Conference Proceedings of the Society for Experimental Mechanics Series

Tom Proulx *Editor*

Dynamic Behavior of Materials, Volume 1

Proceedings of the 2010 Annual Conference on Experimental and Applied Mechanics

SEM

Springer

Conference Proceedings of the Society for Experimental Mechanics Series

For other titles published in this series, go to
www.springer.com/series/8922

Tom Proulx
Editor

Dynamic Behavior of Materials, Volume 1

Proceedings of the 2010 Annual Conference on Experimental and Applied Mechanics

Springer

Editor
Tom Proulx
Society for Experimental Mechanics, Inc.
7 School Street
Bethel, CT 06801-1405
USA
tom@sem1.com

ISBN 978-1-4419-8227-8 e-ISBN 978-1-4419-8228-5
DOI 10.1007/978-1-4419-8228-5
Springer New York Dordrecht Heidelberg London

Library of Congress Control Number: 2011922268

© The Society for Experimental Mechanics, Inc. 2011
All rights reserved. This work may not be translated or copied in whole or in part without the written permission of the publisher (Springer Science+Business Media, LLC, 233 Spring Street, New York, NY 10013, USA), except for brief excerpts in connection with reviews or scholarly analysis. Use in connection with any form of information storage and retrieval, electronic adaptation, computer software, or by similar or dissimilar methodology now known or hereafter developed is forbidden.
The use in this publication of trade names, trademarks, service marks, and similar terms, even if they are not identified as such, is not to be taken as an expression of opinion as to whether or not they are subject to proprietary rights.

Printed on acid-free paper

Springer is part of Springer Science+Business Media (www.springer.com)

Preface

Dynamic Behavior of Materials represents one of six tracks of technical papers presented at the Society for Experimental Mechanics Annual Conference & Exposition on Experimental and Applied Mechanics, held at Indianapolis, Indiana, June 7-10, 2010. The full proceedings also includes volumes on Application of Imaging Techniques, the Role of Experimental Mechanics on Emerging Energy Systems and Materials, Experimental and Applied Mechanics, the 11th International Symposium on MEMS and Nanotechnology, and the Symposium on Time Dependent Constitutive Behavior and Failure/Fracture Processes.

Each collection presents early findings from experimental and computational investigations on an important area within Experimental Mechanics. The current volume on Dynamic Behavior of Materials includes studies on:

Composite Materials, Dynamic Failure and Fracture, Dynamic Materials Response, Novel Testing Techniques, Low Impedance Materials, Metallic Materials, Response of Brittle Materials, Time Dependent Materials, High Strain Rate Testing of Biological and Soft Materials, Shock and High Pressure Response, Energetic Materials, Optical Techniques for Imaging High Strain Rate Material Response, and Modeling of Dynamic Response.

Dynamic behavior of materials represents an ever expanding area of broad interest to the SEM community, as evidenced by the increased number of papers and attendance in recent years. This track was initiated in 2005 and reflects our efforts to bring together researchers interested in the dynamic response and behavior of materials, and provide a forum to facilitate technical interaction and exchange. The sessions within this track are organized to cover the wide range of experimental research being conducted in this area by scientists from around the world. A modeling session is also included in the 2010 program.

The contributed papers span numerous technical divisions within SEM. It is our hope that these topics will be of interest to the dynamic behavior of materials community as well as the traditional mechanics and materials community.

The organizers thank the authors, presenters, organizers, and session chairs for their participation in this track. We are grateful to the TD chairs who co-sponsored and organized sessions in this track (e.g., Composite Materials, Optical Techniques for Imaging High Strain Rate Events). We also acknowledge the SEM support staff for their devoted efforts in accommodating the large number of submissions this year.

The Society would also like to thank the organizers of the track, Kathryn A. Dannemann, *Southwest Research Institute*; Vijay Chalivendra, *University of Massachusetts, Dartmouth*; and Bo Song, *Sandia National Laboratories* for their efforts.

Bethel, Connecticut

Dr. Thomas Proulx
Society for Experimental Mechanics, Inc

Contents

1 **Dynamic Material Property Characterization With Kolsky Bars** 1
W.W. Chen

2 **Dynamic Triaxial Test on Sand** 7
Md. E. Kabir, W.W. Chen

3 **Mechanically Similar Gel Simulants for Brain Tissues** 9
F. Pervin, W.W. Chen

4 **Loading Rate Effect on Tensile Failure Behavior of Gelatins Under Mode I** 15
P. Moy, M. Foster, C.A. Gunnarsson, T. Weerasooriya

5 **On Failure and Dynamic Performance of Materials** 25
N.K. Bourne

6 **In-situ Optical Investigations of Hypervelocity Impact Induced Dynamic Fracture** 31
L.E. Lamberson, A.J. Rosakis, V. Eliasson

7 **A Dynamic CCNBD Method for Measuring Dynamic Fracture Parameters** 39
F. Dai, R. Chen, K. Xia

8 **New "Fish Tank" Approach to Evaluate Durability and Dynamic Failure of Marine Composites** 49
A. Krishnan, L.R. Xu

9 **Large Field Photogrammetry Techniques in Aircraft and Spacecraft Impact Testing** 55
J.D. Littell

10 **Properties of Elastomer-based Particulate Composites** 69
A.V. Amirkhizi, J. Qiao, K. Schaaf, S. Nemat-Nasser

11 **Dynamic-tensile-extrusion Response of Polytetrafluoroethylene (PTFE) and Polychlorotrifluoroethylene (PCTFE)** 73
C.P. Trujillo, E.N. Brown, G.T. Gray, III

12 **Dynamic Compression of an Interpenetrating Phase Composite (IPC) Foam: Measurements and Finite Element Modeling** 77
C. Periasamy, H.V. Tippur

13 **Improved Mechanical Properties of Nano-nickel Strengthened Open Cell Metal Foams** 83
A. Jung, H. Natter, R. Hempelmann, S. Diebels, E. Lach

14 **A Numerical and Experimental Study of High Strain-rate Compression and Tension Response of Concrete** 89
A. Samiee, J. Isaacs, S. Nemat-Nasser

15 **Impact Behavior and Dynamic Failure of PMMA and PC Plates** 93
W. Zhang, S.A. Tekalur, L. Huynh

16 **Experimental Investigation on Dynamic Crack Propagation Through Interface in Glass** 105
H. Park, W. Chen

17 **Effect of Temperature and Crack Tip Velocity on the Crack Growth in Functionally Graded Materials** 113
A. Kidane, V.B. Chalivendra, A. Shukla

18 **Characterization of Polymeric Foams Under Muli-axial Static and Dynamic Loading** 121
I.M. Daniel, J.-M. Cho

19 **Effects of Fiber Gripping Methods on Single Fiber Tensile Test Using Kolsky Bar** 131
J.H. Kim, R.L. Rhorer, H. Kobayashi, W.G. McDonough, G.A. Holmes

20 **Mechanical Behavior of A265 Single Fibers** 137
J. Lim, J.Q. Zheng, K. Masters, W.W. Chen

21 **Experimental Study of Dynamic Behavior of Kevlar 49 Single Yarn** 147
D. Zhu, B. Mobasher, S.D. Rajan

22 **Dynamic Response of Fiber Bundle Under Transverse Impact** 153
B. Song, W.-Y. Lu

23 **Impact Experiments to Validate Material Models for Kevlar KM2 Composite Laminates** 155
T. Weerasooriya, C.A. Gunnarsson, P. Moy

24 **Numerical Study of Composite Panels Subjected to Underwater Blasts** 169
R. Bellur-Ramaswamy, F. Latourte, W.W. Chen, H.D. Espinosa

25 **Non-shock Initiation Model for Explosive Families-Experimental Results** 171
M.U. Anderson, S.N. Todd, T.L. Caipen, C.B. Jensen, C.G. Hugh

26 **Modeling for Non-shock Initiation** 179
S.N. Todd, M.U. Anderson, T.L. Caipen

27 **Stress and Strain Analysis of Metal Plates With Holes** 187
B. Hu, S. Yoshida, J.A. Gaffney

28 **Impact Response of PC/PMMA Composites** 195
C.A. Gunnarsson, T. Weerasooriya, P. Moy

29 **Performance of Polymer-steel Bi-layers Under Blast** 211
A. Samiee, A.V. Amirkhizi, S. Nemat-Nasser

30 **The Blast Response of Sandwich Composites With a Functionally Graded Core and Polyurea Interlayer** 215
N. Gardner, A. Shukla

31 **The Blast Response of Sandwich Composites With In-plane Pre-loading** 225
E. Wang, A. Shukla

32 **Laboratory Blast Simulator for Composite Materials Characterization** 233
G. Li, D. Liu

33 **Experimental Characterization of Composite Structures Subjected to Underwater Impulsive Loadings** 239
F. Latourte, D. Grégoire, H.D. Espinosa

34 **Controlling Wave Propagation in Solids Using Spatially Variable Elastic Anisotropy** 241
A. Tehranian, A. Amirkhizi, S. Nemat-Nasser

35 **Constitutive Characterization of Multi-constituent Particulate Composite** 245
J.L. Jordan, J.E. Spowart, D.W. Richards

36 **Dynamic Strain Rate Response With Changing Temperatures for Wax-coated Granular Composites** 253
J.W. Bridge, M.L. Peterson, C.W. McIlwraith

37 **Strain Solitary Waves in Polymeric Nanocomposites** 261
I.V. Semenova, G.V. Dreiden, A.M. Samsonov

38 **Measurement of High-strain-rate Strength of a Metal-matrix Composite Conductor** 269
P.J. Joyce, L.P. Brown, D. Landen, S. Satapathy

39 **A Revisit to High-rate Mode-II Fracture Characterization of Composites With Kolsky Bar Techniques** 277
W.-Y. Lu, B. Song, H. Jin

40 **The Influences of Residual Stress in Epoxy Carbon-fiber Composite Under High Strain-rate** 281
H.-C. Lee, S.-H. Wang, C.-C. Chiang, L. Tsai

41 **Strain Rate-dependent and Temperature- dependent Compressive Properties of 2DCf/SiC Composite** 287
Y. Wang, S. Li, J. Liu

42 **Compression Behavior of Near-UFG AZ31 Mg-Alloy at High Strain Rates** 295
M. Hokka, J. Seidt, T. Matrka, A. Gilat, V.-T. Kuokkala, J. Nykänen, S. Müller

43 **Dynamic Torsion Properties of Ultrafine Grained Aluminum** 303
M. Hokka, J. Kokkonen, J. Seidt, T. Matrka, A. Gilat, V.-T. Kuokkala

44 **Effect of Aging Treatment on Dynamic Behavior of Mg-Gd-Y Alloy** 311
L. Wang, Q.-Y. Qin, C.-W. Tan, F. Zhang, S.-K. Li

45 **Plasticity Under Pressure Using a Windowed Pressure-shear Impact Experiment** 319
J.N. Florando, T. Jiao, S.E. Grunschel, R.J. Clifton, D.H. Lassila, L. Ferranti,
R.C. Becker, R.W. Minich, G. Bazan

46 **The Effect of Tungsten Additions on the Shock Response of Tantalum** 321
J.C.F. Millett, M. Cotton, S.M. Stirk, N.K. Bourne, N.J. Park

47 **Stress Perturbations Caused by Longitudinal Stress Gauges** 327
R.E. Winter, P.T. Keightley

48 **Measuring Strength at Ultrahigh Strain Rates** 329
T.J. Vogler

49 **Shear Stress Measurements in Stainless Steel 2169 Under 1D Shock Loading** 333
G. Whiteman, J.C.F. Millett

50 **Spall Strength of AS800 Silicon Nitride Under Combined Compression and Shear Impact Loading** 339
V. Prakash, D. Nathenson, F. Yuan

51 **Spallation of 1100-O Aluminum Under Plate Impact Loading** 349
C. Williams, D. Dandekar, K.T. Ramesh

52 **Line VISAR and Post-shot Metallography Comparisons for Spall Analysis** 351
M.D. Furnish, G.T. Gray, III, J.F. Bingert

53 **Failure of Firefighter Escape Rope Under Dynamic Loading and Elevated Temperatures** 353
G.P. Horn, P. Kurath

54 **Determination of True Stress-true Strain Curves of Auto-body Plastics** 361
C.H. Park, J.S. Kim, H. Huh, C.N. Ahn

55 **Elasto-viscoplasticity Behavior of a Structural Adhesive Under Compression Loadings** 369
D. Morin, G. Haugou, F. Lauro, B. Bennani

56 **Dynamic Behaviors of Fiber Reinforced Aerogel and Mg/Aerogel Composite** 379
S. Li, J. Liu, J. Yang, Y. Wang, L. Yan

57 **Mechanisms of Slip Weakening and Healing in Glass at Co-seismic Slip Rates** 387
V. Prakash, F. Yuan, N. Parikh

58 **Rate Dependent Response and Failure of a Ductile Epoxy and Carbon Fiber Reinforced Epoxy Composite** 401
E.N. Brown, P.J. Rae, D.M. Dattelbaum, D. Stahl

59 **High Pressure Hugoniot Measurements Using Converging Shocks** 403
J.L. Brown, G. Ravichandran

60 **Photonic Doppler Velocimetry Measurements of Materials Under Dynamic Compression** 411
T. Ao, D.H. Dolan

61 **Dynamic Equibiaxial Flexural Strength of Borosilicate Glass at High Temperatures** 413
T. Ao, D.H. Dolan

62 **Measurement of Stresses and Strains in High Rate Triaxial Experiments** 415
Md. E. Kabir, W.W. Chen, V.-T. Kuokkala

63 **A New Technique for Combined Dynamic Compression-shear Test** 417
P.D. Zhao, F.Y. Lu, R. Chen, G.L. Sun, Y.L.

64 **A New Compression Intermediate Strain-Rate Testing Apparatus** 425
A. Gilat, T.A. Matrka

65 **A Modified Kolsky Bar System for Testing Ultra-soft Materials Under Intermediate Strain-Rates** 431
R. Chen, S. Huang, K. Xia

66 **Visualization and Measurements of Wave Propagations in Slurry Hammers** 439
K. Inaba, H. Takahashi, N. Kollika, K. Kishimoto

67 A Newly Developed Kolsky Tension Bar 447
B. Song, B.R. Antoun, K. Connelly, J. Korellis, W.-Y. Lu

68 Evaluation of Welded Tensile Specimens in the Hopkinson Bar 449
K.A. Dannemann, S. Chocron, A.E. Nicholls

69 Effect of Aspect Ratio of Cylindrical Pulse Shapers on Force Equilibrium in Hopkinson Pressure Bar Experiments 453
S. Abotula, V.B. Chalivendra

70 Interferometric Measurement Techniques for Small Diameter Kolsky Bars 463
D.T. Casem, S.E. Grunschel, B.E. Schuster

71 A Kolsky Bar With a Hollow Incident Tube 471
O.J. Guzman, D.J. Frew, W.W. Chen

Proceedings of the SEM Annual Conference
June 7-10, 2010 Indianapolis, Indiana USA
©2010 Society for Experimental Mechanics Inc.

Dynamic Material Property Characterization with Kolsky Bars

Weinong W. Chen

Schools of Aeronautics/Astronautics, and Materials Engineering, Purdue University
701 West Stadium Avenue, West Lafayette, IN 47907-2045, USA
Phone: 1-765-494-1788, Email: wchen@purdue.edu

ABSTRACT

Split Hopkinson pressure bars (SHPB), also called Kolsky bars, have been widely used to determine the stress-strain response of materials in the strain-rate range 10^2 – 10^4/s. Unlike quasi-static testing methods for material properties, the high-rate Kolsky bar technique does not have a closed-loop control system to monitor and adjust testing conditions on the specimen to specified levels. There are no standards to guide the experimental design either. This presentation briefly reviews the physical nature of Kolsky bar experiments and recent modifications in the attempt to conduct experiments for more accurate results. The main approach for obtaining improved results is to deform the specimen uniformly under an equilibrated stress state at a constant strain rate. Examples of experiment design to achieve the desired testing conditions are presented.

KOLSKY BARS (SHPB)

Most material properties such as yield stress and ultimate strength are obtained under quasi-static loading conditions using common testing load frames with the guidance of standardized testing procedures. To ensure product quality and reliability under impact conditions such as those encountered in the drop of personal electronic devices, vehicle collision, and sports impact, the mechanical responses of materials under such loading conditions must be characterized accurately. To obtain dynamic response of materials under laboratory controlled conditions, Kolsky [1] placed two elastic rods on both sides of the specimen and then stuck one of the rods with an explosive blast. This concept is schematically shown in Fig. 1, where the elastic rod between the external impact and the specimen is called the incident bar and that rod on the other side the transmission bar. With this arrangement, when the incident bar is loaded by external impact, a compressive stress wave is generated and then propagates towards the specimen, moving the bar material towards the specimen as it sweeps by. When the wave arrives at the interface between the incident bar and the specimen, part of the wave is reflected back into the incident bar and the rest transmits through the specimen into the transmission bar. Laboratory instrumentation can record the stress waves in the incident bar propagating towards the specimen and being reflected back from the specimen and the wave in the transmission bar. Under this arrangement the impact event is controllable and quantitative. Analysis on the recorded waves results in information regarding the loading conditions and deformation states in the specimen. This system has been called the Kolsky bar or a split-Hopkinson pressure bar (SHPB).

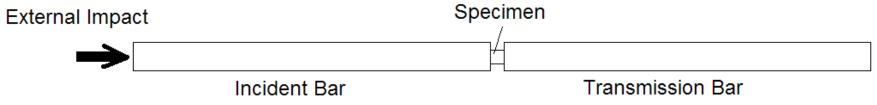

Figure 1: A schematic of a Kolsky bar

T. Proulx (ed.), *Dynamic Behavior of Materials, Volume 1*, Conference Proceedings of the Society for Experimental Mechanics Series,
DOI 10.1007/978-1-4419-8228-5_1, © The Society for Experimental Mechanics, Inc. 2011

Based on the principle, the Kolsky bar was modified continuously by many researchers for various applications. Lindhom’s design in 1964 [2] became a popular template for Kolsky bar setups and is still widely used today. Besides the original compression version of the Kolsky bar, there are also tension, torsion, and the combination versions that share the same principle. There have been a number of excellent review articles documenting the working principle of Kolsky bar. This paper focuses on the testing conditions on the specimen and the experimental methods to achieve the desired conditions.

The Kolsky bar has two distinct features that are different from a conventional material testing machine. One is that the loading-axis stiffness is low due to the small-diameter bars, in contrast to the typical massive stiffness in hydraulic or screw-driven testing machines. The other difference is that the Kolsky bar does not have a closed-loop feed-back control system for real-time monitoring and adjustment of the loading conditions on the specimen. The low stiffness means that the specimen response cannot be ignored in experiment design. For example, loaded by identical loading pulses, the deformation of an aluminum specimen is drastically different from that of a ceramic specimen. Without a feed-back control system, the Kolsky bar experiments can only be conducted in an open-loop manner to approach desired testing conditions. These features make it more challenging to design Kolsky bar experiments. In order to achieve desired testing conditions on the specimen, the loading conditions in Kolsky bar experiments must be determined according to the specimen’s response that is initially unknown.

SHAPE THE INCIDENT PULSE

In a Kolsky bar experient, to control the impact conditions such that the specimen undergoes desired state of loading and deformation, the control over the incident pulse profiles in an open-loop manner is the most commonly used approach. Pulse shaping is used to facilitate stress equilibrium and constant strain rate deformation in the specimen through adjusting the profile of the incident pulse based on specimen response. Pulse shaping technique has been developed over the past three decades. Duffy et al. [3] were probably the first authors to use pulse shapers to smooth pulses generated by explosive loading for a torsional Kolsky bar. Christensen et al. [4] might be the first authors to employ a pulse shaping technique in the compression version of Kolsky bar. Ellwood et al. [5] generated incident pulses similar to the transmitted signals (specimen responses) but at higher amplitude, subjecting the specimen to a nearly constant strain rate deformation. Nemat-Nasser et al. [6] might be the first authors to analytically model the pulse-shaping process. Frew et al. [7] presented a more extensive analysis that includes the use of compound pulse shapers. Figure 2 shows such a compound pulse shaper. Upon impact by the striker, the momentum in the striker has to enter the incident bar through the momentum passage controlled by the pulse shaper. The way the pulse shaper deforms depicts the profile of the incident pulse, which is the subject of the quantitative analysis performed by Frew et al. [7]. In the following sections, three examples of Kolsky bar experiments are illustrated with their incident pulses controlled.

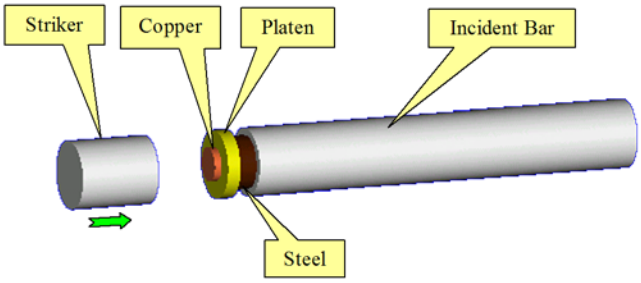

Figure 2: A compound pulse shaper

COMPRESSION EXPERIMENTS ON A MILD STEEL

Figure 3(a) shows incident, reflected, and transmitted signals recorded from a typical experiment on the 1046 steel [8]. With pulse shaping, the incident pulse was modified to produce a reflected signal with a nearly flat top that indicates a constant strain rate history in the specimen. Furthermore, there is a small amplitude precursor ahead of the main reflected signal. Detailed data reduction reveals that this corresponds to the elastic deformation, whereas the main reflected signal corresponds to the dynamic plastic flow in the specimen. During the elastic deformation, the specimen is stiff and deforms at a much lower strain rate. The details of this initial plateau in the reflected signal corresponding to the elastic deformation in the specimen are shown in Fig. 3(b) [8]. When the stress exceeds the dynamic yield strength, the stiffness of the specimen decreases significantly due to plastic flow, and this causes a much higher strain rate in the specimen. Figure 4 shows the dynamic compressive stress-strain curves from the experiments with and without pulse shaping at a close strain rate. The comparison shows that the difference in the elastic responses is significant. The two curves start to merge after about 4% of strain.

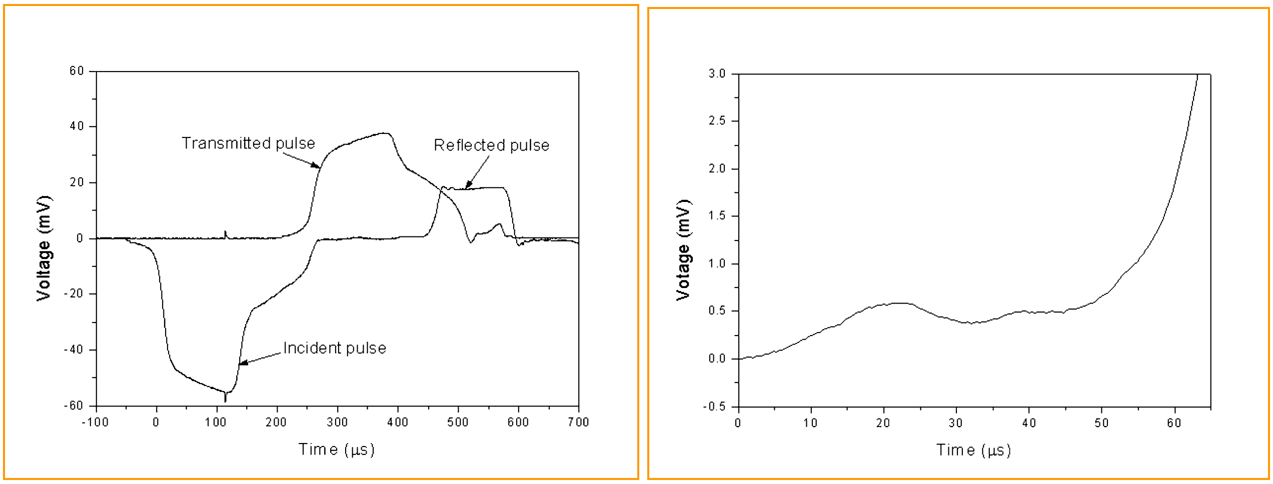

(a) (b)

Figure 3: Records in a Kolsky bar experiment on 1046 steel (a) and the beginning of reflected pulse (b)

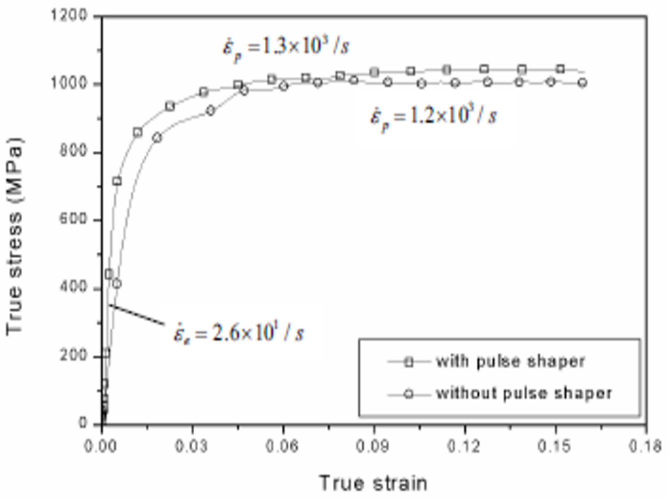

Figure 4: Dynamic stress-strain curves of 1046 steel obtained with and without pulse shaping

EXPERIMENTS ON SHAPE MEMORY ALLOYS

The loading and unloading responses of a shape memory alloy are different. Instead of a conventional stress-strain curve for most metals, a stress-strain loop that includes both loading and unloading portions must be characterized at a common constant strain rate. In this example, we present the design of a set of such experiments where both the loading and unloading portions of the loading pulses are controlled by pulse shaping [9]. In addition to the pulse shaping for the loading portion of the incident pulse, a reverse pulse-shaping technique was used to generate an unloading profile at deforms the specimen at the same constant strain rate as the loading strain rate under dynamic stress equilibrium. Using this technique, the dynamic stress-strain loop at a strain rate of 420 s^{-1} for a NiTi shape memory alloy was determined [9]. The shape memory alloy studied in these experiments is composed of nominal 55.8% nickel by weight and the balance is titanium. The NiTi shape memory alloy has a specified density of 6.5 g/cm^3, an austenite finish transition temperature A_f of 5-18˚C, and a melting point of 1310˚C. The cylindrical specimens had a dimension of 4.76-mm diameter by 4.76-mm long. Figure 5 shows the incident, reflected, and transmitted pulses at the strain rate of 420 s^{-1} obtained with the modified Kolsky bar during both loading and unloading phases [9]. The strain-rate history, which is proportional to the reflected pulse in Fig. 5, indicates that both the loading strain rate and the unloading strain rate were maintained at the same constant value (420 s^{-1}) for most of the experiment duration. The strain-rate signal flipped its sign from compression (loading) to tension (unloading) at the peak of the loading. The resultant dynamic stress-strain loop at the strain rate of 420 s^{-1}, together with its quasi-static counterparts, is shown in Fig. 6.

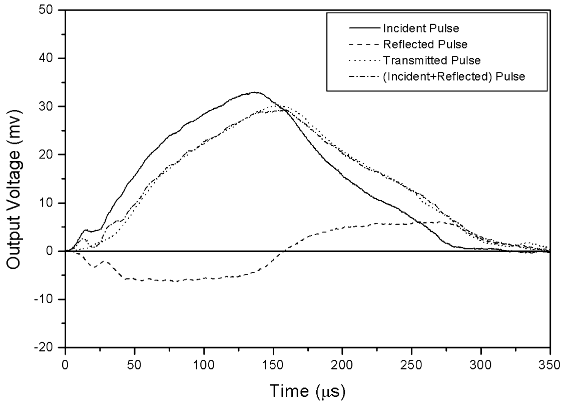

Figure 5: A test on a shape memory alloy

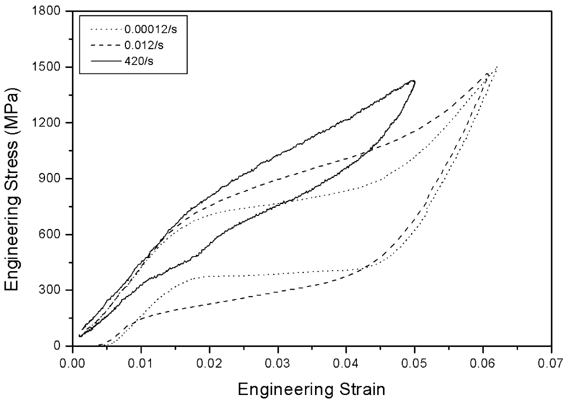

Figure 6: Stress-strain loops of the SMA

LOADING-RELOADING EXPERIMENTS ON A CERAMIC

In impact applications, the dynamic compressive response of dynamically damaged ceramics is desired. We present the design of a set of experiments where an alumina ceramic is dynamically loaded by two consecutive stress pulses [10]. The first pulse determines the dynamic response of the intact ceramic material while crushing the specimen and the second pulse determines the dynamic compressive constitutive behavior of the crushed ceramic rubble. In order to produce two consecutive stress pulses, a striker train of two elastic rods separated by pulse shapers is employed to replace the single striker bar in a conventional Kolsky bar setup. A schematic illustration of the modified Kolsky bar used in this ceramic study is shown in Fig. 7 [10], where two strikers are seen inside the barrel of the gas gun of a Kolsky bar setup. The first striker is a maraging steel rod (ϕ19 mm × 152 mm), which creates the first stress pulse to crush the intact ceramic specimen. The second striker is either an aluminum bar or a steel bar with the dimension of ϕ19 mm × 203 mm to compress the crushed ceramic rubble at a different strain rate. As is the case when testing any brittle material in a Kolsky device, pulse shaping is needed to ensure the specimen deforms at nearly a constant strain rate under dynamic stress equilibrium during both dynamic loadings. Pulse shaping also controls the amplitudes of the loading pulses, the values of strain rates, the maximum strains in the rubble specimens, and the proper separation time between the two loading pulses.

A typical set of the incident, reflected, and transmitted pulses obtained from such a pulse shaping experiment are shown in the Fig. 8. The first pulse has a triangular shape with a loading time of ~80 μs. The rise-side of this triangle is a linear ramp which is necessary to achieve a constant strain rate on the intact ceramic specimen possessing a linearly elastic brittle response. Approximately 30 μs after the first pulse is completed; the second pulse produced by the second striker in association with the tube pulse shaper arrives. Due to the first ramp pulse, the first reflected signal maintains at a constant level for ~80 μs starting from the instant of 620 μs. This nearly flat reflected signal over the entire first loading period indicates that a nearly constant strain-rate has been achieved in the intact specimen. The amplitude of the first reflected signal then increases drastically, indicating that the damaged specimen has a reduced resistance to the motion of the incident bar end. The second reflected signal also exhibits a nearly flat portion, indicating a constant strain rate in the rubble specimen. the transmitted signal also contains two pulses corresponding to the two loading periods. The first portion shows a typical brittle specimen response, where the load increases nearly linearly until a sudden drop due to the crushing of the specimen. The load does not immediately drop to zero because the specimen is crushed but not shattered due to the confining metal sleeve. The second portion of the transmitted signal shows a flow-like behavior of the pulverized specimen.

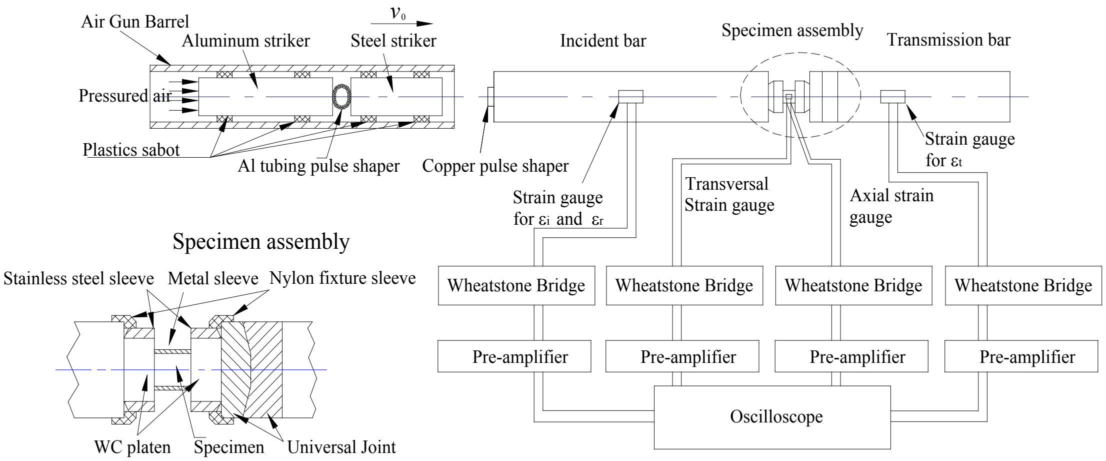
Air Gun Barrel
Aluminum striker
v_0
Steel striker
Incident bar
Specimen assembly
Transmission bar
Pressured air
Plastics sabot
Al tubing pulse shaper
Copper pulse shaper
Strain gauge for ε_i and ε_r
Transversal Strain gauge
Axial strain gauge
Strain gauge for ε_t
Specimen assembly
Stainless steel sleeve
Metal sleeve
Nylon fixture sleeve
WC platen
Specimen
Universal Joint
Wheatstone Bridge
Wheatstone Bridge
Wheatstone Bridge
Wheatstone Bridge
Pre-amplifier
Pre-amplifier
Pre-amplifier
Pre-amplifier
Oscilloscope

Figure 7: Kolsky bar set-up for loading and reloading experiments

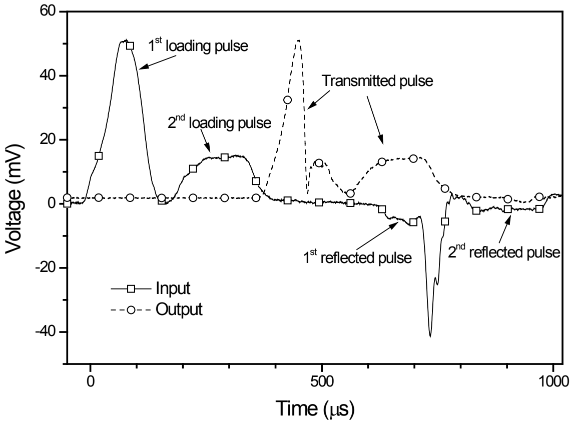

Figure 8: Record from a loading/reloading experiment

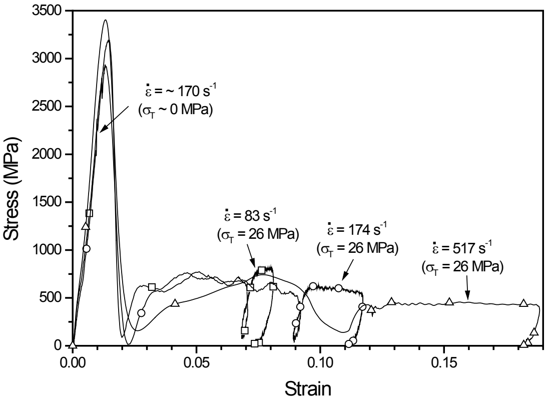

Figure9: Stress-strain curves

Three resultant dynamic compressive stress-strain curves of AD995 ceramic are shown in Fig. 9. The strain rates are commonly ~170 s^{-1} for the intact alumina and 83, 174, and 517 s^{-1} for the damaged specimen from three experiments. The variation in the strain rates in the crushed specimens is achieved by changing the second striker material (aluminum or steel) and the second pulse shaper. As shown in Fig. 9, the ceramic specimen initially behaves as a typical brittle material exhibiting a linear stress-strain response with peak stresses in the range of 2.8-3.4 GPa. As the sample is being crushed, the lateral confinement from the thin metal sleeve causes an axial stress increasing from nearly zero at the beginning of crush to 500-700 MPa near the unloading of the first pulse. The incident pulse was controlled such that unloading started shortly after the peak load when the specimen was crushed to a desired level. It should be noted that the results from this crushing phase of the experiment may not be reliable since the specimen was not in dynamic stress equilibrium during this phase. The second pulse came after the end of the unloading from the first stress pulse. During the dynamic compression from the second pulse, the sample stress ascends to a "flow" stress of about 500-700 MPa. This portion of stress-strain curve in each of the three experiments represents the dynamic compressive response of the crushed ceramic specimen to impact loading.

In the conference presentation, additional examples will be illustrated.

REFERENCES

[1] Kolsky, H., “An Investigation of the Mechanical Properties of Materials at Very High Rates of Loading,” Proc. Royal Soc. Lond., B, **62**, 676-700, (1949).

[2] Lindholm, U.S. and Yeakley, L.M., “High Strain Rate Testing: Tension and Compression,” Experimental Mechanics, **8**, 1-9 (1968).

[3] Duffy, J., Campbell, J. D., and Hawley, R. H., “On the Use of a Torsional Split Hopkinson Bar to Study Rate Effects in 1100-0 Aluminum,” ASME J. Appl. Mech., **37**, 83-91, (1971).

[4] Christensen, R. J., Swanson, S. R., and Brown, W. S., ”Split-Hopkinson-Bar Tests on Rock Under Confining Pressure,” EXPERIMENTAL MECHANICS, **29**, 508-513, (1972).

[5] Ellwood, S., Griffiths, L. J., and Parry, D. J., “Materials Testing at High Constant Strain Rates,” J. Phys. E: Sci. Instrum., 15, 280-282 (1982).

[6] Nemat-Nasser, S., Isaacs, J. B. and Starrett, J. E., “Hopkinson Techniques for Dynamic Recovery Experiments,” Proc. R. Soc. Lond., A, **435**, 371-391 (1991).

[7] Frew, D. J., Forrestal, M. J., and Chen, W., “Pulse Shaping Techniques for Testing High-Strength Steel with a Split Hopkinson Pressure Bar,” Experimental Mechanics, **45**, 186-195 (2005).

[8] Chen, W., Song, B., Frew, D. J., and Forrestal, M. J., “Dynamic Small Strain Measurement with a Split Hopkinson Pressure Bar,” Experimental Mechanics, **43**, 20-23 (2003).

[9] Chen, W. and Song, B., “Temperature Dependence of a NiTi Shape Memory Alloy’s Superelastic Behavior at a High Strain Rate,” Journal of Mechanics of Materials and Structures, **1**, 339-356 (2006).

[10] Chen, W. and Luo, H., “Dynamic Compressive Responses of Intact and Damaged Ceramics from a Single Split Hopkinson Pressure Bar Experiment,” Experimental Mechanics, **44**, 295-299 (2004).

Proceedings of the SEM Annual Conference
June 7-10, 2010 Indianapolis, Indiana USA
©2010 Society for Experimental Mechanics Inc.

Dynamic Triaxial Test on Sand

Md. E. Kabir
Schools of Aeronautics and Astronautics, Purdue University
701 West Stadium Avenue, West Lafayette, IN 47907-2045, USA
Phone: 1-765-494-7419, Email: mkabir@purdue.edu

Weinong W. Chen
Schools of Aeronautics/Astronautics, and Materials Engineering, Purdue University
701 West Stadium Avenue, West Lafayette, IN 47907-2045, USA

ABSTRACT

Triaxial experiments are a common method for measuring shear strength. Usually the loading in the shear phase in these experiments are done at a quasi-static rate but in many real instances the loading is dynamic in nature. Therefore, a triaxial setup has been developed based on a Kolsky bar experimental technique to characterize the shear response of the material at high rates. Using this setup, a systematic investigation of the undrained behavior of sand at high pressures has been performed to study the rate effects on the stress-strain behavior. The dynamic experiment results show that the stress-strain response of the sand specimens is only sensitive to pressure levels while it is insensitive to loading rates.

INTRODUCTION

Historically, triaxial experiments involve low and/or intermediate rate of loadings. But in many cases, the stress environments of the soil are dynamic in nature. Therefore, it is necessary to perform high rate triaxial experiments on sand to quantify the sand response at these stress environments. To explore the high rate response, Kolsky bar has been modified in the past where the radial confinement to sand was applied using rigid jackets around the sand specimen [1-2]. However, the rigid jacket does not provide a controllable confining pressure throughout the experiment. Other group of researchers [3, 4] has used a combination of confined fluid media and servo-hydraulic load frames in modified Kolsky bar apparatuses to obtain a hydrostatic state of stress in a test sample. A dynamic triaxial experimental setup has been recently developed based on Christensen work [5]. In this setup, two pressure chambers are integrated with a Kolsky bar to apply a triaxial stress state. The isotropic pressure loading on the specimen is still applied quasi-statically; however, the specimen experiences a stress-wave loading from the Kolsky bar in the shear phase of the experiment. In the following sections, the experimental setup, specimen preparation, and measurement techniques for high-rate triaxial experiments on dry sand have been described.

EXPERIMENT

Two hydraulic pressure cells are incorporated with the Kolsky bar. One cell is located at the end of the transmission bar and other one is surrounding the specimen. In the hydrostatic phase of the experiment the pressure cell at the end of the transmission bar applies the axial load on the specimen, while the pressure cell surrounding the specimen applies the radial load. Quikrete #1961® fine grain sand has been used as sample materials. All specimens have a diameter of 19 mm and length of 9.3 mm. The small specimen length is required to ensure stress equilibrium within the specimen. All specimens are confined by a polyolefin heat shrink tube. A heat gun is used to shrink the tube to the desired diameter. Two steel discs are used to hold the sand. The specimen thickness was checked through verification of alignments between the edges of the tube and the marked lines on the transmission bar. The measurement techniques for load and deformation have been described elsewhere [6]

T. Proulx (ed.), *Dynamic Behavior of Materials, Volume 1*, Conference Proceedings of the Society for Experimental Mechanics Series,
DOI 10.1007/978-1-4419-8228-5_2, © The Society for Experimental Mechanics, Inc. 2011

RESULTS

The stress-strain response of the specimen is plotted in Figure 1 at strain-rates of 1000 and 500 s^{-1}, respectively. The stress-strain response indicates that, this material is pressure dependent.

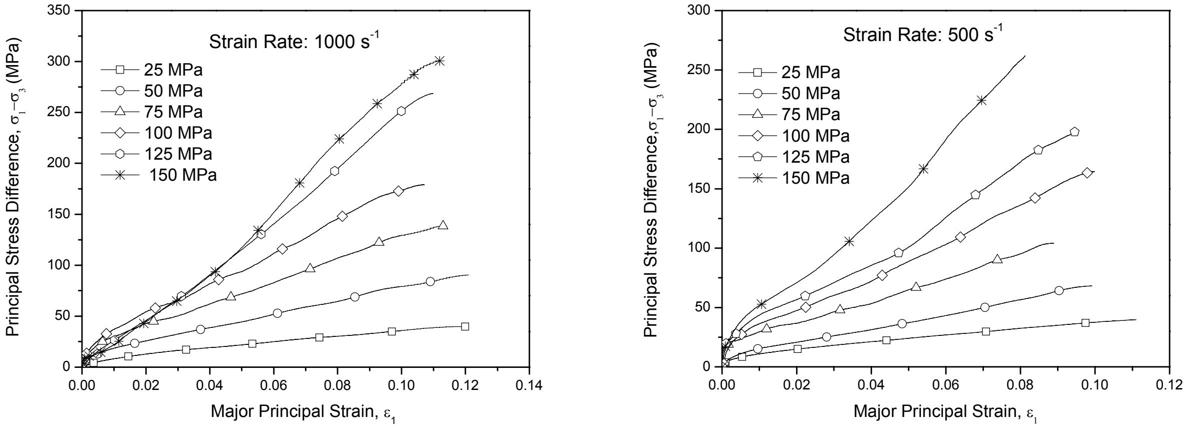

(A) (B)

Fig. 1: Stress-strain response for high rate triaxial experiments at strain-rate of (A) 1000 s^{-1} strain-rate (B) 500 s^{-1}

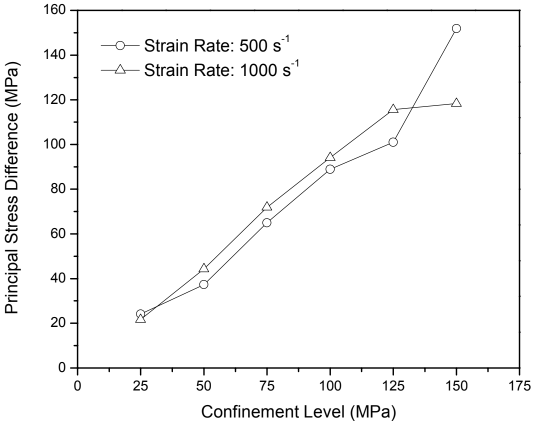

Fig. 2: Principle stress difference at 5% axial strain as a function of confining pressure

To compare the strain rate effects, principal stress difference at 5% axial strain is plotted for different confinement levels in Figure 2. This clearly indicates that there in no significant strain-rate effect for the shear property of sand at these strain rate levels.

CONCLUSION

The results show that the stress-strain response of the sand specimens is only sensitive to pressure levels while it is insensitive to high loading rates.

ACKNOWLEDGEMENT

This research is sponsored by the Sandia National Laboratories, which is operated by Sandia Corporation, a Lockheed Martin Company, for the United States Department of Energy under Contract DE-AC04-94AL85000.

REFERENCE

1. Bragov, A.M., Grushevsky, G.M., Lomunov, A.K., Use of the Kolsky Method for Confined Tests of Soft Soils. Exp. Mech. 36(3), 237-242, 1996.
2. Charlie, W. A., Ross, C.A., Pierce, S.J., Split-Hopkinson Pressure Bar Testing of Unsaturated Sand. Geotechnical Testing Journal GTJODJ 13(4), 291-300, 1990.
3. Christensen, R. J., Swanson, S. R., and Brown, W. S., Split-Hopkinson-Bar Tests on Rock under Confining Pressure, Exper. Mech., 29, 508-513, 1972.
4. Lindholm, U. S., Yeakley, L. M., and Nagy, A., The Dynamic Strength and Fracture Properties of Dresser Basalt, Int. J. Rock Mech. Min. Sci. & Geomech. Abstr., 11, 181-191, 1970.
5. Frew, D. J., Akers, S. A., Chen, W.W., and Green, M.L., Development of a Dynamic Tri-axial Kolsky Bar, Submitted to Experimental Mechanics, 2009.
6. Kabir, M. E. and Chen, W. W., Measurement of Stresses and Strains on the High Strain Rate Triaxial Test, Review of Scientific Instruments 80 (12), doi:10.1063/1.3271538, 2009.

Proceedings of the SEM Annual Conference
June 7-10, 2010 Indianapolis, Indiana USA
©2010 Society for Experimental Mechanics Inc.

Mechanically Similar Gel Simulants for Brain Tissues

Farhana Pervin

Schools of Aeronautics and Astronautics, Purdue University
B173 Neil Armstrong Hall of Engineering
701 West Stadium Avenue, West Lafayette, IN 47907-2045
Phone: 1-765-494-7419, Email: fpervin@purdue.edu

Weinong W. Chen

Schools of Aeronautics/Astronautics, and Materials Engineering, Purdue University
701 West Stadium Avenue, West Lafayette, IN 47907-2045

ABSTRACT

Various gels have been used to evaluate the dynamic response of soft tissues. In dynamic experiments studying the brain response to impact loading, gel materials are used as surrogates in the exploration and calibration stages of the experimental research. Gels are simpler in handling and can be made in large quantities. In such experiments, it is clear that the dynamic mechanical behavior of the gels must be similar to that of the brain tissues they are representing. The objective of this study is to experimentally determine the mechanical properties of artificial gels over a wide range of strain rates, in addition to rheological analysis. The behaviors are then compared to that of the brain tissues under identical loading conditions to find candidate gel materials that respond to dynamic loading in a similar manner as the brain tissues. The gels investigated include Perma gel, collagen gel, and Agarose gel. Each type of the gels has multiple concentration levels. The results show that the mechanical properties of agarose gel with concentration of 0.4-0.6% are close to that of brain tissues.

INTRODUCTION

Different types of gels have been generally used for the cell culture of soft tissues [1]. Gel has unique feature which has drawn attention to the researchers. These gels are chemically and electrically neutral and have good elasticity. They are available easily and easy to fabricate. The mechanical behaviors of gels are important since these gels will be used to model the human head to study the injury mechanism. Agarose is a natural polysaccharide. It has the greatest gelling capacity. The contents of agarose vary depending on the source from which the agar was extracted. This fact is important as it will affect the physicochemical, mechanical, and rheological properties of agar [2]. Traditionally, ballistics gelatins have been used as human tissue simulants in a wide variety of impact and injury studies and provided a natural initial material [3]. The limitations of traditional gelatins include room temperature decomposition, translucence, and single use behavior. Perma-Gel^{TM} ballistics gelatin is characterized as a styrene-ethylene-butylene copolymer. The benefits of the Perma-Gel^{TM} gelatin over traditional gelatins include the superior transparency and lack of decomposition at room temperature. This allows for multiple uses of the gelatin by melting and recasting of the model. In this present study, the dynamic mechanical properties of gel materials at different strain rate have been characterized. Our concentration is on the agar gel.

T. Proulx (ed.), *Dynamic Behavior of Materials, Volume 1*, Conference Proceedings of the Society for Experimental Mechanics Series,
DOI 10.1007/978-1-4419-8228-5_3, © The Society for Experimental Mechanics, Inc. 2011

Dynamic mechanical analysis (DMA) on gel materials can be used to validate dynamic measurement as well as to provide better understanding for the mechanical response of the brain tissues to the dynamic loading in artificial brain tissue studies. DMA is a non-destructive technique to characterize the viscoelastic properties of materials. This instrument deforms a sample in a constant or step fashion or under fixed rate or in a sinusoidal oscillation (stress or strain); and measures the sample response as function of time or temperature. The mechanical response monitored in DMA instrument can be termed as elastic modulus, viscous modulus and the phase angle or phase shift between the deformation and response. The DMA compressive test provides information for low to moderate modulus materials such as foams, gel and elastomer. A DMA compression experiment has advantage to directly measure the frequency-dependency of the materials, and has a better comparability with dynamic material testing experiment. Chen et al [4] performed dynamic mechanical analysis on agarose gel to validate the magnetic resonance elastography measurement. They investigated systematically the effect of sample thickness, shear strain, testing frequency and compressive clamping strain in DMA shear modulus measurements. Their multi-frequency sweep data showed that the shear modulus increased slowly with the frequency.

MANUFACTURING METHOD

Several procedures for the preparation of gel material are available in literature (2). Here, we have fabricated the agarose gel. Gels with agarose (Agarose, BPI 365-100, Fisher Scientific, USA) concentration (weight/volume, w/v) of 0.6%, 0.5%, 0.4%, and 0.3% were prepared by dissolving powdered agarose in distilled water. The solution was sealed and heated for 15 mins at 90-95 ^{0}C and magnetically stirred; and finally cooled down to 35 ^{o}C (gelation temperature) which is then poured into a vertical mold for curing. The mold is kept at room temperature overnight to cure the gel. The sheet was kept in Ziploc bag to maintain humidity. The mold is designed to prepare 3 mm thick sheet. Here, we have discussed the fabrication of agarose gel only.

EXPERIMENTAL METHOD

Dynamic Mechanical Analysis

For the DMA experiment, cylindrical specimen of 16 mm diameter and 3 mm thickness were cut from the 3mm thick sheet with a punch. The samples are taken from the top and bottom part of the sheets to check the density difference of the material. Dynamic mechanical analysis was performed in frequency sweep compression mode at 30 ^{o}C temperature with DMA (Q800-0127, TA instrument) over a frequency range 0.1-100 Hz at constant amplitude of 15 µm with 1% strain. Samples were subjected to 0.01N preloading before testing. Storage modulus and loss modulus were recorded.

Mechanical Analysis (quasi static, low and intermediate strain rates)

Quasi-static, low and intermediate experiments were performed using a hydraulically driven machine (MTS810). The MTS machine was set to the mode of displacement control at five speeds, which correspond to the strain rate 0.01/s, 0.1/s, 1/s, 10/s and 100 /s. 25 lb load cell (1500 Standard low capacity, Interface, Arizona) was used for quasi-static and 50lb low impedance piezoelectric load cell (9712A50, Kistler Inc. Corp, NY, USA) was used for intermediate strain rates. Samples with OD 10 mm and ID 5 mm and thickness of 1.7 mm were taken from the sheet.

RESULTS AND DISCUSSION

Figure 1-3 show the experimental results obtained from uniaxial compression tests conducted at quasi-static and intermediate strain rates. At each strain-rate, five repeated experiments were performed under identical testing conditions. These results reveal that the each gel material exhibits non-linear stress-strain behavior. The gel’s responses stiffen up with increasing loading rates, suggesting the rate dependency of the gels.

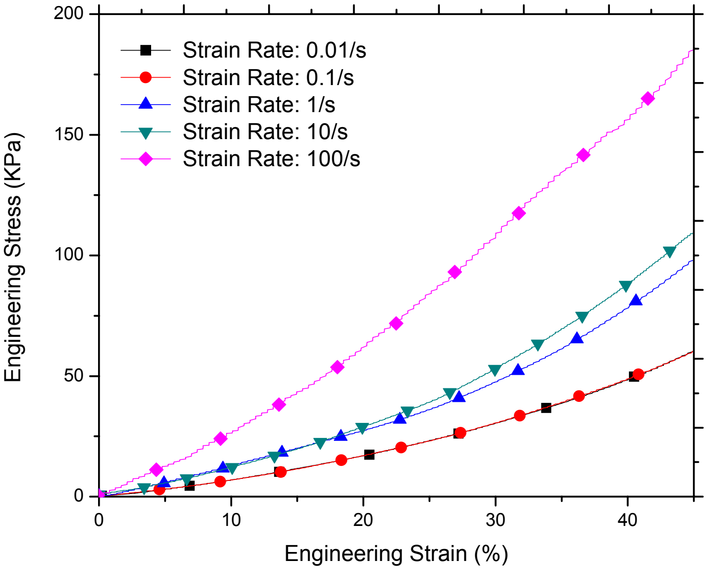

Figure 1: Compressive stress-strain response of Perma gel

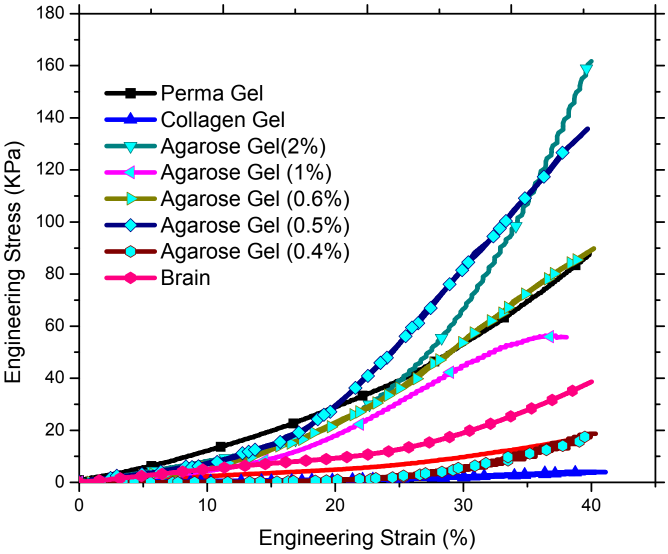

Figure 2: Average stress-strain curve of different gel materials at strain rate of 10/s

Figure 2 represents the average stress- strain curve of different gel materials at strain rate of 10/s. The brain response of bovine white matter was compared with the different candidate gels and it was found that agarose 0.4% has close mechanical properties compared to the brain tissue response. The DMA data shows that the elastic modulus and viscous modulus of the gel increase significantly with the frequency and gel concentration (Fig 2). These are consistent with the previous study [1, 2, 4, 5, 6 and 7]. Agarose 0.5% shows a decrease in modulus resulted from irreversible effects such as slippage or micro-cracking that occurred at high frequency

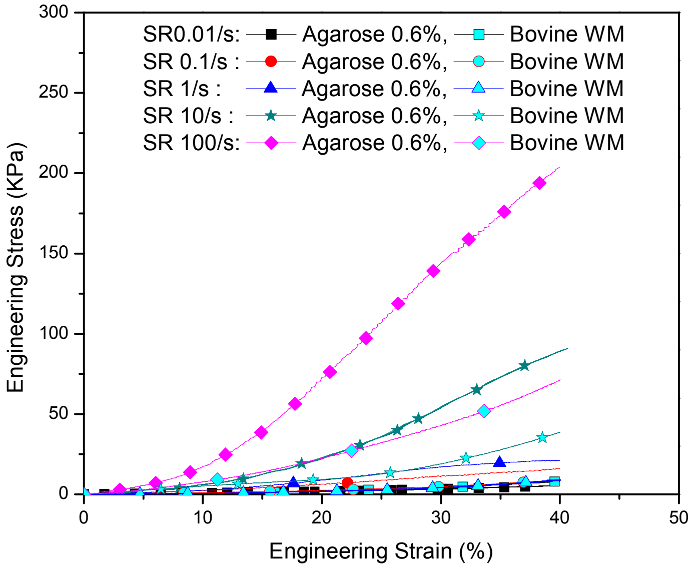

Figure 3: Comparison of stress-strain behavior of Agarose gel with concentration of 0.6% and brain white matter

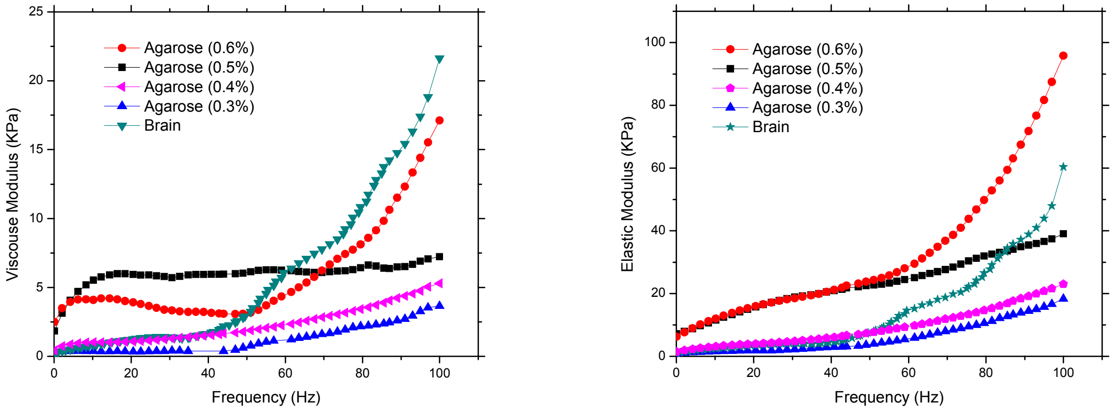

Figure 4: Average viscous and elastic modulus of agarose gel with different concentration as a function of frequency

CONCLUSIONS

This study involved manufacturing candidate gel material to simulate the brain tissue behavior. The mechanical behaviors of gels must closely match the tissues they are simulating to produce realistic results. In this study we experimentally determined the dynamic mechanical properties of gels with different integrants and concentrations to evaluate the stress-strain behavior of gel materials for wide range of strain and strain rates. The mechanical and rheological behaviors are then compared to that of the brain tissues under identical loading conditions to find candidate gel materials that respond to the loading in a similar manner as the brain tissues. This study evaluated the candidate gel materials for simulated brain tissues and agarose gel with concentration of 0.4~0.6% could be a good candidate for brain tissues. The mechanical properties of gel materials are critical for designing and performing the measurements on gels for various biomedical investigation purposes and also developing a model head for numerical simulations.

Acknowledgement:
This research was supported by US Army Research Office (ARO) and Joint Improvised Explosive Device Defeat Organization (JIEDO) through Massachusetts Institute of Technology (MIT).

Reference:

1. Chahine, N. Albro, M. Lima, E. Wei, V. Dubois, C. Hung, C. and Ateshian, G. Effect of dynamic loading on the transportation of solutes into agarose hydrogels. Biophysical Journal, 97, 968-975, 2009.
2. Ross, K. Notle, L. and Campanella, O. The effect of mixing conditions on the mechanical properties of an agar gel-microstructural and macrostructural considerations. Food Hydrocolloids, 20, 79-87, 2006.
3. Moy, P. Gunnarsson, C. and Weerasooriya, T. Tensile deformation and fracture of ballistic gelatin as a function of loading rate. Proceedings of the SEM Annual Conference, 2009.
4. Chen, Q. Ringleb, S.Hulshizer, T. and An, K. Identification of the testing parameters in high frequency dynamic shear measurement on agarose gels. Journal of Biomechanics, 38, 959-963, 2005.
5. Chen, Q. Suki, B. and An K. 2003. Dynamic mechanical properties of agarose gel by a fractional derivative model. Summer Bioengineering Conference, Sonesta Beach Resort in Key Biscayne, Florida.
6. Mohammed, Z. Hember, M. Richardson, R. and Morris, E. Kinetic and equilibrium process in the formation and melting of agarose gels. Carbohydrate polymers, 36, 15-26, 1998.
7. Salisbury, C. and Cronin, D. Mechanical properties of ballistic gelatin at high deformation rates. Experimental Mechanics, 49, 829-840, 2009.

Proceedings of the SEM Annual Conference
June 7-10, 2010 Indianapolis, Indiana USA
©2010 Society for Experimental Mechanics Inc.

Loading Rate Effect on Tensile Failure Behavior of Gelatins under Mode I

Paul Moy
(pmoy@arl.army.mil)

Mark Foster
(mark.foster12@us.army.mil)

C. Allan Gunnarsson
(allan.gunnarsson@us.army.mil)

Tusit Weerasooriya
tusitw@arl.army.mil

Army Research Laboratory
Weapons and Materials Research Directorate
Bldg 4600 Deer Creek Loop
Aberdeen Proving Ground, MD 21005-5069

ABSTRACT

For decades, ballistic gelatin has been used as a tissue surrogate to test and evaluate bullets and firearms due to its similar viscosity to natural tissue. However, the high water content in ballistic gelatin makes it unstable at room temperature, and therefore causes it to have a poor shelf life. The development of polymer-based gels has shown promise as an alternative tissue surrogate. Polymer gels such as Perma-Gel are stable at room temperature and can be stored for long periods of time. Gels often fail due to tensile stresses during penetration. The failure behavior in tension is highly influenced by the presence of defects, such as cracks and voids, in the bulk material. A mode I experimental method was developed to obtain tensile failure criteria for the initiation and propagation behavior of these types of soft materials. Digital image correlation is used to determine the full-field surface strains around the crack tip to obtain a quantitative measure of the critical strain-field required for initiation and propagation of failure due to a defect. This systematic study utilizes these experimental techniques to determine the critical criteria for crack growth initiation and crack propagation of ballistic gelatins and a polymer gel as a function of loading rate. This paper presents experimental methodologies and results from Mode I fracture experiments including measured critical energy and strain-based criteria for failure initiation and growth, as well as their dependence on the rate of loading.

INTRODUCTION

For decades, the tissue surrogate ballistic gelatin has been used as a standard target to test and evaluate bullets and firearms [1]. This material has the approximate density and viscosity of biological tissues and thus provides an excellent substitute for biological subjects. Typically, ballistic gelatin of a certain mixture and size is shot with a firearm from a standard distance. The bullet would lodge within the gelatin and the depth of penetration would be measured to determine the approximate effect of the projectile on tissue. Other ballistic studies on gelatins have involved the use of high speed imaging to examine the temporary and permanent cavities inflicted by the penetration of the bullet [2-4]. The study of the formation of these cavities in ballistic gelatin was typically a qualitative investigation rather than a quantitative one. Nevertheless, these efforts offered an insight into the effectiveness of the bullet or weapon.

T. Proulx (ed.), *Dynamic Behavior of Materials, Volume 1*, Conference Proceedings of the Society for Experimental Mechanics Series,
DOI 10.1007/978-1-4419-8228-5_4, © The Society for Experimental Mechanics, Inc. 2011

Ballistic gelatin is produced from a mixture of protein-based powder and water; this causes it to degrade over time and thus having a short shelf life. It has been noted that the mechanical properties of ballistic gelatin will begin to change in as short of a time as 1-2 days, or even shorter if left out at room temperature and exposed to dehydration due to evaporation. Recently, polymer based gels, such as Perma-Gel™ has been introduced to the market as an alternative to ballistic gelatin. According to the manufacturer of Perma-Gel (Perma-Gel, Inc., Albany, OR), the material is 100% synthetic, clear, and reusable. Also, the manufacturer maintains that this polymer gel is closely matched in physical and mechanical properties to 10% ballistic gelatin. It differs significantly from 20% ballistic gelatin, which is another tissue surrogate used by NATO [5]. An advantage of polymer based gels is the ability to tailor them to potentially simulate the physical and mechanical properties of actual tissues and organs. This is not possible with ballistic gelatin due to its inherent homogeneity and fixed mechanical properties, which is unlike most biological tissues.

Tissue simulants provide valuable information about penetration and wound mechanics; therefore, when gelatins are used as tissue simulants, it is necessary to fully understand the mechanical responses of them under these impact conditions to obtain material models for different stress states. During these impact and penetration events, these tissue simulants fail most frequently due to tensile stresses at high loading rates, causing a pre-existing defect to grow. Therefore, it is essential to obtain the constitutive and failure behavior of these gelatins under tensile loading conditions up to high loading rates, as well as other stress states.

Gelatin like material has been characterized for mechanical responses using several different techniques. Moy et al [6] conducted uniaxial compression of 20% ballistic gelatin as well as physically associating gels at intermediate and high strain rates. Their high strain rate experiments were performed using aluminum Split-Hopkinson Pressure Bars under dynamic stress equilibrium. Similarly, Salisbury et al [7] characterized ballistic gelatin under compression at different loading rates including high rates using a polymeric Hopkinson bar apparatus. Juliano et al investigated multiple mechanical characterization methods of biomimetic gels and explained the modulus relationship between these techniques [8].

There are only few studies on the tensile behavior of soft materials, such as tissue simulants, due to a lack of good experimental methods including gripping techniques. Additionally, there are even fewer studies in literature on fracture behavior of soft materials due to the difficulty in measurement of strain and displacement fields around the crack-tip. Previously, the authors developed experimental methods to obtain the tensile behavior of 20% ballistic gelatin under different strain rates up to 1/s [9]. Gelatins have similar characteristics to elastomers, which include a high stretch ratio. Zhang et al [10] investigated the resistance to Mode I fracture of natural rubber with crystallite fillers. They used a photo-elastic technique to determine the strain field at the notch-tip, and were able to study the fracture speeds as a function of elastic stored energy, thus obtaining the effect of crystallites on the fracture behavior. An experimental technique was developed by the authors previously to perform notched tensile fracture experiments on ballistic gelatin at low loading rate [11]. The work in this paper extends previous effort to obtain the fracture behavior for both 10% and 20% ballistic gelatin and the polymer gel commercially known as Perma-Gel, as a function of loading rate.

The major challenge associated with fracture experiments on ballistic gelatin is accurately measuring strain in the gage section of the specimen to obtain the strain distribution around the crack. Digital image correlation (DIC) technique was used to measure strain fields in the gage area and around the crack, similarly to the method used previously for tensile experiments [9] and fracture experiments [11]. DIC is a non-contact optical technique to measure surface displacements. Digital images are acquired during the test and, subsequently, the images are post processed with specialized software to convert pixel patterns into displacement/strains [12-16].

In the past several years, commercially available DIC systems have been extensively used to obtain axial and shear strains simultaneously. DIC systems can measure strain in complex states, and have the unique ability to acquire full-field strain measurements over a large area. Strain gages and extensometers are generally applicable for only one-dimensional strain measurements, and provide an average strain at a single point. Furthermore, strain gages and clip-on extensometers are not feasible for use on gelatin or other soft materials due to their susceptibility to damage the soft material. The sharp edges of an extensometer or metal foil gage would lead to premature failure at these locations during loading. The DIC technique allows better full-field measurement of displacement and deformation while eliminating any possible damage due to instrumentation.

MATERIAL

Both 10% and 20% (by mass) ballistic gelatin samples were made of 250 bloom type A ordnance gelatin (GELITA USA Inc., Sioux City, IA) with 40°C ultra-pure filtered water. The mixture was stirred slowly with a cake mixer to dissolve all the particles and to remove air bubbles. The solution was then poured into aluminum molds in the shape of the tensile specimen geometry. It is vital that the solution be poured into the molds in a very slow and deliberate manner to avoid frothing of the solution and formation of air bubbles in the gage length. Specimens with bubbles in or near the gage length are deemed unusable for experiments. The gelatin mixture begins to congeal gradually even at room temperature, at which the mold is then placed in a refrigerator. The ballistic gelatin specimens are prepared when the experiments are to be carried out the following day to ensure that the properties do not change. The specimens tend to dehydrate and thus the surfaces become hard when left at ambient room conditions. Therefore, individual ballistic gelatin specimens were removed from the molds just prior to testing.

Perma-Gel was acquired as a test block form about the size of a typical ballistic gelatin target (444 mm x 292 mm x 127 mm). To fabricate the Perma-Gel specimens, small pieces were extracted from the block and placed in an open-faced aluminum mold over a hot plate that was set to a temperature of about 120°C. The melting point for Perma-Gel is about 70°C. This procedure was repeated several times until the Perma-Gel filled the mold and matched the mold surface evenly.

MODE I FRACTURE EXPERIMENTS

Fracture experiments on gelatin were conducted using a tensile specimen that was inserted into the loading machine with special grips; a 1.75 mm deep pre-crack was created in the specimen just prior to testing. Since both the ballistic gelatin and Perma-Gel are so supple, the pre-crack was carefully initiated with a razor blade that was pressed across the edge of the gel specimen at the center of the gage length while it was in the grips. Notching after mounting the specimen into the grips ensured that no further crack growth was caused by handling the specimen. A custom designed jig was used to hold the razor blade and provide a fixed depth of the notch at the center of the sample; a backing piece was used to prevent the specimen from being "pushed" or bent by the razor.

The authors designed a "shoulder supported" tensile grip made from acrylic for the gelatin specimens. Schematic drawings of the specimen and grip fixture are shown in Figure 1. The dimensions in the drawing are displayed in inches. The gage length of the specimen is 25.4 mm, with a width (parallel to the crack) of 12.7 mm and a thickness of 9.5 mm. Also, the curvature of the shoulder was optimized to mitigate failure outside the gage section. Before settling with the shoulder curvature in the figure, several design iterations of the curvature were explored. It was determined that the radius of approximately 53.98 mm at the shoulder minimized the failure of the gelatin at the gage length/grip interface.

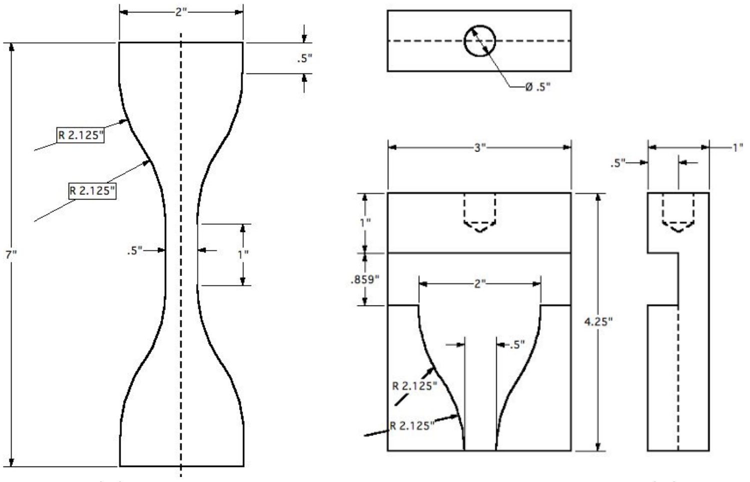

(a) (b)

Figure 1. Schematic Drawing of the Ballistic Gelatin (a) Specimen Geometry and (b) Tensile/Fracture Gripping Fixture

Prior to testing, the entire gage area of the specimen was speckled with a dark-colored ink using an airbrush for the digital image correlation measurements. Compared to the speckle pattern used for tensile experiments in the previous study [9], a much finer pattern was applied for these experiments. This finer speckles allowed measurement of the strain field around the crack tip at higher resolution during initiation and propagation of the crack compared to the previous study [11]. The measured load and displacement data were recorded and synchronized with the corresponding digital images taken during loading. The experiments were conducted at two different constant displacement rates: 0.127 mm/s (slow rate) and 127 mm/s (high rate). A single camera was configured to record images for 2D correlation, assuming minimum out-of-plane displacement during the experiment. Two different cameras were used for the two displacement rates. A Photron APX-RS camera, set to a frame rate of 1000 fps with resolution of 1024 by 1024, was used for the high rate experiments. The test images for the low rate experiments were recorded with a Point Grey Research camera at a frame rate of 4 fps and 1024 by 1024 resolution.

RESULTS AND DISCUSSION

Data obtained from a typical experiment are shown in Figures 2-7, in this case, for 20% ballistic gelatin at slow loading rate. Figure 2 shows the load-displacement plot from the fracture experiment for this gelatin with a series of corresponding correlated images at discrete times during the test. Each of the contour pictures represents the 2D strain field in the direction of loading and noted as e_{yy}. The color scale on the first four correlated images (0.13 to 0.23) is different from the scale on the last four images (0.1 to 0.4). The maximum e_{yy} value was extracted in the vicinity of the crack tip from the correlated images. The values are indicated below on each picture of the graph. There is a critical point at which the crack “pops” and begins to propagate across the specimen. This occurs 82.7 seconds after the test begins. Up until this point, the crack-tip-opening-displacement (CTOD) grows in the vertical direction, but the length of the crack remains constant. The maximum e_{yy} strain reaches a critical value of 0.18, when the pre-crack begins to propagate. The load at this point is 4.1 N, which is lower than the maximum load. The load increases beyond the critical point to a maximum of 4.7 N and then starts to decrease rapidly as the crack tip accelerates to failure. The maximum strain measured at the vicinity of the crack tip reaches 0.22 at the maximum load of 4.7 N. Subsequently, the maximum e_{yy} strain continues to increase after the peak load up to about 0.38 just before complete specimen failure.

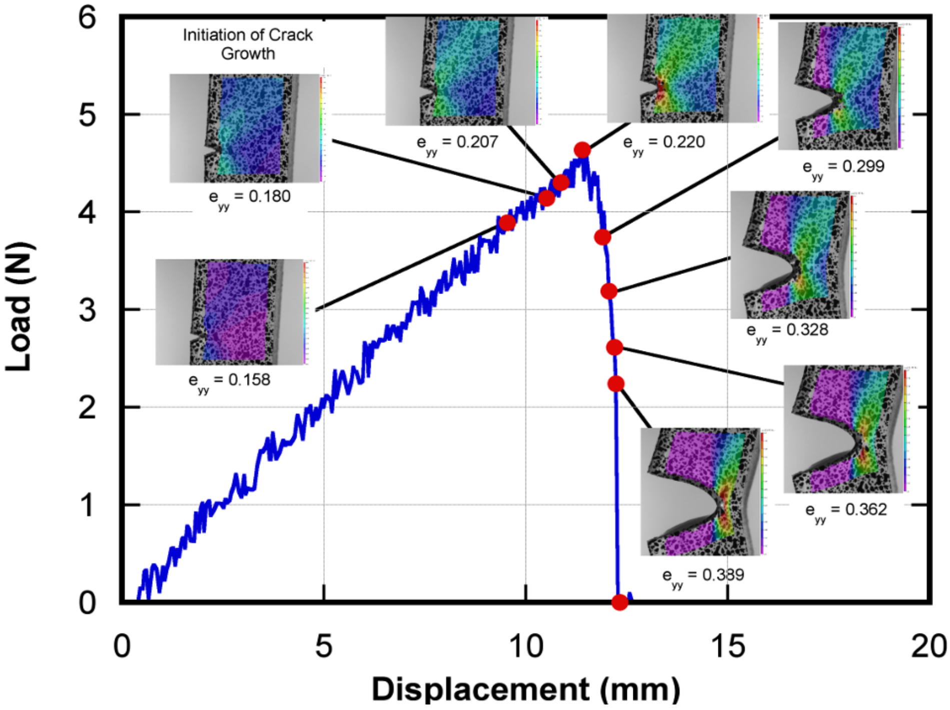

Figure 2. Load-Displacement for 20% Ballistic Gelatin Fracture Experiment at Low Rate with Measured Strain Fields in the Loading Direction Around the Crack-tip

Figure 3 displays the images that are embedded in Figure 2 with more detailed e_{yy} fields at corresponding times; time of zero ms corresponds to the beginning of loading. These pictures provide a close-up view of the strain field including the minimum and maximum values of the color contour scale. From these set of pictures, it can be seen that the strain field is symmetrically distributed along the crack tip during the entire experiment. The strain fields are entirely concentrated at the crack tip. The strain is nearly zero directly above and below the cracked surface in the ballistic gelatin.

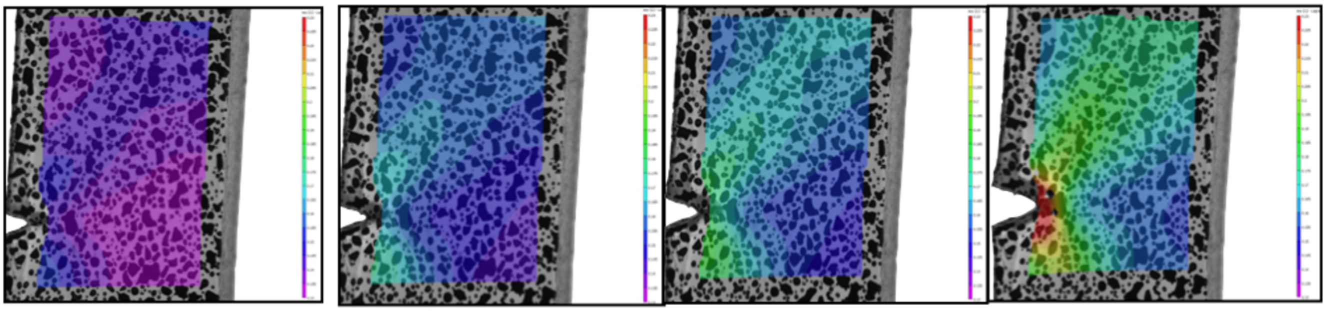

e_yy = 0.158;Time=75.1s
Red=0.23; Purple=0.13

e_yy = 0.180;Time=82.7s
Red=0.23; Purple=0.13

e_yy = 0.207;Time=85.6s
Red=0.23; Purple=0.13

e_yy = 0.220;Time=89.6s
Red=0.23; Purple=0.13

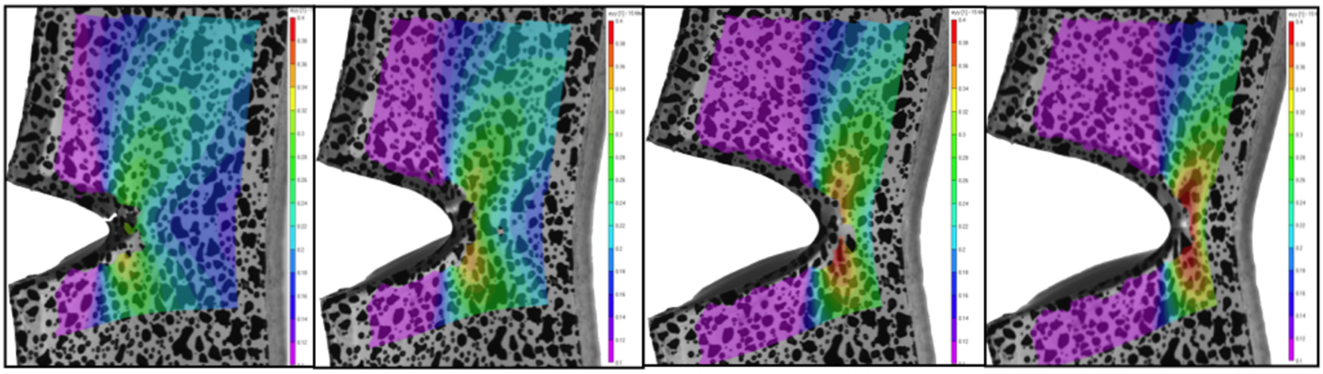

e_yy = 0.299;Time=93.1s
Red=0.4; Purple=0.1

e_yy = 0.328;Time=94.4s
Red=0.4; Purple=0.1

e_yy = 0.362;Time=95.3s
Red=0.4; Purple=0.1

e_yy = 0.389;Time=96.4s
Red=0.4; Purple=0.1

Figure 3. Strain-Field Around the Crack-Tip for 20% Ballistic Gelatin at Low Rate Showing Maximum Strain Values in the Loading Direction. Crack growth begins second picture, top row (82.7 seconds).

The maximum strain vs. time for 20% ballistic gelatin at slow rate is shown in Figure 4. The strain data is the maximum value obtained at the crack tip and is in the direction of loading. The figure also includes the corresponding load history of the experiment. The measured e_{yy} strain is constant up to the time at 82.7 seconds, which is when the crack begins to grow across the specimen. The black markers in all the figures indicate the point where the crack growth initiates. The load continues to increase at a constant rate for a period of time after crack initiation; it then starts to decrease rapidly as the specimen fails. The maximum strain, e_{yy}, increases approximately linearly at low rate until the load reaches the critical point. After this point, the rate of increase of e_{yy} is significantly higher compared to the initial rate before the critical load.

The crack length and load history plots for 20% ballistic gelatin at slow rate is shown in Figure 5. The crack length grows at a much higher rate after the critical point, which is indicated in the graph by the black markers. From the crack length measurements, the crack tip velocity was derived and is shown in Figure 6. Again, the crack tip velocity increases significantly after the critical crack initiation point. In both Figures 5 and 6, crack length and crack-tip velocity do not deviate significantly from their initial values until the load reaches the critical point.

Figure 7 shows the energy imparted to the 20% ballistic gelatin as a function of the measured crack velocity at slow rate. The energy is calculated by integrating the load vs. displacement curve. The displacement in this case is the relative displacement at the loading grips. The black marker indicates the critical energy (22.1 mJ) at the crack growth initiation point. Energy imparted to the specimen increases rapidly as the velocity of the crack-tip increases. When the crack-tip velocity reaches around 1 mm/s, subsequent crack growth occurs at an approximate steady value of 29 mJ energy.

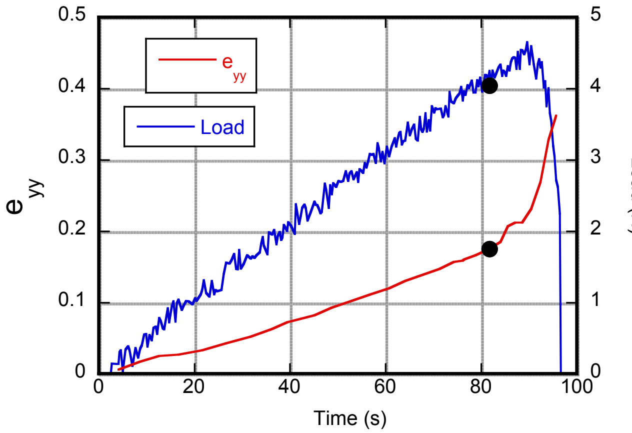

Figure 4. Maximum Strain and Load vs. Time for 20% Ballistic Gelatin at Low Rate

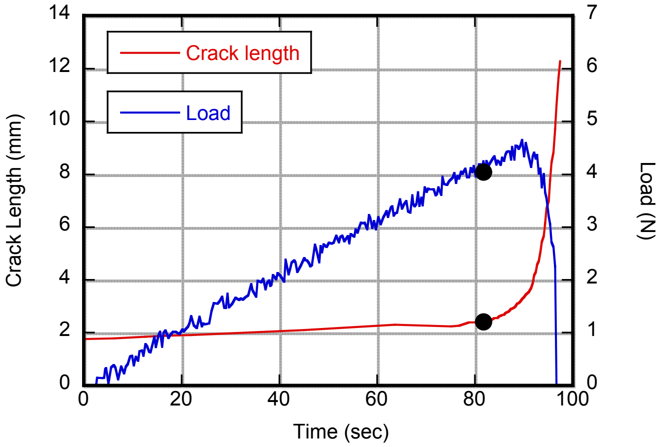

Figure 5. Crack Length and Load vs. Time for 20% Ballistic Gelatin at Low Rate

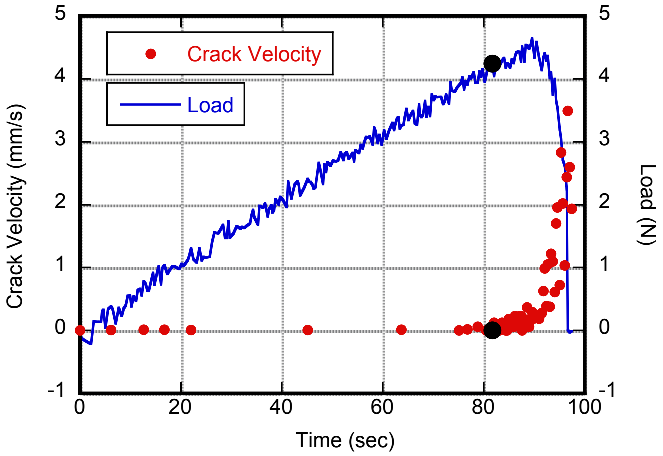

Figure 6. Crack Velocity and Load vs. Time for 20% Ballistic Gelatin at Low Rate

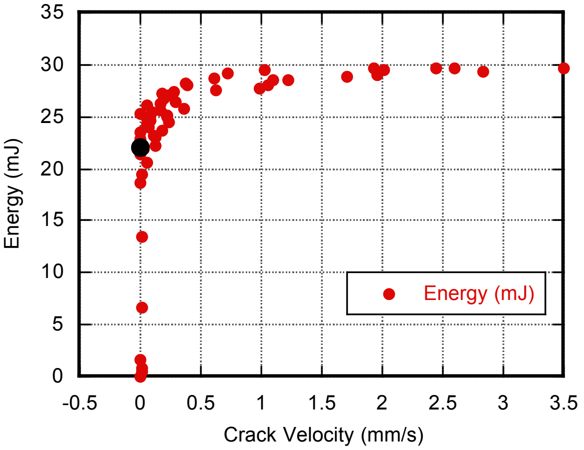

Figure 7. Energy vs. Crack Velocity for 20% Ballistic Gelatin at Low Rate

The preceding data is representative of the data obtained for 10% and 20% ballistic gelatin at low and high rates, and for Perma-Gel at low rate. Valid results for the Perma-Gel fracture experiments at 127 mm/s could not be obtained; the test machine reached its maximum extension (100 mm) prior to the crack propagating at this rate. The crack eventually would propagate to failure after being stretched to the maximum machine displacement and held there for a few seconds. In all cases, the fracture surfaces of the 10% and 20% ballistic gelatin as well as the Perma-Gel were very smooth and flat.

The complete data sets for all of the experiments that were conducted are not shown in this paper for brevity; the results are summarized in Table 1. There is a significant difference between the loading rates for 20% and 10% ballistic gelatins for identical displacement rates. At high rate, the average loading rate for 20% ballistic gelatin is about twice that of the 10%; the load at the initiation of crack growth is about 4 times higher in the 20% ballistic gelatin than the 10%. However, the load for initiation of crack growth for Perma-Gel at the low rate is lower than the 20% ballistic gelatin, yet the critical energy required for crack growth is higher. The total displacement to reach crack propagation for the Perma-Gel is higher than for both ballistic gelatins. In fact, the total displacement is about 40 mm for the Perma-Gel to reach complete specimen failure. For both ballistic gelatins, the corresponding extension is about 10-12 mm. The critical e_{yy} strain at the initiation of crack growth is ~0.20, approximately the same magnitude for the 10% and 20% ballistic gelatin; for the Perma-Gel it was 0.68, three times the value for the ballistic gelatins.

Table 1. Summary of Gelatin Fracture Experimental Results

Initial Crack Length (a) = 1.75 mm Width = 12.7 mm Thickness = 9.5 mm	**10% Ballistic Gelatin**		**20% Ballistic Gelatin**		**Perma-Gel^{TM}**	
Displacement Rate (mm/s)	0.127	127	0.127	127	0.127	127
Avg. Loading Rate (N/s)	0.00956	10.90	0.05020	20.86	0.00088	-
Load for Initiation of Crack Growth (N)	0.66	3.05	4.25	12.25	1.42	-
Critical Energy for Initiation of Crack Growth (mJ)	2.71	66.48	22.05	455.11	27.83	-
Critical e-yy for Initiation of Crack Growth	0.20	1.56	0.17	2.70	0.68	-

The energy imparted for both 10% and 20% ballistic gelatin as a function of the crack velocity at the displacement rate of 127 mm/s are shown in Figure 8(a). The black markers are the critical energy at crack initiation for each material. The critical energy for crack growth for the 10% and 20% ballistic gelatin is about 455 mJ and 67 mJ, respectively. For the Perma-Gel, at 127 mm/s, the crack growth never started; at maximum displacement, the energy level had already reached ~300 mJ. With about twice the amount of gelatin power by mass, the 20% ballistic gelatin is much more resilient to crack initiation than the 10% ballistic gelatin. After crack initiation, the crack would grow at a steady energy level for 10% ballistic gelatin. In contrast, the energy required for crack growth increases with crack velocity for 20% ballistic gelatin, after the start of crack growth. Figure 8(b) shows the energy as a function of crack velocity at the lower loading rate for both ballistic gelatins and the Perma-Gel.

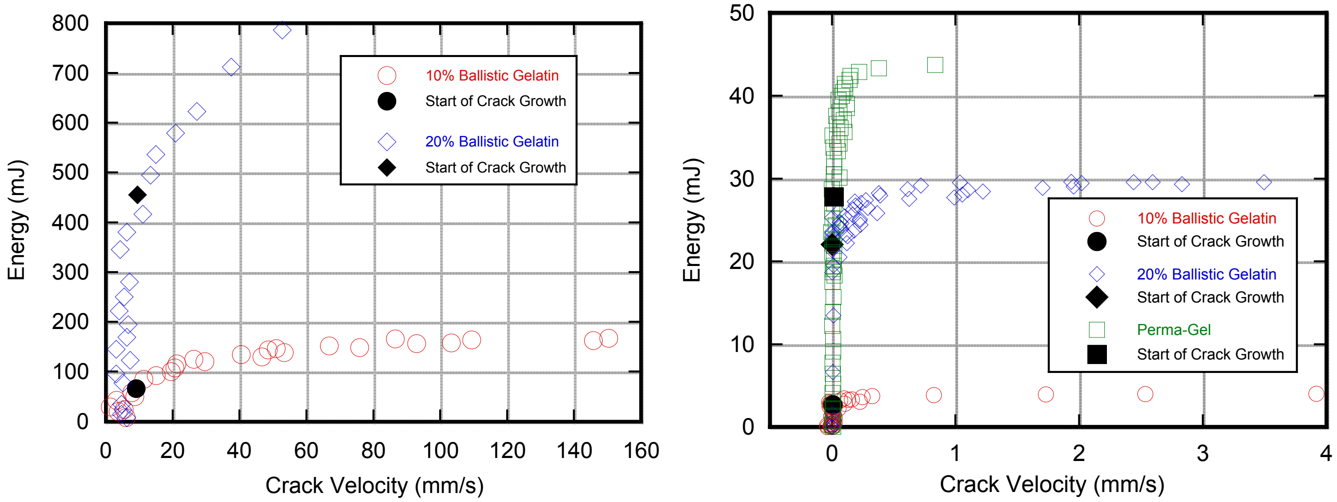

(a) (b)

Figure 8. Energy as a Function of Crack Velocity for all Gelatins at (a) High Rate and (b) Slow Rate

The critical energy for Perma-Gel (27 mJ) is similar to the 20% ballistic gelatin at 22 mJ, and both are significantly greater than 10% ballistic gelatin (2.7 mJ). As can be seen in Figure 8(b), even after crack initiation in the Perma-Gel at low rate, the energy continues to increase until it reaches 43 mJ and levels off shortly before complete fracture. This continuation of increased energy absorption after crack initiation demonstrates just how much tougher the Perma-Gel is compared to the ballistic gelatins. This is also demonstrated by the fact that the Perma-Gel reached maximum displacement before crack initiation at the 127 mm/s rate. Also, at this loading rate, the critical energy required for crack growth for both gelatins decreases significantly in comparison with the high loading rate experiments.

All of the gelatins are much more resistance to crack initiation and propagation at higher rates. At the slower rate, there is more time for the crack to start during the experiment. The test time duration at the slower rate is about

90 seconds for the 10% and 20% gelatins whereas the Perma-Gel test ran for an average test time of 3 minutes to reach complete fracture. Furthermore, the time to reach the onset of the crack initiation in the Perma-Gel is much longer. The polymer gel is relatively tacky and this may have further increased its crack resistance. After notching, the crack in the Perma-Gel appears to seal itself.

Both at low and high rates, the energy required for crack initiation and growth for 10% and 20% ballistic gelatins are shown in Figures 9(a) and 9(b), respectively. Each plot also includes an expanded view of the low rate experiments. For both 10% and 20% ballistic gelatins, the energy required for crack initiation and growth is higher at the higher loading rate. Energy levels are higher for 20% gelatins compared to 10% gelatin for both initiation and growth of the crack for corresponding velocities of the crack. In both types of ballistic gelatins, at the slower loading rate, energy reached a steady value for further crack growth after initiation; however, for the higher loading rate, the energy did not reach a steady value during the crack growth.

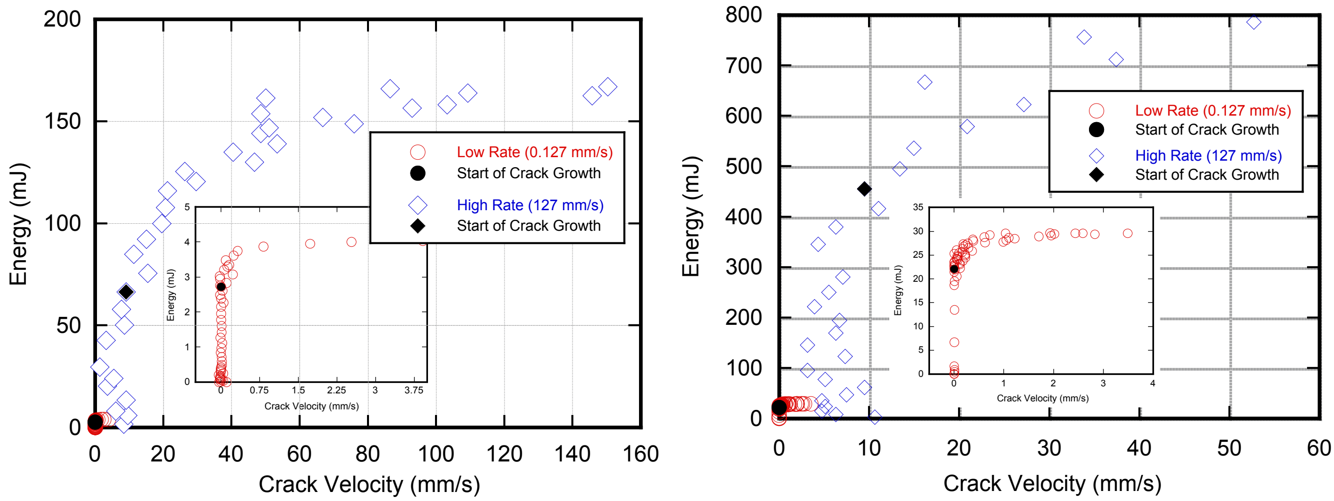

(a)

(b)

Figure 9. Energy as a Function of Crack Velocity at Low Rate and High Rate for (a) 10% Ballistic Gelatin and (b) 20% Ballistic Gelatin

SUMMARY AND CONCLUSIONS

Experimental methods were developed to obtain tensile failure criteria. These can be used for simulation of projectile penetration into different gels. Mode I fracture experiments, using single edge-notched specimens, were conducted at two different loading rates on three gelatins: 10% and 20% ballistic gelatin and polymer based Perma-Gel. Digital image correlation was used to measure the strain field at the crack tip during initiation and propagation. The critical energy for crack initiation and growth were determined from the experiments for all three gelatins at low loading rates; they were also determined for the two ballistic gelatins at high loading rate. Critical maximum strain in the loading direction for crack growth was obtained from the measured strain fields at the crack-tip. Results show a significant increase in the critical energy required for crack initiation and subsequent growth for both ballistic gelatins at the high rate compared to the slow rate. At the lower rate, Perma-Gel requires a higher critical energy for the crack initiation than both 10% and 20% ballistic gelatins. For the low loading rate, energy for further growth reached a steady value until complete failure; in contrast, for the high loading rate, the energy required for crack growth after initiation did not reach a steady value.

The critical maximum strain in the loading direction at the crack growth initiation was obtained for the gelatins at the tested loading rates. The critical maximum strain for crack growth initiation was an order of magnitude higher for the high loading rate, compared to the low rate. For Perma-Gel, the critical strain was about three times higher compared to that for ballistic gels at the slower rate of loading; comparatively, the critical strain for 10% and 20% ballistic gels were approximately at the same level for this loading rate. At the high loading rate, critical strain for the 20% gelatin was about two times higher. Results from these fracture experiments indicate that all the gelatins are rate sensitive and each gelatin behaves differently with respect to one another. These critical energy and strain-based criteria can be used as failure criteria during simulation of penetration into gels.

ACKNOWLEDGEMENTS

The authors wish to acknowledge the following individuals at the U.S. Army Research Laboratory for providing the Perma-Gel material and information on the procedure to fabricate these materials: Mr. Larry Long and Mr Richard Merrill.

Certain commercial equipment and materials are identified in this paper in order to specify adequately to the experimental procedure. In no case does such identification imply recommendation by the Army Research Laboratory nor does it imply that the material or equipment identified is necessarily the best available for this purpose.

REFERENCES

1. Peterson, B. Ballistic Gelatin Lethality Performance of 0.375-in Ball Bearings and MAAWS 401B Flechettes. Army Research Laboratory Technical Report. ARL-TR-4153. 2007
2. Nicolas, N. C. and Welsch, J. R. Ballistic Gelatin, Institute for Non-Lethal Defense Technologies Report, The Pennsylvania State University Applied Research Laboratory.
3. MacPherson, D. Bullet Penetration: Modeling the Dynamics and the Incapacitation Resulting from Wound Trauma. Ballistic Publications. 1994.
4. Fackler, M. L. Ordnance Gelatin for Ballistic Studies. Association of Firearm and Toolmark Examiners Journal. 4:403-5. 1987.
5. http://en.wikipedia.org/wiki/ballistic_gelatin
6. Moy, P., Weerasooriya, T., Juliano, T.F., VanLandingham, M.R., and Chen, W. Dynamic Response of an Alternative Tissue Simulant, Physically Associating Gels (PAG). Proceedings of the 2006 SEM Annual Conference. St. Louis, MO. 2006.
7. Salisbury, C.P. and Cronin, D.S., Mechanical Properties of Ballistic Gelatin at High Deformation Rates, Experimental Mechanics. 2009.
8. Juliano, T.F., Forster, A. M., Drzal, P.L., Weerasooriya, T., Moy, P., and VanLandingham, M.R., Multiscale Mechanical Characterization of Biomimetic Physically Associating Gels. J. Mater. Res., Vol 21, No. 8, Aug 2006.
9. Moy, P., Weerasooriya, T., and Gunnarsson, C. A., Tensile Deformation of Ballistic Gelatin as a Function of Loading Rate. Proceedings of the 2008 SEM Annual Conference. Orlando, FL. 2008.
10. Zhang, H. P., Niemczura, J., Dennis, G., Ravi-Chandar, K., and Marder, M. Toughening Effect of Strain-Induced Crystallites in Natural Rubber. Physical Review Letters, Vol. 102, Issue 24, id. 245503. June 2009.
11. Moy, P., Weerasooriya, T., and Gunnarsson, C. A., Tensile Deformation and Fracture of Ballistic Gelatin as a Function of Loading Rate. Proceedings of the 2009 SEM Annual Conference. Albuquerque, NM. June 2009.
12. Chu, T. C., Ranson, W. F., Sutton, M. A., and Peters, W. H. Applications of Digital-Image-Correlation Techniques to Experimental Mechanics. Experimental Mechanics. September 1995.
13. Sutton, M. A., Wolters, W. J., Peters, W. H., Ranson, W. F., and McNeill, S. R. Determination of Displacements Using an Improved Digital Image Correlation Method. Computer Vision. August 1983.
14. Bruck, H. A., McNeill, S. R., Russell S. S., Sutton, M. A. Use of Digital Image Correlation for Determination of Displacements and Strains. Non-Destructive Evaluation for Aerospace Requirements. 1989.
15. Sutton, M. A., McNeill, S. R., Helm, J. D., Schreier, H. Full-Field Non-Contacting Measurement of Surface Deformation on Planar or Curved Surfaces Using Advanced Vision Systems. Proceedings of the International Conference on Advanced Technology in Experimental Mechanics. July 1999.
16. Sutton, M. A., McNeill, S. R., Helm, and Chao, Y. J. Advances in Two-Dimensional and Three-Dimensional Computer Vision. Photomechanics. Volume 77. 2000.

Proceedings of the SEM Annual Conference
June 7-10, 2010 Indianapolis, Indiana USA
©2010 Society for Experimental Mechanics Inc.

On failure and dynamic performance of materials

N.K. Bourne

AWE, Aldermaston, Reading RG7 4PR, United Kingdom
email – neil.bourne@awe.co.uk

ABSTRACT

The performance of armour materials depends upon deformation mechanisms operating during the penetration process. The critical mechanisms determining the behaviour of armour ceramics have not been isolated using traditional ballistics. It has recently become possible to measure strength histories in materials under shock. The data gained for the failed strength of the armour are shown to relate directly to the penetration measured. Further it has been demonstrated in 1D strain that the material can be loaded and recovered for post-mortem examination. Failure is by micro-fracture that is a function of the defects and then cracking activated by plasticity mechanisms within the grains and failure at grain boundaries in the amorphous intergranular phase. Thus it appears that the shock-induced plastic yielding of grains at the impact face that determines the later time penetration through the tile.

INTRODUCTION

The dynamic response of materials and structures is determined by a range of mechanisms operating within materials at the microstructural length scale [1, 2]. These are fixed by the boundary conditions applied by the load which the structure sees. The resulting response at the continuum is the integrated response of these operating mechanisms.

Work has progressed with both metals and brittle materials and has determined, for a limited number within this set, a complete history of test data across a suite of impulses that gives an overview of the time evolution of the state of a material after compressive loading [3, 4]. The final observed properties of an impact-loaded material appear as an integration of these operating mechanisms with their different thresholds and timescales. In one-dimensional loading, only target recovery, developed to ensure precisely known continuum loading conditions, allows uniequivocal exploration of operating mechanisms [5]. These processes occur over a small time and a restricted volume but represent critical processes that condition the target for the entry of a projectile and flow of fractured material around it at later times.

The inhomogeneities within a brittle material cause local, mesoscale damage to propagate into the material failing the material from its elastic state and defining the onset of inelastic behaviour within it. It is possible to suppress failure in the continuum in a one dimensional experiment since these global boundary conditions constrain the failure. However, introducing a flaw into a material by design allows the propagation of the front to progress from a line source on the impact face and gives a measure of the initial value of the failed strength.

When a long, dense metal rod strikes a ceramic armour panel there are high transient stresses driven in behind shock fronts generated beneath its nose6. This impacted zone initiates damage that determines the resistance to the penetrator as it enters the armour. Surface effects known as dwell represent a conditioning enviroment for failure with its own failure kinetics. Inertial confinement defines a high-pressure environment that causes metallic armour to yield by plastic flow accompanied by processes such as shear banding, whereas penetration mechanisms in ceramics involve micro-fracture and fragmentation. The resistance experienced by a penetrating long rod is in the wake of failed material by a propagating shock ahead. It follows in material which is in a different state to that at the shock front but follows the failed isentrope fo the material in its state. The steady penetration phase is governed by flow through this medium with resistance supplied by the target material described analytically by the Alexeevski-Tate equation [7, 8]. In such cases the appropriate material strength is that of the failed material mediated by the integrated effects of other operating mechanisms such as friction or shear. If the inelastic failure of the material controls the penetration then the first transition to a failed state with be a critical step in the penetration. This hypothesis is investigated in the rest of this paper.

T. Proulx (ed.), *Dynamic Behavior of Materials, Volume 1*, Conference Proceedings of the Society for Experimental Mechanics Series,
DOI 10.1007/978-1-4419-8228-5_5, © The Society for Experimental Mechanics, Inc. 2011

It is possible to measure the inelastic strength of materials in an idealized loading geometry at an appropriate rate, and then apply the data derived to define the conditions operating during the impact event. An idealized experiment of choice has geometrically simple boundary conditions to allow material properties to be unequivocally defined. For the regime ahead of a penetrator, plate impact loading provides the correct range of conditions appropriate to the impact event considered. In the following sections, a series of experiments will be described in which the results obtained from such tests will be shown to determine penetration into armour ceramics. The mechanisms operating in metals and ceramics proceed at different timescales by dint of the restricted plastic flow possible in brittle solids. Dislocation motion and twinning are operative on nanosecond timescales whereas the volume additive process, fracture, operates several orders of magnitude more slowly. This high resistance to flow directly determines the ballistic properties of an armour.

EXPERIMENTAL PROCEDURE

A plate impact experiment delivers a well-defined pulse into the stationary target that allows tracking of material properties experimentally as the pulse disperses. On the impact face, the pulse is square and as it progresses through the target the elastic wave travels faster than the plastic so that dispersion occurs and a step develops. The position of a stress sensor determines a Lagrangian station at which a continuum state variable is monitored. There is a uniaxial strain but a biaxial, cylindrically symmetric stress state in the target at the continuum but a fully three-dimensional state at inhomogeneities in the microstructure. The longitudinal stress may be measured with a suitably mounted sensor. Now the direct measurement of the lateral stress with piezoresistive gauges has been developed to allow use of the sensor in impact experiments. Gauges are mounted at a known distance from the impact face in a target reassembled from two tiles with a gauge mounted between. The geometrical arrangement for this is shown in Fig. 1. In some cases two gauges are mounted into the target to monitor wave development at a particular stress level.

As has been mentioned previously, it is possible to suppress failure in the continuum in plate impact experiments on ceramics by symmetrical impact reducing lateral strains at the impact face. Using different impedance materials and a sectioned sample allows a failure zone to be propogated from the surface. This allows the determination of an upper bound upon the initial value of the failed strength.

Longitudinal stress profiles were measured with commercial manganin stress gauges embedded between two blocks bonded together. Targets were flat to within 5 fringes across the surface. These gauges (Micromeasurements type LM-SS-125CH-048) have been calibrated and used widely in plate impact over many years9, 10. Lateral stresses were also measured using manganin stress gauges, this time of type J2M-SS-580SF-025 (resistance 25 Ω). The data collected cannot be used directly to infer the lateral stress. Thus they were reduced using a new analysis requiring no knowledge of the longitudinal stress11. The gauges were mounted at two positions within the target (usually 2 and 6 mm from the impact face) and the lateral stress histories were recorded simultaneously at each position. The experimental target arrangement is shown in figure 1.

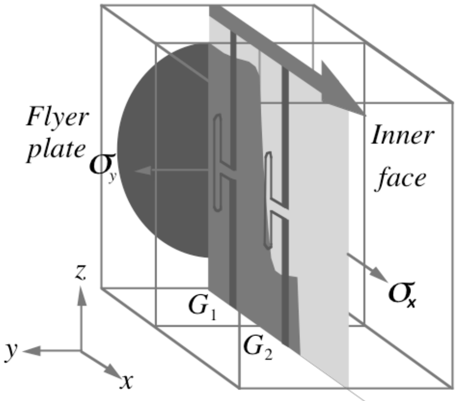

Figure 1 Experimental arrangement used in experiments showing sectioning of target and insertion of gauges.

The signals were recorded using a fast (2 GS s-1) digital storage oscilloscope and transferred onto a microcomputer for data reduction. Impact velocity was measured to an accuracy of 0.5% using a sequential pin-shorting method and tilt was made less than 1 mrad by means of an adjustable specimen mount. Impactor plates were made from lapped tungsten alloy, copper and aluminium discs and were mounted onto a polycarbonate sabot with a recessed front surface in order that the rear of the flyer plate was a free surface.

The lateral stress, σy, was used along with measurements of the longitudinal stress, σx, to calculate the shear strength τ of the material using

$$2\tau = \sigma_x - \sigma_y\,. \quad (1)$$

This quantity has already been shown to be an indicator of the ballistic performance of materials in previous work12-14. This method of measuring shear strength also has the advantage of being direct since no computation of the hydrostat is required. Additionally, its expected value can be calculated within the elastic range using the well-known relations

$$\sigma_y = \frac{\nu}{1 - \nu}\sigma_x \text{ and thus } 2\tau = \frac{1 - 2\nu}{1 - \nu}\sigma_x\,, \quad (2)$$

where v is the Poisson's ratio.

MATERIALS

Materials' properties are presented in Table 1. Details for each of the materials tested can be found in the papers from which results are taken.

	ρ (±0.05 g cm^{-3})	E (GPa)	μ (GPa)	ν	c_L (±0.01 mm μs^{-1})	c_S (±0.01 mm μs^{-1})	HEL (±0.5 GPa)	2 τ (±0.2 GPa)
4340	7.85	277	83	0.30	5.94	3.26	1.0	1.0
SL	2.49	73	30	0.23	5.84	3.46	4.0	1.9
AD85	3.42	221	91	0.22	8.81	5.24	6.1	5.3
AD995	3.89	436	151	0.23	10.66	6.28	6.7	5.5
B_4C	2.51	451	192	0.18	13.90	8.70	16.0	7.1
SiC	3.16	422	181	0.16	11.94	7.57	13.5	11.4
TiB_2	4.48	522	238	0.09	10.91	7.31	15.0[1]	13.0

[1] the upper

Table 1. Selected properties of the materials studied in this work.

Experimental work published previously is used here to assess the correlation between failed strength and depth of penetration (DoP) [15, 16]. Out of the large quantity of data presented in these, this work focuses on experiments conducted so that impact velocity was held constant and normal penetration into tiles of large areal extent and constant thickness occurred. A further feature of these studies was that the penetrator material and its geometry were also held constant in each experiment, and adequate control on pitch and yore gave confidence in the reproducibility of results.

RESULTS

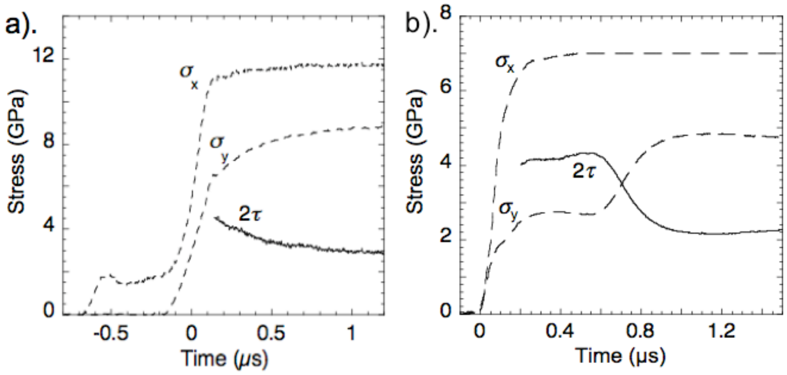

Figure 2. Longitudinal and lateral stress histories for a) BCC tantalum and b) SL glass targets. The response in the elastic region where gauge equilibration occurs is not shown.

Fig. 2 shows the impulse recorded at a Lagrangian sensor for a BCC metal and a glass. The longitudinal and lateral stress components of the axisymmetic stress field are shown in dashed lines for each material. In the case of the BCC Ta shown, the longitudinal stress pulse shows that an elastic precursor has arrived before the plastic front rises to the Hugoniot stress at the gauge station17. The sensors are limited in their response times. The lateral gauge takes time to equilibrate to the flow field in materials where the impedances of gauge and target are not close. Thus the first 150 ns of the stress history are not shown since the sensor does not reliably track the target for this time period. The lateral stress rises more slowly to this peak behind the front. Thus the solid curve shows twice the strength behind the pulse at ca. 4 GPa when the gauges are active, decaying after 1 μs to around 2 GPa. This reduction occurs over a time interval which is an order of magnitude slower for a BCC material then is the case for an FCC one which indicates the speed of operating dislocation generation and storage mechanisms behind the shock for the two different crystal structures18. It is this defect activation and equilibration time which differentiates material classes and leads to differences in the observed dynamic response in continuum experiments.

Fig. 2 b) shows longitudinal and lateral stress histories for a shot at a stress above the elastic limit of soda-lime glass. Again both the stress traces show similar behaviour for the first 500 ns after which a drop occurs from ca. 4 to 2 GPa. This corresponds with the arrival of a fracture front driven from the impact face of the glass and known as a failure wave19-21. The metal and the glass are displaying the same behaviour consistent with their microstructural response to the step impact load. In the first moments both adopt an elastic state with corresponding elastic strength. Defects within the microstructure propagate from nucleation sites until they can interact and take the material to a plastic state. In the tantalum, the defects are dislocations that travel from the existing population in the metal. In a glass, the means of relieving the shear stresses is by crack nucleation and propagation at the Rayleigh wavespeed in the material (90% of the shear wave speed in glass). These processes and defect densities mean that the elastic state starts to relax after ca. 100 ps in a metal whereas in glass that time is ca. 500 ns.

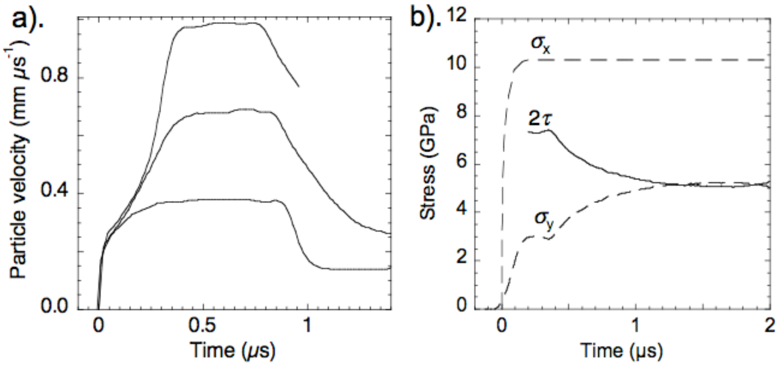

Figure 3 a). Longitudinal particle velocities for AD995 recorded from the work of Grady[22]. b). Longitudinal and lateral stress histories (dashed) and shear stress history (solid) for AD995.

These times reflect two factors which control the strength. Defect density in the as-received microstructure and the mechanism of deformation that operates to define the inelastic state. Dislocation activation, transport and interaction in polycrystalline metals occurs three orders of magnitude faster than fracture that leads to comminution in amorphous glass. This illustrates how materials with limited ductility but equivalent hardness make better armour materials than metals by virtue of slower failure kinetics. Further, these experiments define not only the kinetics but also the strengths of the materials as a function of pressure.

When the shock reaches a gauge station, material around it must initially respond in an elastic manner to the stimulus. Over some time processes will take place that allow the material to attain an inelastic state and these proceed reducing the shear stress in the material, by dislocation motion in metals and micro-fracture in brittle materials. The initial value of the lateral stress and the strength is given by the equations (2) which determine the initial state of the material. The kinetics of the processes leading to inelastic deformation determine the time taken to achieve the inelastic state. In the case of the glass, the initial strength for the shock (seen in Fig. 2 b) is the elastic strength for the glass at a longitudinal stress of 7 GPa whereas the failed strength is 2.3 GPa which compares with 2.6 GPa derived using a simple Griffith's fracture criterion. Thus the glass retains its elastic strength for 0.5 μs until cracks interconnect and it fails to a fracture-controlled yield surface.

Fig. 3 shows the response of the armour alumina, AD995 [23]. In Fig. 3 a). three wave profiles are shown taken from the work of Grady [22]. The histories show typical form for aluminas. There is a rapid rise to the first elastic limit, then a convex region to a point of inflexion and then a concave section rising (at the highest stress amplitudes) to the peak of the shock. It has been shown that the convex part of the pulse; from the first break from the elastic rise to the second point of inflexion on the rising pulse, corresponds to the mixed response region resulting from grain anisotropy [23]. The lower yield corresponds to slip in the basal plane and the upper to shock down the c-axis of the alumina grain which has no resolved stresses in this plane. In a polycrystalline target this means that an assemblage of elastically deformed grains exists within a matrix of plastically deformed grains favouring fracture at the weakly bound grain boundaries. Further twinning in the grains is favoured over slip and so fracture across grains down twin boundaries is also observed [24].

Figure 3 b) shows an experiment at the lower of these stress levels to ca. 10 GPa. The HEL of the ceramic, AD995 is 6.71 GPa [23]. The longitudinal and lateral stresses rise to the HEL quickly but then more slowly to the Hugoniot stress. Near to the impact face the stress remains high for around 500 ns before decaying to a lower value. Again, the material can display an elastic strength for some time before it returns to an inelastic state. The damaged material on the other hand has a failed strength of *ca*. 5 GPa at this stress level.

It may be hypothesized that the failed strength, determined in plate impact in the manner described for alumina above, might correlate with the penetration of a rod in a DoP test. A series of such experiments have been conducted and their results have been collated here to test this hypothesis. Further, the failed strengths of a range of ceramics corresponding to these ballistic experiments have been conducted and are documented elsewhere [12].

Figure 4 shows the data for three thicknesses of five ceramics placed onto a steel semi-infinite witness block and laterally confined, and impacted with the same projectile. The curves show the depth of penetration recorded in ceramic and steel, converted (in the Fig. 4 b). to areal density, ρ_A, to mediate for the differing densities encountered between the different ceramics thus

$$\rho_A = \rho_C t + \rho_{4340} d , \qquad (3)$$

where *t* represents the thickness of ceramic plate whose density is ρ_C, and *d* represents the penetration distance into 4340 (ρ_{4340}). There is an additional point where no ceramic plate was added to the block and impact was allowed to occur directly upon it.

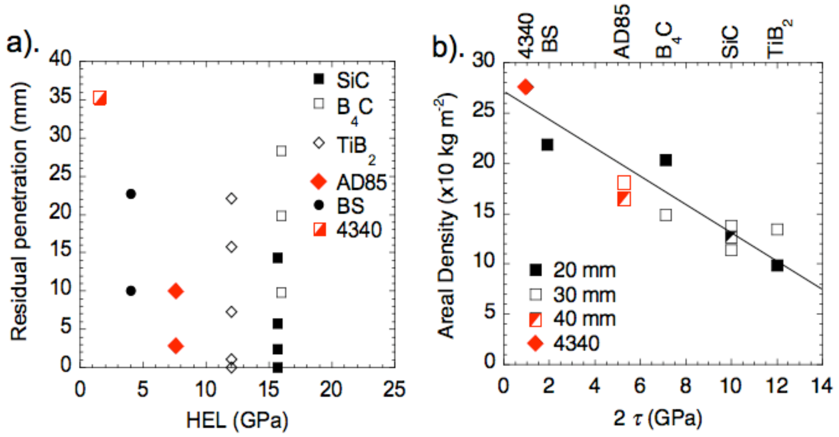

Figure 4a). Residual penetration *vs*. HEL for the six materials. b). Areal density *vs*. strength in the failed state for 4340 steel and armour ceramics subject to normal impact at 1750 m s^{-1}. Red points indicate the metal and alumina targets discussed earlier.

In all experiments, residual penetration depth was measured into a block of 4340 steel with ceramic tiles of different target strengths bonded to the front. Each tile/backing laminate was impacted by a 25.4 mm long, 6.35 mm diameter (L/D 4) tungsten rod at 1750±50 m s^{-1} [15]. One point, at a penetration depth of 35.3 mm, was obtained by the rod impacting a monolith consisting just of the semi-infinite 4340 steel backing block. Fig. 4 a). shows the correlation between penetration depth and strength. Clearly there is little obvious dependence discernable from this measure. Neither are there other correlations with other properties of the as received material. However, Fig. 4 b). shows a clear correlation between failed strength and areal density. Considering that there is a spread of velocities, and that a range of processes operate in the flow around a projectile through a comminuted ceramic that are not reproduced in plate impact, the relation is strong. It is particularly noticeable that the metal too follows the trend established by the ceramics. The points in red represent values for steel and alumina since these were discussed earlier. The steel is a BCC metal and shares some properties with the pure tantalum shown earlier. The AD85 has a lower alumina content than AD995 but similar mechanisms will be operating to define its response. It is interesting to note that the material with the highest HEL, B_4C, does not have the best performance as might be expected on the basis of purely its strength since beyond this elastic value its strength rapidly falls away relative to the other ceramics.

CONCLUSIONS

Results have been presented from a series of experiments in which the strength of ceramic facing materials has been related to ballistic performance of a laminate target. Continuum measurements of strength histories near the impact face of metals and ceramics have shown that the strength decays from an elastic to a plastic state with kinetics dependent upon operating mechanisms. In the case of BCC metals, high Peierls barriers to slip slow relaxation from an elastic to a plastic state in ca. 500 ns. In the case of glasses the material holds its elastic strength for a similar time before the strength starts to decay to its inelastic state by the interconnection of microcracks.

The alumina AD995 has grains, within which slip systems are limited, and a brittle intergranular glass phase. It too shows itself capable of retaining its elastic strength for around 500 ns before relaxing to a failed state. Shock and recovery of AD995 alumina has shown evidence of twinning in the grains above the lower elastic limit of the composite ceramic and trans- and intergranular fracture within the microstructure in this range.

Micromechanics control the conditioning of the impact zone ahead of an incoming penetrator and the density of nucleation sites and nature of fracture in the projectile’s path. Penetration depth into the ceramic scales with the failed strength of the materials independent of whether the targets are metals, brittle glasses or polycrystalline ceramics. The processes described above are operating in the initial stages of the impact process and at the surface where different process occur. The kinetics of damage and flow are set up in these initial states and the times taken for failure are of a different magnitude to those that occur in steady state penetration that occurs later. The nature of the states achieved however are material properties of the failed material and are related.

Thus the ultimate strength of strong ceramics controls conditions in the impact zone that define the failure of the material. This is a function of the point at which they undergo plastic flow. Failure in these materials is by micro-fracture which is a function of the density of defects activated by plasticity mechanisms within the grains and in the amorphous intergranular phase. Future work must completely define the mechanisms by which materials operate when subjected to load. Understanding the kinetics at work within the materials in these states will allow better design of protective structures for civilian protection in the future.

British Crown Copyright MoD/2010

REFERENCES

1. Y. M. Gupta: Mater. Res. Soc. Symp. Proc., 1999, 538, 139-150.
2. Y. M. Gupta: in 'Shock Compression of Condensed Matter - 1999', (eds. M. D. Furnish, et al.), 3-10; 2000.
3. Z. Rosenberg: in 'Shock and Impact on Structures', (eds. C. A. Brebbia, et al.), 73-105; 1994, Southampton, Computational Mechanics Publications.
4. N. K. Bourne, J. C. F. Millett, Z. Rosenberg, N. H. Murray: J. Mech. Phys. Solids, 1998, 46, 1887-1908.
5. N. K. Bourne, W. H. Green, and D. P. Dandekar: Proc. R. Soc. A 2006, 462(2074), 3197-3212.
6. J. Lankford: Intl. J. Applied Ceramic Technology, 2004, 1(3), 205-210.
7. V. P. Alekseevskii: Fizika Goreniya Vzryra, 1966, 2, 99.
8. A. Tate: J. Mech. Phys. Solids, 1967, 15, 387-399.
9. Z. Rosenberg, Y. Partom, and D. Yaziv, J. Appl. Phys., 1981, 52, 755-758.
10. Z. Rosenberg: in 'Shock Compression of Condensed Matter - 1999', (eds. M. D. Furnish, et al.), 1033-1037; 2000, Melville, New York, American Institute of Physics.
11. J. C. F. Millett, N. K. Bourne, and Z. Rosenberg, J. Phys. D: Appl. Phys., 1996, 29, 2466-2472.
12. N. K. Bourne: Int. J. Imp. Engng., 2008, 35, 674-683.
13. Z. Rosenberg, S. J. Bless, and N. S. Brar, Int. J. Impact Engng, 1990, 9, 45-49.
14. Z. Rosenberg and Y. Yeshurun: Int. J. Impact Engng, 1988, 7, 357-362.
15. J. Reaugh, A. Holt, M. Wilkins, B. Cunningham, B. Hord, A. Kusubov, Int.J.Imp.Eng., 1999, 23, 771-782.
16. Z. Rosenberg, E. Dekel, V. Hohler, A. J. Stilp, and K. Weber: in 'Shock Compression of Condensed Matter 1997', 917-920; 1998, Woodbury, New York, American Institute of Physics.
17. G. T. Gray III, N. K. Bourne, and J. C. F. Millett: J. Appl. Phys., 2003, 94, 6430-6436.
18. N. K. Bourne, G. T. Gray III, and J. C. F. Millett: J. Mat. Sci., 2009, in press.
19. N. K. Bourne, J. C. F. Millett, and J. E. Field: Proc. R. Soc.,1999, 455, 1275-1282.
20. N. K. Bourne and Z. Rosenberg: in 'Shock Compression of Condensed Matter 1995', (eds. S. C. Schmidt, et al.), 567-572; 1996, Woodbury, New York, American Institute of Physics.
21. N. K. Bourne, Z. Rosenberg, and J. E. Field: J. Appl. Phys., 1995, 78, 3736-3739.
22. D. E. Grady: 'Shock wave compression of brittle solids', Mech. Mater., 1998, 29, 181-203.
23. N. K. Bourne, J. Millett, M. Chen, D. P. Dandekar, J. W. MacCauley: J. Appl. Phys., 2007, 102, 073514.
24. M. W. Chen, J. W. McCauley, D. P. Dandekar, and N. K. Bourne: Nature Materials, 2006, 5(8), 614-618.

Proceedings of the SEM Annual Conference
June 7-10, 2010 Indianapolis, Indiana USA
©2010 Society for Experimental Mechanics Inc.

In-situ Optical Investigations of Hypervelocity Impact Induced Dynamic Fracture

Leslie E. Lamberson[1], Ares J. Rosakis
Graduate Aerospace Laboratories
California Institute of Technology
Pasadena, California 91125
Email: les@caltech.edu

Veronica Eliasson
Department of Mechanical & Aerospace Engineering
University of Southern California
Los Angeles, California 90089

ABSTRACT

Two independent optical methods are used to analyze the dynamic material behavior of Mylar and Homalite-100 subjected to hypervelocity impact. Birefringent targets are loaded in tension inside a two-stage light-gas gun vacuum chamber, and are impacted with a 5 mg nylon slug at velocities between 3 and 6 km/s. Caustics and photoelasticity combined with high-speed photography are used to determine dynamic stress intensity behavior around the crack tip during and after impact. Homalite-100 lower crack tip speeds are subjected to reflecting boundary shear waves from the nylon impact, and thereby the crack path exhibits distinct kinks; whereas Mylar higher crack tip speeds provides distinguishable isochromatic patterns and an unadulterated fracture surface. Shear wave patterns in the target from photoelastic effects are compared to results from numerical simulations using the Overture Suite, which solves linear elasticity equations on overlapping curvilinear grids by means of adaptive mesh refinement.

Introduction

Micrometeoroid and orbital debris (MMOD) damage from hypervelocity impact is a growing concern in space asset design. According to NASA Johnson's Orbital Debris Program Office there are currently over 7,000 pieces of tracked space debris in low Earth orbit (reaching up to 2 km above Earth's surface) over 1 cm in diameter and an estimated 50,000 pieces untracked of the same size [6]. Moreover, the International Space Station (ISS) currently has roughly 100 different types of MMOD shielding and still executes debris avoidance procedures [4]. While the size of the debris and micrometeoroids is relatively small, these impacts can induce strain rates up to $10^{-11}\mathrm{s}^{-1}$ and pressure rates in the Mbar range which can compromise the structural integrity as well as the optical, thermal or electrical functionality of a space vehicle. The threat of hypervelocity impact is real, yet little has been investigated involving the damage evolution resulting from these high-energy density events. This paper addresses the dynamic fracture behavior of brittle polymers subjected to hypervelocity impact.

While a generous amount of work has been done by NASA facilities investigating damage of various metals and composite materials from hypervelocity impacts, these studies mainly focus on generating equations to predict impact crater geometry [8]. What makes this study unique is that the dynamic fracture behavior of brittle polymers from this out-of-plane high-speed loading condition has never been rigorously investigated, yet brittle materials are often a critical component of space vehicles. For example, the James Webb Space Telescope scheduled to launch in 2013 has a tennis court sized sun-shield made of thin sheets of Kapton (a Mylar-like polymer) [1] and the newly finished Cupola on the ISS 'window to the world' is made from thick pieces of fused silica glass [5], while all windows on the current shuttle orbiter are a form of brittle

---

[1] Address all correspondence to this author.

T. Proulx (ed.), *Dynamic Behavior of Materials, Volume 1*, Conference Proceedings of the Society for Experimental Mechanics Series,
DOI 10.1007/978-1-4419-8228-5_6, © The Society for Experimental Mechanics, Inc. 2011

polymer. During hypervelocity impact, the incoming micrometeoroids and space debris are traveling at velocities at least 3 to over 10 times faster than the target material pressure wave speed, and as a result the inertial stresses outweigh the material strength in damage evolution.

The mechanics of a hypervelocity impact strike can be described from a fundamental perspective of a right-cylinder (length equal to diameter) impacting a semi-infinite plate of the same thickness as the projectile at a normal angle of incidence with hypervelocity speed. Upon contact, a shock wave travels to the rear of the projectile as well as to the rear of the target plate. At almost the same instant, rarefaction waves are generated on the boundary of impactor due to its much smaller size than the plate and propagate towards its axis of symmetry. A short time later the shock waves reach the rear surface of the plate and the projectile and reflect back as rarefaction waves to satisfy the stress free boundary conditions. The rarefaction waves can be thought of a tensile waves in the sense that if they are greater than the fracture strength of the material, the material will fracture (often as spall) in either the target or projectile material. When this occurs a new free surface is generated and a new rarefaction wave is created to satisfy the boundary conditions on the freshly created boundary. If the new rarefaction wave is greater than the fracture strength another fracture will occur, creating new spall and further damage. Consequently, the fracture process of hypervelocity impact can be described as a multiple spallation process initiated at fracture surfaces. Additionally, the initial shocking process is nonisentropic and rarefactions are isentropic. This mismatch in entropy generates energy often in the form of heat which contributes to the melting, vaporization and plasma formation at the strike site [3].

Experimental Configuration

Hypervelocity impacts were generated in the laboratory utilizing a two-stage light-gas gun jointly owned between NASA's Jet Propulsion Laboratory and the California Institute of Technology called the Small Particle Hypervelocity Impact Range (SPHIR). The two-stage light-gas gun creates micrometeoroid and orbital debris strikes initiating with a Sako 22-250 rifle action using 0.9 grams of smokeless gunpowder. This chemical ignition then sets in motion a small high-density polyethylene piston which compresses 150 psi of hydrogen in the pump-tube generating a high energy shock wave in stage one. From there, the gas is further accelerated in a small converging shape nozzle called the area-reservoir (AR) section where the piston gets extruded and stopped. On the downrange side of the AR section, a 5 mil thick film of Mylar is burst creating a uniform shock wave release on the launch package housed in the launch tube in stage two. In this case, launch packages are all nylon 6/6 right cylindrical slugs 5 mg with a length and diameter of 1.8 mm. Impact speeds ranged from 3 to 6 km/s. The projectile then goes into free flight under 1 Torr vacuum for 4 meters until striking the polymer plate in the target chamber. Two brittle polymer plates were considered in this investigation, Mylar and Homalite-100, between 1 and 6 mm in thickness and 150 mm in diameter. The plates were given notches and in some cases small pre-cracks (1-3 mm in length) and held in nominal tensile loads between 0.5 and 4 MPa on a load frame housed inside the target tank. These small loads helped to instigate mode-I crack growth (opening crack mode) and could serve as simulated membrane stresses of an external tank or cooling pipe or functional load on a working component of a space asset. A photograph of the SPHIR laboratory as well as a schematic of the optical diagnostics configuration is shown in Figures (1,2).

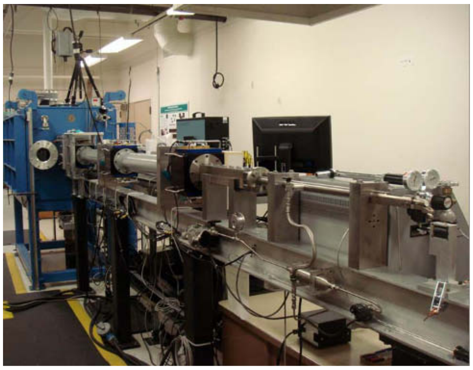

Figure 1: Photograph of SPHIR Laboratory.

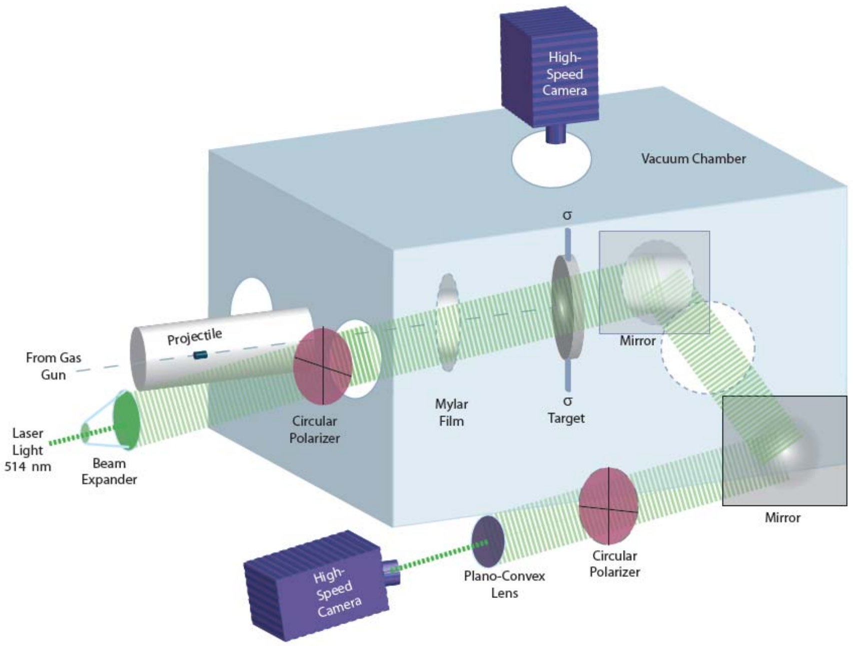
High-Speed Camera
Vacuum Chamber
σ
Mirror
Projectile
From Gas Gun
Laser Light 514 nm
Beam Expander
Circular Polarizer
Mylar Film
σ
Target
Mirror
Circular Polarizer
Plano-Convex Lens
High-Speed Camera

Figure 2: Schematic of optical diagnostics and high-speed photography configuration.

Method of Caustics

All optical analysis was performed in transmission. A monochromatic light source from an Argon-Ion laser was expanded to 100 mm diameter and fed into the target chamber of the two-stage light-gas gun, illuminating the target. A CORDIN 214-8 camera capable of capturing 8 frames at up to 100 million frames per second was set to focus on a virtual object plane at a distance z_0 behind the specimen. Due to the localized thinning at the crack tip, the incident light is refracted away generating a characteristic shadow spot near the region of the crack tip due to the displaced imaging plane [10]. While a circular polariscope was used to qualitatively investigate isochromatic patterns near the crack tip, caustics was used to quantitatively determine the energy ahead of the moving crack tip via the dynamic stress intensity factor. An example schematic of the caustics configuration is shown in Figure (3).

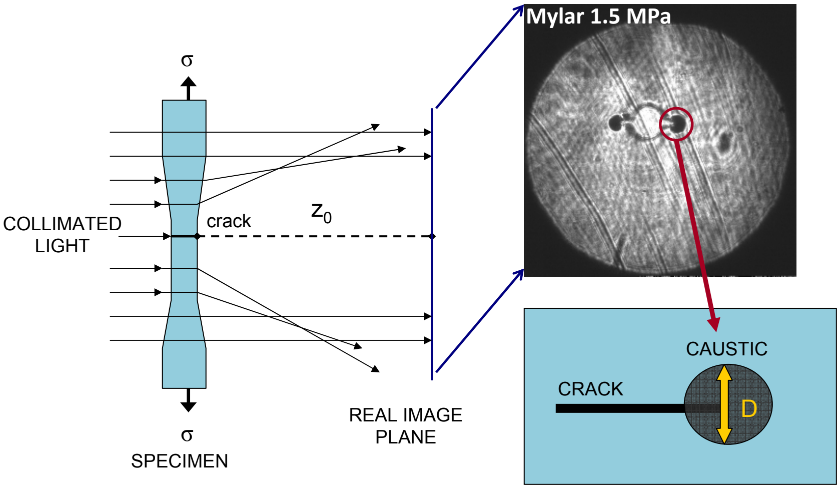
σ
COLLIMATED LIGHT
crack
z_0
σ
SPECIMEN
REAL IMAGE PLANE
Mylar 1.5 MPa
CAUSTIC
CRACK
D

Figure 3: Schematic of method of caustics in transmission.

The method of caustics uses the dimensions of the shadow or caustic formed which dictates the value of the stress intensity factor at that instant in time. Assuming the near-tip stress distribution is characterized by only the first term of the steady-state asmyptotic stress solution originally proposed by Griffith in steady-state expansion [7] and the initial curve is approximated by a circle, the equation expressing the relationship is as follows

$$K_I^{dyn} = \frac{2}{3}\frac{\sqrt{2\pi}}{z_0 C t}\left(\frac{D}{3.163}\right)^{5/2}\frac{4\beta_1\beta_2 - (1+\beta_2^2)^2}{(\beta_1^2-\beta_2^2)(1+\beta_2^2)} \tag{1}$$

where D is the transverse diameter of the caustic, C is the stress optic coefficient, t is plate thickness, z_0 is the distance between the screen and the specimen, and $\beta_1 = (1 - \nu^2/c_1^2)$ and $\beta_2 = (1 - \nu^2/c_2^2)$, ν being the crack speed and c_1 and c_2 being the dilatational and distortional wave speeds of the plate [2]. The 3.163 value is empirically determined for these materials assuming optical isotropy [11].

By using the method of caustics to determine K_I^{dyn} we are pre-supposing that the fracture behavior will remain K-I dominant at the crack tip even though it is instigated by an extreme out-of-plane dynamic loading event. Depending on the results, we can then determine both if our mode-I dominant fracture criterion is appropriate and if local symmetry typically assumed at the crack tip on more classical mixed-mode loading problems is a valid approach to characterizing this complex phenomenon [9].

Results

Crack velocities were averaged using a secant method. No statistically significant correlation was determined between the location of the hypervelocity impact and resulting crack tip speeds, nor with the incoming projectile velocity and the resulting crack tip speeds. Resulting dynamic stress intensity values nondimensionalized by the material equivalent static value is plotted versus the crack speed nondimensionalized by the material Rayleigh wave speed and shown in Figure (4). While crack speeds seemed to be slightly slower in Homalite-100, on average, this material also tended to exhibit more transient crack behavior ahead of the crack tip. The nature of the transient crack behavior could be seen both in the dynamically changing sizes of the caustics in time of Homalite-100 as well as the distinct jagged or kinking behavior exhibited in the microscopy of the resulting crack taken after the impact event.

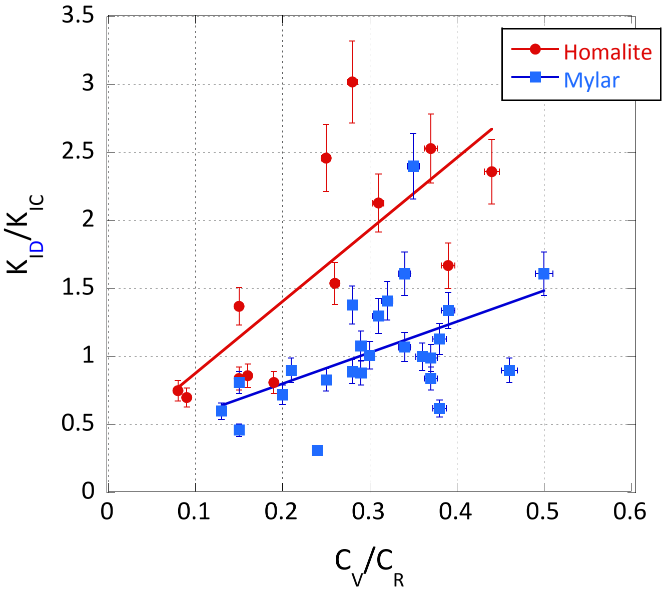

Figure 4: Plot of Mylar and Homalite-100 dynamic stress intensity factor normalized by static fracture toughness value versus the crack velocities normalized by the material Rayleigh wave speed.

Table 1: Summarized results of hypervelocity impact damage of brittle polymer investigation.

	Homalite-100	Mylar
P wave speed [m/s]	2145	2447
S wave speed [m/s]	1082	1185
Static Fracture Toughness [MPa/$\sqrt{m}$]	0.45	1.0
Averaged crack tip velocity [m/s]	230	330
Averaged Dynamic Stress Intensity [MPa/$\sqrt{m}$]	0.73	1.0
Crack path appearance	kinked	smooth

Generally, Mylar tended to transition from crack initiation to crack propagation sooner by approximately 20 ms than Homalite-100. Therefore, Mylar was able to completely fail before significant wave reflections and boundary interactions affected the moving crack. As a result, Mylar had a smooth and unadulterated crack path appearance and tended to follow directly behind the propagating shear wave from the impact site. Curiously, crack speeds remained relatively subsonic in nature, remaining between 0.2 to 0.5 the material Rayleigh wave speeds, yet there seemed to be an absence of extensive crazing ahead of the crack tip in Mylar. Branching was only seen when crack speeds reached its highest values in Homalite-100 and was not a common site along the crack path in post-analysis. Furthermore, Homalite-100 took longer to initiate cracking and as such had more complex wave action at the crack tip, most likely causing the crack path to continuously seek its local opening mode (or mode I crack growth) resulting in a kinked crack path appearance. Table (1) summarizes the results of the caustic investigation.

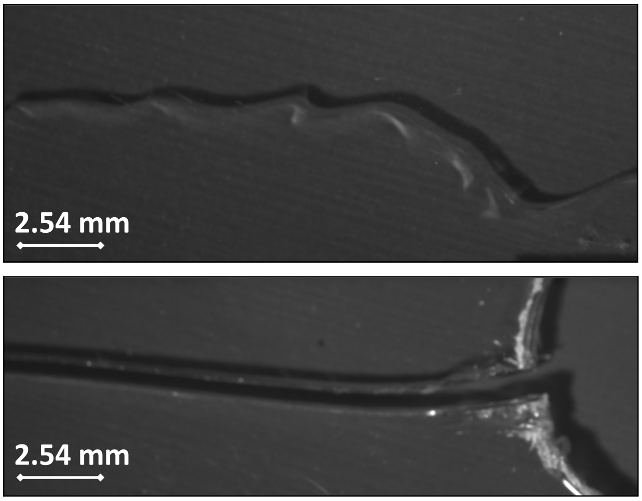

Figure 5: *(Top)* Homalite-100 microscopy image of kinked crack path appearance. *(Bottom)* Mylar microscopy image of smooth crack path appearance.

Overall the range of crack tip velocities and dynamic stress intensity values of both Mylar and Homalite-100 remained in a regime typically cited in literature under traditional in-plane lower loading rates to quasi-static loading rate behavior. The general noted trend of increasing dynamic stress intensity factor with increasing crack velocities can be seen. Error in the analysis predominantly came from the mismatch in the lack of temporal resolution in the full-field CORDIN images. Namely, the 8 images taken during the fracture initiated by the impact event had a 10 to 20 μs time scale, yet the behavior at the crack tip was dynamically changing on a time scale closer to 1 μs down to nanosecond scale. Additionally, the integrity of the measurement of the caustic could be questioned due to the multiple energetic phenomena happening in the region during impact including debris cloud and eject formation, vaporization of the projectile and melting. Despite of all the sources of error, the mixed-mode initiation loading conditions and the highly energetic interaction between the projectile and the target, the predominant failure mode remained in-plane. This is most likely due to the fact that the slowest moving Rayleigh wave did not have time to propagate and interact with the boundaries enough to generate an out-of-plane bending moment before fracture completed. Therefore, in averaged sense, K_I or opening mode fracture criterion is relatively valid even in the complex event of a micrometeoroid and orbital debris strike.

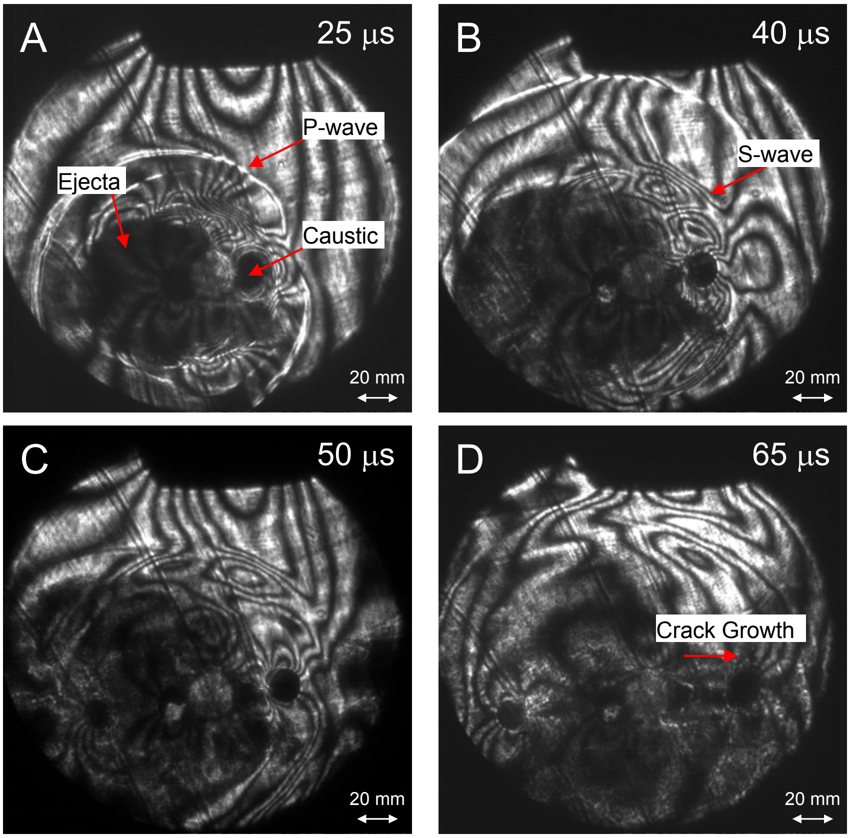

Figure 6: Caustics and isochromatic fringe patterns illustrating crack growth resulting from a hypervelocity impact strike on Mylar 1.6 mm thick at 5 km/s. (A) Shows initial P-wave radiating from impact site 25 μs after impact. Ejecta cloud at impact site can be seen. (B) Shows S-wave propagating soon after impact. Impact hole location and damage is clearly visible. (C),(D) Show noticeable crack growth via caustics as ejecta cloud disperses and stress wave patterns become more complex.

Next steps in this research include taking the results of the experimental fracture behavior of these brittle polymer plates under hypervelocity impacts and comparing them to numerical results from a 2-D in-plane code. In this case, initial endeavors in modeling the complex stress wave behavior from impact are being investigated using the Overture Suite, an adaptive mesh refinement finite difference method which solves the linear elasticity equations. Initial results indicate reasonable qualitative agreement in resulting wave pattern structure from computations and those captured with high-speed photography in the experiments. Future work will develop the code to output the difference in principle stress values in order to compare one-to-one with the isochromatic fringe patterns from the results at various times of interest during fracture. Lastly, future experimental investigations should probe conditions where, even in the averaged sense, the fracture criterion begins to fail by examining variables such as plate thickness (into plane strain regime), impact velocities, nominal tensile loads, initial crack sizes, and the like.

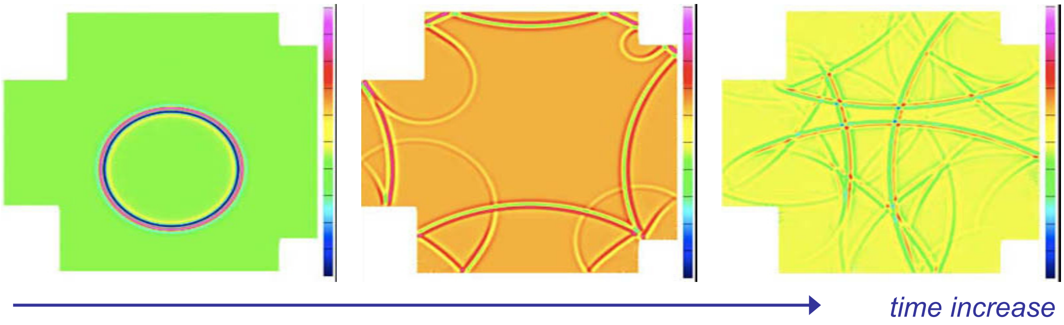

Figure 7: Example qualitative results from Overture of pressure wave patterns in Mylar from impact conditions as illustrated by color bar, which corresponds to the magnitude of the divergence. Left surface is clamped boundary condition, all others are free.

The authors acknowledge support from the Department of Energy Award DE-PS52-07NA28208 through the National Nuclear Security Administration, National Science Foundation Graduate Research Fellowship, as well as the NASA Aeronautics Scholarship Program through the American Society of Engineering Education.

References

[1] Jeanna Bryner. Huge sun shield built for space telescope. *SPACE*, December 2008.

[2] K. Ravi-Chandar C. Taudou. Experimental determination of the dynamic stress-intensity factor using caustics and photoelasticity. *Experimental Mechanics*, 32(3):203–210, 1992.

[3] A.R McMillan C.J. Maiden. An investigation of the protection afforded a spacecraft by a thin shield. *AIAA Journal*, 2(11):1992–1998, 1964.

[4] Aeronautics Committee on International Space Station Meteoriod/Debris Risk Management, Commission on Engineering Space Engineering Board, and National Research Council Technical Systems. *Protecting the Space Station from Meteoroids and Orbital Debris*. National Academy Press, 1997.

[5] Marcia Cunn. International space station gets a bay window. *Sci-Tech Today*, February 2010.

[6] Jr. D. F. Portree J. P. Loftus. Orbital debris: A chronology. Technical Report TP-1999-208856, NASA, 1999.

[7] L.B. Freund. *Dynamic Fracture Mechanics*. Cambridge University Press, 1990.

[8] S. A. Hill. Determination of an empirical model for the prediction of penetration hole diameter in thin plates from hypervelocity impact. *International Journal of Impact Engineering*, 30:303–321, 2004.

[9] K. Ravi-Chandar. Dynamic fracture of nominally brittle materials. *International Journal of Fracture*, 90:83–102, 1998.

[10] R. J. Rosakis S. Krishnaswamy. On the extent of dominance of asymptotic elastodynamic crack-tip fields; part i: and experimental study using bifocal caustics. *Journal of Applied Mechanics*, 8:87–95, 1991.

[11] George C. Sih, editor. *Experimental evalution of stress concentration and intensity factors*. Mechanics of Fracture 7. Martinus Nijhoff Publishers, 1981.

Proceedings of the SEM Annual Conference
June 7-10, 2010 Indianapolis, Indiana USA
©2010 Society for Experimental Mechanics Inc.

A Dynamic CCNBD Method for Measuring Dynamic Fracture Parameters

Feng Dai , Rong Chen and Kaiwen Xia [*]

Department of Civil Engineering and Lassonde Institute, University of Toronto
Toronto, Ontario, Canada M5S 1A4
*Corresponding author: kaiwen@ecf.utroronto.ca

Abstract: The cracked chevron notch Brazilian disc (CCNBD) method is widely used in characterizing static rock fracture toughness. We explore here the possibility of extending the CCNBD method to characterizing the dynamic fracture parameters of rocks. The relevant fracture parameters are the initiation fracture toughness, fracture energy, propagation toughness, and fracture velocity. The dynamic load is applied with a split Hopkinson pressure bar (SHPB) apparatus. A strain gauge is mounted on the sample surface near the notch tip to detect the fracture-induced strain release on the sample surface, and a laser gap gauge (LGG) is used to monitor the crack surface opening distance (CSOD) during the test. With dynamic force balance achieved in the tests, the stable-unstable transition of the crack propagation crack is observed and the initiation fracture toughness is obtained from the peak load. The dynamic fracture initiation toughness values obtained for the chosen rock (Laurentian granite) using this method are consistent with those reported in the literature. The fracture energy, propagation toughness and the fracture velocity are deduced using an approach based on energy conservation.

1 INTRODUCTION

Dynamic fracture is frequently encountered in various geophysical processes and engineering applications (e.g., earthquakes, airplane crashes, projectile penetrations, rock bursts and blasts). These processes are governed by rock dynamic fracture parameters, such as initiation fracture toughness, fracture energy, propagation fracture toughness, and fracture velocity. Therefore, accurate determination of these fracture parameters is crucial for understanding mechanisms of dynamic fracture and is also beneficial for hazards prevention and mitigation.
Most of the existing studies on rock fracture are focused on the fracture initiation toughness measurement, mainly under quasi-static loading conditions. Fracture initiation toughness depicts the material resistance to crack reactivation. For brittle materials such as rocks, one can not simply use the standard methods of fracture tests developed for metals. Special sample geometries have been developed for fracture toughness measurements for brittle solids like ceramics and rocks. For example, the International Society for Rock Mechanics (ISRM) recommended two methods with three types of core-based specimens for determining the fracture toughness of rocks: chevron bend (CB) and short rod (SR) specimens in 1988 [1], and cracked chevron notched Brazilian disc (CCNBD) specimen in 1995 [2].

Limited attempts have been made to measure the dynamic initiation fracture toughness of brittle solids, primarily due to the difficulties in experimentation and subsequent data interpretation. As reported by Böhme and Kalthoff [3], high loading rate test features significant inertial effect due to stress wave loading and this inertial effect complicates the data reduction. They demonstrated the inertial effect using a three point bending configuration loaded by a drop weight. They showed that the measured crack tip stress intensity factor (SIF) history using the shadow optical method of caustics did not synchronize with the load histories at supports. Tang and Xu [4] tried to measure dynamic fracture toughness of rocks using three point impact with a single Hopkinson bar, and Zhang et al. [5,6] employed the split Hopkinson pressure bar (SHPB) technique to measure the dynamic fracture toughness of rocks with SR specimen. In these attempts, the evolution of SIF and the fracture toughness were calculated using quasi-static formulas. However, because of the steep rising of the load, the inertial effect prevails and the resulting error is significant [7].

T. Proulx (ed.), *Dynamic Behavior of Materials, Volume 1*, Conference Proceedings of the Society for Experimental Mechanics Series,
DOI 10.1007/978-1-4419-8228-5_7, © The Society for Experimental Mechanics, Inc. 2011

To minimize the error induced by inertial effects, pulse shaping technique was employed to conduct dynamic fracture tests with the SHPB [8,9]. The pulse shaping technique [10,11] facilitates dynamic force equilibrium and thus minimizes inertial effects. The fracture sample is therefore in a quasi-static state of deformation. Indeed, as was observed by Owen et al. [12], the SIF value obtained by directly measuring the crack tip opening is consistent with that calculated with the quasi-static equation, as long as the dynamic force balance is roughly achieved in split Hopkinson tension bar tests. The dynamic fracture energy and the propagation fracture toughness of materials are directly related to the energy consumption during dynamic failures. For transparent polymers or polished metals, those properties could be readily measured with optical methods [12,13]. For rocks, the measurements on these fracture properties are rarely reported in the literature, albeit their direct relevance to the energy consumption during dynamic fracture [14].

Recently, a semi-circular bend (SCB) technique in SHPB tests has been proposed to measure dynamic fracture parameters of rocks [7]. Provided that the force balance is achieved with pulse shaping, the initiation fracture toughness can be obtained by substituting the peak load into the static calculation equation. A laser gap gauge (LGG) system was developed to measure the crack surface opening displacement (CSOD) history. From this history and the stress wave measurements in the bars, the average fracture energy, the average propagation fracture toughness, and the average fracture velocity were determined [7]. A fundamental prerequire for fracture testing via this dynamic SCB method was the fabrication of notch with a sharp tip. The authors first made a 1 mm notch in the semi-circular rock disc (with 40 mm in diameter) and then sharpened the crack tip with a diamond wire saw to achieve a tip radius of 0.25 mm. For the granite tested, the average grain size is about 0.5 mm. The radius of the tip is thus smaller than the thickness of naturally formed cracks in this rock. This argument is also supported by Lim et al. [15] that pre-cracking for certain rocks is not necessary if the notch is sufficiently small (<0.8 mm). Compared to coarse-grained rocks, pre-cracking is likely necessary whereas is tedious and difficult for fine-grained brittle materials, if it is not impossible.

To overcome the technical difficulties associated with making a sharp notch, V shaped (or chevron) notch (e.g. CB, SR and CCNBD specimens by ISRM suggested methods [1,2]) was proposed. The V shaped ligament facilitates crack initiation emanating from the notch tip and thus avoids pre-cracking in the brittle solids. The crack propagates in a stable fashion until it reaches the critical crack length where the crack growth transits to be unstable. If the load is static, the load reaches its maximum at this critical crack length while the corresponding SIF has a minimum value. The V notched specimen has been conducted in the SHPB fracture test for rocks [5,6], and ceramics [9]. Zhang et al. [5,6] conducted dynamic SHPB wedge tests with SR rock samples. Quasi-static equation proposed in the ISRM 1988 method was employed to determine the fracture toughness without evaluating the stress state in the sample. Weerasooriya et al. [9] employed a V notched four point bend specimen to measure dynamic initiation toughness of ceramics. They applied pulse shaping technique to achieve force balance in the SHPB tests. The time varying forces on both ends of the sample is almost the same during the loading. They thus concluded that the sample is in a quasi-static loading condition and a quasi-static data reduction is valid. We noticed that in these attempts on the dynamic initiation toughness measurements employing V notched samples [5,6,9], no detailed evaluation has been conducted on the measurement principles. In addition, key fracture parameters such as dynamic fracture energy and the propagation fracture toughness are not measured. A thorough investigation on the dynamic fracture test employing the sample with a chevron notch is thus desirable.

Among three standard ISRM specimens [1,2], the CCNBD specimen owns special merits such as higher failure load, fewer restrictions on the testing apparatus, larger tolerance on the specimen machining error, simpler testing procedure and lower scatter of test results [2]. The CCNBD method thus has been widely used [16,17] and is chosen in this research to conduct our dynamic tests.

In this study, we use a 25 mm SHPB system to load the CCNBD specimen. LGG [7] is used to monitor CSOD of the CCNBD specimen during SHPB testing. With pulse shaping technique employed, the dynamic forces on both ends of the sample are balanced. The stable-unstable transition of the fracture propagation is observed and the peak load matches in time with the transition point of the stable-unstable fracture propagation. The initiation fracture toughness is thus calculated with a quasi-static equation [2]. Based on the first law of thermodynamics, the fracture energy and the propagation toughness are obtained. Using the CSOD data, we can also distinguish the completion time of the stable and unstable fracture growth; the corresponding fracture velocities thus are estimated. We demonstrate our proposed methodology with Laurentian granite.

2 EXPERIMENTAL SETUP

2.1 Modified split Hopkinson pressure bar

A 25mm diameter SHPB system (Fig. 1) is used in this study. The SHPB, originally developed by Kolsky [18], has been widely employed to investigate mechanical properties of engineering materials at high strain rates. It is composed of a striker, an incident bar and a transmitted bar, all made of high strength maraging steel. The lengths of the striker bar, the incident (input) bar and the transmitted (output) bar are 200 mm, 1500 mm and 1000 mm respectively. One strain gauge is cemented on the incident bar with 787 mm away from the impact end of the bar to measure the incident and reflected waves (i.e. ε_i and ε_r); and another on the transmitted bar, 522 mm away from the sample to measure the transmitted wave (i.e. ε_t). Assuming one-dimensional stress wave propagation, the forces on both ends of the sample are [19]:

$$P_1 = A_0 E_0(\varepsilon_i + \varepsilon_r), P_2 = A_0 E_0 \varepsilon_t \tag{1}$$

where P_1 is the force on the incident end of the specimen, and P_2, the transmitted end. E_0 is Young's modulus of the bar material and A_0 is the cross-sectional area of the bar. A laser detector system is used to measure the velocity of the striker bar. An eight-channel Sigma digital oscilloscope is used to record and store the strain signals collected from the Wheatstone bridge circuits after amplification, together with the signal from LGG system as well as the strain gauge signal from the sample surface which will be discussed later.

The pulse shaper technique is used to achieve dynamic force equilibrium in the specimen during the experiment. This technique was discussed in detail by Frew et al. for SHPB tests of brittle materials [11] and was recently used by Xia et al. in rock compressive tests [20] and Dai et al. in rock tensile tests [21]. In conventional SHPB tests, the incident wave has a rectangular shape and thus a sharp rising edge. This may induce undesired damage to the sample upon impact of the incident bar with the specimen. In the current research, a C11000 copper disc is placed on the impact end of the incident bar to shape the incident wave from a rectangle pulse to a ramp pulse. In addition, a rubber disc is tipped in front of the copper shaper to further decrease the rising slope of the incident pulse.

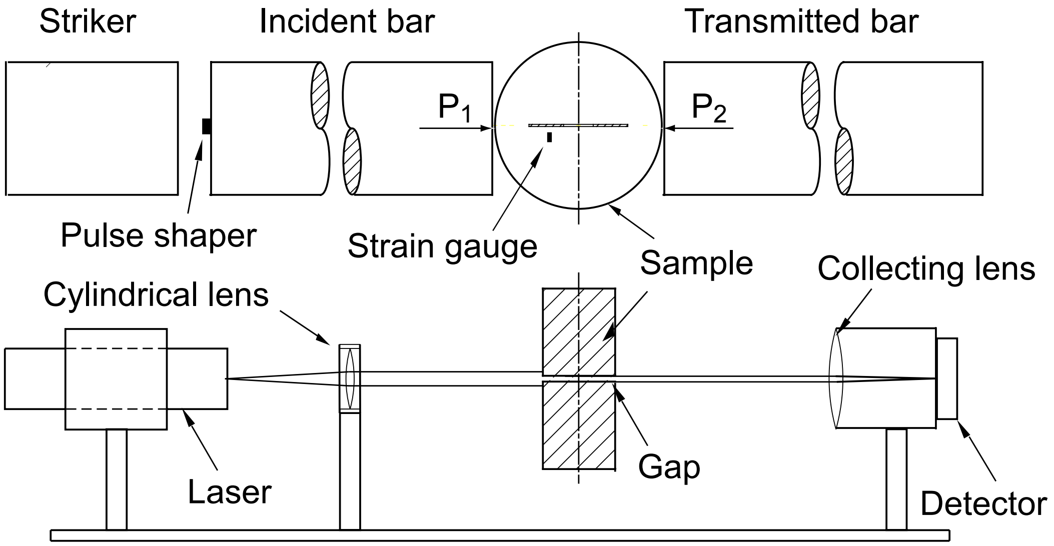

Fig. 1. Schematics of the spit Hopkinson pressure bar (SHPB) system and the laser gap gauge (LGG) system.

2.2 The Laser Gap Gauge system

The LGG system is developed to monitor the CSOD [7]. As shown schematically in Fig. 1, the system consists of two major components: the collimated line laser source and the sensing system. The plane of the laser sheet is orientated orthogonally to the CCNBD surface and the notch surface. The specimen blocks the laser sheet except the notched portion in the center. During the test, as the notch opens up, the amount of light passing through increases. This will lead to an increase of the voltage output from the detector. By recording this voltage output of the photodiode, the gap opening distance (i.e., CSOD) ant thus the opening velocity can be obtained with pre-calibration.

2.3 Sample configuration

Laurentian granite (LG) is selected in this study. It is a widely studied isotropic granite [22]. LG is from the Laurentian region of Grenville province of the Precambrian Canadian Shield, north of St. Lawrence and north-west of Quebec City, Canada. The mineral grain size of Laurentian granite varies from 0.2 to 2 mm with the average quartz grain size of 0.5 mm and the average feldspar grain size of 0.4 mm, with feldspar dominated (60 %) followed by quartz (33 %). Biotite grain size is of the order of 0.3 mm and constitutes 3–5 % of this rock. The physical and strength properties of LG are well documented in the literature[23].

Rock cores with a nominal diameter of 40 mm are first drilled from the rock block. We then slice the rock cores to obtain disk samples with an average thickness of 16 mm. All these disk samples are polished afterwards. A diamond impregnated blade saw is used to fabricate the notch in the middle of the disc. The geometry of the CCNBD specimen is shown in Fig. 2. All the dimensions are normalized by the specimen radius R as shown in Table 1. A strain gauge is cemented on the sample surface to monitor the fracture initiation and propagation during the test. The crack emits elastic release wave upon fracture initiation and propagation, and this wave causes changes in the recorded strain gauge signal [24].

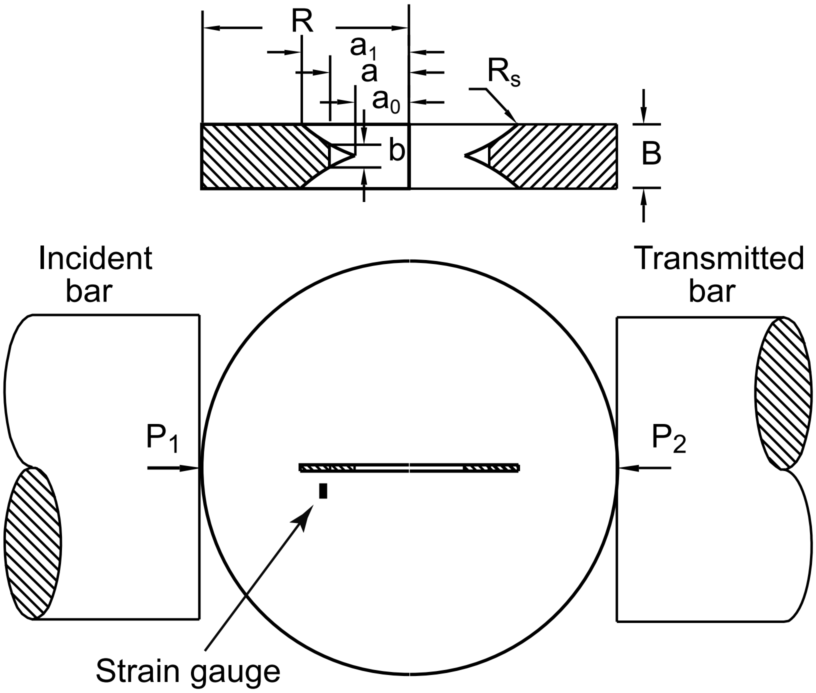

Fig.2 The CCNBD specimen in the SHPB system.

Table 1 CCNBD geometrical dimensions used in this study

Descriptions	Values (mm)	Dimensionless expression
Diameter D (mm)	40.0	
Thickness *B* (mm)	16.0	$\alpha_B = B / R = 0.800$
Initial crack length a_0 (mm)	3.57	$\alpha_0 = a_0 / R = 0.179$ $\alpha_1 = a_1 / R = 0.593$
Final crack length a_1 (mm)	11.85	$\alpha_s = D_s / D = 0.625$
Saw diameter *D*s (mm)	25	

3 MEASUREMENT PRINCIPLES

3.1 Initiation fracture toughness

Provided a quasi-static state of the specimen has been achieved during the SHPB test with pulse shaping, the initiation fracture toughness KIC of CCNBD specimen is then determined by the ISRM suggested method [2]:

$$K_{IC} = \frac{P_{\max}}{B\sqrt{R}} Y^*_{\min} \tag{2}$$

where Pmax is the measured maximum load, B and R are the thickness and radius of the disc respectively, $Y^*_{\min}$ is the minimum value of Y^*, and Y^* is the dimensionless SIF and can be determined in advance by numerical calibrations according to Eq. (3):

$$Y^* = K_I /(\frac{P}{B\sqrt{R}}) \tag{3}$$

As a critical factor for determining fracture toughness, $Y^*_{\min}$ corresponds to the dimensionless SIF at the critical dimensionless crack length αm (αm = am /R and am is the critical crack length), where the load is maximum.

For a given CCNBD sample configuration, the critical dimensionless SIF $Y^*_{\min}$ can be found from the ISRM suggested method [2]. However, the corresponding critical dimensionless crack length α_m is not explicitly documented [2]. A commercial finite element analysis software ANSYS is used in this work to determine the critical dimensionless crack length α_m and the corresponding dimensionless SIF $Y^*_{\min}$ .To achieve accurate SIF values, a sub-modeling technique is adopted to achieve a fine mesh zone around the crack front. A typical sub-modeling sequence is twofold in practice. A full-model, generally with a coarse mesh, is first analyzed. This is followed by analyzing the zone of interest sliced from the full model using a finely meshed sub-model. Sub-modeling is also known as the cut-boundary displacement method or the specified boundary displacement method. The boundary of the sub-model inherits the displacement obtained from the analysis of the full model [25]. Before we calculate the SIF of the CCNBD specimen, the analysis capabilities of the ANSYS sub-modeling technique on three dimensional crack problems are evaluated by several benchmark problems, involving the calculation of SIFs for a penny-shaped crack and an elliptic crack in an infinite domain under remote uniform traction. The results are highly satisfactory, with the maximum error less than 0.4% compared to the theoretical results. We then conduct elaborate analysis on the CCNBD specimen with the ANSYS sub-modeling technique. Due to symmetry, one eighth of the specimen is first modeled. Solid 92 elements (10-node tetrahedral structural solid) are used in the mesh. The total model is meshed with 34907 elements and 50427 nodes as shown in Fig. 3. We cut a brick from the model enclosing the straight crack front (shown in Fig. 3) and analyze it as a sub-model. Solid 95 elements (20-node brick shaped element) are used. This sub-model is meshed with 6258 elements and 25829 nodes as shown in Fig. 4. Specifically, to simulate the stress singularity of $r^{-1/2}$ near the crack tip (r is the radius to the crack tip), quarter-nodal elements [26] are used to mesh the region adjacent to the crack front. For the CCNBD sample configurations used in this research (see Table 1.), the calculated dimensionless SIFs vary with the dimensionless crack length α (Fig. 5) [27]. $Y^*_{\min}$ is found as 0.6 and the corresponding critical dimensionless crack length α_m is 0.43.

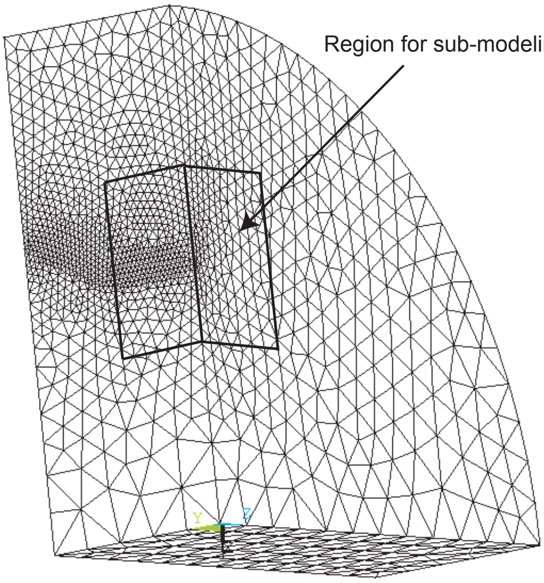

Fig. 3 Mesh of one eighth of the CCNBD specimen as well as the cut-boundary of the sub-model.

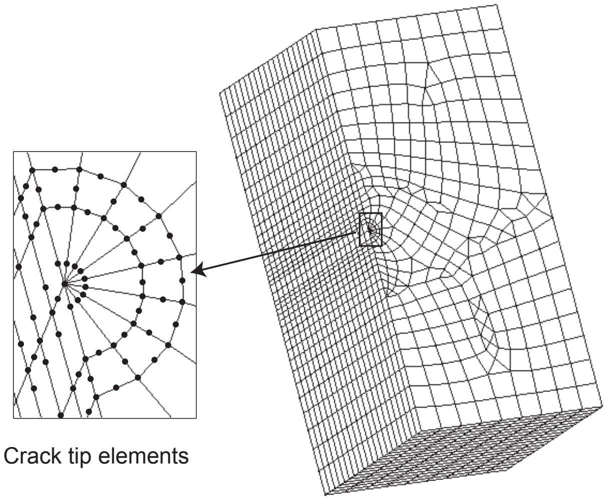

Fig.4 Mesh of the sub-model; a close view of the crack tip elements is also illustrated.

3.2 Fracture energy and propagation toughness

Based on the first law of thermodynamics, the energy consumed during dynamic fracture in SHPB test can be quantified [7]. During the dynamic test, the energy dissipation (ΔW) pertaining to the CCNBD specimen is the energy difference between the input energy (Wi) and the summation of the energy reflected (Wr) and transmitted (Wt):

$$\Delta W = W_i - W_r - W_t \tag{4}$$

where W is the energy carried by the stress wave can be calculated as follows [28]:

$$W = \int_0^t E_0 \varepsilon^2 A_0 C_0 d\tau \tag{5}$$

where E_0 and C_0 are the Young's modulus and wave speed of the bar material respectively. A0 is the cross-sectional area of the bar and ε denotes the time-resolved strain induced by the stress wave. This energy dissipation ΔW has two parts: the energy consumed to create new crack surfaces WG and the residue kinetic energy in the two cracked fragments K. The kinetic energy K can be calculated with $K = mv^2/2$, where m is the mass of the specimen and v is the translation velocity of the fragment, which can be deduced from the CSOD history data using with our optical device. The energy consumed in generating new cracks thus can be reduced as WG = ΔW - K. Consequently, the average propagation fracture energy is determined with Eq. (6) below:

$$G_c = W_G / A_c \tag{6}$$

where Ac is the area of the new generated crack surfaces. Assuming plane strain, the average dynamic propagation fracture toughness can be attained:

$$K_I^P = \sqrt{G_c E / (1 - \nu^2)} \tag{7}$$

where E and v are the Young's modulus and Poisson's ratio of the sample material respectively.

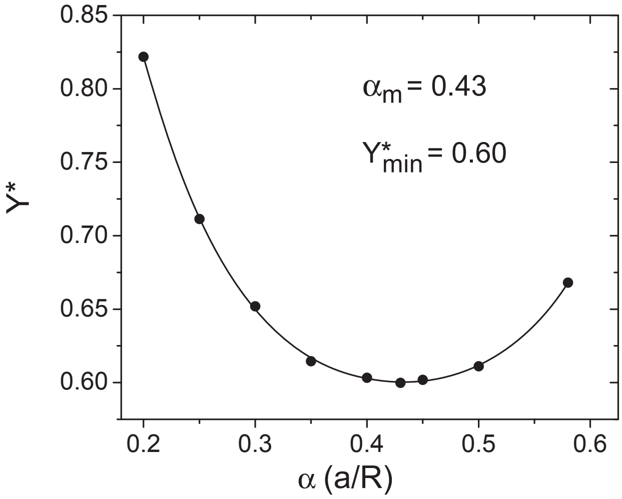

Fig.5 The dimensionless SIF of CCNBD specimen.

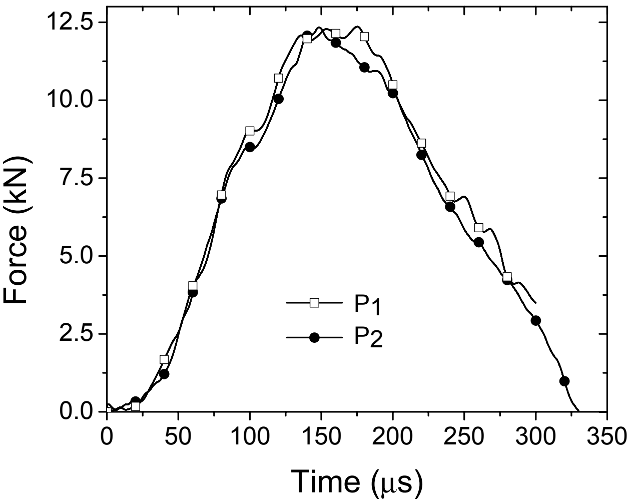

Fig.6 Dynamic force balance in a typical CCNBD-SHPB test with pulse shaping.

4. RESULTS

4.1 Stable-unstable crack propagation transition

We employ pulse shaping technique for all our dynamic CCNBD tests. The dynamic forces on both loading ends of the sample are critically assessed (Eq. 1). To compare the dynamic force histories, the time zeros of the incident and reflection stress waves are shifted to the sample-incident bar interface and the time zero of the transmitted stress wave is shifted to the sample-transmitted bar interface invoking 1D stress wave theory. Hereafter, a typical dynamic CCNBD test is shown and discussed. Fig. 6 compares the time-varying forces on both ends of the sample for this test. The dynamic forces on both sides of the samples are almost identical throughout the dynamic loading period. Obviously, the dynamic forces on both ends of the sample are balanced and the inertial effects are thus eliminated because there is no global force difference in the specimen to induce inertial force [8, 14].

Fig. 7 shows the measured CSOD by LGG as well as the strain history measured with the gauge mounted on the sample, along with the transmitted force (P2) in the SHPB test. With dynamic force balance (Fig. 6), the transmitted force P_2 can be regarded as the loading to the sample, as in the quasi-static case. The strain gauge signal is used to detect the fracture initiation and propagation. The fracture initiation from the notch tip will result in a decrease in the strain gauge signal, denoted as point C in Fig. 7. This fracture initiation coincides with the turning point A in the loading. After this instant, to further drive the propagation of the crack, the load has to increase until the peak point B. At this instant, the crack reaches the critical crack length (with dimensionless crack length α_m) and the unloading starts due to transition of crack growth from stable to unstable. The peak B of P2 occurs at time 149 μs, 4 μs after the critical crack length is reached as indicated on the strain gauge signal as point D. We believe that the peak of the loading corresponds to the moment when the crack reaches the critical crack length. The delay in time between point B and D can be explained in this way. The load on the specimen increases before the propagating crack reaches critical crack length, when the release waves are emitted at the sound speed of the rock material. The distance between crack tip and the transmitted loading end is about 20 mm and it thus takes around 4 μs for the first release wave to reach the transmitted end of the specimen. It is noted also that the measured CSOD curve from the LGG system exhibits an obvious linear segment after point E is reached at 227 μs. The slope of this linear segment indicates constant departure velocity of the two fractured fragments. The point E thus designates the complete separation of the two fragments of the CCNBD specimen.

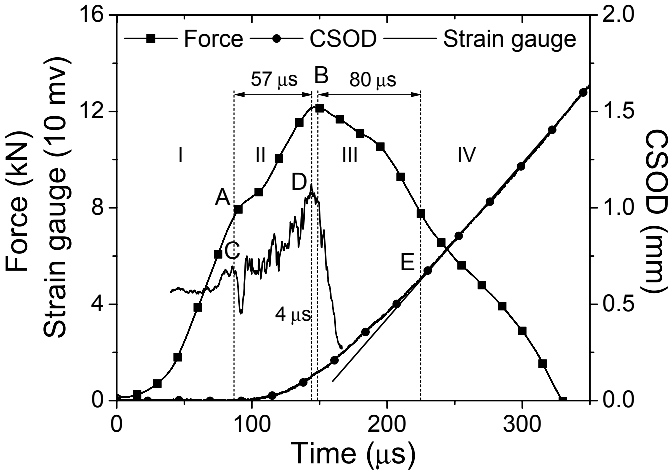

Fig.7 LGG measured CSOD and strain gauge signal along with the transmitted force in a SHPB test with pulse shaping.

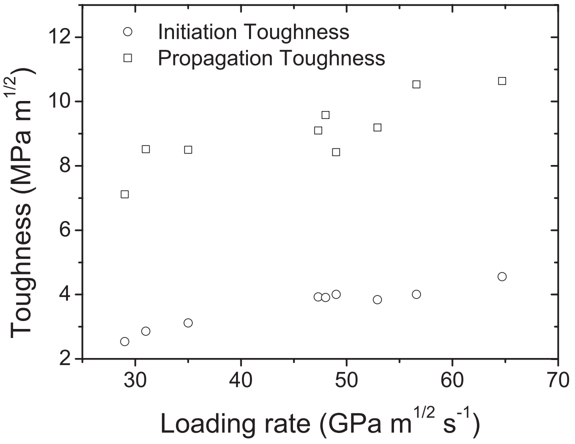

Fig.8 The effect of loading rate on the fracture initiation toughness and the average propagation toughness.

The dynamic fracture process of the CCNBD specimen in SHPB test can be divided into four stages, separated by three vertical lines through points A, B, and E (denoted by I-IV in Fig. 7). The elastic deformation of the CCNBD specimen dominates stage I. At the end of the stage I, the crack initiates from the notch tip, and propagates until the turning point B, when the propagating crack reaches the critical crack length am (stage II). We believe that point B designates the transition of stable to unstable crack propagation. In stage II, the crack propagates stably while in stage III, the crack propagates in an unstable manner. Finally, the sample is cracked completely into two half fragments in stage IV.

Both stable and unstable crack propagation velocities can be estimated. For the typical test, the stable crack propagation lasts around Δts = 57 μs in stage II and the distance of the crack propagation during this stage can be calculated by our finite element analysis: Ls = a_m - a_0 = 5.0 mm. The average velocity of the stable crack growth is then Vs = Ls / Δts = 88 m/s. The unstable crack propagation, shown in stage III, lasts around Δtus = 80 μs. The unstable crack growth distance Lus = R - am = 11.4 mm. The average unstable crack propagation velocity is thus determined as Vus = Lus / Δtus = 143 m/s.

4.2 Fracture initiation and propagation toughness

Fig. 8 illustrates the measured dynamic mode-I fracture initiation toughness and the average propagation toughness of LG with respect to the loading rate. The fracture loading rate is determined from the slope of the loading curve before fracture initiation. Within the range of loading rates from 30 to 70 GPa $m^{1/2}s^{-1}$, both toughness values increase almost linearly with the loading rate. Fig. 9 shows the average stable and unstable fracture velocities as a function of the loading rate. The unstable fracture velocity is always larger than the stable fracture velocity for each test (two to three times). It is also noticed that both velocities are weakly dependent on the loading rate.

The measured fracture initiation toughness values from our dynamic CCNBD method are comparable with those from dynamic SCB tests [7] as shown in Fig. 10. We are thus confident that the measured fracture initiation toughness results from dynamic CCNBD tests are reliable. It is noticed that we can not compare the fracture energy values obtained from both methods. This is because of the difference in failure mode of the two specimen configurations: unstable fracture for SCB and stable-unstable fracture transition for CCNBD. The fracture energy or fracture propagation toughness is strongly influenced by the mode of failure. As a consequence of this difference in failure modes, the variation of fracture velocity observed in dynamic SCB tests [14] is missing for the dynamic CCNBD results (Fig. 9), where the stable and unstable fracture velocities are almost constant.

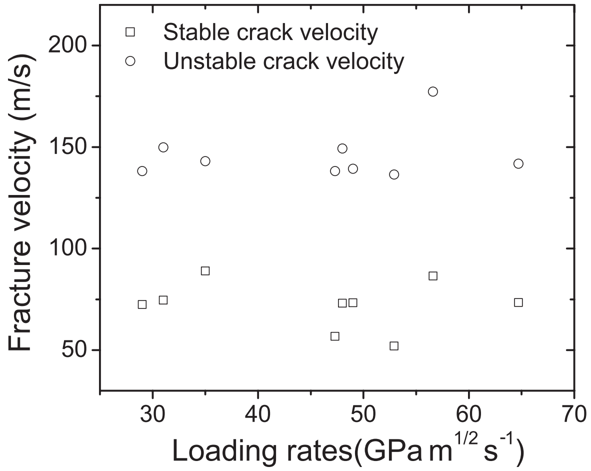

Fig.9 The average stable and unstable crack velocities as a function of the loading rate.

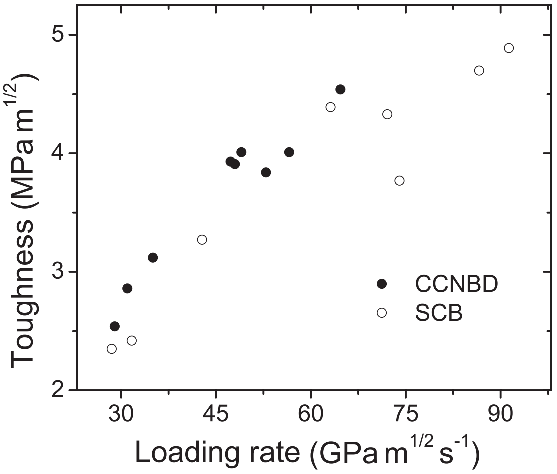

Fig.10 Comparison of the initiation toughness from the CCNBD method and the SCB method[7].

5 CONCLUSIONS

We proposed a SHPB fracture testing technique using ISRM suggested method-cracked chevron notch Brazilian disc (CCNBD) for determining the dynamic mode-I fracture parameters of rocks. Using this dynamic CCNBD method, various fracture parameters can be determined. Laurentian granite is employed to demonstrate this feasibility of this method. A strain gauge is mounted on the sample surface near the notch tip to monitor the fracture initiation and propagation. A LGG system is utilized to measure the CSOD history of the sample. Combined with SHPB measurements, the crack initiation from the notch tip, the transition of stable-unstable crack growth and the complete cracking of the sample are explicitly observed, provided the dynamic forces are balanced during the SHPB testing. Consequently, the dynamic initiation fracture toughness, the dynamic fracture energy, the propagation fracture toughness and fracture velocity are calculated. Both the initiation and propagation toughness of studied rock are loading rate dependent. The propagation toughness is larger than the initiation toughness in a given test. This dynamic CCNBD technique is readily to be implemented and thus can be applied to investigating dynamic fracture mechanics of a variety of rocks.

Acknowledgements

F.D. and K.X. acknowledge the support by NSERC/Discovery Grant No.72031326. R.C. is partially supported by China Scholarship Council for his research in University of Toronto.

References

[1] Ouchterlony F. "Suggested methods for determining the fracture toughness of rock", International Journal of Rock Mechanics and Mining Sciences & Geomechanics Abstracts 25(2): 71-96 (1988).
[2] Fowell R. J., Hudson J. A., Xu C. et al. "Suggested method for determining mode-I fracture toughness using cracked chevron-notched Brazilian disc (CCNBD) specimens", International Journal of Rock Mechanics and Mining Sciences & Geomechanics Abstracts 32(1): 57-64 (1995).
[3] Böhme W., Kalthoff J. F. "The behavior of notched bend specimens in impact testing", International Journal of Fracture 20(4): R139-R143 (1982).
[4] Tang C. N., Xu X. H. "A new method for measuring dynamic fracture-toughness of rock", Engineering Fracture Mechanics 35(4-5): 783-789 (1990).
[5] Zhang Z. X., Kou S. Q., Yu J. et al. "Effects of loading rate on rock fracture", International Journal of Rock Mechanics and Mining Sciences 36(5): 597-611 (1999).
[6] Zhang Z. X., Kou S. Q., Jiang L. G. et al. "Effects of loading rate on rock fracture: fracture characteristics and energy partitioning", International Journal of Rock Mechanics and Mining Sciences 37(5): 745-762 (2000).

[7] Chen R., Xia K., Dai F. et al. "Determination of dynamic fracture parameters using a semi-circular bend technique in split Hopkinson pressure bar testing", Engineering Fracture Mechanics 76(9): 1268-1276 (2009).

[8] Jiang F. C., Vecchio K. S. "Experimental investigation of dynamic effects in a two-bar/three-point bend fracture test", Review of Scientific Instruments 78(6): 063903 (2007).

[9] Weerasooriya T., Moy P., Casem D. et al. "A four-point bend technique to determine dynamic fracture toughness of ceramics", Journal of the American Ceramic Society 89(3): 990-995 (2006).

[10]Frew D. J., Forrestal M. J., Chen W. "A split Hopkinson pressure bar technique to determine compressive stress-strain data for rock materials", Experimental Mechanics 41(1): 40-46 (2001).

[11]Frew D. J., Forrestal M. J., Chen W. "Pulse shaping techniques for testing brittle materials with a split Hopkinson pressure bar", Experimental Mechanics 42(1): 93-106 (2002).

[12]Owen D. M., Zhuang S., Rosakis A. J. et al. "Experimental determination of dynamic crack initiation and propagation fracture toughness in thin aluminum sheets", International Journal of Fracture 90(1-2): 153-174 (1998).

[13]Xia K., Chalivendra V. B., Rosakis A. J. "Observing ideal "self-similar" crack growth in experiments", Engineering Fracture Mechanics 73(18): 2748-2755 (2006).

[14]Bertram A., Kalthoff J. F.,"Crack propagation toughness of rock for the range of low to very high crack speeds", in Advances in Fracture and Damage Mechanics Key engineering materials, Trans Tech Publications, Uetikon-Zurich, Vol. 251-252, pp. 423-430, (2003).

[15]Lim I. L., Johnston I. W., Choi S. K. et al. "Fracture testing of a soft rock with semicircular specimens under 3-point bending. 1. Mode-I", International Journal of Rock Mechanics and Mining Sciences & Geomechanics Abstracts 31(3): 185-197 (1994).

[16]Dwivedi R. D., Soni A. K., Goel R. K. et al. "Fracture toughness of rocks under sub-zero temperature conditions", International Journal of Rock Mechanics and Mining Sciences 37(8): 1267-1275 (2000).

[17]Iqbal M. J., Mohanty B. "Experimental calibration of ISRM suggested fracture toughness measurement techniques in selected brittle rocks", Rock Mechanics and Rock Engineering 40(5): 453-475 (2007).

[18]Kolsky H. "An investigation of the mechanical properties of materials at very high rates of loading", Proceedings of the Royal Society A-Mathematical Physical and Engineering Sciences B62: 676-700 (1949).

[19]Kolsky H. "Stress waves in solids", Clarendon Press, Oxford, pp. 212 (1953).

[20]Xia K., Nasseri M. H. B., Mohanty B. et al. "Effects of microstructures on dynamic compression of Barre granite", International Journal of Rock Mechanics and Mining Sciences 45(6): 879-887 (2008).

[21]Dai F., Xia K. W., Luo S. N. "Semi-circular bend testing with split Hopkinson pressure bar for measuring dynamic tensile strength of brittle solids", Review of Scientific Instruments 79(12) (2008).

[22]Nasseri M. H. B., Mohanty B. "Fracture toughness anisotropy in granitic rocks", International Journal of Rock Mechanics and Mining Sciences 45(2): 167-193 (2008).

[23]Iqbal N., Mohanty B. "Experimental calibration of stress intensity factors of the ISRM suggested cracked chevron-notched Brazilian disc specimen used for determination of mode-I fracture toughness", International Journal of Rock Mechanics and Mining Sciences 43(8): 1270-1276 (2006).

[24]Jiang F. C., Liu R. T., Zhang X. X. et al. "Evaluation of dynamic fracture toughness K-Id by Hopkinson pressure bar loaded instrumented Charpy impact test", Engineering Fracture Mechanics 71(3): 279-287 (2004).

[25]ANSYS Inc. Advanced Analysis Techniques Guide (1999).

[26]Barsoum R. S. "Triangular quarter-point elements as elastic and perfectly-plastic crack tip elements", International Journal for Numerical Methods in Engineering 11(1): 85-98 (1977).

[27]Fowell R. J., Xu C. "The use of the cracked Brazilian disc geometry for rock fracture investigations", International Journal of Rock Mechanics and Mining Sciences & Geomechanics Abstracts 31(6): 571-579 (1994).

[28]Song B., Chen W. "Energy for specimen deformation in a split Hopkinson pressure bar experiment", Experimental Mechanics 46(3): 407-410 (2006).

Proceedings of the SEM Annual Conference
June 7-10, 2010 Indianapolis, Indiana USA
©2010 Society for Experimental Mechanics Inc.

New ‘Fish Tank’ approach to evaluate durability and dynamic failure of marine composites

Arun Krishnan and L. Roy Xu[1]
Department of Civil and Environmental Engineering
Station B 351831, Vanderbilt University, Nashville, TN 37235, USA

ABSTRACT

The major objectives of this paper include: 1) developing a novel approach to accurately simulate the material/mechanics conditions of composite structures in seawater; 2) characterizing the impact damage, and the residual compression strength of marine composites as a function of time of seawater exposure; and 3) conducting a combined experimental and numerical investigation of the compression failure of marine composite with impact damage. In this study, a new composite “fish tank” approach was developed. Four E-glass/vinyl ester composite specimens were weakly bonded together and inserted into a polymethyl methacrylate (PMMA) base plate. Only one surface of the composite specimen was exposed to seawater. This surface will be subjected to the drop weight impact, which is very similar to the dynamic failure of ship structures subjected to underwater explosion. The specimens will then be subjected to compression until failure. For the simulation of the compressive failure after impact, finite element method with cohesive element was employed.

INTRODUCTION

Composites are frequently used in naval construction and in underwater structures. Constant exposure to seawater makes durability and dynamic failure properties critical for naval composite ships. However, previous approaches and measurements have significantly underestimated the actual durability of a composite structure inside seawater. For a composite ship as shown in Fig. 1, a rectangular composite specimen, which is a part of an “infinite” large panel, only has one external face exposed to seawater.

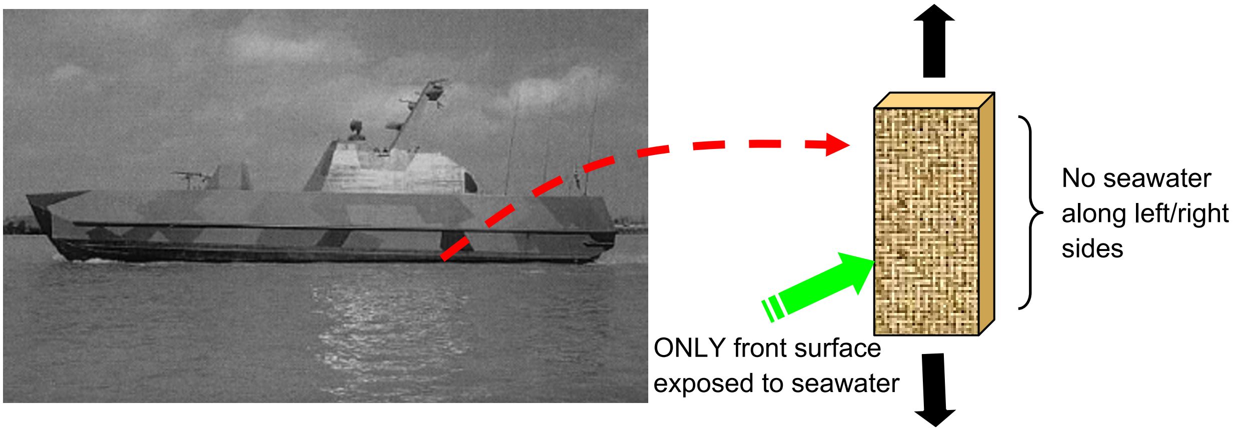

Fig. 1 A composite sample from a composite ship should represent the actual material and loading conditions--- its left/right sides and back surface are not exposed to seawater

During an underwater explosion, only this front surface is subjected to shock loading first. During the life time of the composite ship only the front surface of a composite panel will be directly exposed to seawater. Therefore, property degradation and damage from the front surface will be a major issue to determine the durability and life of the composite ship structure. However, almost all previous experiments have ignored this “single-surface environment effect”. For example, Karasek et al. [1] have evaluated the influence of temperature and moisture on the impact resistance of epoxy/graphite fiber composites. They found that only at elevated temperatures did

---

[1] Corresponding Author, Tel: 615-343-4891, Fax: 615-322-3365. E-mail: l.roy.xu@vanderbilt.edu

T. Proulx (ed.), *Dynamic Behavior of Materials, Volume 1*, Conference Proceedings of the Society for Experimental Mechanics Series,
DOI 10.1007/978-1-4419-8228-5_8, © The Society for Experimental Mechanics, Inc. 2011

moisture have a significant effect on damage initiation energy and that the energy required to initiate damage was found to decrease with temperature. Impact damage resistance and tolerance of two high performance polymeric systems was studied after exposure to environmental aging. For cross-ply laminates, the post-impact tensile strength values fell significantly (by maximum 70–75% of original composite strength) depending on ageing time, environment and impact velocity. Sala [2] found that barely visible impact damage, due to the impact of 1 J/mm (for 2.2-mm laminate thickness) increased the moisture saturation level from 4.8% to 6% for aramid fiber-reinforced laminates and enhanced the absorption rate. Very recently, Imielinska and Guillaumat [3] investigated two different woven glass–aramid-fiber/epoxy laminates subjected to water immersion ageing followed by instrumented low velocity impact testing. The impacted plates were retested statically in compression to determine residual strength for assessment of damage tolerance. The delamination threshold load and impact energy absorption were not significantly affected by the absorbed water. Due to low fiber–matrix adhesion, the prevailing failure modes at low impact energy were fiber/matrix debonding and interfacial cracking. The compression strength suffered significant reductions with water absorbed (28%) and impact (maximum 42%). In addition to impact experiments, other mechanical experiments related to seawater durability also reported similar approaches using fully immersed composite specimens [4-7]. In these previous specimens, property degradation such as matrix cracks in two vertical edges occurred, while these cracks never had the chance to initiate in a closed-edge, “infinite large” composite ship hull. Therefore, the previous data significantly underestimated the actual durability of composite structures inside seawater. In this paper, our new “composite fish tank” will provide more accurate measurements for composite durability.

MATERIALS AND SAMPLE PREPARATION

Glass fiber reinforced vinyl ester (glass/VE) panels were produced using vacuum assisted resin transfer molding (VARTM) by Prof. U. Vaidya’s group at the University of Alabama at Birmingham [8]. Eight layers of plain weave glass fabric (CWR 2400/50 plain weave, Composites One, LLC) were used to produce the panels with approximately 5mm thickness which is required by ASTM D 7137 “Standard Test Method for Compressive Residual Strength Properties of Damaged Polymer Matrix Composite Plates”. The fiber fraction of the panels was found to be 54% vol. after burn off testing was conducted. Compression after impact (CAI) testing samples with a dimension of 101.6 mm x 152.4 mm (4” x 6”) were cut and machined to meet the strict dimension requirement specified in ASTM D 7137.

As shown in Fig. 2, silicone rubber as aquarium sealant (Perfecto Manufacturing, Noblesville, IN) were applied to four slots of a base PMMA plate before four composite specimens were inserted. PMMA has very little reaction with seawater. The reason to use silicone rubber is that it provides enough bonding strength under water pressure, at the same time, it is not too strong for us to break this tank for future impact experiments. After one week of the construction of this tank (full bonding strength), it was filled with synthetic seawater (Ricca Chemical Co., TX). This tank will be disassembled after certain periods of time such as three months, six months etc. to conduct impact and compression experiments (see Fig. 3). The impact experiments of dry specimens were conducted to provide baseline data for future durability experiments.

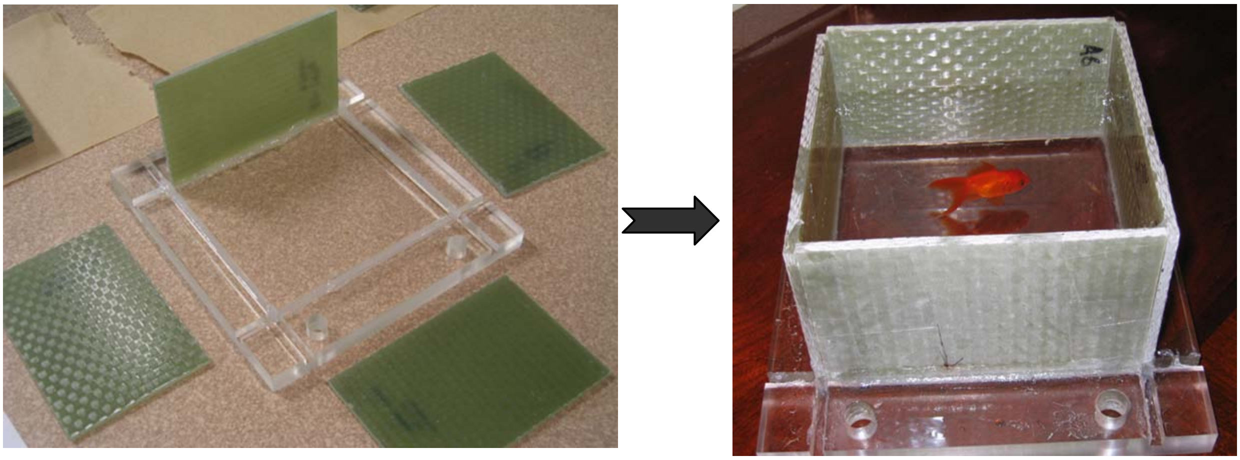

Fig. 2. A composite tank before construction (left) and after construction with seawater inside (right)

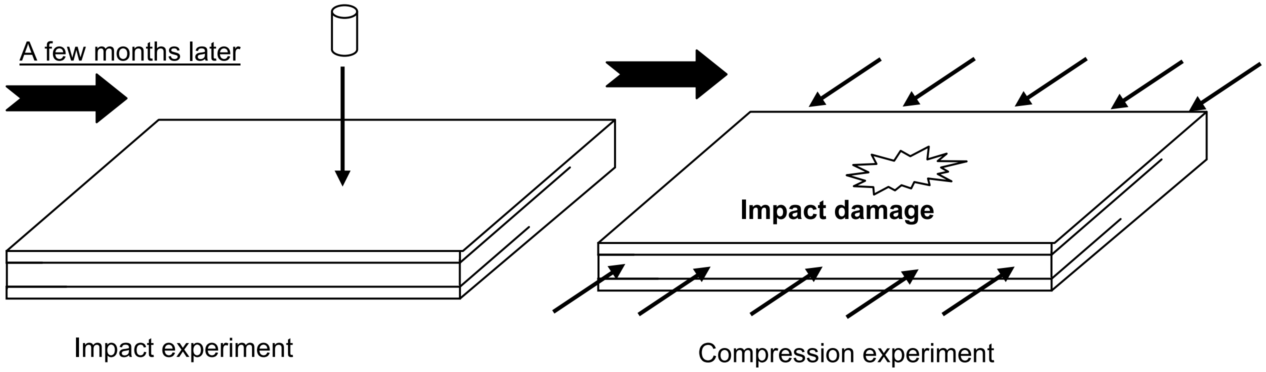
A few months later
Impact damage
Impact experiment
Compression experiment

Fig. 3. Layered composite specimens subjected to out-of-plane impact and compression

EXPERIMENTAL METHODS INVOLVING IMPACT EXPERIMENTS

Impact damage was introduced using a drop tower setup [9]. All samples (fixed four edges) were subjected to an impact (60 joules impact energy) using a 16mm (5/8") diameter hemisphere impactor. Damage zones of the impacted samples are clearly seen in Fig. 4(a), (b). For the front surface directly subjected to impact, dark areas represent internal delamination, with possible several delaminations at the different interfaces. As discussed by Xu and Rosakis [10], these delaminations are mainly shear-dominated so the interlaminar shear strength is an important parameter for delamination resistance characterization.

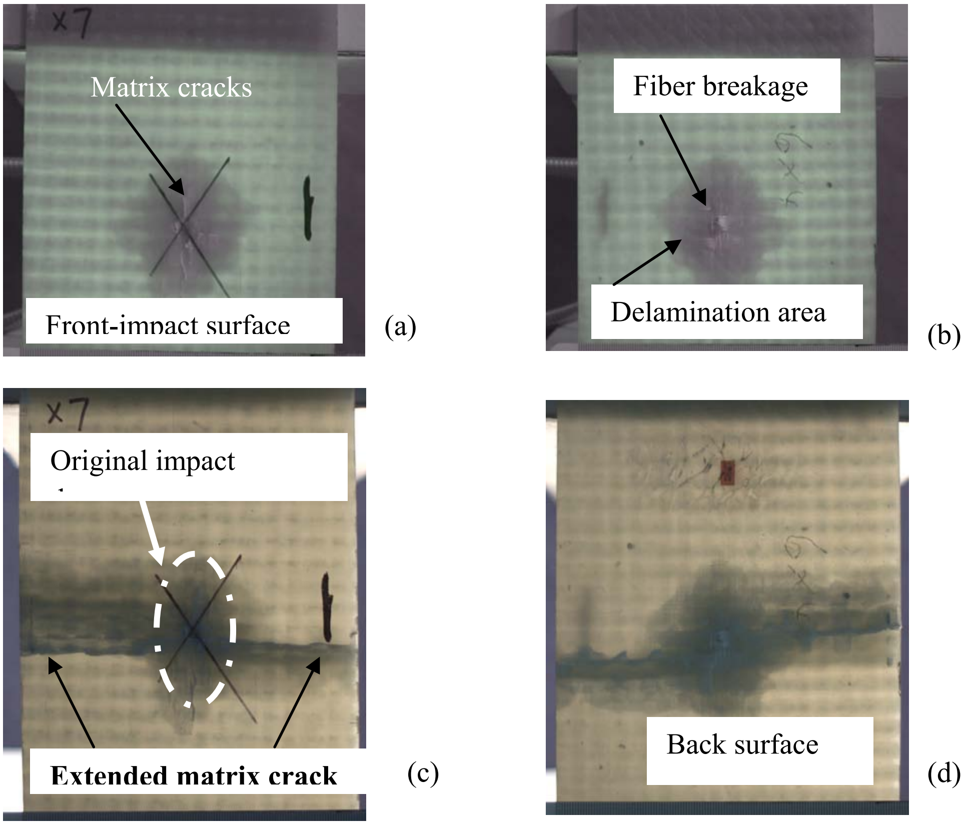
x7
Matrix cracks
Front-impact surface
(a)
Fiber breakage
Delamination area
(b)
x7
Original impact
Extended matrix crack
(c)
Back surface
(d)

Fig. 4. Typical impact damage on the front and back surfaces, (a) and (b), and typical compression failure of the impacted specimen (c) and (d).

Also, two major matrix cracks were observed near the impact site (as shown by two dark mark lines). One matrix crack was along the horizontal direction and the other one was along the vertical direction. On the back surface of the impacted specimen, fiber breakage was observed at the impact site and this failure mode contributed to major impact energy absorption. Meanwhile, fiber/matrix debonding appeared as white thin lines on the back surface of the impacted specimens. These four major failure modes indeed make different contributions to the composite impact resistance [11], and we believe fiber breakage and delamination play the major role to absorb impact energy.

COMPRESSION TESTS FOR IMPACTED SPECIMENS

Impacted samples were mounted into a compression fixture. Strain gages were attached on the sample back and front surfaces to monitor the strain variations at both surfaces during compression. The reason to use strain monitoring is to avoid any global laminate buckling during compression because buckling failure leads to positive and negative strain readings from both surfaces, while a valid compression failure should lead to the same negative strains of both sides of the specimen. A loading rate of 1 mm/min was used. The progressive compression failure started from the impact damage as shown in Fig. 4. Initially, as the compression load increased, delamination from the previous impact propagated in a local buckling form (see more details by Kadomateas [12]). Unlike impact-induced delamination, its propagation is mainly opening-dominated. Notice that delamination also appeared along the horizontal matrix crack and this matrix crack extended to the two edges as the compressive loading increased, as seen in Figure 4. The final failure (maximum load) was controlled by a shear crack near the horizontal matrix crack as seen in Fig. 5. An inclined angle around 30-45 degrees (with respect to the compressive loading direction) was observed from the two vertical edges of the failed specimen. These results are similar to previous compressive failure results by Daniel [13], Tsai and Sun [14], Oguni and Ravichandran [15]. A load-displacement curve is illustrated in Figure 5 for a compressive experiment of an impacted specimen. The initial non-linear part is caused by the initial gap of the compressive fixture. Then a long linear load-displacement part was recorded. The failure mode starts from the opening delamination from the impacted-induced delamination (shear-dominated), followed by a sudden propagation of the longitudinal matrix crack and a final shear crack appeared along the specimen edge based on the recorded high-definition video.

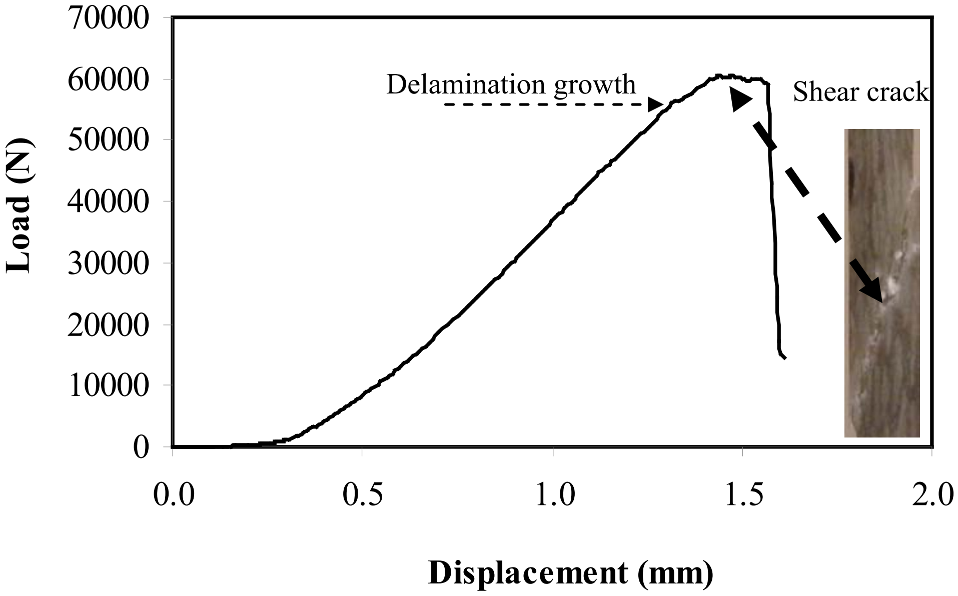

Fig. 5. A typical load-displacement curve of an impacted marine composite laminate in compression

RESULTS AND CONCLUSIONS

Table 1 depicts CAI data up to 13 months. The dry specimen was used as a baseline specimen or comparison. Since the CAI strength combines the effects of the seawater exposure and impact damage, it is very convenient to be used as a durability property plus the dynamic failure behavior. From the table, we notice that the CAI strength reduction is less than 10% after one-year seawater exposure. This is much lesser than 40% as reported by Imielinska and Guillaumat [3] on the same compression after impact experiments with different composite materials. This comparison confirms that our new approach produces more reasonable data as our experiments simulate the right material conditions. These CAI data are also plotted in Figure 6. A slight increase in CAI strength for the specimen after four-month seawater exposure is probably due to the specimen size effect. The average thickness of this set of specimens is at least 10% higher than other specimens. The CAI strength is not a material property as it is sensitive to the specimen size especially the specimen thickness.

Table 1. Variation of Compression-After-Impact (CAI) Strength with seawater exposure time

	Dry	**Seawater exposure**		
Time (months)	0	4	9.5	13
Mean CAI (MPa)	132.98 ±7.59	140.4 ± 4.38	121.38 ± 10.98	125.63 ±10.82
Reduction in CAI (%)	baseline	+5.580	-8.723	-5.527

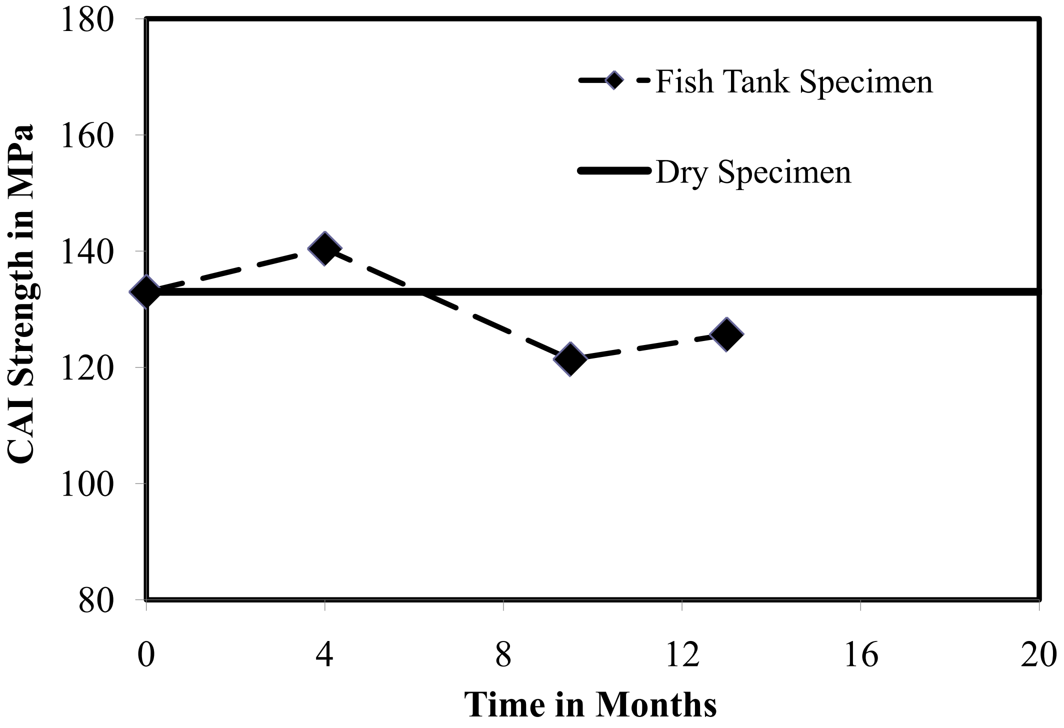

Fig. 6. Change in compressive strength (CAI) as a function of seawater exposure time

ACKNOWLEDGEMENT

The authors acknowledge the support from the Office of Naval Research (Program manager Dr. Yapa D.S. Rajapakse)

REFERENCES

1. Karasek, M.C., Strait, L.H., and Amateau, M.F., Effect of temperature and moisture on the impact behaviour of graphite/epoxy composites: parts I and II. Journal of Material Res Technol 17(1), 3–15, 1995.
2. Sala, G., Composite degradation to fluid absorption. Composites Part B 31, 357-377, 2000.
3. Imielinska, K. and Guillaumat, L., The effect of water immersion ageing on low-velocity impact behaviour of woven aramid–glass fibre/epoxy composites, Composite Science and Technology, 64, 2271–2278, 2004.
4. Smith, L.V., and Weitsman, Y. J., The immersed fatigue response of polymer composites, International Journal of Fracture, 82, 31-42, 1996.
5. Strait, L.H., Karasek, M.L. and Amateau, M.F., Effects of seawater immersion on the impact resistance of glass fiber reinforced epoxy composites, Journal of Composite Materials, 26(14), 2118- 2133, 1992.
6. Wood, C.A., and Bradley, W., Determination of the effect of seawater on the interfacial strength of an interlayer E-glass/graphite/epoxy composite by in situ observation of transverse cracking in an environmental SEM. Composite Science and Technology, 57, 1033-1045, 1997.
7. Weitsman, Y.J., and Elahi, M., Effects of fluids on the deformation, strength and durability of polymeric composites—an overview. Mechanical Time- Dependent Materials, 4,107–126, 2000.
8. Pillay, S., Vaidya U.K., and Janowski, G.M., Liquid molding of carbon fabric-reinforced nylon matrix composite laminates. Journal of Thermoplastic Composite Materials, 18 (6), 509-527, 2005.
9. Ulven, C., and Vaidya, U. K., Post-fire low velocity impact response of marine grade sandwich composites. Composites Part A, 37 (7), 997-1004, 2006.
10. Xu, L. R. and Rosakis, A. J., Impact failure characteristics in sandwich structures; Part I: Basic Failure Mode Selections. International Journal of Solids and Structures, 39, 4215-4235, 2002.
11. Abrate, S., Impact on composite structures, Cambridge University Press, New York, 1998.
12. Kadomateas, G.A., Post-buckling and growth behavior of face-sheet delaminations in sandwich composites. AMD-Vol. 235, Thick Composites for Load Bearing Structures, (Y.D.S. Rajapakse and G.A. Kadomateas, Ed.), 51-60, 1999.
13. Daniel, I. M. http://www.composites.northwestern.edu/
14. Tsai, J. and Sun, C.T., Dynamic compressive strength of polymeric composites, International Journal of Solids and Structures, 41, 3211-3224, 2004.
15. Oguni, K., and Ravichandran, G., Dynamic compressive behavior of unidirectional E-glass/vinylester composites. Journal of Materials Science, 36, 831-838, 2001.

Proceedings of the SEM Annual Conference
June 7-10, 2010 Indianapolis, Indiana USA
©2010 Society for Experimental Mechanics Inc.

Large Field Photogrammetry Techniques in Aircraft and Spacecraft Impact Testing

Justin D. Littell Ph.D.

ATK Space Systems

NASA Langley Research Center MS 495

12 W. Bush Rd.

Hampton, Virginia 23681

Justin.D.Littell@nasa.gov

Abstract

The Landing and Impact Research Facility (LandIR) at NASA Langley Research Center is a 240 ft. high A-frame structure which is used for full-scale crash testing of aircraft and rotorcraft vehicles. Because the LandIR provides a unique capability to introduce impact velocities in the forward and vertical directions, it is also serving as the facility for landing tests on full-scale and sub-scale Orion spacecraft mass simulators. Recently, a three-dimensional photogrammetry system was acquired to assist with the gathering of vehicle flight data before, throughout and after the impact. This data provides the basis for the post-test analysis and data reduction.

Experimental setups for pendulum swing tests on vehicles having both forward and vertical velocities can extend to 50 x 50 x 50 foot cubes, while weather, vehicle geometry, and other constraints make each experimental setup unique to each test. This paper will discuss the specific calibration techniques for large fields of views, camera and lens selection, data processing, as well as best practice techniques learned from using the large field of view photogrammetry on a multitude of crash and landing test scenarios unique to the LandIR.

Background

The Landing and Impact Research Facility (LandIR) at NASA Langley Research Center is a 240 ft. high by 400 ft. long gantry structure. The facility was originally built in 1965 to train the Apollo astronauts for lunar landings [1]. Following the Apollo program, the Lunar Landing Research Facility (LLRF) was converted to the Impact Dynamics Research Facility (IDRF) for use as a full-scale aircraft crash test facility [2]. To date, over 150 vehicles comprising a mix of general aviation aircraft, helicopters, and fuselage subsections have been tested at the recently renamed LandIR. [3] Currently, the facility supports NASA's Constellation and Subsonic Rotary Wing programs for Orion crew module landing and rotorcraft impact testing.

Due to the size of the vehicles tested at the LandIR (commonly known as and referred to herein as the *Gantry*), all testing is conducted outdoors, either under the 240 ft high A-frame structure or a 70 ft vertical drop tower structure depending on the type of test. Figure 1 shows pictures of the LandIR facility and of the 70 ft drop tower.

T. Proulx (ed.), *Dynamic Behavior of Materials, Volume 1*, Conference Proceedings of the Society for Experimental Mechanics Series,
DOI 10.1007/978-1-4419-8228-5_9, © The Society for Experimental Mechanics, Inc. 2011

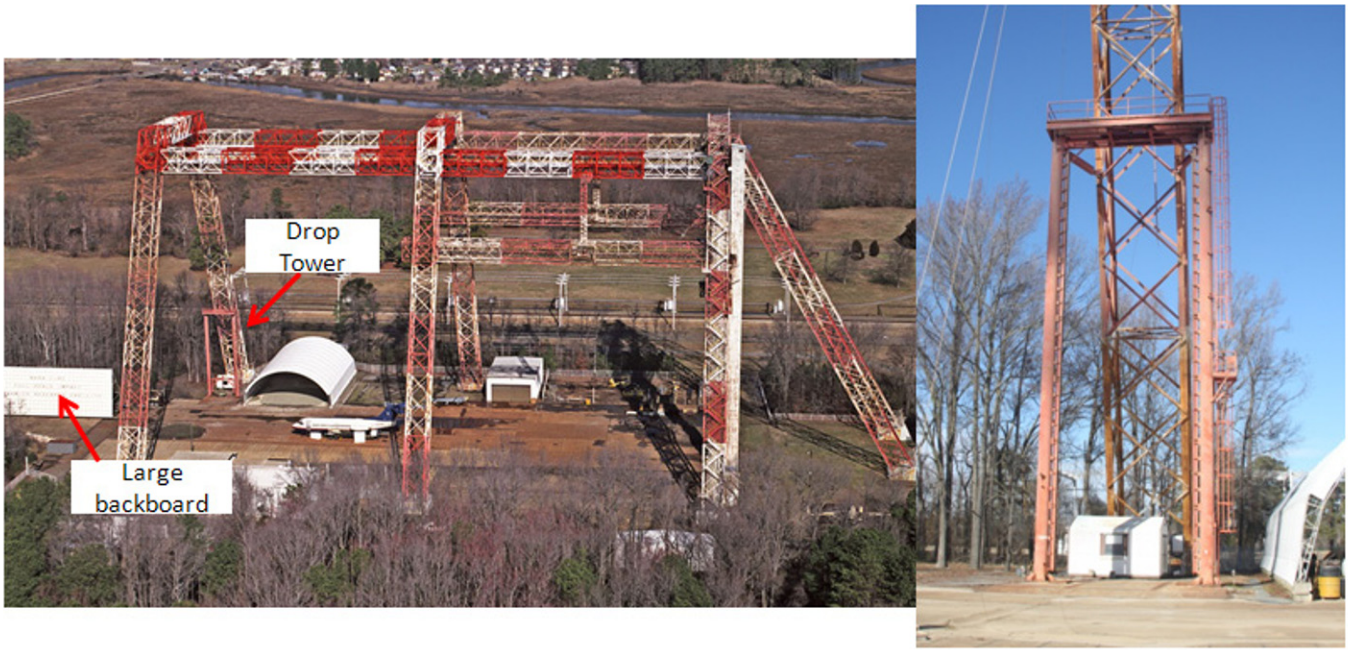

Figure 1 – Landing and Dynamics Research Facility (LandIR) (left), and 70’ vertical drop tower (right)

The large size and scale of tests conducted requires particular care for the experimental photogrammetry setup because aspects typically not seen in a controlled laboratory environment must be considered. For further reading on test setups at the Gantry, a detailed description on test preparation and experimental methods can be found in ref. [2]. Ever changing factors in the weather such as wind, clouds, and time of day can affect lighting conditions, along with camera exposure values and aperture settings. Since no two tests are alike, once the test article is moved to the test site, final test preparations can take anywhere from two to four hours. The preparations typically involve various vehicle cabling and roping safety attachments, pyrotechnics placement and arming procedures, final data acquisition system checkouts, and leveling and balancing the vehicles before the final lift, all of which could be happening simultaneously. These items are all mentioned because they can involve personnel and/or equipment such as forklifts or cranes interfering with the photogrammetry field of view from minutes to hours, interfering with camera setup time and/or potentially moving cameras from their calibrated position. Finally, as all tests conducted use very large field of views, typical methods of obtaining conventional photogrammetry calibrations with hand held panels do not work, so alternative calibration procedures are needed. This paper will describe the methods used at the LandIR facility to overcome the above mentioned constraints to obtain well conditioned calibrations with specific examples and results. This paper will focus on applications of a photogrammetry system, rather than a discussion on the theoretical basis behind the specific algorithms used in photogrammetry.

Photogrammetry, in generalized terms, is the analysis to determine geometric properties and specific spatial information of photographed objects. It has been historically used for terrain mapping, civil engineering, accident investigations and automotive crash testing. The automotive industry has been using various forms of photogrammetry in automotive crash tests for the determination of occupant motion [4] and vehicle deformation [5] for many years. Large field photogrammetry has been used for terrain mapping for Geographic Information Systems (GIS), and numerous articles are available in the literature describing features and functions [6][7][8]. In aerospace applications, two dimensional photogrammetry has been used in the past for impact testing of Crew Exploration Vehicle capsules [9], while three-dimensional photogrammetry has been used on solar sails and gossamer structures for dynamic characterization [10]. The objective of this paper is to familiarize the reader with the typical setup steps, constraints, challenges, and lessons learned from outdoor large field three-dimensional photogrammetry, while providing specific examples and test setups, where applicable.

LandIR Calibration Procedures

The LandIR facility has two types of custom made large field calibration objects. Purely vertical impact tests conducted under the 70 ft drop tower mainly use a portable calibration backboard, whereas full-scale swing tests conducted under the Gantry use a calibration grid present on a large backboard. The portable backboard is on rollers, making it easy to move and position to cater to each specific test. The large backboard is only partially movable along railroad tracks in the Gantry's east/west (shown left to right in Figure 1) direction only. Each calibration object has an array of targets positioned at known distances apart. Each target has arc segments appearing at specified angular locations around a center dot such that no two targets have the same "code". The large backboard has 24 coded targets, placed in a 50 ft. x 36 ft. array, while the small portable backboard has 16 coded targets, arranged in a 10 ft. x 6 ft. array. Figure 2 shows both calibration objects.

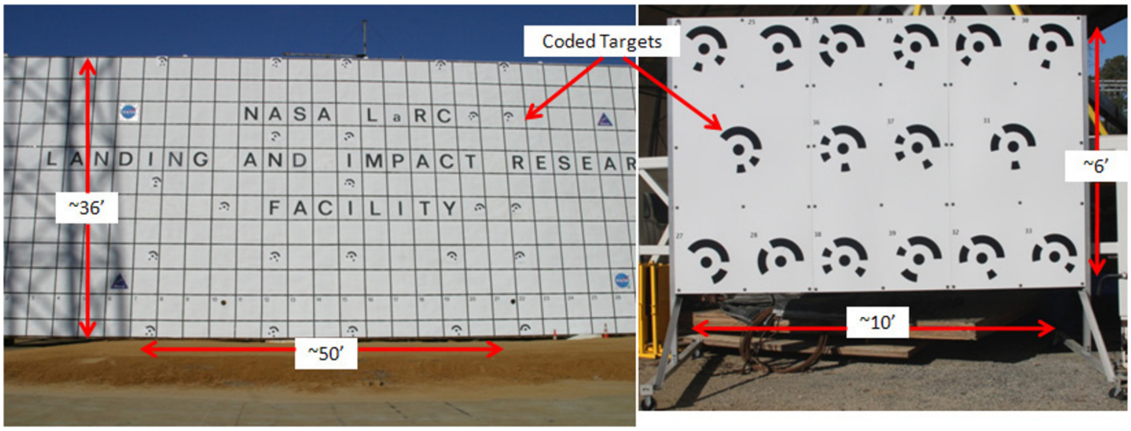

Figure 2 – Large (left) and portable (right) calibration backboards

As with the smaller field calibration procedures, the large field calibration method starts with first determining the approximate size of the field of view needed and determining the lens sizes required. Once the field of view has been determined and the lens has been selected, the technique used for the portable and large backboards is largely the same. Three-dimensional photogrammetry, unlike two-dimensional photogrammetry, uses two or more cameras to create a three-dimensional calibrated volume unique for each test. The off-axis viewing angle of the volume by each camera allows the third, or out of plane, dimension to be triangulated. All three-dimensional photogrammetry techniques require three basic steps for proper calibration, which will be briefly mentioned here. A full procedure can be found in ref [11]. The first step is the removal of camera lens distortion. Camera lens distortions become evident when a circular lens is placed on a camera using a rectangular sensor, and is inherent to varying degrees in all cameras. Parts of the image near the edge of the frame will have a slight curvature about them, in which straight lines will no longer be completely straight. These nonlinear and generally radial lens distortions can be controlled using optical algorithm corrections. Secondly, a three-dimensional "cube", or volume in space, must be generated. Ideally, this region will be comprised of a defined space around the test article's impact location, with enough distance next to or behind the impact location for the placement of static points to establish a reference frame or coordinate system. Finally, the procedure must establish fixed locations for each camera when viewing the newly created calibrated volume. The location and focus for each camera cannot change once these locations have been established. Steps two and three are used in an algorithm typically known as the *bundle adjustment.* This algorithm uses the pictures and user definitions of known distances in the pictures to determine three-dimensional coordinates of the coded targets in space during the calibration procedures.

All tests were filmed with Phantom 9 cameras at a rate of 1000 frames per second at full camera resolution (1632x1200 pixels). Care was taken to maintain camera settings such as aperture settings, focal length, exposure, etc. the same for the calibration pictures as used for the test. To obtain large field of views under current safety requirements, cameras with 24 mm. lenses were for swing tests. Typical full-scale swing setups required that the cameras be positioned at least 50 ft. from the test articles (and 80 ft. to 90 ft. from the large backboard). Focal depth was set to infinity such that both the test article and backboard were in focus. This configuration typically gave field of views for the full-scale swing tests of approximately 62 ft. wide by 45 ft. tall and greater than 30 ft. for the depth. Tests are normally conducted with the backboards in the cameras field of views such that some of the coded targets used for calibration can also be used for coordinate/reference frame definitions.

All cameras (along with all other data acquisition equipment used for each test) were connected to an IRIG-B time code generator. The IRIG-B allows data collected on multiple, otherwise incompatible, systems to be synchronized to a common time stamp to facilitate post-test data reduction and post processing. Thus, results presented in the following sections will be plotted against the seconds unit of IRIG time.

When calibrating, a set of 16-25 pictures was taken with each camera. Due to the large size of the calibration objects and unlike smaller calibration procedures, the large field calibration procedure fixed the calibration backboard and moved the camera instead. A series of four to eight pictures was taken with the target array centered and at the extreme edges of the camera's field of view to compensate for the camera lens distortion. The next set of ten to twenty pictures was taken to obtain the calibrated volume. This series acquired images of the backboard from each camera from as much as 40 degrees off axis to the left and 30 ft. away from the backboard to 40 degrees off axis to the right and 120 ft. away from the backboard, with images being captured at regular intermediate intervals in a grid-like pattern. Finally, each camera was mounted in a fixed location, where it remained for the entire test.

Outside lighting and contrast was determined to be extremely important for each calibration. In varying lighting conditions, the photogrammetry software handled images with flat contrast much better than images with sharp contrast, as illustrated in Figure 3. Normally, sharply contrasting images are desired when finding and tracking targets. Shadowing from the gantry structure, clouds, and supports cables pose unwanted dark spots that are not easy mitigate. Camera settings were established prior to impact testing for bright sunshine or cloudy conditions. However, the conditions can change from sunny to cloudy or vice verse from the time the cameras were set until the impact occurred. Setting up for cloudy conditions is preferred for photogrammetric measurements because shadowing is minimized. Sharp contrast imaging is most desired for qualitative observations and visual inspections.

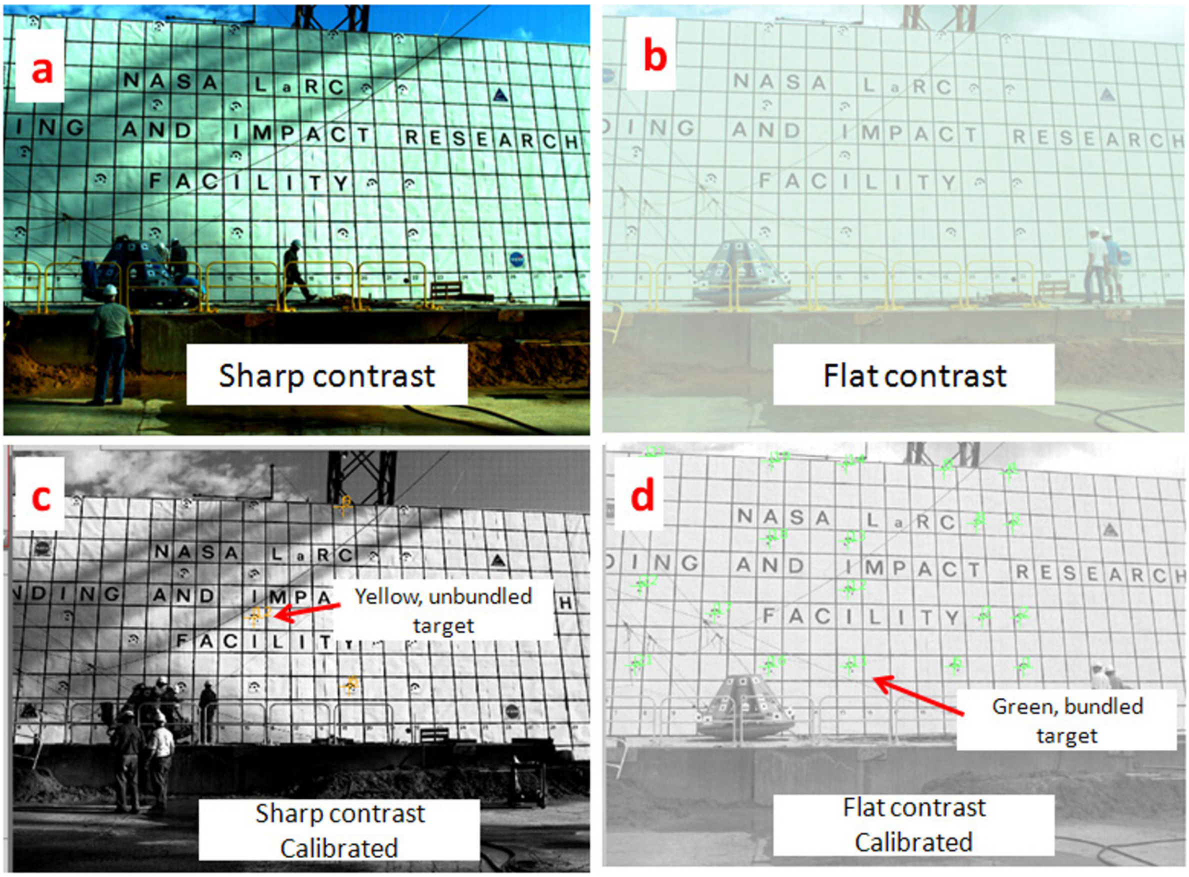

Figure 3 – Calibration findings using sharp contrast (left two images) and flat contrast (right two images)

Figures 3(a) and 3(b) are from the final mounted location of the left camera taken approximately a half hour apart during the morning of a sunny day in the late summer of 2009. The sun position and lighting conditions were approximately the same for both figures. Figure 3(a) shows a shadow from one of the Gantry legs on the large backboard taken at the camera contrast used for a typical test. The shadow is obscuring approximately one third of the target array, mainly in the upper left corner. The image in Figure 3(b) is taken with the contrast artificially adjusted, whereas all of the other test variables were the same. Figures 3(c) and 3(d) are screenshots from the photogrammetry calibration software. Figure 3(c) shows the identification of three of the coded targets on the array displayed in yellow. Yellow indicates that the three targets were identified but the bundle adjustment failed to converge the coordinates of the targets between the left and right (view not shown) cameras. However, the calibration shown in Figure 3(d) identifies the majority of targets. In addition the green color indicates that the bundle adjustment has occurred successfully. It is believed that by adjusting the contrast on the images to give an artificially flat result allows for the software pattern recognition capabilities to resolve areas between light and dark more easily if all of the lighter areas are of the same lightness and all of the darker areas are of the same darkness. For the sharply contrasted images, Figures 3(a) and 3(c), the contrast between the light and dark areas for those targets in the shadow is different than the contrast in light and dark areas for those targets in the sun. This difference leads to misidentification and/or no identification from the software. After this finding, care has been taken to artificially flatten all calibration (and test) images on bright and sunny days. During cloudy days, the clouds artificially flatten the images, so no adjustments are made.

Experimental Setups

Since 2009, three-dimensional photogrammetry has been used on a series of full-scale impact tests conducted at the LandIR facility for both NASA's Constellation [12] and Subsonic Rotary Wing [13] Programs. A summary of the specific test setups and preparations used are provided in this section. This section also provides a subset of tests to illustrate the capabilities and limitations of a photogrammetry system seen on large scale testing conducted on aircraft and spacecraft. The section will start with the simplest setups and proceed to the most involved, and do not necessarily follow chronological order.

MD-500 Mass Simulator Swing Testing

One of the first instances where three-dimensional target tracking photogrammetry was used was on an impact test of a helicopter mass simulator. The test article consisted of a 3,000 lb aluminum flat plate with skid gears, representing an approximate test configuration of a 3,000 lb MD-500 helicopter. This mass simulator was used to obtain baseline accelerations when tested with a foam block under the plate acting as an impact energy attenuation mechanism. In addition, the test article contained a replacement shock absorbing strut as the interface between the skid gear and airframe. The plate was instrumented with 32 channels recording accelerations at various locations and 11 photogrammetric targets. Figure 4 shows the experimental setup with camera locations, test article and calibrated volume highlighted.

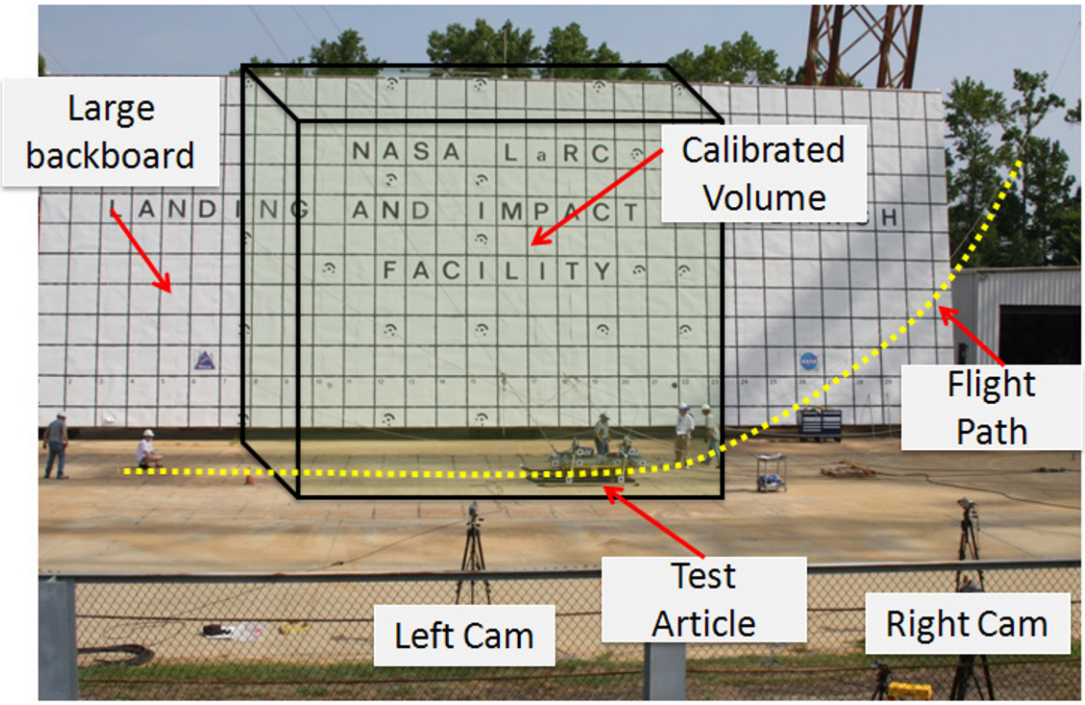
Large backboard
Calibrated Volume
Flight Path
Test Article
Left Cam
Right Cam

Figure 4 – MD-500 Mass simulator full-scale swing test setup

The flight path of the vehicle was from the right to the left as shown by the yellow line in Figure 4. The test article is positioned at the approximate impact location in the figure. Most of the calibrated volume was to the left of the impact location, which allowed for post-impact slide out data to be collected. Figure 4 also shows the cameras in their fixed position for the test, 50 feet away from the test article, 80 feet away from the large backboard and approximately 24 feet apart. These dimensions result in a 15 degree angle to the normal direction of the vehicle's flight path.

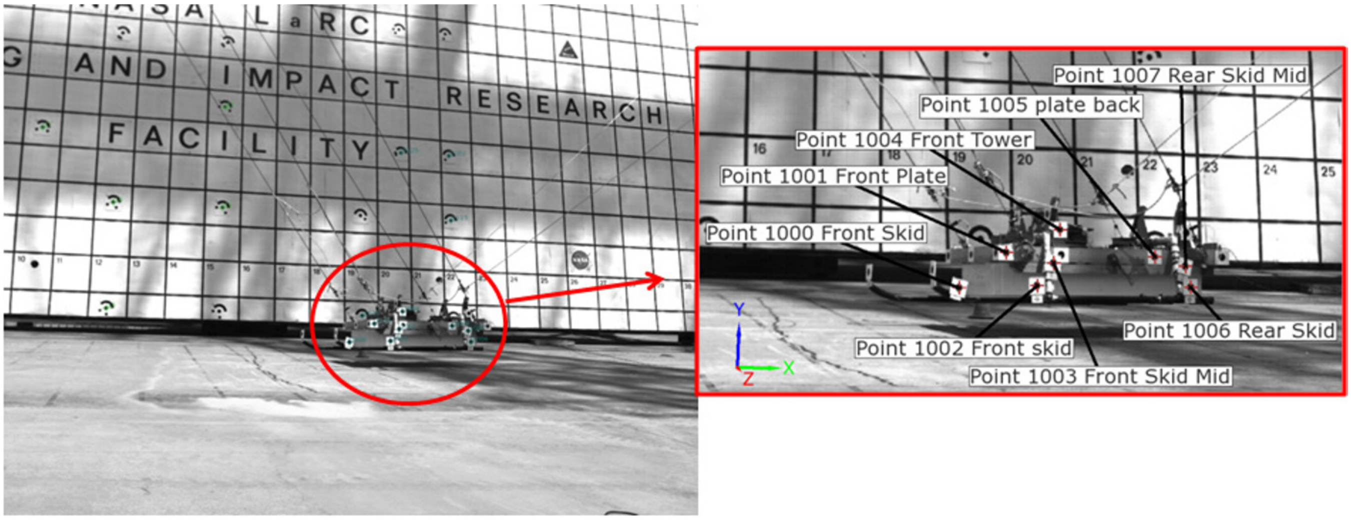
Point 1007 Rear Skid Mid
Point 1005 plate back
Point 1004 Front Tower
Point 1001 Front Plate
Point 1000 Front Skid
Point 1006 Rear Skid
Point 1002 Front skid
Point 1003 Front Skid Mid
Y
X
Z

Figure 5 – Flat plate swing test full view (left) and close up showing target locations/identifications (right)

Figure 5 shows a frame of the high speed video from the left camera immediately before test article impact and subsequent target identification as processed by the photogrammetry system. One target in Figure 5 was not tracked, which was a consistent problem in subsequent frames of data for this specific test. This target was located below Point 1004. The large relative motion between the skid gear and the flat plate caused some of the targets on the skid gear (Points 1000, 1002, 1003, 1006, 1007) to overlap some of the targets on the plate (Points 1001, 1004, and 1005). A major lesson learned from this test was that targets should not be placed too close together and thus interfere with identification during impact. An additional item of interest learned specifically from this test was that the targets on the skid gear were attached to the gear by a series of flexible standoffs, which caused the targets to oscillate. Figure 6 shows post impact lateral displacement comparison between the skid gear and flat plate for the first 0.5 seconds after impact. There are very slight oscillations from the flat plate due to the foam compression, but the pronounced oscillations occurred in the target (Point 1000) attached to the front skid gear. The vertical red line represents the time of the vehicle impact. Subsequent tests for this test article and others had the targets rigidly attached to the skid gears or other rigid locations and further apart to avoid overlap and cover.

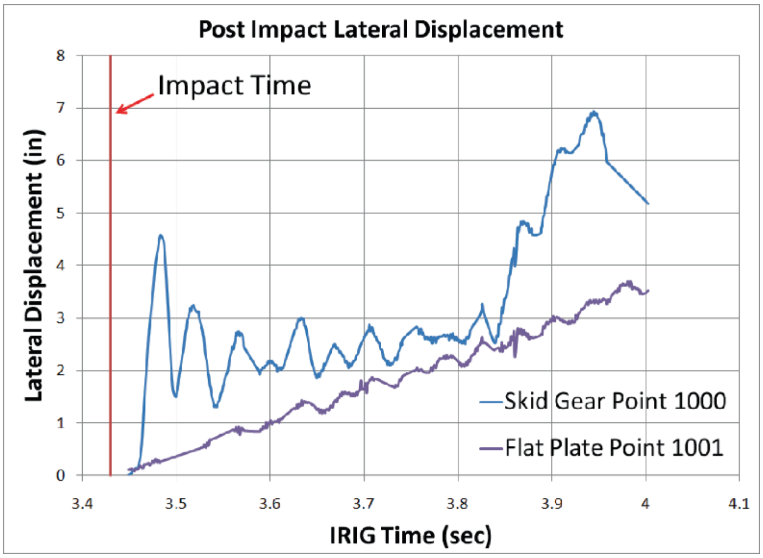

Figure 6 – Relative lateral motion comparison between the skid gear and rigid plate

In order to process the vehicle data, a coordinate system had to be established such that the three orthogonal axes represented the three directions of motion from the vehicle. The coordinate system was created on the large backboard by using the static coded targets present. A coordinate system was created by first defining a plane using three targets, typically those in the corners of the field of view. Then, a positive x axis was defined using two of the targets lying in the same horizontal plane. Finally, an origin was defined using one of the targets in the lower left hand corner of the backboard. In the coordinate system, the x direction represented horizontal velocity, y direction represented vertical velocity and z direction represented out-of-plane, or lateral velocity. Impact velocities were taken as the average of all the vehicle target points at the time of ground contact as determined by visual inspection of the high speed video. Pitch, roll, and yaw angles were found by creating projection angles in the xy, xz, and yz directions using artificially created lines on the vehicle and artificial lines created on the backboard. Figure 7 shows a schematic on the projection angle methodology. Vehicle pitch was determined by calculating an xy projection angle between a horizontal line on the vehicle (Points 1001 to 1005) and a horizontal line on the backboard. Vehicle yaw was calculated by creating an xz projection angle between a horizontal line on the vehicle and a horizontal line on the backboard. Vehicle roll was calculated by creating a yz projection angle between a vertical line on the vehicle and vertical line on the backboard. All of these angles can be differentiated (by the software) to give angular rates at impact as necessary.

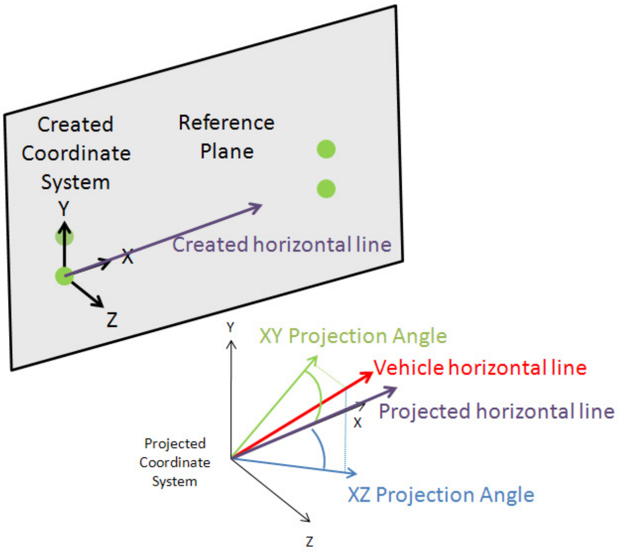
Created
Coordinate
System
Reference
Plane
Y
X
Z
Created horizontal line
Y
XY Projection Angle
Vehicle horizontal line
Projected horizontal line
X
Projected
Coordinate
System
XZ Projection Angle
Z

Figure 7 – Projection angle methodology

For the MD-500 mass simulator, the impact velocities were computed to be 27.1 ft/sec horizontal and 17.5 ft/sec vertical with 1.8 degree pitch, 6.7 degree yaw and 3.4 deg roll angles. These values deviate from the planned conditions of 28 ft/sec horizontal, 18.2 ft/sec vertical velocities with 0.0 degree pitch, roll and yaw angles.

Finally, target displacements on the large backboard were checked. It was assumed that the large backboard and targets attached to large backboard remained stationary during tests. As such, the amount of displacement computed by the photogrammetry software was the noise level, or the amount of uncertainty in the measurements. Three targets were picked to examine the noise levels; 11, 13, 16, because they represented a large area of the backboard far enough away from the mass simulator test article and cabling as to remain visible. The target locations and resultant root-sum-squared displacements are shown in Figure 8. The majority of the data resides within the ±0.05 inch range for all three targets. This 0.10 inch noise range over the length of 62 feet represented a 0.01% error in the data.

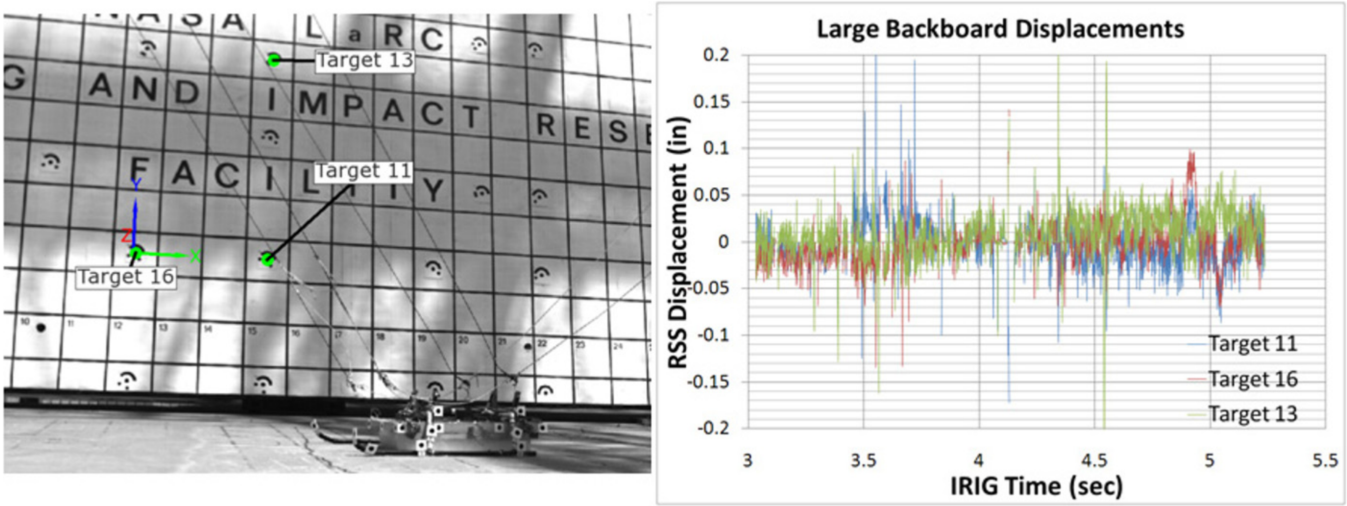

Figure 8 – Backboard Target Locations (left) and displacements (right)

Subscale Orion Swing Testing

A series of 5 swing tests was conducted by the Constellation program in the summer of 2009. This program tested a 5146 lb, 8 ft. diameter Subscale Orion mass simulator boilerplate to assess abort land landing conditions. The Subscale Orion impacted a 4 ft. high by 20 ft. wide by 78 ft. long sand bed at various vertical and horizontal velocities to assess the effects of horizontal velocity in the vehicle response. Capsule deformations were not considered for these tests as the capsule was assumed to be a rigid structure. This series of tests, however, brought about increasing photogrammetric complexity because the fabricated sand bed obscured the bottom row of coded targets on the large backboard. After several attempts to calibrate, the problem was remedied by taking extra calibration pictures such that the first visible row of calibration targets on the backboard was captured near the bottom of the cameras' sensors to ensure that lens distortions were removed. Then, the cameras were tilted slightly such that the bottom of the calibrated cube would be on the surface of the sand bed approximately 4 ft. off the ground. Figure 9 shows a picture of the test setup taken from the right photogrammetry high speed camera. Note that the image has been artificially flattened as described previously to give an even white/black contrast on the entire backboard.

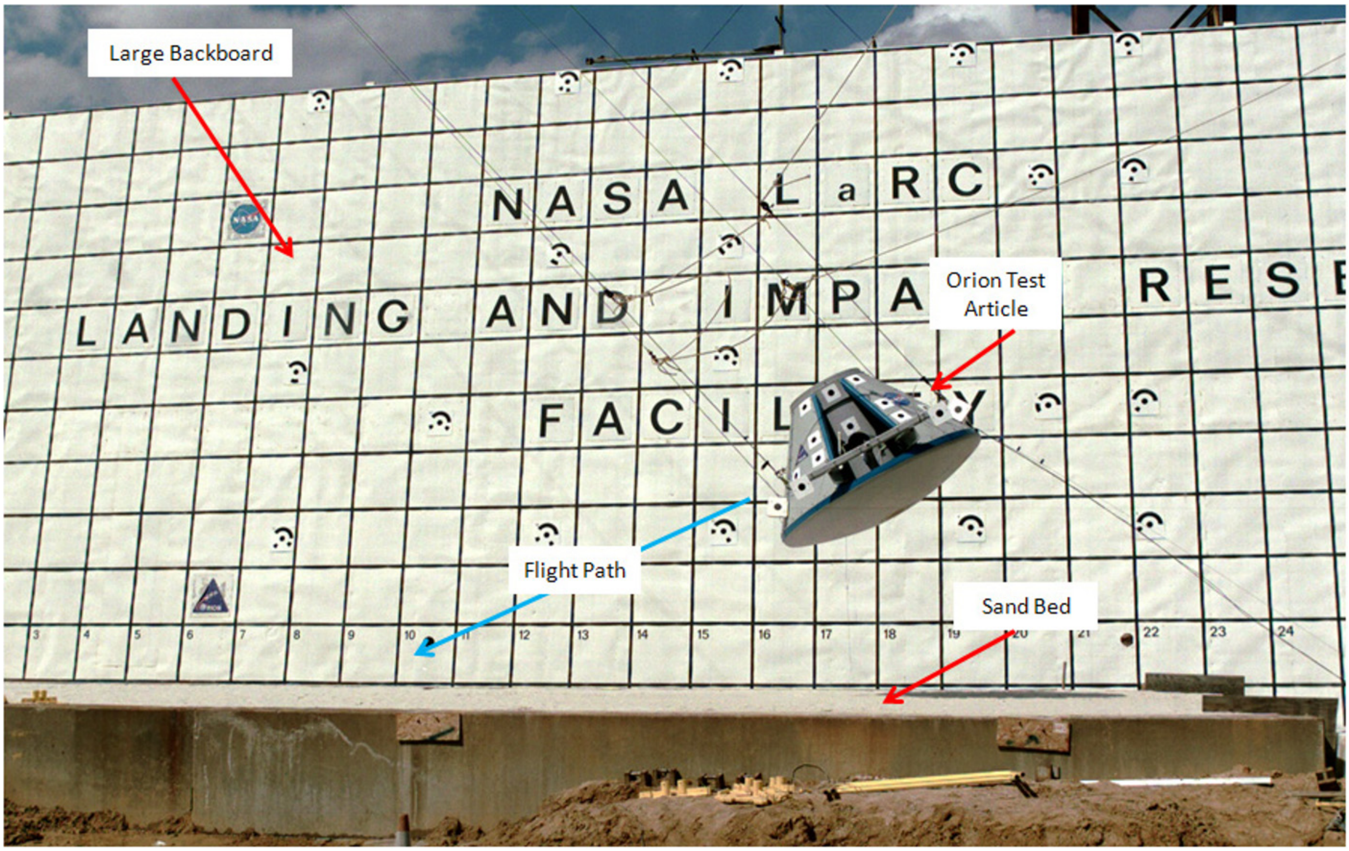

Figure 9 – Test setup for the Subscale Orion Swing tests

Ten targets were located on the vehicle. Eight of these targets were located on the vehicle's skin, and two were located on an out-rigging bar, which provided the Gantry's lifting/swinging interface point. Often times when conducting full-scale swing tests, extra lifting and/or swinging hardware is added to facilitate interface with gantry cabling systems. This extra hardware is ideal for photogrammetry target placement as these points can be thought of as rigid locations which minimally deform. Figure 10, left, shows the tracked targets on the Subscale Orion while Figure 10, right, shows approximately ½ second (500 images) of vehicle velocity time history data. For the Subscale Orion test presented, the vehicle impacted the soil at 29.8 ft/sec horizontal, 24.7 ft/sec vertical and 0 ft/sec lateral velocities, corresponding with the nominal 30 ft/sec horizontal, 25 ft/sec vertical and 0 ft/sec lateral velocities.

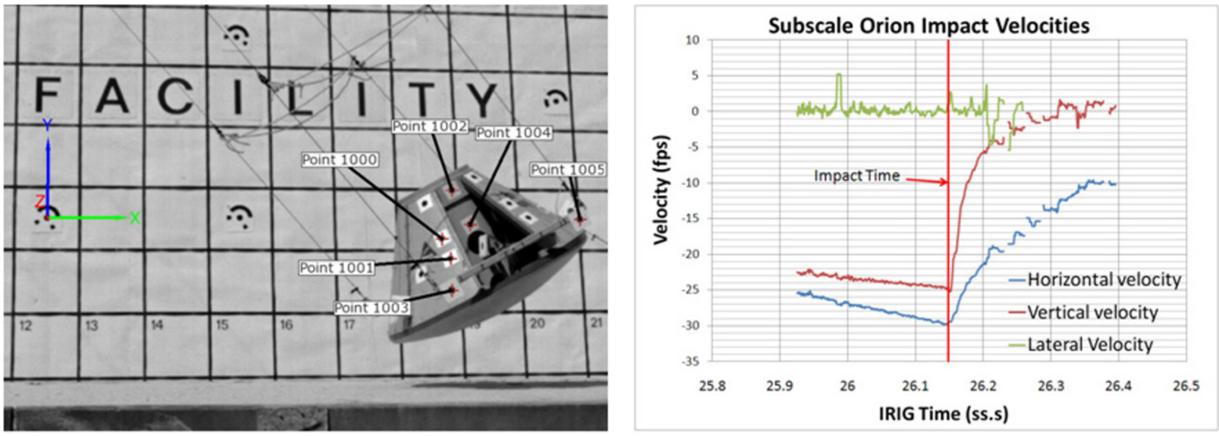

Figure 10 – Tracked targets on the Subscale Orion (left) and impact velocities (right)

MD-500 Full-Scale Swing Test

Photogrammetry techniques were used for a full-scale crash test of an MD-500 helicopter in December 2009. This crash test was the most complex in that both the target tracking and full field strain capabilities of the system were implemented. The purpose of this test was to evaluate a prototype composite energy absorbing concept to reduce the risk of crew injury during accidents. As a result, vehicle deformations and impact conditions were critical to evaluate the energy absorber's capabilities. The helicopter was instrumented with 160 data channels recording strain, acceleration, load and occupant data, but also instrumented with a grid of targets on the side of the airframe, along with targets on the tail, rotor mount, skid gear and belly to record both vehicle impact conditions and also gross vehicle deformation. As a proof of concept, the tail skin was also painted with a white/black speckle pattern to enable full-field strain photogrammetry. Targets used for the target tracking photogrammetry were approximately 3 in. diameter, whereas the black dots used in the full-field strain photogrammetry were 1 in. diameter. Figure 11 shows a picture of the instrumented helicopter.

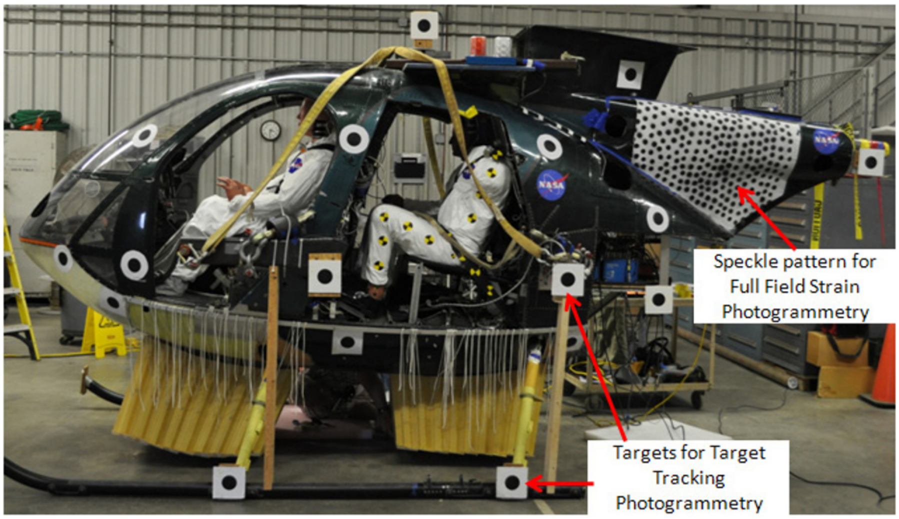
Speckle pattern for Full Field Strain Photogrammetry
Targets for Target Tracking Photogrammetry

Figure 11 – Fully Instrumented MD-500 helicopter

Information to assess the helicopter's impact velocities along with pitch, roll and yaw impact angles was ultimately needed. However, because the helicopter was considered a deformable structure, structural deformations also were of interest to assess the integrity of the airframe post-impact. Figure 12 shows the un-coded targets tracked on the vehicle (Points 1000 – 1013), static coded targets found on the backboard (Point 6, 8, 12, 13, 15, 16, 17, 18, 21, and 22) and the coordinate system created (lower left hand corner of Figure 12, right)

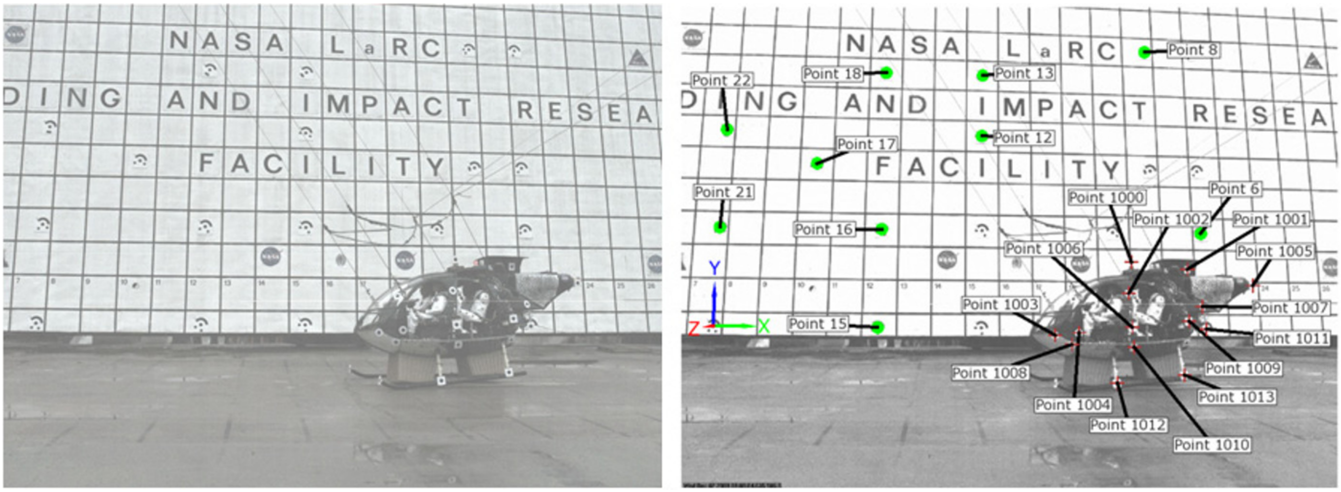
NASA LaRC
DING AND IMPACT RESEA
FACILITY
Point 8
Point 18
Point 13
Point 22
Point 17
Point 12
Point 21
Point 1000
Point 6
Point 1002
Point 1001
Point 16
Point 1006
Point 1005
Y
Point 1003
Point 1007
Z
X
Point 15
Point 1011
Point 1008
Point 1009
Point 1004
Point 1013
Point 1012
Point 1010

Figure 12 –Single image captured from high speed movie (left) and post processed photogrammetry data (right)

As with the Subscale Orion tests, impact velocity conditions were determined from an average of all points on the vehicle at impact, while pitch and yaw angles and angular rates were taken from an average of xy and xz projected angles from the lifting hardware (Points 1006 and 1009) and skid gear (Points 1012 and 1013) with respect the horizontal axis, defined by the x axis in Figure 12. Roll angle and angular rate were obtained from measuring the angle of a yz projected line. This measurement was more complicated, since no two targets were in the same vertical plane on the vehicle. By using Points 1006 and 1002 and subtracting out the built- in angle on the vehicle, roll parameters were computed. The photogrammetric results showed the vehicle impacted at 38.7 ft/sec horizontal and 25.5 ft/sec vertical velocities, with 5.7 degrees pitch, 9.3 degrees yaw and 7.0 degrees roll with angular rates of 4.8 deg/sec yaw and 1.1 deg/sec roll. Figure 13 shows these results, along with results for about 800 ms after vehicle impact. The red vertical line is included to show the impact time (4.605 seconds).

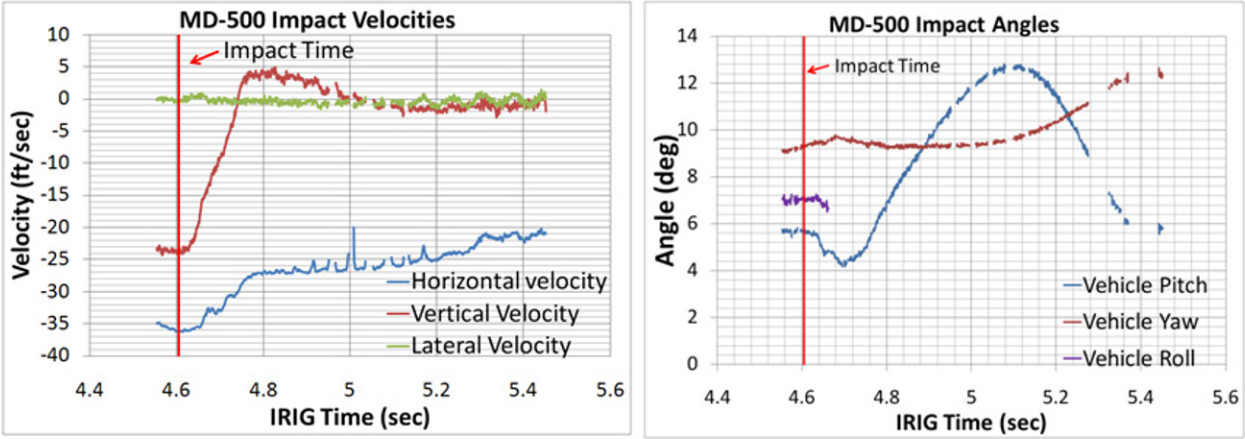

Figure 13 – Impact conditions of the MD-500 helicopter

Care was taken to locate specific target locations on the vehicle such that the structural integrity of the vehicle could be analyzed post test. The targeting scheme can be summarized as follows: two targets measured the relative motion of the skid gear (Points 1012 and 1013), three targets measured the waterline deformation of the vehicle (Points 1003, 1008, 1010), four points formed a horizontal line in-line with the lifting hardware (Points 1003, 1004, 1006, 1009) and created the “seat” line for the occupants, three points defined the helicopter’s nose deformation (Points 1003, 1008, 1004), two points define the structural integrity of the data acquisition system mounting hardware (Points 1007, and 1011), and separate points define the locations for the top rotor mass ballast (Point 1000), occupant “head” line (1002), rear engine fairing (Point 1001) and rear tail (Point 1005). Note that some of the targets were used for multiple functions. Structural integrity of the airframe was determined by examining the time history of the change in distance between the various targets on the airframe. The maximum deformation was found (and reported as strain) while the time history was examined to determine if the maximum deformation stayed constant at the max value, or began to unload toward a zero value. Target distances and maximum permanent deformations are listed in Table 1.

Table 1 – Deformation Measurements of the MD-500 helicopter

Location (Target Numbers)	Nominal Distance (in.)	Max Strain (%)	Permanent
Nose to Water Line (1003 – 1008)	14.14	0.85	No
“Seat” line, Nose (1003 – 1004)	17.80	0.47	No
Water Line (1008 – 1010)	47.48	0.17	No
DAS Shelf (1007 – 1011)	17.34	0.98	No
Top mass to front lifting fixture (1000 – 1006)	64.70	0.32	No
Top mass to rear lifting fixture (1000 – 1009)	66.73	0.34	No
Rear Engine Fairing to rear lifting fixture (1001 – 1009)	54.80	0.40	No
Tail to rear lifting fixture (1005 – 1009)	83.79	0.24	No

The results in Table 1, along with visual inspections and strain gage data on keel beams and bulkheads, helped to indicate that very little permanent deformation occurred on the airframe, and thus it was suitable for reuse. Areas showing permanent deformation (mainly forward lower skin areas) and buckling have been removed and repaired.

Finally, a proof of concept using the full field strain measurement system was completed on the MD-500 tail skin. This was to evaluate if the dot pattern was acceptable to resolve full field strains on a full-scale vehicle crash test. As a check, a strain gage rosette was wired in the lower quadrant of the tail skin, which was then painted over by the speckle pattern. Results show that the full field strain measurement system was able to resolve a strain field, however the size of the dots were large and did not capture the localized effects captured by the strain gauge rosette. The rosette featured three 0.125 in. length gages arranged in a 0 /45 /90 deg arrangement covering an approximate 1 square inch area, whereas the resolved grid pattern of results for the full field strain photogrammetry system was approximately 1.5” apart. Data for each point in the grid pattern used multiple adjacent grid point locations in an averaging function to obtain results for each discrete position, such that the actual gage size for the full field strain measurement was on the order of 6”. Future investigations are necessary to address the issues of capturing more localized defects by reducing dot size, decreasing the camera field of view, or using alternate hardware. However, the proof of concept in taking measurements on a large structure was successful.

Discussion and Conclusion

Large field three-dimensional photogrammetry techniques have been used for approximately 20 full-scale aircraft and spacecraft impact tests for determination of vehicle impact conditions and also structural deformations. Representative individual results for the full six degree of freedom impact conditions have been presented as examples of capabilities of the applied techniques. Specific examples included in this paper are results for Subscale Orion swing tests, impact conditions on MD-500 mass simulator and helicopter swing tests, and structural deformations on the MD-500 helicopter during a full scale crash test.

Since 2009, the LandIR at NASA Langley Research Center has been using three-dimensional photogrammetry for both aircraft crash and spacecraft impact tests. Obstacles faced in conducting photogrammetry setups in outdoor large field of view environments have been described, and solutions to these obstacles have been provided. Mitigation strategies due to specific hardware and facility constraints, such as the immobility of the large backboard and the impact of vehicles above the ground surface were provided. Many of the techniques described were developed in tandem with the testing, basing updated procedures on previous sets of findings and results. For example, backboard target interference due to shadows hindered target recognition, which was resolved by trial and error flattening of the image series.

Processes to document results in the photogrammetry software for the full six degree of freedom solution were developed in tandem with photogrammetry setup procedures. Target placement techniques have been refined to eliminate overlap and lost data, while a methodology has been developed for optimum placement of targets for angle analyses in two separate planes. Static targets were added to all tests such that coordinate transformation techniques could be implemented. This is especially critical for tests conducted with the large backboard, which was rotated at an angle of 9.4 degrees from the vertical. Finally, noise levels were checked within the measurements by examining backboard fixed target displacements.

References

[1] O'Bryan, Thomas C., and Hewes, Donald E., "Operational Features of the Langley Lunar Landing Research Facility," NASA Technical Note, TN D-3828, February 1967.

[2] Vaughan, Jr., Victor L. and Alfaro-Bou, Emilio, "Impact Dynamics Research Facility for Full-Scale Aircraft Crash Testing," NASA Technical Note, TN D-8179, April 1976.

[3] Jackson, K.E., et al. A History of Full-Scale Aircraft and Rotorcraft Crash Testing and Simulation at NASA Langley Research Center. NASA TM 20040191337. 2004.

[4] McClenathan, R.V. et al. Use of Photogrammetry in Extracting 3D Structural Deformation/Dummy Occupant Movement Time History During Vehicle Crashes. SAE 2005 World Congress and Exhibition. SAE Paper # 2005-01-0740. 2005.

[5] Fenton, S. et al. Using Digital Photogrammetry to Determine Vehicle Crush and Equivalent Barrier Speed (EBS). SAE International Congress and Exposition 1999. SAE Paper # 1999-01-0439. 1999.

[6] Bulner, M.H. et al. How to use Fiducial-Based Photogrammetry to Track large-Scale Outdoor Motion. Experimental Techniques. Pp 40-47. 2010.

[7] Lane, S.N. et al. Application of Digital Photogrammetry to Complex Topography for Geomorphological Research. Photogrammetric Record, 19(95). Pg 793-821. 2000.

[8] Collin, R.L and Chisholm, N.W.T. Geomorphological Photogrammetry. Photogrammetric Record 13(78). Pg 845-854. 1991.

[9] Barrows, D. et al. Photogrammetric measurements of CEV Airbag Attenuation Systems. 46th AIAA Aerospace Sciences Meeting and Exhibit. AIAA Paper 2008-846. 2008.

[10] Black, J.T. et al. Photogrammetry and Videogrammetry methods for Solar Sails and Other Gossamer structures. 45th AIAA/ASME/ASCE/AHS/ASC Structures, Structural Dynamics and Materials Conference. AIAA Paper 2004-1662. 2004.

[11] GOM mbH “PONTOS User Manual – Software” GOM mbH, Germany. 2008.

[12] Baumeister, J. NASA’s Constellation Program. NASA/CP—2009-215677. 2009

[13] Jackson, K.E., Fuchs, Y. T., and Kellas, S., “Overview of the NASA Subsonic Rotary Wing Aeronautics Research Program in Rotorcraft Crashworthiness” Journal of Aerospace Engineering, Special Issue on Ballistic Impact and Crashworthiness of Aerospace Structures, Volume 22, No. 3, July 2009, pp. 229-239.

Proceedings of the SEM Annual Conference
June 7-10, 2010 Indianapolis, Indiana USA
©2010 Society for Experimental Mechanics Inc.

Properties of Elastomer-based Particulate Composites

A.V. Amirkhizi[a], J. Qiao[b,a], K. Schaaf[a], S. Nemat-Nasser[a]

[a] Department of Mechanical and Aerospace Engineering, Center of Excellence for Advanced Materials, University of California, San Diego, 9500 Gilman Drive, La Jolla, CA 92093-0416, USA
[b] School of Materials Science and Engineering, Harbin Institute of Technology, Harbin 150001, China

ABSTRACT

In this work, an attempt has been made to develop fly ash filled polyurea matrix composites with low density and good dynamic mechanical behavior. Fly ash (105μm –149μm in diameter) was introduced into polyurea, and its volume fraction was varied to study its effects on the overall properties of the composites. Scanning electron microscopy was used to observe the morphology of the composites. The storage and loss moduli of the composites were determined using dynamic mechanical analysis (DMA) from -80 to 70°C at low frequencies and using ultrasonic measurements at high frequencies under ambient conditions. Results showed that fly ash particles were distributed homogeneously in the polyurea matrix, and the density of the composites decreased as the volume fraction of fly ash increased. Compared to neat polyurea, increases in storage and loss moduli at high temperature were achieved by increasing fly ash content. The peak in the ratio of the moduli of the composites system over that of neat polyurea occurred near glass transition temperature T_g. The speed of sound in the composites increased with increasing fly ash content. Longitudinal modulus and acoustic impedance had similar trends.

Keywords: polyurea elastomer, fly ash, composites, dynamic mechanical properties, acoustic properties

1. INTRODUCTION

Polyurea, which is widely used for coating applications, has attracted the attention of material scientists all over the world due to its excellent impact properties as a protective coating. Many researchers have worked on its application in impact-resistant steel structures, and the results have shown that the polyurea coating is able to enhance the energy absorption and dynamic performance of structures[1-4]. This ability can be greatly enhanced by optimal microstructural modifications.

The addition of particulate fillers to polymers is a very widely used technique, particularly when polymer properties need to be modified. The presence of fillers may lead to significant changes in the rheological and chemical structure of polymers that host them[5]. Due to low density and hollow structure, fly ash has been utilized as filler in metal-matrix composites and polymer-matrix composites to achieve high damping and impact properties. Use of fly ash is also attractive because it is inexpensive and its use can reduce the environmental pollution.

In this work, polyurea filled with fly ash is studied to obtain a promising, advanced low density composite. An attempt has been made to investigate the effect of fly ash content in polyurea-based composites on the overall dynamic properties. Four kinds of composites with fly ash volume fractions from 5% to 30% were prepared and their densities and mechanical behavior were determined by dynamic mechanical analysis (DMA) and ultrasonic measurements. The results were compared with the properties of neat polyurea.

2. EXPERIMENTAL DETAILS

2.1 Material

Polyurea elastomer obtained from the reaction of diisocyanate and diamine components was employed as the matrix. We used Isonate 2143L, which is a polycarbodiimide-modified diphenylmethane diisocyanate[6], and

T. Proulx (ed.), *Dynamic Behavior of Materials, Volume 1*, Conference Proceedings of the Society for Experimental Mechanics Series, DOI 10.1007/978-1-4419-8228-5_10, © The Society for Experimental Mechanics, Inc. 2011

Versalink P1000, an oligomeric diamine [7]. Theoretically, Isonate 2143L and Versalink P1000 must be mixed in a stoichiometric ratio of 1:1, i.e., the total number of isocyanate groups must equal the total number of hydroxyl groups in order to avoid a product with undesirable physical or chemical properties. However, a slight excess of Isonat 2143L was used so as to ensure that the reaction went to completion and produced some cross-linking between the hard domains formed from semi-crystallization of diamine molecules. The amount of excess Isonate 2143L was estimated through weight measurements of containers before and after the processing.

Fly ash particulates originating from coal combustion were applied as the filler. They were sieved with a standard mesh sieve column on a mechanical shaker, and the particle sizes in the range of 105μm –149μm in diameter were used in this study. The density of fly ash particulate is about 0.78g/cm^3 and its constituents, which were experimentally determined through X-Ray Fluorescence Spectrometer, are listed in Table 1.

Table 1. Chemical composition of fly ash [8]

Chemical Composition	Content (Wt.%)
Al_2O_3	26.07
SiO_2	58.83
K_2O	6.26
Fe_2O_3	3.64
MgO	1.57
TiO_2	1.03
Na_2O	1.16
CaO	0.74
Other	0.70

2.2 Preparation of composites

Due to the short gel time of polyurea at room temperature, fly ash was added to Versalink P1000 (the more viscous component) prior to the polymerization process of polyurea in order to achieve a homogenous distribution throughout the matrix. The procedure was designed as follows: first, fly ash particles, which were preheated at 110°C for 1 hour and cooled under dry conditions, were introduced into Versalink P-1000 in a predetermined proportion and this blend was mixed thoroughly to ensure the fly ash would not be removed by air in the subsequent degassing process. Second, using a magnetic stirrer, the above blend was stirred for 2 hours while being degassed in order to achieve a homogenous distribution. Meanwhile, the Isonate 2143L was degassed separately until most of the entrapped air bubbles were removed. Third, these two components were mixed rapidly for five minutes while degassing. Finally, the mixture was cured in a teflon mold at room temperature for one week to obtain the test specimens. In order to control humidity levels, the mold was placed in an environmental chamber that maintained a relative humidity level of 10%.

The fly ash volume fractions in the final composites were 5%, 10%, 20%, and 30%.

2.3 Scanning Electron Microscopy (SEM)

SEM was conducted using a Philips XL30 ESEM scanning electron microscope to observe the distribution of fly ash in the matrix. Composite specimens were immersed in liquid nitrogen until thermal equilibrium was achieved, at which point they were removed and immediately fractured with a hammer. Due to poor conductivity, the fragments were coated with a thin layer of iridium (75 nm thick) in an automatic sputter coater and then the fracture surfaces were observed using an acceleration potential of 15KV.

2.4 Density characterization

The density of the material was determined through the application of Archimedes' principle by measurement of the weight of the specimen in air and in water, respectively:

$$\rho = \frac{m_{Air}}{m_{Air} - m_{Water}} \cdot \rho_{Water} \tag{1}$$

Here, m_{Air} and m_{Water} are the measured weight of composite in air and in water, respectively, and ρ_{Water} is the density of water. At least five samples were measured for each category.

2.5 Dynamic mechanical analysis

Dynamic mechanical analysis was carried out using a TA Instruments DMA 2980, using the corresponding software to collect and analyze the experimental data. The specimens measured approximately 3 mm thick by 10 mm wide and were clamped at a free length of 17.5 mm by a single cantilever clamp. They were constrained from rotation at both ends by clamping plates and excited into a sinusoidal transverse displacement at one end at a constant strain amplitude of 15 μm. The experiments were performed over the temperature range from -80°C to 70°C, stepping upwards in increments of 3°C. At each temperature step, five frequencies of 1, 2, 5, 10 and 20 Hz were tested sequentially. Thermal soaking times of 3 minutes at the beginning of each step minimized the effects of thermal gradients. Liquid nitrogen was used to cool the system to sub-ambient temperature. For each category, sets of three samples were tested, two from the same batch and the third from a secondary batch.

2.6 **Ultrasonic measurement**

Direct contact measurement was used to measure the speed of sound in the composites. The experimental setup consists of a desktop computer containing a Matec TB-1000 Toneburst Card, two Panametrics videoscan transducers, an attenuator box, and a digital Oscilloscope. As shown in Fig.1, toneburst signals of various frequencies are sent from the card to the attenuator box, fed via BM-174-3 cables to the generating transducer. The received signal is sent directly to the oscilloscope and displayed on the oscilloscope where the amplitude and travel time are measured. Samples were sandwiched between a pair of longitudinal transducers using a custom-made holder. Tests were conducted at 1MHz. The speed of sound was determined by measuring the time of travel through the sample.

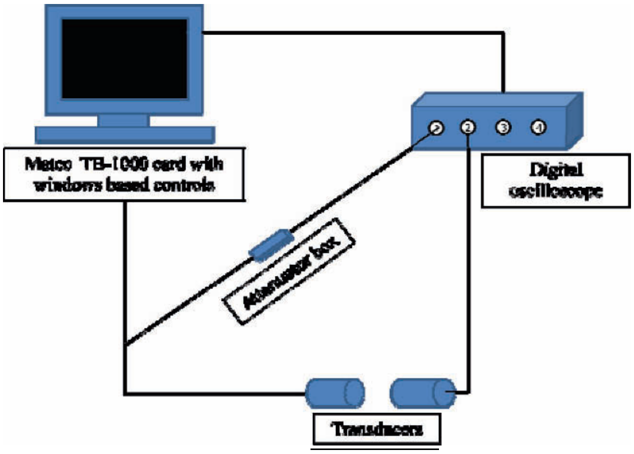

Fig. 1 Ultrasonic experimental setup

3. RESULTS AND DISCUSSION

3.1 Density

Densities of composites specimens were determined for all volume fractions. As expected, the density of the composite material decreased as the volume fraction of fly ash increased. When the volume fraction increased up to 30%, the density of the composite material is lower than water, about 11.3% less than the neat polyurea.

3.2 Microstructure

From the fractographs of the composites filled with various volume fractions of fly ash, it is clear that the polyurea matrix is very dense and there are no obvious micropores, and the fly ash particles are distributed homogeneously in the matrix with no signs of agglomerates. Furthermore, there are no observable cracks or voids between the remaining fly ash and the matrix, indicating that the fly ash particles have good interfacial adhesion with the matrix.

3.3 Dynamic mechanical analysis

The storage modulus of the composites increases by increasing the volume fraction of fly ash, and the increment is more pronounced in the rubbery zone ($T>T_g$) than in the glassy region ($T<T_g$). There is a jump in the relative modulus E_c'/E_m' (E_c' and E_m' are the storage moduli of the composites and polyurea matrix, respectively) near T_g, and the magnitude of this jump increases as the fly ash volume fraction increases. A theory based upon the concept that there are some particle-particle contacts in doublets and in agglomerates containing a larger number of particles was developed by Lee[9]. A similar trend can be observed in the case of loss modulus.

Glass transition temperature T_g is measured as the temperature at the peak of the loss modulus at 1Hz. It increases with the increasing fly ash content which may be due to the segmental immobilization of the fly ash surface. This result suggests that the degree of crosslinking may increase as a result of the addition of fly ash.

3.4 Ultrasonic properties

The speed of sound increases almost linearly with the increasing fly ash content. At a volume fraction of 30%, the speed of sound in the composites is 20% higher than that in neat polyurea. The longitudinal modulus and acoustic impedance of the composites were calculated from

$$\mathrm{L} = \mathrm{v}^2 \cdot \rho \tag{2}$$

$$\mathrm{Z} = \rho \cdot \mathrm{v} \tag{3}$$

In these equations, L is the longitudinal modulus(Pa), v is the speed of sound in the composites(m/s), ρ is the density(kg/m^3) and Z is the acousitc impedance of the composites(kg/m^2-s). These quantities demonstrate the similar trend as the sound speed in the composites.

ACKNOWLEDGEMENTS

This research has been conducted at the Center of Excellence for Advanced Materials (CEAM) at the University of California, San Diego. The authors thank Professor Gaohui Wu of Harbin Institute of Technology for supplying the fly ash utilized in this study. This work was partially supported through the Office of Naval Research (ONR) grant N00014-09-1-1126 to University of California, San Diego.

REFERENCES

[1] Mock. W; Balizer, E., Penetration protection of steel plates with polyurea layer, Presented at Polyurea Properties and Enhancement of Structures under Dynamic Loads, 2005, Airlie, VA.

[2] Amini, M.R.; Isaacs, J.B.; Nemat-Nasser, S., Effect of polyurea on the dynamic response of steel plates, Proceedings of the 2006 SEM Annual Conference and Exposition on Experimental and Applied Mechanics, St Louis, MO. June 4-7, 2006.

[3] Bahei-el-din, Y.A.; Dvorak, G.J., A blast-tolerant sandwich plate design with a polyurea interlayer, International Journal of Solids and Structures, 43(25-26), 7644-7658, 2006

[4] Tekalur, S.A.; Shukla, A.; Shivakumar, K., Blast resistance of polyurea based layered composite materials, Composite Structures, 84, 271-281, 2008

[5] Oliver P., Ioualalen K., Cottu J.P., Dynamic Mechanical Spectrometry Analysis of Modifications in the Cure Kinetics of Polyepoxy Composites, Journal of Applied Polymer Science, 63(6), 745-760, 1998

[6] The Dow Chemical Company, Isonate 143L; Modified MDI (Dow Chemical, Midland, MI, 2001).

[7] Air Products Chemicals, Inc., Polyurethane Specialty Products (Air Products and Chemicals, Allentown, PA, 2003).

[8] Dou, Z.Y. Study of damping and impact energy absorption behaviors and mechanisms of cenosphere/Al porous meterials, PhD dissertation, Harbin Institute of Technology , 2008

[9] Lee, B.L.; Nielsen, L.E., Temperature dependence of the dynamic mechanical properties of filled polymers, Journal of Polymer Science Part B: Polymer Physics, 15, 683-692, 1997

Proceedings of the SEM Annual Conference
June 7-10, 2010 Indianapolis, Indiana USA
©2010 Society for Experimental Mechanics Inc.

Dynamic-tensile-extrusion response of polytetrafluoroethylene (PTFE) and polychlorotrifluoroethylene (PCTFE)

Carl P. Trujillo[1], Eric N. Brown[2], G.T. Gray III[1]
[1]Los Alamos National Laboratory, MST-8, Los Alamos, NM 87545 USA
[2]Los Alamos National Laboratory, ADW, Los Alamos, NM 87545 USA

ABSTRACT

Dynamic-Tensile-Extrusion (Dyn-Ten-Ext) experiments have been utilized to probe the dynamic tensile responses of polytetrafluoroethylene (PTFE) and polychlorotrifluoroethylene (PCTFE). These fluoropolymers exhibit more irregular deformation and stochastic-based damage and failure mechanisms than the stable plastic elongation and shear instabilities observed in metals. The technique elucidates a number of tensile mechanisms that are consistent with quasi-static, SHPB, and Taylor Impact results. Similar to the observed ductile-to-brittle transition for Taylor Impact loading, PCTFE failure occurs at a peak velocity greater than for PTFE. However, for the Dyn-Ten-Ext PCTFE exhibits even greater resistance to failure due to the tensile stress-state. While PTFE generates a large number of small fragments when extruded through the die, PCTFE draws out a smaller number of larger particles that dynamically evolve during the extrusion process through a combination of local necking mechanisms and bulk relaxation. Under Dyn-Ten-Ext loading, the propensity of PTFE to fail along normal planes is observed without indication of any localization, while the PCTFE clearly forms necks during the initial extrusion process that continue to evolve.

INTRODUCTION

The quasi-static and dynamic responses of polytetrafluoroethylene (PTFE, Teflon) [1–15] and polychlorotrifluoroethylene (PCTFE, Kel-F 81) [1,16] have been extensively characterized. Both polymers are semicrystalline, with PCTFE having one out of every four fluorine atoms along the polymer backbone substitutive with a chlorine atom. Structurally, this substitution does not significantly change the level of crystallinity or the density, but does suppress the crystalline phase transitions observed in PTFE [2–6]. The properties are more notably modified by this addition, with the longitudinal and transverse sound speeds increased by approximately 50% and the flow stress of PCTFE being two to four times greater than that of PTFE for a given condition of temperatures ranging from -100 to 150°C and strain rates from 10-4 to 3200 s-1 [1,6,7,16]. The two polymers also exhibit signifi-cantly different failure behavior under tensile loading. Polytetrafluoroethylene resists formation of a neck and exhibits significant strain hardening. Independent of temperature or strain rate, PTFE sustains true strains to failure of approximately 1.5. On the other hand, PCTFE consistently necks at true strains of ~0.05 [16]. Below the glass transition temperature (48°C) in PCTFE necking is unstable, resulting in either a decreasing ability to bare load or dynamic failure. Above the glass transition temperature, the neck is stable but the total elongation remains significantly less than observed for PTFE.

In this study we investigate the response of PCTFE and PTFE under Dynamic-Tensile-Extrusion (Dyn-Ten-Ext). The Dyn-Ten-Ext technique was original developed for metals and applied to copper and tantalum spheres by Gray et al., [17,18] as a tensile corollary to compressive Taylor Cylinder Impact testing [19]. Similar to Taylor testing, Dyn-Ten-Ext is a strongly integrated test, probing a wide range of strain rates, plastic strains, and stress states. A light gas gun is employed to drive 7.62 mm diameter samples at velocities on the order of hundreds of meters per second. However, unlike the case of the Taylor Impact test where a rod is driven into a semi-infinite steel block, the Dyn-Ten-Ext test drives the sample through an extrusion die. The resulting stress state is more dominantly tensile leading to dynamic tensile elongation followed by necking, particulation, and finally failure.

EXPERIMENTAL TECHNIQUES

This investigation was performed on semi-crystalline PTFE and PCTFE commercial plate materials. The pedigree of these materials has been characterized and key properties are presented in Table 1. Spherical specimens, 7.58 mm in diameter, where machined from the two polymers. Dynamic tensile extrusion tests were conducted in a modified 7.62 mm diameter Taylor cylinder facility [17,18]. Polymer spheres were accelerated in a He-gas

T. Proulx (ed.), *Dynamic Behavior of Materials, Volume 1*, Conference Proceedings of the Society for Experimental Mechanics Series,
DOI 10.1007/978-1-4419-8228-5_11, © The Society for Experimental Mechanics, Inc. 2011

launcher at a range of speeds up to 1000 m s-1 into a high-strength steel extrusion die (A2 or S7 tool steel with Rockwell hardness 56 and 54, respectively) designed with an entrance diameter of 7.62 mm and an exit diameter of 2.8 mm (a reduction of 63%). The post-extrusion macroscopic evolution of the samples upon exiting the extrusion die was captured using high-speed photography and segments coming out of the die were soft captured by a technique described in Refs. [17,19]. An Imacon 200 high-speed camera was used to photograph the experiments. This camera is capable of taking up to 16 frames at a maximum rate corresponding to 200x106 frames/s. The exposure time and inter-frame time (IFT) of each exposure are fully programmable, and set to 500 ns and 15 µs respectively.

DISCUSSION AND CONCLUSIONS

A more complete discussion of Dyn-Ten-Ext measurements on PTFE and PCTFE with associated complete photographic sequences have recently been reported by Brown et al. [20, 21]. Both polymers investigated by the Dyn-Ten-Ext technique in the current work exhibited a threshold under which extrusion through the die was not observed: 164 and 259 m s-1 for PTFE and PCTFE, respectively. This threshold is analogous to the ductile-to-brittle transition previously reported for Taylor Impact loading of these two polymers. Similar to the observed ductile-to-brittle transition for Taylor Impact loading, PCTFE failure occurs at a peak velocity greater than for PTFE. However, for the Dyn-Ten-Ext PCTFE exhibits even greater resistance to failure due to the tensile stress-state. While PTFE generates a large number of small fragments when extruded through the die, PCTFE draws out a smaller number of larger particles that dynamically evolve during the extrusion process through a combination of local necking mechanisms and bulk relaxation. Under Dyn-Ten-Ext loading, the propensity of PTFE to fail along normal planes is observed without indication of any localization, while the PCTFE clearly forms necks during the initial extrusion process that continue to evolve. There is clearly greater opportunity to investigate the extruded samples post mortem towards understanding the active deformation mechanisms and the below threshold spheres for deformation and any onset of damage, these will be a focus of future work.

ACKNOWLEDGMENTS

Los Alamos National Laboratory is operated by LANS, LLC, for the NNSA of the US Department of Energy under contract DE-AC52-06NA25396. This research was supported under the auspices of the US Department of Energy and the Joint DoD/DOE Munitions Program.

REFERENCES

1. Brown E.N., Rae P.J., Gray G.T. III, “The influence of temperature and strain rate on the tensile and compressive constitutive response of four fluoropolymers” J. de Physic. IV 134, 935, 2006.
2. Brown E.N. and Dattelbaum D.M., “The role of crystalline phase on fracture and microstructure evolution of polytetrafluoroethylene (PTFE)” Polymer 46, 3056, 2005.
3. Rae P.J., Brown E.N., Clements B.E., and Dattelbaum D.M., “Pressure-induced phase change in poly(tetrafluoroethylene) at modest impact velocities” J. Appl. Phys. 98, 063521, 2005.
4. Bourne N.K., Brown E.N., Millett J.C.F., Gray G.T. III, “Shock, release and Taylor impact of the semicrystalline thermoplastic polytetrafluoroethylene” J. Appl. Phys. 103, 074902, 2008.
5. Brown E.N., Dattelbaum D.M., Brown D.W., Rae P.J., Clausen B., “A new strain path to inducing phase transitions in semi-crystalline polymers” Polymer 48, 2531, 2007.
6. Rae P.J. and Brown E.N., “The properties of poly(tetrafluoroethylene) (PTFE) in tension” Polymer 46, 8128, 2005.
7. Rae P.J. and Dattelbaum D.M., “The properties of poly (tetrafluoroethylene) (PTFE) in compression” Polymer 45, 7615, 2004.
8. Jordan J.L., Siviour C.R., Foley J.R., Brown E.N., “Compressive properties of extruded polytetrafluoroethylene” Polymer 48, 4184, 2007.
9. Brown E.N., Rae P.J., Dattelbaum D.M., Clausen B., Brown D.W., “In-situ measurement of crystalline lattice strains in polytetrafluoroethylene” Experimental Mechanics 48, 119, 2008.
10. Brown E.N., Clausen B., Brown D.W., “In situ measurement of crystalline lattice strains in phase IV polytetrafluoroethylene” J. Neutron Res. 15, 139, 2007.
11. Bourne N.K., Millett J.C.F., Brown E.N., Gray G.T. III, “Effect of halogenation on the shock properties of semicrystalline thermoplastics” J. Appl. Phys. 102, 063510, 2007.
12. Brown E.N., Rae P.J., Liu C., “Mixed-mode-I/II fracture of polytetrafluoroethylene” Maters. Sci. Engng. A 468–470, 253, 2007.

13. Brown E.N., Trujillo C.P., Gray G.T. III, Rae P.J., Bourne N.K., “Soft recovery of polytetrafluoroethylene shocked through the crystalline phase II-III transition” J. Appl. Phys. 101, 024916, 2007.
14. Brown E.N., Rae P.J., Orler E.B. Gray G.T. III, and Dattelbaum D.M., “The effect of crystallinity on the fracture of polytetrafluoroethylene (PTFE)” Mater. Sci. Engng. C 26, 1338, 2006.
15. Bourne N.K., Gray G.T. III, “Equation of state of polytetrafluoroethylene” J. Appl. Phys. 93, 8966, 2003.
16. Brown E.N., Rae P.J., Orler E.B., “The influence of temperature and strain rate on the constitutive and damage responses of polychlorotrifluoroethylene (PCTFE, Kel-F 81)” Polymer 47, 7506, 2006.
17. Gray III G.T., Cerreta E., Yablinsky C.A., Addessio L.B., Henrie B.L., Sencer B.H., Burkett M., Maudlin P.J., Maloy S.A., Trujillo C.P., Lopez M.F., “Influence of Shock Prestraining and Grain Size on the Dynamic-Tensile-Extrusion Response of Copper: Experiments and Simulation” in Shock Compression of Condensed Matter, 2007 (M. Elbert, M.D. Furnish, R. Chau, N. Holmes, J. Nguyen, eds.) pp. 725-728.
18. Cao F., Cerreta E.K., Trujillo C.P., Gray G.T. III, “Dynamic tensile extrusion response of tantalum” Acta Materialia 56, 5804, 2008.
19. Taylor G.I., “The use of flat-ended projectiles for determining dynamic yield stress. 1. Theoretical considerations” Proc. Roy. Soc. London A 194, 289, 1948.
20. Brown E.N., Trujillo C.P., Gray G.T. III “Influence of necking propensity on the dynamic-tensile-extrusion response of fluoropolymers” in DYMAT 2009: 9th International Conference on the Mechanical and Physical Behaviour of Materials Under Dynamic Loading, Vol. 1, 171-177, 2009.
21. Brown E.N., Trujillo C.P., Gray G.T. III, “Dynamic-Tensile-Extrusion Response of Fluoropolymers” in Conference of the American-Physical-Society-Topical-Group on Shock Compression of Condensed Matter, Vol. 2, Pages: 1233-1236, 2009

Proceedings of the SEM Annual Conference
June 7-10, 2010 Indianapolis, Indiana USA
©2010 Society for Experimental Mechanics Inc.

Dynamic Compression of an Interpenetrating Phase Composite (IPC) Foam: Measurements and Finite Element Modeling

Chandru Periasamy and Hareesh Tippur
Department of Mechanical Engineering
Auburn University, AL 36849
htippur@eng.auburn.edu

ABSTRACT

Dynamic compression response of Syntactic Foam (SF)–aluminum foam Interpenetrating Phase Composites (IPC) is measured. By infusing uncured syntactic foam (epoxy filled with hollow microballoons) into an open-cell aluminum network, a 3D interpenetrating structure is obtained. The uniaxial compression responses are measured at ~1500 /sec using a split Hopkinson pressure bar set up. The effect of volume fraction of microballoons on the compression response of IPC is examined in terms of yield stress, plateau stress and energy absorption. The response of IPC samples are also compared with those made using syntactic foam alone. For all volume fractions of microballoons, the IPC samples have better compression characteristics when compared to the corresponding syntactic foam samples. The failure modes of SF and IPC foams are examined both optically (using high-speed photography) and microscopically. The measured dynamic responses of SF are used in a finite element model based on a Kelvin cell representation of the IPC structure. Using infinite elements and measured particle velocity histories as input boundary conditions, the compression response of IPC foams have been successfully captured.

INTRODUCTION

Aerospace, automotive and marine industries demand novel multifunctional material solutions for structural problems. A class of composites called Interpenetrating Phase Composites (IPC) [1] has been gaining reputation recently mainly for their multifunctional capabilities. The IPC used in this work is a syntactic foam (SF) - aluminum foam based IPC. Syntactic foam is made by mixing hollow glass microballoons in epoxy. The IPC is made by infusing uncured syntactic foam into open cell aluminum foam prior to curing. In the current work, high-strain rate (~1500 per second) compression properties of IPCs made of four different volume fractions (V_f) of microballoons in SF are analyzed and compared with the pure SF counterparts. Surface analysis of real time deformation of samples and microscopic analysis of sectioned samples are also performed to understand the failure mechanisms. A unit cell based finite element model of the IPC is developed in which the aluminum structure is idealized as a tetrakaidecahedron (a 14 sided polyhedron) called Kelvin cell [2]. Experimentally measured material properties of SF are used for the SF region in the computational model. Infinite elements [3] are used to model the far field region surrounding the unit cell. Finite element results of IPC compare well with those from experiments.

MATERIAL SPECIFICATIONS

The SF foam is prepared by first mixing low viscosity epoxy (Epo-Thin^{TM} from Beuhler, Inc. USA, mass density of resin ~1100 kg/m^3) and hollow glass microballoons (K-1^{TM} microballoons from 3M Corp., bulk density 125 kg/m^3) of average diameter ~60 μm and wall thickness ~0.6. The uncured SF is then transferred into a silicone rubber mold after vacuuming to remove any trapped air bubbles. The mixture is then allowed to cure for seven days before being removed and machined to size. The aluminum foam used in the IPC is a commercially available open-cell Duocel® aluminum (Al6101-T6) foam (ERG aerospace Corp., with a pore density of 40 pores per inch; ~8% relative density). The metal foam is cleaned with acetone and then coated with silane to enhance the bond strength between the aluminum ligaments and the SF. To prepare the IPC, the degassed, uncured SF is prepared the same way as before. Then, the silane coated aluminum foam is slowly inserted into the mold containing the uncured syntactic foam so that the syntactic foam fills in the open pores of the aluminum network. After curing, the unfinished sample is removed from the mold for machining. The length and diameter of the machined samples used in the dynamic tests are 9.5 mm and 12.7 mm, respectively.

T. Proulx (ed.), *Dynamic Behavior of Materials, Volume 1*, Conference Proceedings of the Society for Experimental Mechanics Series,
DOI 10.1007/978-1-4419-8228-5_12, © The Society for Experimental Mechanics, Inc. 2011

EXPERIMENTAL RESULTS

SF and IPC samples with 10%, 20%, 30% and 40% microballoon volume fractions in SF were tested at a strain rate of ~1500 per second using a split Hopkinson pressure bar (SHPB) [4] developed for this purpose. The stress-strain responses, energy absorption capacities and failure processes of SF and IPC samples are discussed below.

Stress-strain response

The dynamic true stress – true strain response of syntactic foam has two distinct regions (Fig 1(a)). An initial linear elastic response is followed by a monotonically decreasing stress region with increasing strain. The compressive strengths of the 10%, 20%, 30% and 40% volume fraction SF samples are approximately 104 MPa, 80 MPa, 62 MPa and 50 MPa, respectively. The relative decrease in the compressive strengths for every 10% increase in the microballoon volume fraction is ~20%. The tendency for the SF with lower volume fraction of microballoons (10% and 20%) to soften after attaining the maximum stress is somewhat more distinct than for the ones with higher volume fraction of microballoons (30% and 40%). After yielding, the stresses for SF with lower V_f of microballoons remain consistently higher than that for SF with higher V_f. The difference in stress values after yielding between specimens with different volume fraction of microballoons is approximately constant at all strains (within the observation window). The dynamic compression response (Fig 1(b)) of IPC foams follow trends similar to that of the corresponding V_f syntactic foams. In the order of increasing microballoon V_f, the maximum stress values attained by IPC are approximately 120 MPa, 100 MPa, 80 MPa and 60 MPa. The percentage decrease in the compressive strength for the IPC-20 with respect to that of IPC-10 is 17%, and that of IPC-30 with respect to that of IPC-20 is 20%. The IPC-40 has a 25% decrease in compressive strength with respect to the IPC-30. In general, for all volume fractions, the yield strengths of IPC are higher than that of corresponding SF.

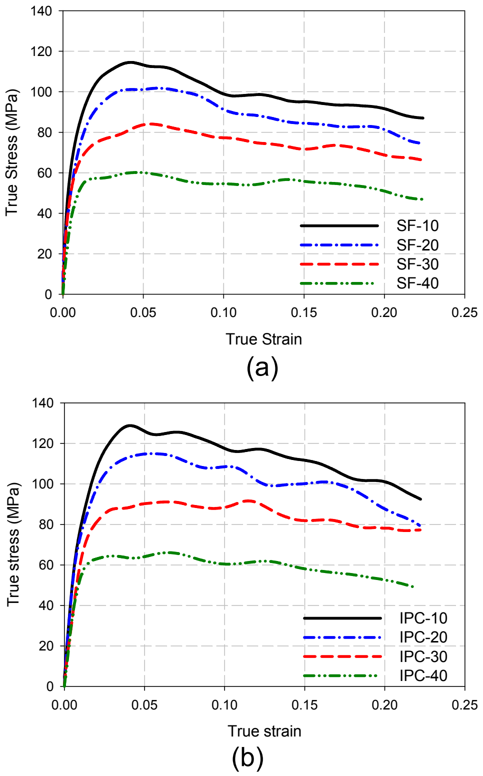

(a)

(b)

Figure 1: Dynamic compression responses of (a) SF and (b) IPC foams (Strain rate ~ 1500/s)

Energy absorption

The energy absorbed per unit volume by SF and IPC were evaluated up to a strain value of 22% as $U_{0.22}$ and are shown in Fig 2. Energy absorbed by SF-10, SF-20, SF-30 and SF-40 samples are 21.9 MJ/m^3, 19.6 MJ/m^3, 16.4 MJ/m^3 and 12.1 MJ/m^3, respectively and that by IPC-10, IPC-20, IPC-30 and IPC-40 samples are 24.5 MJ/m^3, 22.0 MJ/m^3, 18.3 MJ/m^3 and 12.7 MJ/m^3, respectively. The percentage reduction in $U_{0.22}$ per unit volume for the SF-20 / SF-10, SF-30 / SF-20 and the SF-40 / SF-30 pairs are approximately 11%, 16% and 26% respectively. The percentage reduction in $U_{0.22}$ per unit volume for the IPC-20 / IPC-10, IPC-30 / IPC-20 and the IPC-40 / IPC-30 pairs are approximately 10%, 17% and 30%, respectively. The trend of the percentage reduction in the energy absorption per unit volume suggests that the rate of reduction in $U_{0.22}$ would be greater than the rate of increase of the microballoon volume fraction for dynamic loading. Also, IPC samples have higher energy absorption capacities per unit volume when compared to corresponding SF samples.

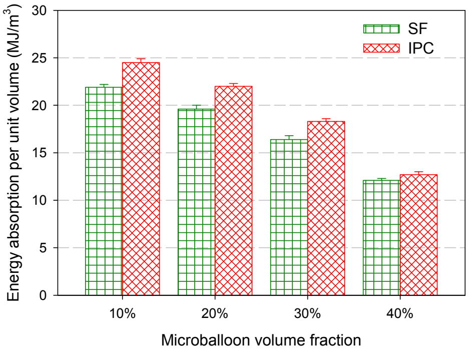

Figure 2: Energy absorbed per unit volume by SF and IPC under dynamic loading up to 22% true strain

Failure progression

Another interesting outcome under dynamic loading conditions is strain recovery in SF and IPC foam samples. The final lengths of the deformed samples were measured after the tests for both SF and IPC. Interestingly, for SF samples, the final measured lengths were more than that predicted by the SHPB equations following a 25% engineering strain. This suggests that the SF samples had partially recovered (sprung-back) after deformation.

However, this phenomenon was negligible in case of IPC samples. The spring back in the SF is potentially overcome in the IPC by the aluminum ligaments. Once aluminum ligaments undergo plastic deformation, they prevent the SF from spring-back. The spring-back phenomenon was verified by recording the failure of SF and IPC foams in real-time using high-speed photography. Backlit photographs of deformed SF and IPC samples with 30% V_f of microballoons are shown in Fig 3. A network of shear bands crisscrossing the entire sample and oriented at approximately ±45° to the loading direction can be readily seen. Micrographs of deformed 30% V_f SF and IPC specimens are shown in Fig 4. The cracks that appear in the images are skewed at an angle of approximately 45° to the direction of application of the load suggesting failure due to shear localization. In regions away from the crack, the microballoon footprints are circular suggesting very little deformation. However, shear bands in IPC are interrupted by the metallic ligaments. The other type of failure in IPC, which is absent in pure SF samples, is the debonding of the interfaces between the syntactic foam and the aluminum ligaments.

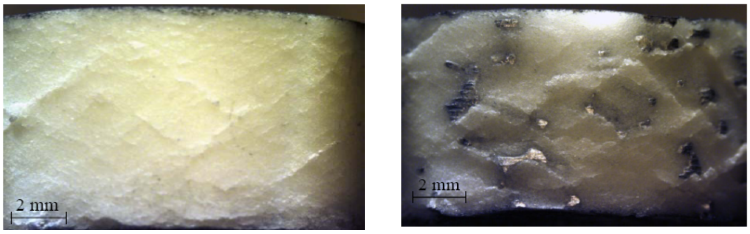

(a) (b)

Figure 3: Side view of dynamically deformed (a) SF and (b) IPC samples (Loading was along the vertical direction)

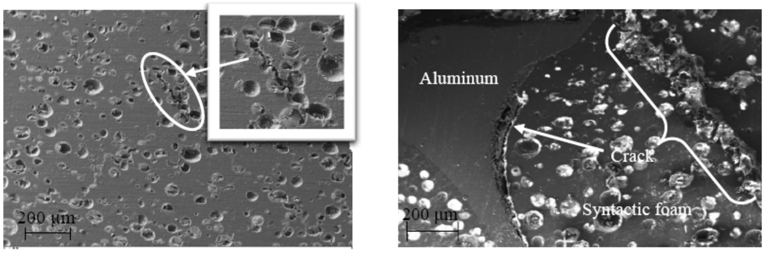

(a) (b)

Figure 4: SEM image of cross section of dynamically deformed (a) SF and (b) IPC samples (Loading was along the vertical direction)

FINITE ELEMENT MODELING

A unit cell finite element model of the IPC foam was used to predict the dynamic compression response. The geometry was modeled using the solid modeling software Solid Edge and imported into the finite element analysis software ABAQUS. The three dimensional connectivity of aluminum ligaments of the cell was modeled as an idealized 14 sided polyhedron (tetrakaidecahedron). Based on the measurements on the ligaments of the actual aluminum foam and the volume fraction of aluminum in the actual IPC, the dimensions of the ligament were chosen. Accordingly, the length of the ligaments is 1.5 mm and the cross section is triangular with ~0.78 mm edges. In a dynamically loaded sample, stress waves travel through the entire length of the sample before reflecting at the end of the sample, whereas in the model the stress waves would get reflected at the boundaries of the cell itself.

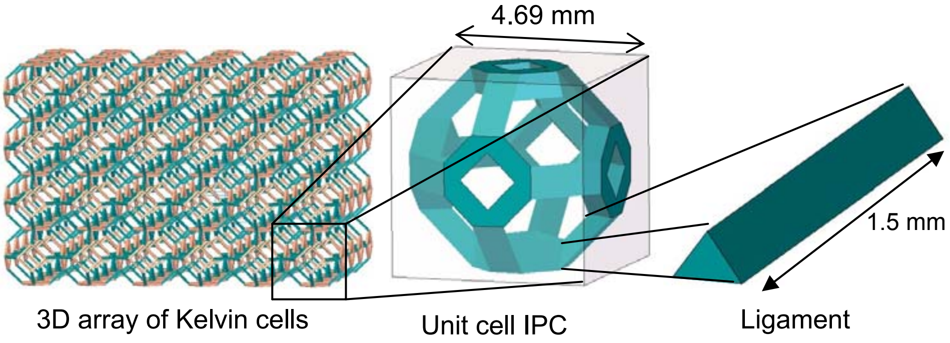

Figure 5: Schematics representing the building blocks of an idealized Kelvin cell based IPC

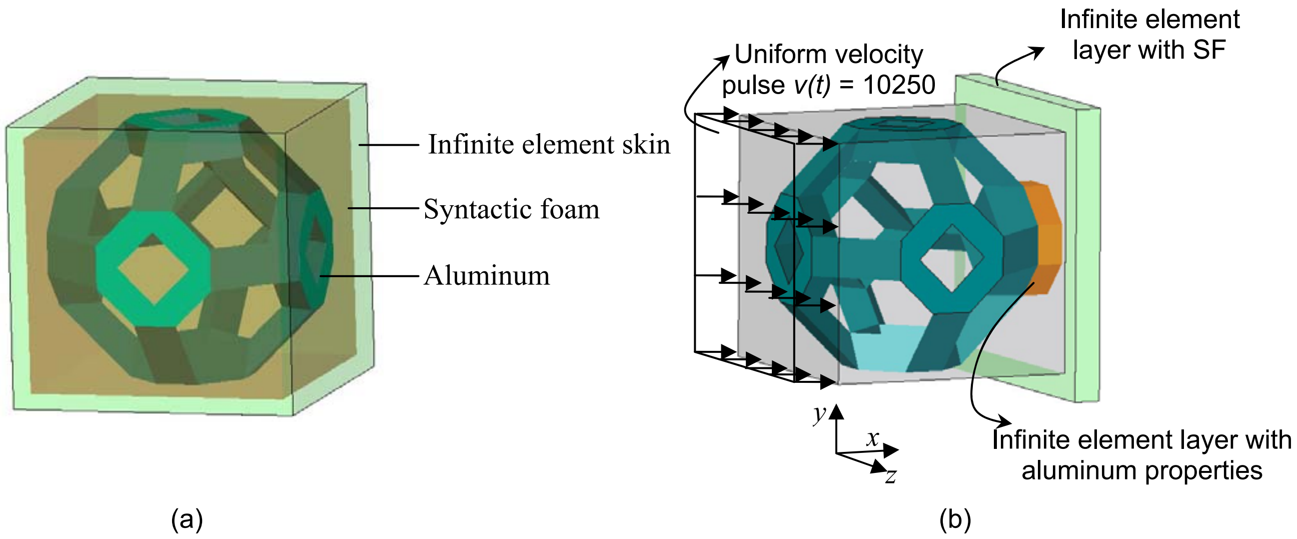
Infinite element skin
Syntactic foam
Aluminum
Uniform velocity pulse $v(t)$ = 10250
Infinite element layer with SF
y
x
z
Infinite element layer with aluminum properties

(a) (b)

Figure 6: (a) Unit cell model with outer infinite element layer. (b) Load and boundary conditions

To overcome this shortcoming, a skin of SF and aluminum material was modeled adjacent to the corresponding material at the boundary of the cell. This skin was discretized using the so-called *infinite elements* to represent the far field regions surrounding the unit cell. Figure 5 shows the schematic of the building blocks of the model and the boundary conditions applied are shown in Figs. 6 (a) and (b).

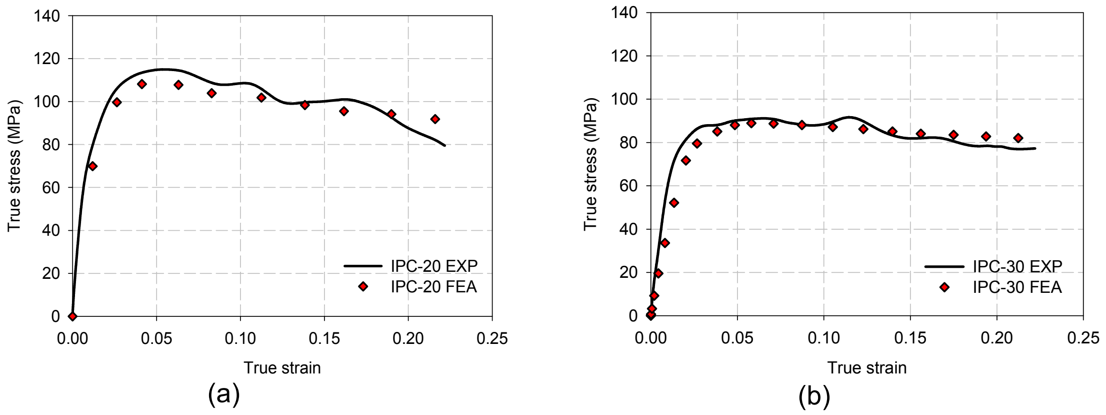

(a) (b)

Figure 7: Comparison of experimental and FEA results of (a) IPC-20, (b) IPC-30

The measured particle velocity history (10250 mm/s for ~ 250 microseconds) in the incident bar of the SHPB was used as the load input to the computational model. The input velocity pulse was applied on the surface of the unit cell which marks the boundary between the unit cell IPC and the infinite element layer on one side. IPC models corresponding to all four volume fractions of microballoons were simulated and the results are compared to that of the experiments. In Fig 7 the results for 20% and 30% volume fraction microballoons in SF are shown. Evidently, a good agreement between computations and measurements exists.

SUMMARY

Uniaxial compression characteristics of Interpenetrating Phase Composite (IPC) foams have been studied under dynamic loading conditions using a split Hopkinson pressure bar apparatus. The IPC foams were made by infusing uncured epoxy-based syntactic foam (SF) into open-cell aluminum preforms. Curing of SF resulted in an IPC structural foam with a 3D interconnectivity. The dynamic compression responses of IPC foams made of SF with 10% - 40% V_f of hollow glass microballoons have been studied. The responses of IPC foams have also been evaluated relative to their pure SF counterparts. The V_f of microballoons in SF plays a dominant role in the overall response of the SF and IPC foams studied. A monotonic increase in elastic modulus, yield stress, and plateau stress are evident as V_f of microballoons decrease. The IPC foams consistently have higher value of each of these characteristics relative to the corresponding SF. The energy absorbed per unit volume by the IPC under dynamic conditions is about ~10% higher than the SF counterparts. The failure of SF and IPC under dynamic conditions is dominated by the formation of an extensive network of shear bands in SF. In addition to microballoon crushing as seen in SF, IPC samples show debonding of aluminum ligaments from the surrounding SF. A unit cell model of the IPC using a space-filling polyhedron – tetrakaidecahedron has been successfully developed using ABAQUS. Infinite elements were used to model the far field region of the computational model. The stress-strain responses of the model IPC's have been compared to those from experiments. A good agreement between the simulated and the experimental results has been observed.

REFERENCES

1. Clark D. R., 'Interpenetrating phase composites', *Journal of the American Ceramic Society*, 75(4), pp 739-759, 1992.
2. Thompson W (Lord Kelvin), 'On the division of space with minimum partitional area', *Philosophical Mag.*, 24, pp 503-514, 1887.
3. Bettess P, 'Infinite elements', *International Journal for numerical methods in engineering*, 11, pp 53-64, 1977.
4. Kolsky, H., 'An investigation of the mechanical properties of materials at very high rates of strain', *Proceedings of the Physical Society*, Section B, 62, 676-700, 1949.

Proceedings of the SEM Annual Conference
June 7-10, 2010 Indianapolis, Indiana USA
©2010 Society for Experimental Mechanics Inc.

Improved Mechanical Properties of Nano-nickel Strengthened Open Cell Metal Foams

Dipl.-Chem. Anne Jung[1,2,3], Dr. Harald Natter[1], Prof. Dr. Rolf Hempelmann[1],
Prof. Dr. Stefan Diebels[2], Dr. Erhardt Lach[3]

[1] Saarland University, Physical Chemistry, 66123 Saarbruecken, Germany
[2] Saarland University, Applied Mechanics, 66123 Saarbruecken, Germany
[3] French-German Research Institute of Saint-Louis (ISL), 68301 Saint-Louis, France

Dipl.-Chem. Anne Jung
Am Markt – Zeile 3
66125 Saarbruecken
D-Germany
anne.jung@mx.uni-saarland.de

ABSTRACT

Metal foams are low impedance materials which are often used as light weight construction elements, energy absorber and for structural damping. We have coated open cell aluminum foams by a nanocrystalline nickel coating via an electrodeposition process and in this way we could improve the stiffness, energy absorption capacity and the damping behavior of the foams. The mechanical behavior of the coated foams could be tuned by the crystallite size and the thickness of the coating. The foams were characterized in quasi-static compression tests as well as in dynamic compression tests, using a Split Hopkinson pressure bar (SHPB). At the optimized coating thickness of 150 µm Ni, there was an enhancement effect of the energy absorption capability of 800% for 10 ppi foams. Ballistic tests showed the applicability of the foams as splinter shield. A big opportunity of open cell metal foams is that they can be filled for example with elastomeric materials and build a composite structure.

INTRODUCTION

Metal foams are solid foams, so called metal cellular structures, containing a large volume fraction of gas-filled pores. They mimic the construction elements of bones as the spongiosa, honeycombs, cellular structure elements of wood or cork. Based on the nature of their pores, metal foams are classified in open cell metal foams with an interconnected framework of pores and closed cell metal foams with sealed pores. The ppi number is the number of pores per inch and acts as a measure to characterize the structure of open cell metal foams. According to their high stiffness to weight ratio metal foams are used as lightweight construction elements. The special stress vs. strain characteristics of metal foams is favorable for applications as energy absorber and for structural damping [1].

Open cell aluminum foams, purchased from m-pore, Dresden, were used as substrate in a coating process via electrodeposition. A detailed description of the coating process, the special conditions needed for complex three dimensional substrates as metal foams and the optimization of this coating process has been presented in previous works [2-4].

MECHANICAL CHARACTERIZATION

The stress vs. strain characteristics of metal foams is divided into three parts. The first part is the linear elastic deformation of the foam according to Hooke's law. At the plastic collapse stress the first cell of the foam deforms plastically and undergoes large deformation at a nearly constant stress, the plateau stress. This is a

T. Proulx (ed.), *Dynamic Behavior of Materials, Volume 1*, Conference Proceedings of the Society for Experimental Mechanics Series,
DOI 10.1007/978-1-4419-8228-5_13, © The Society for Experimental Mechanics, Inc. 2011

result of the bending and fracturing of the cell edges. At the densification point there is a strong rise in stress. The foam shows the behavior of a bulk material made of the same metal as the foam. The integral of the stress up to a certain strain is the amount of mechanical energy absorbed by the foam.

Quasi-static compression test

In a previous work, it could be shown that a coating of nanostructured nickel with a crystallite size of 43 nm is the best coating metal to increase the stiffness, the strength and the energy absorption capacity of open cell aluminum foams [5]. Cubic nickel coated 10 ppi foams with an edge length of 40 mm and plate-shaped 30 ppi foams with an area of 40 x 40 mm^2 and a thickness of 5 mm have been tested on a INSTRON universal testing machine under compressive loading at strain rates of $5 \cdot 10^{-3}$ s^{-1}. Based on the fact that metal foams are very complex structures and to have better statistics of the results, for each sample type the tests were carried out at least three times. Figure 1 shows the effect of the pore size (1a) and the coating thickness (1b, 10 ppi foams) on the stress vs. strain characteristics.

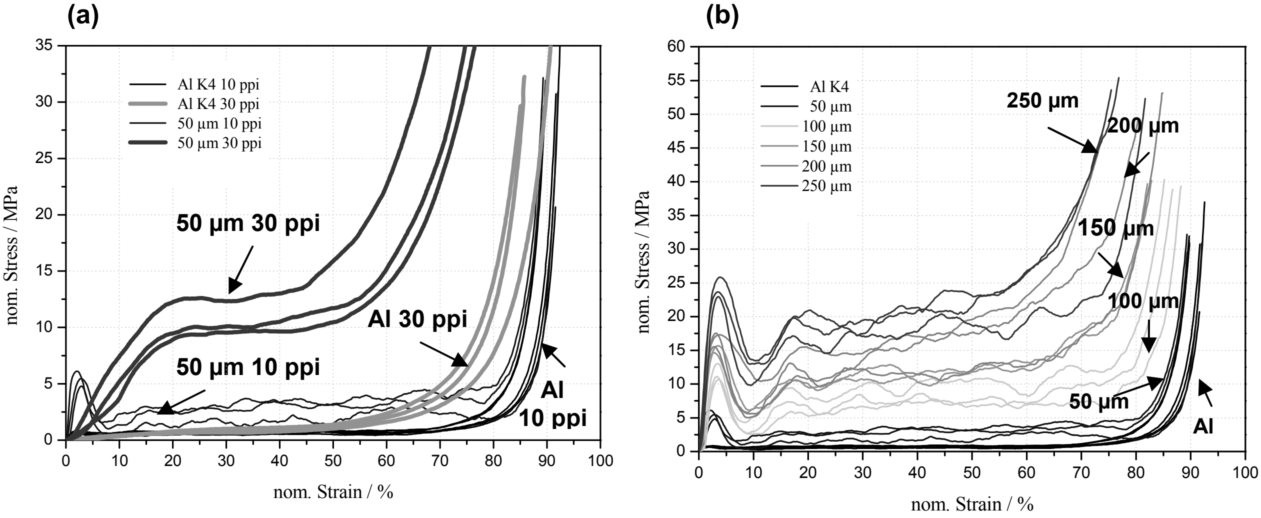

Figure 1: Effect of the pore size (1a) and the coating thickness (1b, 10 ppi foams) on the stress vs. strain characteristics.

For 30 ppi foams, the excessive stress of the plastic collapse in comparison to the plateau stress is much lower than for 10 ppi foams. Higher ppi-numbers are correlated with smaller pore sizes. The decrease in the excessive stress at the plastic collapse and the increase of the plateau stress for smaller pore sizes can be explained by the smaller bending length of the cells [6].

Figure 1b outlines the effect of an increasing coating thickness of nickel on the cubic 10 ppi foams. The plastic collapse stress and the plateau stress of the foams increase linearly with an increasing coating thickness, the densification and compression points decrease.

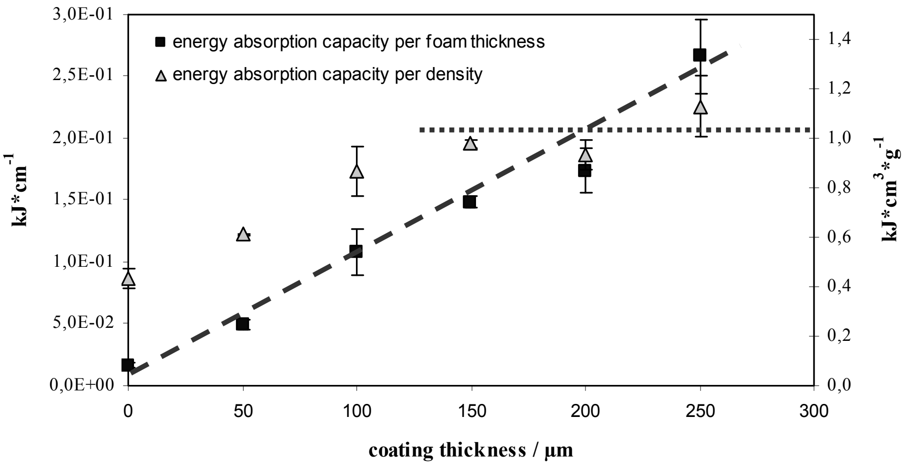

Figure 2: Dependency of the specific energy absorption capacity of nickel coated 10 ppi foams from the coating thickness.

The dependency of the specific energy absorption capacities of the nickel coated 10 ppi foams on the coating thickness is shown in figure 2. There is also a linear increase of the absolute values and the specific energy absorption capacity per foam thickness of the foams with an increasing coating thickness. But for the specific energy absorption capacity per density for coating thickness higher than 150 µm Ni the mass increase overcompensates the increase in the energy absorption capacity. Hence, there is an optimal coating thickness of 150 µm Ni. With this coating thickness the energy absorption capacity could be enhanced by factor of 8.

Dynamic compression tests

For an application as crash absorber or lightweight armor the material behavior under dynamic loading is very important. Dynamic compression tests have been performed at strain rates up to 5000 s^{-1} using a classical Split Hopkinson pressure bar (SHPB) apparatus [7]. The bars are made of Zicral (AlZn 7075) and had a diameter of 20 mm. The samples consist of 30 ppi foams with a diameter of 20 mm and a thickness of 5 mm with no coating or a coating thickness of 50 µm and 75 µm Ni, respectively. For reason of better statistics each test has been repeated at least three times.

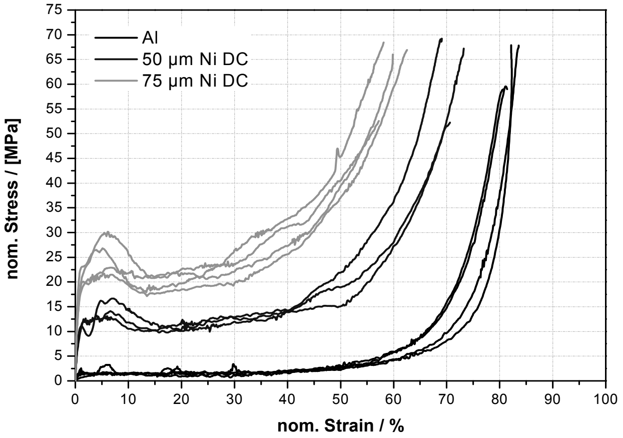

Figure 3: Stress vs. strain characteristics under dynamic loading.

Figure 3 shows the results of the SHPB tests. The plastic collapse stress and the plateau stress increase linearly with the coating thickness, the densification and compression points decrease. There is also a linear increase of the absolute value of energy absorption capacity and the specific energy absorption capacity per foam thickness (about 300% for 75 µm Ni) but there is a decrease of the specific energy absorption capacity per mass and per density with increasing coating thickness of about 3% for 50 µm Ni and 12% for 75 µm Ni in comparison to the uncoated foams.

Ballistic tests

In order to investigate the applicability of the strengthened foams as armor for slow bullets or as splinter shield ballistic tests have been performed. Metal foams show a high strength of the complete structure but only a low strength of a single strut. Compared with the abovementioned compression tests in the ballistic tests there is a more point-shape loading of the foams. Hence, the point-shape loading of the bullet has to be distributed over the foam to create a more areal loading. In this study the distribution of the loading on the foams has been done by shielding plates made of aluminum (Al 99.5%, thickness 1 mm). The ballistic tests were performed by using a steel bullet (1.4034 / X 46 Cr 13 / DIN EN 10088) with a diameter of 10 mm and a mass of 4.0 g. The bullet has been accelerated by a nitrogen driven compressed air gun. The impact velocity on the target was about 300 m/s. The tests have been observed with a high speed camera and analyzed via the residual velocity of the bullet after the perforation of the target. The nine different tested target types which are a combination of different foams and a certain number of shielding plates are listed in table 1.

Table 1: target types

Type of the target	**description**
Typ A	stack of 3 foams (10 ppi) with a thickness of 10 mm and 4 shielding plates
Typ B	stack of 3 foams (30 ppi) with a thickness of 10 mm and 4 shielding plates
Typ C	stack of one foam (10 ppi) with a thickness of 30 mm and 2 shielding plates
Typ D	stack of one foam (30 ppi) with a thickness of 30 mm and 2 shielding plates
Typ E	stack of 4 shielding plates with interspaces of 10 mm

The foams and the shielding plates were stacked alternatingly. Target type marked with an “N” after the type consist of coated foams with a coating thickness of 150 µm Ni for the 10 ppi foams and 75 µm Ni for the 30 ppi foams, respectively.

Figure 4 shows a comparison of the flight length of the bullet in millimeter after the perforation of the targets 400 µs after the impact of the bullet on the target. The target types C and D show a worse performance than type E which is only a stacking of the four shielding plates with interspaces of 10 mm. The target type D with the small pore structure (30 ppi) was a little bit better than the 10 ppi foam. Both for the 10 ppi and for the 30 ppi foams the energy absorbed by the deformation of the target could by increased by the nickel coating and the coated types CN and DN are better than the reference type E.

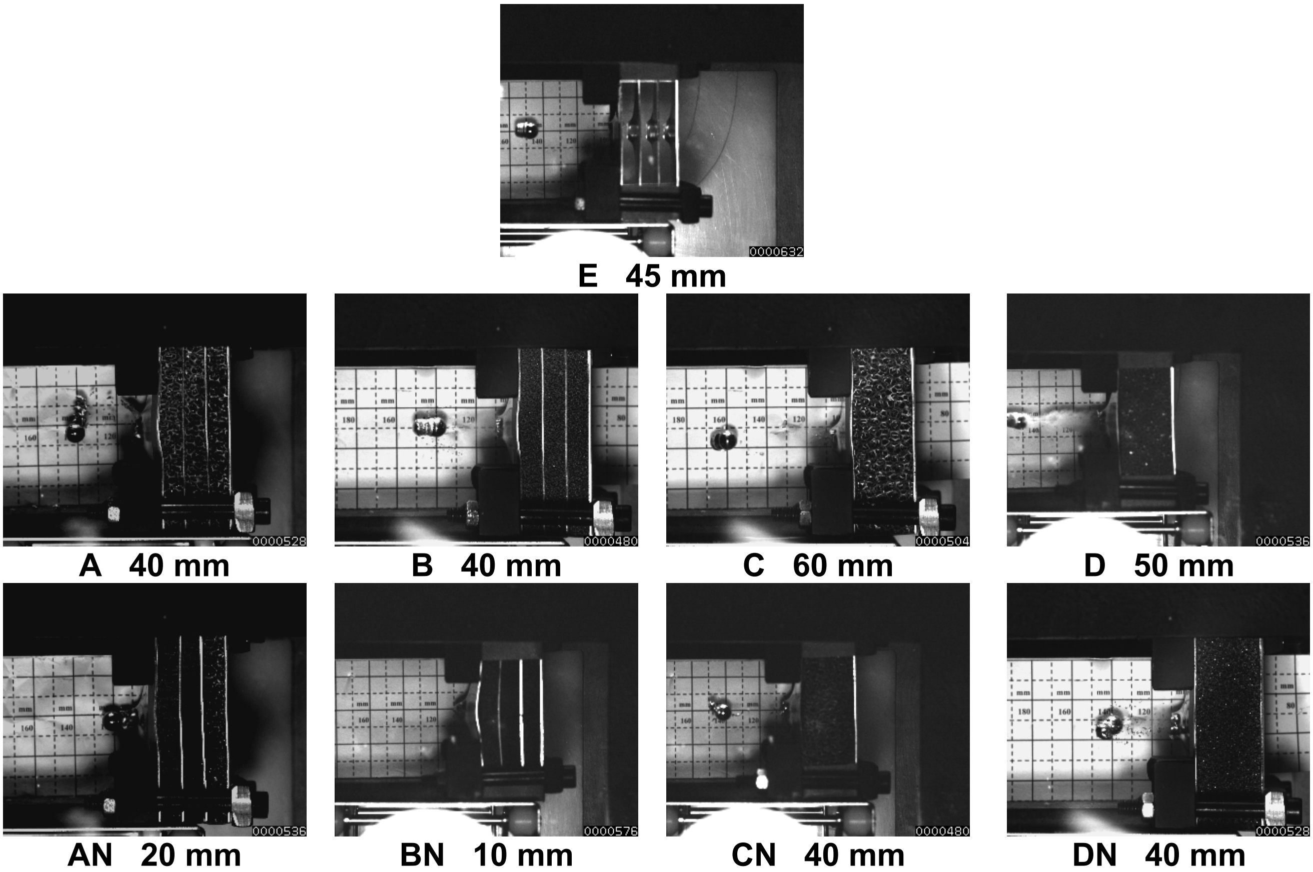
E 45 mm

A 40 mm

B 40 mm

C 60 mm

D 50 mm

AN 20 mm

BN 10 mm

CN 40 mm

DN 40 mm

Figure 4: Comparison of the flight distance of the bullet after the perforation of the target 400 µs after the impact of the bullet on the target.

For the alternating stacking of three foams and four shielding plates there is a shorter flight distance of the bullet after the perforation which is equivalent to a higher amount of the energy of the bullet absorbed by the target structure. By coating the foams (type AN and BN) the absorbed deformation energy by the target in relation to the uncoated foams is higher than for the types CN and DN. This is a proof for the assumptions of a distribution of the point-shape loading of the energy of the bullet by the incorporation of shielding plates. The best performance as splinter shield and as armor for slow flying bullets has been shown by the stacking of three nickel coated 30 ppi foams and 4 shielding plates (type BN). The residual velocity of the bullet was so low that the bullet had not left the back of the target 400 µs after the impact yet.

CONCLUSION

Coating open cell metal foams with nanocrystalline nickel is a good way to improve the stiffness, strength and the energy absorption capacity of open cell metal foams. The coated foams show a kind of twin-wall sheet effect. The light aluminum foam only acts as support for the coating and has hardly any effect on the mechanical properties of coated foams. The stiffness, strength and stability which do also affect the energy absorption capacity do completely result from the thin, nanostructured nickel coating. Up to a critical coating thickness the specific energy absorption capacity per density increases linearly with the coating thickness, then the mass increase overcompensates the increase in the energy absorption capacity. At the optimized coating thickness of 150 µm Ni, there was an enhancement effect of the energy absorption capability of 800% for 10 ppi foams.

The coated foams resist dynamic impact loading without a global collapse of the complete foam structure. There is no predetermined breaking point introduced by the stiff, nanostructured coating. The decrease of the specific energy absorption capacity per density and per mass outlines that under dynamic loading such strengthened foams show a higher potential for stationary applications than for mobile applications.

The ballistic tests showed that coated metal foams have potential for applications as splinter shield or protective barriers. A combination of several thin foam plates and shielding plates in a stack is necessary to distribute point-shape loading over the complete foam structure and hence to increase the absorbed impact energy of a bullet. Smaller pore sizes, which are correlated to higher ppi numbers are better than larger pores.

A big opportunity of coated open cell metal foams for a further improvement of their ability for the absorption of kinetic energies or as armor is that they can be filled for example with elastomeric materials and thus form a composite structure. This work is in progress now.

REFERENCES

[1] Ashby MF et al, Metal Foams: a Design Guide (Butterworth-Heinemann, Woburn, 2000) pp. 1-5.

[2] Hempelmann R, Jung A, Natter H, Lach E, Metal Foams, EP 09 007 696.9.

[3] Jung A, Natter H, Hempelmann R, Diebels S, Koblischka MR, Hartmann U, Lach E, Electrodeposition of nanocrystalline metals on open cell metal foams: improved mechanical properties, ECS-Transactions, 216th Meeting, Vienna (accepted).

[4] Jung A, Natter H, Hempelmann R, Diebels S, Koblischka MR, Hartmann U, Lach E, Study of the magnetic flux density distribution of nickel coated aluminum foams, J.Phys. Conf. Ser, 200, 082011, 2010.

[5] Jung A, Natter H, Lach E, Hempelmann R, Nano nickel strengthened open cell metal foams under quasistatic and dynamic loading, Proceedings DYMAT, 7.– 11. September 2009, Brussels, Belgium

[6] Zhou J, Shrotriya P, Soboyejo WI, Mechanisms and mechanics of compressive deformation in open-cell Al foams, Mech. Mater. 36, 781-797, 2004.

[7] Hopkinson B, A method of measuring the pressure in the detonation of high explosives or by the impact of bullets, Philos. Trans. R. Soc. Lond. A, 213A, 437-456, 1914.

Proceedings of the SEM Annual Conference
June 7-10, 2010 Indianapolis, Indiana USA
©2010 Society for Experimental Mechanics Inc.

A Numerical and Experimental Study of High Strain-rate Compression and Tension Response of Concrete

Ahsan Samiee[1*], Jon Isaacs[1], and Sia Nemat-Nasser[1]
[1] Center of Excellence for Advanced Materials, Department of Mechanical and Aerospace Engineering, University of California at San Diego, 9500 Gilman Drive, La Jolla, CA 92093-0416, USA
* asamiee@ucsd.edu

ABSTRACT

Unconfined compression and tension tests have been performed on cylindrical samples prepared from a newly developed concrete. A 3-inch Hopkinson bar setup has been employed to experimentally extract the stress-strain relation of the concrete at different strain rates. A novel procedure is introduced to conduct tension tests. Initiation and propagation of cracks in concrete samples are captured by high-speed photography. The experimental data will be used to improve the existing concrete material models.

Extracting stress-strain relations from the Hopkinson-bar experimentally obtained data requires assumptions about the sample size and interface friction between the sample and the bars. The effect of violating these assumptions on the validity of experimentally acquired stress-strain results is explored by performing a full-scale finite element simulation of the entire process. A new method of accounting for the dispersion in the Hokinson cylindrical bars using the finite-element results is introduced and verified by comparing these results with the generally used analytical method. Numerical results reveal that the strain and stress history are not uniform within the sample. The usual method of analyzing the Hopkinson bar experimental results that generally overlook this fact can be corrected by minor calibration on the data.

Keywords: concrete, compression test, tension test, Hopkinson bar, SHPB

EXTENDED ABSTRACT

To characterize the mechanical properties of a newly developed concrete when subjected to dynamic loads, unconfined compression and tension tests have been performed on cylindrical concrete samples. A 3” Split-Hopkinson Pressure Bar (SHPB) has been employed to perform the experiments. SHPB consists of two cylindrical bars, known as incident bar and transmission bar, and a striker, all made from some high-strength material. A relatively thin sample is placed between the bars. A gas gun is employed to accelerate the striker towards the incident bar. The impact between the two generates a pressure pulse inside the incident bar. The shape, amplitude and duration of the pulse can be designed by altering the shape, size and impact velocity of the projectile. When the pulse reaches the sample, some of it is reflected due to impedance mismatch between the bar and sample and some of it is transmitted to the transmission bar. The reflected and transmitted pulses are captured by surface-mounted strain gages on the bars.

Using one-dimensional uniaxial stress wave theory, stress and strain experienced by the sample can be retrieved from the strain gages data (see Nemat-Nasser et al. [1]and Gray [2]) using the following formulas:

T. Proulx (ed.), *Dynamic Behavior of Materials, Volume 1*, Conference Proceedings of the Society for Experimental Mechanics Series, DOI 10.1007/978-1-4419-8228-5_14, © The Society for Experimental Mechanics, Inc. 2011

$$\varepsilon_s(t) = -\frac{2C_0}{L_s}\int_0^t \varepsilon_R(t)dt \qquad (1)$$

$$\sigma_s(t) = -E_0\frac{A_0}{A_s}\varepsilon_T(t) \qquad (2)$$

where C_0, A_0 and E_0 are sound speed, cross-sectional area and elastic modulus of the bars, respectively. ε_R and ε_T are the strain histories in incident and transmission bars which can be evaluated from the strain gage data. A few assumptions are made in derivation of these equations. For example, the width of the sample is neglected and the bars have to remain in their elastic region during the experiment. Dispersion of the travelling wave in the bars, which happens because waves with different frequencies travel with different velocities, is also not considered in these formulas. Therefore, generally small samples are used and a dispersion correction routine is used to account for these assumptions. Figure (1) illustrates the schematic view of HSPB for compression tests.

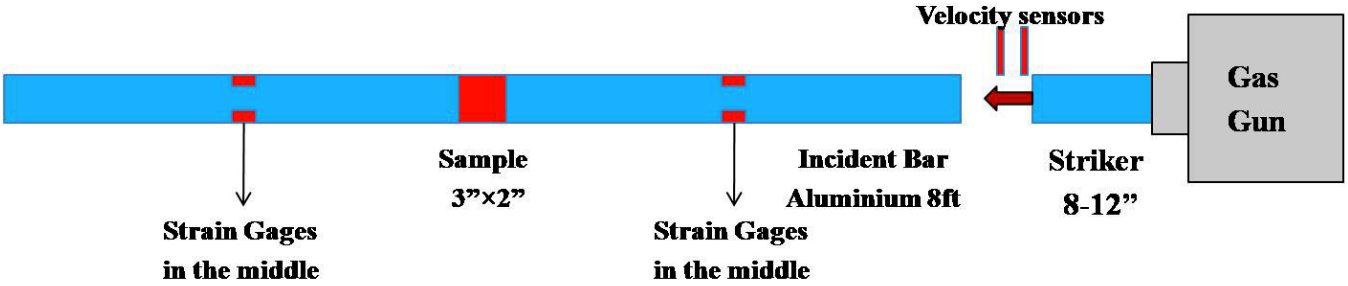
Velocity sensors
Gas Gun
Sample 3"×2"
Incident Bar Aluminium 8ft
Striker 8-12"
Strain Gages in the middle
Strain Gages in the middle

Figure 1. The schematic view of the HSPB for compression tests

Figure (2) shows the compression and tension samples. The average size of the aggregate in the concrete is a defining factor in designing these specimens. The samples are made large enough to ensure that they represent the concrete rather than its components, e.g. aggregate or cement. Therefore 3-inch diameter was chosen for the specimens.

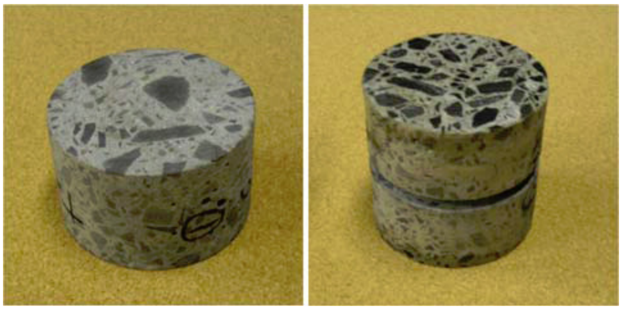

Figure 2. Left: compression sample, Right: tension sample

To generate different strain rates, strikers with different lengths were designed. Figure (3) shows three different input pulses generated for compression tests. A total of 27 tests were carried out and the strain gage data was recorded for each experiment. Using this data, the stress-strain curves at different strain rates were plotted for this concrete.

A finite element model for these experiments was developed to investigate the validity and accuracy of equations (1) and (2) in this case. A well-established concrete material model was used. This model uses the pressure pulse from the experiments (which is captured by strain gages) as an input. Using the simulation results, the stress-strain curve inside the sample is plotted. Also, the time-history of the strain at the location of strain gages in the finite element model is available. Therefore, the stress-strain curve can be plotted using equations (1) and (2). Our simulation results reveal that these two curves are different but close. Therefore, although the specimens are large, using equations (1) and (2) to calculate the stress-strain curve for the concrete is acceptable.

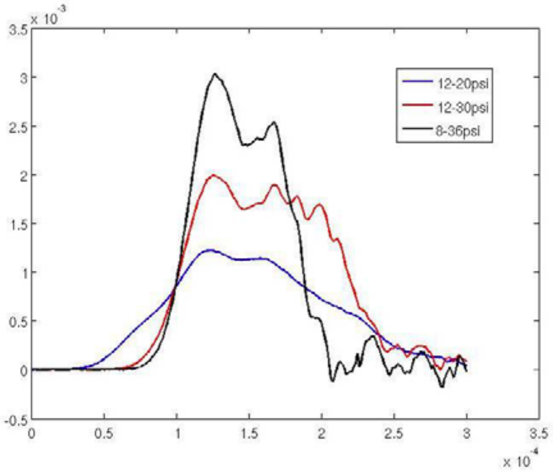

Figure 3. Three different input pulses

ACKNOWLEDGEMENTS

The experimental work has been conducted at the Center of Excellence in Advanced Materials (CEAM), Mechanical and Aerospace Engineering Department, University of California, San Diego, and has been supported by Karagozian & Case Company.

REFERENCES

[1] Nemat-Nasser, S., J.B. Isaacs, and J.E. Starrett, "Hopkinson Techniques for Dynamic Recovery Experiments", *Proceedings of the Royal Society of London*, A, Vol. 435 (1991) 371-391.
[2] *Gray, G.T., "*Classic Split-Hopkinson Pressure Bar Technique", *LA-UR-99-2347, Los Alamos National Laboratory* (1999).

Proceedings of the SEM Annual Conference
June 7-10, 2010 Indianapolis, Indiana USA
©2010 Society for Experimental Mechanics Inc.

Impact Behavior and Dynamic Failure of PMMA and PC Plates

Wei Zhang[1], Srinivasan Arjun Tekalur[2] and L. Huynh
[1]PhD candidate, Dept. of Mechanical Engineering, Michigan State University, East Lansing, MI 48824. E-mail: zhangw31@egr.msu.edu
[2]Assistant Professor, Dept. of Mechanical Engineering, Michigan State University, East Lansing, MI 48824. E-mail: tsarjun@egr.msu.edu

ABSTRACT

Dynamic failure of monolithic poly methyl methacrylate (PMMA) plates subjected to low velocity dynamic loading was studied using an instrumented drop weight tower. The investigation was carried out at various combinations of impact velocities and drop-weights on the monolithic PMMA plates to examine their threshold impact energy and impact behavior. To examine the beneficial effect of layering, experiments were conducted using the following combinations of plates reinforced with weak and strong adhesive interface bonding: PMMA and PC bi-layered plates, and PMMA and PMMA bi-layered plates. Energy dissipation, time to crack, reaction force, and fragmentation pattern were compared for different combinations of velocity and drop weight. The recorded loading histories were used as inputs to finite element (FE) models, which were achieved using a commercial FE software, ABAQUS. The FE modeling provided a detailed insight of the energy dissipations of the impact events, which showed good agreement with the experimental results. From these results, we conclude that layered structures are beneficial to improve the impact resistance and the interfacial bonding plays an important role in determining the extent of the same.

1. Introduction

Due to its high toughness and transparency, Poly methyl methacrylate (PMMA) plates have been widely used in both military structures, such as transparent armor, as well as for civilian applications, such as residential and commercial aquariums, automobile windshield, aircraft windows etc. However, as a viscoelastic polymer, PMMA exhibits high brittleness in service. The susceptibility to impact loading due to its brittle nature greatly limits its application. Thus, the study of the impact response of PMMA structures under dynamic loading is of great engineering interest.

Generally, impact test can be classified into three categories according to its impact velocities, which are low velocity drop weight impact test [1-8], high velocity impact by use of air gun [9-16], and shock wave impact by use of explosives [8]. Among them, low velocity drop weight test is popularly used to evaluate the threshold conditions indicating the onset of damage and to investigate the failure mechanism of the tested material. Liu [1] conducted a low velocity drop weight impact test on monolithic PMMA plate using an Instron Dynatup drop

T. Proulx (ed.), *Dynamic Behavior of Materials, Volume 1*, Conference Proceedings of the Society for Experimental Mechanics Series,
DOI 10.1007/978-1-4419-8228-5_15, © The Society for Experimental Mechanics, Inc. 2011

weight impact tester, where the variations of force with time, and strain energy release rate were examined. The brittle-ductile transition temperature of PMMA was also evaluated to be in the range of 185 F to 205 F [1]. A low velocity impact and quasi-static failure of PMMA, based on global and local strain measurements, were conducted by Pearson and his colleagues [2]. In their work, Fiber Bragg Grating (FBG) sensors were used to measure local strains, which were combined with the measurements from quasi-static indentation and low-velocity impact test to examine the failure mechanisms of PMMA. Multiple strikes were applied to the PMMA sample till failure. Stenzler [3] investigated the impact mechanics of transparent multi-layered polymer composites using an instrumented intermediate velocity impact test facility. The multi-layered structures with various boning adhesives were investigated to improve the impact performance [3]. The ballistic impact response of PMMA plate structures attracts high attention due to its wide application in military defense [11, 13-14]. Sarva [13] studied impact of PMMA /PC hierarchical assembly by a projectile at the impact velocities ranging from 300 to 550 m/s. It was shown that a hierarchical assembly exhibited higher penetration resistance compared to uniform distributed PMMA discs structure [13]. Hsieh [12] measured the ballistic impact response of coextruded PC/PMMA multilayered composites, the thickness of PMMA plate of which was proved to play an important role in improving the ballistic performance of the same. With the development of computational techniques, finite element modeling method has been widely used in the study of the mechanical response of materials subjected to dynamic loading [1, 13, 17-20]. A finite element model was developed to predict the dynamic response of PMMA plates [1] and fibrous composite panels [17] subjected to low velocity drop weight respectively. A computational model [13] was used to study the ballistic impact response of PMMA plate structures.

The objective of the paper is to investigate the failure mechanism of monolithic PMMA plates and layered configurations comprising PMMA and PC plates subjected to low velocity impact loading. Experimental measurements were used to examine the failure behavior including threshold conditions, energy dissipation, and crack pattern of the tested structures. A Finite element model, achieved using a commercial software, ABAQUS, was developed to show a detailed insight of the energy dissipation mechanism of the impact events.

2. Experimental procedures and results

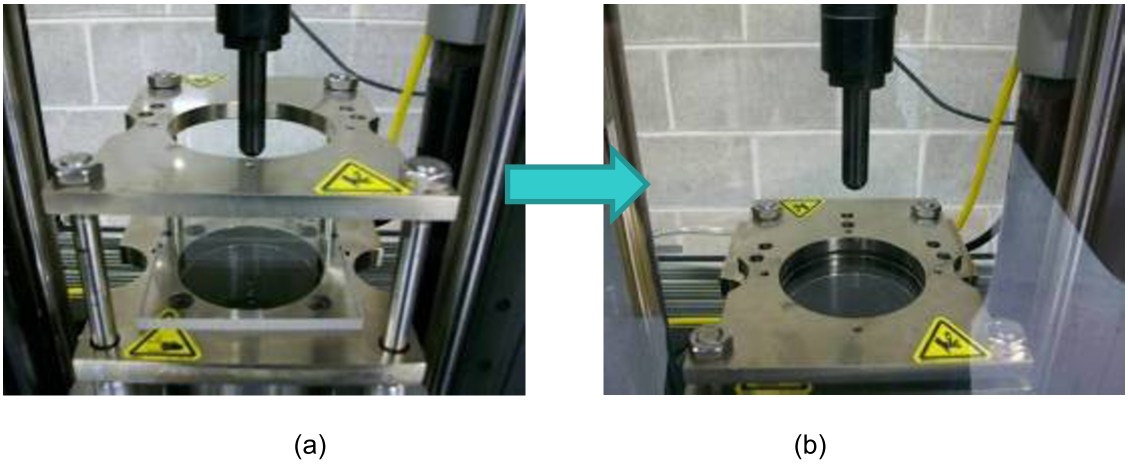
(a) (b)

Figure 1: Instron Dynatup 9250 drop weight tower:(a) before clamping; (b) after clamping

The drop weight impact tests were carried out through an Instron Dynatup 9250 drop weight tower (Fig. 1), which is equipped with a load cell above the impactor to record the force history and the impact energy during the test. A velocity detector was mounted on the tup to measure the initial velocity of the impact. During the test, the 12.7 mm diameter hemispherical impactor was raised to a specific height above the specimen and allowed to drop the drop weight onto that specimen. The drop weight ranges are 2.7-14.7 kg for the low weight drop. The tested specimens are PMMA and PC plates, which are square plates (100 mm x 100 mm) with thickness of quarter inch for monolithic plate and 0.125 inch for each of the plates in a layered configuration. The mechanical and physical properties are summarized in Table 1. When the impact tower was armed, the specimen was fixed by a hydraulic clamp with a diameter of 76.2 mm. To avoid double impact, a rebound brake cylinder caught the specimen after the first impact. All the experiments were preformed at room temperature.

Table 1: Mechanical and physical properties of PMMA and PC plate.

Specimen	Density (kg/mm3)	Modulus of Elasticity (MPa)	Poisson's Ratio	Tensile strength (MPa)	Shear Strength (MPa)	Compression Strength (MPa)
PC	1.2x10-6	2344	0.38	65.5	68.9	86
PMMA	1.19x10-6	3100	0.38	74.4	68.9	120.66

2.1 Monolithic PMMA plates

To examine the threshold energy of mono-PMMA plates, multiple tests were conducted. The combinations included constant impact mass (6.95 kg) with various impact velocities and constant energy (12J) with various velocities and mass. For comparison, the results of monolithic PMMA plate with constant energy are shown along with the results for the bi-layered plates.

The plots of force versus time and energy versus time of monolithic PMMA plates with constant impact mass are shown in Fig. 2 & 3 respectively. The velocity ranges from 0.7 m/s to 5.0 m/s. The test showed good repetitive results. It was observed that no visible cracks were induced on the tested specimen with the impact velocity of 0.7 m/s, and 4 to 6 radial cracks propagated in the specimen with the velocities of 1.0 m/s and 2.0 m/s. Serious damages were induced on specimen with velocities of 3.0 m/s and 5.0 m/s. Fig.5 (a) and (d) show the conditions of the specimens after being impacted with velocity of 2.0 m/s and 3.0 m/s. It can be seen that the crack pattern of the monolithic plate was purely brittle, and the impactor penetrated through the specimen when the velocity was 3.0m/s. Fig. 2 shows that a smooth force curve was induced on the specimen with the velocity 0.7m/s when no crack was initiated, and the time to peak force was around 3.0 ms. All the other force curves gradually reached the peak load, and then suddenly dropped to zero due to the initiation of crack, the oscillations being caused by vibration induced while cracking. It can be seen that higher velocities induced higher peak force and lessened the time to initiate crack. The time to reach the peak force was around 2.1 ms, 0.76 ms, 0.73 ms and 0.38 ms for the velocities from 1.0 m/s, 2.0 m/s, 3.0 m/s, and 5.0 m/s respectively. The average threshold energies examined for different velocities are shown in Fig. 4. It can be seen that the threshold energy had small deviations when the velocity was changed. The threshold energy was examined to be 2.7 - 3 J for monolithic PMMA plates. Fig.3 shows that the maximum impact energy of mono-layered PMMA with the impact velocity of 0.7 m/s was around 1.7 J which was lower than the crack propagation energy. Thus, no crack was induced on the specimen with velocity of 0.7m/s. When the impact energy reached the threshold value, cracks initiated in the bottom of the PMMA plates, and propagated onto the top because the bottom face attained the maximum tensile stresses due to bending.

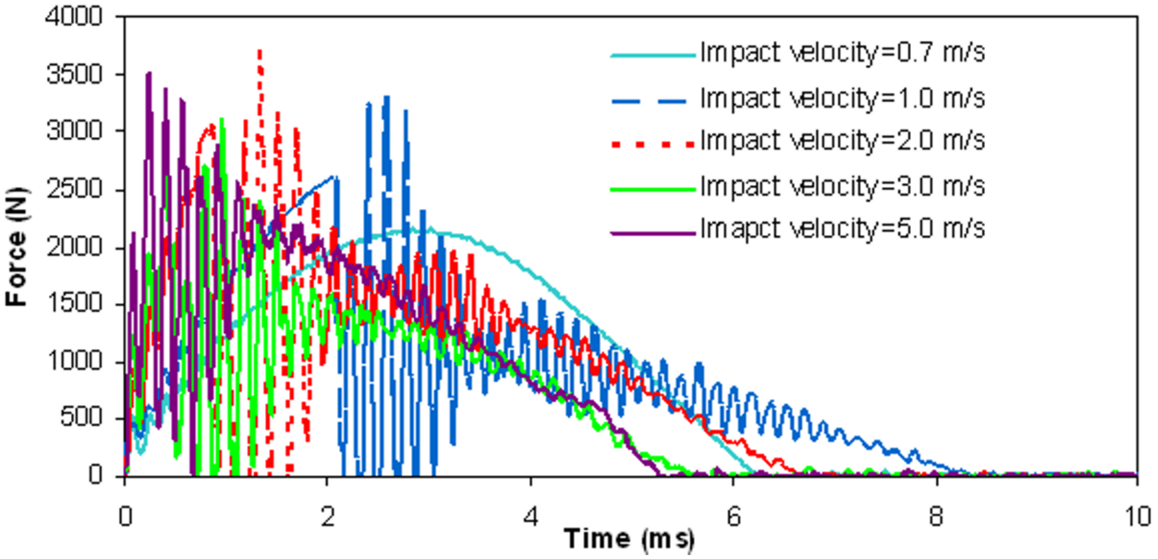

Figure 2: Reaction force of mono-PMMA plates under various impact velocities with constant impact mass

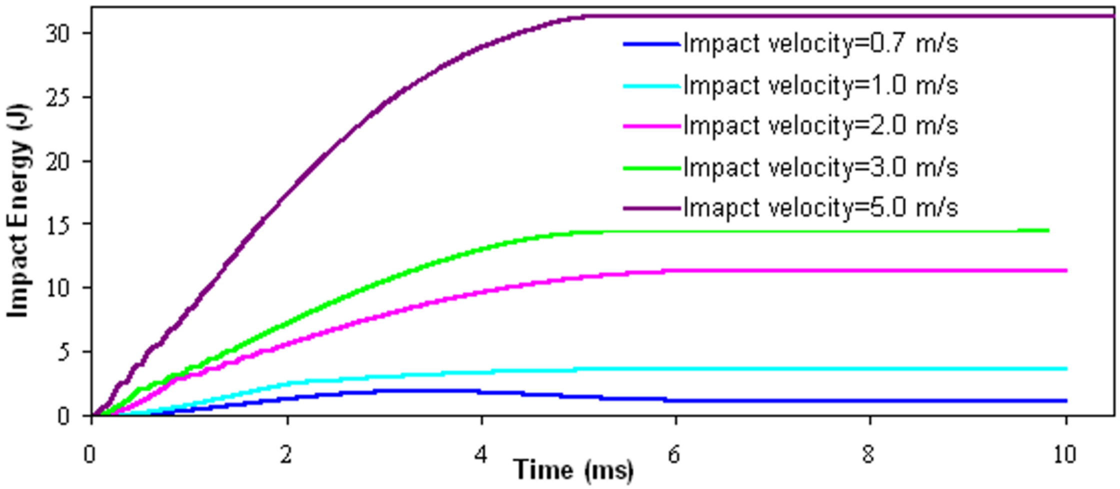

Figure 3: Impact energy of mono-PMMA plates under various impact velocities with constant impact mass.

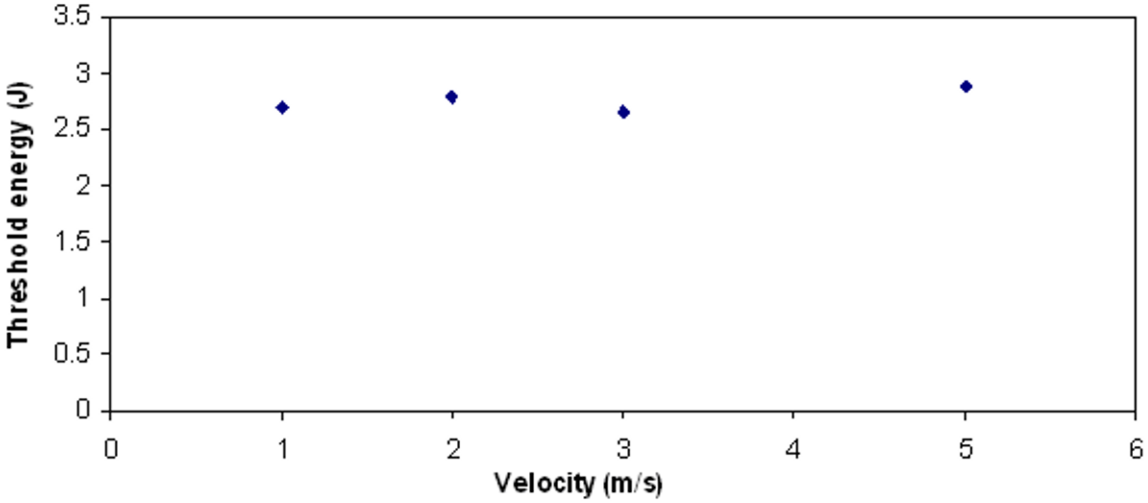

Figure 4: Threshold energy of mono-PMMA plates under various impact velocities mass.

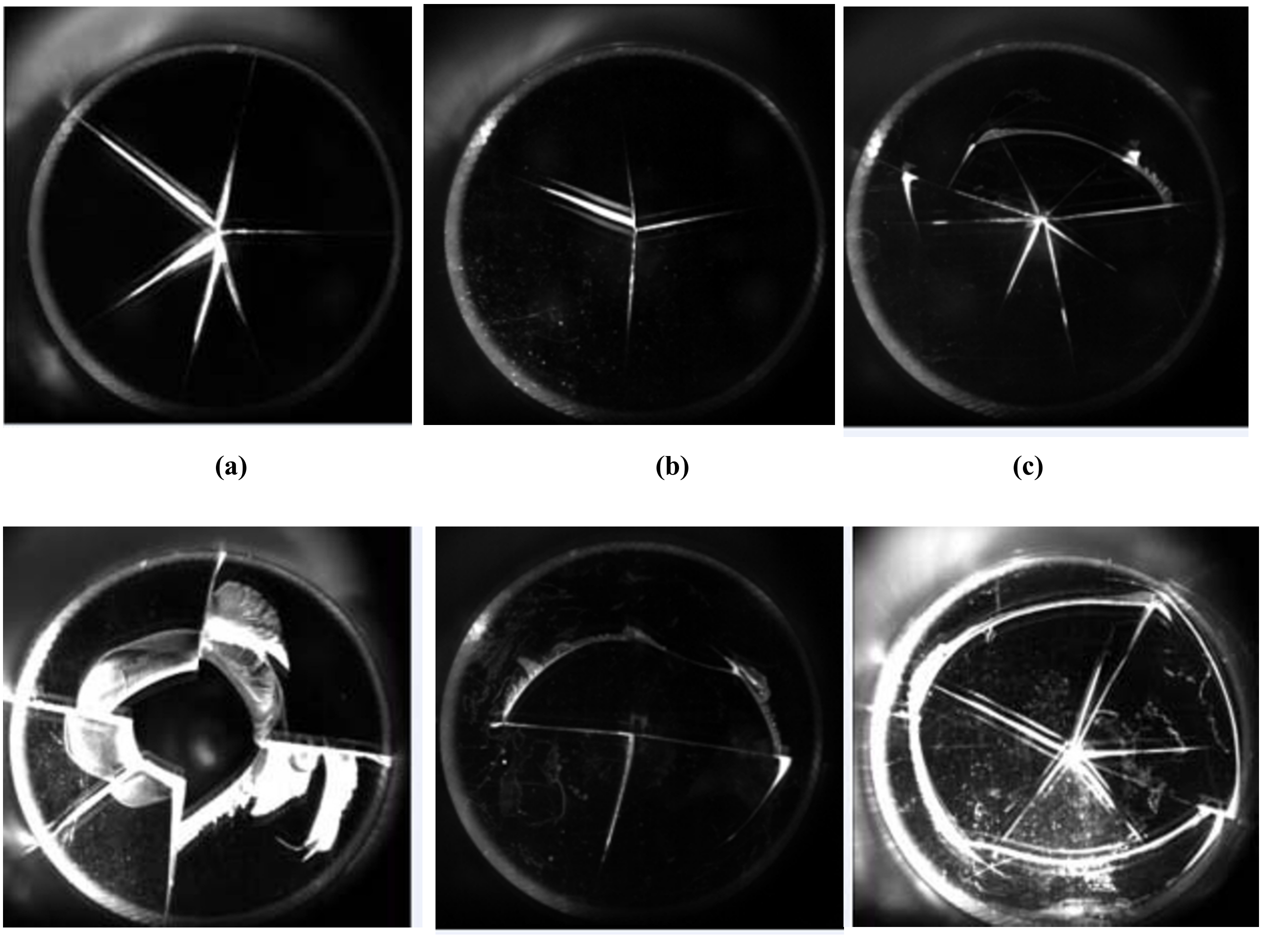

(a) (b) (c)

(d) (e) (f)

Figure 5: Post-failure images of PMMA plates under various impact velocities with constant impact mass: (a) Mono_PMMA_V=2.0 m/s; (b) PMMA/PC_strong_V=2.0 m/s; (c) PMMA/PMMA_strong_V=2.0 m/s; (d) Mono_PMMA_V=3.0 m/s; (e) PMMA/PC_strong_V=3.0 m/s; (f) PMMA/PMMA_strong_V=3.0 m/s.

2.2 Layered plates

The bi-layered PMMA and PC plates with weak and strong interface bonding were designed to examine the effect of layered structure. The weak bonding was created by placing two plates together without adhesive. The strong bonding was achieved by using Loctite 3336 Epoxy adhesive between two layers of PMMA/PC or PMMA/PMMA plates. The adhesive was dispensed using a dispensing gun and was cured at room temperature for 2 hours, followed by heating in an oven at 65°C for 8 hours.

The layered combinations tested, included PMMA on the top of PC plates, PC on the top of PMMA plates, and bi-layered PMMA plate structures. No visible crack was observed on PC plates for both the weakly bonded bi-layered structures with PMMA on top of PC and PC on the top of PMMA with velocity of 2.0 m/s and 3.0 m/s. In contrast, 3 to 5 radial cracks, which were governed by brittle failure, were observed on PMMA plates for all the experiments with velocity of 2.0 m/s and 3.0 m/s. No ductile deformation on the PMMA plates was observed. It was further found that impact results of the bi-layered PMMA/PC structures with strong interface bonding were very similar to the same with weak bonding. The post impact pictures of PMMA/PC bi-layered structures with strong interfacial bonding are shown in Fig.5 (b) & (e). Brittle failure, revealed by radial cracking pattern, was observed on each PMMA plate for the bi-layer PMMA/PMMA structures with weak bonding. However,

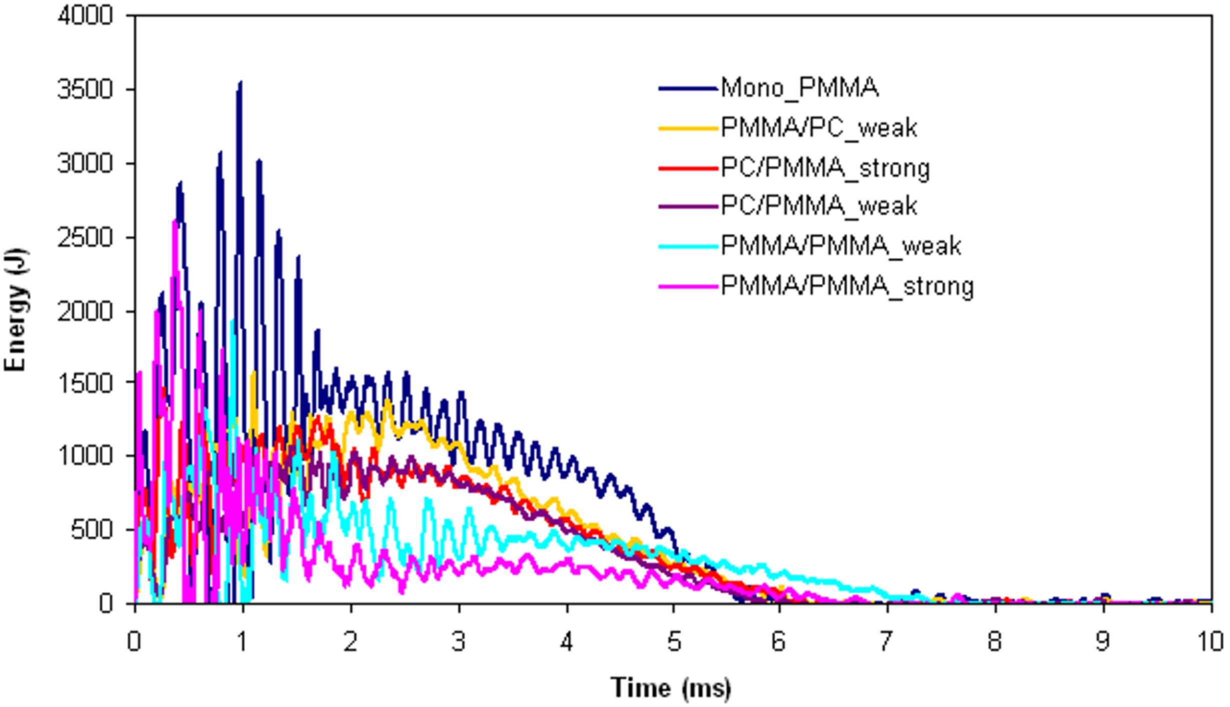

Figure 6: Comparison of reaction force of mono-PMMA plates to layered structures with weak bonding under velocity of 3.0 m/s.

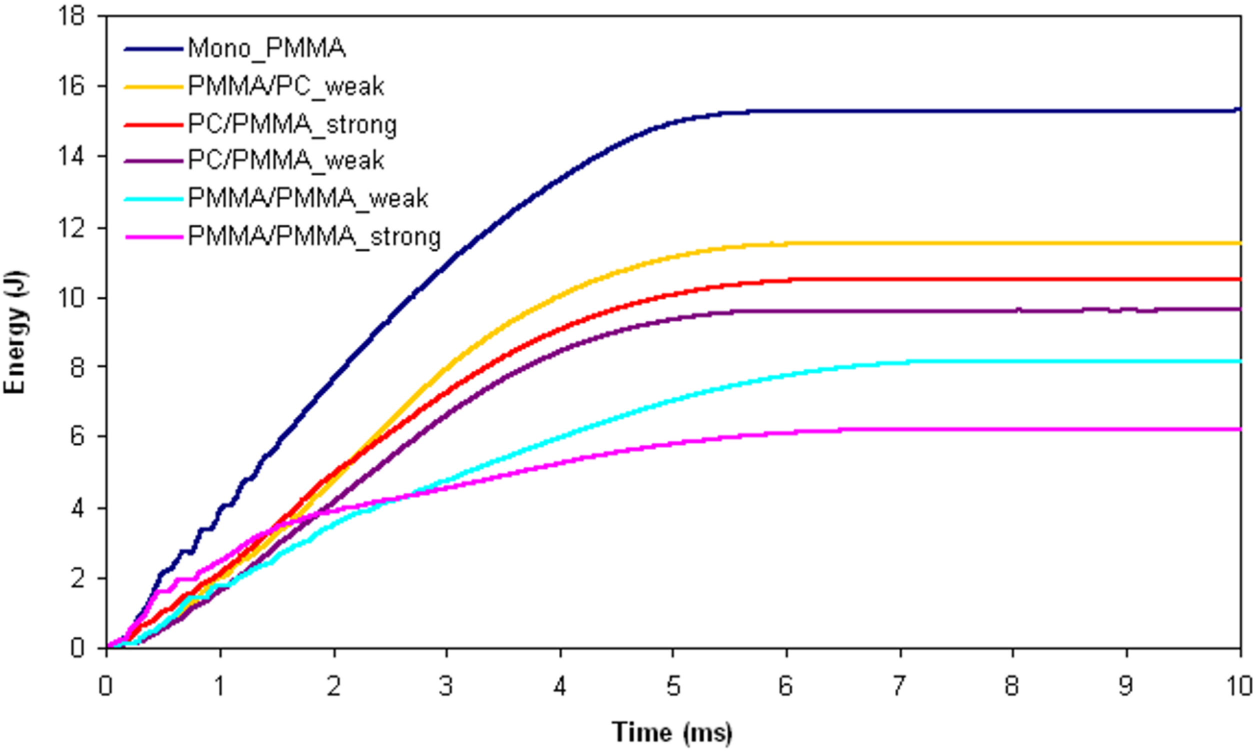

Figure 7: Comparison of energy of mono-PMMA plates to layered structures with weak bonding under velocity of 3.0 m/s.

compared to the weakly bonded structures, the bi-layer PMMA/PMMA structures with strong bonding exhibited mixed failure mode comprising brittle radial cracking and circular ductile cracking [12].

The post-impact pictures of the PMMA/PMMA bi-layered structure with strong bonding for velocity of 2.0 m/s and 3.0 m/ are shown in the Fig.5 (c) & (f) respectively. Fig. 6 & 7 show the comparisons of the reaction forces and impact energy of the layered structure to the Mono-PMMA plate with constant impact mass under impact velocities of 3.0 m/s. The results show that the bi-layered structures lead to lower contact forces compared to monolithic PMMA plates. The peak force for bi-layered structure seems to be half of the same for mono-layered PMMA plates. Bi-layered structure seemed to take longer time for crack initiation and attaining peak force.

It was seen that during impact, monolithic PMMA plate dissipated most energy due to more severe cracking induced, compared to the bi-layered structures. It is therefore concluded that layered-structures are beneficial to improve the impact resistance of the PMMA plates. Fig. 7 shows that bi-layered PMMA/PMMA structure dissipated less energy compared to the PMMA/PC structure. Thus, interface bonding was found to play a role on improving the compliance of PMMA structure.

Table 2: Velocities and corresponding mass with the constant energy of 12 J.

Trail Name	Specimen	Velocity(m/s)	Total mass(kg)	Energy(J)
Bialyer_NA_CE_1	PMMA/PC	1.89	6.69	12
Bialyer_NA_CE_2	PMMA/PC	1.36	12.91	12
Bialyer_NA_CE_3	PMMA/PC	1.14	18.6	12
Bialyer_NA_CE_4	PMMA/PC	0.97	25.57	12
Mono_CE_1	PMMA	1.89	6.69	12
Mono_CE_2	PMMA	1.36	12.91	12
Mono_CE_3	PMMA	1.14	18.6	12
Mono_CE_4	PMMA	0.97	25.57	12

To further evaluate the beneficial effect of the bi-layered structure, multiple runs with a constant energy of 12 J were conducted on the bi-layered structures comprising of PMMA and PC plates, the results of which were compared to monolithic PMMA plates. The conditions of velocities and mass used in the experiments are shown in Table 2. The order of PMMA and PC plates in the bi-layered configuration seems that there is no obvious effect on the impact response according to previous examination. Thus, all the tests for bi-layered structures focus on the case of PMMA on the top of PC plates.

The variations of reaction force and impact energy with time are shown in Fig. 8, 9, 10 & 11. It can be seen that the average peak force for the mono-PMMA plate is around 2500 N, and is 1400 N for the bi-layered structure. The results further confirm that the reaction force of bi-layered structures was around half of the same for monolithic PMMA plates. Fig.8 & 9 also show that the time for the force to reach a peak value is around 2.2 ms for the bi-layered structure, and 1.7 ms for the mono-PMMA plate. The bi-layered structures seem to delay the crack initiation by 22% of that of mono-PMMA plate. The interface bonding between the PMMA and PC plates acts as a gap, which interfered with the wave propagation during the impact.

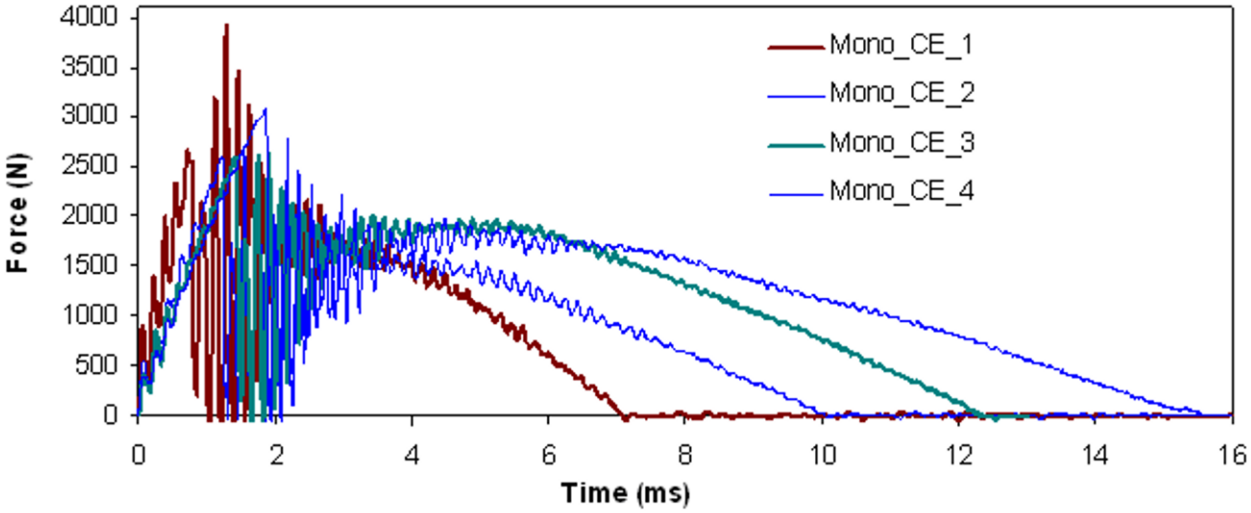

Figure 8: Reaction force of mono-PMMA plates to under constant energy of 12J.

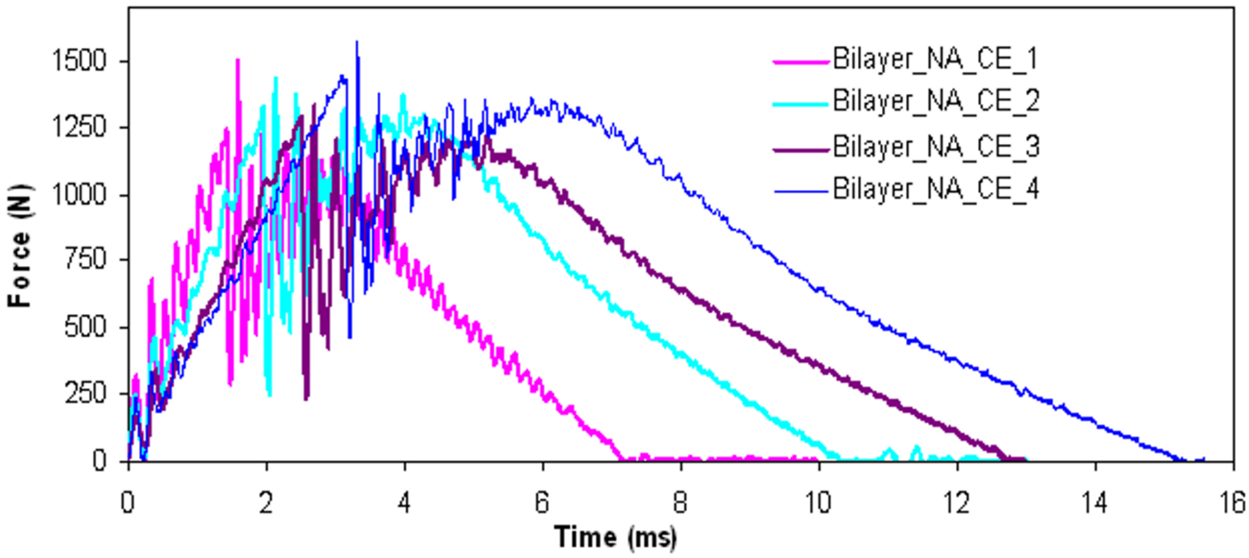

Figure 9: Reaction force of bi-layered structures under constant energy of 12J.

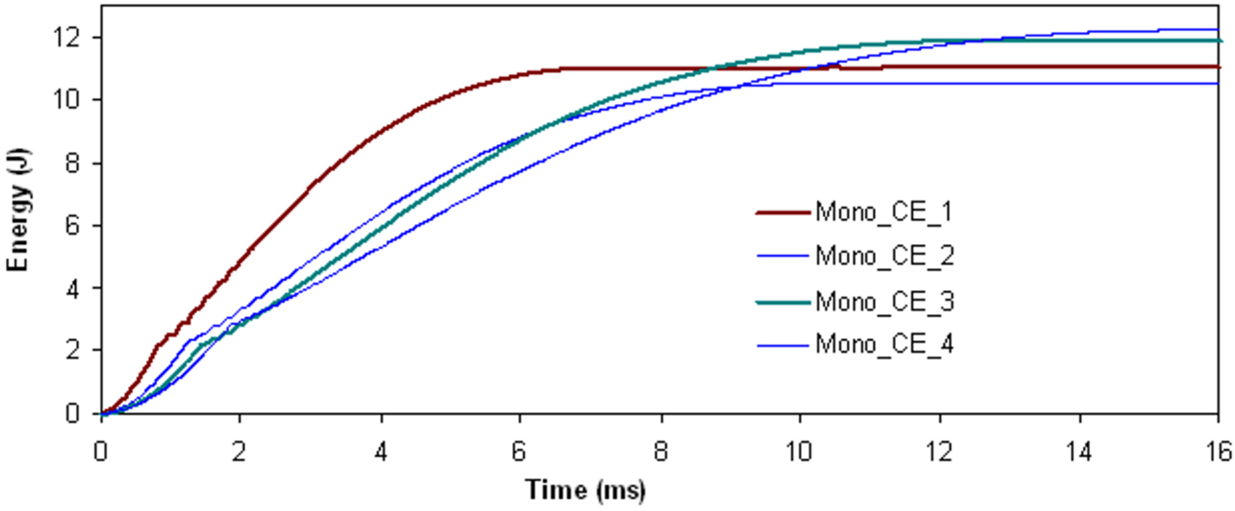

Figure 10: Impact energy of mono-PMMA plates to under constant energy of 12J

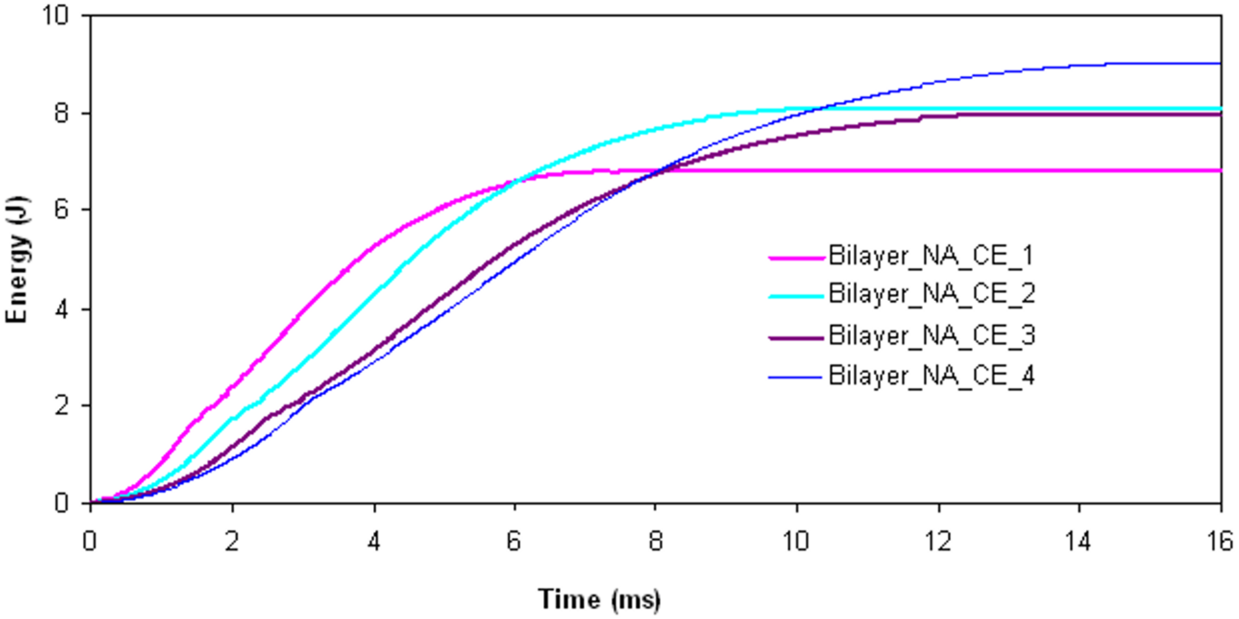

Figure 11: Impact energy of bi-layered structures under constant energy of 12J

3. Finite element simulations

A finite element model, achieved by a commercial software ABAQUS, was used to further quantify the energy dissipations during impact. The impactor was modeled as a rigid body and 8-node CD38R element was used for modeling the specimen. The mesh density of the specimen was chosen based on the low cost of computation without compromising on the accuracy of the results. Griffith surface energy criterion was used in analysis, which states that when the maximum surface energy exceeds the crack opening energy, crack will initiate until failure of the element. The geometry and mesh of the FE analysis of mono-PMMA plates are shown in Fig. 13. Fig. 12 & 14 show FE simulation results for velocity of 1.0 m/s. It can be seen that the reaction force of the FEM simulations perfectly agree with the experiment. It further verifies our previous conclusions, where the threshold energy of Mono-PMMA was about 2.7 J (Fig. 14), which was stored as strain energy in the specimen. The time to crack was 2.1 ms at which the vertices of the curves of kinetic energy, impact energy and strain energy exhibit. It was also found that the strain energy reached its maximum at the onset of crack.

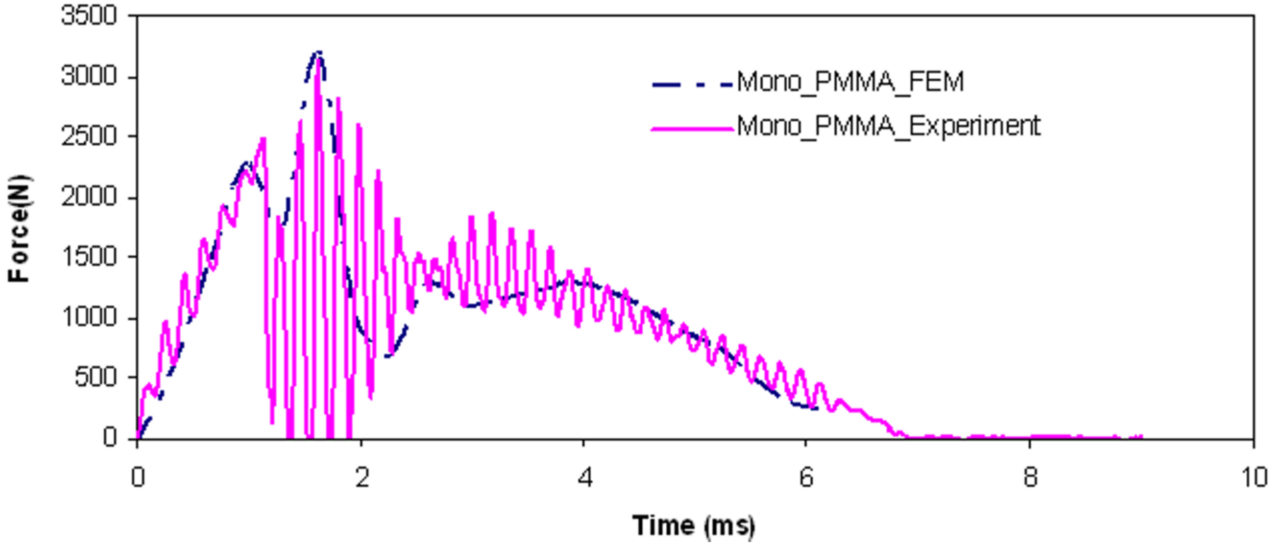

Figure 12: Comparison of reaction force of FEM simulation to experimental result under velocity of 1.0 m/s with constant mass.

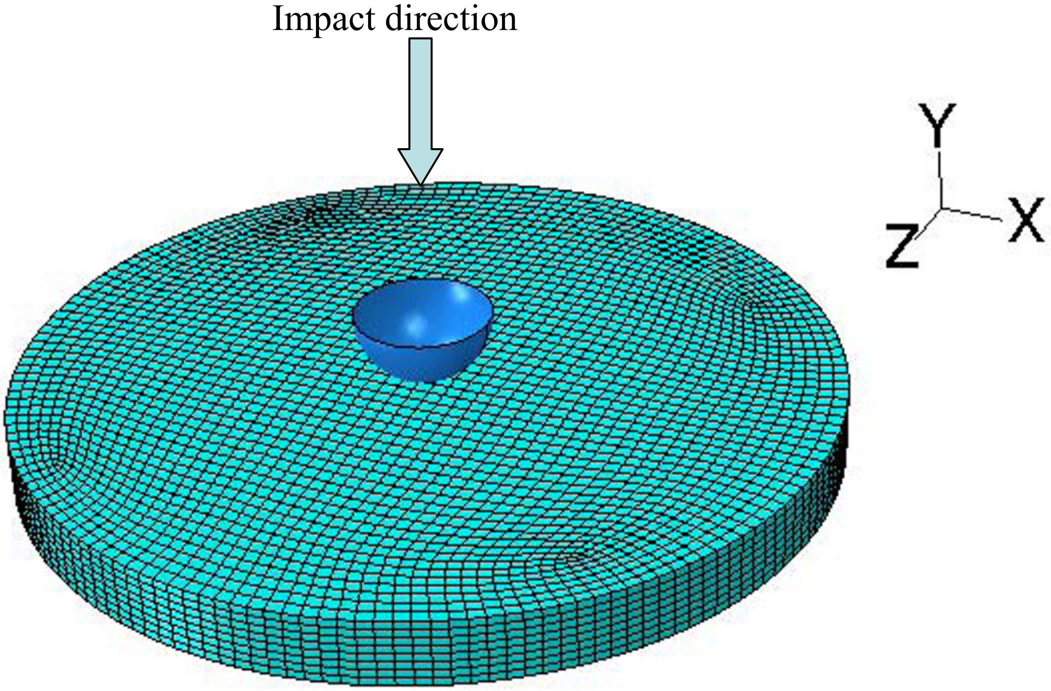

Figure 13: Geometry and mesh of FEM simulation

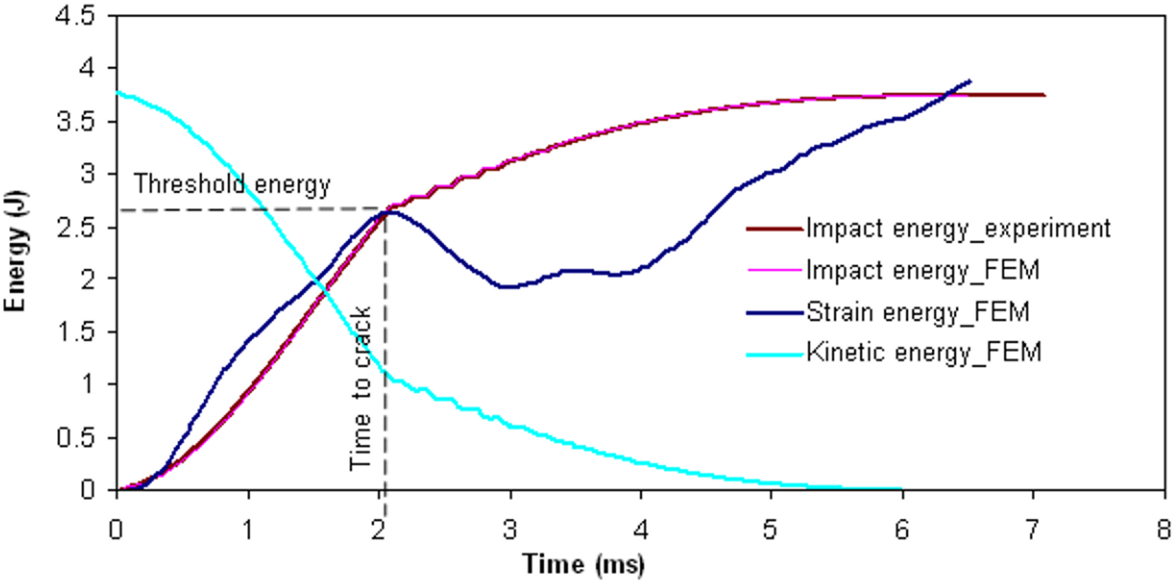

Figure 14: Energy dissipation of Mono-PMMA plates under velocity of 1.0 m/s with constant mass.

4. Conclusion

The low velocity impact response of monolithic and multi-layered PMMA and PC plates with weak and strong interface bonding were studied by both experimental and finite element methods. The threshold impact energy of monolithic PMMA plates was found to be in the range of 2.7 to 3.0J. It was found that the time to crack depended on the impact velocity. Higher velocity took less time to initiate crack. The crack initiation force for bi-layered structure seemed to be half as much of the mono-layered PMMA plate. The bi-layered structures exhibited lighter deformation compared to the monolithic PMMA plates. The interfacial adhesive improved the compliance of bi-layered PMMA structures. A mixed failure mode comprising brittle failure (revealed by radial crack) and ductile deformation (revealed by circular crack) was observed on bi-layered PMMA structures with strong bonding, when impacted with a velocity of 3.0 m/s. Results of this works clearly demonstrate that layered-structures are beneficial to improve the impact resistance of the PMMA plates and the interfacial bonding plays a role in determining the extent of the same.

The optimization of the layered PMMA plate structures are left as a future study. The critical thickness of single PMMA plate and the numbers of layers in the layered configuration exhibiting higher impact resistant will be determined through the optimization.

Reference

1. Y.X. Liu and B. Liaw, ‘Drop-weight impact tests and finite element modeling of cast acrylic plates’, Polymer Testing 28, 2009, Pp: 599-611.

2. J.D. Pearson, M.A. Ziky, M. Prabhugoud and K. Peters, ‘Measurement of low velocity and quasi-static failure modes of PMMA’, Polymer Composites, 2007, Pp: 381-391.

3. J.S. Stenzler and N.C. Goulbourne, ‘Impact mechanics of transparent multi-layered polymer composites’, Society for Experimental Mechanics-SEM Annual Conference and Exposition on Experimental and Applied Mechanics, 2009, V3, Pp 1963-1982

4. H. Chai and G.U. Ravichandran, ‘On the mechanics of fracture in monoliths and multilayers from low-velocity impact by sharp or blunt-tip projectiles’, International Journal of Impact Engineering 36, 2009, Pp: 375-385.

5. M. A. Hazizan and W.J. Gantwell, ‘The low velocity impact response of foam-based sandwich structures’, Composites Part B 33, 2002, Pp: 193-204.

6. I.H. Choi and C.H. Lim, ‘Low-velocity impact analysis of composite laminates using linearized contact law’, Composite Structures 66, 2004, Pp: 125-132.

7. M.A. Hazizan and W.J. Cantwell, ‘The low velocity impact response of an aluminum honeycomb sandwich structure’, Composites Part B 34, 2003, Pp: 679-687.

8. M. Hebert, C. E. Rousseau and A. Shukla, ‘Shock loading and drop weight impact response of glass reinforced polymer composites’, Composite Structure 84, 2009, Pp: 199-208.

9. S. Orgihara, T. Ishigure and A. Kobayashi, ‘Study on impact perforation fracture mechanism in PMMA’, Journal of Material Science Letters 17, 1998, Pp:691-692.

10. S. Sahraqui and J.L. Lataillade, ‘Deformation and fracture of PMMA at high rates of loading’, Journal of Applied Polymer Sciences 51, 1994, Pp: 1527-1532.

11. L.R. Xu and A.J. Rosakis, ‘An experimental study of impact-induced failure events in homogeneous layered materials using dynamic photoelasticity and high-speed photography’, Optics and Lasers in

Engineering 40 (2003) Pp: 263-288.

12. A.J. Hsieh and J.W. Song, ‘Measurement of ballistic impact response of novel coextruded PC/PMMA multilayered-composites’, Journal of Reinforced Plastics and Composites 20, 2001, Pp: 239-254.

13. S. Sarva, A.D. Mulliken and M.C. Boyce, ‘Mechanics of transparent polymeric material assemblies under projectile impact: simulations and experiments’, Proceeding for the Army Science Conference (24th) Held on 29 Novermber-2 December 2005 in Orlando, Florida.

14. A.J. Hsieh, ‘Ballistic impact measurements of polycarbonate layered-silicate nanocomposites’, Conference proceeding, Society of Plastics Engineering, V 2, 2001 Pp: 2185-2191.

15. M.A. Grinfeld, J. W. McCauley, S. E. Schoenfeld and T. W. Wright, ‘Failure pattern formation in brittle ceramics and glasses’, 23RD International Symposium on Ballistics Tarragona, Spain 16-20 April 2007, Pp: 953-963.

16. E.Strassburger, P. Patel, J. W. McCauley, C. Kovalchick, K.T. Ramesh, and D.W. Templeton, ‘High-speed transmission shadowgraphic and dynamic photoelasticity study of stress wave and impact damage propagation in transparent materials and laminates using the Edge-On Impact (EOI) method’, 25th Army Science Conference, Orlando, FL, November 2006, Pp: 27-30.

17. U. Faroop and K. Gregory, ‘Computational modeling and simulation of low velocity impact on fibrous composite panels drop_weight un_partitioned model’, Journal of Engineering and Applied Sciences, 2009, Pp: 1819-6608.

18. M. Park, J. Yoo and D.T. Chung, ‘An optimization of a multi-layered plate under ballistic impact’, International Journal of Solids and Structures 42, 2005, Pp: 123-137.

19. P.Z. Qiao, F. Asce, M.J. Yang, and F. Bobaru, ‘Impact mechanics and high-energy absorbing materials: Review’, Journal of Aerospace Engineering, 2008, Pp: 0893-1321.

20. Y.M. Gupta and J.L. Ding, ‘Impact load spreading in layered materials and structures: concept and quantitative measure’, International Journal of Impact Engineering 27, 2002, Pp: 277-291.

Proceedings of the SEM Annual Conference
June 7-10, 2010 Indianapolis, Indiana USA
©2010 Society for Experimental Mechanics Inc.

Experimental Investigation on Dynamic Crack Propagation Through Interface in Glass

Hwun Park[1] and Weinong Chen[2]
School of Aeronautics and Astronautics, Purdue University
701 West Stadium Avenue
West Lafayette, Indiana 47907-2045

ABSTRACT

Experimental analyses are conducted to investigate the dynamic crack propagation through the interface in glass. Failure wave, which is a dense crack network initiated from a surface, is a characteristic of dynamic failure of glass. It has been observed that the cracks driven by a high dynamic load may stop at an interface even though the stress wave goes through it. The cracks can also pass through the interface if the stress is high enough. To understand the behavior of the failure wave, the interaction between a propagating crack and an interface needs to be investigated. In this study, the behavior of a single dynamic crack as it interacts with an interface is investigated. High speed photography and optical methods are employed to visualize the phenomena. A notched glass sample having an interface is impacted with a projectile. A single crack is initiated at the notch tip by the dynamic loading and propagates into the interface. The crack stops if the interface has no adhesive. The crack passes through the interface if it has a very thin layer of adhesive. The crack branches into multiple cracks if the interface has a finite thick layer of adhesive or the impact speed is very high. The branch patterns depend on the thickness of adhesive layer and loading condition.

INTRODUCTION

Glass has been used in transparent armors. It is desired to predict the impact response and failure behavior of the armors. However, the phenomenon of dynamic failure of glass under a high speed impact is very complicated and successful models have not been developed. Under intensive dynamic loading, glass has a unique dynamic failure phenomenon known as failure wave. It is referred as dense crack networks propagating behind shock waves. Comminuted materials having very low tensile strength are created behind the failure wave, which affects the resistance to impact. This phenomenon has been explored in many studies but has not been understood completely [1,2]. If there is an interface in the way of the failure-wave propagation, the failure wave initiates with the interface and may stop at the interface even though stress waves pass across the interface. After pausing at the interface, the failure wave may reinitiate from the interface [3]. There are many cracks in the failure wave that interact with each other, making it difficult to investigate the phenomenon quantitatively in experiments with proper instrumentation. On the other hand, the theory and experimental analysis on single crack growth has been studied extensively [4,5]. Therefore, to understand the interactions between the failure wave and the glass interface, a feasible approach is to first understand the interaction between a single dynamic crack and an interface, and then expand the scope to include the interactions among cracks.

The single crack propagation at the interface has been investigated by many studies. It has been known that a crack may stop at the interface of two different media when it propagates in perpendicular to the interface. The static stress field of the crack tip ending in an interface has been obtained analytically; and it was found that the rate of singularity and the principal stress direction depended on the properties of two media [6]. The crack behavior at the interface of duplex specimen has been investigated with photoelasticity. A crack growth initiated by static loading stopped abruptly at the interface; but it penetrated the interface when the load was high enough. The stress intensity factor decreased at the interface and increased sharply after the crack reinitiated at the second medium [7]. A crack growth initiated by a drop weight in bi-material was investigated with the method of caustics. The stress intensity factor was found to increase before the interface, decrease abruptly at the interface

---

[1] Ph.D. Student, hpark@purdue.edu
[2] Corresponding author, Professor, wchen@purdue.edu

T. Proulx (ed.), *Dynamic Behavior of Materials, Volume 1*, Conference Proceedings of the Society for Experimental Mechanics Series,
DOI 10.1007/978-1-4419-8228-5_16, © The Society for Experimental Mechanics, Inc. 2011

and increase again at the second medium. When the crack penetrated, it paused for tens of microseconds at the interface and reinitiated at the second medium. It was also observed that the crack branched into multiple cracks in some cases [8]. The crack propagation driven by low impact loading through interfaces was investigated with photoelasticity. The crack behavior was found to depend on the strength of adhesive. Cracks were arrested at the interface having low strength adhesive because two media were detached due to their weak bonding [9].

All those experiments were conducted under static or low impact loading conditions on brittle polymers such as epoxy or Homalite, which does not have any failure wave phenomenon. It is more challenging to investigate the dynamic fracture of glass because of its much faster crack speeds and lower photoelastic constants. The single crack propagation at an interface of glass driven by a dynamic load has not been investigated yet, which is the focus of this research.

EXPERIMENTS

To produce high dynamic loading, a projectile is discharged into a glass specimen. In this study, a 63.5 mm light gas was employed to produce consistent high velocity impact. Figure 1 shows the configuration of the experimental setup. The couples of lasers and sensors detect the passage of the projectile. The velocity of the projectile is obtained from the sensor signals by comparing the time interval between the projectile passing through the two sensors. The high speed camera triggered by the laser and sensors begins to record the images of crack propagation at the instant when the projectile impacts the specimen.

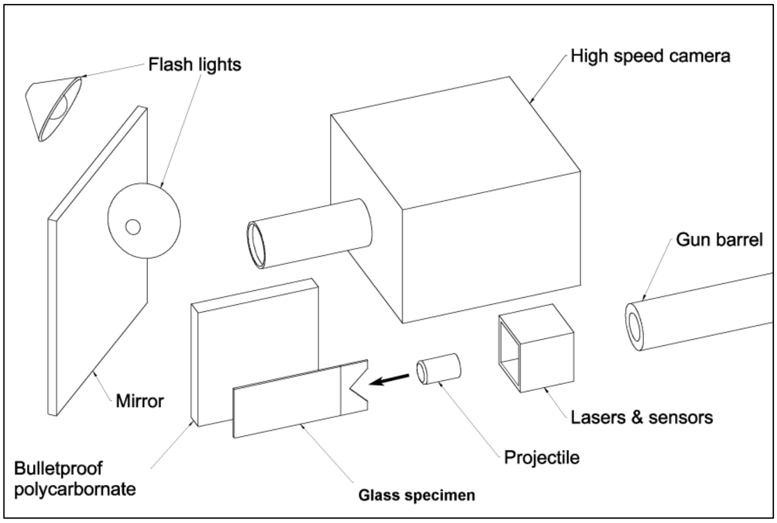

Figure 1. Configuration of experimental setup

Figure 2 shows the dimensions of the projectile and specimen. The projectile strikes the notch, initiating a dynamic crack at the tip of the notch. The specimen is sufficiently long to prevent a reflected tensile wave from separating the glass specimen at the interface. The glass specimens were made with commercial soda-lime glass and Loctite E-30CL epoxy glass bond. The thickness of adhesive is controlled with shims and was measured with an optical magnifier. The projectile material requires low hardness and strength to prevent damage on the glass surface where the projectile initially contacts. Otherwise, the contact surface is subjected to developing fragmentations immediately when a harder projectile touches, because of the brittleness of glass. Smooth-On Featherlite™, casting polyurethane, was chosen for its low hardness and light weight. High speed images and post-mortem observations verified that the cracks always initiate at the notch first instead of at the contact surfaces between the projectile and the glass specimen.

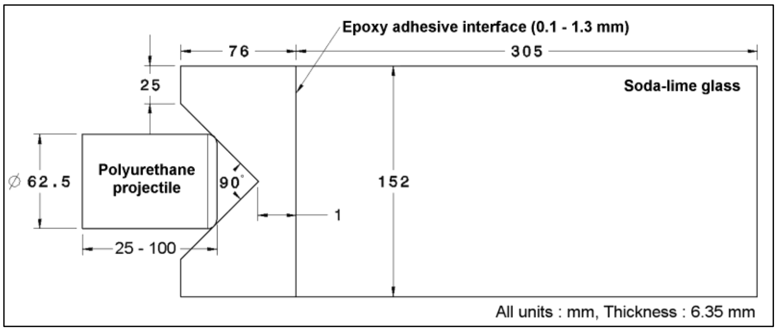
Epoxy adhesive interface (0.1 - 1.3 mm)
76
305
25
Soda-lime glass
∅ 62.5
Polyurethane projectile
90°
152
1
25 - 100
All units : mm, Thickness : 6.35 mm

Figure 2. Dimensions of projectile and specimen

To obtain more quantitative information about the crack propagating in the glass plates, the method of caustics was employed to track the tip of cracks and to estimate stress intensity factors. The glass has very small photoelastic constants and the corresponding size of caustics is very small. The size of caustics in glass is only a few millimeters, making it difficult to obtain the exact value of stress intensity factor of each crack [10]. However, it is still possible to estimate the change of the stress intensity factor and compare the relative value of each branched crack.

RESULTS

The high speed camera recorded the images of crack propagation and its interaction with the interface at a frame interval between 5 μs and 20 μs. Figure 3 shows the crack propagation on a specimen having two glass panels touching along the interface without adhesive bonding. The propagating crack from the notch tip stopped at the interface. Similar phenomenon was observed in another study [9], where a crack was observed to be arrested at the adhesive interface because the two sides of the interface were detached before the crack arrived. Besides the initial cracks, more cracks developed from the interface toward the notch later, which were generated by the tensile waves reflected from the side edges of the specimen, as shown in the image on the right side of Figure 3.

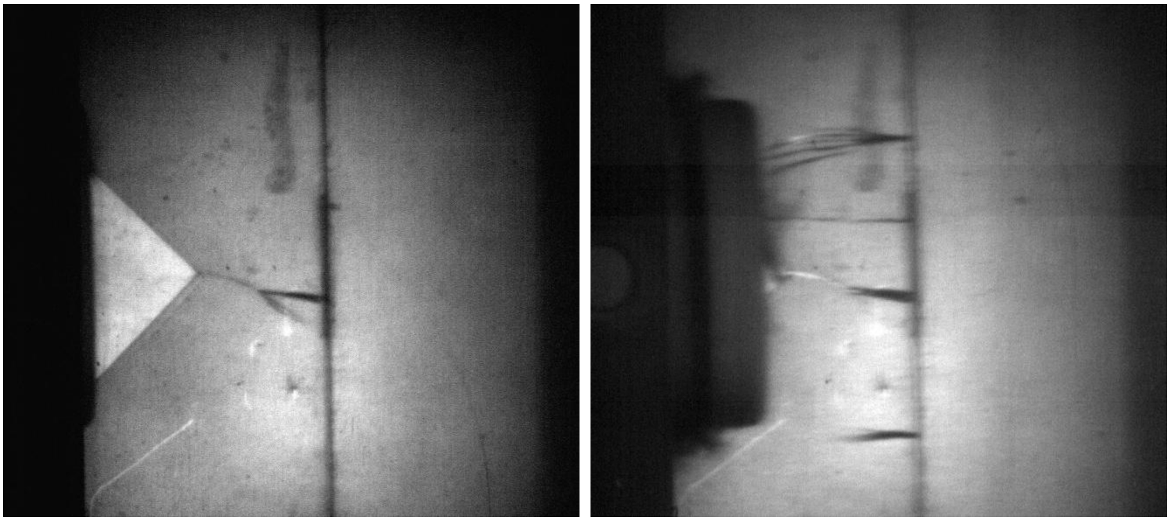

Figure 3. Crack propagation across an interface without adhesive (projectile: 217 g, 212 m/s, K.E.: 4880 J)

Figure 4 shows the crack propagation across an interface bonded with an adhesive layer of less than 0.1-mm thick. In this case, two glass plates were bonded without any shims. The images in Figure 4 show that the crack passed across the interface without deflecting or branching. The propagation of the crack paused at the interface for 5 μs approximately. A similar delay was also observed in another study [8].

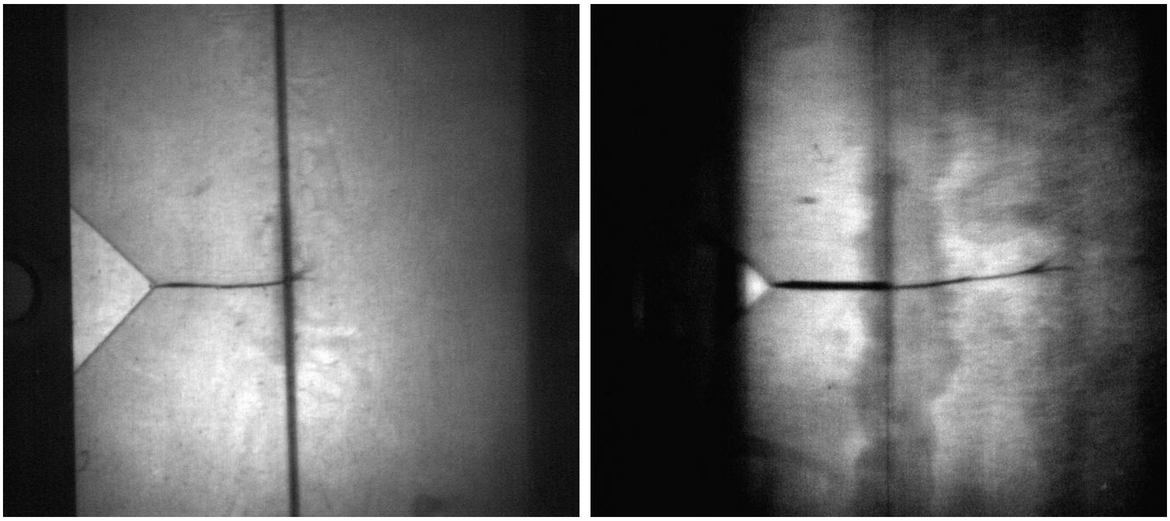

Figure 4. Crack Propagation across a very thin interface (projectile: 162 g, 229 m/s, K.E.: 4250 J)

Figure 5 shows the behavior of a crack propagating through an interface bonded with an adhesive layer of 0.13-mm thick. The crack also paused at the interface for 10 μs approximately when crossing the interface. The crack then branched into multiple cracks after it passed across the interface. Comparing to the behavior of the crack interaction with a thin interface where no branching or defecting occurred despite higher impact energy as shown in Figure 4, this branching-after-interface phenomenon is an interesting phenomenon worth further exploration.

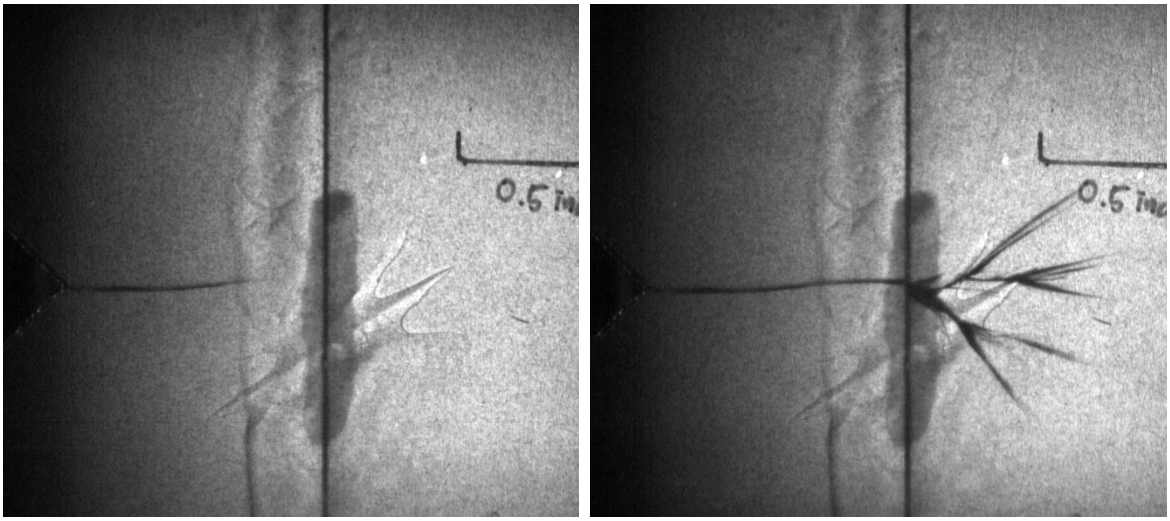

Figure 5. Crack propagation across a 0.13 mm-thick interface (projectile: 124 g, 192 m/s, K.E.: 2290 J)

It is suspected that the branching is caused by the accumulation of strain energy in the ductile adhesive layer that is suddenly released at the initiation of the crack after the interface. To further explore the relation between the available strain energy and the branching behavior, the specimen having a much thicker (1.3-mm) layer of adhesive was impacted as shown in 6. The crack had more branches than that happened in the specimen having the 0.13-mm thick adhesive layer as shown in Figure 5, in spite of similar impact energy. The thickness of the interface is concluded to affect the pattern of the crack branching.

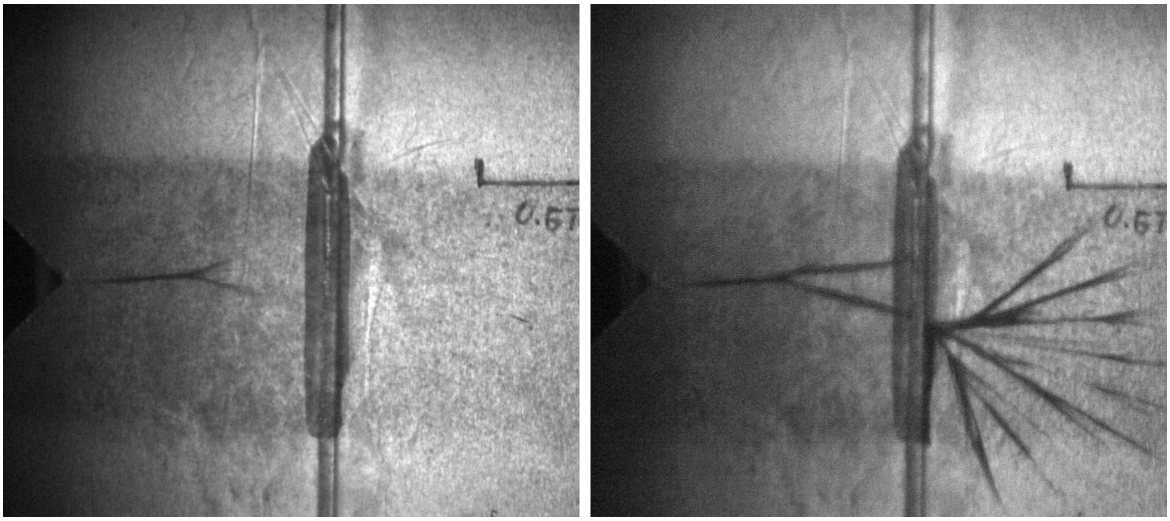

Figure 6. Crack propagation across a 1.3 mm-thick interface (projectile: 135 g, 200 m/s, K.E.: 2700 J)

It was also observed in this experiment that the crack branched before reaching the interface. The upper crack branch stopped at the interface while the lower branch penetrated the interface.
Another approach to vary the strain energy in the specimen is to increase the striking velocity of the projectile. Figure 7 shows the crack branching in the specimen impacted by the projectile at a higher speed of 660 m/s. With more energy available in the specimen, it is seen that the high-speed impact caused severe crack branching in the glass specimen after the interface. The initial crack also branched into multiple cracks at the very early time before reaching the interface. The dense crack in the glass after the interface is quite different from the other cracks in glass observed in normal static or low speed dynamic experiments, such as the ones shown in Figures 4 and 5.

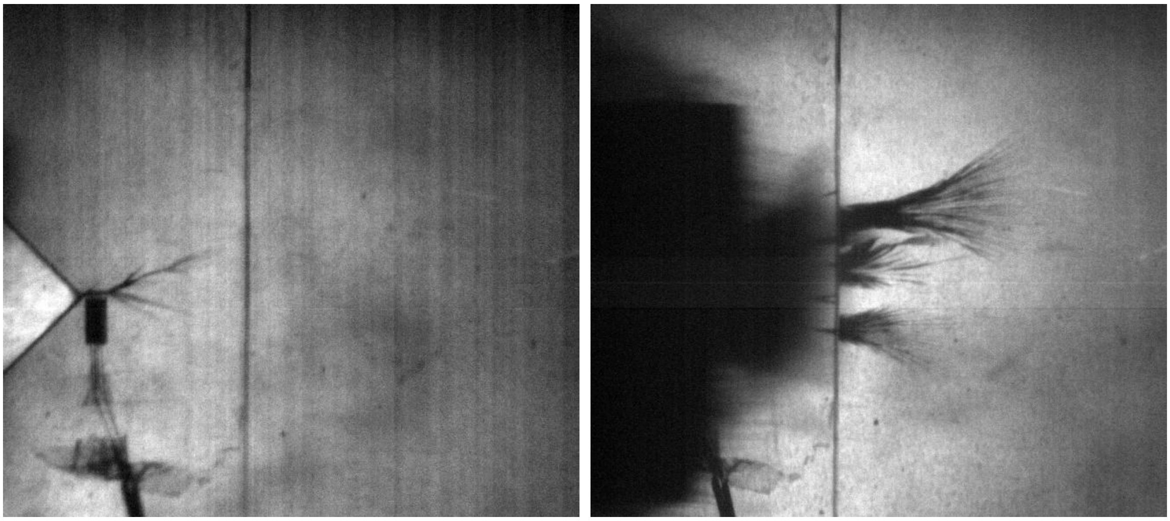

Figure 7. Crack propagation across a 0.38 mm-thick interface (projectile: 77 g, 660 m/s, K.E.: 16800 J)

To compare the relative stress intensity factors associated with each of the crack tip, the method of caustics was employed. Figure 8 shows the images of caustics from such an experiment. The vertical black line is the interface having a 0.5-mm thick adhesive layer. The horizontal black line at the center is a shadow that is not covered by laser pulses and should be ignored. The size of caustics is approximately 1 mm but the exact size can not be obtained due to low resolution of the images. As shown in the figure, the initial crack was branched before it reached the interface, which is similar to that of Figure 6. Comparing the sizes of caustics, crack 1 has the higher stress intensity factor than crack 2 initially. But when they reached the interface, crack 2 had a higher stress intensity factor; and it penetrated the interface and then branched in to multiple cracks. This phenomenon indicates that the main crack driving force may switch from one crack to another when the cracks approach an interface delaying their propagation. The information obtained from the caustics shed insights into why one crack penetrates the interface while other crack stops at the interface even though they are branched from a single crack.

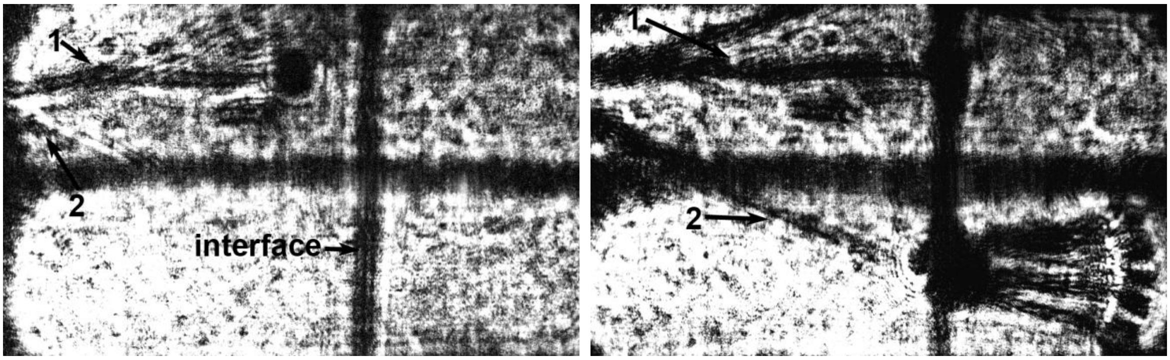

Figure 8. Caustic of crack propagation across a 0.5 mm-thick interface (projectile: 84 g, 262 m/s, K.E.: 16660 J)

DISCUSSIONS

It is known that elastic energy in a specimen is transferred into a growing crack. The crack propagation speed is an important factor to dissipate the stored energy [4]. Under dynamic loading conditions, the energy in the specimen increases rapidly and a delay in crack propagation may let excessive energy store in the specimen. Such excessive energy leads to crack branching. The mechanism of crack branching have not been explained clearly. The definition of the critical conditions for crack bifurcation have been attempted in various ways such as a critical velocity, a stress intensity factor, a strain release energy, and a surface roughness [12,13]. Even though the definite model for crack branching does not exist this time, it is obvious that excessive energy in loaded specimen causes crack branching. The surface roughness transition known as mirror-mist-hackle of a fractured surface shows the excessive energy dissipation through the surface when a crack branches into multiple crack [13].

It is experimentally determined that the crack propagation is delayed longer as the thickness of adhesive increases. One of the reasons is that the crack speed in epoxy is much lower than that of glass. It was also observed that the initiation of crack in the glass after the interface takes a certain amount of time even when the duplex specimen did not have any adhesive layer [8]. If the duration of delay is very short, the stored energy in the specimen is not big enough to cause crack branching as show in Figure 4. However, if the impact velocity is high, even a short duration of delay can cause crack branching because of the excessive energy accumulated in the specimen. As show in Figure 7, very sever crack branching was observed in spite of a relatively thin 0.38 mm-thick adhesive layer.

CONCLUSIONS

Projectile impact speed and thickness of adhesive layer affect the patterns of the crack propagation across an interface in notched glass specimens. The crack penetrates the interface with a very thin layer of adhesive at a moderate impact speed. The crack branches into multiple cracks if the layer has a finite thickness or the impact speed is high. The crack stops at the interface without any adhesion. The stress intensity factor of each branched crack may increase or decrease when the cracks approach the interface.

REFERENCES

1. Kanel G. I., Razorenov S. V., Fortov V.E., Shock-wave Phenomena and the Properties of Condensed Matter, Springer, 2004.
2. Feng R., Formation and Propagation of Failure in Shocked Glass, *J. App. Phy.*, **87**, 1693-1700, 2000.
3. Kanel G. I., Bogatch A. A., Razorenov S. V., Chen Z., Transformation of Shock Compression Pulses in Glass due to the Failure Wave Phenomena, *J. App. Phy.*, **92**, 5045-52, 2002.
4. Freund L. B., Dynamic Fracture Mechanics, Cambridge, 1990.

5. Ravi-Chandar K., Dynamic Fracture, Elsevier, 2004.
6. Zak A. R., Williams M. L., Crack Point Stress Singularities at a Bi-Material Interface, *Tran. ASME*, **3**, 142-143, 1963.
7. Dally J. W., Kobayashi T., Crack Arrest in Duplex Specimens, *Int. J. Sol. Struc*., **14**, 121-129, 1977.
8. Theocaris P. S., Milios J., Crack-arrest at a Bimaterial Interface, *Int. J. Sol. Struc.*, 1**7**, 217-230, 1981.
9. Xu L. R., Rosakis A. J., An Experimental Study of Impact-involved Failure Events in Homogeneous Layered Materials Using Dynamic Photoelasticity and High-speed Photography, *Opt. Laser. Eng.,* **40**, 263-288, 2003.
10. Takahashi K., Fast Fracture in Tempered Glass, *Key Eng. Mat.,* **166**, 9-16, 1999.
11. Schardin H., Velocity Effects in Fracture, *Fracture : Proc. Int. Conf. Atomic. Mech. Frac. Help in Swampscott*, Massachusetts, 297-330, 1959.
12. Ramulu M., Kobayashi A. S., Mechanics of Crack Curving and Branching – a Dynamic Fracture Analysis, *Int. J. Frac*., **27**,187-201, 1985.
13. Ravi-Chandar K., Knauss W. G., An Experimental Investigation into Dynamic Fracture: **III**. On Steady-state Crack Propagation and Crack Branching, *Int. J. Frac*., **26**, 141-154, 1984.

Proceedings of the SEM Annual Conference
June 7-10, 2010 Indianapolis, Indiana USA
©2010 Society for Experimental Mechanics Inc.

Effect of Temperature and Crack Tip Velocity on the Crack Growth in Functionally Graded Materials

Addis Kidane[1*], Vijaya B. Chalivendra[2], Arun Shukla[3],

[1]Graduate Aeronautical Laboratory, California Institute of Technology

[*]1200 E. Californian Blvd. MC 205-45, Pasadena, CA 91125, Email: addis@caltech.edu

[2]Department of Mechanical Engineering, University of Massachusetts Dartmouth, North Dartmouth, MA 02747

[3]Dynamic Photomechanics Laboratory, Department of Mechanical Engineering & Applied Mechanics
The University of Rhode Island, Kingston, RI 02881

ABSTRACT

The stress-fields near the crack tip for mixed-mode thermo-mechanical loading in functionally graded material (FGM) are developed using displacement potentials in conjugation with an asymptotic approach. The shear modulus, mass density and coefficient of thermal expansion of the FGM are assumed to vary exponentially along the gradation direction. Using insulated crack face boundary condition and steady state heat conduction assumption, the temperature field near to the crack tip is developed. By incorporating the developed temperature field equations with the displacement potentials, asymptotic thermo-mechanical stress field equations are derived. Finally, utilizing the minimum strain energy density criterion and the maximum circumferential stress criterion, the crack growth direction for various crack-tip speeds, non-homogeneity coefficients and temperature fields are determined.

INTRODUCTION

Functionally graded materials (FGMs) are essentially non-homogeneous composites which have characteristics of spatially varying microstructure and mechanical/thermal properties to meet a predetermined functional performance [1, 2]. Although their performance in real-life engineering applications are still under investigation, FGMs have shown promising results when they are subjected to thermo-mechanical loading [2]. A few studies on the quasi-static fracture of FGMs under thermo-mechanical loading have been reported. Assuming exponential variation of material properties, Jin and Noda [3] investigated the steady thermal stress intensity factors in the functionally gradient semi-infinite space with an edge crack subjected to thermal load. Later, Erdogan and Wu [4] also determined the steady thermal stress intensity factor of a FGM layer with a surface crack perpendicular to the boundaries. By employing a finite element method (FEM), Noda [5] analyzed an edge crack problem in a zirconia/titanium FGM plate subjected to cyclic thermal loads. Using FEM and boundary element method, Jin and Paulino [6] studied transient thermal stresses in an FGM with an edge crack and having constant Young's modulus and Poisson's ratio but varying thermal properties along the thickness direction.

The above studies provide closed form solutions for stress intensity factors under thermo-mechanical loading conditions; however for extracting fracture parameters from experimental studies, asymptotic expansion of thermo-mechanical stress fields around the crack tip are essential. In this direction, recently, Jain et al., [7] developed quasi-static stress and displacement fields for a crack in an infinite FGM medium under thermo-mechanical loading conditions. Very recently, Lee et al. [8] developed analytical expressions for dynamic crack-tip stress and displacement fields under thermo-mechanical loading in FGM. In the solution development process, the authors employed twice-scaled Laplacian equations that led to complex set of stress expressions. These stress expressions are fairly difficult to interpret and use in extracting fracture parameters from experimental studies. Motivated by this limitation, we now propose a simpler solution methodology [9] in evaluating mixed-mode stress fields for a propagating crack at uniform speed along the direction of mechanical and thermal

T. Proulx (ed.), *Dynamic Behavior of Materials, Volume 1*, Conference Proceedings of the Society for Experimental Mechanics Series, DOI 10.1007/978-1-4419-8228-5_17, © The Society for Experimental Mechanics, Inc. 2011

property variation in a FGM under thermo-mechanical loading. The crack growth direction as a function of temperature, nonhomogeneity parameter and crack-tip velocity is also evaluated using both circumferential stress and minimum strain energy density criterions.

THEORETICAL FORMULATION

An asymptotic analysis is used to expand the stress field around a mixed-mode propagating crack in functionally graded materials under thermo-mechanical loading.

Shear modulus (μ), Lame's constant (λ), density (ρ), thermal expansion (α) and heat conductivity (k) of the FGM are assumed to vary in an exponential manner as shown in Eq. (1), whereas Poisson's ratio (ν) is assumed to be a constant.

$$\mu = \mu_0 \, exp\left(\zeta X\right), \; \lambda = \lambda_0 \, exp\left(\zeta X\right), \; \rho = \rho_0 \, exp\left(\zeta X\right) \tag{1a}$$

$$\alpha = \alpha_o \, exp\left(\beta X\right), \; k = k_o \exp\left(\beta X\right) \tag{1b}$$

The equations of motion for a plane problem are given by Eq.(2)

$$\frac{\partial \sigma_{XX}}{\partial X} + \frac{\partial \tau_{XY}}{\partial Y} = \rho \frac{\partial^2 u}{\partial t^2}, \; \frac{\partial \tau_{XY}}{\partial X} + \frac{\partial \sigma_{YY}}{\partial Y} = \rho \frac{\partial^2 v}{\partial t^2} \tag{2}$$

The relationship between stresses and strains for a thermo-mechanical problems can be written as

$$\sigma_{XX} = \exp\left(\zeta X\right)\left[(\lambda_0 + 2\mu_0)\varepsilon_{XX} + \lambda_0 \varepsilon_{YY} - (3\lambda_0 + 2\mu_0)\alpha_0 \exp(\beta X) T\right] \tag{3a}$$

$$\sigma_{YY} = \exp\left(\zeta X\right)\left[\lambda_0 \varepsilon_{XX} + (\lambda_0 + 2\mu_0)\varepsilon_{YY} - (3\lambda_0 + 2\mu_0)\alpha_0 \exp(\beta X) T\right] \tag{3b}$$

$$\tau_{XY} = \exp\left(\zeta X\right)\mu_0 \gamma_{XY} \tag{3c}$$

where X and Y are reference coordinates, σ_{ij} and ε_{ij} $\left(where \; i = X, \, Y \; and \; j = X, Y\right)$ are in-plane stress and strain components, λ and μ denote Lame's constant and shear modulus respectively and subscript "o" means at $X = 0$ as shown in Fig. 1. T represents the change in temperature in the infinite medium, ζ and β are nonhomogeneity constants that have the dimension (length)$^{-1}$.

For plane strain deformation, the displacements u and v are derived from dilatational and shear wave potentials Φ and Ψ. For a propagating crack shown in Fig. 1, the transformed crack tip coordinates can be written as $x = X - ct$, $y = Y$, where *c* is constant crack tip speed. It is assumed that in the above transformation, the fields Φ and ψ do not depend explicitly on time in the moving coordinate reference and their time dependence is only through the transformation *x* = *X*-*ct*.

In the asymptotic analysis, first a new set of coordinates is introduced as defined as

$$\eta_1 = x/\varepsilon \;\; , \;\; \eta_2 = y/\varepsilon \;\; and \;\; 0 < \varepsilon < 1$$

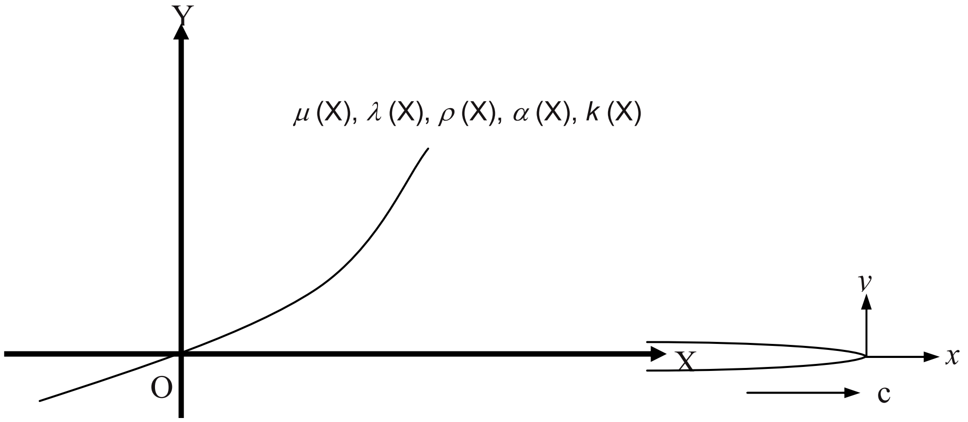

Fig 1. Propagating crack tip orientation with respect to reference coordinate configuration

Then, the equations of motion are written in these scaled coordinate and the displacement fields Φ and ψ and T are assumed as a power of series expansion in ε . By considering the first few terms, the solution for Φ and ψ in the scaled coordinate are obtained by solving a set of partial differential equations corresponding to each power of ε ($\varepsilon^{1/2}$, ε, $\varepsilon^{3/2}$…). Finally by transforming back to the X-Y plane, the solution for Φ and ψ can be written as Eq. (4a and 4b),

$$\begin{aligned}\phi = {} & r_l^{3/2}\left\{A_0\cos\left(\frac{3}{2}\theta_l\right)+C_0\sin\left(\frac{3}{2}\theta_l\right)\right\}+r_l^2\left\{A_1\cos(2\theta_l)+C_1\sin(2\theta_l)\right\} \\ & +r_l^{5/2}\left\{A_2\cos\left(\frac{5}{2}\theta_l\right)+C_2\sin\left(\frac{5}{2}\theta_l\right)\right\}-\frac{1}{4}\frac{\zeta}{\alpha_l^2}r_l^{5/2}\left\{A_0\cos\left(\frac{1}{2}\theta_l\right)+C_0\sin\left(\frac{1}{2}\theta_l\right)\right\} \\ & -\frac{2}{5}\frac{\zeta}{\delta+2}\frac{\alpha_s}{\alpha_l^2-\alpha_s^2}r_s^{5/2}\left\{B_0\cos\left(\frac{5}{2}\theta_s\right)+D_0\sin\left(\frac{5}{2}\theta_s\right)\right\}+\frac{4}{15}\frac{3\delta+2}{\delta+2}\frac{\alpha_c}{\alpha_l^2-1}q_0 r^{5/2}\cos\left(\frac{5}{2}\theta\right)\end{aligned} \tag{4a}$$

$$\begin{aligned}\psi = {} & r_s^{3/2}\left\{B_0\sin\left(\frac{3}{2}\theta_s\right)+D_0\cos\left(\frac{3}{2}\theta_s\right)\right\}+r_s^2\left\{B_1\sin(2\theta_s)+D_1\cos(2\theta_s)\right\} \\ & +\rho_s^{5/2}\left\{B_2\sin\left(\frac{5}{2}\theta_s\right)+D_2\cos\left(\frac{5}{2}\theta_s\right)\right\}-\frac{1}{4}\frac{\zeta}{\alpha_s^2}\rho_s^{5/2}\left\{B_0\sin\left(\frac{1}{2}\theta_s\right)+D_0\cos\left(\frac{1}{2}\theta_s\right)\right\} \\ & -\frac{2}{5}\delta\frac{\zeta\alpha_l}{\alpha_l^2-\alpha_s^2}\rho_l^{5/2}\left\{A_0\sin\left(\frac{5}{2}\theta_l\right)+C_0\cos\left(\frac{5}{2}\theta_l\right)\right\}\end{aligned} \tag{4b}$$

TEMPERATURE FIELDS AROUND THE CRACK TIP

In this analysis it is assumed that the temperature field around the crack tip changes asymptotically. Also, the transient effects are neglected. The developed field equations can be used for situations of small temperature gradient thermal loading conditions. The heat conductivity is assumed to vary exponentially as given by Eq. (1b). The steady state heat conduction equation can be written as

$$\frac{\partial}{\partial X}\left(k\frac{\partial T}{\partial X}\right)+\frac{\partial}{\partial Y}\left(k\frac{\partial T}{\partial Y}\right)=0 \tag{5}$$

The heat conductivity relation given by Eq. (1b) is substituted in the above equation and the equation is transformed to the crack tip coordinate. Using asymptotic expansion, the governing equation is written in scaled coordinate. At this time, It is assumed that *T* is represented as a power series expansion in ε. The equation is valid by solving a set of partial differential equations corresponding to each power of ε ($\varepsilon^{1/2}$, ε, $\varepsilon^{3/2}$…). This gives a solution for *T* in the scaled coordinate. Finally by transforming back to the crack tip coordinate *x* and *y*, the temperature fields near to the crack tip can be given as

$$T = q_0 r^{1/2} \sin(\frac{1}{2}\theta) + q_1 r \cos(\theta) + q_2 r^{3/2} \sin(\frac{3}{2}\theta) + \frac{1}{4} q_0 \beta r^{3/2} \sin(\frac{1}{2}\theta) \tag{6}$$

Where, q_0, q_1 and q_2 are real constants, $r = \left(x^2 + y^2\right)^{1/2}$ and $\theta = \tan^{-1}(y/x)$.

THERMO-MECHANICAL STRESS FIELDS

The above definitions of the displacement potentials with Eq. (4) are now used to get the displacements fields. These displacement fields are then used to get strain fields. These strain fields and Eq. (6) are substituted into Eq. (3) to obtain in-plane stress fields around the crack tip Eq. (7).

$$\sigma_{ij} = \frac{(K_{Id}, K_{IId})}{(2\pi r)^{1/2}} F_{ij}(r, \theta, T, \xi, c) \tag{7}$$

Using the definition of dynamic stress intensity factor K_{ID} and K_{IID} for opening mode and shear mode [26] the relation between A_o and K_{ID} and C_o and K_{IID} are obtained.

$$A_0 = \frac{4(1+\alpha_s^2)}{4\alpha_l \alpha_s - (1+\alpha_s^2)^2} \frac{K_{ID}}{\mu_c \sqrt{2\pi}}, \tag{8}$$

$$C_0 = \frac{4(\alpha_s}{3(4\alpha_l \alpha_s - (1+\alpha_s^2)^2)} \frac{K_{IiD}}{\mu_c \sqrt{2\pi}}, \tag{9}$$

Where μ_c is crack-tip shear modulus, K_{ID} and K_{IID} are mode-I and mode-II dynamic stress intensity factors respectively.

Now considering the crack face boundary conditions $\sigma_{22} = 0$ *and* $\sigma_{12} = 0$ we can also obtain the following relationship between A_o and B_o and C_o and D_o

$$B_o = \frac{-2\alpha_l}{1+\alpha_s^2} A_o \tag{10}$$

$$D_o = \frac{1+\alpha_s^2}{2\alpha_s} C_o \tag{11}$$

CRACK EXTENSION ANGLE

A dynamically moving crack tends to deviate from its path due to crack-tip instability conditions. The crack tip instability becomes predominant when the cracks tend to propagate in non-homogeneous materials under thermo-mechanical loading. In the present study, using the derived thermo-mechanical stress field equations, the effects of temperature, crack-tip velocity and material non-homogeneity on the crack-tip instability are presented. The theoretical prediction of crack extension angle is investigated by using the two well-known fracture criterions: minimum strain energy density (S-criterion) and maximum circumferential stress ($\sigma_{\theta\theta}$ -criterion).

Minimum strain-energy density (MSED) criterion

According to this criterion [10], the crack initiates when the strain energy density achieves a critical value and propagates in the direction of minimum strain-energy density value. The strain energy density *dW/dV* near the crack tip for an FGM is given as

$$dW/dV = S = \frac{1}{4\mu e^{\zeta X}}\left\{(1-\nu)\left\{\sigma_{xx}^{2}+\sigma_{yy}^{2}\right\}-2\nu\sigma_{xx}\sigma_{yy}+2\sigma_{xy}^{2}\right\} \tag{12}$$

Fracture takes place in the direction of minimum S, and the condition can be obtained by using Eq. (13)

$$\frac{\partial S}{\partial \theta}=0 \quad ;\frac{d^{2}S}{d\theta^{2}}>0 \qquad at\ S=S_{c} \tag{13}$$

where S_c is the critical strain energy density.

Variations of strain energy density with angle θ from $-\pi$ to π around the crack–tip for mixed-mode thermo-mechanical loading in an FGM for several values of the temperature coefficient are investigated. The angle at which the strain energy density reaches a minimum value changes with temperature and the non-homogeneity parameter.

Maximum circumferential-stress (MCS) criterion

The maximum circumferential stress criterion [11] states that, crack growth will occur in the direction of the maximum circumferential stress and will take place when the maximum circumferential stress reaches a critical value, and it can be given as Eq. (14)

$$\frac{\partial \sigma_{\theta\theta}}{\partial \theta}=0, \quad \frac{\partial^{2}\sigma_{\theta\theta}}{\partial \theta^{2}}=<0 \qquad at \quad \sigma_{\theta\theta}=\sigma_{\theta\theta cri} \tag{14}$$

where $\sigma_{\theta\theta cri}$ is the critical circumferential stress.

Variations of circumferential stress with angle around the crack–tip for mixed mode thermo-mechanical loading in an FGM for several values of temperature coefficients are investigated. The angle at which the circumferential stress reaches a maximum value changes with temperature and non-homogeneity parameter.
Based on the above two criteria's, the effects of velocity, non-homogeneity and temperature on the crack extension angle (θ) are further investigated.

Effect of Crack tip velocity

The crack extension angles as a function of crack tip velocities as predicted by the above two criterions are shown in Fig. 2. For pure mode-I loading ($K_{IID}/K_{ID}=0$), the crack extends along $\theta=0$ until the crack tip velocity reaches a critical value at which instability occurs [12]. When the crack tip velocity reaches the critical value, the crack deviates and extends at a different angle. For example at a crack tip velocity of $c/c_s=0.7$, the MSED criterion predicts a crack extension angle of about -55° and the MCS criterion predicts about -38° for pure mode-I loading conditions. For any crack tip velocity shown in figure, as the value of K_{IID}/K_{ID} increases from 0 to 1 and later from 1 to ∞ the crack extension angle increases monotonically. Broek [13], in his book gives the crack extension angles for mixed-mode quasi static loading and his results match perfectly with the predictions from the current study.

Effect of Non homogeneity

The effect of non-homogeneity parameter on crack extension angle for a crack-tip velocity of 0.5c_s at room temperature (q_0 = 0) is shown in Fig. 3. For both homogenous material (i.e. $\xi = 0$) and a FGM with increasing stiffness in the direction of crack growth (i.e. $\xi > 0$), the MCS criterion provides a maximum value and the MSED criterion provides a minimum value along $\theta = 0$ under pure mode-I loading (K_{IID}/K_{ID} =0). However, for a FGM with decreasing stiffness in the direction of crack growth (i.e. $\xi < 0$), the MCS criterion predicts a kink angle of about -55° and the MSED criterion gives a kink angle of about -28°. It can be also observed that for complete range of K_{IID}/K_{ID} values, a FGM with $\xi < 0$ has larger crack extension angle compared to both homogenous and a FGM with $\xi > 0$. This could be attributed to the presence of a compliant material ahead of the crack tip in which the peak stress occurred at higher angle.

Effect of temperature

The effect of temperature field on the crack extension angle for a crack tip velocity of 0.5c_s is shown in Fig. 4. Both the criterion show that, for homogeneous material, the crack extension direction at room temperature is along $\theta = -30^o$ and the value decreases slowly with increase in applied temperature field. For FGM with $\xi > 0$, the crack extension angle is along $\theta = -15^o$ at room temperature and again the value decreases with increase in applied temperature field. In the case of FGM with $\xi < 0$, the crack extension angle is about -50° at room temperature and increases in magnitude as the temperature increases. The increased temperature field increases the compliance of the already compliant material (in case of $\xi < 0$) ahead of the crack tip and creates stresses and strain energy density that peak at higher values of angle.

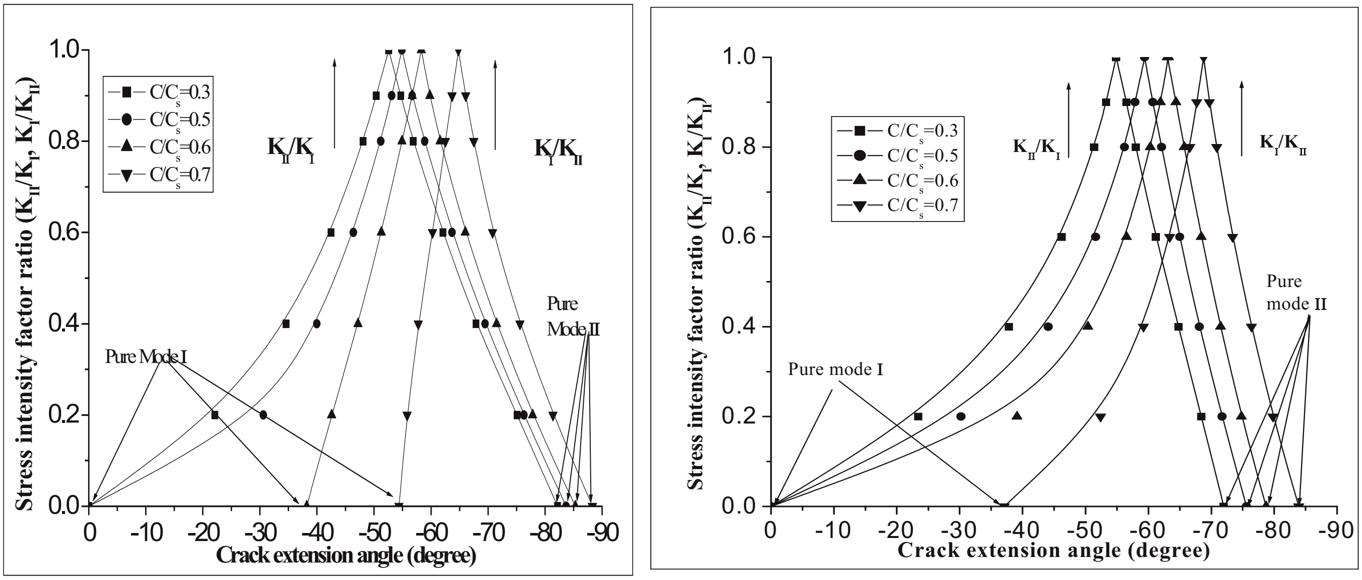

a) Minimum strain energy density criterion   b) Maximum circumferential stress criterion

Fig 2. Crack extension angle as a function of crack tip velocity for mixed mode thermo-mechanical loading in homogeneous material (ζ *=0, r=0.002m*)

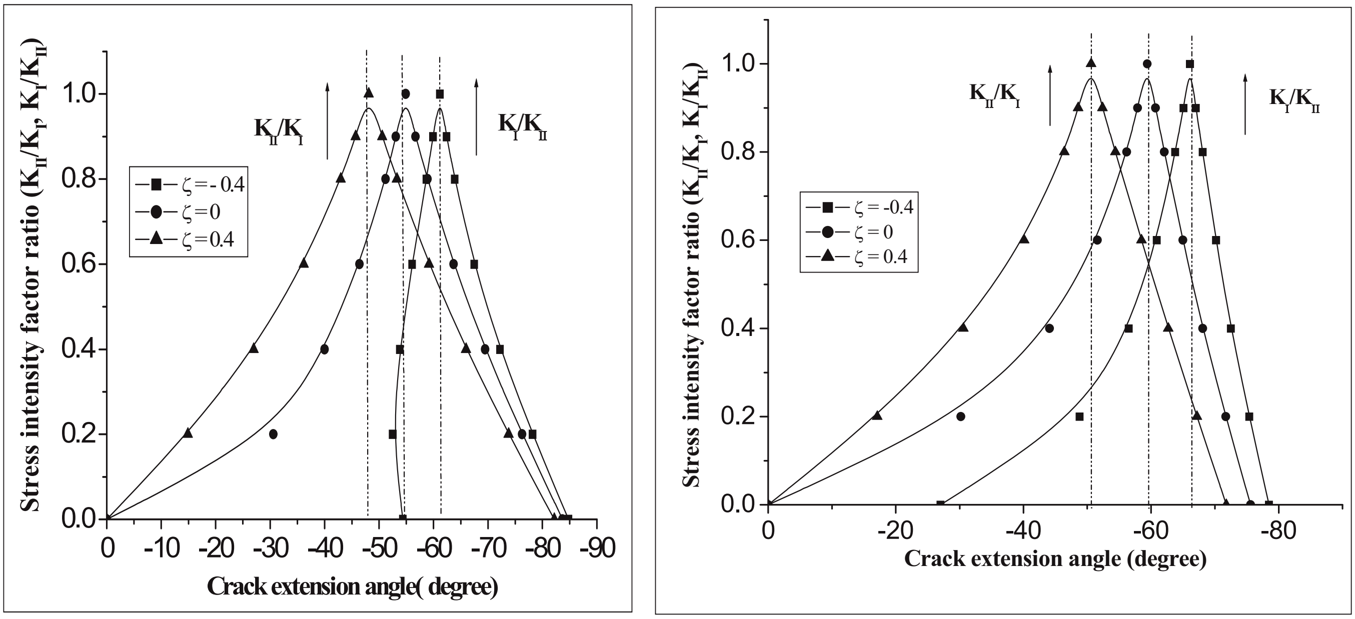

a) Minimum strain energy density criterion

b) Maximum circumferential stress criterion

Fig. 3 Crack extension angle as a function of non-homogeneity parameter for mixed mode crack with no temperature field ($c/c_s=0.5$, $r=0.002m$)

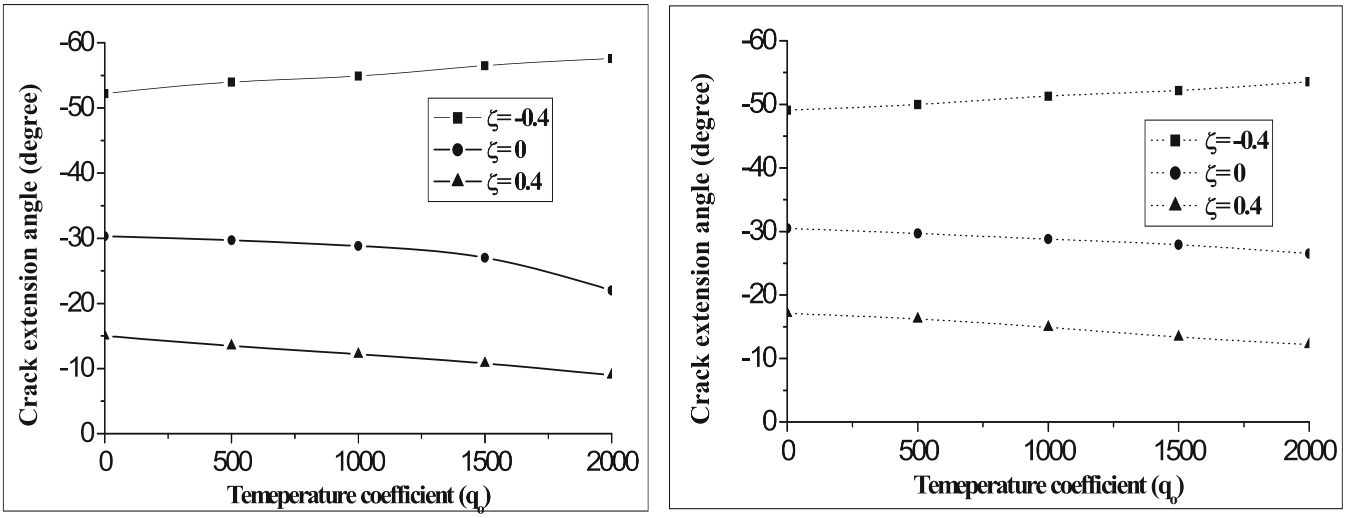

a) Minimum strain energy density criterion

b) Maximum circumferential stress criterion

Fig. 4 Effect of temperature on the crack extension angle for mixed mode loading in FGM ($K_{IID}/K_{ID}=0.2$, $c/c_s=0.5$, $r=0.002m$)

SUMMARY

The stress-fields near the crack tip for mixed-mode thermo-mechanical loading in graded materials are developed using displacement potentials in conjugation with an asymptotic approach. The following key points are observed.

- The thermo-mechanical stress fields around the crack tip are significantly affected by the non-homogeneity parameter. The temperature coefficients considered in this study show little variation in the stress fields.
- The crack extension angle depends on the crack tip velocity. The crack deviates from the original path and starts to kink after the crack tip velocity reaches a critical value (about c/c_s>0.5). Furthermore the crack extension angle increases with the increase in crack tip velocity.
- The increase in the temperature field decreases the crack extension angle in the case of homogeneous materials and FGMs with increasing stiffness along the crack direction.
- The increases in temperature field increases the crack extension angle in the case of FGMs with decreasing stiffness along the crack direction.
- The crack extension angle decreases with increases in the non-homogeneity parameter.

REFERENCE

1. M. Niino, T. Hirai and R. Watanabe, The Functionally Gradient Materials, J. Jap. Soc. Comp. Mater., vol.13, no.1, pp. 257, 1987.
2. S. Suresh and A. Mortensen, Fundamentals of functionally graded materials, processing and thermomechanical behavior of graded metals and metal-ceramic composites. IOM Communications Ltd., London, 1998.
3. Z. H. Jin and N. Noda, Crack-Tip Singular Fields in Nonhomogeneous Materials,J. Appl. Mech., vol. 61, pp. 738-740, 1994.
4. Erdogan and Wu, Crack problems in FGM layers under thermal stresses, J Therm Stress.1996; 19: 237-265.
5. N. Noda, Thermal stress intensity for functionally graded plate with an edge crack, J. Therm Stresses., 1997; 20: 373-387.
6. Z.-H.Jin and G. H. Paulino, Transient thermal stress analysis of an edge crack in a functionally graded materials, Int. J. Fract., 2001; 107: 73-98.
7. Jain, A Shukla and R. Chona, Asymptotic stress fields for thermomechanically loaded cracks in FGMs, J ASTM Int., 2006; 3(7): 88-90.
8. Lee K.H, Chalivendra V.B, Shukla. A. Dynamic crack-tip stress and displacement fields under thermomechanical loading in functionally graded materials. J. Appl. Mech 2008; 75 (5): 1–7.
9. Parameswaran V. and Shukla A. Crack-tip stress fields for dynamic fracture in functionally gradient materials. Mech Mater 1999; 31: 579–596.
10. Sih G.C. Strain-energy-density factor applied to mixed mode crack problems. Int J Fract 1974; 10(3): 305-321.
11. Erdogan F, Sih G. C. On the crack extension in plates under plane loading and transverse shear, J of Basic Eng, 1963; 85: 519-527.
12. Yoffe E. H. The moving griffith crack. Philosophical Magazine 1952; 42: 739-750.
13. Broek D. Elementary engineering fracture mechanics, Martinus Nishoff Publishers, 1978.

Proceedings of the SEM Annual Conference
June 7-10, 2010 Indianapolis, Indiana USA
©2010 Society for Experimental Mechanics Inc.

Characterization of Polymeric Foams under Multi-Axial Static and Dynamic Loading

Isaac M. Daniel and Jeong-Min Cho

Robert R. McCormick School of Engineering and Applied Science
Northwestern University
Evanston, IL 60208
imdaniel@northwestern.edu

ABSTRACT

An orthotropic polymeric foam with transverse isotropy (Divinycell H250) used in composite sandwich structures was characterized under multi-axial quasi-static and dynamic loading. Quasi-static tests were conducted along principal material axes as well as along off-axis directions under tension, compression, and shear. An optimum specimen aspect ratio of 10 was selected based on finite element analysis. Stress-controlled and strain-controlled experiments were conducted. The former yielded engineering material constants such as Young's and shear moduli and Poisson's ratios; the latter yielded mathematical stiffness constants, i. e., C_{ij} . Intermediate strain rate tests were conducted in a servo-hydraulic machine. High strain rate tests were conducted using a split Hopkinson Pressure Bar system built for the purpose. This SHPB system was made of polymeric (polycarbonate) bars. The polycarbonate material has an impedance that is closer to that of foam than metals. The system was analyzed and calibrated to account for the viscoelastic response of its bars. Material properties of the foam were obtained at three strain rates, quasi-static (10^{-4} s^{-1}), intermediate (1 s^{-1}), and high (10^{3} s^{-1}) strain rates.

Introduction

A great deal of work is being reported by other investigators dealing with analysis and simulation of impact and blast loading of composite and sandwich structures. The usefulness of the results obtained depends on the type of inputs used for loading pulses and material behavior. Loading pulse information may be obtained from the literature, however, no realistic models are available for the facesheet and core materials under multi-axial dynamic loading, especially models including hygrothermal effects of long term environmental exposure. Characterization and modeling of facesheet composite materials is being addressed and reported in many sources. However, not enough work has been devoted to characterization and constitutive modeling of structural foams used in sandwich construction. Such work is needed to develop numerical models capable of capturing the dynamic response of composite and sandwich structures under realistic impact and blast loadings and design novel structures for mitigation of severe threats.

Cellular foams are commonly used as core materials in sandwich structures. They are usually made of polyvinyl chloride (PVC), polyurethane (PUR) and polystyrene. The properties of foams depend on the structure of the cells and the density of the material. The mechanical behavior of cellular foams has been investigated and discussed in the literature [1-5]. A thorough discussion of mechanical behavior of polymeric foams is given in the book by Gibson and Ashby [1]. However, characterization has been in general inadequate, and few of the models can capture all the characteristic features of structural foams. Sandwich foam core materials, such as PVC foams (especially higher density ones), are strain rate dependent anisotropic elastic/viscoplastic materials. Their deformation history during dynamic loading affects critically the integrity of the sandwich structure. A few studies have been reported on dynamic characterization of foams [6-9]. Constitutive modeling has lagged because of the finite deformations and the anisotropy involved in some foams, with few works reported in the literature [10-12]. Gielen [12] developed a constitutive model including elastic-plastic behavior and damage progression. However, the

T. Proulx (ed.), *Dynamic Behavior of Materials, Volume 1*, Conference Proceedings of the Society for Experimental Mechanics Series,
DOI 10.1007/978-1-4419-8228-5_18, © The Society for Experimental Mechanics, Inc. 2011

model is not easily applicable in analyses. Considering the loading-unloading-reloading test results in [4], a realistic modeling approach is needed based on an elastic-plastic-damage formulation in strain space.

The present paper extends the multi-axial characterization of an anisotropic foam by means of off-axis testing and stress-controlled and strain-controlled experiments. Rate effects were also studied by using a Hopkinson bar system with impedance-matched polymeric rods.

Experimental Procedures

The material studied was a closed cell PVC foam, Divinycell H250, having a density of 250 kg/m^3. The material was obtained in the form of 25 mm thick panels. It is an orthotropic/transversely isotropic material with principal axes as shown in Fig. 1. This material has been characterized before under loading along the principal material axes as shown in Fig.2.

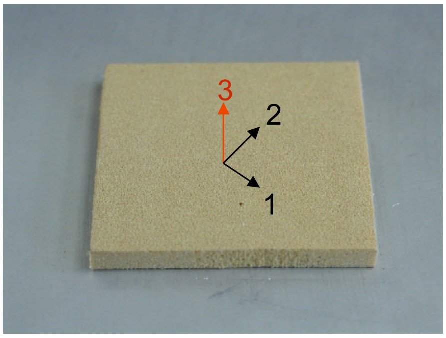

Figure 1. Principal material axes of Divinycell H250 foam

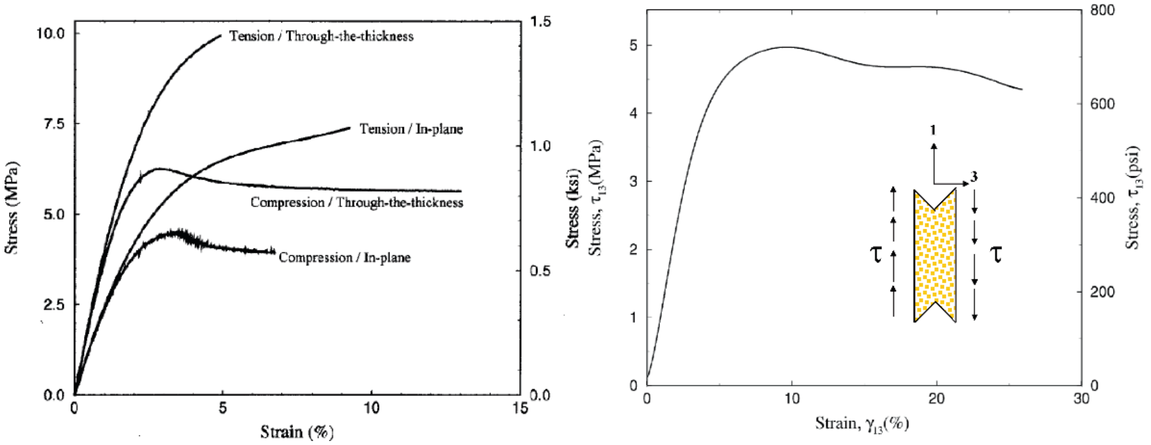

Figure 2. Typical stress-strain curves of Divinycell H250 foam loade along principal directions[2].

A more complete characterization of this material was performed by means of static and high rate tests along principal material axes as well as off-axis directions under tension, compression, and shear (at orientations of 0, 20, 45, 70, and 90 deg with the 3-axis, Fig. 3).

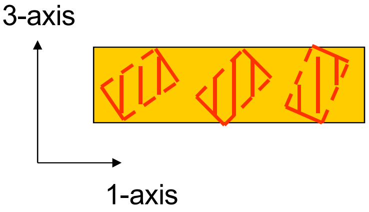

Figure 3. Off-axis testing of foam specimens

On-axis and off-axis coupons were tested under stress control as shown in Fig. 4. Strains were measured by means of Moiré gratings photoprinted on the specimen surface.

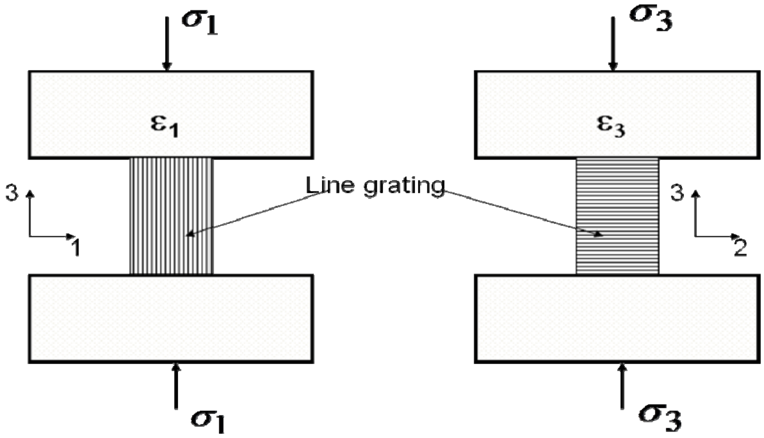

Figure 4. Stress-controlled experiments

Strain-controlled experiments were conducted using specimens and fixtures such as those shown in Fig. 5 at quasi-static and moderate strain rates. These tests, corresponding to strain rates of 10^{-4} and 1 s^{-1}, respectively, were conducted in a servo-hydraulic machine. The optimum specimen aspect ratio was determined by Finite Element Analysis (Fig. 6). The higher the aspect ratio the more homogeneous is the state of strain. An aspect ratio of 10 was deemed suitable for the experiments.

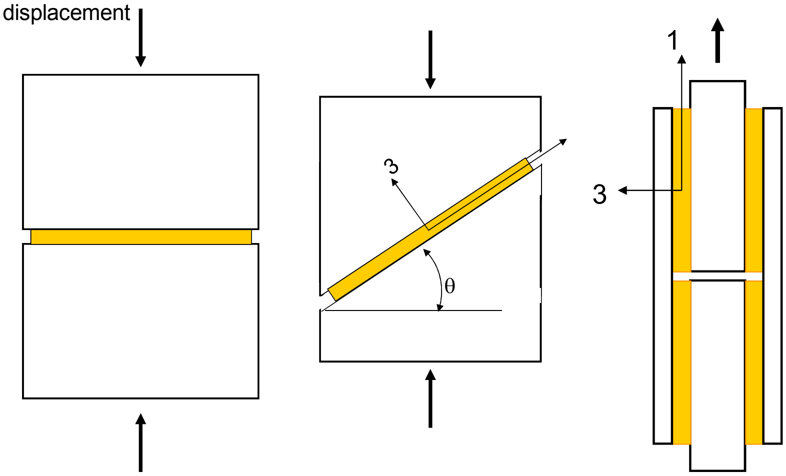

Figure 5. Strain-controlled experiments.

High strain rate tests were conducted using a split Hopkinson Pressure Bar (SHPB) system built for the purpose (Fig. 5). This SHPB system was made of polymeric (polycarbonate) bars. The polycarbonate material has an impedance that is closer to that of foam than metals as shown in Table 1 below. The viscoelastic wave propagation in the polycarbonate rods was analyzed by FFT and the frequency dependence of the attenuation and phase velocity in the rods was determined. The transformed strain, velocity and force (stress) in the specimen were obtained as a function of frequency.

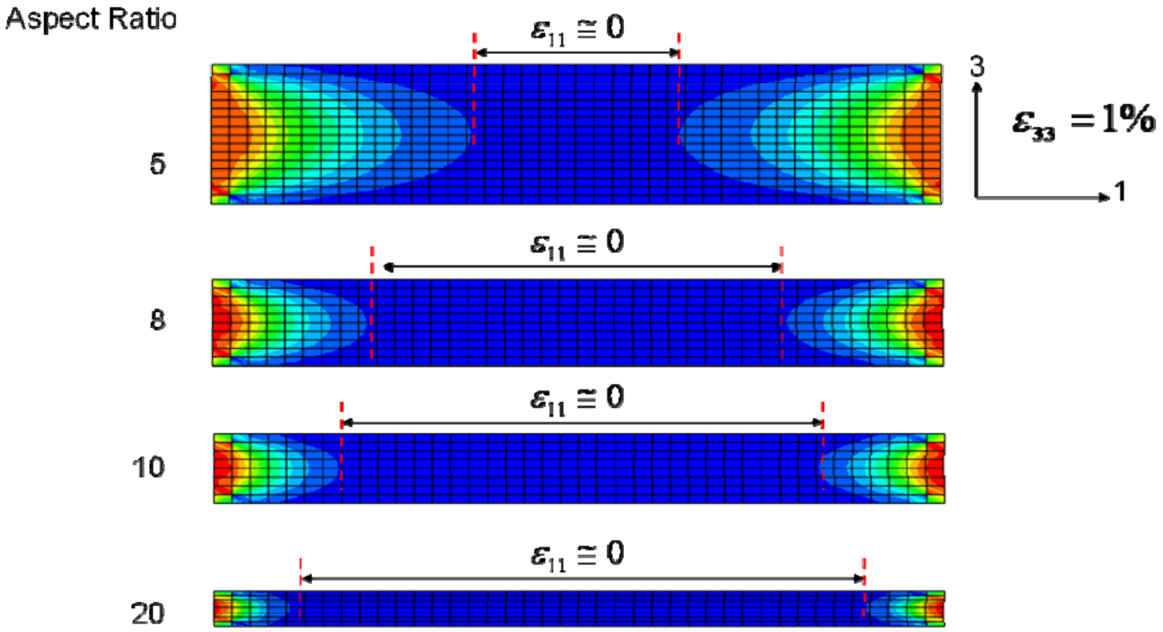

Figure 6. Selection of specimen aspect ratio for strain-controlled experiments

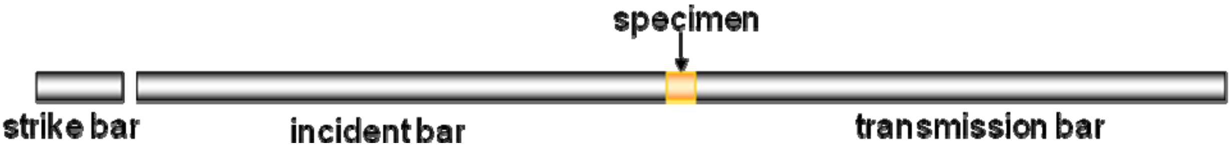
specimen
strike bar
incident bar
transmission bar

Figure 7. Split Hopkinson pressure bar with polymeric bars for testing foam materials

Table 1. Impedances of Hopkinson bar and foam materials

Material	*E*, MPa	ρ, kg/m^3	$Z(=\rho c)$, kg/m^{2}s
Steel	207,000	7,800	4.0×10^7
Aluminum	73,000	2,800	1.4×10^7
Polycarbonate	2,410	1,200	1.7×10^6
PVC Foam (DIAB H250)	322 (through-thickness)	250	2.8×10^5
PVC Foam (DIAB H250)	207 (in-plane)	250	2.3×10^5

Stress-Controlled Experiments

Compressive stress-strain curves for the off-axis specimens tested under stress-controlled conditions are shown in Fig. 8. The effect of anisotropy and stress biaxiality is reflected in the variation in axial modulus and characteristic first peak in the stress-strain curve. The latter is the "critical point" of initiation of local collapse of the cell structure. The variation of the axial modulus and this critical point with load orientation is shown in Figs. 9 and 10.

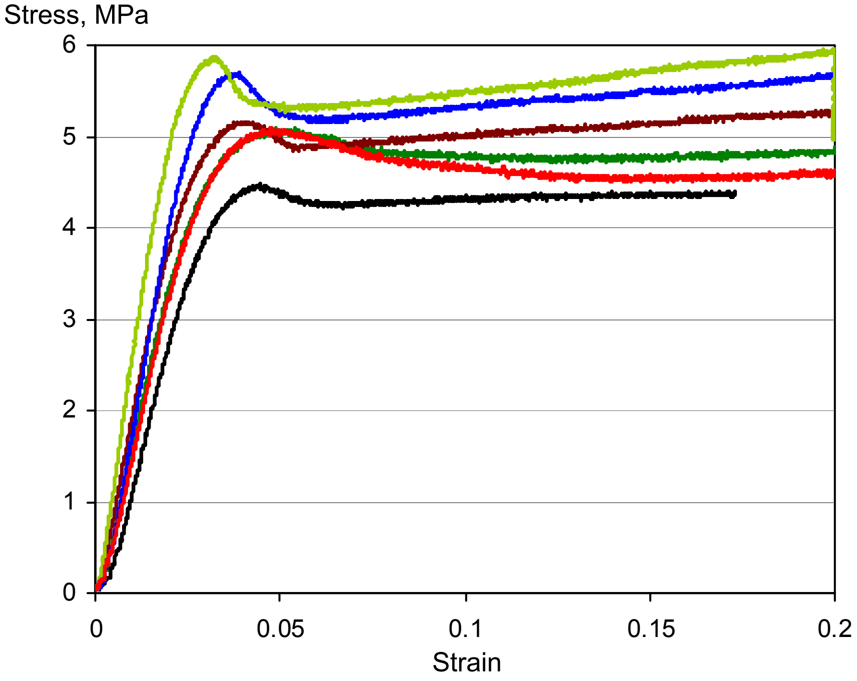

Figure 8. Compressive stress-strain curves of off-axis specimens for loading orientations of 0, 20, 45, 70, and 90 deg with the 1-2 plane.

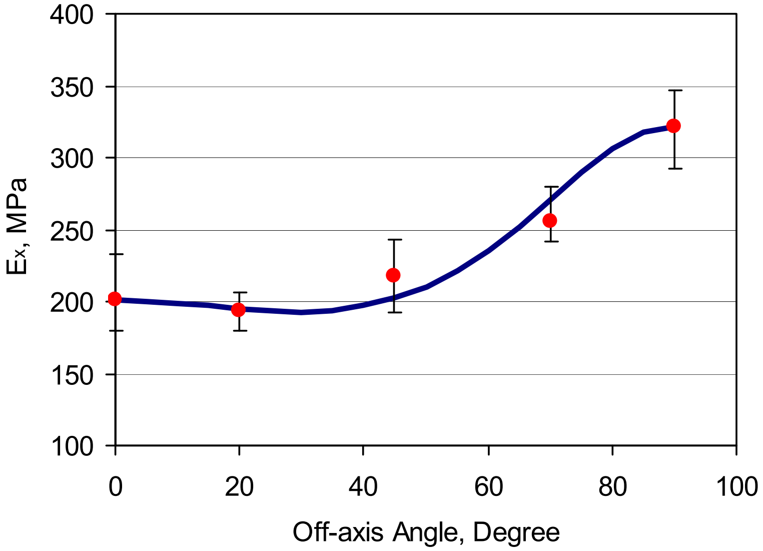

Figure 9. Variation of axial modulus with load orientation from the 1-2 plane

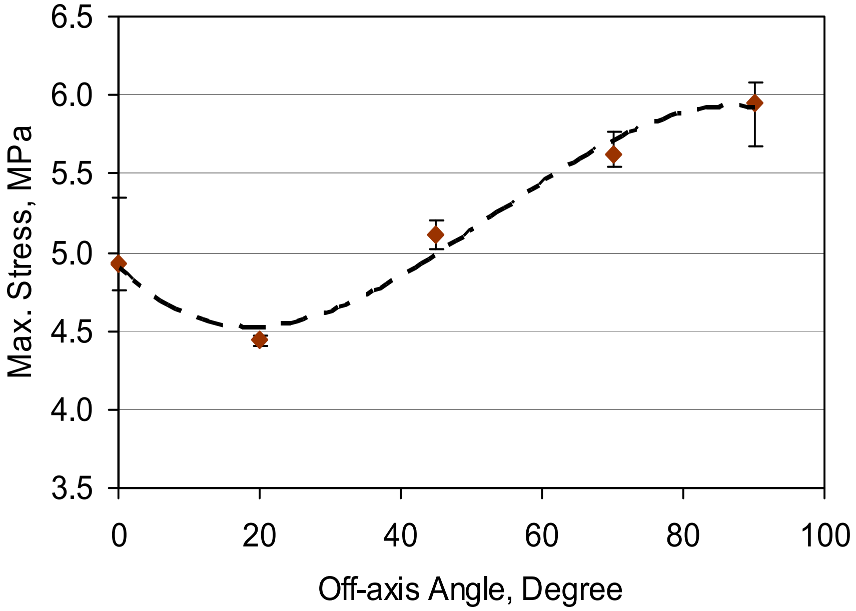

Figure 10. Variation of “critical stress” of cell structure with load orientation from the 1-2 plane

The above tests yielded the engineering constants, $E_1 = E_2$, E_3 , v_{12} , $v_{13} = v_{23}$, G_{12} , $G_{13} = G_{23}$ of the material shown in Table 2.

Strain-Controlled Experiments

Compressive stress-strain curves along the in-plane and through-thickness directions for the strain-controlled (constrained) experiments are shown in Fig. 11. All strain components other than the one measured are constrained to be zero. These curves yield the stiffnesses $C_{11} = C_{22}$ and C_{33}.

$$\varepsilon_{ij} \cong 0 \qquad \varepsilon_{33} \neq 0$$

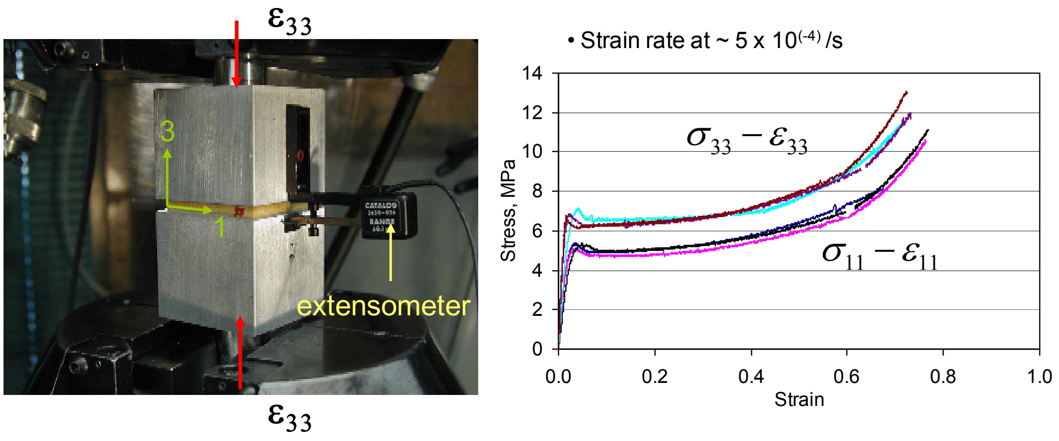

Figure 11. Stress-strain curves under uniaxial strain compression

Shear stress-strain curves are shown in Fig. 12. Only shear strain was applied, all other normal strains were zero. This test yields the shear moduli G_{12} and G_{13} .

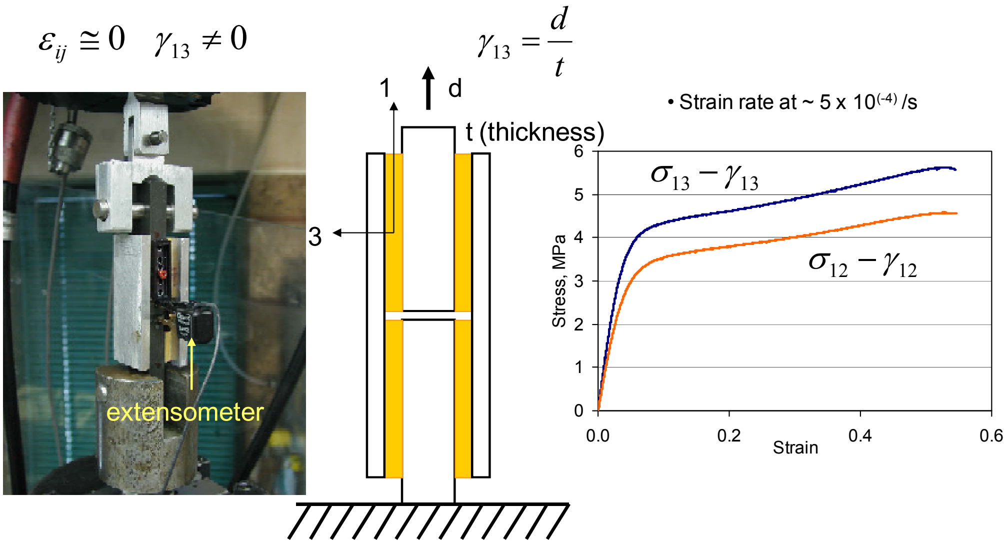

Figure 12. Strain-controlled shear stress-strain curves on the 1-2 and 1-3 planes.

Stress-strain curves under strain-controlled conditions were obtained at three strain rates and are shown in Fig. 13. Results at the highest rate of 10^3 s^{-1} were obtained with the SHPB system.

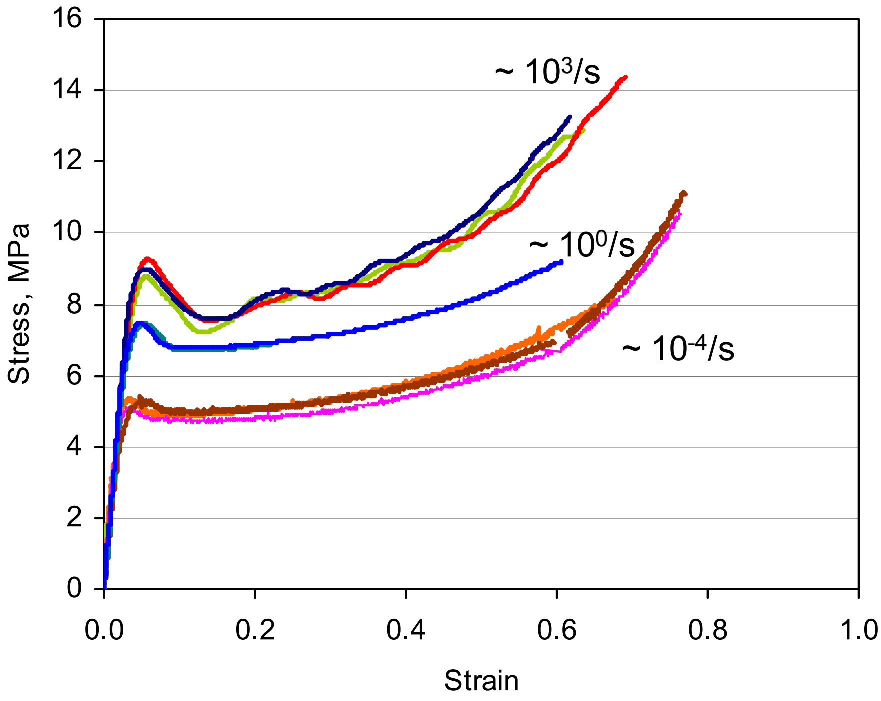

Figure 9. Compressive stress-strain curves in the in-plane (1 or 2) direction obtained under strain- controlled conditions.

The strain-controlled experiments did not yield the Poisson's ratios directly. These were calculated by the known interrelations between the engineering and mathematical stiffness constants.The mathematical constants $C_{11} = C_{22}$ and C_{33} are related to the engineering constants as follows:

$$C_{11} = \frac{E_1\left(E_1 - \nu_{13}^2 E_3\right)}{\left(E_1\left(1-\nu_{12}\right) - 2\nu_{13}^2 E_3\right)\left(1+\nu_{12}\right)} \tag{1}$$

$$C_{33} = \frac{E_1 E_3\left(1-\nu_{12}\right)}{\left(E_1\left(1-\nu_{12}\right) - 2\nu_{13}^2 E_3\right)} \tag{2}$$

From the above, we can obtain the Poisson's ratios as follows:

$$\nu_{12} = \frac{-\dfrac{E_1}{E_3}\dfrac{C_{33}}{C_{11}}\left(1-\dfrac{E_3}{C_{33}}\right) \pm \sqrt{\left(\dfrac{E_1}{E_3}\dfrac{C_{33}}{C_{11}}\left(1-\dfrac{E_3}{C_{33}}\right)\right)^2 - 8\dfrac{E_1}{E_3}\dfrac{C_{33}}{C_{11}}\left(1+\dfrac{E_3}{C_{33}}\right)+16}}{4} \tag{3}$$

$$\nu_{13} = \sqrt{\frac{E_1\left(1-\nu_{12}\right)}{2E_3}\left(1-\frac{E_3}{C_{33}}\right)} \tag{4}$$

Results from the second set of tests are summarized in Table 2 below.

Table 2. Mechanical Properties of Divinycell H250

Property	Strain Rate, s^{-1}		
	10^{-4}	1	10^{-3}
In-plane Young's Modulus $E_1 = E_2$, MPa	207		
Through-thickness Young's Modulus E_3, MPa	322		
Poisson's Ratio, ν_{12}	0.29	0.26	0.26
Poisson's Ratio, $\nu_{13} = \nu_{23}$	0.20	0.19	0.19
In-plane Shear Modulus, G_{12}, MPa	85	87	
Through-thickness Shear Modulus $G_{13} = G_{23}$, MPa	110	111	
Stiffness, $C_{11} = C_{22}$, MPa	250	247	254
Stiffness, C_{33}, MPa	388	378	399

Summary and Conclusions

An anisotropic cellular foam, Divinycell H250, used in sandwich structures was characterized under quasi-static and dynamic loading conditions. Two types of tests were conducted under quasi-static loading, stress-controlled and strain-controlled tests. Tests were run at various orientations with respect to the principal material axes. These tests allowed the determination of the complete set of both engineering and mathematical stiffness constants. Tests were also conducted at an intermediate strain rate of 1 s^{-1} and also at a high rate of 10^3 s^{-1} by means of a Split Hopkinson Pressure Bar. It was observed that the stiffness, based on the initial slope of the stress-strain curves, did not change with strain rate. However, the characteristic peak following the proportional limit increased noticeably with strain rate. This peak is the "critical point" corresponding to collapse initiation of the cells in the foam. This peak is followed by a "strain hardening" region before densification at very high strains.

Acknowledgement

The work described in this paper was sponsored by the Office of Naval Research (ONR). We are grateful to Dr. Y. D. S. Rajapakse of ONR for his encouragement and cooperation.

References

[1] Gibson, L.J. and M.F. Ashby, Cellular Solids. 2nd ed., New York: Cambridge University Press (1997).

[2] Daniel, I.M., E.E. Gdoutos, K.-A. Wang and J.L. Abot, "Failure Modes of Composite Sandwich Beams," International Journal of Damage Mechanics, **11**, 309-334 (2002).

[3] Gdoutos, E.E., I.M. Daniel, and K.A. Wang, "Failure of Cellular Foams under Multiaxial Loading," Composites Part A, **33**, 163-176, (2002).

[4] Flores-Johnson, E.A. and Q.A. Li, "Degradation of Elastic Modulus of Progressively Crushable Foams in Uniaxial Compression," Journal of Cellular Plastics, 44, 415-434, (2008).

[5] Abrate, S., "Criteria for Yielding or Failure of Cellular Materials," Journal of Sandwich Structures and Materials, **10**, 5-51, (2008).

[6] Ramon, O. and J. Mintz, "Prediction of Dynamic Properties of Plastic Foams from Constant Strain Rate Measurements," J. Appl. Polym. Scie., **40**(9-10),1683-1692 (1990).

[7] Daniel, I.M. and S. Rao, "Dynamic Mechanical Properties and Failure Mechanisms of PVC Foams," Dynamic Failure in Composite Materials and Structures, ASME Mechanical Engineering Congress and Exposition, AMD-Vol. **243**, 37-48 (2000).

[8] Viot, P., F. Beani and J.-L. Latallade,"Polymeric foam behavior under dynamic compressive loading," J. Mat. Scie., **40,** 5829-5837 (2005).

[9] Lee, Y.S., N.H. Park and H.S. Yoon, "Dynamic Mechanical Characteristics of Expanded Polypropylene Foams," J. Cellular Plastics, 46, 43-55 (2010).

[10] Zhang, Y., N. Kikuchi, V. Li, A. Yee and G. Nusholtz, "Constitutive Modeling of Polymeric Foam Material Subjected to Dynamic Crash Loading," International Journal of Impact Engineering, vol. 21, No. 5, pp. 369 386, 1998.

[11] Tagariellia, V.L., V.S. Deshpande, N.A. Fleck, and C. Chen, "A constitutive model for transversely isotropic foams, and its application to the indentation of balsa wood," International Journal of Mechanical Sciences, **47**, 666-686, (2005).

[12] Gielen, A.W.J., "A PVC-foam material model based on a thermodynamically elasto-plastic-damage framework exhibiting failure and crushing," International Journal of Solids and Structures, vol. 45, pp. 1896–1917, 2008.

Proceedings of the SEM Annual Conference
June 7-10, 2010 Indianapolis, Indiana USA
©2010 Society for Experimental Mechanics Inc.

Effects of fiber gripping methods on single fiber tensile test using Kolsky bar[1]

J.H. Kim, R.L. Rhorer*, H. Kobayashi, W.G. McDonough, G.A Holmes**

Polymers Division (M/S 8541), Manufacturing Metrology Division* (M/S 8223)

National Institute of Standards and Technology

Gaithersburg, MD 20899

**Corresponding author: gale.holmes@nist.gov

ABSTRACT

Preliminary data for testing fibers at high strain rates using the Kolsky bar test by Ming Cheng et al. [1] indicate minimal effect of strain rate on the tensile stress-strain behavior of poly (p-phenylene terephathalamide) fibers. However, technical issues associated with specimen preparation appear to limit the number of samples that can be tested in a reasonable time. In addition, under the Kolsky bar testing condition fiber fracture may occur at the interface between the fiber and adhesive rather than in the gage section. In this study, the authors investigate the effects of different gripping methods in order to establish a reliable, reproducible, and accurate Kolsky bar test methodology for single fiber tensile testing. As many single fiber tests have been carried out associated with ballistic research, we compare the Kolsky bar test results with the quasi-static test results to determine the tensile behavior over a wide range of strain rates.

1. INTRODUCTION

The desire for lightweight soft body armor (SBA) that enhances the survivability and comfort level of the first responder remains the development focus of new ballistic fibers or nanotechnology enhanced fiber technologies whose ballistic fiber responses and long-term durability to various environmental conditions are unknown. Furthermore, the lack of reliable deformation data at rates approximating ballistic impact speeds continues to vex

---

[1] "Official contribution of the National Institute of Standards and Technology; not subject to copyright in the United States."

T. Proulx (ed.), *Dynamic Behavior of Materials, Volume 1*, Conference Proceedings of the Society for Experimental Mechanics Series, DOI 10.1007/978-1-4419-8228-5_19, © The Society for Experimental Mechanics, Inc. 2011

committees whose primary role is to develop certification protocols that ensure the reliability of SBAs over the projected lifespan of the product.

Within this framework, the Kolsky bar test (see Figure 1) has emerged as a promising measurement technique for providing the critical data needed to accurately assess material properties in ballistic performance that may result from different environmental exposure conditions. Compared with the conventional Kolsky bar, the setup shown in Figure 1 was designed for conducting single fiber tensile tests at high strain rates [1, 2]. The incident stress pulse generation method and the incident bar are the same as a conventional Kolsky bar, but a sensitive quartz transducer is used to detect the transmitted force signal for stress evaluation in the specimen. To carry out a successful test, the gage length of the fiber specimen is limited to a few millimeters to ensure a state of dynamic force equilibrium in the fiber specimen during an experiment.

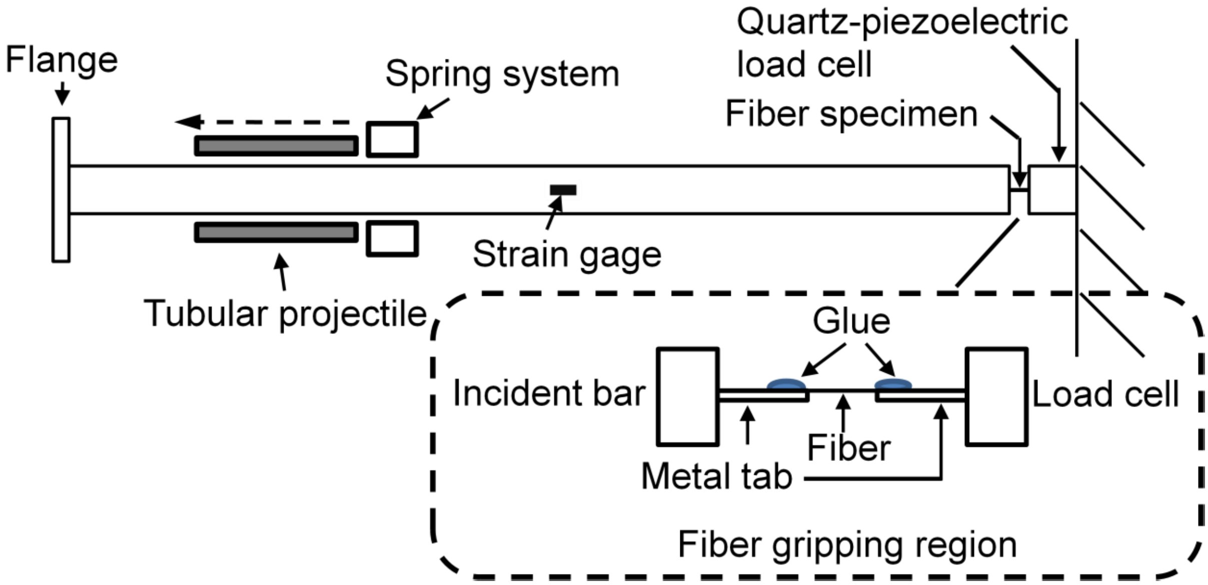

Figure 1. Schematic of the experimental setup for single fiber tensile tests using Kolsky bar.

For ballistic fibers with nominal fiber diameters of 10 µm to 15 µm, the 2 mm length used in the research has an aspect ratio of approximately 133 to 200. Until 1998, the recommended minimum recommended aspect ratio via ASTM D3379-75 [3] for static single fiber testing was 2000. This was done to minimize the amount of tested gage length perturbed by the gripping process. ASTM D3379-75 was superseded by ASTM C1557-03 in part because of the technical inaccuracies associated with the use of the average of the cross-sectional area of several fibers for the calculation of individual fiber strengths. ASTM C1557-03 allows testing of shorter lengths as long as the gage length is reported [4].

Implicit in this protocol change is the belief that the perturbed stress fields in the gripping regions are constant in the standard testing configuration. However, a problem experienced by many researchers in preparing single fiber test samples with small gage lengths is the wicking of glue that has a moderate or low viscosity along the fiber length that effectively seals flaws on the fiber surface and enhances fiber strength [5], since the effective gage length is now much shorter and essentially unknown. To avoid the influence of the glue on the test results, and to be able to conduct rapid assessment of single fiber properties such as tensile strength, modulus and ultimate strain, a direct gripping method is being evaluated for the small gage length test. In this study, single fiber tensile tests under quasi-static conditions are carried out to investigate the feasibility of the new fiber gripping device in the Kolsky bar test.

2. ISSUES ON SINGLE FIBER TEST

When measuring the fiber tensile strength in the single fiber tensile test, there is a certain probability that the fiber fails within the adhesives or tab. To address the issue of failing in the gripping area, Phoenix [6] proposed a model that depends on the fiber Weibull parameters and the fiber stress distribution within the load transfer zone. Assuming perfect alignment and the presence of a shear stress that arises between the matrix that holds the fibers in place and the fiber surface when an external force is applied, several cases are theorized to exist. In the case 1, the fiber tensile stress varies linearly within the whole clamping region. For the case 2, the stress also varies linearly but requires only a portion of the matrix to completely transfer the stress to the fiber. Therefore the difference between the case 1 and 2 is mainly the length of fiber section needed to completely transfer the stress from the matrix to the fiber embedded in the clamp matrix. The case 3 is the ideal situation which has no shear stress in the clamp area (i.e., the stress transfer is instantaneous). This last case is almost impossible to achieve with conventional test procedure. One possible approach may be to directly clamp the fiber between two metallic plates. However, this has the potential to perturb the stress in the gage length. Numerical analyses indicate that the rate of fiber failure within the clamp area (outside of gage length) increases rapidly with decreasing gage length, which may be problematic for testing in reality. [6]

On the other hand, tensile test results of fibers with high strength and modulus are often scattered due to the presence of flaws introduced during processing and handling. Assuming stress concentrations near the end of the fiber close to the grip (clamp), fibers are likely to fail due to the testing method rather than the flaw population alone. Stoner et al. [7] and Newell et al.[8] have suggested a model to account for failures caused by end effects .

In this model the survival probability of the fiber is considered to be the product of the fiber intrinsic flaws (S_f) and the end effects (S_e) (see equation 1). The probability for survival (S_t) of the fiber associated with flaws (S_f) and end effect (S_e) can be expressed in equations 2 and 3, respectively.

$$S_t = S_f \cdot S_e \qquad (1)$$

$$S_f = exp\left(-L\left(\frac{\sigma}{\gamma 1}\right)^{\beta 1}\right) \qquad (2)$$

$$S_e = exp\left(-\left(\frac{\sigma}{\gamma 2}\right)^{\beta 2}\right) \qquad (3)$$

L is the fiber length being tested, and β and γ are the Weibull parameters. Fitting the fiber strengths to the combined Weibull model in equation 1 results in an estimation of the two failure mechanisms that dominate fiber fracture during single fiber tensile test [8]. To obtain the optimized parameters for the model, statistical analyses were performed on the fiber strength distribution for several fiber lengths using the maximum likelihood estimation procedure. Using the same type of fibers, test results are shown to demonstrate the effect of fiber length and gripping method achieved from the quasi-static test (Strain rate, 0.00056 s^{-1}). These data are compared with the failure behavior predicted from the above model.

3. EXPERIMENTAL PROCEDURE

3.1 Quasi-static loading

For the tensile test under quasi-static loading, poly (p-phenylene terephthalamide) fibers (PPT) were used. Two types of fiber gripping techniques were introduced for the quasi-static tensile tests. For the test using grip 1 as shown in Figure 2 (a), the specimens and loading procedure were prepared based on ASTM C1577-03. A brief procedure for preparing single fiber tensile test specimens using grip 1 is as follows: after measuring fiber diameters on the optical microscope, individual fibers were temporarily attached to paper templates with double-sided tape. Small strips of silver reflective tape were applied to the template at the top and bottom of the section with the tabs of each fiber sample. The reflective tape allows direct elongation measurements to be made by a laser extensometer during tensile testing, so calculating the actual strain by determining the system compliance is not needed. Finally the fiber was adhered to the paper template using epoxy which was cured at room temperature for at least 48 h before the tensile test was performed. Maintaining an identical shear stress level for multiple specimens using adhesives is somewhat difficult due to various parameters such as air pockets and irregular mixing of two component adhesives, etc. For tensile testing at high strain rates, the influence from these issues may be more remarkable than for the quasi-static test due to the inconsistent internal structure of material for rapid response.

For the mechanical grip procedure (grip 2) shown in Figure 2 (b), a single PPT fiber is directly clamped between two blocks on both ends and the clamping force of the blocks is controlled by tightening a spring. A unique aspect of this test set up is measuring fiber diameter using a vibration method instead of an optical microscope.

The gage lengths of the fiber specimens on both gripping methods were 2 mm and 60 mm to investigate the effect of the fiber length on the tensile properties under the constant strain rate 0.00056 s^{-1}. Three different loading devices were used for the tensile tests due to the limitation of measurable sample size. The tensile test using grip 1 with gage length 2 mm was performed by an electro magnet driven actuator and the uncertainty of this test in load cell is 0.38 %. The tensile test using grip 1 with gage length 60 mm was performed by a screw driven machine and its uncertainty of the test in load cell is reported in elsewhere [4]. The tests using grip 2 with gage length 2 mm and 60 mm were performed by a commercial single fiber testing machine and its uncertainty in the load cell is 0.1 %.

(a) Fiber grip with adhesives (grip 1)

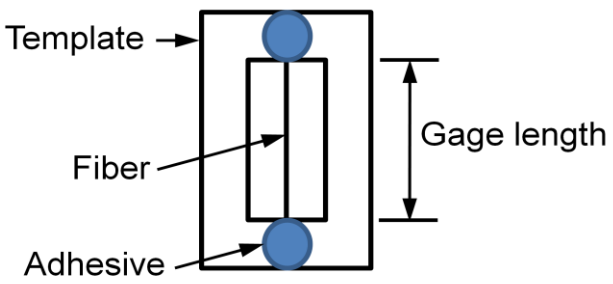

(b) Mechanical grip (grip 2)

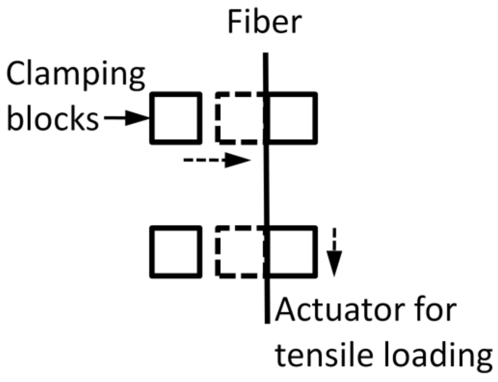

Figure 2. Schematic and closed up of the mechanical grips for quasi-static loading

3.2 High strain rate loading

In order to determine the tensile response of the PPT fiber under high strain rate, a Kolsky bar was used in this study. Owing to the small size of the specimen, the Kolsky bar as proposed by Ming Cheng et al [1]. has a load cell instead of a transmission bar to detect the failure load of a single fiber. As mentioned earlier, this study focuses on developing new fiber gripping device for the high strain rate test using the Kolsky bar. Two gripping methods tested in quasi-static test are introduced in this test. To accommodate the small bar diameter of the Kolsky bar, several modifications were performed, but the fiber gripping mechanism was the same. Detailed information of the Kolksy bar grips will be shown in the presentation.

4. RESULTS AND DISCUSSION

Figure 3 shows the survivability data for 2 mm and 60 mm gage length fibers tested by the two gripping methods. These data are further compared with the expected survivability data predicted by equation 1. The strength data were ordered from strongest to weakest based on its ranking, n, which can be expressed by (n-0.5)/total number of data points. The probability of survival of the PPT fibers was determined by plotting the fiber tensile strengths to each model. The Weibull parameters used in the model are those obtained by Newell and Sagendorf ($\beta1=4.61$, $\gamma1=3.44$, $\beta2=5.23$, $\gamma2=1.59$) [8] since the fibers used in both studies are PPT fibers and the gage lengths are comparable. For the experimental data in this report, the predicted combined probability model (equation 1, red curve) does not agree with any of the data. The reason of this discrepancy between the model and current experimental data is not known. However, differences in sample preparation and/or differences in the testing conditions and/or batch to batch differences between the PPT fibers are being investigated.

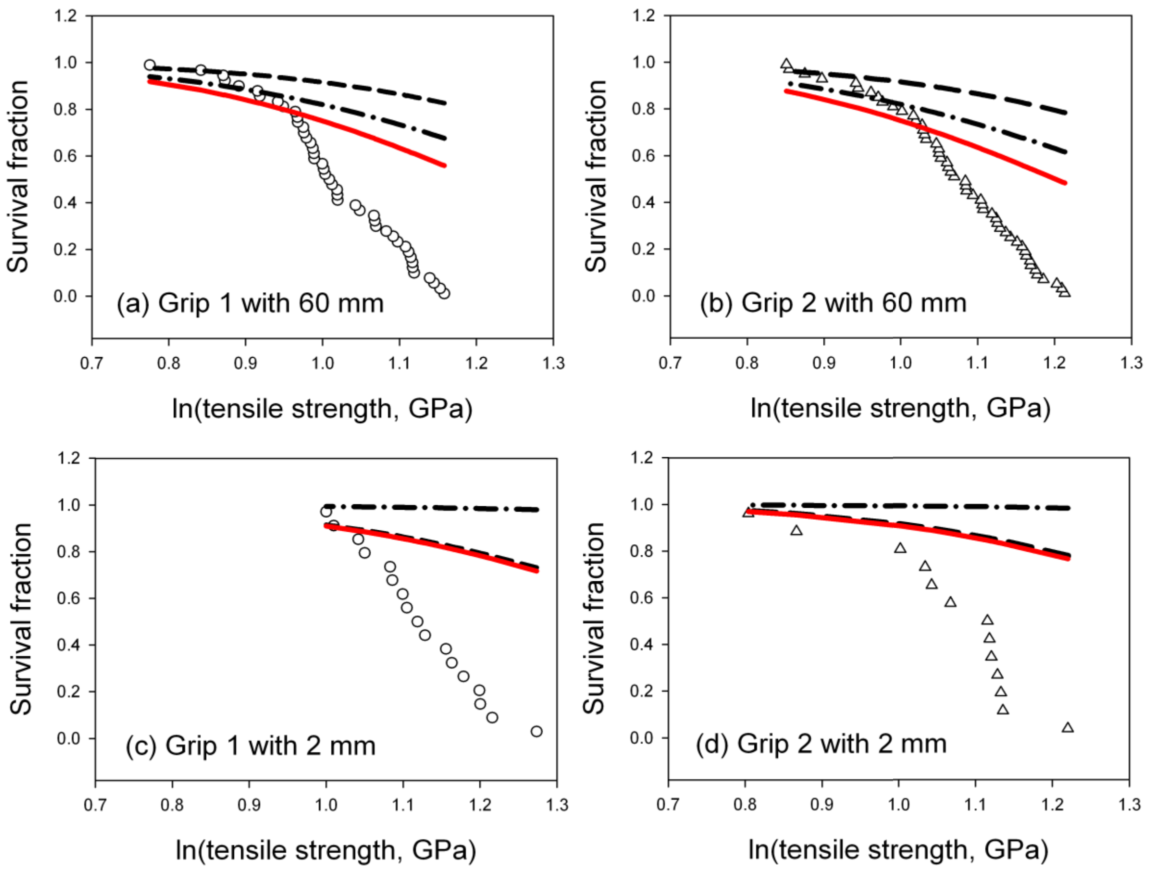

Figure 3. Survival probability plots of the fiber strengths using grip 1 and 2 with 60 mm and 2 mm gage lengths (Strain rate, 0.00056 s^{-1}). Symbols indicate the fiber strength values obtained by each test condition. Solid lines represent the survival probability of the fibers based on the total effect model, and dashed lines (– –) and dashed dot lines (–•–) represent the contribution to the survival probability based on the end effect and flaw effect, respectively.

It is worth noting that the predicted end effect and flaw effect contributions invert as the gage length changes. Although the data generated in this report do not agree, a significant change in the overall failure behavior is observed as the gage length is changed. A more detailed discussion of these results is expected with continued research.

5. CONCLUSIONS

The fiber tensile tests with multiple fiber lengths and gripping methods have been carried out under the quasi-static loading condition to assess the feasibility of gripping for high strain rate tests using the Kolsky bar. Since fiber lengths for the Kolsky bar test that have been reported are only a few millimeters, the influences of the testing conditions (especially fiber gripping) and fiber flaws on the fiber strength of samples with small gage lengths are important in determining true values under high strain loading. Preliminary results show the survival probability of the fibers with the 60 mm gage length is different from the case of fibers that had the 2 mm gage length. These differences are discussed in terms of the influence of the intrinsic fiber flaw and the impact of gripping on the fiber strength that results with changes in the fiber gage length. Additional data measured in various fiber gage lengths will clarify the effects of these two factors (i.e., intrinsic flaw and gripping method).

Reference

[1] Cheng, M., W. N. Chen, T. Weerasooriya, Mechanical properties of Kevlar (R) KM2 single fiber, *Journal of Engineering Materials and Technology-Transactions of the Asme, 127*, 197, **2005**

[2] Lim, J., J. Q. Zheng, K. Masters, W. N. W. Chen, Mechanical behavior of A265 single fibers, *Journal of Materials Science, 45*, 652, **2010**

[3] Whitney, J. M., I. M. Daniel, R. B. Pipes, Experimental Mechanics of Fiber Reinforced Composite Materials, in , The Society for Experimental Stress Analysis (SESA), Brookefield Center, Connecticut **1982**, 151.

[4] Kim, J., W. G. McDonough, W. Blair, G. A. Holmes, The Modified-single fiber test: A methodology for monitoring ballistic performance, *Journal of Applied Polymer Science, 108*, 876, **2008**

[5] Thomason, J. L., G. Kalinka, A Technique for the Measurement of Reinforcement Fibre Tensile Strength at Sub-Millimetre Gauge Lengths, *Compos Part A-Appl S, 32*, 85, **2001**

[6] Phoenix, S. L., R. G. Sexsmith, Clamp Effects in Fiber Testing, *Journal of Composite Materials, 6*, 322-&, **1972**

[7] Stoner, E. G., D. D. Edie, S. D. Durham, An End-Effect Model for the Single-Filament Tensile Test, *Journal of Materials Science, 29*, 6561, **1994**

[8] Newell, J. A., M. T. Sagendorf, Experimental verification of the end-effect Weibull model as a predictor of the tensile strength of Kevlar-29 (poly p-phenyleneterephthalamide) fibres at different gauge lengths, *High Performance Polymers, 11*, 297, **1999**

Proceedings of the SEM Annual Conference
June 7-10, 2010 Indianapolis, Indiana USA
©2010 Society for Experimental Mechanics Inc.

Mechanical Behavior of A265 Single Fibers

Jaeyoung Lim[a], James Q. Zheng[b], Karl Masters[b], and Weinong W Chen[a,*]

[a] Schools of Aeronautics/Astronautics and Materials Engineering, Purdue University, West Lafayette, IN 47907-2045

[b] US Army PM-Soldier Equipment , Haymarket, VA 20169

Abstract

The mechanical behavior of A265 high-performance fibers was experimentally investigated at both low and high strain rates. Axial, transverse, and torsional experiments were performed to measure the five material constants on a single fiber assumed as a linear, transversely isotropic material. A miniature tension kolsky bar was modified to conduct high-rate tension experiments. A pulse shaper technique was adopted to generate a smooth and constant-amplitude incident pulse to produce deformation in the fiber specimen at a nearly constant strain rate. Quasi-static tensile tests performed at five different gage lengths showed the dependence of the tensile strength of this fiber on gage length. The transverse compression results in the large deformation range showed the transverse compressive behavior to be nonlinear and pseudo-elastic. The tensile strength of the fiber increased as the strain rate was increased from 0.001/s to 1500/s. Thus, unlike Kevlar® fibers, the tensile strength of the A265 fiber exhibits both rate and gage length effects.

1. Introduction

High-performance fiber with high strength, light weight and good resistance to high temperatures has been developed for an increased demand in body and vehicle armors. To develop predictive capabilities of impact events involving high-performance fibers, determining single filament properties both at low and high strain rate is critical to understand their performance during impact. High performance fibers are typically very strong under axial tension but much weaker in the transverse directions [1, 2].

There has been some research on the mechanical behavior of high performance fabrics or fiber bundles at high strain rate [3-6]. Shim et al. [4] have observed that Twaron fabrics, similar to the commonly known Kevlar, is

---

[*] Tel.: 765-494-1788; fax: 765-494-0307; E-mail: wchen@purdue.edu

T. Proulx (ed.), *Dynamic Behavior of Materials, Volume 1*, Conference Proceedings of the Society for Experimental Mechanics Series, DOI 10.1007/978-1-4419-8228-5_20, © The Society for Experimental Mechanics, Inc. 2011

highly strain-rate dependent. In their tested results, both the tensile strength and modulus increase with strain rate while the failure strain decrease. The phenomenon was related to the ductile-brittle transition at high strain rate. Recently, Languerand et al. [6] investigated the tensile behavior and failure mechanism of PPTA fiber bundles at high strain rate using a conventional tension kolsky bar and showed the strain rate effects on the elastic modulus in PPTA fiber bundles is insignificant. For a single fiber test at high strain rate, few experimental results are available due to the technical difficulties in tests despite their importance in application to ballistic impact. Cheng et al. [7] observed the loading rate effects on tensile behavior of Kevlar® KM2 single fiber at both quasi-static and high strain rate is insignificant. In addition to longitudinal strength and Young's modulus, there have been many experiments to measure other properties on the transverse compression behavior [8-10] as well as the longitudinal shear behavior [11].

In this study, we examine the mechanical behaviors of a single A265 fiber at both quasi-static and high strain rates. The mechanical constants are determined by adopting three different types of experiments. The strain effects on the longitudinal behavior of A265 fiber are also investigated. A modified kolsky tension bar is used to conduct the dynamic tensile tests at the strain rate of $\dot{\varepsilon} \approx 1000 s^{-1}$, and then the tested results will be compared with the tensile properties at quasi-static by considering the gage length effects.

2. Experimental Procedure and Results

2.1 Materials

The material is a high-performance A265 "Termotex" single fiber, which is a 29.4 tex co-polymer aramid Rusar fiber containing 5-amino-2-(p-amino phenyl)-benzimidazole or related monomers. It has a density of 1,450 kg/m^3. The diameter of each fiber was measured individually using a high-resolution scanning electron microscope (SEM) for accurate stress calculation. The average fiber diameter measured from 15 fibers is 9.28±0.17 μm.

2.2 Axial Tension Experiments

The quasi-static axial tension experiments are performed according to the ASTM standard test method for tensile strength and Young's Modulus of fibers (C1577-03). This standard technique is a mounting method used for very fine specimens. Quasi-static tensile experiments are performed at five gage lengths of 2.5, 5.5, 10, 50 and 100 mm to investigate the gage length effects on the tensile strength. All experiments are performed at the same quasi-static strain rate of 0.001/s. The gage-length effect may provide a measure of the defect distribution along the length of the fiber. A significant defect will limit the tensile strength as measured. The experimentally determined values of the tensile strengths of A256 fibers with different gage lengths are summarized in Table 1. At each gage length, 15 tests are repeated. The results listed in Table 1 are with 95% confidence interval from the results of the 15 repeated experiments.

The experimental results show that the ultimate tensile strength of a single A265 fiber depends on the gage length, as shown in Fig. 1. The tensile strength increases with decreasing gage length. The gage-length effects on the A265 fiber also become insignificant when the gage length is increased beyond 10 mm, which is also shown in Fig. 1. This experimentally measured trend indicates that, for this specific fiber, a strength-limiting defect is very likely to exist in the fiber with a length of at least 10 mm.

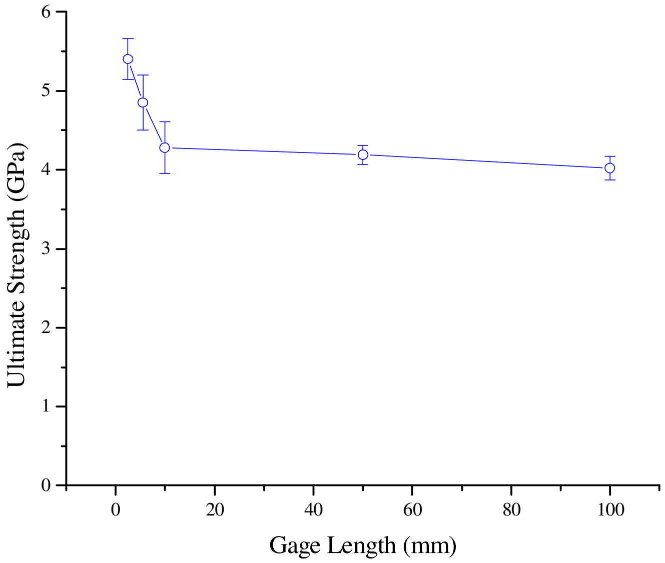

Fig. 1 Variation of the ultimate strength of A256 fibers over the gage length

Table 1 Longitudinal mechanical properties of A265 fiber deforming at quasi-static rates

Gage Length l (mm)	Tenacity (g/denier)	Failure Load (N)	Ultimate Strength (GPa)	Failure Strain (%)	Young's Modulus (GPa)
2.5	42.52	0.36±0.02	5.40±0.26	5.79±0.28	91.39±4.96
5.5	38.19	0.33±0.03	4.85±0.35	3.63±0.28	126.66±5.08
10	33.70	0.29±0.02	4.28±0.33	3.05±0.25	140.51±2.32
50	32.99	0.28±0.01	4.19±0.12	2.77±0.13	151.06±3.98
100	31.65	0.27±0.01	4.02±0.15	2.56±0.15	156.72±3.33

2.3 Transverse Compression Experiments

An experimental setup is modified to investigate the transverse mechanical behavior of a single A265 high-performance fiber. The system includes a piezoelectric translator (Physik Instrument LVPZT, P840.20) traveling up to 30 micrometers, push and supporting rods, and a precision vertical translation stage for the proper positioning and alignment. Transverse compressive loading and displacement are measured directly by a low profile load cell with a capacity of 22.24 N (5 lbf) and a capacitive displacement sensor with sub-nanometer resolution (Physik Instrument D510.100), respectively.

The transverse modulus of a single fiber from the compression experiments can be obtained through an analytical solution with measurements of Poisson's ratios and longitudinal modulus. In this study, the relations between displacement and applied load based on the Hertz and McEwen's solution are introduced. After normalizing the compressive load and the displacement by the diameter of the fiber, the equation is as follows [10]:

$$\overline{U} = \frac{4\overline{\sigma}}{\pi b^2}\left[\left(-\frac{\nu_{12}}{E_1}-\frac{\nu_{31}^2}{E_3}\right)\left(\sqrt{b^2+r^2}-r\right)r+\left(\frac{1}{E_1}-\frac{\nu_{31}^2}{E_3}\right)b^2\ln\frac{\sqrt{b^2+r^2}+r}{b}\right] \tag{1}$$

where b is given by:

$$b=\sqrt{\frac{8\overline{\sigma}r}{\pi}\left(\frac{1}{E_1}-\frac{\nu_{31}^2}{E_3}\right)} \tag{2}$$

where E_1 and E_3 are transverse and longitudinal Young's modulus respectively, which are constant within small deformation. v_{12} and v_{31} are transverse and longitudinal Poisson's ratios, respectively. b is half of the width of the contact zone. r is the radius of the fiber specimen. F stands for the transverse compressive load per unit length along the fiber axial direction, and δ is the transverse displacement. Finally, $\overline{\sigma}$ and $\overline{U}$ are the nominal compressive stress and nominal compressive strain, respectively. The transverse Young's modulus E_1 of A265 single fibers is determined by matching the nominal compressive stress and nominal strain curves obtained from experiments and from analytical modeling with the modulus as parameter. The stress-strain curves of A265 fibers from the transverse compression tests and theoretical solutions derived in Eqs. (1) ~ (2) are compared in Fig. 2. The results show that the transverse Young's modulus is 1.83 GPa from Eqs. (1) and (2). The theoretical predications for the transverse compressive behavior agree well with experimental measurements at small strains of <5%, as shown in Fig. 2.

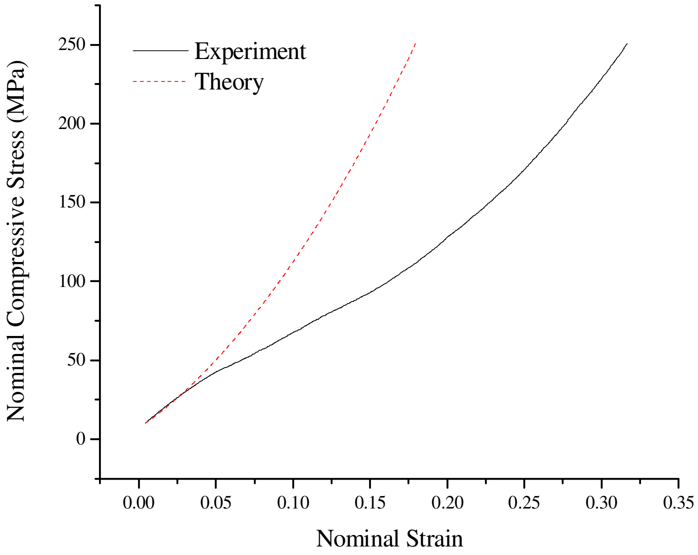

Fig. 2 Comparison between model prediction and experimental data of an A265 single fiber

2.4 Tensile Behavior at High Strain Rates

To determine the tensile response of the fiber at high rates, we modified a Kolsky tensile bar, which is also known as a split Hopkinson tension bar (SHTB), for single-fiber experiments. Due to the small size of the specimen investigated in this study, we used a miniature version of a tension bar, which is shown in Fig. 3. The miniature tension bar consists of an incident bar with a flange, a fiber specimen, and a load cell. For measuring the elastic waves in the incident bar, while eliminating the effect of bending from impact, two high-resistance semiconductor strain gages (KYOWA KSP-2-1K-E4) are mounted in opposite positions of a circumference on the bar. In this system, the transmission bar is replaced by a quartz-piezoelectric load cell (Kistler 9712B5) with a capacity of 22.24 N (5 lbf) since the transmitted force level is very low. The fiber's axial stress is calculated by dividing the measured force by the cross-sectional area of the fiber.

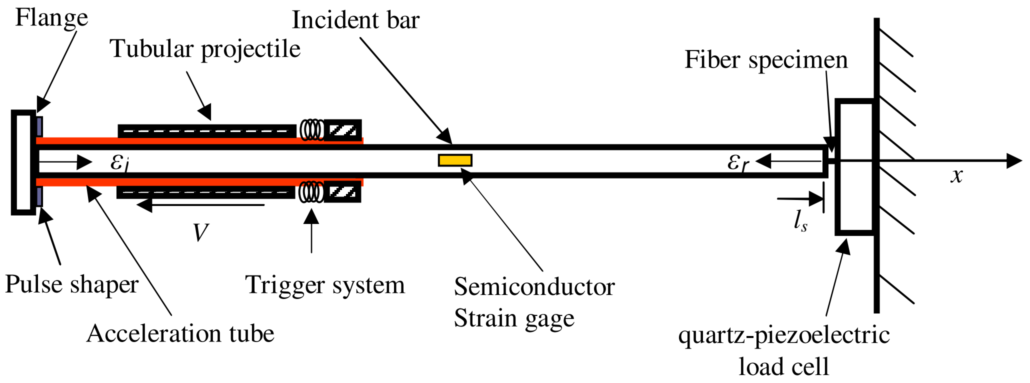
Flange
Tubular projectile
Incident bar
Fiber specimen
ε_i
ε_r
x
V
l_s
Pulse shaper
Trigger system
Semiconductor Strain gage
Acceleration tube
quartz-piezoelectric load cell

Fig. 3 The experimental setup of a miniature tension bar

By introducing the D'Alembert solution, which is the general solution to the one-dimensional wave equation, the strain rate ($\dot{\varepsilon}$) and the strain (ε) of the fiber specimen are calculated using the following equations:

$$\begin{aligned} \dot{\varepsilon} &= -\frac{v}{l_s} = \frac{c_0}{l_s}\left(\varepsilon_i - \varepsilon_r\right) \\ \varepsilon &= \int_0^t \frac{c_0}{l_s}\left(\varepsilon_i - \varepsilon_r\right) d\tau \end{aligned} \qquad (3)$$

where v is the particle velocity at the end of the incident bar, l_s is the length of the specimen, c_0 is the elastic bar wave velocity in the rod, and ε_i and ε_r are incident and reflected strains respectively.

The experimental values of the longitudinal mechanical properties for the A265 fiber at the high strain rate are summarized in Table 2. Graphically, Figs. 4 and 5 show the distribution of tensile strength data of A265 fiber strength at high strain rates around 1,000/s obtained at two gage lengths of 2.5 and 10 mm. As a comparison, the strength data obtained quasi-statically are also displayed. As shown in Figs. 4 and 5, the average tensile strength of the A265 fiber increases by 16.6 % when the strain rate is increased from quasi-static to dynamic. In a range of strains rate around 1,000/s, the failure strength of A265 fibers are 6.41±0.34 GPa and 5.18±0.22 GPa at the gage lengths of 2.5 and 10 mm, respectively, as averaged from 15 experiments at each length. These results clearly show that the tensile strength of the fiber is both rate and gage-length dependent.

Table 2 Longitudinal mechanical properties of A265 fibers at high strain-rate

Gage Length *l* (mm)	Tenacity (g/denier)	Ultimate Strength (GPa)	Young's Modulus (GPa)
2.5	50.47	6.41±0.34	154.09±8.34
10	40.78	5.18±0.22	164.44±11.19

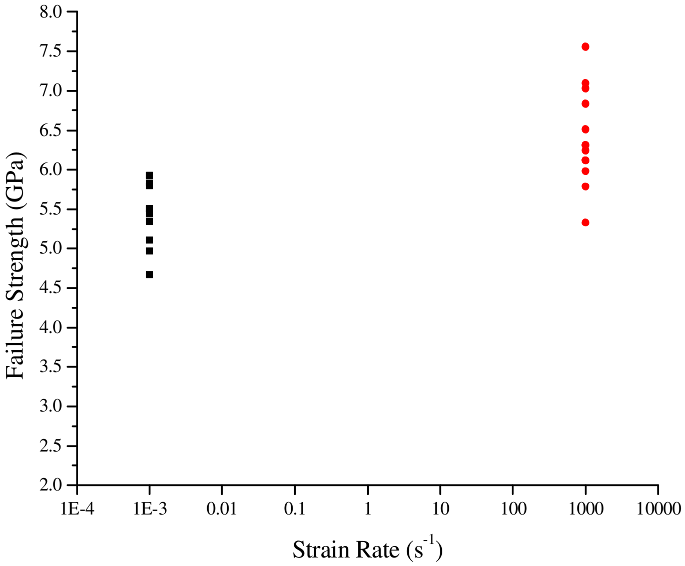

Fig. 4 Strain rate effects of A265 single fibers at the gage length of 2.5 mm

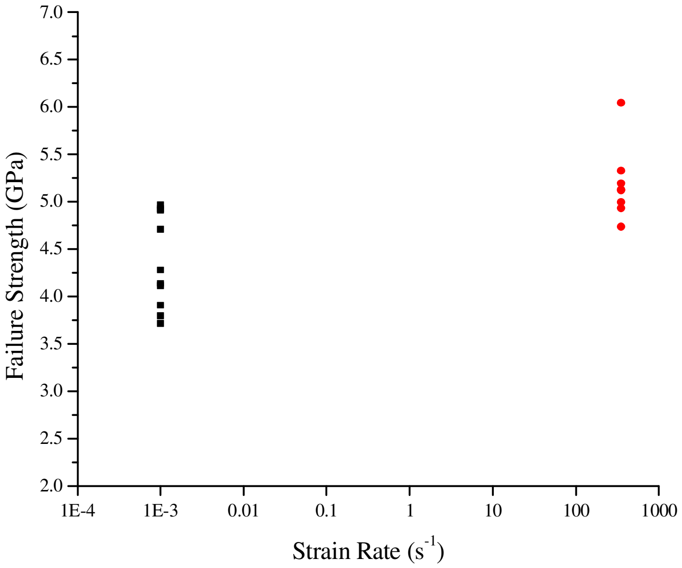

Fig. 5 Strain rate effects of A265 single fibers at the gage length of 10 mm

3. Conclusions

Experiments on single A256 fibers were performed to determine the mechanical properties of this high-performance fiber. Four elastic constants were obtained from longitudinal tensile tests, transverse compression tests, and torsional tests. Transverse Young's modulus (E_1), longitudinal Young's modulus (E_3), longitudinal shear modulus (G_{13}) and longitudinal Poisson's ratios (ν_{31}) obtained are 1.83 GPa, 159.78±3.21 GPa, 12.03±0.78 GPa and 0.402, respectively. A miniature tension bar was used to investigate the strain-rate sensitivity of the fiber in its axial tensile behavior. The experimental results show that the behavior of a single A265 fiber is strain-rate sensitive. As the strain rate increases from $\dot{\varepsilon} = 0.001s^{-1}$ to $\dot{\varepsilon} \approx 1000s^{-1}$, the tensile strength increases by 16.6%. The high-rate experiments also confirm that the gage-length effects also exist in high-rate tensile strength data.

References

1. Yang, H.H., Kevlar Aramid Fiber, John Wiley & Sons, New York, NY, 1992

2. Morton, W.E., and Hearle, J.W.S., Physical Properties of Textile Fibres, Published by the Textile Institute, UK, 1993

3. Wang, Y., and Xia, Y., The effects of strain rate on the mechanical behavior of Kevlar fibre bundles: an experimental and theoretical study, Composites A **29A**, pp. 1411-1415, 1998

4. Shim, V.P.W., Lim, C.T., and Foo, K.J., Dynamic mechanical properties of fabric armor, International Journal of Impact Engineering, **25**, pp.1-15, 2001

5. Creasy, T.S., Modeling Analysis of Tensile Tests of Bundled Filaments with a Bimodal Weibull Survival Function, Journal of Composite Materials, 36, pp. 183-194, 2002

6. Languerand, D.L., Zhang, H., Murthy, N.S., Ramesh, K.T., and Sanoz, F., Inelastic behavior and fracture of high modulus polymeric fiber bundles at high strain rates, Material Science and Engineering **A 500**, pp. 216-224, 2009

7. Cheng, M., and Chen, W., Mechanical Properties of Kevlar® KM2e Fiber, ASME Journal of Engineering Materials and Technology, **127**, pp. 197-203, 2005

8. Kawabata, S., Measurement of the Transverse Mechanical Properties of High performance Fibres, Journal of the Textile Institute, Vol. **81**, pp. 432-447, 1990

9. Singletary, J., Davis, H., Ramasubramanian, M.K., Knoff, W., and Toney, M., The Transverse Compression of PPTA fibers, Journal of Materials Science, **35**, pp. 573-581, 2000

10. Cheng, M., Chen, W., and Weerasooriya, T., Experimental Investigation of the Transverse Mechanical Properties of a Single Kevlar® KM2e Fiber, International Journal of Solids and Structures, **42**, pp. 6215-6232, 2004

11. Tsai, C.-L., and Daniel, I.M., Determination of Shear Modulus of Single Fibers, Experimental Mechanics, **39**(4), pp. 284-286, 1999

Proceedings of the SEM Annual Conference
June 7-10, 2010 Indianapolis, Indiana USA
©2010 Society for Experimental Mechanics Inc.

Experimental Study of Dynamic Behavior of Kevlar 49 Single Yarn

Deju Zhu (1), Barzin Mobasher*(2), S.D. Rajan(3)

[1] Graduate Research Associate, Department of Civil and Environmental Engineering, Arizona State University, Tempe, AZ, 85287, E-mail: Deju.Zhu@asu.edu
[2] Professor, Ph.D., P.E., Department of Civil and Environmental Engineering, Arizona State University, Tempe, AZ, 85287, corresponding author, E-mail: Barzin@asu.edu
[3] Professor, Ph.D., Department of Civil and Environmental Engineering, Arizona State University, Tempe, AZ, 85287, E-mail: S.Rajan@asu.edu

ABSTRACT

Aramid and other high strength fibers and fabrics have been studied extensively due to their application in a wide range of products such as bullet-proof vests, confinement chambers for jet engines, cut-resistant gloves et al. These applications have created a demand for numerical modeling of the fabrics and more in depth information about the behavior of fibrous materials and yarns. Manufacturers of yams usually provide quasi-static tensile strength for the single fiber form of the material. However, this information cannot be scaled up directly for a yarn consisting of many fibers. Also, the strain rate at which this information is obtained is not in the same order of magnitude as the strain rates observed in ballistic applications. In this study, Kevlar 49® single yarn was tested in tension within a strain rate range of 20 to 100 s^{-1} using a high speed servo-hydraulic testing system. The failure behavior of test specimen was recorded by a high speed digital camera. Results were used to investigate the strain rate effect on the dynamic material properties in terms of Young's modulus, tensile strength, maximum strain and toughness. The dependence of dynamic material properties on the strain rate was discussed.

Keywords: Kevlar 49, Single yarn, Strain rate, Dynamic material properties

1. Introduction

Aramid and other high strength fibers and fabrics have been studied extensively due to their application in a wide range of products such as bullet-proof vests, confinement chambers for jet engines, cut-resistant gloves et al. These applications have created a demand for numerical modeling of the fabrics and more in depth information about the behavior of fibrous materials and yarns. Manufacturers of yams usually provide quasi-static tensile strength for the single fibre form of the material. However, this information cannot be scaled up directly for a yarn consisting of many fibers. Also, the strain rate at which this information is obtained is not in the same order of magnitude as the strain rates observed in ballistic applications. Different types of testing techniques have been used to generate data under dynamic conditions. Each serves for a specific range of strain rates and provides a specific type of information. There is a lack of general agreement about the standards and methodology used to conduct dynamic tensile tests [1]. A number of experimental techniques exist to investigate high strain rate material properties including: split Hopkinson pressure bar (SHPB), falling weight devices, flywheel facilities, hydraulic machine, etc. [2, 3, 4, 5]. The use of servo-hydraulic machines in intermediate strain rate tensile testing was reported for steels [6, 7], plastics [1, 8], woven fabrics [9, 10] and composite materials [11, 12, 13].

Kevlar® 49 is a registered trademark of E.I. du Pont de Nemours & Co., has been used in many engineering applications due to its high strength, modulus, and strength-to-weight ratio. Research on quasi-static strength of yarns along with studies of dynamic strength has been reported by several authors. Farsi Dooraki et al. [14] studied the parameters that affect the quasi-static and dynamic strength of five different yarns (Kevlar® 129, Kevlar® KM2, Kevlar® LT, Twaron and Zylon) using hydraulic and Hopkinson bar testing methods. The failure strengths of Kevlar products showed limited dependence on strain rate, while Twaron and Zylon showed a more significant strain rate dependency. Wagner et al. [15] reported that Kevlar® 29, Kevlar® 49, and Kevlar® 149 fibers

T. Proulx (ed.), *Dynamic Behavior of Materials, Volume 1*, Conference Proceedings of the Society for Experimental Mechanics Series, DOI 10.1007/978-1-4419-8228-5_21, © The Society for Experimental Mechanics, Inc. 2011

were insensitive to the strain rate in the range of $3\text{x}10^{-4}$ to 0.024 s^{-1}. Amaniampong and Burgoyne [16] studied the effect of gage length and strain rate from $3\text{x}10^{-4}$ to 0.003 s^{-1} on the failure stress and failure strain of Kevlar® 49 yarns. Yarn strength decreases slightly as the gage length increases; whereas the failure strain of the Kevlar® 49 yarns was independent of the gage length, however decreased slightly as the strain rate increased. Sharda et al. [17] and Rajan et al. [18] studied the quasi-static properties of Kevlar® 49 (17x17) and Zylon AS (35x35) fabric in tension at a strain rate of $1.4\text{x}10^{-4}$ s^{-1} and the load-deflection response of single layer and multiple layers in static penetration test. The material behavior obtained from the experimental study was then used as the constitutive model in a finite element simulation of the static test. Xia and Wang [19] studied the strain rate dependence of the Young's modulus, the failure stress, and the failure strain of Kevlar® 49 fiber bundle over a strain rate range of 10^{-4} to 1350 s^{-1}. It was observed that failure stress, failure strain, and Young's modulus were directly proportional with the strain rate.

The purpose of this paper is to study the effects of strain rate on the tensile mechanical properties of Kevlar 49 single yarn by using a dynamic tensile testing method, and to evaluate the Weibull statistical distribution parameters.

2. Methodology

2.1 Specimen Preparation

Kevlar® 49 fabric is manufactured using a plain weave of 6.7×6.7 yarns/cm (17×17 yarns/inch). The yarns in the woven structure consist of hundreds of filaments. The modulus of elasticity of Kevlar® 49 is 110 GPa, the bulk density and linear density are 1.44 g/cm^3, 1.656(10^{-3}) g/cm, respectively [20]. The cross-sectional area of single yarn which is 0.115 mm^2 is calculated by taking into account the linear density of the material and dividing it by its bulk density. The single yarn specimens with gage lengths of 25 mm and 50 mm were constructed as shown in Figure 1(a) & (b). The fabric was cut to the width using an electric scissor allowing eight yarns in the section of gage length. Thin aluminum sheets were glued on specimen ends using epoxy to reduce the stress concentration and improve load transfer in grips. When the epoxy was cured, one yarn in the central position was remained in the section of gage length by removing the rest. The 25 mm specimens were tested at three strain rates, i.e. 30, 50, and 100 s^{-1}, and the 50 mm specimens were tested at strain rates of 20 and 60 s^{-1}. Six replicates were tested for each specimen size at each strain rate.

Figure 1- Constructed test specimens: (a) 50 mm and (b) 25 mm gauge Length

2.2 Test Setup

The dynamic tensile tests were conducted using an MTS high speed servo-hydraulic testing machine. The speed of the actuator is controlled by the opening and closing of the servo-valve of hydraulic supply. By manually turning the servo-valve, the rate of flow of hydraulic fluid can be controlled, resulting in different actuator speeds. According to the calibration records, the actuator can reach a maximum speed of 14 m/s with a load capacity of 25 kN. The high strain rate testing system includes the loading frame, MTS Flex SE control panels, and a high speed data acquisition card, a Phantom v.7 high speed digital camera.

Figure 2(a) presents the schematic diagram of test setup. The load train consists of a piezoelectric load washer, upper and lower grips, test specimen, a slack adaptor. The specimen is mounted between the upper and lower grips. As the test is initiated, the actuator accelerates until it reaches a constant pre-determined velocity. The constant velocity is transferred to the specimen using a slack adaptor which consists of a sliding bar with a conical tip moving inside a hollow tube. As the actuator accelerates downwards, the hollow tube travels freely over a distance to reach a specified velocity before making contact with the cone-shaped surface of the sliding bar. The slack adaptor eliminates the inertia effect of the lower grip and actuator in its acceleration stage.

Using the Phantom high speed digital camera with a 2 GB onboard memory, tests were recorded at sample rates of 10,000 fps (time interval, 100μs) with exposure time of 95 μs and resolution of 256×512 pixels. Two high intensity lamps were used for illumination to capture high quality images. Figure 2(b) shows the images of 25 mm gage length single yarn specimen captured by the high speed camera during a test at a strain rate of 50 s^{-1}. The load was measured by a Kistler 9041A piezoelectric load washer with a capacity of 90 kN and rigidity of 7.5 kN/μm. The response frequency of the load washer is 33 kHz. The load signal was amplified through a Kistler 5010B dual mode charge amplifier. A high speed digitizer was used to collect the signal from actuator to measure the deformation of test specimen and the force signal from the piezoelectric load washer at a sampling rate of 250 kHz.

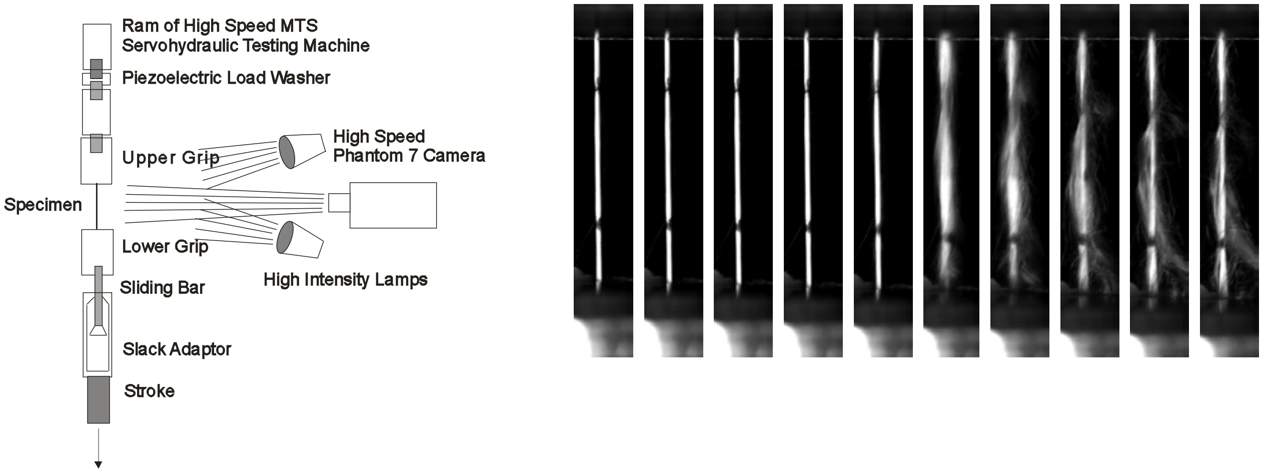
Ram of High Speed MTS Servohydraulic Testing Machine
Piezoelectric Load Washer
High Speed Phantom 7 Camera
Upper Grip
Specimen
Lower Grip
Sliding Bar
High Intensity Lamps
Slack Adaptor
Stroke

(a)

(b)

Figure 2- Test setup: (a) schematic, (b) yarn images at a strain rate of 45 s^{-1} with time interval of 100 μs

2.3 Data Processing

It's quite cumbersome to process the data in dynamic testing as the data is not as clean as static test. In this work, the signals from load washer, LVDT of actuator were recorded at sampling rate of 250 kHz. The signals contain high frequency noises which require taking certain measures to clean up the signals in order to obtain the response of the test specimen. During the data processing, a low-pass filter with a cut-off frequency of 3 kHz was used to eliminate high frequency noise.

Figure 3 shows the stress-strain relation of a test specimen obtained by the data processing procedure which was discussed in previous work [9]. The behavior of the single yarn has four distinct regions during loading: (I) crimp region, (II) elastic region, (III) non-linear failure region, and (IV) post-peak region. In the crimp region, the stress-strain graph shows a relative large increase in strain for a very small increase in load. Single yarn inherently has crimp defined as the initial curvature of the weaving pattern in fabric, and in this portion, the load essentially straightens the yarns by removing the crimp. As the load increases, the elastic region is approached - the straightened yarns start to take more loads, and the stress-strain graph exhibits an increased slope. Young's modulus of the fabric is defined as the slope of the curve in elastic region. Prior to reaching the tensile strength, the stress-strain response exhibits nonlinearity (nonlinear failure region). This is possibly due to random failure of the individual filaments within the yarn. The final stage (IV) is due to a rapid decrease in the stress beyond the tensile strength that is characteristic of progressive yarn failure (post-peak region). The stress-strain curves were analyzed to measure the Young's modulus, tensile strength, ultimate strain (strain at failure stress), maximum strain and toughness for all the specimens. The toughness is evaluated using the area under the stress-strain curve.

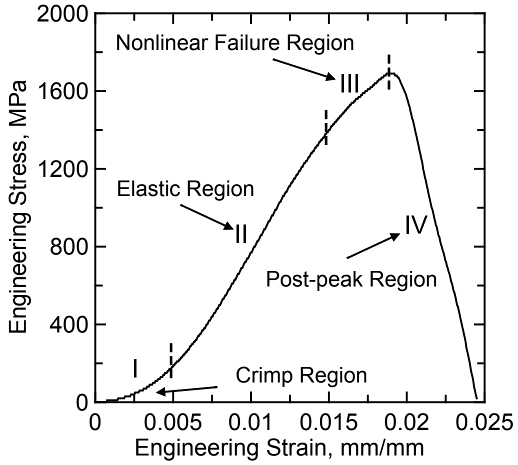

Figure 3- Four regions of the stress-strain curve obtained from a typical test

3. Results and Discussion

3.1 Strain rate effect on dynamic material properties

Figure 4(a)-(d) shows the dependence of the dynamic material properties of Kevlar 49 single yarn, defined in terms of Young's modulus, tensile strength, maximum strain, and toughness on strain rates, respectively. There is an apparent dependence of the dynamic material properties on the strain rates discussed as follows: For 25 mm gage length specimen, the Young's modulus increases from 109±11 GPa at strain rate of 30 s^{-1} to 111±10 and 128±11 GPa at strain rates of 50 and 100 s^{-1} respectively. The tensile strength increases from 1622±104 MPa at strain rates of 30 s^{-1} to 1675±51 and 1707±82 MPa at strain rates of 50 and 100 s^{-1} respectively. Maximum strain increases from 2.45±0.30% to 2.53±0.17% and then to 2.82±0.22%, and toughness increases from 20.1±2.6 to 20.5±1.4 and to 26.0±4.3 MPa when the strain rates increases from 30 to 50 and then to 100 s^{-1}. For 50 mm gage length specimen, the Young's modulus increases from 118 ±28 to 121 ±22 GPa, the tensile strength increases from 1579±100 to 1874±110 MPa, the maximum strain increases from 2.17±0.30% to 2.50±0.26%, and toughness increases from 18.8±2.5 to 24.3±4.0 MPa when the strain rate increases from 20 to 60s^{-1}.

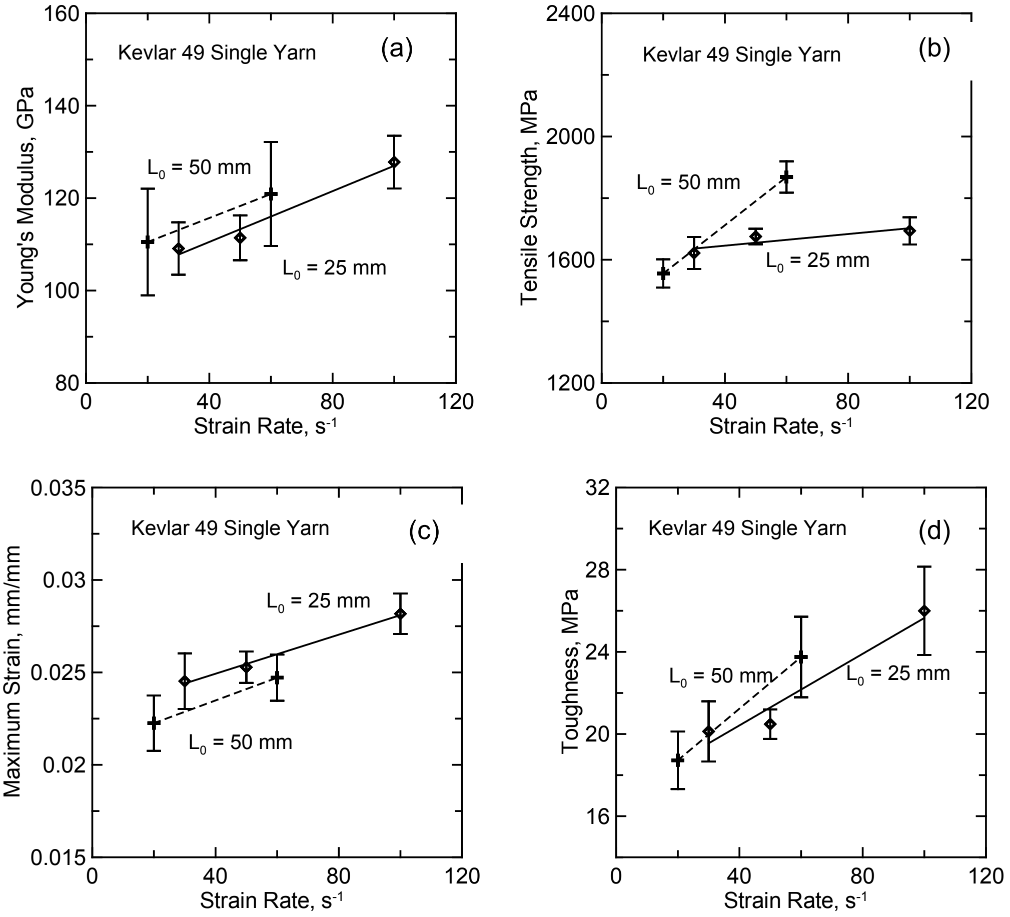

Figure 4- Strain rate effect on (a) Young's modulus, (b) tensile strength, (c) maximum strain, and (e) toughness

3.2 Weibull analysis

Kevlar 49 single yarn exhibited variability in tensile strength. The variability can be explained by the distribution of defects within the fibers. The strength data presented in terms of Weibull cumulative probability of failure of a yarn of length *L* at stress σ is given by:

$$P_f(\sigma,L)=1-\exp\left[-\frac{L}{L_0}\left(\frac{\sigma}{\sigma_0}\right)^m\right] \tag{1}$$

where σ_0 is the characteristic yarn strength at gage length L_0 and m is the Weibull modulus or shape parameter, characterizing the spread in the distribution of strengths at any gage length.

Weibull parameters are obtained for the characteristic length ($L=L_0$) using a two-parameter Weibull equation:

$$P_f(\sigma) = 1 - \exp\left[-\left(\frac{\sigma}{\sigma_0}\right)^m\right] \tag{2}$$

where the cumulative probability density, P_f is estimated using the following equation:

$$P_f = \frac{i}{N+1} \tag{3}$$

where N is the total number of tests and i is the current test number.

Weibull parameters were computed by fitting cumulative probability distribution of the test data in least square sense. Figure 5 represents the Weibull curve fitting to the experimental data using a least-square method. The Weibull parameters thus obtained are listed in Table 1. For all the specimens with same gage length, the σ_0 increases with increasing strain rate. This is due to strain rate effect on the tensile strength of Kevlar 49 single yarn.

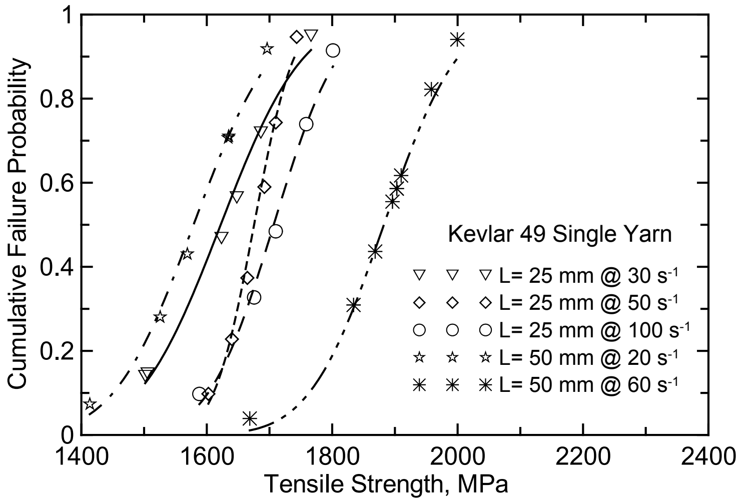

Figure 5-Comparison of cumulative failure probability versus tensile strength for different strain rates and gage lengths

Table 1 Weibull parameters obtained from experimental data

Gage Length, mm	25			50	
Strain Rate, s^{-1}	30	50	100	20	60
σ_0, MPa	1642.2	1680.4	1710.5	1599.3	1907.6
m	13.83	32.47	26.10	19.66	34.12

4. Conclusions

A high strain rate testing system built on a high speed servo-hydraulic machine, the corresponding test procedure and data processing method were presented in this study. Kevlar 49 single yarn specimens of two gage lengths (25 mm and 50 mm) was tested at strain rates ranging from 20 to 100 s^{-1}. The failure behavior of single yarn specimens was recorded by a high speed digital camera. The dynamic material properties - i.e. Young's modulus, tensile strength, maximum strain, and toughness – were investigated within the range of strain rates. For both of the specimen sizes, these dynamic material properties increased with increasing strain rate. The Weibull parameters were identified by least-square fitting. In the future research, these results will be used to verify a new constitutive model of single yarn implemented in finite element software and an analytical model based on the Weibull strength failure distribution.

Acknowledgements

The authors wish to thank William Emmerling, Donald Altobelli and Chip Queitzsch of the Federal Aviation Administration's Aircraft Catastrophic Failure Prevention Research Program for their support and guidance. Funding for this effort was provided by the FAA.

Reference

[1] Xiao, X.R. Dynamic Tensile Testing of Plastic Materials. *Polymer Testing*, 27, 164-178, 2008.

[2] Meyers, M.A. *Dynamic Behavior of Materials*, John Wiley & Sons, New York, 1994.

[3] Nicholas, T. Tensile Testing of Material at High Rates of Strain. *Experimental Mechanics*, 21, 177-185, 1981.

[4] Kenneth, G. H. Influence of Strain Rate on Mechanical Properties of 6061.T6 Aluminum under Uniaxial and Biaxial States of Stress. *Experimental Mechanics*, 6(4), 204-211, 1966.

[5] Zabotkin, K., O'Toole, B. and Trabia, M. Identification of the Dynamic Properties of Materials under Moderate Strain Rates. *16th ASCE Engineering Mechanics Conference.* Seattle, WA, 2003.

[6] Bastias, P.C., Kulkarni, S.M., Kim, K.Y. and Gargas, J. Noncontacting Strain Measurements during Tensile Tests. *Experimental Mechanics,* 78, 78–83, 1996.

[7] Bruce, D.M., Matlock, D.K., Speer, J.G. and De, A.K. Assessment of the Strain-Rate Dependent Tensile Properties of Automotive Sheet Steels. *SAE*, 0507, 2004.

[8] Hill, S. and Sjöblom, P. Practical Considerations in Determining High Strain Rate Matererial Properties, *SAE*, 981136, 1998.

[9] Zhu, D., Mobasher, B., Rajan, S.D. High strain rate testing of Kevlar 49 fabric. In: Society for Experimental Mechanics, 11th International Congress and Exhibition on Experimental and Applied Mechanics, v1, p. 34-35, 2008.

[10] Zhu, D., Mobasher, B., Rajan, S.D. Image Analysis of Kevlar 49 Fabric at High Strain Rate. In: Society for Experimental Mechanics, 11th International Congress and Exhibition on Experimental and Applied Mechanics, v2, p. 986-991, 2008.

[11] Silva, F., Zhu, D., Soranakom, C., Mobasher, B., Toledo Filho, R. High Speed Tensile Behavior of Sisal Fiber Cement Composites. *Materials Science and Engineering: A*, 527(3), 544-552, 2010.

[12] Zhu, D., Peled, A., Mobasher, B. Dynamic Tensile Testing of Fabric-Cement Composites. Construction & Building Materials, (in revision), 2009.

[13] Fitoussi, J., Meraghni, F., Jendli, Z., Hug, G., and Baptiste, D. Experimental Methodology for High Strain Rates Tensile Behavior Analysis of Polymer Matrix Composites. *Composite Science Technology*, 65, 2174–2188, 2005.

[14] Farsi, D. B., Nemes, J. A. and Bolduc, M. Study of Parameters Affecting the Strength of Yarns. *Journal of Physics IV*, 134, 1183-1188, 2006.

[15] Wagner, H.D., Aronhime, J. and Marom, G. Dependence of Tensile Strength of Pitch-based Carbon and Para-aramid Fibres on the Rate of Strain. *Proc.the Royal Society of London*, A428, 493-510, 1990.

[16] Amaniampong, G. and Burgoyne, C. J. Statistical Variability in the Strength and Failure Strain of Aramid and Polyester Yarns. *Journal of Material Science*, 29, 5141-5152, 1994.

[17] Sharda, J., Deenadayalu, C., Mobasher, B. and Rajan S. D. Modeling of Multi-Layer Composite Fabrics for Gas Turbine Engine Containment Systems. *Journal of Aerospace Engineering*, 19(1), 38-45, 2006.

[18] Rajan, S. D., Mobasher, B., Sharda, J., and Deenadayalu, C. Explicit Finite Element Analysis Modeling of Multilayer Composite Fabric for Gas Turbine Engines Containment Systems. Part 1: Static Tests and Modeling. Final Report: DOT/FAA/AR-04/40, P1 Office of Aviation Research, Washington, D.C., 2004.

[19] Xia, Y., and Wang, Y. The Effects of Strain Rate on the Mechanical Behavior of Kevlar Fibre Bundles: An experimental and Theoretical Study. *Composites Part A*, 29A, 1411-1415, 1999.

[20] Simons, J., Erlich, D., and Shockey, D. Explicit Finite Element Modeling of Multi-layer Composite Fabric for Gas Turbine Engine Containment Systems. Part 3: Model Development and Simulation of Experiments. Final Rep. No. DOT/FAA/AR-04/40/P3, Washington, D.C., 2004.

Proceedings of the SEM Annual Conference
June 7-10, 2010 Indianapolis, Indiana USA
©2010 Society for Experimental Mechanics Inc.

Dynamic Response of Fiber Bundle under Transverse Impact

Bo Song, Wei-Yang Lu

Sandia National Laboratories, Livermore, CA 94551-0969, USA

Research and development of soft body armor have been extremely critical to efficiently protect the soldiers and law enforcement personnel from ballistic injury. High strength ballistic fabrics have been developed and utilized in soft body armors. Improvement of the fabrics performance against ballistic impact is still ongoing. It is desirable to understand the dynamic response of the fabrics under high-speed transverse impact. Technically it is a good start to investigate the transverse impact response of the fiber bundles that are primary components in fabrics.

When a fiber bundle is subjected to transverse impact, both longitudinal and transverse stress waves are generated and then propagate in the fiber bundle. The longitudinal wave stretches the fiber bundle, which produces stress and strain in the fiber bundle. The transverse wave changes the shape of the fiber bundle [1]. The longitudinal stress wave is a characteristic parameter, which is usually a constant for a certain material regardless of loading condition. However, the transverse stress wave is dependent on the loading condition. For example, the transverse wave speed may depend on the external transverse impact speed. A higher transverse wave speed is favorable to transmit the external impact energy outwards so that the strain localization at the impact contact can be avoided [1, 2]. This consequently improves the ballistic performance of the fiber bundle. Unlike longitudinal wave speed, the transverse wave speed is dominated by many material parameters as well as loading conditions. Models are possibly used to correlate the transverse wave speed with the material constants and loading conditions. However, precise models rely on valid experimental data and in-depth understanding of the mechanism of dynamic response of the fiber bundle under transverse impact. In this study, we used a Kolsky bar as the loading device and high-speed photography to investigate the dynamic transverse response of fiber bundle.

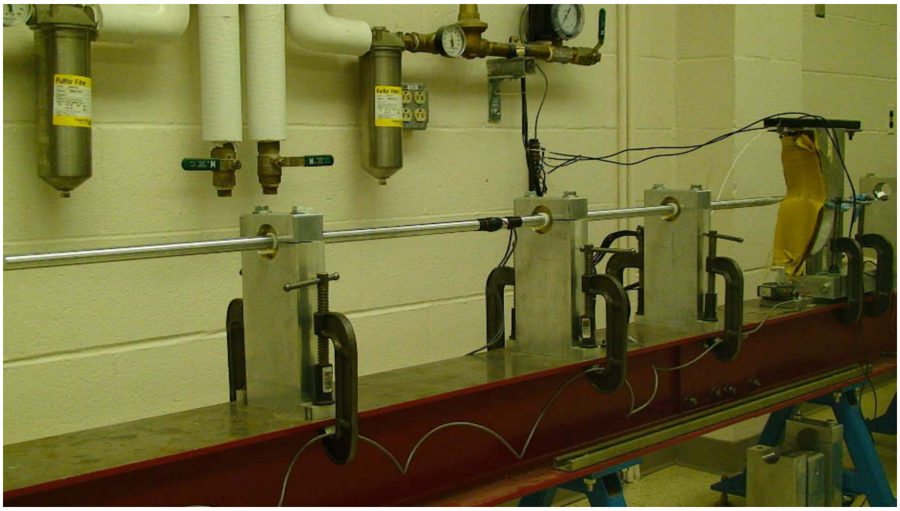

Fig. 1. A schematic of the Kolsky-bar apparatus

T. Proulx (ed.), *Dynamic Behavior of Materials, Volume 1*, Conference Proceedings of the Society for Experimental Mechanics Series, DOI 10.1007/978-1-4419-8228-5_22, © The Society for Experimental Mechanics, Inc. 2011

The Kolsky bar setup we used in this study is shown in Fig. 1. In comparison of conventional Kolsky bar, the transmission bar was removed. The specimen end of the incident bar was tapered to a wedge, as shown in Fig. 2. As an alternative method, a separate wedge was also glued on the flat surface of the incident bar. The bar is 19.05 mm in diameter, which is made of 7075-T651 aluminum. Two different strikers, which are 610- and 305-mm long, respectively, were used to impact on the incident bar with velocities varying from 8 to 53 m/s. Two high speed cameras were employed to photograph the high-speed deformation of the fiber bundle under transverse impact, which are set in different scales in both time and zooming. A Phantom v12.1 digital camera takes the images of overall deformation of the fiber bundle with a large time scale (a few milliseconds) while a Cordin 550 high speed digital camera zooms in the impact portion of the fiber bundle over the first loading duration (a few microseconds) only. The fiber bundle we studied is Kevlar® KM2 bundle removed from a commercial woven fabric.

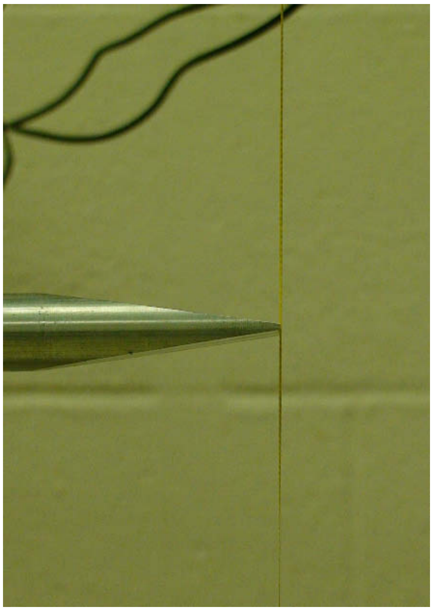

Fig. 2. An image of testing section

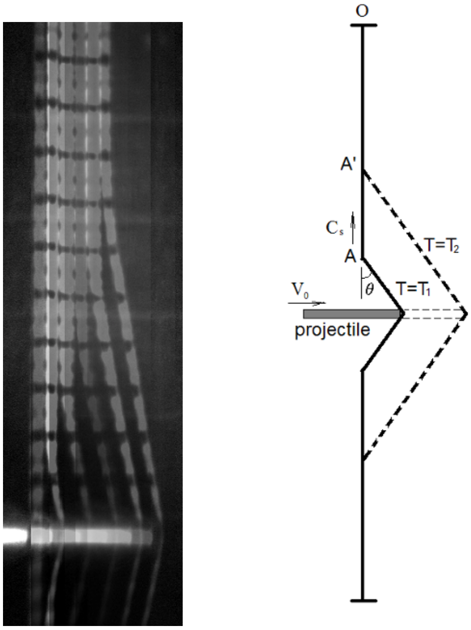

(a) (b)

Fig. 3. High speed deformation of fiber bundle

Figure 3(a) shows the high-speed deformation of the fiber bundle. This image consists of several sequent individual images taken by the Cordin 550 camera to show the propagation of transverse wave. The transverse wave here represents the change in shape of the fiber bundle. After the transverse wave passes, the fiber bundles changes to a cone shape, producing an angle (θ in Fig. 3(b)) with the original vertical straight line. It is clearly seen that the transverse wave propagates outwards from the impact contact. The angle, θ, did not significantly change during transverse impact at a constant speed, which is illustrated in Fig. 3(b). Experiments for different impact speeds were performed and the results show that both the transverse wave speed and the angle significantly depend on the transverse impact speed, but nonlinearly.

ACKNOWLEDGEMENTS

Sandia is a multiprogram laboratory operated by Sandia Corporation, a Lockheed Martin Company, for the United States Department of Energy under Contract DE-ACO4-94AL85000.

REFERENCES

1. Field, J. E., and Sun, Q., 1990, “A high speed photographic study of impact on fibres and woven fabrics,” SPIE Vol. 1358, pp703-712.
2. Wang, L.-L., Foundations of stress waves, Elsevier, 2007.

Proceedings of the SEM Annual Conference
June 7-10, 2010 Indianapolis, Indiana USA
©2010 Society for Experimental Mechanics Inc.

Impact Experiments to Validate Material Models for Kevlar KM2 Composite Laminates

Tusit Weerasooriya
tusitw@arl.army.mil

C. Allan Gunnarsson
allan.gunnarsson@arl.army.mil

Paul Moy
pmoy@arl.army.mil

Army Research Laboratory
Weapons and Materials Research Directorate
Aberdeen Proving Ground, MD 21005-5069

ABSTRACT

Blunt impact experiments were conducted on single and multi-layered Kevlar KM2 (Style 706) fabric at various velocities. To complement previous experiments with multi-ply fabric layers without resins, multi-ply laminates were fabricated from single or multiple plies of Kevlar fabric hot-pressed with a blended polyolefin (PO) resin consisting primarily of low molecular weight polyethylene to form a relatively rigid panel while maintaining a high fiber volume. During impact, full-field, back surface displacements were obtained using digital image correlation (DIC) technique using a pair of high-speed digital cameras configured stereoscopically. This allowed the full-field measurement of the fabric panel in three dimensions. These experimental results are to be used to evaluate different types of fabric and composite laminate models and simulation methodologies that are in literature. In this paper, experimental measurements are presented.

INTRODUCTION

KM2 yarn is one of the variations of DuPont's line of Kevlar fiber products. When the yarns are formed into a woven fabric, due to its effective resistance to high velocity fragments, it is widely used in body armor. Although this material is used for protection in impact scenarios, the dynamic behavior of these fabrics is not completely understood. Because of the lack of dynamic properties of fabrics including the dynamic deformation and failure mechanisms, there are no comprehensive computer simulations of impact on fabrics in literature.

There is past research focused on investigation of the dynamic behavior of a single fiber. Cheng et al [1 - 3] investigated the longitudinal and transverse properties of a single Kevlar KM2 fiber. Their results show that the Kevlar behaves nonlinearly and has a pseudo-elastic transverse property. In addition, the loading rates on the single KM2 fiber did not have any significant effect on the fibers in the transverse direction. Also, Raftenberg et al [4, 5] conducted quasi-static tensile experiments of the woven Kevlar KM2 fabric and reported the failure conditions based on the warp and weft direction of the yarns. Both of these efforts also provided some degree of modeling of the material response of Kevlar for those cases studied.

More sophisticated fabric models are also proposed by other researchers. One such approach is by King et al [6]. Here, the fabric is modeled as a continuum, but details of the model are based on micro-mechanics at the yarn level. The unit cell of fabric configuration is represented by pin-joined beam elements. A similar continuum level approach is also followed by Yen et al [7]. In their case, the unit cell of fiber bundle is represented as a shell element. Zhou et al [8] have proposed a micro level model to represent fabric deformation behavior. In their approach, yarn or sub-yarns are represented by digital-chains of rod-elements.

T. Proulx (ed.), *Dynamic Behavior of Materials, Volume 1*, Conference Proceedings of the Society for Experimental Mechanics Series,
DOI 10.1007/978-1-4419-8228-5_23, © The Society for Experimental Mechanics, Inc. 2011

Whether it is a single fiber or a fabric, the material model development will actually depend on the assumptions and the approach being used [9]. Therefore, to validate different modeling efforts related to impact on fabrics, the authors developed an experimental technique to obtain the quantitative impact behavior data for a single ply of woven Kevlar KM2 fabric [10] and for multi-ply woven Kevlar KM2 fabric [11]. This type of data is essential for validation or refinement of the deformation and failure models for fabrics. Single-ply data obtained was used to validate different fabric models and simulation methodologies [12-13].

For some impact experiments, the deformation of the back surface of a target is determined from a witness plate placed behind the target [14]. The measurements of the displacement from the witness plate are conducted after the impact. Most witness plates are simply thin sheets of aluminum or in some cases a block of ballistic clay placed at the back of the target [15]. These methods provide only the final maximum displacements of the target. In addition, these witness plates may affect the response of the target. Other researchers, who provided quantitative back surface displacement data for model validation, used high-speed cameras to visually capture the event during the target deflection. Though this method provided low-resolution quantitative transient data of the back surface, it was restricted to the displacements at the impact point. The ability to acquire higher resolution full-field transient measurements at the surrounding area of the impact zone provides more detailed data to compare with corresponding results from computer simulations of impact on fabrics. This allows the researchers to validate proposed material models and computational methodologies for fabrics in greater detail.

With the same objective, similar work was conducted by Weerasooriya [16] using a Shadow-Moiré method on different composite materials. In contrast to acquiring deformation through tracking changing line patterns in Shadow-Moiré method, in this study, the transient deformation is monitored using digital image correlation (DIC), where movement of speckles are tracked. Similar to Shadow-Moiré method, DIC is a non-contact optical technique, capable of measuring full-field, out-of-plane displacement. However, the experimental techniques for the two methods are quite different.

For DIC, a speckle pattern is directly applied to the surface of the sample. The pattern is typically produced by using consumer spray paints of black and white, which offers the high contrast for the monochromatic cameras that were used for the impact experiments. The deformation of the speckled surface is captured by two high-speed digital cameras configured stereoscopically. Thus, the dual camera setup provides images for out-of-plane (z-direction) measurements. This DIC method allows the authors to obtain deformation data at a much higher resolution than the Shadow-Moiré method used in the previous study.

Through post-processing of the recorded digital images, the algorithms in the DIC software determines the surface displacement of a deforming object by tracking a series of gray scale pixel arrays [17-21]. The software used in this work is Vic-3D, a commercially available product from Correlated Solutions, Inc. The camera's physical attributes, such as focal length and relative position, were determined using the built in calibration feature, by capturing several dozen pictures of a special grid. After inputting grid properties, such as grid spacing and size, the software calculated the necessary attributes. Using the calibration data, the program analyzed the gray-scale pattern from the area of interest and calculated the full-field displacements and strains (ε_{xx}, ε_{yy}, ε_{xy}, and, ε_1 and ε_2). Highly detailed images of the displacement and strain fields are produced with the DIC method. Furthermore, sample preparation for DIC is relatively non-intrusive, particularly significant when working with textiles and composite laminates. The KM2 fabric laminates only require an application of a speckle pattern created with household black and white spray paint.

In a previous paper, authors reported back surface measurements on a single Kevlar ply with square and circular fixed boundary conditions [10]. In addition, the authors have conducted similar studies on multi-ply fabric systems without any bonding between fabric layers [11]. The work reported in this paper extends these studies to multi-ply laminates of Kevlar fabric bonded with a resin (in this case with polyolefin formulation consisting primarily of low molecular weight polyethylene), impacted with the same projectile under fixed circular-framed boundary condition. The two impact velocities of the projectile that were used for the experiments were selected to avoid penetration of the laminates. The measured maximum displacements are presented as a function of time for the two velocities, and also as a function of ply count. In addition, sectional profiles through the impact point are presented at discrete time points during impact. In this paper, the measured hot-pressed laminate results are presented and compared to the corresponding data from the fabric configurations without resin.

These experimental data on multi-plies are being used to evaluate different fabric/laminate models and simulation methodologies at the Army Research Laboratory (ARL) and Institute of Soldier Nanotechnology at the Massachusetts Institute of Technology (ISN-MIT), similar to the work reported in [12-13].

MATERIAL AND TARGET PREPARATION

The laminates used in this study were fabricated using 600-denier Kevlar KM2 fabric sheets. Typical properties of the woven Kevlar KM2 fabric used in this study are shown in table 1 (from online Hexcel performance data).

Table 1. Typical Properties of Kevlar KM2*

Style	706
Weave	Plain
Warp Count	34 yarns/inch
Fill Count	34 yarns/inch
Fabric Weight	5.3 oz/yd2
	180 g/m2
Fabric Thickness	9 mils
	0.23 mm
Breaking Strength	775 lbf/in (warp)
	880 lbf/in (fill)

The size of each fabric sheet was approximately 304.8 mm (12 in) by 304.8 mm (12 in). The Kevlar plies were stacked with the polyolefin resin, and created using a hot-press. The laminates were then fastened onto a square wood frame with a circular cut-out using a pneumatic staple gun. The frame outside dimension was 304.8 mm (12 in), and the inside cut-out diameter was 254 mm (10 in); it was made from 19 mm (0.75 in) thick plywood. The exposed circular area inside the frame was 0.051 m^2. The fabric was kept taught preventing any wrinkling in the effective target zone as shown in Figures 2. The direction of the yarns, was aligned parallel to the edges of the wooden frame.

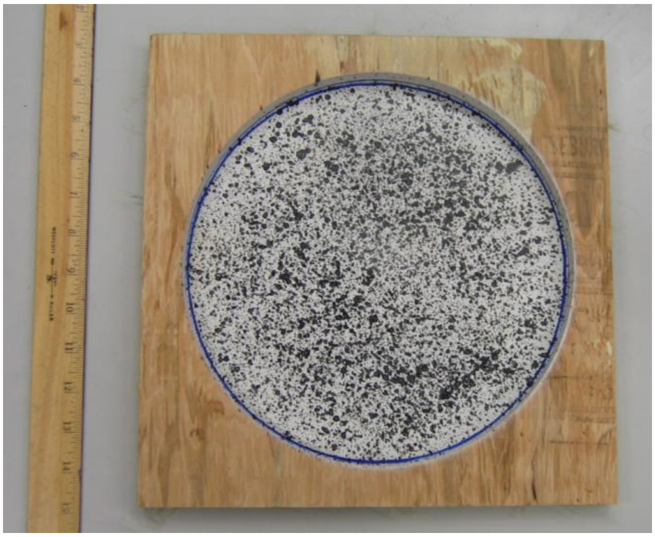

Figure 2. “Circular Picture Frame” Mounted Kevlar KM2 with Speckles

The picture frame was clamped between two aluminum plates of similar dimensions. A coarse grit paper was adhered on the surface of the aluminum plate that comes in contact with the fabric. This mitigated any slipping of the laminate during impact. The inside edge of the Kevlar next to the wooden frame was traced with a marker to allow any slipping to be identified. This can be seen in Figure 2 as the blue line around the edge of the exposed fabric circle.

In preparation for DIC measurements, the backside of the laminate panels were spray-painted white, followed by a speckling of black paint to create a random pattern. A high density of speckles is necessary to increase the data resolution generated by the DIC software.

IMPACT EXPERIMENTS

Impact experiments were conducted on single and multi-ply (two and four plies) 600-denier plain weave Kevlar KM2 (style 706) laminates that were hot-pressed with a polyolefin (PO) resin consisting primarily of low molecular weight polyethylene. The experiments consisted of propelling a projectile towards the center of the laminate using a laboratory gas gun. The experiments were performed with the laminates under fixed-circular boundary conditions. The projectile was made from Maraging 350 steel with a total mass of 104 grams. This total mass includes the mass of the sabot. Impact nose of the projectile is of hemispherical shape, with a 6.35 mm (0.25 in) radius (See Figure 1 for details). The dimensions indicated in the drawing are in inches.

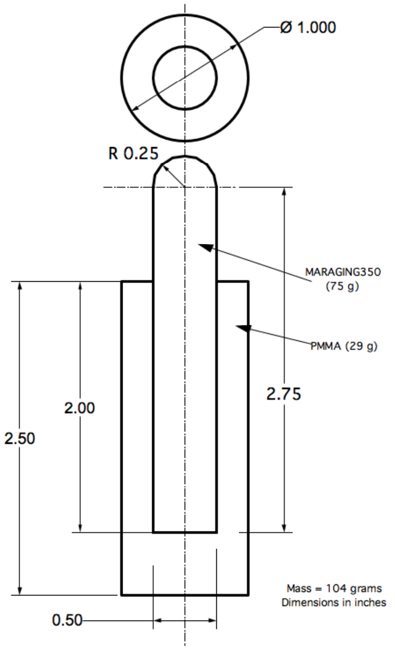

Figure 1. Hemispherical Steel Projectile with Acrylic Sabot (all dimensions are in inches)

EXPERIMENTAL METHOD

The experimental set-up consisted of two high-speed digital cameras, an aluminum mount which held the Kevlar laminate and wood frame, gas gun, velocity measuring system and a high-speed oscilloscope. A schematic of the experimental setup is shown in Figure 3. Velocity of the projectile is measured at the outlet of the gun tube using a three-laser beam/detector system with a fixed known distance between the lasers. The gun tube has a bore diameter of 25 mm, which is the same diameter as the acrylic sabot of the projectile. Interruption of three laser beams by the projectile produces a change in voltage from the detector. A three-stepped voltage drop is recorded in a digital oscilloscope providing the time of travel between each laser beam. For all experiments that were conducted, the approximate impact velocities were 22 m/s or 30 m/s, to match the previous work conducted on untreated Kevlar. These velocities correspond to approximate kinetic energies of 25.6 and 46.8 J for the projectile.

The laser velocity measuring system also acts as the trigger mechanism for the high speed digital cameras. When the digital oscilloscope is triggered by the interruption of the first laser beam, it is configured to send a TTL pulse directly to the high-speed digital cameras. The two high-speed cameras used in this study are Photron APX-RS. A photograph of the impact setup is shown in Figure 3, without the safety enclosures.

When the TTL pulse triggers the cameras, digital images of the speckled back-surface of the laminates are recorded and stored on the camera-memory. The corresponding photographs from each camera were correlated using DIC software to obtain the full field deformation of the back surface of the fabric.

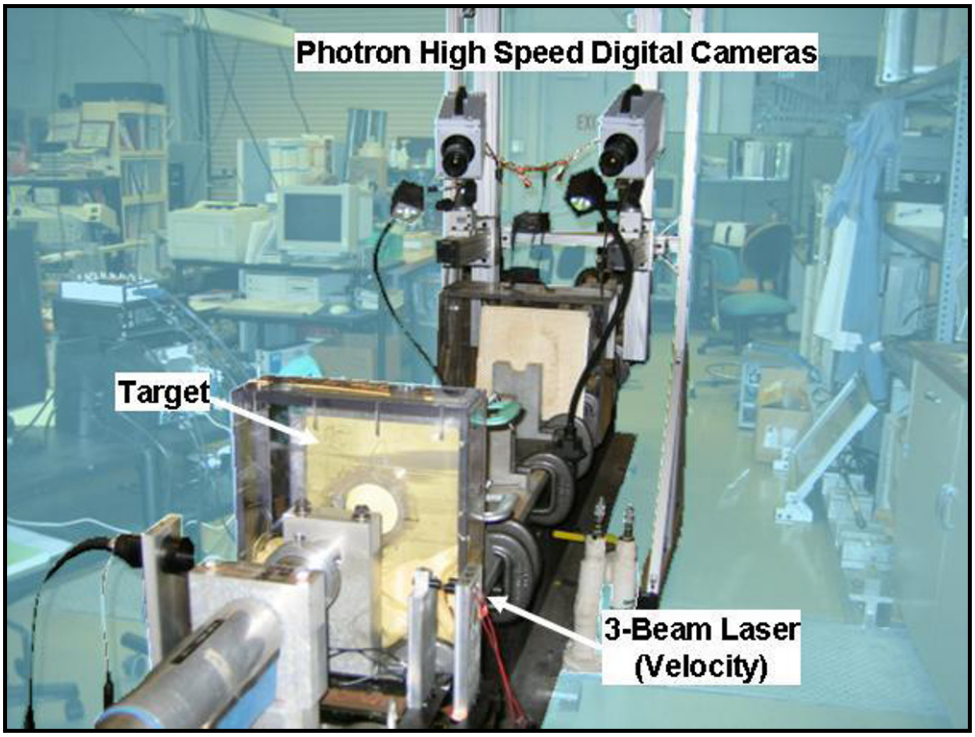

Figure 3. Photograph of Impact Setup at ARL

RESULTS AND DISCUSSION

For all the experiments conducted, there was no appreciable slip of the Kevlar KM2 fabric at the circular edges. This is indicated by lack of any deviation between the traced inside edge of the Kevlar and the wood frame after the impact experiments. Additionally, changes in x and y position are measured by the DIC method and, at the edge, there is no significant displacement of the circular edge towards the center. Inspection of the panels after the experiments also showed no appreciable displacement or stretch of the fabric at the staples. The absence of slipping is most likely attributed to the large (~50 per side) number of staples used to mount the target as well as the friction between the grit paper on the aluminum surface of the holder frame and the fabric.

Using the DIC system, the displacement data points of the back surface were extracted from each experiment. In all the plots, time at zero milliseconds (ms) corresponds to the starting-time of the impact. For comparison, all the measured experimental data from this study on laminates are presented with the corresponding uncured (unlaminated) Kevlar KM2 experimental results from the previous study [11].

Figure 4 compares the impact point displacement for laminated Kevlar to untreated Kevlar in (a) 1-ply, (b) 2-ply, and (c) 4-ply configurations for an impact velocity of 22 m/s. For the 2 and 4-ply configurations at this impact velocity, out-of-plane deflection of the impact location is identical up to the maximum point of displacement. However, after the maximum point, response of the laminated and untreated configurations deviated. In contrast, the response of the single-ply with polyolefin (PO) resin deviated from the untreated single-ply fabric, after initially having similar responses up to about 1 ms. Maximum displacement attained by the ply without PO resin was significantly higher than the PO resin treated fabric. Upon reaching the peak displacement, the displacement data shows an attenuating-like behavior for both treated and untreated Kevlar fabric. However, the amplitude of this reverberation decreases dramatically for the Kevlar fabric treated with the PO resin. This is possibly due to the fact that the PO resin treated fabric is relatively stiffer than the dry single ply KM2.

The displacement data for the single-ply both with and without PO at 30 m/s impact velocity is shown in Figure 5. At this velocity, the deflection at the impact location begins to extend to a point where the fabric begins to tear and the projectile starts to penetrate through the woven Kevlar. Nevertheless, with the DIC method we were able to obtain the full-field displacement data of the back-surface, including the out-of-plane maximum displacement, until just before penetration of the fabric by the projectile. The maximum out-of-plane displacement reached by the fabric (30 mm) with PO was significantly lower than the corresponding displacement (37mm) reached by the untreated fabric layer.

Figure 6 shows the maximum out-of-plane displacement for the 2 and 4--ply configurations at the velocity of 30 m/s. The projectile did not penetrate any of the fabric configurations. The maximum deflections for untreated and laminated 2-ply configuration were 38 mm and 34 mm, respectively. For the 4-ply configurations, the corresponding deflections were 33.5 mm for untreated and 31 mm for laminated fabrics. Maximum deflection reached by the untreated configuration was higher than the laminated configuration for both 2 and 4-ply configurations. This is expected since the cured laminate is able to resist higher loads since it acts as a unit rather than individual plies. During the experiments, impact point response was approximately similar for laminated and untreated cases, until the maximum out-of-plane deflection is reached by the laminate. After this point, the response of the laminated and unlaminated configurations deviated from each other.

Figure 7 (1-ply), Figure 8 (2-ply), and Figure 9 (4-ply) show the sectional displacement profiles at different times through the impact point for (a) untreated and (b) laminated configurations at the 22 m/s impact velocity. Each plotted line is a representation of the yarn across the plane of the fabric through the impact point. Different plotted lines correspond to different times (noted in the legend key) throughout the experiment. Figure 10 (2-ply) and Figure 11 (4-ply) show the displacement profiles through the impact point for (a) untreated and (b) laminated configurations at an impact velocity of 30 m/s. In all these cases, shapes of the sectional profiles are approximately similar between laminated and untreated Kevlar for the two velocities studied.

Figure 12 compares the displacement profiles at the maximum displacement for the laminated Kevlar to untreated Kevlar in (a) 1-ply, (b) 2-ply, and (c) 4-ply configurations for the 22 m/s impact velocity. Figure 13 compares the displacement profiles at maximum of the laminated Kevlar to untreated Kevlar in (a) 2-ply and (b) 4-ply configurations for the 30 m/s impact velocity. As discussed earlier, the shape of the sectional profiles are quite similar for both laminated and untreated Kevlar configurations, although, especially at the higher velocity, the maximum displacements of the untreated Kelvar is higher than the laminate.

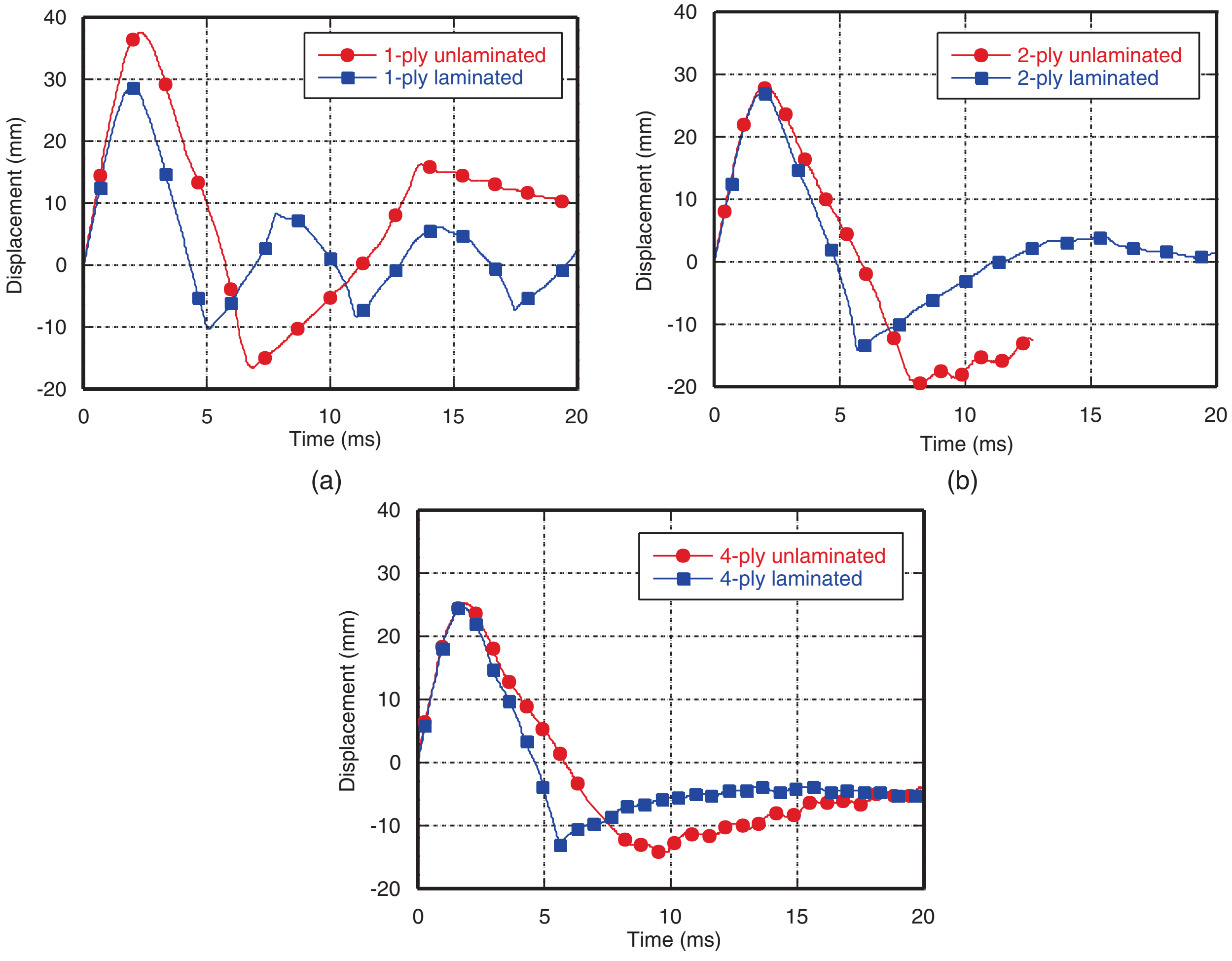

(a) (b)

(c)

Figure 4. Impact Point Displacement Comparisons of Unlaminated and Laminated Kevlar for (a) 1-ply (b) 2-ply and (c) 4-ply Configurations at 22 m/s.

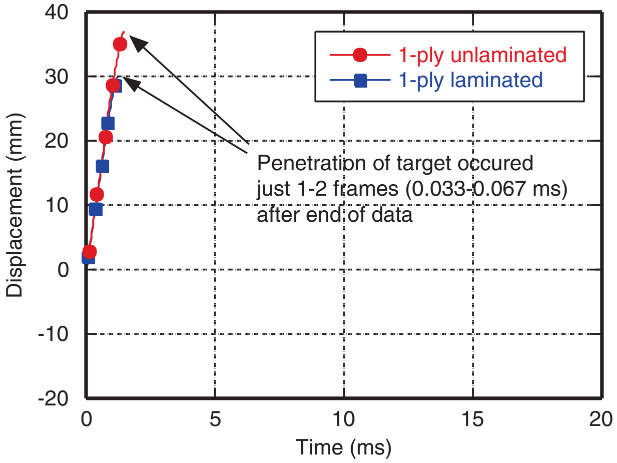

Penetration of target occured just 1-2 frames (0.033-0.067 ms) after end of data

Figure 5. Impact Point Displacement Comparisons of Resin-Treated and Untreated Kevlar for 1-ply Configurations at 30 m/s.

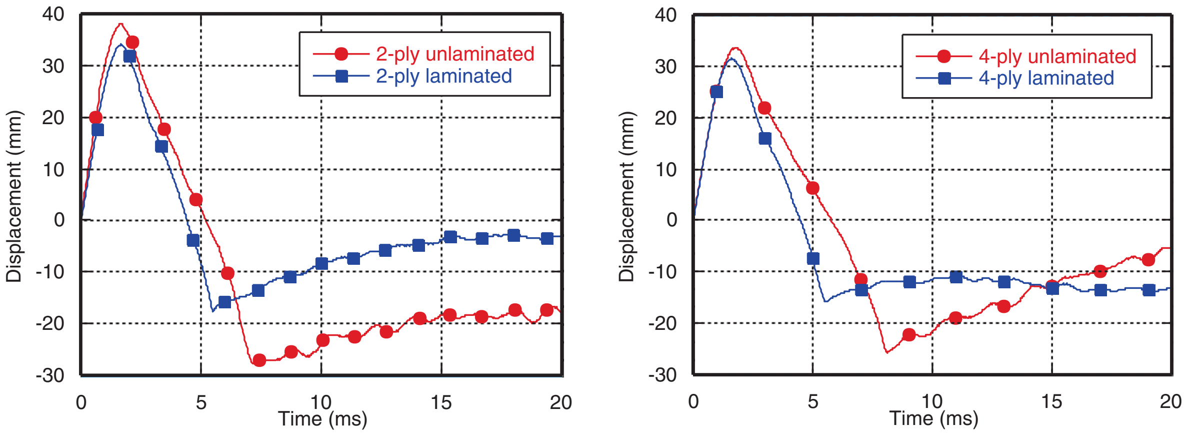

(a) (b)

Figure 6. Impact Point Displacement Comparisons of Unlaminated and Laminated Kevlar for (a) 2-ply and (b) 4-ply Configurations at 30 m/s.

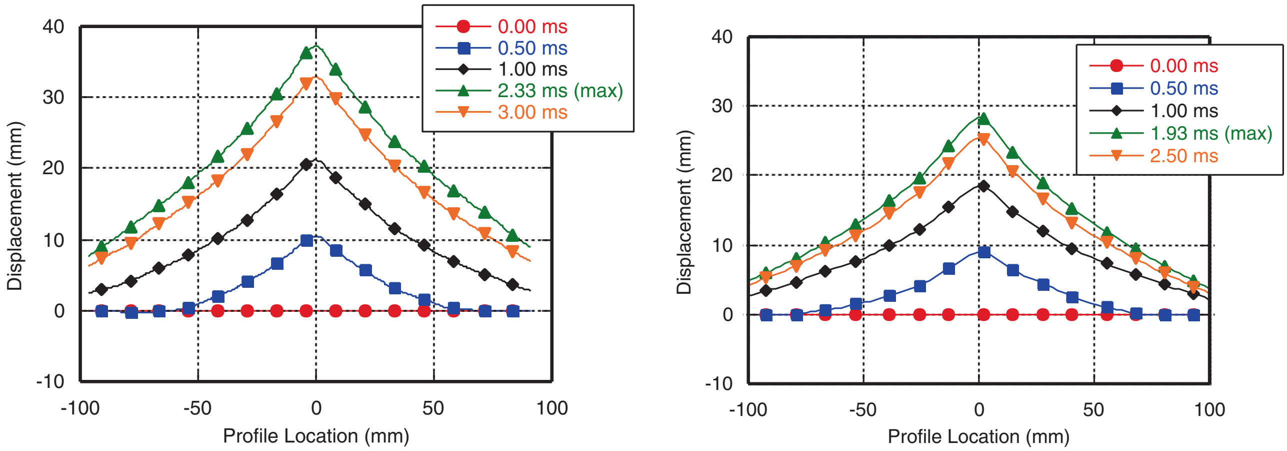

(a) (b)

Figure 7. Displacement Profiles of Kevlar for 1-ply (a) Untreated and (b) Resin Treated Configurations at 22 m/s.

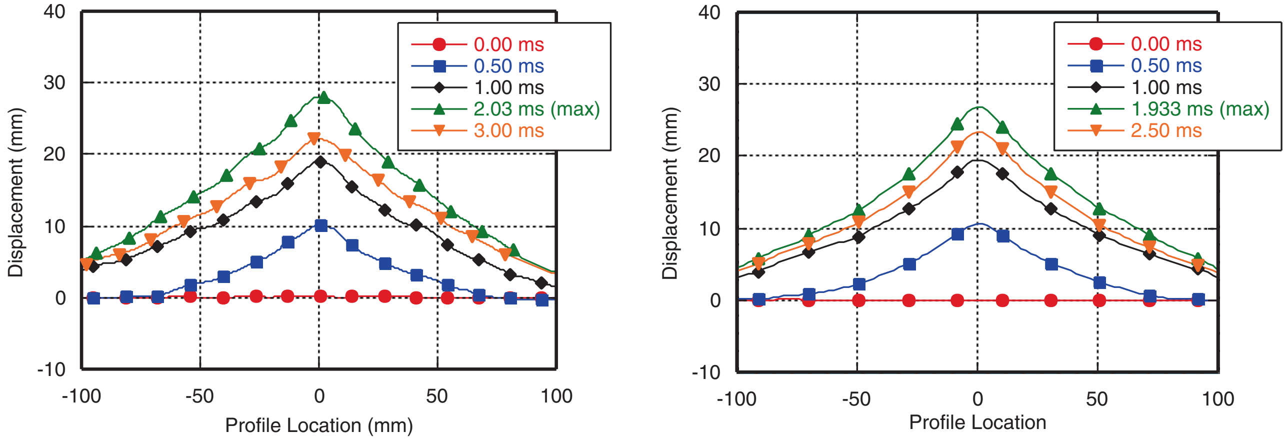

(a) (b)

Figure 8. Displacement Profiles of Kevlar for 2-ply (a) Unlaminated and (b) Laminated Configurations at 22 m/s.

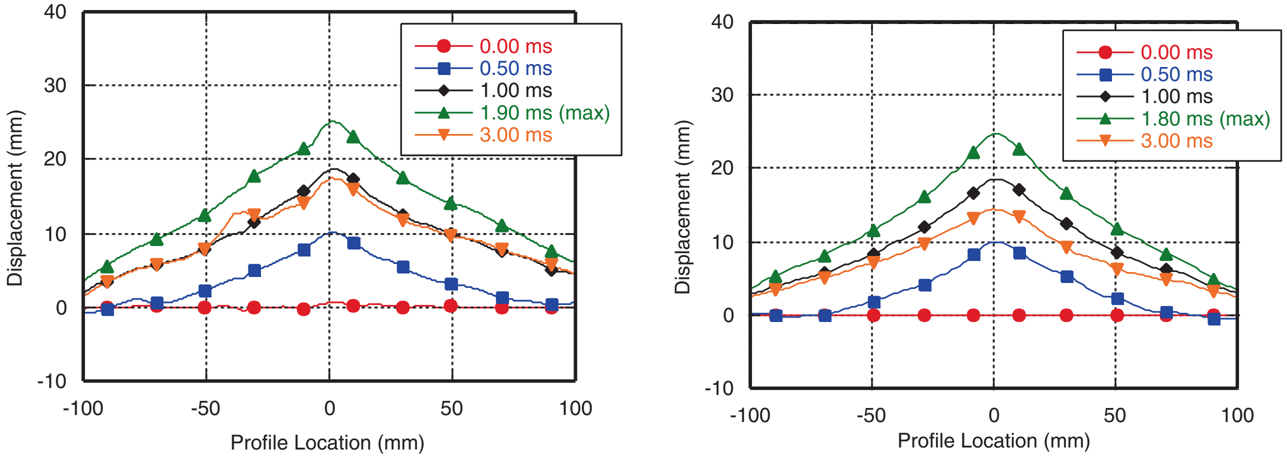

(a) (b)

Figure 9. Displacement Profiles of Kevlar for 4-ply (a) Unlaminated and (b) Laminated Configurations at 22 m/s.

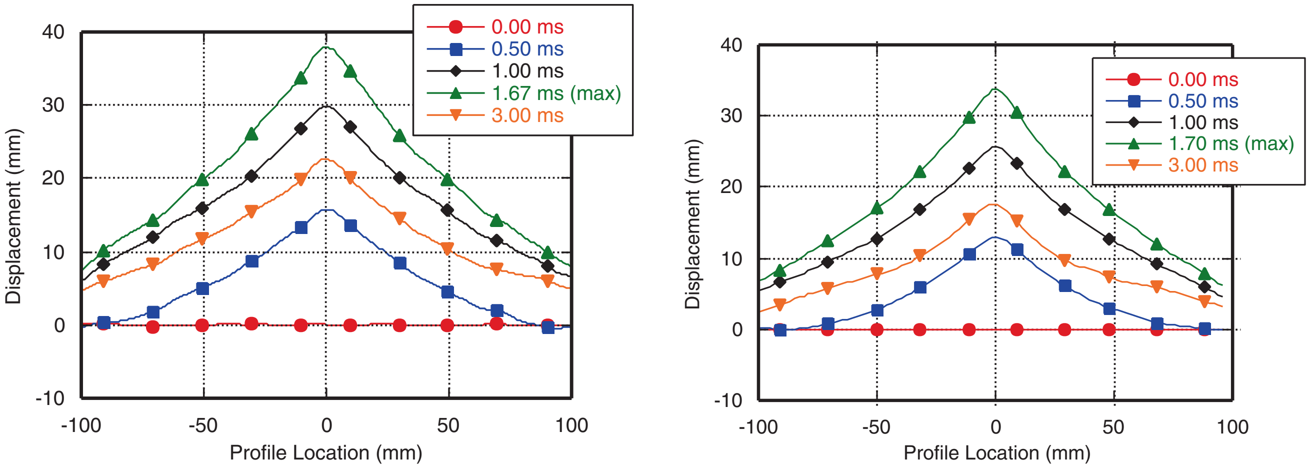

(a) (b)

Figure 10. Displacement Profiles of Kevlar for 2-ply (a) Unlaminated and (b) Laminated Configurations at 30 m/s.

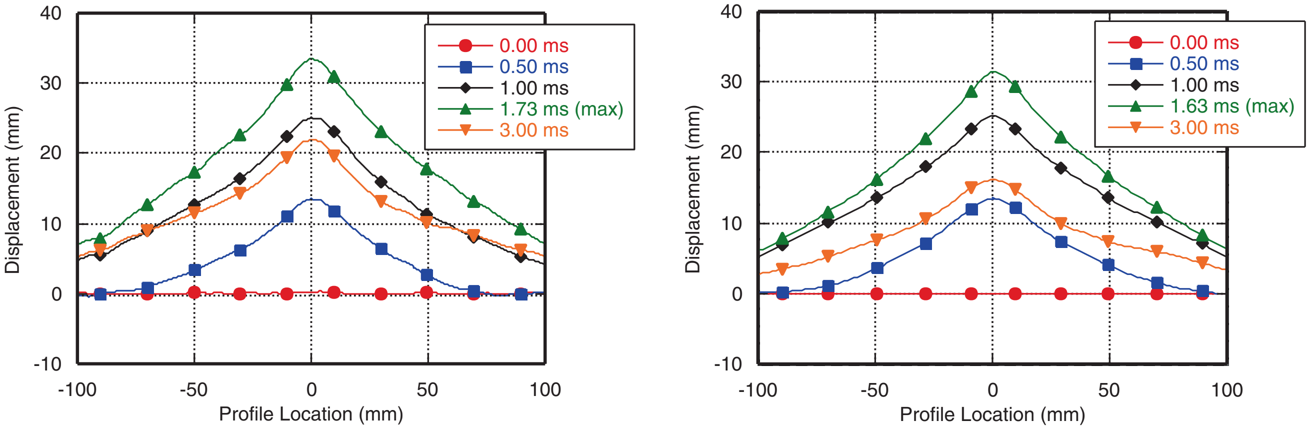

(a) (b)

Figure 11. Displacement Profiles of Kevlar for 4-ply (a) Unlaminated and (b) Laminated Configurations at 30 m/s.

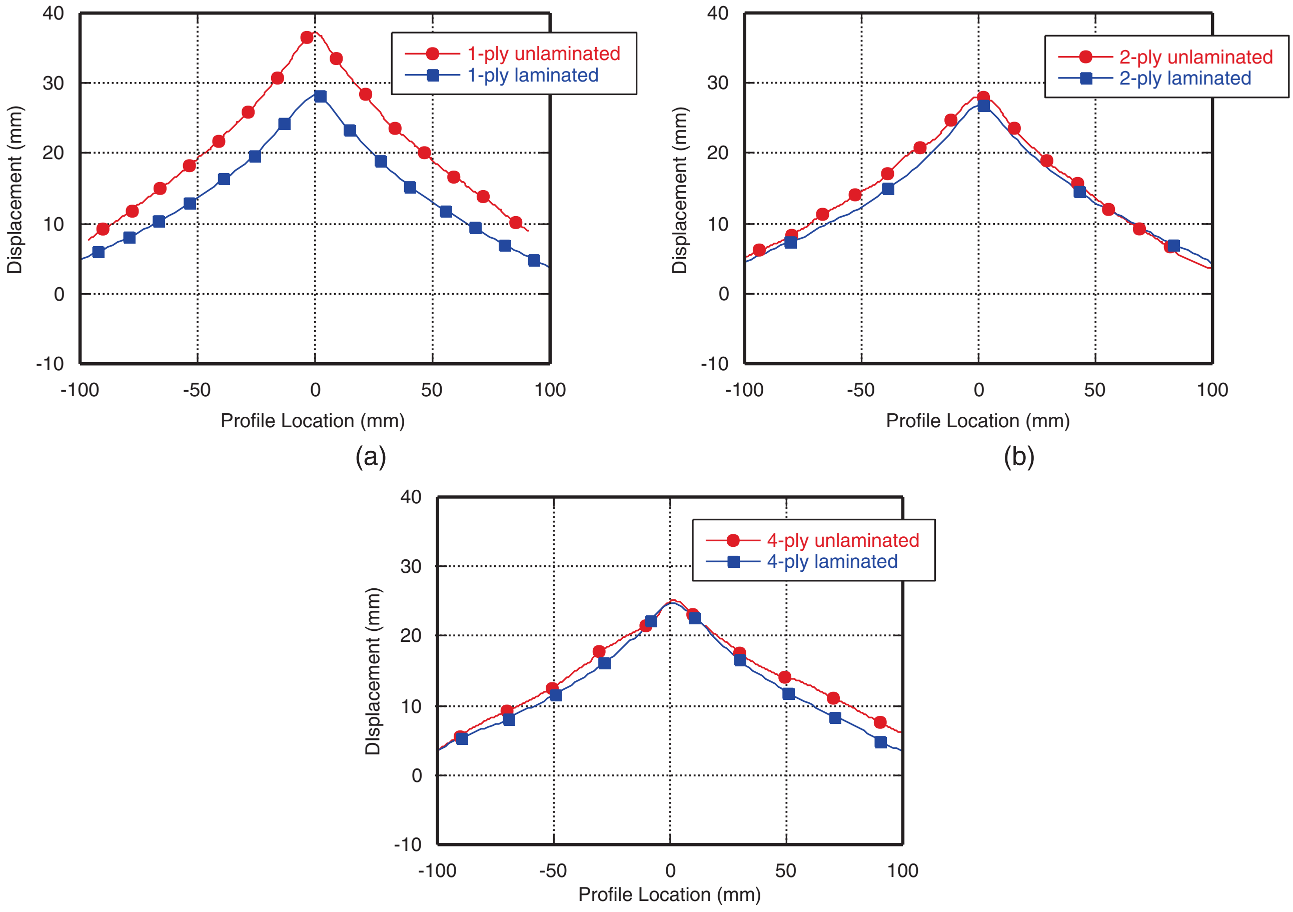

(a)

(b)

(c)

Figure 12. Maximum Displacement Profile Comparison of Unlaminated and Laminated Kevlar Configurations for (a) 1-ply (b) 2-ply and (c) 4-ply at 22 m/s.

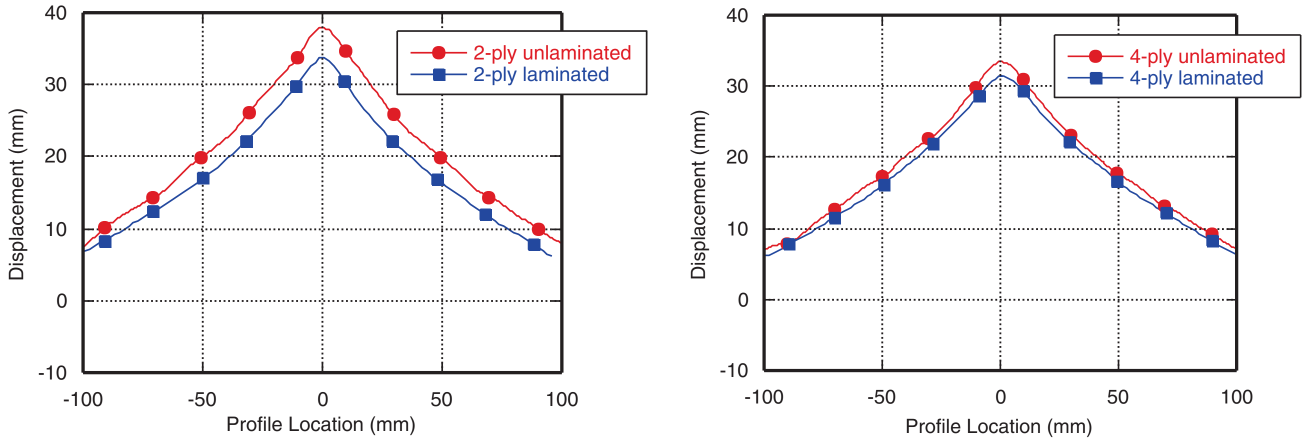

(a)

(b)

Figure 13. Maximum Displacement Profile Comparison of Unlaminated and Laminated Kevlar Configurations for (a) 2-ply and (b) 4-ply at 30 m/s.

The summary of maximum displacement at the impact point is shown as a function of impact velocity for all of the Kevlar KM2 configurations in Figure 14. The increase of impact velocity from 22 m/s to 30 m/s had a smaller effect on the laminated configurations than the unlaminated ones. Also, it can be seen that the treating of 1-ply Kevlar with PO resin had a much more dramatic effect than on the other ply counts.

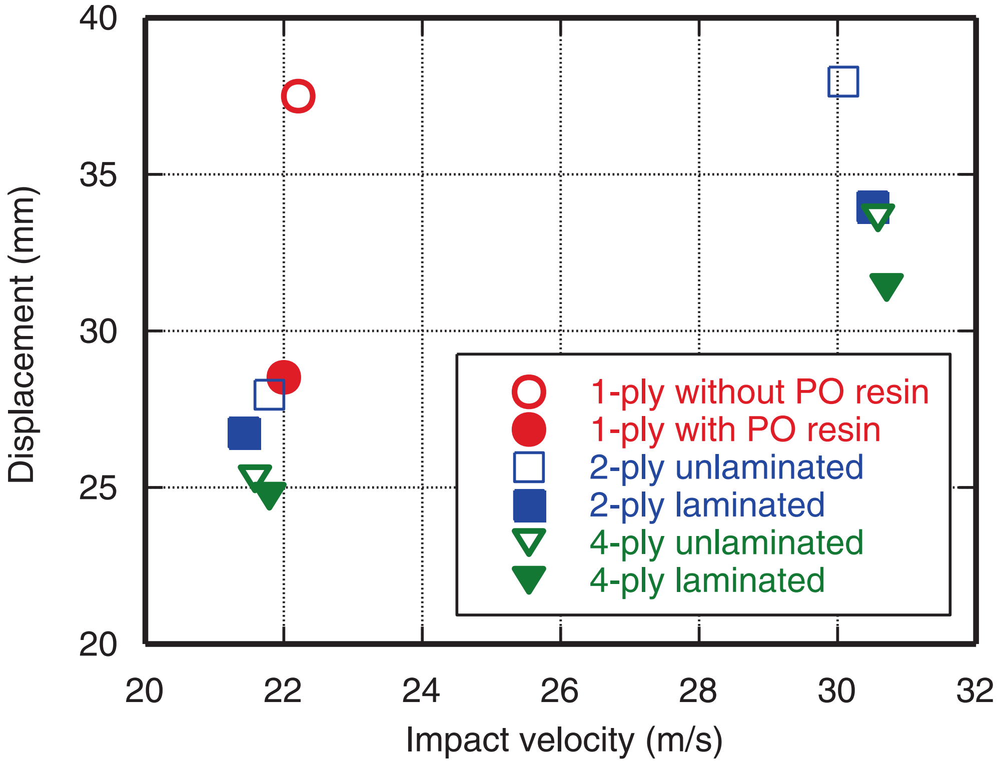

Figure 14. Maximum displacement of impact point as a function of impact velocity for all Kevlar configurations

SUMMARY

Experimental techniques were developed to measure full-field transient deformation of the back surface of the multi-layer circular configurations of Kevlar KM2 fabric (style 706) during impact by a hemispherical projectile at two different velocities. To complement our previous multi-ply impact studies without resins, cured 1, 2 and 4-ply laminate configurations with polyolefin resin were used in the series of experiments conducted under this study. A DIC method was used to obtain the full-field transient deformation of the back surface of the fabric during impact. The correlated results show that the experimental methods developed can be used to obtain maximum transient displacement as well as sectional profile of the displaced fabric as a function of time during impact. Experimental results show that there is very little difference between the response of the laminated and untreated 2 and 4-ply configurations for both velocities during the time to the maximum displacement. Response after the maximum displacement point was different for cured laminate and uncured laminate for both velocities. For single-ply configuration, uncured, KM2 fabric displaces more than the laminated Kevlar composite. For 30 m/s velocity, the projectile penetrated single fabric configuration. For all the cases studied, the results indicate as a function of ply count, the peak displacement decreases as the ply count increases. The data are being used to evaluate fabric models that are proposed in the literature. In addition, these results are being used to validate simulation methodologies that are being developed for multi-layer fabric/laminate configurations.

ACKNOWLEDGEMENTS

The authors wish to extend their gratitude to fellow colleague Dr. Chian-Fong Yen at the Army Research Laboratory (ARL) and Prof. Simona Socrate of the Institute for Soldier Nanotechnology (ISN) at the Massachusetts Institute of Technology (MIT) for providing the motivation to develop the experimental methodology and conduct the work reported in this paper. We would also like to thank Mr. James Wolbert of ARL for fabricating the Kevlar panels for this study.

Certain commercial equipment and materials are identified in this paper in order to specify adequately to the experimental procedure. In no case does such identification imply recommendation by the Army Research Laboratory nor does it imply that the material or equipment identified is necessarily the best available for this purpose.

REFERENCES

1. Cheng, M., Chen, W., Weerasooriya, T. Experimental Investigation of the Transverse Mechanical Properties of a Single Kevlar KM2 Fiber. International Journal of Solids and Structures. Vol 41, Iss 22-23, pp 6215-6232. Nov 2004.
2. Cheng, M., Chen, W., Weerasooriya, T. Mechanical Properties of Kevlar KM2 Single Fiber. Journal of Engineering Materials and Technology. Vol 127, Iss 2, pp 197-203. April 2005.
3. Cheng, M. and Chen, W. Modeling Transverse Behavior of Kevlar KM2 Single Fibers with Deformation-Induced Daamge. International Journal of Damage Mechanics. Vol 15, No 2, pp 121-132. 2006.
4. Raftenberg, M. N., Scheidler, M., Moynihan, T. J., Smith, C. A. Plain Woven, 600-Denier Kevlar KM2 Fabric under Quasi-Static, Uniaxial Tension. ARL-TR-3437. March 2005.
5. Raftenberg, M. N., Mulkern, T. J., Quasi-Static Uniaxial Tension Characteristics of Plain-Woven Kevlar Fabric. ARL-TR-2891. December 2002.
6. King, M.J., Jearanaisilawong, P., Socrate S. A Continuum Constitutive Model for the Mechanical Behavior of Woven Fabrics. International Journal of Solids and Structures. Vol 42. pp 3867. 2005.
7. Yen, C.-F., Scott, B., Dehmer, P., and Cheeseman, B. A Comparison between Experiment and Numerical Simulation of Fabric Ballistic Impact. Proc. 23rd Int. Ballistic Symposium. Tarragona, Spain. 2007.
8. Zhou, Guangming, Xuekun Sun and Youqi Wang. Multi-Chain Digital Element Analysis in Textile Mechanics. Journal of Composites Science and Technology. 2003.
9. King, M. J. A Continuum Constitutive Model for the Mechanical Behavior of Woven Fabrics Including Slip and Failure. MIT Doctor of Philosophy Thesis. June 2006.
10. Tusit Weerasooriya, Allan Gunnarsson and Paul Moy, Measurement of Full-Field Transient Deformation of the Back Surface of a Kevlar KM2 Fabric during Impact for Material Model Validation, Proceedings of the 2008 International Congress and Exposition on Experimental Mechanics and Applied Mechanics, June 2-5, Orlando, FL, 2008
11. Tusit Weerasooriya, Allan Gunnarsson and Paul Moy, Measurement of Full-Field Transient Deformation of the Back Surface of Multi-layered Kevlar KM2 Fabric Configurations during Impact for Material Model Validation, Proceedings of the 2009 SEM Conference and Exposition on Experimental and Applied Mechanics, June 1-4, Albuquerque, NM, 2009
12. Yen. C., Weerasooriya T., Moy, P., Scott, B. and Cheeseman, B., Experimental Validation of a Kevlar Fabric Model for Ballistic Impact, 24th National Symposium on Ballistics, New Oleans, LA, pp 51-58, September, 2008
13. Ethan Parsons, Simona Socrate, Tusit Weerasooriya and Sai Sarva, Continuum Model Simulations and Experimental Projectile Impact on Woven Fabric, 26th Army Science Conference, Orlando, FL, December 2008
14. ARMY MIL-STD-662F. V50 Ballistic Test for Armor.
15. Wetzel, E.D., Lee, Y.S., Egres, R.G., Kirkwood, K.M., Kirkwood, J.E., and Wagner, N.J. The Effect of Rheological Parameters on the Ballistic Properties of Shear Thickening Fluid (STF) – Kevlar Composites. NUMIFORM. Columbus, OH. 2004
16. Weerasooriya, T. Full Field Out-of-Plane Transient Deformation for Several Composites on Impact. ARL Technical Report to be published.
17. Chu, T. C., Ranson, W. F., Sutton, M. A., and Peters, W. H. Applications of Digital-Image-Correlation Techniques to Experimental Mechanics. Experimental Mechanics. September 1995.
18. Sutton, M. A., Wolters, W. J., Peters, W. H., Ranson, W. F., and McNeill, S. R. Determination of Displacements Using an Improved Digital Image Correlation Method. Computer Vision. August 1983.
19. Bruck, H. A., McNeill, S. R., Russell S. S., Sutton, M. A. Use of Digital Image Correlation for Determination of Displacements and Strains. Non-Destructive Evaluation for Aerospace Requirements. 1989.

20. Sutton, M. A., McNeill, S. R., Helm, J. D., Schreier, H. Full-Field Non-Contacting Measurement of Surface Deformation on Planar or Curved Surfaces Using Advanced Vision Systems. Proceedings of the International Conference on Advanced Technology in Experimental Mechanics. July 1999.

21. Sutton, M. A., McNeill, S. R., Helm, and Chao, Y. J. Advances in Two-Dimensional and Three-Dimensional Computer Vision. Photomechanics. Volume 77. 2000.

Proceedings of the SEM Annual Conference
June 7-10, 2010 Indianapolis, Indiana USA
©2010 Society for Experimental Mechanics Inc.

Numerical Study of Composite Panels Subjected to Underwater Blasts

R. Bellur-Ramaswamy, F. Latourte, W. Chen, H.D. Espinosa*
Northwestern University, Department of Mechanical Engineering, 2145 Sheridan Road,
Evanston IL 60201, USA
* Corresponding author: espinosa@northwestern.edu

ABSTRACT

In this work, we characterize the performance of composite panels subjected to underwater impulsive loadings by finite element analysis (FEA). First, we present a finite element model that simulates the fluid-structure interaction experiment developed in our laboratory for testing the underwater blast resistance of marine composite panels. Then, we present the methodology used to calibrate this model (possessing a high number of degrees of freedom) from available experimental data presented in another talk. Both deflection profile histories and damage maps are used as a metric to identify unknown model parameters. The dynamic model incorporates layered-shell elements, damage initiation by Hashin criterion and damage evolution laws for laminæ and interfaces. The calibrated model will help to improve the blast performance of marine structures by design optimization studies of solid and sandwich panels

Introduction

Over the years, due to advancement of computer hardware and software, computer-based simulations have become an integral part of several areas of science and engineering research. In fact, it is now considered crucial to possess computational predictive capability in order to maintain a lead in science and technology, as recently reported by World Technology Evaluation Center, Inc., supported by the leading national laboratories of the USA [1]. Furthermore it is now common in the defense and industry to possess computational capability to drastically cut down product release time and gain an edge over the competition. In light of this, predictive capabilities are being developed in newer and newer frontiers. In the present work, we are particularly interested in the design and optimization of marine sandwich composites. Although attempts have been made in developing predictive capability for foam sandwich composites [2-5], they lack validation, which is an important component of developing a predictive tool. A major aspect of composite-material based simulation is the ability to predict the initiation and evolution of damage. Several composite damage models are available in the literature, but none of them can be concluded to be the best for all given material and loading conditions [6-9]. Moreover, not many models are available to be directly applied to highly dynamic problems. This work aims at developing a predictive capability via a finite element analysis for the response of marine sandwich composite panels subjected to underwater blasts. Numerically obtained results can be correlated to Fluid Structure Interaction (FSI) experiments results (the experimental apparatus was used earlier to characterize steel sandwich panels and also validate related computational models [10-12]). The experimental results on composite panels are presented in another talk, and will be used here to attempt a calibration of the numerical model. A major interest of the validated computational model is to help designing optimized composites panels for given loading conditions. Moreover, limited information can be obtained in the underwater blast experiment because of the limitations in instrumentation and highly dynamic nature of the phenomenon. Hence, the computational model is helpful in providing additional understanding of the mechanisms of dynamic failure of composite panels, as well as assessing the capabilities of the Hashin composite failure model [13].

Finite Element Model

Because of the quasi-isotropic layup of the composite panel, only a quarter of the composite panel is modeled using layered continuum shell elements. Each shell element is a laminate with 4 plies of different orientation. The

T. Proulx (ed.), *Dynamic Behavior of Materials, Volume 1*, Conference Proceedings of the Society for Experimental Mechanics Series, DOI 10.1007/978-1-4419-8228-5_24, © The Society for Experimental Mechanics, Inc. 2011

layers of laminates are tied together by an adhesive, which is modeled by cohesive elements [14] with standard traction-separation laws. Based on the results from the world failure exercise, Hashin-type failure model performs reasonably under tensile loading conditions and is also a simple physically based model. Therefore, it was chosen in this work to model damage initiation along with linear damage evolution law using ABAQUS/Explicit finite element package [15]. A quarter cylindrical column of water (modeled as equation of state material [10]) has surface contact interactions with the composite panel. Cavitation within the water is modeled by applying tensile failure criterion.

Model Calibration and Results

The experiments have been carried out for solid monolithic panels and sandwich panels. The experimental data for solid monolithic panels are utilized to fine tune the composite material damage model parameters. This will be done by comparing the deflection history of the center of panels and also matrix damage and delamination. These calibrated model parameters are further used in modeling the foam sandwich panels and the results will be compared with those from the experiments in terms of the panel center deflection history, panel deflection profiles, foam crushing and composite damage. Sensitivity of the response of the composite panels with respect to boundary conditions and some of the model parameters will also be presented.

References

1. *International Assessment of Research and Development in Simulation-Based Engineering and Science (SBE&S)*. 2009, World Technology Evaluation Center, Inc.
2. Deshpande, V.S. and N.A. Fleck, *One-dimensional response of sandwich plates to underwater shock loading.* Journal of the Mechanics and Physics of Solids, 2005. **53**(11): p. 2347-2383.
3. Hoo Fatt, M.S. and L. Palla, *Analytical Modeling of Composite Sandwich Panels under Blast Loads.* submitted to J. of Sandwich Struct. and Mat.
4. Tilbrook, M.T., V.S. Deshpande, and N.A. Fleck, *Underwater blast loading of sandwich beams: regimes of behaviour.* International Journal of Solids and Structures. **In Press, Accepted Manuscript**.
5. Forghani, A. and R. Vaziri, *Computational Modeling of Damage Development in Composite Laminates Subjected to Transverse Dynamic Loading.* Journal of Applied Mechanics-Transactions of the Asme, 2009. **76**(5).
6. Hinton, M.J., A.S. Kaddour, and P.D. Soden, *A comparison of the predictive capabilities of current failure theories for composite laminates, judged against experimental evidence.* Composites Science and Technology, 2002. **62**(12-13): p. 1725-1797.
7. Soden, P.D., M.J. Hinton, and A.S. Kaddour, *A comparison of the predictive capabilities of current failure theories for composite laminates.* Composites Science and Technology, 1998. **58**(7): p. 1225-1254.
8. Soden, P.D., M.J. Hinton, and A.S. Kaddour, *Biaxial test results for strength and deformation of a range of E-glass and carbon fibre reinforced composite laminates: failure exercise benchmark data.* Composites Science and Technology, 2002. **62**(12-13): p. 1489-1514.
9. Soden, P.D., A.S. Kaddour, and M.J. Hinton, *Recommendations for designers and researchers resulting from the world-wide failure exercise.* Composites Science and Technology, 2004. **64**(3-4): p. 589-604.
10. Espinosa, H., S. Lee, and N. Moldovan, *A Novel Fluid Structure Interaction Experiment to Investigate Deformation of Structural Elements Subjected to Impulsive Loading.* Experimental Mechanics, 2006. **46**(6): p. 805-824.
11. Mori, L.F., et al., *Deformation and fracture modes of sandwich structures subjected to underwater impulsive loads.* Journal Of Mechanics Of Materials And Structures, 2007. **2**(10): p. 1981--2006.
12. Mori, L.F., et al., *Deformation and Failure Modes of I-Core Sandwich Structures Subjected to Underwater Impulsive Loads.* Experimental Mechanics, 2009. **49**(2): p. 257--275.
13. Hashin, Z., *ANALYSIS OF STIFFNESS REDUCTION OF CRACKED CROSS-PLY LAMINATES.* Engineering Fracture Mechanics, 1986. **25**(5-6): p. 771-778.
14. Camanho, P. and C. Dávila, *Mixed-mode decohesion finite elements for the simulation of delamination in composite materials.* NASA-Technical Paper, 2002. **211737**.
15. *ABAQUS User's manual*: Dassault Systèmes Simulia Corp., Providence, RI, USA.

Proceedings of the SEM Annual Conference
June 7-10, 2010 Indianapolis, Indiana USA
©2010 Society for Experimental Mechanics Inc.

Non-Shock Initiation Model for Explosive Families: Experimental Results

Mark U. Anderson*, Steven N. Todd*, Terry L. Caipen^{f}, Charles B. Jensen*, and Chance G. Hughs$^{\aleph}$

*Sandia National Laboratories, Albuquerque, NM, 87185

^{f}Applied Research Associates, Albuquerque, NM, 87110

$^{\aleph}$North Vector, Menlo Park, CA, 94025

Abstract. The "DaMaGe-Initiated-Reaction" (DMGIR) computational model has been developed to predict the response of ideal high explosives to impulsive loading from non-shock mechanical insults. The distinguishing feature of this model is the introduction of a damage variable, which relates the evolution of damage to the initiation of a reaction in the explosive, and its growth to detonation. This model development effort treats the non-shock initiation behavior of explosives by families; rigid plastic bonded, cast, and moldable plastic explosives. Specifically designed experiments were used to study the initiation process of each explosive family with embedded shock sensors and optical diagnostics. The experimental portion of this model development began with a study of PBXN-5 to develop DMGIR model coefficients for the rigid plastic bonded family, followed by studies of the cast, and bulk-moldable explosive families, including the thermal effects on initiation for the cast explosive family. The experimental results show an initiation mechanism that is related to impulsive energy input and material damage, with well defined initiation thresholds for each explosive family. These initiation details will be used to extend the predictive capability of the DMGIR model from the rigid family into the cast and bulk-moldable families.

Introduction

The impulsive load caused by the impact of a projectile or fragment into an energetic material will produce a range of responses that can range from mechanical damage with no reaction to a self-sustaining deflagration that consumes the material at an increasing rate, transitioning into a detonation.

The magnitude of impulsive energy input, and the extent to which damage is generated in the energetic material have a direct effect on the onset and the extent of reaction produced in an explosive sample. Impact-induced deflagrations with sufficient energy input and mechanical damage have been observed to transition within a few microseconds into a growth to detonation. The generation of damage is dependent on the shock loading and unloading profile, and the material strength. Numerical simulations of this damage are used to relate shear-induced strain to explosive initiation by the use of a damage variable which is embedded in the DMGIR non-shock initiation model. This treatment of non-shock initiation

T. Proulx (ed.), *Dynamic Behavior of Materials, Volume 1*, Conference Proceedings of the Society for Experimental Mechanics Series, DOI 10.1007/978-1-4419-8228-5_25, © The Society for Experimental Mechanics, Inc. 2011

allows all ideal explosives to be described numerically in one of the following three explosive families; rigid plastic bonded, cast, and moldable plastic explosives.[1]

An experimental program was designed which made use of embedded shock sensors and optical diagnostics in order to better understand the explosive initiation process of these explosive families from impulsive, non-shock loading.

Experimental Description

A single–stage light gas, or a propellant gun was used in each test to accelerate a projectile to the desired velocity, impacting an explosive test specimen. Projectile free flight of ~8-feet allowed blast protection for the gun. The test specimen was either a solid or a sandwiched cylindrical billet, instrumented with PVDF piezoelectric shock sensors for velocity measurements.[2] Digital framing cameras recorded the details of projectile impact and subsequent reaction on each experiment. Thermal effects on the cast explosive family were evaluated at temperatures that ranged from ambient to 122C. The ambient temperature test configuration is shown schematically in Fig. 1.

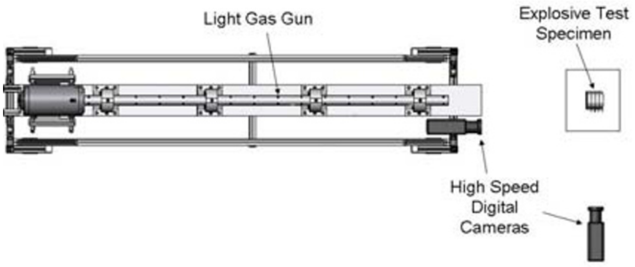

Fig. 1. Gun configuration for explosive study.

The projectile geometry consisted of a blunt-faced, hollow, right circular cylinder with a 0.500-inch diameter and an O-ring groove near the impact face. Projectile materials were aluminum or brass.

This projectile design provided a planar, short duration shock loading pulse, followed immediately by axial and radial rarefaction waves which provide well controlled mechanical damage, as shown in Fig. 2. This controlled damage was intended to simulate the expected profile produced by accidental impact.[3] Impact velocity capabilities range from 0.20 – 1.66 km/s. Explosively driven water blades were also used to generate mechanical damage, although less well controlled.

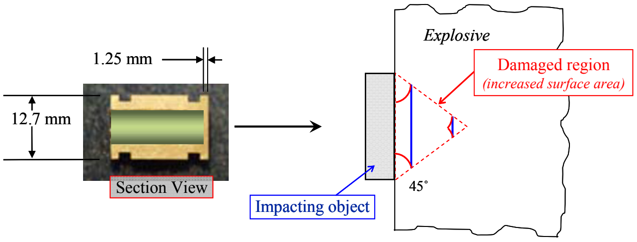

Fig. 2. Shock and release from projectile impact generates a controlled damage region in explosive.

Test Specimen

Ideal explosives are composite materials with explosive crystals embedded in a variety of polymer-based binders, with mechanical properties that depend mainly on the mixture used to form the polymer binder. The three explosive families described in this study were represented by: PBXN-5, ρ=1.80 gm/cc, (rigid plastic bonded), cast Composition-B, ρ=1.61 and 1.67 gm/cc, (cast), and PETN- or RDX-based Primasheet 1000, 2000, and Composition C-4, ρ=1.60 gm/cc (moldable plastic).

The ambient temperature test specimen configurations consisted of a cylindrical billet that was made from sandwiched billets with piezoelectric shock sensors embedded at each interface. Billet diameters were nominally 4.0–inch diameter. The piezoelectric shock sensors measured stress-time history along the axial centerline of the PBXN-5 billet. Shock front arrival times for each sensor location are plotted in Fig. 3 for a collection of PBXN-5 tests, showing the transition region between the mechanical response and the deflagration growth to detonation, as well as prompt detonation response from detonator input.

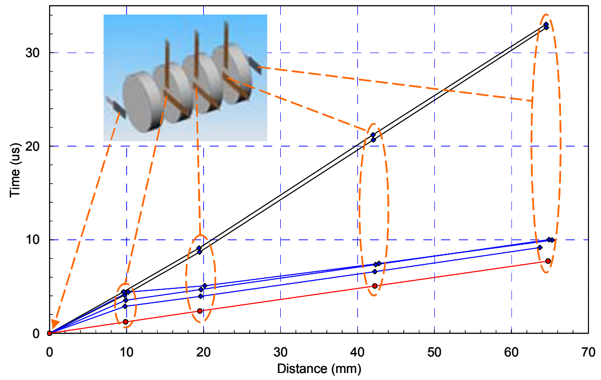

Fig. 3. Instrumented test sample of PBXN-5 with embedded piezoelectric shock sensors. Shock arrival data is plotted for multiple PBXN-5 tests.

The embedded Bauer PVDF shock sensor thickness was 25 µm, insulated on both sides with 50 µm Teflon™. MSI Piezofilm™ sensors were used on front and rear surfaces for timing measurements, augmenting the embedded shock sensor measurements on the sandwiched billets. The impact surface Piezofilm™ sensor also provided the instrumentation trigger signal.

Shock Propagation Results

The piezoelectric output from each shock sensor provides a wave propagation measurement with a timing uncertainty of ± 4 ns, based on the 2 ns sampling interval. Average velocity between each shock sensor location is based on thickness measurements along the billet centerline and transit time between sensor locations. Shock propagation time through each sensor package is removed prior to velocity calculations. Prompt-detonation control experiments were conducted to measure material response for each family under Shock-to-Detonation Transition (SDT) conditions. The PBXN-5 data set from Fig. 3 is plotted in velocity-vs-distance space in Fig. 4 to illustrate the observed non-shock initiation behavior for PBXN-5.

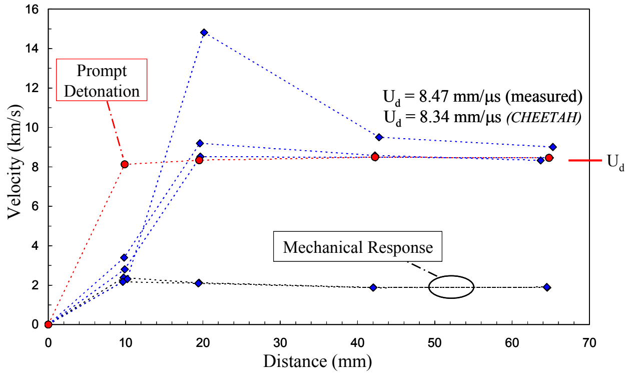

Fig. 4. Velocity calculations from PBXN-5 tests show non-shock initiation results, prompt detonation results, and CHEETAH predictions.

The non-shock insults that result in a mechanical response are observed to initially propagate above the PBXN-5 acoustic velocity (1.35 km/s), with a slight decrease in velocity as a function of distance.[4] The prompt-detonation control experiments show a velocity measurement that asymptotically approaches a steady velocity of 8.47 km/s, which shows that the CHEETAH calculations estimate of 8.34 km/s, is within 1.5% of the experimental velocity. The non-shock, or damage initiated experiments show the initial velocity to be above the detonation velocity followed by a rapid increase through the next 10-mm thick disc to approximately the detonation velocity. The observed transient overshoot in velocity is consistent with a Deflagration-to-Detonation Transition (DDT) in porous explosives, in which the porosity is caused by mechanical damage. This collection of experimental data at increasing impact velocities show that the non-shock initiation behavior, as shown in Figures 3 and 4, is dependent on input energy.

The average shock velocity through the assembled explosive billet is dependent on the specific energy input, as shown in Fig. 5 for each family of ideal explosives.

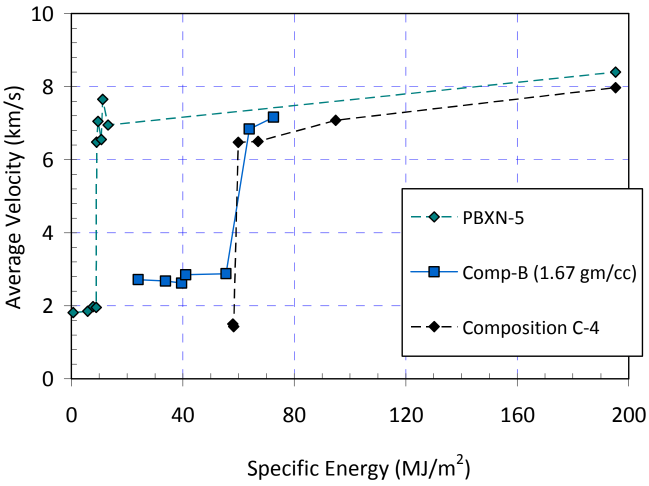

Fig. 5. Average velocity through explosive billet shows distinct transition to near-detonation velocity at initiation threshold, shown by family.

The average shock velocities range from slightly above acoustic velocity for mechanical response to nearly detonation velocity for a SDT-type reaction, with the velocity for non-shock initiations ranging between these limits. For energy inputs above the initiation threshold, the measured shock velocity is dependent on the run distance to the DDT transition. Baseline experiments used a M16 non-electric detonator for a SDT initiation, with a specific energy of 195.3 MJ/m^2.

Experimental results are summarized for the rigid plastic bonded family in Table 1.

Table 1. PBXN-5 results, aluminum projectile.

Impact Velocity (m/s)	Impact Energy (kJ)	Specific Energy (MJ/m^2)	Shock Velocity (km/s)
188	0.080	0.632	1.814
574	0.736	5.810	1.850
682	0.989	7.807	1.976
730	1.133	8.94	1.954
733	1.143	9.02	6.479
735	1.206	9.52	7.050
799	1.358	10.72	6.550
800	1.427	11.26	7.650
802 (tilt)	1.437	11.34	1.727
885	1.666	13.15	6.947
detonator	5.748	195.3	8.396

All damage initiation experiments were focused on specific energy levels below the SDT threshold. The PBXN-5 response to non-shock initiation showed a well defined initiation threshold of 9.0 MJ/m^2, with modest scatter in the average velocity above the initiation threshold. The 802 m/s experiment had a 14-degree tilt angle on impact, resulting in a non-sustained deflagration with an average shock velocity of 1.727 km/s. The modest scatter in shock velocity above the initiation threshold is thought to be caused from lack of tilt control on the smooth-bore gas gun used for the PBXN-5 experiments. Subsequent testing on the cast, and moldable families used a rifled barrel powder gun to control tilt angle on impact.

The study of cast Comp-B used densities of 1.61, and 1.67 gm/cm^3. The results from 1.61 gm/cm3 cast Comp-B are given in Table 2.

Table 2. Cast Comp-B results, see projectile note.

Impact Velocity (m/s)	Impact Energy (kJ)	Specific Energy (MJ/m^2)	Shock Velocity (km/s)
655 (B)	3.352	26.46	6.601
1,095 (A)	8.077	37.15	4.557
796 (B)	4.968	39.22	4.638
1,518 (A)	6.152	48.57	7.245
963 (B)	7.252	57.25	5.428
detonator	5.748	195.3	7.467

The projectile materials for the experiments shown in Table 2 were either aluminum (A) or brass (B) for the Comp-B experimental series, with the material notation following the impact velocity. The results from 1.67 gm/cm3 cast Comp-B are given in Table 3.

Table 3. Cast Comp-B results.

Impact Velocity (m/s)	Impact Energy (kJ)	Specific Energy (MJ/m^2)	Shock Velocity (km/s)
619	3.036	23.96	2.715
734	4.278	33.77	2.678
794	5.006	39.52	2.622
809	5.199	41.04	2.848
941	7.029	55.49	2.880
1010	8.089	63.86	6.841
1076	9.193	72.57	7.162

The cast Comp-B material showed an initiation threshold below 26.5 MJ/m2 for the sample density of 1.61 gm/cm^3, and an initiation threshold of 63.8 MJ/m^2 for a sample density of 1.67 gm/cm^3.

The cast Comp-B initiation response shows a similar behavior to the rigid plastic bonded family for both densities when high quality material was studied. Experimental results from damaged Comp-B show an initiation threshold with a higher specific energy threshold than for the undamaged Comp-B, as shown in Fig 6.

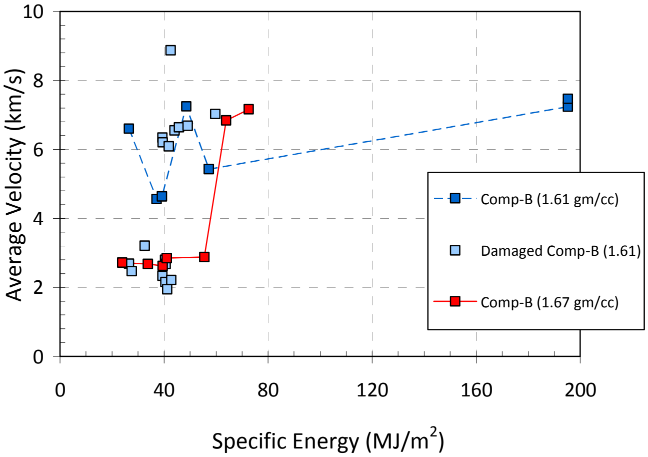

Fig 6. Density effects on Comp-B initiation threshold are observed, as well as the higher initiation threshold for damaged Comp-B.

The measurements on damaged Comp-B show considerable scatter in average velocity-vs-input energy for experiments near the initiation threshold. This scatter appears to be reasonable given that the material damage consists of cracks and voids with a length scale of several millimeters.

The moldable explosive family was investigated initially with a sandwiched billet configuration made with multiple layers of C2-thickness Primasheet 1000 (PETN), and 2000 (RDX) stacked and clamped together with the same arrangement of embedded PVDF shock sensors. Subsequent experiments with bulk moldable Composition C-4 used low density confinement rings to ensure a density of ρ=1.60 gm/cc with known sample thicknesses. The results for the moldable family are shown in Fig. 7, and listed in Tables 4, 5, and 6.

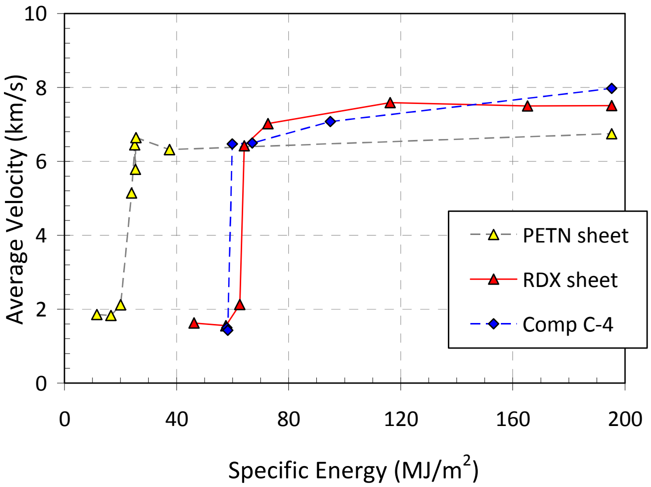

Fig. 7. Initiation thresholds for the moldable plastic explosive family, using both sheet and bulk material.

Table 4. Primasheet 1000 (PETN) results.

Impact Velocity (m/s)	Impact Energy (kJ)	Specific Energy (MJ/m^2)	Shock Velocity (km/s)
432	1.463	11.55	1.859
517	2.100	16.58	1.829
569	2.541	20.06	2.119
622	3.032	23.94	5.145
637	3.178	25.09	6.443
640	3.208	25.32	5.785
642	3.231	25.51	6.643
778	4.746	37.47	6.321
detonator	5.748	195.3	6.748

Table 5. Primasheet 2000 (RDX) results.

Impact Velocity (m/s)	Impact Energy (kJ)	Specific Energy (MJ/m^2)	Shock Velocity (km/s)
865	5.859	46.25	1.626
965	7.294	57.58	1.552
1006	7.927	62.58	2.130
1019	8.130	64.18	6.424
1083	9.201	72.63	7.021
1370	14.73	116.2	7.590
1634	20.93	165.2	7.497
detonator	5.748	195.3	7.506

Table 6. Composition C-4 results.

Impact Velocity (m/s)	Impact Energy (kJ)	Specific Energy (MJ/m^2)	Shock Velocity (km/s)
968	7.339	57.93	1.502
971	7.383	58.29	1.429
985	7.589	59.91	6.475
1041	8.488	67.00	6.498
1238	12.02	94.88	7.078
detonator	5.748	195.3	7.973

The initiation response of the moldable explosive family demonstrates well defined thresholds for the two RDX-based materials, and a more gradual threshold for the PETN material. The RDX-based Primasheet 2000 exhibits no increase in average shock velocity above specific energy levels of 116 MJ/m^2, with a lower detonation velocity than the Composition C-4.

Thermal Effects

The initiation of explosives is known to be effected by initial temperature. The cast Comp-B material was chosen as the candidate material to evaluate the effect of temperature on non-shock initiation. Controlled experiments were conducted on Comp-B at elevated temperatures in the vicinity of the melt region, 63 – 122C using a thin walled, mild steel housing that was designed to retain the same configuration as the ambient temperature experiments, while housing molten Comp-B at the same density (1.67 gm/cm^3). The effect of a mild steel housing was evaluated at ambient temperature in order to separate the effect of a steel housing from the effect of initial temperature. The results of those experiments are compared to ambient temperature tests, with and without a steel housing, as shown in Fig. 8.

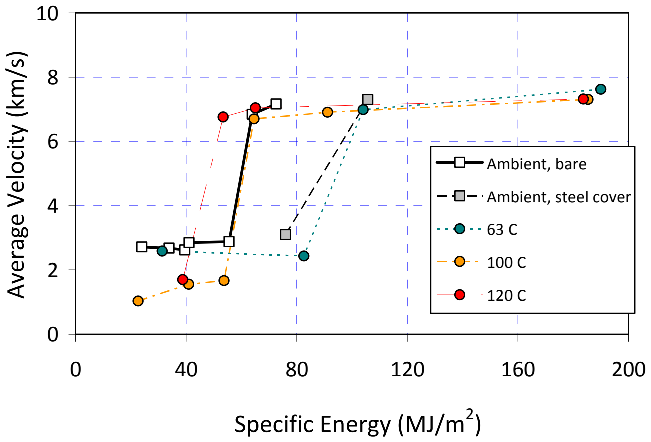

Fig 8. Thermal effect on initiation threshold of Comp-B.

The results of those elevated temperature experiments are listed in Tables 7, 8 and 9.

Table 7. Comp-B results at 63C.

Impact Velocity (m/s)	Impact Energy (kJ)	Specific Energy (MJ/m^2)	Shock Velocity (km/s)
707	3.965	31.30	2.589
1148	10.47	82.64	2.433
1289	13.18	104.1	6.984
1627	24.07	190.0	7.622

Table 8. Comp-B results at 102C.

Impact Velocity (m/s)	Impact Energy (kJ)	Specific Energy (MJ/m^2)	Shock Velocity (km/s)
601	2.866	22.63	1.033
808	5.186	40.94	1.554
926	6.806	53.73	1.667
1015	8.180	64.58	6.696
1206	11.55	91.18	6.904
1609	23.48	185.4	7.305

Table 8. Comp-B results at 122C.

Impact Velocity (m/s)	Impact Energy (kJ)	Specific Energy (MJ/m^2)	Shock Velocity (km/s)
786	4.909	38.75	1.698
903	6.765	53.41	6.755
1019	8.239	65.04	7.041
1597	23.27	183.7	7.316

The effect of initial temperature on non-shock initiation behavior was evaluated both above and below the 85C melt temperature of Comp-B. The observations show that as initial temperature is increased from ambient, there is a slight increase in the specific energy initiation threshold at 63C, followed by progressive decrease in the initiation threshold as the initial temperature is increased above the melt to 122C. For specific energy levels below the initiation threshold, the average shock velocity was observed to decrease at temperatures above the melt. External piezoelectric shock sensors observed a transient overshoot in velocity near the initiation transition region, similar to the ambient temperature experiments.

Summary

The initiation mechanism for ideal explosives subjected to impulsive loading from non-shock mechanical insults appears to be related to the input kinetic energy level and the material damage that is caused by shock and release wave interactions at the impact site that create additional surface area. For the experiments in the present study, the impulsive loading has sufficient time duration to compact this damaged material, initiating a DDT reaction, as evidenced by the transient super detonation velocities, which is observed for all explosive families at ambient temperature, and for Comp-B at elevated temperatures. The initiation thresholds are well defined for each explosive family. The cast Comp-B material with cracks and voids with a length scale of several millimeters appear to have a higher specific energy threshold for initiation, with more scatter than the undamaged Comp-B. The tests with RDX sheet material show that projectile impact at energy levels above 100 MJ/m^2 result in average velocities similar to the SDT initiation tests, even though the material experiences extensive damage from the shock loading and release profiles.

This study is directly coupled to the Damage-Initiated Reaction (DMGIR) model development, which has demonstrated the predictive capability to capture these effects.[5]

Acknowledgements

The authors would like to thank Matthew Heine, Shawn Parks, Jason Podsednik, Don Gilbert and Shirley Smith at Sandia and Dennis Grady at Applied Research Associates for their contributions to this research program. Sandia is a multiprogram laboratory operated by Sandia Corporation, a Lockheed Martin Company, for the United States Department of Energy's National Nuclear Security Administration under Contract DE-AC04-94AL85000.

References

1. Todd, S.N., "*Non-shock initiation model for plastic bonded explosive PBXN-5: empirical and theoretical results*", New Mexico Tech, PhD Dissertation, April 2007.
2. Anderson, M. U., et al, "*Prediction and data analysis of current pulses from impact-loaded piezoelectric polymers (PVDF)",* Shock Compression of Condensed Matter-1989, pp 805-808, 1990.
3. Anderson, M. U., et al, "*Non-Shock Initiation of the Plastic Bonded Explosive PBXN-5: Experimental Results",* Shock Compression of Condensed Matter-2007, pp 959-962, 2007.
4. Brown, G.W., *Dynamic and Quasi-static Measurements of PBXN-5 and Comp-B Explosives*, SEM 2009 Annual Conference and Exposition on Experimental and Applied Mechanics proceedings, June 2009.
5. Todd, S. N., et al, "*Non-Shock Initiation Model for Explosive Families: Numerical Results*", Shock Compression of Condensed Matter-2009, pp 361-364.

Proceedings of the SEM Annual Conference
June 7-10, 2010 Indianapolis, Indiana USA
©2010 Society for Experimental Mechanics Inc.

Modeling for Non-Shock Initiation

Steven N. Todd and Mark U. Anderson
PO Box 5800 MS1133
sntodd@sandia.gov, muander@sandia.gov
Sandia National Laboratories, Albuquerque, NM, 87185

Terry L. Caipen
Applied Research Associates, Inc., 4300 San Mateo Blvd. NE, Suite A-220,
Albuquerque, NM 87110
tcaipen@ara.com

Abstract. A model is being developed to include non-shock energy contributions to explosive detonation. This model does not attempt to include all possible specific initiation mechanisms at the mesoscale, but instead looks at cumulative energy in the explosive through experimental calibration of a small number of coefficients. Both shock pressure and shear stress are accounted for in the summation. The model is designed to be robust, fast-running, and relatively simple to calibrate. The model is implemented into the CTH wave code as an extension to the existing History Variable Reactive Burn (HVRB) model currently used for shock initiation. The expression in the extended model uses the functional form of the Johnson-Cook strength model, as that relation contains terms for confinement, strain and strain rate, which contribute to the overall energy deposition. This form is not unique, other expressions will be examined that may be more comprehensive, but the current relation has provided reasonable results.

INTRODUCTION

A non-shock initiation model has been developed for predicting initiation and growth of reaction in explosives subjected to a mechanical insult. The subsequent task of model validation is in progress. Motivation for this reaction model was based on the need to predict the response of various explosive materials to both shock, and non-shock mechanical insults. The model should also be relatively simple to calibrate, make use of existing codes to the greatest extent possible with minimal code changes, and run on a personal computer for simple geometries.

The DaMage Initiated Reaction” (DMGIR) model is based on existing features found in the CTH shock physics code at Sandia National Laboratories. The ability to predict explosive response to non-shock insults represents a notable change to the initiation and growth models presently used to address shock-to-detonation transitions (SDT). The distinguishing feature of the DMGIR model is the introduction of a damage variable, which relates the evolution of damage to the initiation of a reaction and subsequent growth to a detonation [1].

T. Proulx (ed.), *Dynamic Behavior of Materials, Volume 1*, Conference Proceedings of the Society for Experimental Mechanics Series, DOI 10.1007/978-1-4419-8228-5_26, © The Society for Experimental Mechanics, Inc. 2011

NUMERICAL APPROACH

The DMGIR model represents a modification of the History Variable Reactive Burn (HVRB) model that exists in the Sandia National Laboratories robust multi-material shock physics code CTH. The DMGIR model was embedded into CTH to use the well validated capabilities of CTH. Comparisons of DMGIR model predictions with recent experiments are presented for non-shock initiation experiments on the plastic bonded explosive PBXN-5 and cast Composition B. Further expansion of the model for plastic explosives is planned.

HISTORY VARIABLE REACTIVE BURN (HVRB) MODEL

The HVRB is a pressure–based model used to treat shock induced initiation that grows to a detonation for a heterogeneous explosive material. The HVRB is an extension of the Walker-Wasley relation for critical energy and is calibrated using results obtained in Pop plot experiments (run distance to detonation vs. shock pressure).

The HVRB model uses a mixture rule to yield the following equations of state,

$$P(\rho,T,\lambda) = P_U(\rho,T,)(1-\lambda) + P_R(\rho,T,)\lambda \qquad (1)$$

$$E(\rho,T,\lambda) = E_U(\rho,T,)(1-\lambda) + E_R(\rho,T,)\lambda \qquad (2)$$

where the subscript U identifies the equation of state for the unreacted (solid state) portion of the material and the subscript R identifies the equation of state for the reacted (gaseous state or detonation products) portion of the material. The parameter λ is the extent of reaction and represents the fractional amount of material in the reacted state. When the HVRB is used, the equations of state for the unreacted and reacted phases are usually the Mie–Grüneisen and JWL equations of state, respectively. Most pressure–based reaction models use the pressure–dependent rate law [2].

$$\frac{d\lambda}{dt} = A(1-\lambda)^m f(P) \qquad (3)$$

which sufficiently describes the shock initiation of heterogeneous explosives. The HRVB model uses a simplified version of equation (3),

$$\begin{aligned} \lambda(t) &= \min\left(1, \phi(t)^M\right) \\ &= 1 - \left[1 - \frac{\phi(t)^M}{X}\right]^X \qquad (4) \end{aligned}$$

and

$$\phi(t) = \frac{1}{\tau_0}\int_0^t \left[\frac{(P-P_I)}{P_R}\right]^Z dt \qquad (5)$$

where λ is the extent of reaction parameter, ϕ is the history variable, M controls the time delay to pressure buildup behind the shock wave, *X* governs the rate of reaction, τ_0 is a normalization constant set to $1\,\mu s$, *P* is pressure, P_i is the threshold pressure, P_R is the scaling pressure, and *Z* is the pressure exponent.

The history variable ϕ in equation (5) is dimensionless, and through its integration gives the pressure–time history imposed upon an explosive sample. The HVRB is calibrated by fitting the parameters P_I, P_R, and *Z* to Pop–plot data. The threshold pressure for initiation, P_I, is typically between *0.3* and *1.2 GPa* for a heterogeneous material. Equation (4) describes the reaction growth with time. As the history variable increases, the extent of reaction grows. Once $\lambda = 1$, the mixture equation of state reduces to the reacted–phase equation of state for the explosive [2].

MATERIAL MODELS

In computer codes that model explosive materials, the primary material behavior of interest is the reactive burn characteristics and not the strength or damage behavior. Therefore, there is a significant lack of mechanical response data available to aid the development of constitutive models that can accurately predict the behavior of explosives over a wide range of thermal and mechanical insults. One of the most commonly used constitutive models used in large deformation and hydrodynamic computer codes are the Johnson-Cook strength and fracture models. The Johnson-Cook strength and fracture models are relatively simple computational models used to show the material's behavior to dynamic conditions of large strains, high strain rates, high pressures, and high temperatures. Furthermore, one only needs static, quasi-static, and dynamic tension and torsion test data to obtain the five material constants for each model. Because of these features, Sandia National Laboratories (SNL) chose the Johnson-Cook Strength [equation (6)] and fracture [equation (7)] models to describe the mechanical behavior of PBXN-5 and Composition B-3 to impact insults at standard temperatures and pressures and at elevated temperatures. SNL contracted Los Alamos National Laboratories (LANL) to obtain compressive strength properties for PBXN-5 and Composition B-3 that provided sufficient data to obtain the material constants used in the Johnson-Cook strength and damage model [3]. Although the Johnson-Cook strength and damage model is mainly used for metals, Johnson and Holmquist [4] generate Johnson-Cook strength and damage material constants for 23 different materials, including two polymers.

$$Y = \underbrace{\left[A + B\varepsilon^{n}\right]}_{\substack{Yield\ and \\ Strain-Hardening}} \underbrace{\left[1 + C\ln\dot{\varepsilon}^{*}\right]}_{Strain-Rate} \underbrace{\left[1 - T^{*m}\right]}_{Temperature} \qquad (6)$$

$$\begin{aligned} D &= \sum \frac{\Delta\varepsilon}{\varepsilon_f}, \\ \varepsilon_f &= \underbrace{\left[D_1 + D_2\exp\left(D_3\sigma^{*}\right)\right]}_{pressure} * \\ &\qquad \underbrace{\left[1 + D_4\ln\dot{\varepsilon}^{*}\right]}_{strain-rate} \underbrace{\left[1 - D_5T^{*m}\right]}_{temperature} \end{aligned} \qquad (7)$$

For the Johnson-Cook strength model *A*, *B*, *C*, *n*, and *m* are material constants, ε is the equivalent plastic strain, $\varepsilon^* = \dot{\varepsilon}/\dot{\varepsilon}_0$ is the equivalent plastic strain-rate normalized to $\dot{\varepsilon}_0 = 1.0\,s^{-1}$, and T* is the homologous temperature. Additionally, in the Johnson-Cook damage model D_1, D_2, D_3, D_4, D_5, *m* are material constants, $\Delta\varepsilon$ is the increment of effective plastic strain during incremental loading, ε_f is the effective strain to failure, σ^* is the mean stress/effective stress $\left(\sigma_m/\sigma_{eff}\right)$, $\varepsilon^* = \dot{\varepsilon}/\dot{\varepsilon}_0$ is the equivalent plastic strain-rate normalized to $\dot{\varepsilon}_0 = 1.0\,s^{-1}$, and T* is the homologous temperature. An important benefit of the Johnson-Cook strength and damage model is that only static, quasi-static, and dynamic tension and torsion test data are needed to obtain the five material constants for each model.

DAMAGE INITIATED REACTION (DMGIR) MODEL

The DMGIR complements the HVRB by computing a second extent of reaction parameter

$$\lambda_D(t) = \min\left(1, D^M\right) = 1 - \left[1 - \frac{D^M}{X}\right]^X \qquad (8)$$

with a damage history variable

$$D = \int \frac{d\varepsilon}{\varepsilon_f} \qquad (9)$$

where $d\varepsilon$ is the incremental equivalent deviatoric plastic strain and ε_f is the equivalent failure strain. The equivalent failure strain retains the form of the Johnson – Cook fracture model,

$$\begin{aligned}\varepsilon_{fD} = & \underbrace{\left[D_{R1} + D_{R2}\exp\left(D_{R3}\sigma^*\right)\right]}_{pressure} \times \\ & \underbrace{\left[1 + D_{R4}\ln\dot{\varepsilon}^*\right]}_{strain-rate} \times \underbrace{\left[1 - D_{R5}T_R^{*m}\right]}_{temperature}\end{aligned} \qquad (10)$$

where D_{R1}, D_{R2}, D_{R3}, D_{R4}, and D_{R5} are material constants. Therefore, the DMGIR relates the evolution of damage to the initiation of reaction and the growth to a detonation. During numerical calculations preformed by CTH, the extent of reaction used is the higher value of λ_{HVRB} or λ_D for each time step and cell location to calculate the rate of reaction.

The Johnson-Cook damage model provides a functional form that includes strain-rate and temperature effects. Integrating the DMGIR into the existing CTH code is greatly facilitated by using the same computational form as an existing model, and was done to remain within cost and time constraints. Future work should include improvements to the functional form.

The experimental aspect of the DMGIR model development included gas and powder gun experiments using a 0.5-inch diameter projectile as shown in Figure 3 to impact an instrumented 4-inch diameter, 4-inch long test sample (Fig. 1). Shock sensors were embedded into the test sample as in Fig. 1 with results as shown in Fig. 2.

The projectile is designed so the rarefactions from the thin impact surface web and the radial edges rapidly limit the shock run distance while inducing considerable shear and damage.

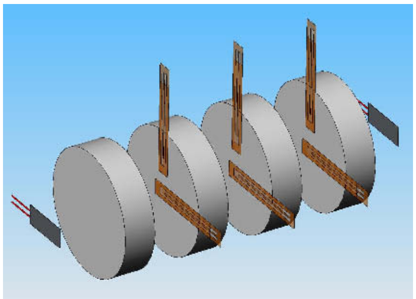

Fig. 1. Gauge arrangement.

Calibration of the model coefficients is currently performed using data from gun-projectile tests on explosive billets. X-T diagrams, such as Figure 5, are constructed from arrival time data at sensors imbedded at specified depths in the billet. For unconfined billets at ambient temperature, coefficients D_2, D_3, and D_5 do not contribute. A value of $D_1=5$ has been found to be reasonable, and the value of D_4 is determined by iteration. The iteration can be performed either to match a known projectile threshold velocity or to match a known initiation depth.

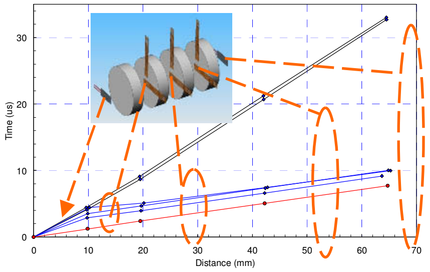

Fig. 2. General X-T diagram from an experiment.

Future configurations will involve confined targets and targets at elevated temperatures. The unused parameters D_2, D_3, and D_5 will be calibrated to these conditions.

RESULTS

Typically, the initiation and growth models used in SDT-type predictions initiate the explosive at a specific point, line, or plane, producing a steady detonation wave that propagates through the material, with the initiation criteria based on temperature and/or pressure. For these predictions, the material yield strength of the explosive is used. However, it often plays a minor role in the initiation process since the input shock strength is significantly larger than the yield strength. This assumption does not necessarily hold for non-shock impulsive loading conditions, where shear/mechanical damage of the explosive plays a greater role in the initiation process. A non-shock impulsive loading condition can be expected to subject the explosive material to shock and release wave interactions at the impact interface, where significant mechanical damage is experienced on the microsecond time scale during the initial portion of the impulsive loading. These shock and release wave (Fig. 3) interactions transform the solid explosive into a more porous explosive bed, drastically altering the initiation process.

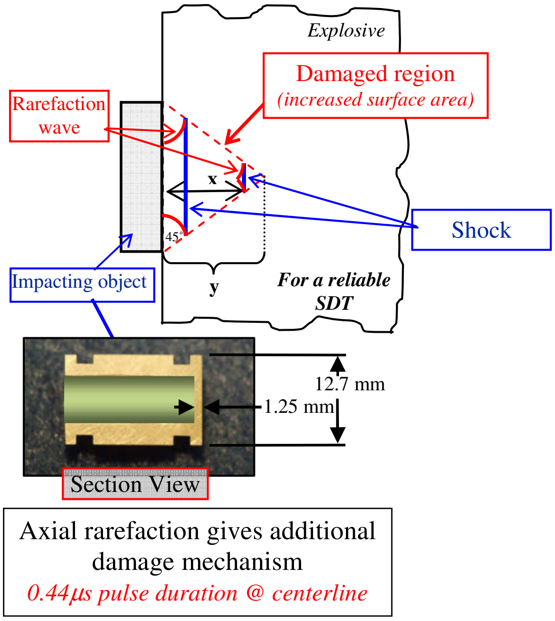
Explosive
Damaged region
(increased surface area)
Rarefaction wave
x
Shock
45°
Impacting object
y
For a reliable SDT
12.7 mm
1.25 mm
Section View
Axial rarefaction gives additional damage mechanism
0.44µs pulse duration @ centerline

Fig. 3. Projectile design and edge/axial relief diagram.

For a non-shock projectile test impact at 733 m/s, the DMGIR model predicts the transition from powder compaction through reactive growth to detonation at a run distance of ~ 10-mm as shown in Fig. 4. The image in Figure 4 shows materials on the left side of centerline, and the extent of reaction on the right side.

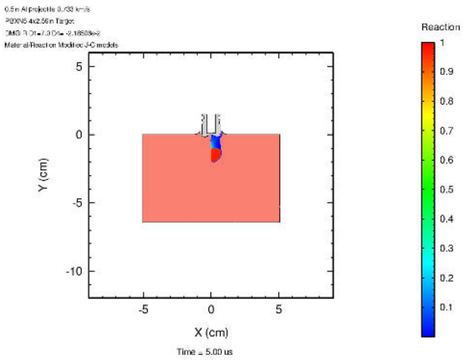

Fig. 4. DMGIR response for 733 m/s.

The HVRB model prediction at 733 m/s does not show agreement with either the transition region, or the growth to detonation behavior, demonstrating the importance of the damage tracking variable in the DMGIR model. However, the X-T results in Fig. 5 for the PBXN-5 impact experiment shows slightly later transition for the DMGIR (green) compared to that of the experiment (blue), but the DMGIR matches the growth to detonation closely. The HVRB (red) does not show damage initiation. A SDT-type initiation, where a boosted detonator provided the stimulus, is shown for comparison (brown) against the damage-induced initiation in Fig. 5.

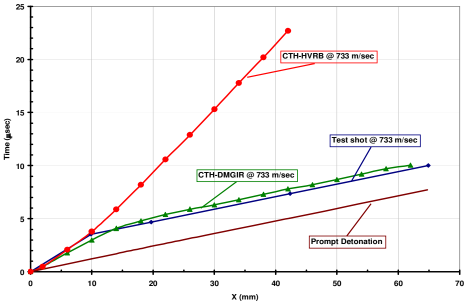

Fig. 5. X-T results for PBXN-5 impact experiment.

Table 1 shows the calculations of the minimum run distances required to generate an SDT with PBXN-5. As one can see, it takes a projectile velocity of 885 m/s or greater to generate an SDT. CTH runs with the HVRB alone show detonation at velocities equal or greater than 907 m/s.

Table 1. Minimum run distance for a shock wave to generate a SDT in PBXN-5.

Projectile impact vel. (m/s)	Interface pressures PBXN-5/PBX-9404 (GPa)	x (mm)	Transit time (ms)	x versus y
682	3.192/3.08*	8.98	2.50	x > 6.35
730	3.471/3.35*	7.92	2.16	x > 6.35
733	3.488/3.36*	7.87	2.14	x > 6.35
799	3.882/3.74*	6.70	1.78	x > 6.35
885	4.412/4.24*	5.54	1.42	x < 6.35

*based on $U = 2.494\left(km/s\right) + 2.093u$

During numerical calculations preformed by CTH, the extent of reaction uses the higher value of *D* or ϕ per cell/time step to calculate the fraction and rate of reaction. However, as shown in Figure 6, the DMGIR dominates the extent of reaction during the early stages or the evolution of damage. At a later point, the pressure (generated by the crush-up of the damaged material) and its duration are enough to allow the HVRB model to dominate the reaction process.

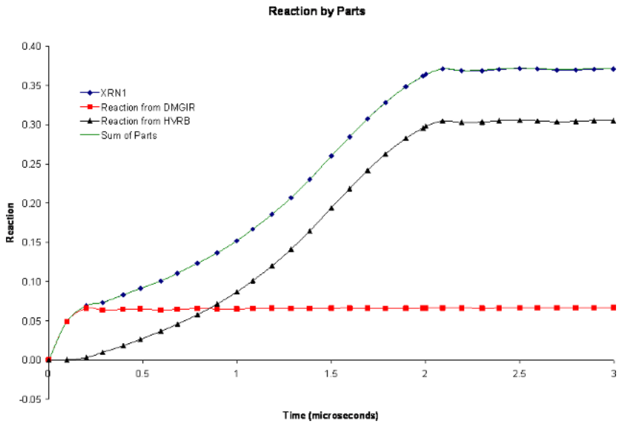

Fig. 6. Reaction by parts.

SUMMARY

During the evolution of damage in a reactive material, the induced damage generates new surfaces and void space. It is the crushing of this void space and related shear that dominates the beginning stages of the initiation process. The DMGIR model captures this initial portion of the process. The HVRB model captures the pressure increases due to hot spot coalescence, which may either produce a detonation or die out, leaving only mechanical damage. Many factors affect reaction growth, including material composition, geometry, rarefactions, void development, and others.

ACKNOWLEDGEMENT

The authors would like to thank Chance Hughs, Shawn Parks, Charles Jensen, and Mark Anderson for their contributions to this research program. Sandia is a multiprogram laboratory operated by Sandia Corporation, a Lockheed Martin Company, for the United States Department of Energy's National Nuclear Security Administration under Contract DE-AC04-94AL85000.

REFERENCES

1. Todd, S.N., Dissertation: *Non-Shock Model for Plastic Bonded Explosive PBXN–5: Empirical and Theoretical Results,* New Mexico Institute of Mining and Technology, April 2007.

2. Hertel, Eugene S. and Kerley, Gerald I., *CTH Reference Manual: The Equation of State Package*, SAND98-0947, pp 57-59, April 1998.

3. Rae, Philip J., *Compression Studies of PBXN-5 and Comp B as a function of Strain-Rate and Temperature*, Report, Los Alamos National Laboratories, July 2008.

4. Johnson, G. R. and Holmquist, T. J., *Test Data and Computational Strength and Fracture Model Constants for 23 Materials Subjected to Large Strains, High Strain Rates, and High Temperatures*, LA-11463-MS, Los Alamos National Laboratories, January 1989.

Proceedings of the SEM Annual Conference
June 7-10, 2010 Indianapolis, Indiana USA
©2010 Society for Experimental Mechanics Inc.

Stress and strain analysis of metal plates with holes

Biyu Hu, Sanichiro Yoshida and John Gaffney

Department of Chemistry and Physics, Southeastern Louisiana University

SLU 10878, Hammond, LA 70402, USA, Biyu.Hu@selu.edu

ABSTRACT For our long-term goal of understanding how metal connectors used for housing respond to hurricanes' wind load, we have conducted Finite Element Analysis (FEA) to compute the stress and strain distributions in tensile-loaded, aluminum and tin plates with holes. The specimen is 20 - 25 mm wide, 0.1 - 10 mm thick, and 100 mm long in the direction of the tensile axis along which two holes are drilled. In addition, we have conducted tensile experiment using an optical interferometer and analyzed the in-plane strain field. Comparison of the FEA and experiments indicate that band-like interferometric fringe patterns representing strain concentration coincide with the region where the von-Mises yield criterion is satisfied, and that the specimen fractures at the hole that shows more concentrated plastic strain. Experimental results show that in the tin samples the fracture lines run through the hole perpendicularly to the tensile axis, while in the aluminum samples the fracture lines run about 45 degrees to the tensile axis. Results of the corresponding FEA are consistent with this observation, showing that the plastic strain patterns observed in the tin samples are much more horizontal than those in the aluminum samples.

Key words: Finite Element Method, White Band, Plasticity

Introduction

Hurricanes are big disaster in coastal areas. To build a strong house to reduce the loss, it is necessary to understand how construction connectors respond to hurricane wind loads. Conventionally researchers employ empirical methods to assess the strength of metal connectors; they look at the stress-strain characteristics and estimate the maximum stress using the stress intensity factor for given geometries. In this study, we focus on the distributions of the deformation, stress and strain over the connectors. Generally speaking, if stress is distributed more evenly over the entire connector body, stress concentration into one specific spot is eased, and consequently, the level of maximum stress is reduced. In industry, due to mass production, a small material reduction can mean a great saving in production cost, as well as contributes to saving energy and natural resources. Thus it is important to find an optimum condition in designing connectors. The goal of the study is to characterize the stress and its distribution in metal connectors under external loads, and explore clues for optimum design parameters under given geometric conditions of connectors.

T. Proulx (ed.), *Dynamic Behavior of Materials, Volume 1*, Conference Proceedings of the Society for Experimental Mechanics Series,
DOI 10.1007/978-1-4419-8228-5_27, © The Society for Experimental Mechanics, Inc. 2011

To this end, we made finite element (FE) analysis on metal samples with holes under tensile loads. We started FEM analysis with simple models, and compared the simulation results with experiment for model validation. As for the experiment, we employed in-plane sensitive electronic speckle-pattern interferometry (ESPI) [1]. The advantage of this technique was that we could visualize strain distribution on a real time basis. After confirming that the simulation and experiment show reasonable agreement, we conducted FE analysis under various conditions varying the dimensions of the specimen to see how each parameter contributes to the reduction of stress concentration.

Background

Fracture mechanics has a long history. Conventional fracture mechanics [2] relies on stress concentration and stress intensity factors instead of stress distribution. These factors heavily depend on geometric conditions such as numbers of holes and width-hole-diameter ratio. However, experiments indicate that different patterns of fracture depending on conditions (e.g., aluminum fractures diagonally, tin fractures transversely). Therefore, it is important to look at stress distributions.

In industry, the test method of connector manufactures is not realistic. For instance, sometime, they test connectors only by monotonic loading test and asses the strength by a predefined stress value. For actual manufacturing, they multiply the design parameters obtained in this fashion with a safety factor. This does not represent realistic hurricane wind loads properly, and often the design requirement is too conservative leading to the use of the material for unnecessary amounts.

Our previous experiments based on optical interferometry (ESPI) indicate that when a bright pattern appears, regardless of the shape of the specimen, fracture occurs soon at the point where the bright spot appears [3-5]. In the case of metals with holes, an X shaped bright pattern appears around the hole. However, fracture mechanical conditions under which such a bright spot appears have not been understood. Through comparison the experimental results with Finite Element (FE) simulation, we found out that the appearance of X-bands is in good agreement with the timing and zone of equivalent plastic strain based on the von Mises yield condition [2].

Methodology

Both optical interferometry test and Finite Element Method (FEM) were applied to conduct this research. As the small equipment in our lab cannot conduct the experimental test under realistic conditions, we employed FEM to conduct numerical simulation. The small equipment is used to validate the FE model under simple conditions. Thus we divided this study into the following two steps.

Step 1: Validation of the FE model via comparison experimental test results with FE simulation solutions.

Experimental test

Figure 1 illustrates the experimental setup. A dual-beam, vertically sensitive Electron Speckle Pattern Interferometry (ESPI) interferometer was set up on the front side of the specimen attached to a test machine. The light source of the interferometer was a 0.5mW helium-neon laser. The specimen was a rectangular tin alloy plate with a hole at the center of the plate. The plate was a 100 mm long, 20 mm wide and 0.4 mm thick. The diameter of the hole was 2mm, which was 10% of the width. A charge coupled device (CCD) camera took the image of the specimen at a rate of 30 frame/s, and a frame grabber stored all the image data into computer memory at the same frame rate. By subtracting the image taken at each time step from the image taken at the following time step, we formed interferometric fringe patterns. Here each fringe patterns represents the displacements of all the points on the sample caused by the deformation that the sample experiences during the interval between the two time steps. The interferometer was sensitive to horizontal displacement.

In this step, we built a simple model to validate the FE analysis. The specimen was the tin plate with one hole at the center. In the experiment, we applied a tensile load at a constant crosshead speed of typically 0.02 mm/s to the tin plate. Fig. 2 shows fringe images at four representative points along with the corresponding loading curve. The four points are labeled A – D, and their locations are indicated on the loading curve.

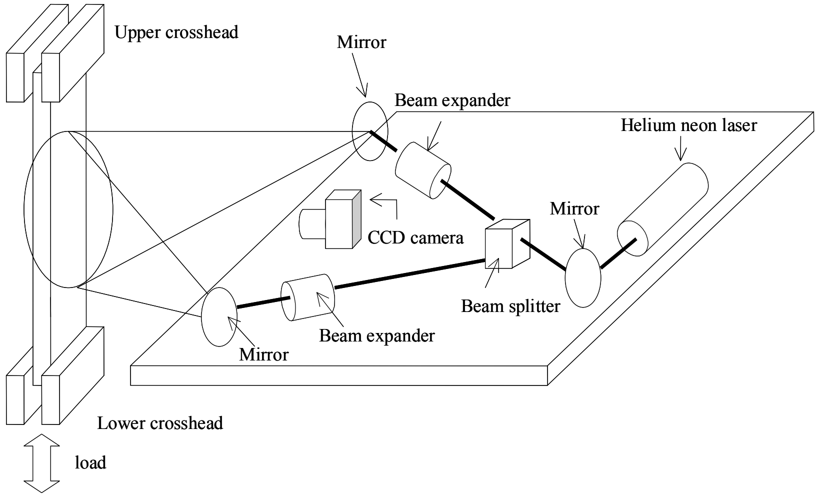

Fig. 1. Experimental setup

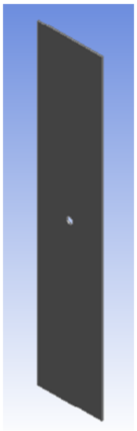

Fig.3. Metal plate with one hole

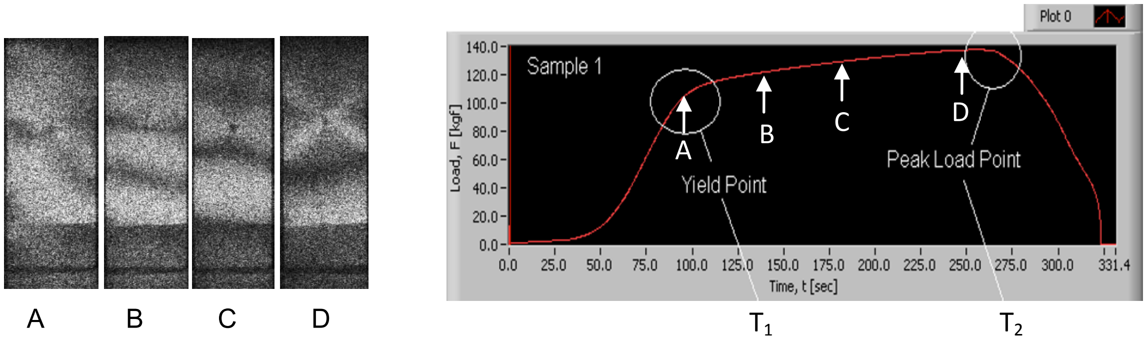

Fig. 2 Four fringe patterns (left) and corresponding points on the loading curve (right). The clock of the FEM simulation was synchronized with the experiment at the yield point and maximum stress point (labeled T_1 and T_2, respectively, in the figure).

The interferometric fringes shown in Fig. 2 represent contours of equi-horizontal-displacement (because the interferometer is sensitive to horizontal displacement). Generally speaking, therefore, vertically parallel fringes indicate that the displacement is constant along the vertical axis, hence the specimen experiences uniform stretch or compression in the horizontal direction, whereas horizontally parallel fringes indicate that the specimen experience either pure shear or rotation. During elastic deformation of a tensile test, fringes representing horizontal displacement normally show the vertical parallel pattern because the material deforms uniformly causing the specimen to compress uniformly.

Fringe A was taken when the stress level is about to reach the yield point, i.e., the beginning of plastic deformation. As expected, the fringes show the transitional stage from vertically parallel to the horizontally parallel pattern (the above-mentioned pure compression due to elastic deformation to shear or rotation in the plastic regime). Fringe B was taken after the stress passes the yield point. It is seen that the fringes are more horizontally parallel, indicating that the degree of plasticity increases so that the deformation is more shear/rotation dominating. (There is no way to distinguish the horizontally parallel fringe due to pure shear from pure rotation from the fringe patterns). Fringe C was taken when the deformation further developed toward the maximum stress level. The fringes appear to be concentrated towards the hole. In other words, the fringe density becomes denser near the hole as compared with away from the hole. Denser fringe represents higher strain, and this observation can be interpreted as the stress is getting concentrated around the hole at this stage. Finally, slightly before the stress reaches the maximum point, the fringe density becomes so high that the pattern appears to be a conspicuous X-shaped bright bands crossing at the hole. We compared the experimental fringe patters with corresponding FEM analysis at these four representative points, as discussed below.

Finite Element Analysis

We built a three-dimensional FE model (Fig. 3) to simulate the above-mentioned tensile experiment with the tin specimen. The Young's modulus and Poisson ratio used for this simulation were 50 GPa and 0.36. To simulate the tensile experiment, we fixed the bottom surface of the specimen stationary and displaced the top surface at a constant speed. To model plasticity of the plate, we used experimentally observed stress-strain characteristics as input to the FE model. In addition, we synchronized clock of the FEM code with the actual time as indicated in Fig. 2. We computed plastic strain (equivalent strain based on von Mises yield criterion), equivalent stress, and deformation. In Fig.4, we show the results of FEM simulation at the above four representative points A, B, C and D to compare with the experiment. The comparison leads to the following findings.

1. The FEM result indicates that starting at point A, concentrated plastic strain develops from the edge of the hole toward the edges of the specimen.
2. At point C, the computed deformation starts to be concentrated around the hole. This is similar to the experimental fringes get concentrated around the hole (Fig. 2 C).
3. At point D where the experimental fringe image shows the bright X-shaped band patters, the FEM result shows the equivalent plastic strain concentrated around the hole bridges the specimen transversally. Moreover, the shape of the concentrated plastic strain pattern is very similar to the experimental bright pattern.
4. The computed plastic stress pattern drastically changes from point C to D, indicating that the appearance of the bridged X-shaped strain concentration, hence the appearance of the experimentally observed X-shaped bright pattern, is abrupt.
5. Since the FE model uses the von Mises yield criterion to compute the equivalent plastic strain, the resemblance between the experiment and FEM at point D strongly indicates that the X-shaped bright pattern observed in fringe image represents the von Mises yield criterion.

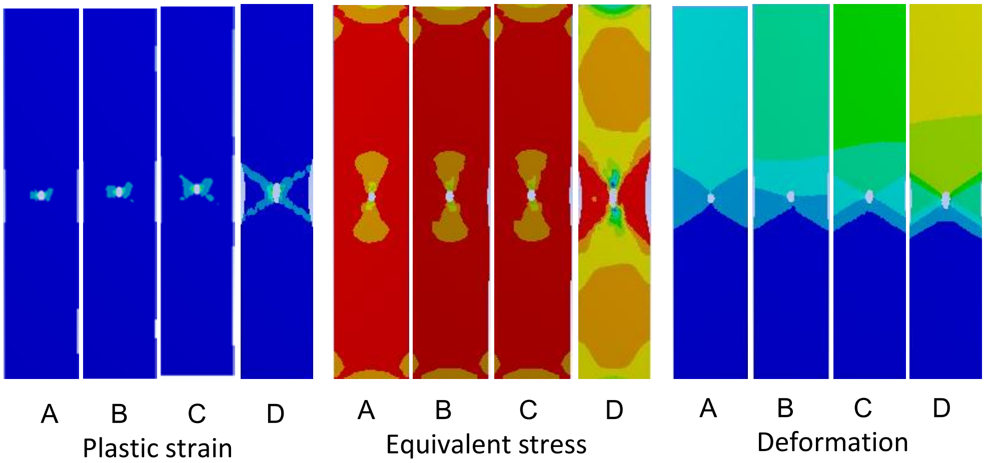

Fig. 4 Results of FEM simulation at the four critical points

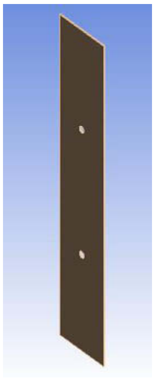

Fig.5. Metal plate with 2 holes

We next conducted similar investigation using tin and aluminum specimens with two holes, and found the following observations. See Fig. 6.

1. FE simulation results always indicated that under the present condition the strain was concentrated at the lower hole for tin and the upper hole for aluminum. Experiment showed the tin and aluminum specimens dominantly fractures at the same hole as the simulation. The reason is not clear at this point.
2. In experiment, the fracture line of the tin specimen was always horizontal while the fracture line of the aluminum specimen was always diagonal. The corresponding simulation showed that the concentrated plastic strain of the tin specimen was much more horizontal than the concentrated plastic strain.

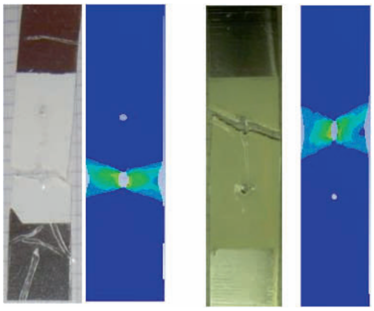

Fig. 6.1 (tin) Fig. 6.2 (Al)

Fig. 6. Fracutre on the plate (Left), plastic strain pattern(Right)

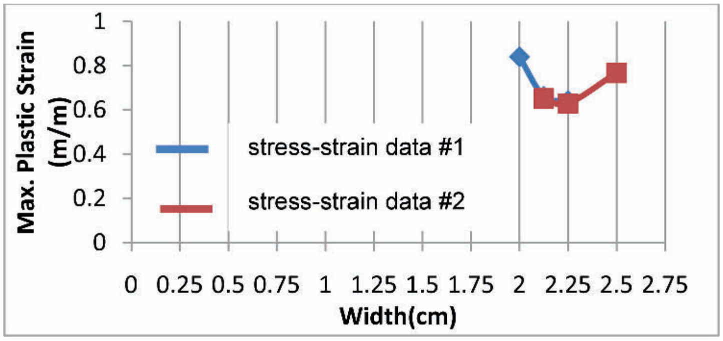

Fig. 8 Max. plastic strain value vs. Width of the plate

Design optimization

In this step, we varied the thickness, width and the number and location of the hole on the tin and aluminum plates respectively to find out the condition where the plastic strain was most uniformly distributed over the specimen. Fig. 7 shows the plastic strain patterns computed under the various thicknesses shown in table 1 (0.005 cm – 0.4 cm) where the other dimensions were kept constant. Note that the more evenly distributed the plastic strain, the less the maximum strain. Thus we judged that under this condition, the thickness of 0.04 cm was optimum. In this particular case, the least maximum plastic strain of 0.48 was observed when the thickness was 0.04 cm and the plastic strain was most evenly distributed.

Table 1. Max. plastic strain values vs. thickness

Thickness(cm)	0.005	0.01	0.02	0.04	0.08	0.16	0.2	0.32	0.4
Max. plastic strain Value (m/m)	1.154	1.2495	0.88956	0.47891	0.52941	0.96478	0.94516	0.91811	0.9134

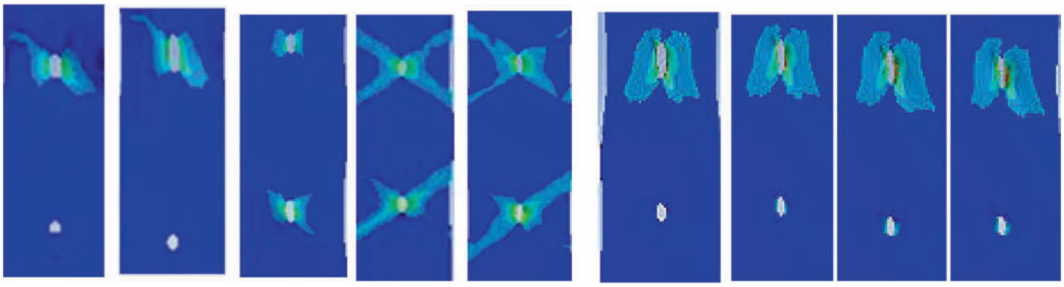

Fig. 7. Plastic strain patterns

To investigate the effect of the width of the plate on the plastic strain, we varied the width in the range of 2.0 cm to 2.5cm. Two series experimental observed are applied to conduct the simulations. The maximum plastic strain values are shown on Fig. 8 where the results with the two stress-strain data show very similar dependence on the specimen width. The maximum plastic strain was lowest when the width was 2.25 cm.

To investigate the effect of the location of the hole on the plastic strain, we moved the single hole along the central axis of the plate as shown in Fig. 9. Three series of simulations with width of 2.0cm.2.25cm and 2.5cm were conducted and the maximum plastic strain values of each width are shown in Figure10.

It is observed from the graph in Figure 10, when the width of the plate is 2.25 cm, the average maximum plastic strain value is the lowest, which consistent with Figure 8.

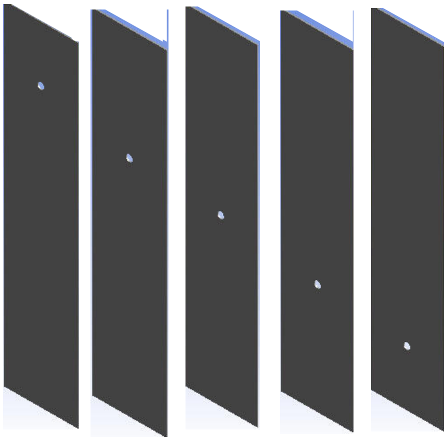

Fig. 9. Plates with different location of the hole

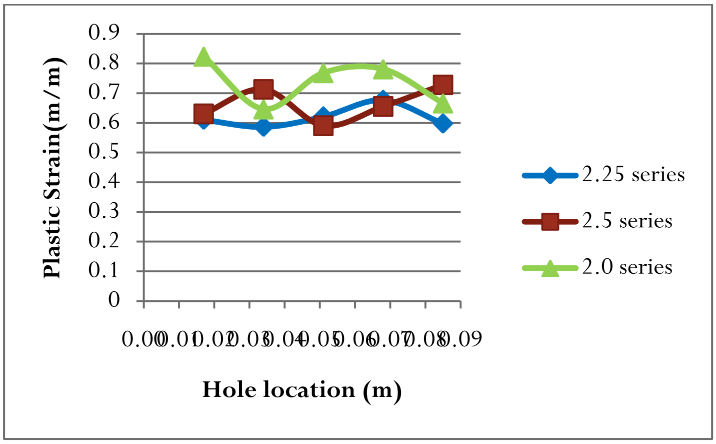

Fig.10. Plastic strain value vs. location of hole

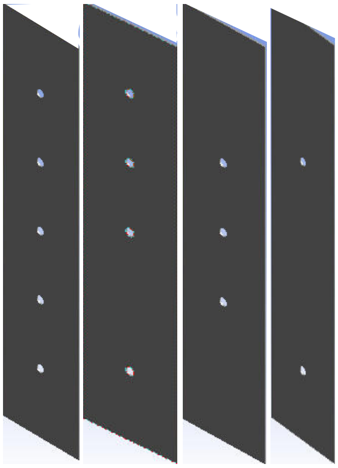

Fig.11. Plates with different numbers of hole

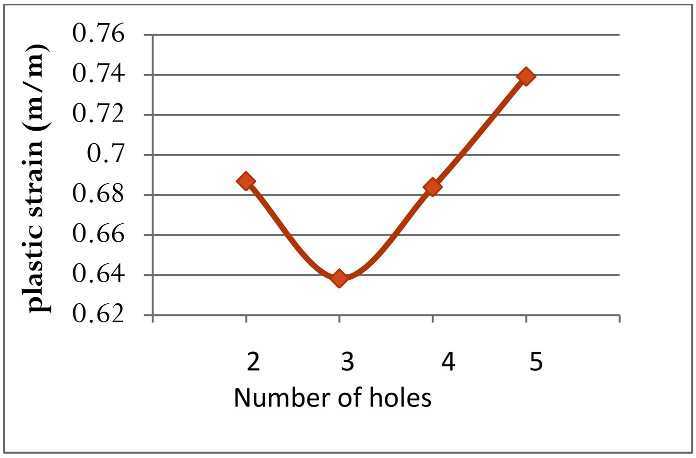

Fig.12. Plastic strain vs. number of hole

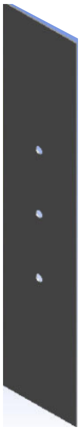

Fig.13. Optimum design

To investigate the effect of the number of the hole on the plastic strain values, the FE simulations with 2 holes, 3 holes, 4 holes and 5 holes (Fig. 11) are conducted and the maximum plastic strain value of each simulation is shown in Fig. 12. It is observed from Fig. 12 that when the number of the hole is 3, the maximum plastic strain value is the lowest.

The above results show that under the given condition, the optimal design of the connector for a given hole diameter are: thickness = 0.04 cm, width = 2.25 cm and number of holes = 3. Fig.13 shows the shape of this optimum design.

Conclusions

We built finite element models of thin plates with holes to investigate the behavior of the plate when external tensile loads are applied. To validate the models, we conducted experiment using optical interferometry.

Experimental and finite element simulations basically show good agreement in terms of strain distribution and other parameter investigated. In addition, comparison of experimental and theoretical plastic strain indicates that the previously observed bright interferometric band pattern is most likely represents the von Mises yield criterion. The subsequent simulation studies we conducted varying geometric parameters such as the plate's dimensions and holes location indicate that it is possible to reduce the level of maximum stress and that when the stress is more evenly distributed the maximum stress level is minimized. Although this optimization is limited to the presently given condition, the results of this study provide some insights for optimization for general cases.

Acknowledgement

We are grateful for the financial support by the Southeastern Louisiana University Alumni Association and College of Science and Technology.

References

1. O. J. Løkberg, "Recent Developments in Video Speckle Interferometry," in *Speckle Metrology*, R. S. Sirohi, ed Optical Engineering, Vol. 38, Marcel Dekker, New York, Basel, Hong Kong, pp. 157-194 (1993)
2. A. S. Teelman and A. J. McEvily, Jr., *Fracture of structural materials*, John Wliley & Sons, Inc., New York (1967)
3. Sanichiro Yoshida*, Muchiar, I. Muhamad, R. Widiastuti and A. Kusnowo, "Optical interferometric technique for deformation analysis", Opt. Exp. 2, 13, 516-530 (1998)
4. S. Yoshida, H. Ishii, K. Ichinose, K. Gomi, K. Taniuchi, "Observation of Optical Interferometric Band Structure Representing Plastic Deformation Front under Cyclic Loading", Jap. J. of Appl. Phys. 43, 8A, 2004, 5451-5454 (2004).
5. S. Yoshida, S. Toyooka, "Field theoretical interpretation of dynamics of plastic deformation- Portevin –Le Chatelie effect and propagation of shear band", J. Phys: Condensed Matter 13, 6741-6757 (2001).

Proceedings of the SEM Annual Conference
June 7-10, 2010 Indianapolis, Indiana USA
©2010 Society for Experimental Mechanics Inc.

Impact Response of PC/PMMA Composites

C. Allan Gunnarsson
allan.gunnarsson@us.army.mil

Tusit Weerasooriya
tusitw@us.army.mil

Paul Moy
pmoy@us.army.mil

Army Research Laboratory
Aberdeen Proving Ground, MD 21005-5069

ABSTRACT

Polycarbonate (PC) and polymethyl-methacrylate (PMMA) are commonly used materials for transparent protection. For increased effectiveness against impact, PC and PMMA are typically sandwiched and bonded in multiple layers of varying thicknesses to create a composite laminate. To develop high fidelity simulation methodologies for impact behavior for this type of laminated construction, panels were fabricated with different layers of PC and PMMA, on which blunt impact experiments were conducted. A high speed digital image correlation (DIC) technique was used to obtain full-field deformation measurements including out-of-plane displacement and surface strain. The experimental results are used to evaluate constitutive models and simulation methods for these various configurations of PC/PMMA composite laminates. In this paper, experimental technique and results are presented.

INTRODUCTION

Polycarbonate (PC) and polymethyl-methacrylate (PMMA) are the mostly widely used materials for transparent protection. These materials are found in applications for the aerospace and automotive industries, safety glasses, and household windows. Some of the advantages these classes of amorphous glassy polymers have are being lightweight and possessing exceptional clarity as well as their ability to be molded into various shapes and sizes. In addition to these properties, these polymers are used in applications where impact resistance is important because of their high impact strength characteristics.

PC is a thermoplastic polymer that is easily molded and thermoformed. This is due in part to the low glass transition temperature (T_g) of 150°C and melting point of about 267°C [1-2]. The glass transition temperature is the temperature at which an amorphous solid, such as glass or a polymer, becomes brittle on cooling, or soft on heating [3]. The typical density of PC is about 1.21 g/cm^3.

PC has been extensively investigated over the past decades for its toughness, tensile, and compressive strengths. The mechanical properties of polymers are dependent upon two key factors, the rate of deformation and temperature. Polymers, tested at high rates of strain, typically have an increase of the yield strength and the modulus and a decrease in strain to failure when compared to low strain rate results [4, 5].

Work by Moy et al [6] showed that PC is rate sensitive under uniaxial compression. Their research indicates a softening after yielding, followed by a strain hardening phase at low and high strain rates. Mulliken et al [7] reported similar behavior of PC at high strain rates. Their work also included DMA analyses for PC and PMMA to

T. Proulx (ed.), *Dynamic Behavior of Materials, Volume 1*, Conference Proceedings of the Society for Experimental Mechanics Series,
DOI 10.1007/978-1-4419-8228-5_28, © The Society for Experimental Mechanics, Inc. 2011

characterize the viscoelastic behavior for these thermoplastics. Another polymer study by Hall [8] reports that the temperature increases during deformation at high strain rate, whereas no appreciable temperature change occurs during deformation at lower rates. Work by Walley et al [9] has shown that the strain rate and temperature affects the strain hardening behavior of glassy polymers. For both PC and PMMA, Arruda et al [10] and Boyce et al [11, 12] have proposed material models to predict the deformation response for differing strain rates.

PMMA, like PC, is another thermoplastic polymer that is easily molded and thermoformed, and frequently used as a glass substitute due to its ease of manufacturing into complex shapes and clarity at large thickness (greater than 25 mm). It has comparable manufacturing properties and density as PC. PMMA differs from PC in that it behaves in a much more brittle manner when it fails. This brittle failure behavior allows dissipation of energy during impact into cracking. PC, by comparison, is relatively ductile; even when penetrated, it does not fail completely but rather exhibits a “puncture” or tear in the material.

Like its counterpart, PMMA has also been studied to determine its mechanical properties, such as tensile and compressive strengths. Work by Moy et al [13] measured the effect of strain rate on the mechanical properties and failure behavior of PMMA. Their work showed that both modulus and yield strength increased with increasing strain rate, and the failure strain is inversely related to strain rate.

Each of these materials has its own unique beneficial characteristics. Because of this, laminated multi-layered PC and PMMA systems together provide an exceptional transparent protection system with energy dissipation combined with ductility. Hsieh et al [14] conducted V_{50} studies on various layer configurations and material thicknesses with the 0.22 cal fsp (fragmented simulator projectile). Simulating their ballistic experiments, Fountzoulas et al [15] were able predict the observed cracks patterns in the PMMA as well as its V_{50} impact velocity. Typically these multi-layered laminate are bonded together with a polyurethane resin. As such, these resins have also been investigated by Stenzler [16] to determine their impact mechanics.

The research efforts to obtain the constitutive behavior of PC and PMMA experimentally and the development of material models for these materials are well documented. However, the validation of these material models requires a different type of experimental data from the ones used to construct the constitutive model. Therefore, as a compliment to modeling efforts related to impact, an experimental technique was developed to obtain quantitative data under impact loading conditions for PC panels by Gunnarsson et al [17]. This type of data is essential for validation or refinement of the transient deformation and, eventually, failure prediction produced by models. The impact experiments conducted in this report utilize digital image correlation (DIC) as the primary method of instrumentation and measurement [18-22].

DIC is a non-contact, optical technique that tracks the surface deformation of an object under load. This method provides full-field as well as out-of-plane measurements. For DIC, a speckle-like pattern is directly applied to the surface of the sample. The pattern is typically produced by using consumer spray paint of black and white, which offers the best contrast for the monochromatic cameras that were used for the impact experiments. Two high-speed digital cameras, in a stereoscopic setup, captured the deformation of the speckled surface. Thus, the dual camera setup provides images for out-of-plane measurements.

This work extends previous work that was conducted to study impact on single PC panels of varying thicknesses [17]. For increased effectiveness against impact, PC and PMMA are typically sandwiched together and bonded in several layers and thicknesses to create a composite laminate. It is the intent of this work to investigate the impact response of several very basic composite configurations of PC and PMMA. These configurations are described in detail below, and mostly unbonded. The purpose of this work is to validate simulation results using these polymer materials; therefore, it is necessary to investigate basic configurations initially. The measured out-of-plane transient displacement results for these composites are presented here. Future work will extend this to more complicated configurations, including bonding.

Additionally, the transient impact response, for 5.85 mm thick single PMMA panels is studied, as well as the failure velocity. This is done to ensure that the impact response is fully understood for the component materials of the composite configurations; this has been done previously for PC [17]. Determination of the failure velocity is necessary to ensure non-penetration during DIC impact experiments; the transient impact response is necessary to evaluate the material models for PMMA. The measured transient out-of-plane displacement results are presented in this paper, as well as the experimentally determined failure velocity.

EXPERIMENTAL PROCEDURE

Target Preparation

The individual PC and PMMA panels were acquired from a local distributor Sabic Polymer-Shapes (Jessup, Maryland). The PC is a commercial product made by Sheffield Plastics, of Bayer MaterialScience, named Makrolon. The PMMA is a commercial product of Cyro Industries, and its name is Acrylite FF. The size of each panel was 305 mm by 305 mm and 5.85 mm thick. The speckle pattern required for DIC was created on the back surface of the panels by spray painting the back side of the panel surface completely white and then adding random black dots (or speckles) with a coarse application of black spray paint. A panel with applied speckle pattern is shown in Figure 1.

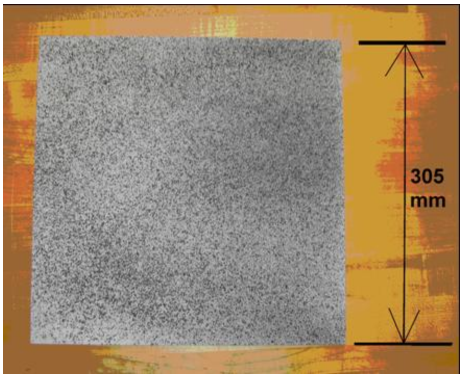

Figure 1. Test Panel with Speckle Pattern for DIC

Composite Configuration

DIC experiments were performed on several different configurations of PC/PMMA composites, as well as single 5.85 mm thick PMMA panels. A graphical summary of the six different configurations from side view is shown in Figure 2, along with an arrow indicating the direction of projectile impact. PMMA is denoted by the letter “M”, PC is denoted by the letter “C”, and the adhesive is denoted by the letter “A”. Configuration C consists of one single panel of 12.32 mm (0.485 in) thick PC. This configuration has been tested previously, and provides reference data to which the other composite configurations can be compared to. Configuration CC consists of two panels of 5.85 mm (0.230”) thick PC mounted together with no bonding agent between them. Configuration CAC consists of two panels of 5.85 mm thick PC bonded together using Deerfield 4700, a thermoplastic polyurethane commonly used to join transparent materials. The panels and polyurethane were vacuum packed, and then pressed and heated using an autoclave. Configuration MC consists of one panel of 5.85 mm thick PC mounted together with one panel of 5.85 mm thick PMMA, with the PMMA being impacted. Configuration CM consists of one panel of 5.85 mm thick PC mounted together with one panel of 5.85 mm thick PMMA, with the PC being impacted. Configuration CMC consists of one panel of 5.85 mm thick PMMA sandwiched between two 5.85 mm thick PC panels. The projectile impacts one of the PC panels.

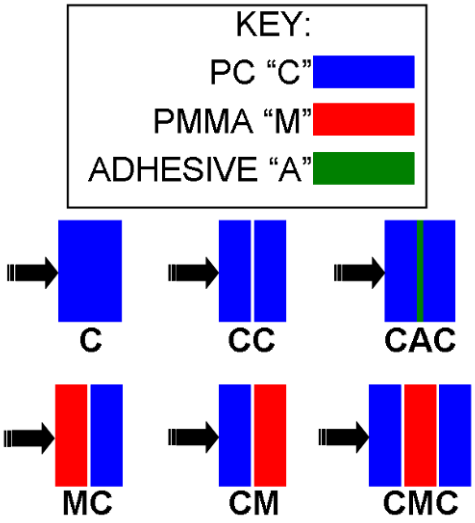

Figure 2. PC/PMMA Composite Configuration Graphical Summary

Mounting

During the impact experiments, the target panels were clamped between an aluminum mounting frame and an aluminum support. The aluminum support increased distribution of the clamping force along the perimeter of the panel. The frame and the support had outside dimensions identical to the targets (305 mm by 305 mm) and were 25.4 mm (1.00 in) thick, leaving a 254 mm by 254 mm (10 in by 10 in) area of the target that was exposed to the camera. The mounting system holds the panels so that the projectile will impact normal to the panel surface. The target panels were aligned so that the impact point is at the center of the panel using a targeting laser inserted into the gun bore. The mounting system of the panels is shown in Figure 3.

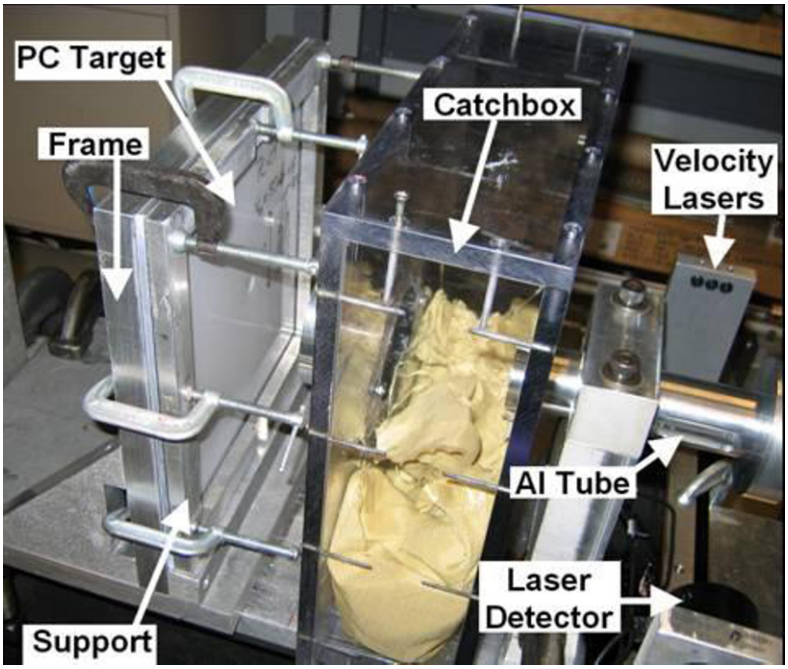
PC Target
Frame
Catchbox
Velocity Lasers
Al Tube
Laser Detector
Support

Figure 3. Composite Mounting Setup for Impact Experiments

Projectile

The impact experiments were conducted using a gas gun with a 25.4 mm diameter bore. The projectile was a Maraging 350 steel rod with hemispherical impact end inserted into an acrylic sabot. The total projectile mass (including sabot) was 104 grams. The projectile was 76.2 mm (3.00 in) long and the hemispherical impact end had a radius of 6.35 mm. The geometry and dimensions can be seen in Figure 4.

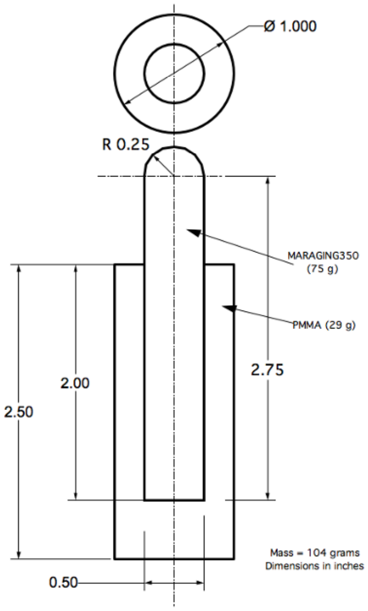
Ø 1.000
R 0.25
MARAGING350
(75 g)
PMMA (29 g)
2.75
2.00
2.50
0.50
Mass = 104 grams
Dimensions in inches

Figure 4. Projectile Geometry and Dimensions

An inert gas (N_2) filled breech was used to propel the projectile to the target. The gas gun was fired remotely, using a fast acting solenoid valve. During DIC testing, the projectile did not penetrate the target and rebounds off the target into the catch-box. To determine the failure velocity, the projectile would penetrate the target and then encounter a secondary catch box filled with unpacked filler to stop it.

Velocity Measurement

A three laser and detector system allow the projectile velocity to be measured during these impact experiments. Interruption of any of the laser beams by the projectile produced a change in output voltage of the detector. A digital oscilloscope is used to record the detector output voltage as the three laser beams are interrupted by the projectile. The times between the step changes in detector output voltage are used with the pre-measured distance between beams to calculate projectile velocity. The oscilloscope also acts as the trigger mechanism for the high-speed digital cameras, sending a TTL pulse to them when the first beam is interrupted.

Camera Setup and DIC Measurement

The DIC system used in these impact experiments consisted of two Photron APX-RS high-speed digital cameras connected to a Windows laptop. The proprietary Photron camera software was used to set-up the cameras and retrieve the back surface images of the panel after impact. After testing, the images from the cameras were post-processed using commercial DIC software from Correlated Solutions Inc. to obtain the three dimensional displacement data of the back-surface of the panel.

The cameras were setup to record at a frame rate of 30,000 frames per second. This frame rate permitted a maximum resolution of 256 by 256 pixels to be used for the images. This provided a good balance between image resolution within the field of view and the number of frames needed to record the relevant impact event. The exposure time was set to the maximum available to allow as much light as possible for the cameras. Sufficient lighting levels were achieved using a light stand that consisted of eight 250W halogen bulbs.

The necessary physical attributes of the cameras, such as focal length and relative position, were determined using the built in calibration feature of the DIC software by capturing several dozen pictures of a special calibration grid. After inputting the grid properties, such as grid spacing and size, the software calculated the attributes. Once calibrated, the software analyzed the speckle pattern present in the area of interest of every picture and calculated the full-field displacement, deformation, and strains (ε_{xx}, ε_{yy}, ε_{xy}, and, ε_1 and ε_2). A schematic of the data acquisition setup is depicted in Figure 5.

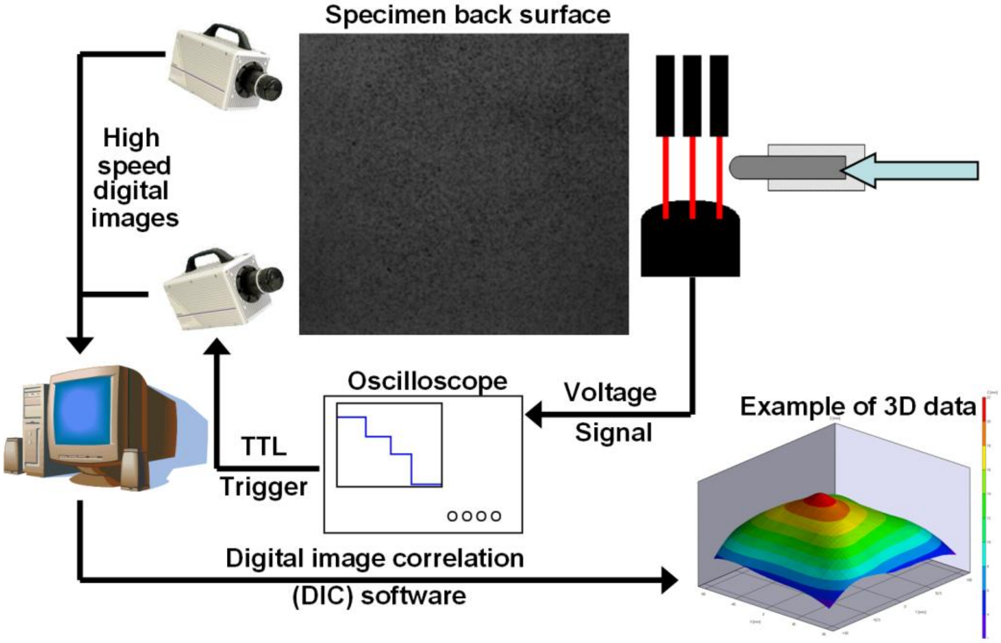

Figure 5. Schematic of Impact Setup using DIC for Back Surface Measurements

RESULTS AND DISCUSSION

PMMA Impact Response and Failure

Experiments were conducted on 5.85 mm (0.23 in) thick PMMA panels to obtain the velocity required for failure. It was found, by incrementally varying impact velocity, that the PMMA panel would fail at an impact velocity of approximately 15 m/s for this projectile mass and geometry. For comparison, the penetration velocity for 5.85 mm thick PC is approximately 80 m/s. This is not surprising as PMMA is brittle, and behaves similarly to glass. During impact, cracks would form and then the panel would shatter. This is contrasted with PC, which is ductile and does not exhibit cracking. During penetration, the PC showed only a small tear in the material. Examples of the failure of the two materials can be seen below in Figure 6, with the failed PMMA on the left and the penetrated PC on the right. However, PC can act in a brittle manner at high velocities; this is known as embrittlement. Similarly, at high velocities, it is possible for PMMA to behave in a ductile manner.

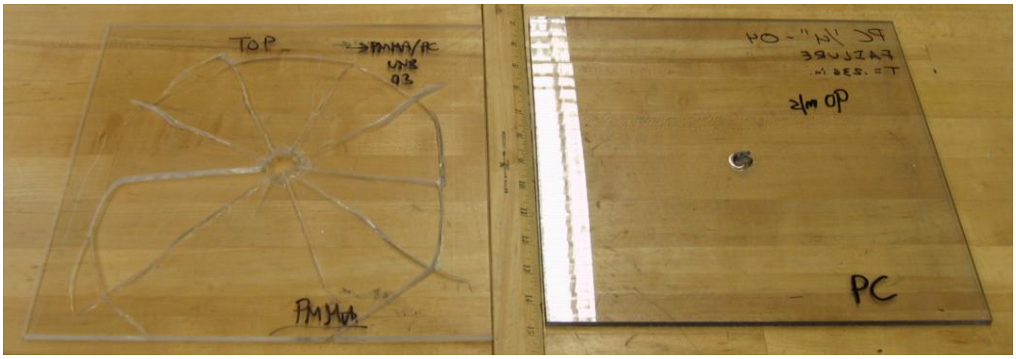

Figure 6. Example of Failed PMMA (left) and PC (right)

The transient deformation data generated by the DIC was used to determine how single 5.85 mm thick PMMA panels behaved during blunt impact. The DIC data is presented both graphically and numerically. The maximum displacement in full-field 2-D and 3-D contour plots at impact velocity of 11.8 m/s for PMMA are shown below in Figure 7(a) and 7(b), respectively. Both contour plots show the maximum out-of-plane displacement (z-direction), which occurs 1.40 ms after impact. In 2-D (a), the deformed image is overlaid with the corresponding full-field deformation map, whereas the 3-D contour (b) is displayed on an x-y-z coordinate axes plot. The 3-D surface map is the same equivalent xy area as the 2-D overlay and not a full representation of the entire PC panel. The z-scale is not proportional to the x-y axes and thus the exaggerated profile in the z-direction. These graphical data are shown here as representations typical of the data acquired for all of the experiments performed.

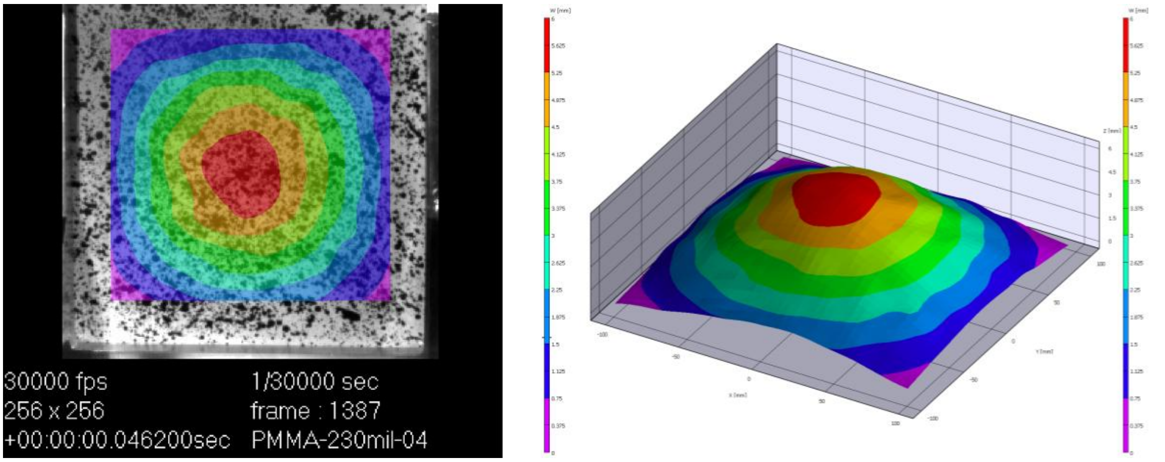

(a) (b)

Figure 7. (a) 2-D and (b) 3-D Maximum Displacement Contour Plots for Single 5.85 mm Thick PMMA at 11.8 m/s (1.40 ms after Impact)

Numerical data was extracted from these graphical data. Shown in Figure 8 below are plots of the out-of-plane displacement as a function of time for the impact point for the three different velocities that were performed on single panel PMMA. The three velocities were 10.6 m/s, 11.8 m/s, and 14.2 m/s. During the 14.2 m/s experiment, the PMMA panel cracked. The DIC analysis broke down due to the change in pattern caused by the cracking sometime prior to the maximum displacement. This causes the 14.2 m/s experiment data set to be shorter than the two other velocities. It can be seen that the displacement is much larger for the 14.2 m/s experiment; this is due to the cracking allowing the panel to extend outward. In all of the figures, time of zero ms corresponds to the time at the beginning of the impact. The maximum displacement values were extracted from the correlated data at the location of impact (panel center). These can be seen on Figure 8; note that the measured 13.4 mm for the 14.2 m/s experiment is not the maximum due to the pattern and analysis failing after cracking began.

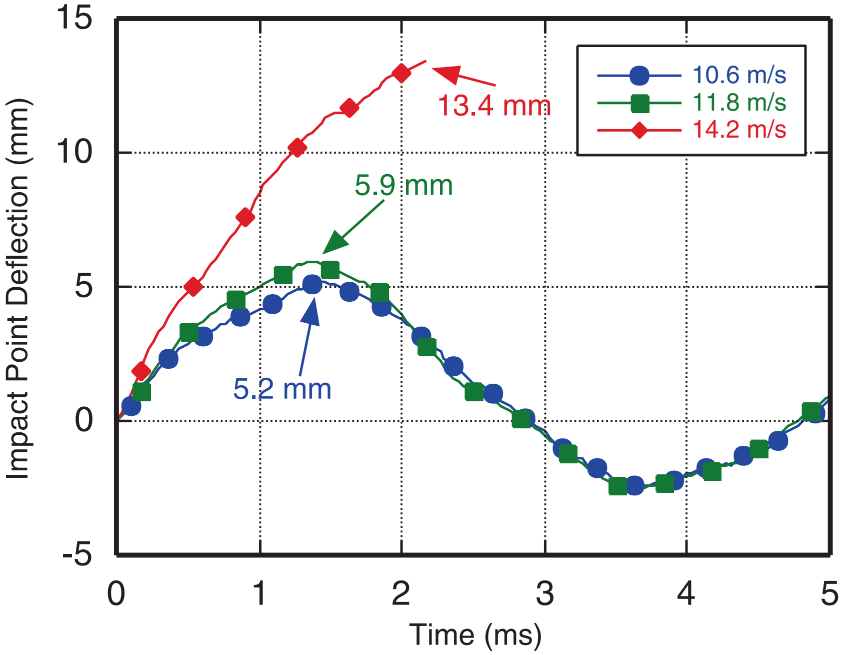

Figure 8. Z-Displacement for 5.85 mm thick PMMA Panels for Velocities of 10.6 m/s, 11.8 m/s, and 14.2 m/s

Using the out-of-plane displacement data at the impact point, the PMMA panels can be compared to previous PC data. Figure 9 shows impact point displacement versus time for approximately10 m/s impact velocity for both PC and PMMA single panels of the same thickness. As is expected, the brittle PMMA deforms less than the ductile PC. However, the PC can withstand much higher velocity impact before failure in these blunt impact experiments.

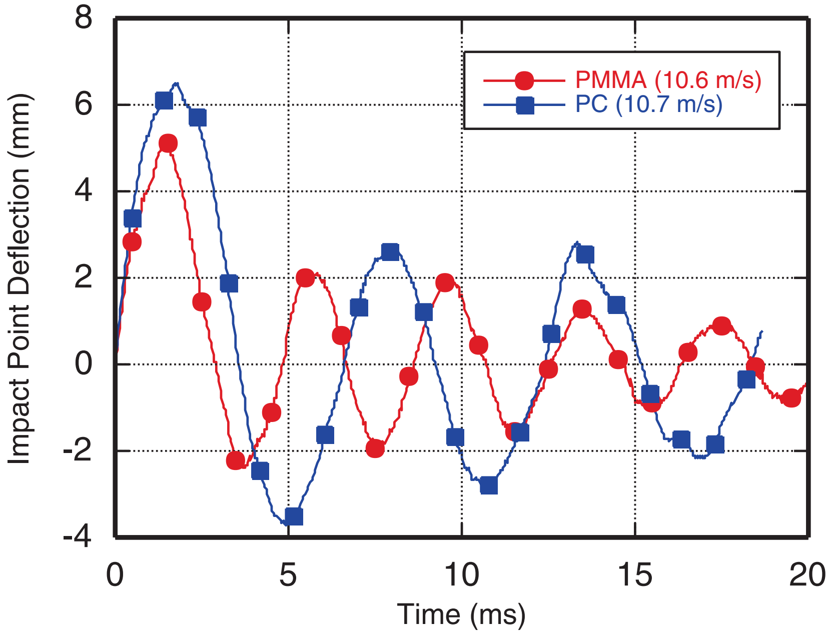

Figure 9. Z-Displacement at 10 m/s Impact Velocity for single 5.85 mm thick PMMA and PC Panels

PC/PMMA Composite Impact Response

The impact response, measured by the back surface deflection at the impact point, of configuration C, single panel of 12.32 mm thick PC, has been published previously. It is presented here again in Figure 10 for continuity and clarity. Maximum deflection for the higher velocity 48.9 m/s is 11 mm compared with the corresponding maximum displacement of 7 mm at 30.0 m/s impact velocity.

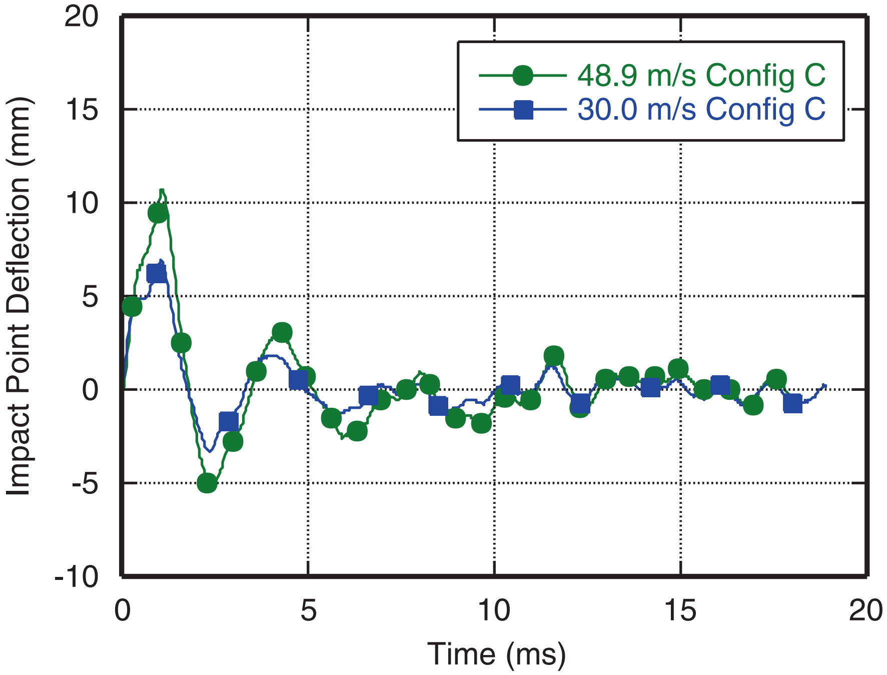

Figure 10. Z-Displacement for Configuration C Panel at Velocities 30 and 49 m/s

The back surface deflection of configuration CC, two un-bonded 5.85 mm thick PC panels, is shown below in Figure 11 for the two impact velocities. Maximum displacements at the velocities 51.1 m/s and 31.1 m/s are 15 mm and 11 mm, respectively.

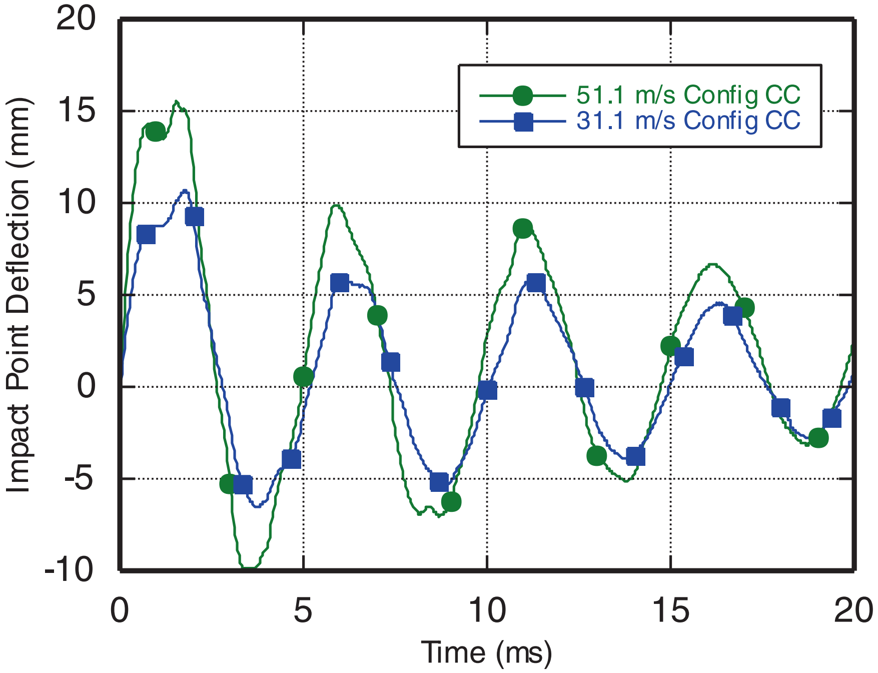

Figure 11. Z-Displacement for Configuration CC Panel at Velocities 31.1 and 51.1 m/s

The back surface deflection of configuration CAC, two bonded 5.85 mm thick PC panels, is shown below in Figure 12 for the two impact velocities. Maximum displacements at the velocities 48.6 m/s and 30.5 m/s are 11 mm and 7 mm, respectively.

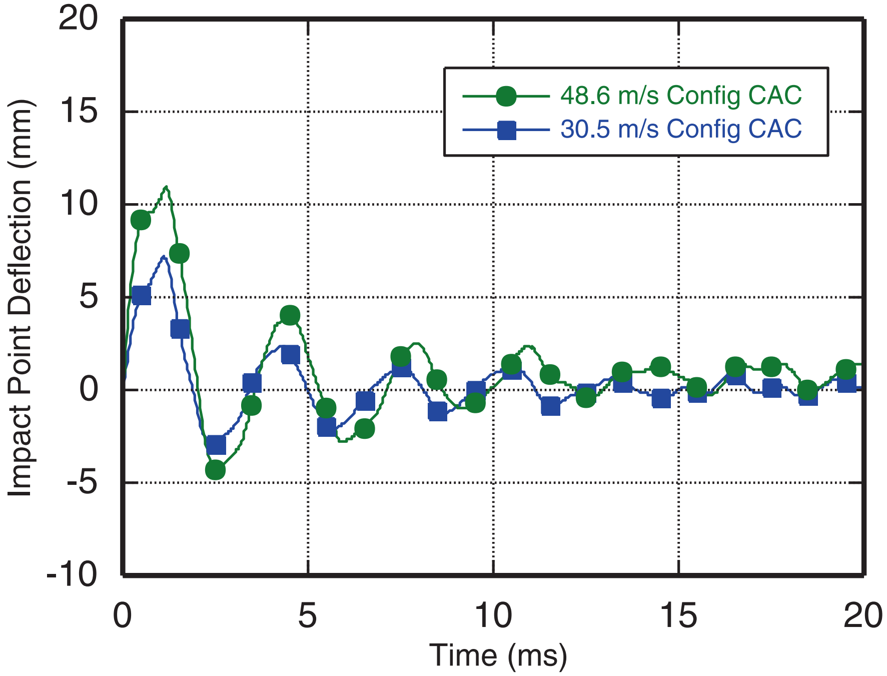

Figure 12. Z-Displacement for Configuration CAC Panel at Velocities 30.5 and 48.6 m/s

The deflection data of configurations C, CC, and CAC at impact velocities of approximately 30 m/s and 50 m/s are plotted together in Figures 13 and 14. As can be seen from the graphs, there is virtually no difference in maximum displacement between a single 12.32 mm thick panel and two bonded 5.85 mm thick panels. Without the polyurethane bonding however, the amount of out-of-plane displacement increases significantly.

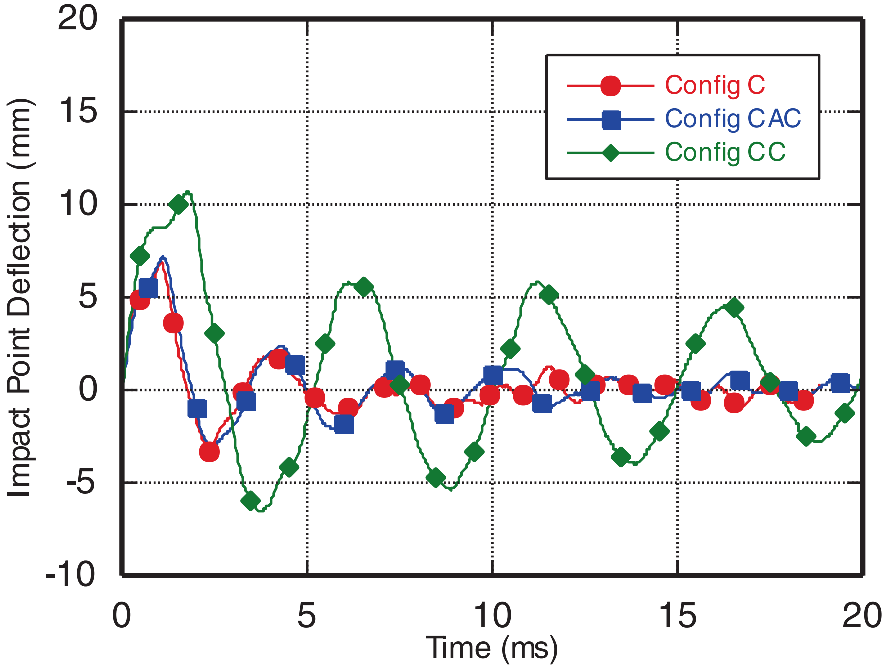

Figure 13. Z-Displacement for Configuration C, CC, and CAC Panels at 30 m/s Velocity

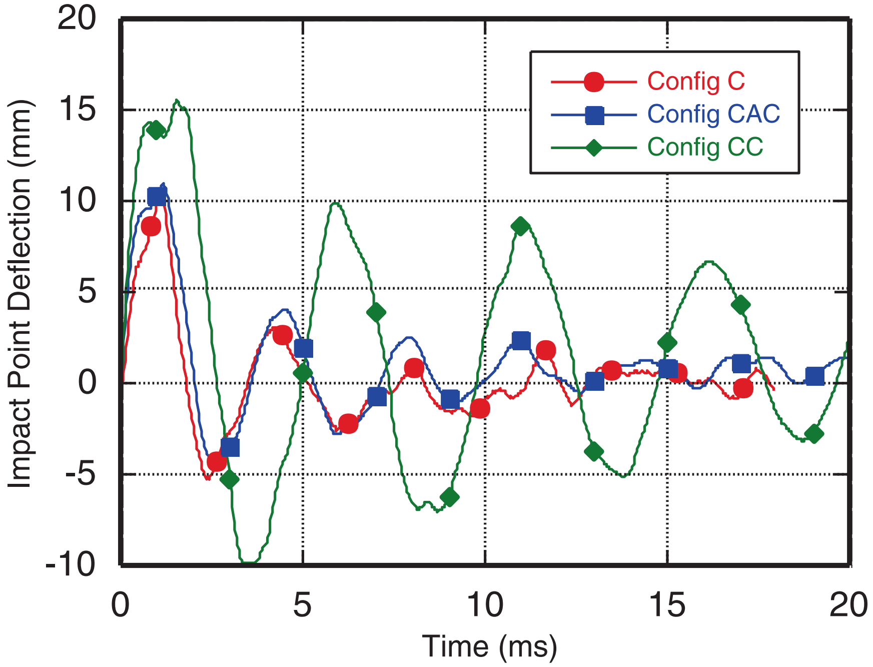

Figure 14. Z-Displacement for Configuration C, CC, and CAC Panels at 50 m/s Velocity

The deflection of configuration MC, un-bonded PMMA (impact side) and PC panel, is shown below in Figure 15 for the two impact velocities. The measured maximum displacements were 17 mm and 12 mm at the respective velocities of 46.0 and 30.5 m/s.

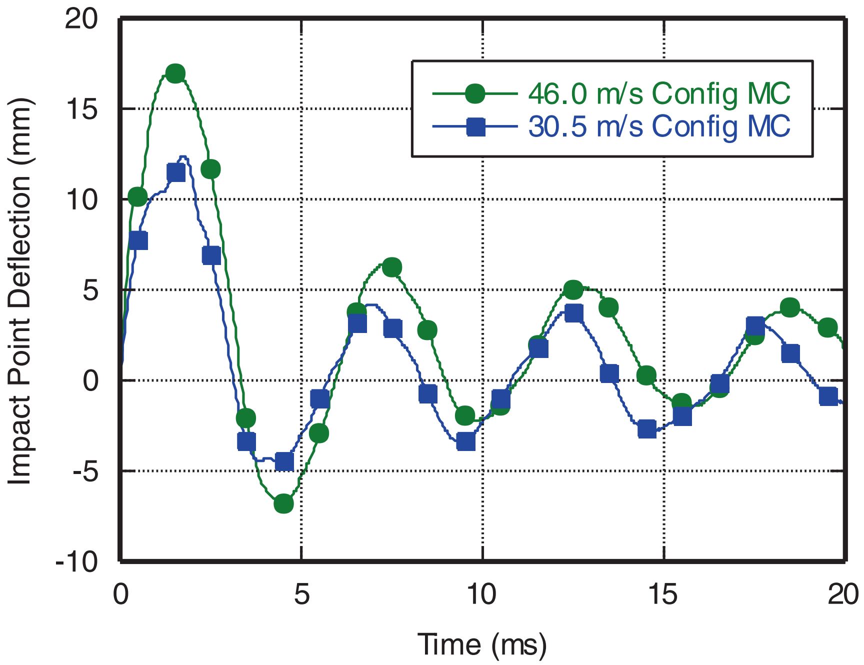

Figure 15. Z-Displacement for Configuration MC Panel at Velocities 30.5 and 48.6 m/s

The deformation of configuration CM, un-bonded PC (impact side) and PMMA, is shown below in Figure 16 for one impact velocity. Only one velocity was performed because it was found that the PMMA back surface would exhibit cracking and failure at even moderate impact velocity. Therefore only one experiment, at 30 m/s, was performed. In this case the PMMA back surface suffered cracking, but did not fail. It was possible to obtain out-of plane displacement. The maximum displacement was 18 mm for this experiment.

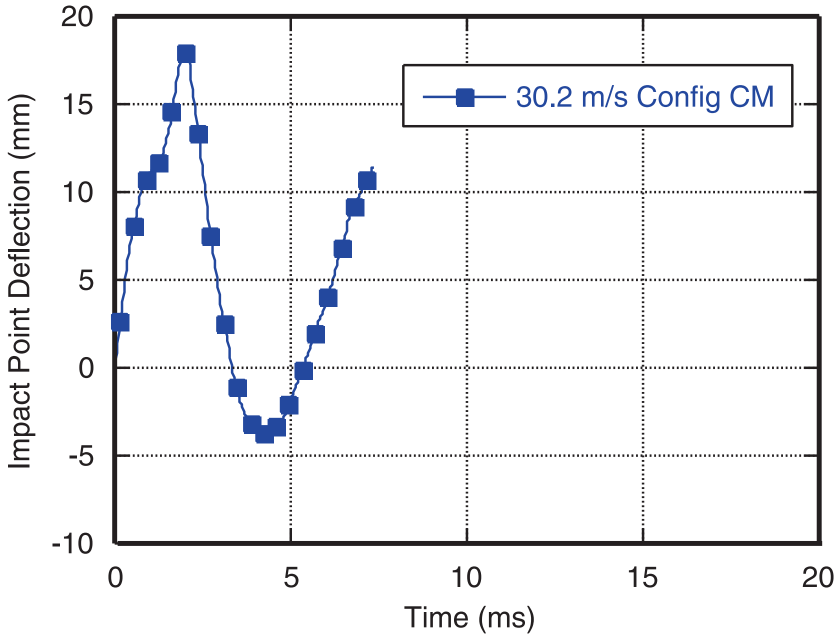

Figure 16. Z-Displacement for Configuration CM Panel for 30.2 m/s Velocity

The displacement data of configurations CC, MC, and CM at impact velocity 30 m/s are plotted together in Figure 17. Configurations CC and MC are plotted together for 50 m/s in Figure 18. As can be seen from the graphs, configuration CC (two un-bonded panels of PC) performed the best in terms of minimum out of plane displacement and configuration CM performed the worst. However, configuration CC did suffer the most rebound. Configuration MC performed almost as well as configuration CC at both velocities even though afterward the PMMA on the impact side was shattered, meaning that configuration MC would not perform well in a multi-impact environment.

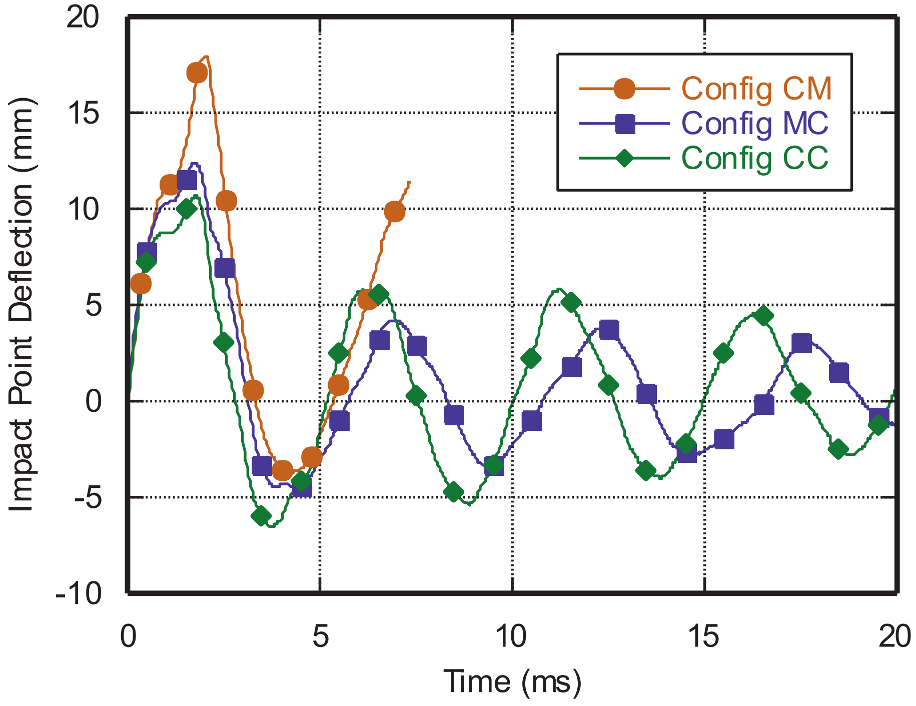

Figure 17. Z-Displacement for Configuration CC, MC, and CM Panels at 30 m/s Velocity

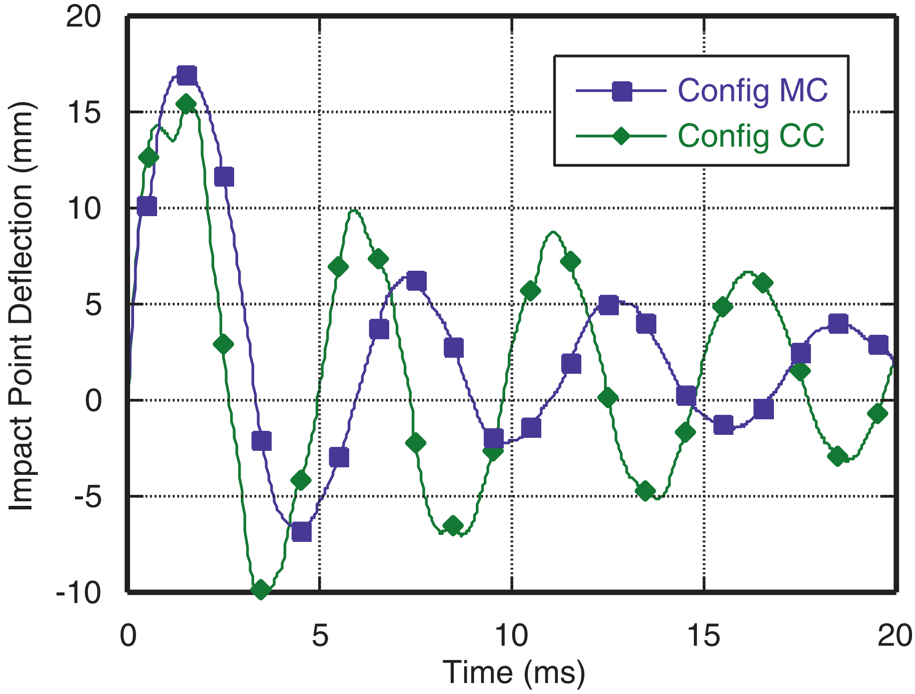

Figure 18. Z-Displacement for Configuration CC and MC Panels at 50 m/s Velocity

The deformation of configuration CMC (un-bonded PC, PMMA, and PC on impact side), is shown below in Figure 19 for the two impact velocities. At both velocities, the center layer of PMMA suffered cracking, but did not fail completely (meaning the entire panel was still intact).

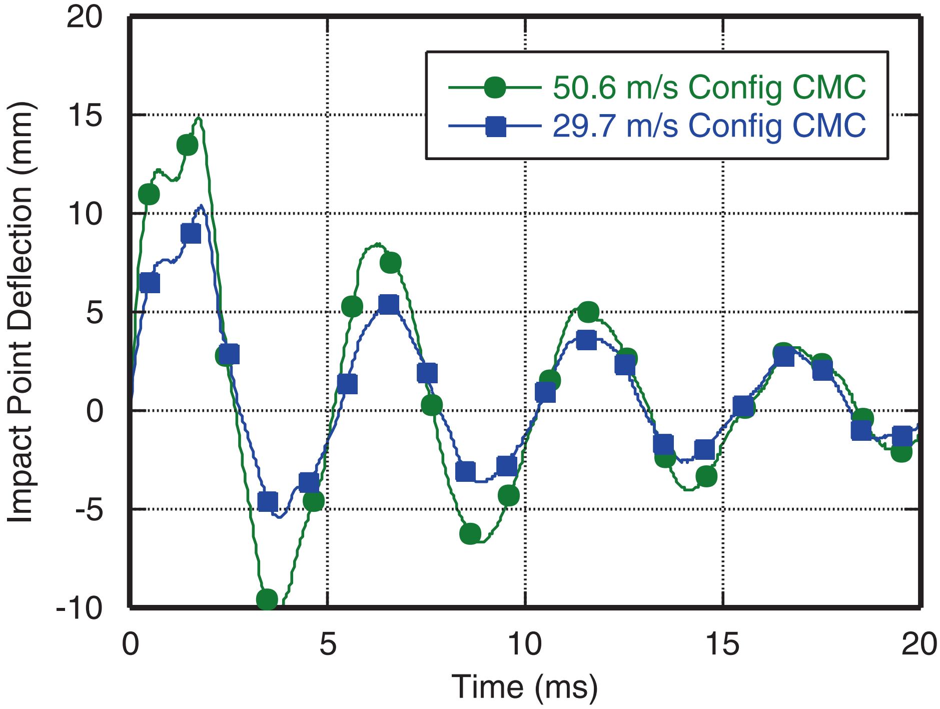

Figure 19. Z-Displacement for Configuration CMC Panel for Velocities 29.7 and 50.6 m/s

The deformation of configurations CMC, C, and CC are show below in Figures 20 and 21 for ~30 and ~50 m/s impact velocities. As can be seen from the graphs, the thickest material, configuration CMC with PMMA between two panels of PC, did not perform better than configuration CC, with two panels of PC alone, when looking at maximum displacement. It can be seen that after peak displacement, the CMC configuration did attenuate to lower amplitude faster than the CC configuration. The single panel of 12.32 mm thick PC outperformed both significantly, as would configuration CAC (two PC panels bonded together), since, as discussed earlier, configuration C and CAC were virtually identical in response.

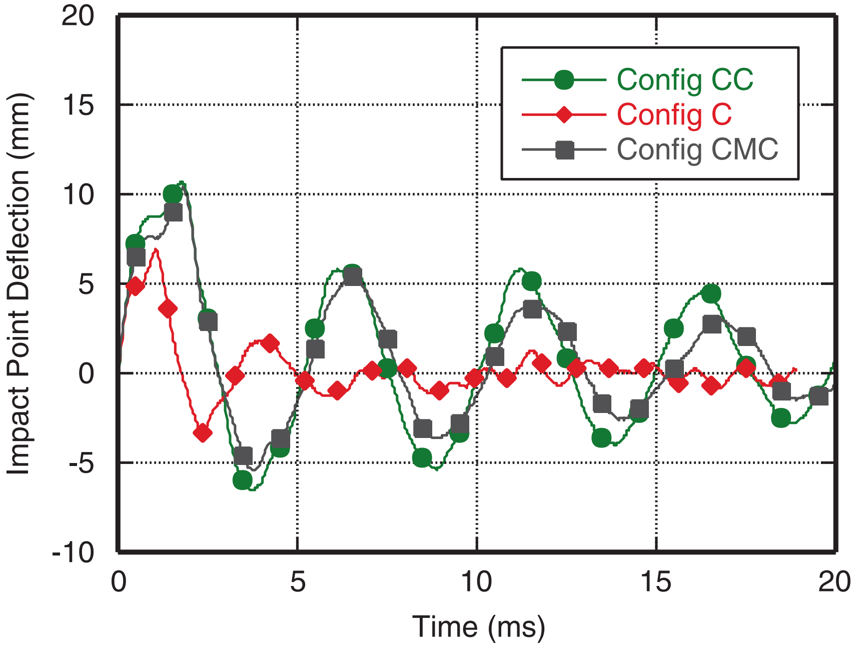

Figure 20. Z-Displacement for Configuration C, CC, and CMC Panel for 30 m/s Velocity

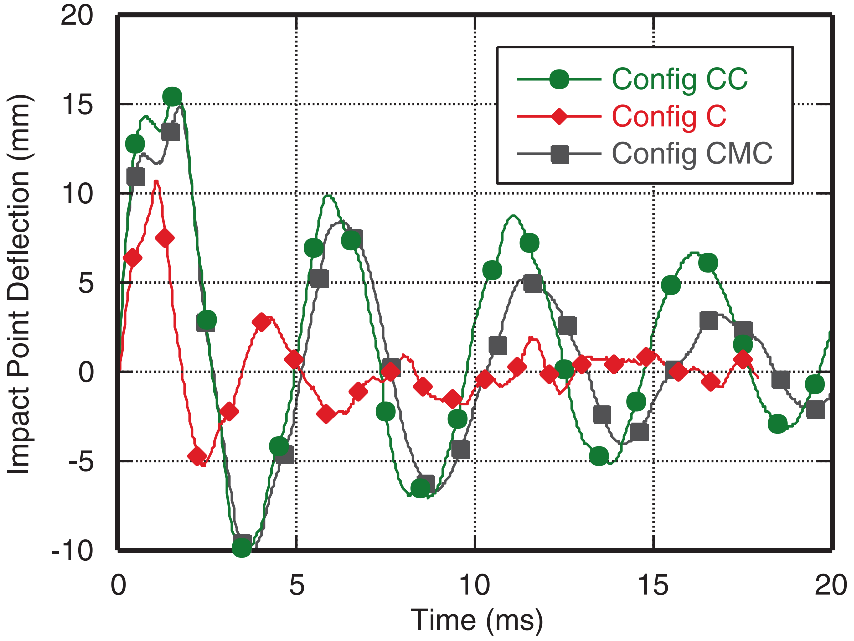

Figure 21. Z-Displacement for Configuration C, CC, and CMC Panel for 50 m/s Velocity

Figure 22 summarizes the maximum deflection of the impact point as a function of impact velocity for all six of the configurations discussed here. Additionally, it includes this data for single panel PMMA and single panel PC, both of 5.85 mm thickness. The PC data has been previously reported, and is included as a comparison tool [17]. Figure 22 reinforces some of the conclusions drawn previously about the performance of these different configurations. As can be seen from the graph, configuration MC does have lower maximum deflection than a single PC panel; however, it does not match the performance of the other two layer composites. The configurations with the lowest maximum deflections are C and CAC, with near identical results. The next lowest deflections are attained by configurations CC and CMC. The additional layer of PMMA in the center of configuration CMC does not appear to make any qualitative difference in back surface deflection compared to configuration CC. However, this conclusion applies only for this range of impact velocities and does not necessarily apply to ballistic performance or reflect on the value of this configuration in other applications.

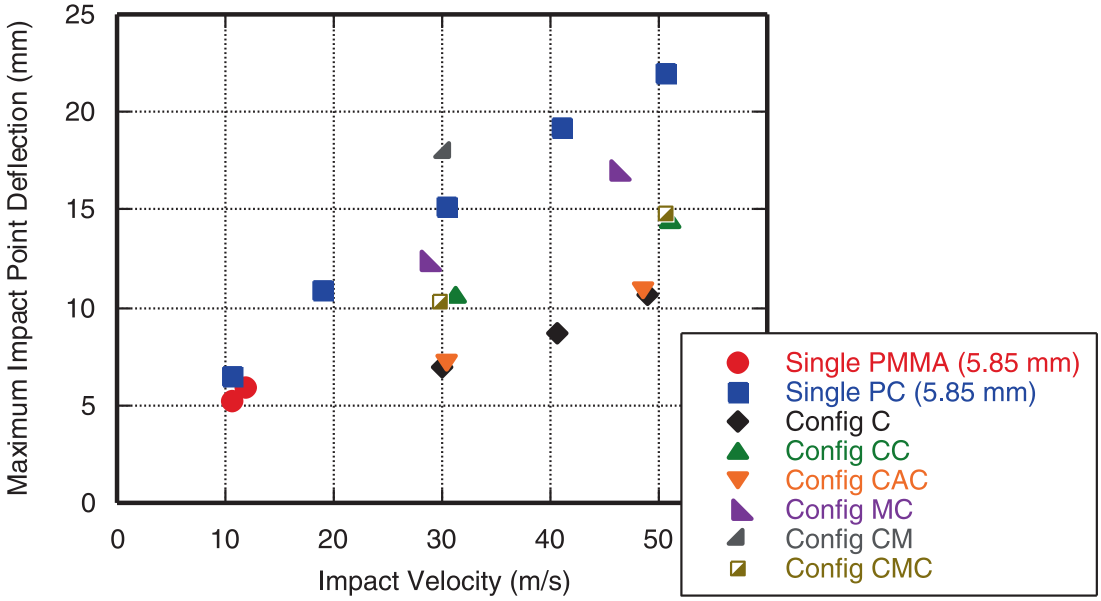

Figure 22. Maximum Impact Point Deflection as a Function of Impact Velocity for all Composite Configurations as well as Single Panel PC and PMMA

SUMMARY

Full-field out-of-plane transient displacements were measured during impact using DIC. The blunt impact response of single panel PMMA at low velocities was obtained. This was compared to previously existing data on PC panels, which showed that PMMA deforms less for a given impact velocity, until its cracking threshold is reached. The penetration velocity for this projectile geometry and mass was determined to be approximately 15 m/s for 5.85 mm thick PMMA panels. The experimental methodology was developed to conduct non-penetrating blunt impact tests on various combinations of PC/PMMA composite panels with a thickness of up to 17.6 mm. The data from these experiments are reported and used to evaluate and refine material models and computational methodologies that are used to predict the impact response of combined PC/PMMA panels. To add to this data, additional impact experiments are being performed to obtain impact response of different/advanced composite configurations, including the effect of bonding between the layers of configurations MC, CM, and CMC.

ACKNOWLEDGEMENTS

The authors would like to acknowledge the following colleagues at the Army Research Laboratory: Mr. Jared Gardner, Mr. James Wolbert, Mr. Terrance Taylor, and Dr. Parimal Patel for their assistance in obtaining and fabricating the material necessary for this work.

Certain commercial equipment and materials are identified in this paper in order to adequately specify the experimental procedure. In no case does such identification imply recommendation by the Army Research Laboratory nor does it imply that the material or equipment identified is necessarily the best available for this purpose.

REFERENCES

1. Myers, F.S. and Brittain, J.O. Mechanical Relaxation in Polycarbonate-Polysulfone Blends. Journal of Applied Polymer Science, 17, pp. 2715-2724. 1973.
2. Petersen, R.J., Corneliussen, R.D., and Rozelle, L.T. Polymer Reprint, 10, pp. 385. 1969.

3. The IUPAC Compendium of Chemical Terminology, 66th Ed., pg 583 (1997).
4. Lo, Y.C. and Halldin, G. W. The Effect of Strain Rate and Degree of Crystallinity on the Solid-Phase Flow Behavior of Thermoplastic. ANTEC '84, pp. 488-491. 1984
5. Kaufman, H. S. Introduction to Polymer Science and Technology. John Wiley and Sons Press, New York. 1977.
6. Moy, P, Weerasooriya, T., Hsieh, A. and Chen, W. Strain Rate Response of a Polycarbonate Under Uniaxial Compression. Proceedings of SEM Annual Conference on Experimental Mechanics. June 2003.
7. Mulliken, A. D. and Boyce, M. C. Mechanics of rate-dependent elastic-plastic deformation of glassy polymers from low to high strain rates. Int. J. Solids Struct. 43:5, pp. 1331–1356. 2006
8. Hall, I. H. The Effect of Strain Rate on the Stress-Strain Curve of Oriented Polymers. II. The Influence of Heat Developed During Extension. Journal of Applied Polymer Science, 12, pp 739. 1968.
9. Walley, S. M., Field, J. E., Pope, P. H., and Stafford, N. A. A Study of the Rapid Deformation Behavior of a Range of Polymers. Philos. Trans. Soc. London, A, 328, pp. 783-811. 1989.
10. Arruda, E. M., Boyce, M. C., and Jayachandran, R. Effects of Strain Rate, Temperature, and Thermomechanical Coupling on the Finite Strain Deformation of Glassy Polymers. Mechanics of Materials, 19, pp. 193-212. 1995
11. Boyce, M. C. Arruda, E. M., Jayachandran, R. The Large Strain Compression, Tension, and Simple Shear of Polycarbonate. Polymer Engineering and Science, Vol. 34, No. 9, pp. 716-725. 1994.
12. Boyce, M.C. and Sarva, S. S. Mechanics of Polycarbonate during High-rate Tension. Journal of Mechanics of Materials and Structures. Volume 2 Issue 10, pp. 1853-1880. December 2007.
13. Moy, P., Weerasooriya, T., Chen, W., and Hsieh, A. Dynamic Stress-Strain Response and Failure Behavior of PMMA. Proceedings of ASME International Mechanical Engineering Congress. November 2003.
14. Hsieh, A. J., DeSchepper, D., Moy, P., Dehmer, P. G., and Song, J. W. The Effects of PMMA on Ballistic Impact Performance of Hybrid Hard/Ductile All-Plastic- and Glass-Plastic-Based Composites. ARL-TR-3155. February 2004.
15. Fountzoulas, C. G., Cheeseman, B. A. Dehmer, P. G., and Sands, J. M. A Computational Study of Laminate Transparent Armor Impacted by FSP. Proceedings of the 23rd International Symposium on Ballistics, Vol. II, pp. 873–881, Tarragona, Spain,16–20 April 2007.
16. Stenzler, J. S., Impact Mechanics of PMMA/PC Multi-Laminates with Soft Polymer Interlayers. Master of Science in Mechanical Engineering Thesis. Virginia Polytechnic Institute and State University. November 2009.
17. Gunnarsson, C. A., Ziemski, B., Weerasooriya, T., and Moy, P. Deformation and Failure of Polycarbonate during Impact as a Function of Thickness. Proceedings of the 2009 International Congress and Exposition on Experimental Mechanics and Applied Mechanics. June 2009.
18. Chu, T. C., Ranson, W. F., Sutton, M. A., and Peters, W. H. Applications of Digital-Image-Correlation Techniques to Experimental Mechanics. Experimental Mechanics. September 1995.
19. Sutton, M. A., Wolters, W. J., Peters, W. H., Ranson, W. F., and McNeill, S. R. Determination of Displacements Using an Improved Digital Image Correlation Method. Computer Vision. August 1983.
20. Bruck, H. A., McNeill, S. R., Russell S. S., Sutton, M. A. Use of Digital Image Correlation for Determination of Displacements and Strains. Non-Destructive Evaluation for Aerospace Requirements. 1989.
21. Sutton, M. A., McNeill, S. R., Helm, J. D., Schreier, H. Full-Field Non-Contacting Measurement of Surface Deformation on Planar or Curved Surfaces Using Advanced Vision Systems. Proceedings of the International Conference on Advanced Technology in Experimental Mechanics. July 1999.
22. Sutton, M. A., McNeill, S. R., Helm, and Chao, Y. J. Advances in Two-Dimensional and Three-Dimensional Computer Vision. Photomechanics. Volume 77. 2000.

Proceedings of the SEM Annual Conference
June 7-10, 2010 Indianapolis, Indiana USA
©2010 Society for Experimental Mechanics Inc.

Performance of polymer-steel bi-layers under blast

Ahsan Samiee[1*], Alireza V. Amirkhizi[1,] and Sia Nemat-Nasser[1]
[1] Center of Excellence for Advanced Materials, Department of Mechanical and Aerospace Engineering, University of California at San Diego, 9500 Gilman Drive, La Jolla, CA 92093-0416, USA
[*]asamiee@ucsd.edu

ABSTRACT

We present results from our numerical simulation of the dynamic response and deformation of 1m diameter circular DH-36 steel plates and DH-36 steel-polyurea bi-layers, subjected to blast loads. Different thicknesses of polyurea are considered, and the effect of polyurea thickness on the performance of steel plates under blast loads is investigated. For each polyurea thickness, we have simulated three cases: 1) polyurea cast on front face (loading face); 2) polyurea cast on back face; and 3) no polyurea, but an increase in steel-plate thickness such that the areal density remains the same in all three cases. Two types of loading are applied to the polyurea-steel system: (1) Direct application of pressure on the bi-layer system, (2) Application of pressure through a separate medium (polyurethane or water).

For numerical simulations, we employed physics-based and experimentally-supported temperature- and rate-sensitive constitutive models for steel and polyurea, including in the latter case, the pressure effects. Results from the simulations reveal that in all cases, polyurea cast on the back face exhibits superior performance relative to the other cases. The differences become more pronounced as polyurea thickness (and the corresponding steel-plate thickness) becomes greater. Also, the differences become less pronounced when direct pressure is applied.

Keywords: polyurea, steel plate, bi-layer, blast

EXTENDED ABSTRACT

Dynamic response of metal sheets and steel plates has been extensively studied by many researches for the last few decades. Numerous applications of steel plates in different industries have motivated researchers to investigate the response of steel plates with different shapes and thicknesses under different loading conditions. (See Jones [1, 2] and Nurick and Martin [3]). Many analytical, experimental and numerical studies have led to practical results which are extensively used by engineers to design stronger structures with lower weight.

Dynamic response and deformation of steel plates under blast and high strain rates can be altered by casting a layer of an energy-dissipating material on the surface. This can improve the performance of steel plates under blast loading while the equivalent mass is kept the same. Amini et al. [4] have reported that casting *polyurea*, an elastomer, on the back surface of steel plates (with respect to the blast loads) delays the necking and rupture process, leading to a better performance. In their experiments, 1mm-thick steel plates are coated with ~3.7mm polyurea.

Polyurea is a well-known polymer in coating industry due to its outstanding reaction and abrasion resistance. It also shows interesting mechanical properties which makes it a possible choice for applications involving energy dissipation. Amirkhizi et al. [20] have systematically studied the viscoelastic properties of polyurea over a wide

T. Proulx (ed.), *Dynamic Behavior of Materials, Volume 1*, Conference Proceedings of the Society for Experimental Mechanics Series, DOI 10.1007/978-1-4419-8228-5_29, © The Society for Experimental Mechanics, Inc. 2011

range of strain rates and temperatures. They have developed a material model for polyurea, suitable for explicit finite element analyses, which is used in our simulations.

A numerical model is proposed to study the dynamic performance and deformation of steel plate-polyurea bi-layers. Figure (1) illustrates an axi-symmetric view of a 3D finite element model developed to run in LS-DYNA, a commercial FEM package well-established in impact engineering applications. In this model, blast is transmitted to bi-layer system through a nearly-incompressible medium. Polyurethane and water material models have been used in our simulations. The bi-layer system in this model consists of a circular steel plate with diameter, D=1.4m and a layer of polyurea cast on the back or front face of the steel plate. In our simulations, DH-36 Naval structural steel is used. A physics-based material model based on the work by Guo and Nemat-Nasser [6] is employed.

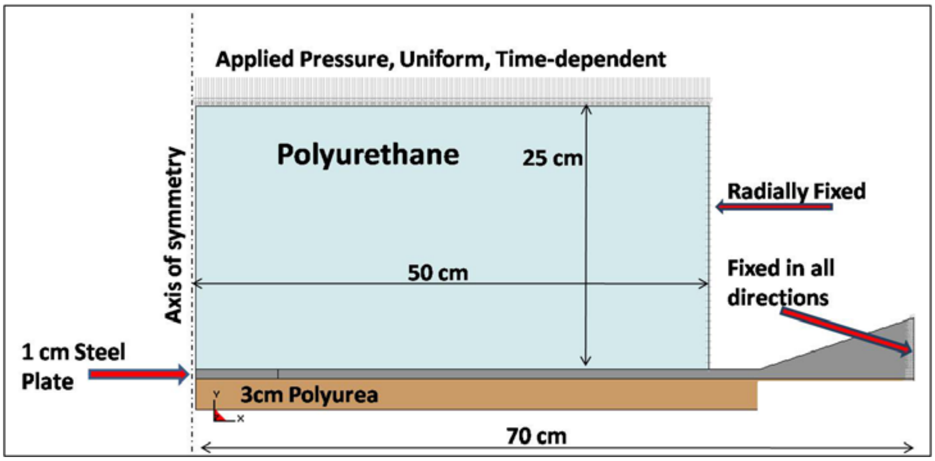

Figure 1. Axi-symmetric view of the FEM model

A uniform, time-varying pressure pulse is applied on top of polyurethane column, which is radially fixed. The pressure pulse travels through the polyurethane column before reaching the bi-layer system. Some of the energy in the pressure pulse is transmitted to the bi-layer system causing it to deform, and some is reflected. The height of the polyurethane column is chosen so that the reflected pulse does not interfere with the further deformation of the bi-layer which is solely preceded by its own momentum. Steel plate is thickened at the outer edge to avoid excessive and unreal stresses at the boundary.

The volumetric average of effective plastic strain (EPS) over a circular part with diameter, D=10cm, at the center of steel plate is used to evaluate the performance of the bi-layer system. The following cases are simulated and compared: (1) Polyurea cast on the back: four thicknesses of polyurea are considered: 1, 2, 3 and 4cm where the thickness of steel plate is 1cm. (2) Polyurea case on the front: four thicknesses of polyurea are considered: 1, 2, 3 and 4cm where the thickness of steel plate is 1cm. (3) No polyurea: four thicknesses of steel plate are considered: 1.14, 1.28, 1.42 and 1.56cm where equivalent areal densities match those from cases (1) and (2). Our simulations reveal that in all cases, polyurea cast on the back face exhibits superior performance relative to the other cases. The differences become more pronounced as polyurea thickness (and the corresponding steel-plate thickness) becomes greater.

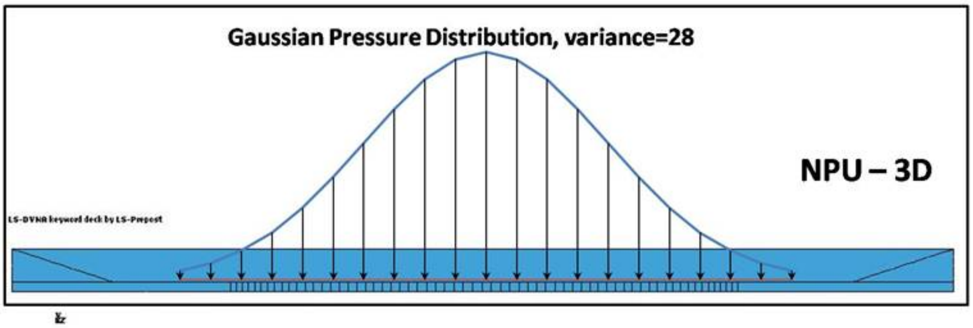
Gaussian Pressure Distribution, variance=28
NPU – 3D
LS-DYNA keyword deck by LS-Prepost

Figure 2. Direct application of pressure pulse. A time-varying pressure pulse with a Gaussian shape is directly applied to the bi-layer system. (NPU: No polyurea)

We also investigated the case where the pressure is directly applied to the bi-layer system. In this case, the pressure-transmitting part (polyurethane or water) is eliminated and a time-varying pressure pulse with a Gaussian shape is directly applied to the bi-layer system (Figure 2). Simulation results suggest that when the pressure transmitting medium is ignored, differences between the cases become less pronounced.

ACKNOWLEDGEMENTS

The experimental work has been conducted at the Center of Excellence in Advanced Materials (CEAM), Mechanical and Aerospace Engineering Department, University of California, San Diego, and has been supported by the Office of Naval Research (ONR) grant number N00014-06-1-0340.

REFERENCES

[1] N. Jones. A literature review of the dynamic plastic response of structures. *The Shock and Vibration Digest 13*, 10:3-16, 1975.

[2] N. Jones. Recent progress in the dynamic plastic behavior of structures: Part i. *The Shock and Vibration Digest 10*, 9:21-33, 1978.

[3] G.N. Nurick and J.B. Martin. Deformation of thin plates subjected to impulsive loading - a review: Part i: Theoretical considerations. *International Journal of Impact Engineering*, 8(2):159-170, 1989.

[4] Mahmoud Amini, Jon Isaacs, and Sia Nemat-Nasser. Effect of polyurea on the dynamic response of steel plates. *Proceedings of the 2006 SEM Annual Conference and Exposition on Experimental and Applied Mechanics*, 2006.

[5] A. V. Amirkhizi, J. Isaacs, J. McGee, and S. Nemat-Nasser. An experimentally-based viscoelastic constitutive model for polyurea, including pressure and temperature effects. *Philosophical Magazine and Philosophical Magazine Letters*, 86:36:5847-5866, 2006.

[21] W. G. Guo Sia Nemat-Nasser. Thermomechanical response of dh- 36 structural steel over a wide range of strain rates and temperatures. *Mechanics of Materials*, 35:1023-1047, 2003.

Proceedings of the SEM Annual Conference
June 7-10, 2010 Indianapolis, Indiana USA
©2010 Society for Experimental Mechanics Inc.

The Blast Response of Sandwich Composites With a Functionally Graded Core and Polyurea Interlayer

Nate Gardner and Arun Shukla
Dynamic Photomechanics Laboratory, Dept. of Mechanical, Industrial & Systems Engineering
University of Rhode Island, 92 Upper College Road, Kingston, RI 02881, USA
ngardner@mail.uri.edu

ABSTRACT

In the present study, the dynamic behavior of two types of sandwich composites made of E-Glass Vinyl-Ester (EVE) face sheets and Corecell ^{TM} A-series foam with a polyurea interlayer was studied using a shock tube apparatus. The materials, as well as the core layer arrangements, were identical, with the only difference arising in the location of the polyurea interlayer. The foam core itself was layered based on monotonically increasing the wave impedance of the core layers, with the lowest wave impedance facing the shock loading. For configuration 1, the polyurea interlayer was placed behind the front face sheet, in front of the foam core, while in configuration 2 it was placed behind the foam core, in front of the back face sheet. A high-speed side-view camera system along with a high-speed back-view Digital Image Correlation (DIC) system was utilized to capture the real time deformation process as well as mechanisms of failure. Post mortem analysis was also carried out to evaluate the overall blast performance of these two configurations. The results indicated that applying polyurea behind the foam core and in front of the back face sheet will reduce the back face deflection, particle velocity, and in-plane strain, thus improving the overall blast performance and maintaining structural integrity.

INTRODUCTION

Core materials play a crucial role in the dynamic behavior of sandwich structures when they are subjected to high-intensity impulse loadings such as air blasts. Their properties assist in dispersing the mechanical impulse that is transmitted into the structure and thus protect anything located behind it [1-3]. Stepwise graded materials, where the material properties vary gradually or layer by layer within the material itself, were utilized as a core material in sandwich composites since their properties can be designed and controlled. Typical core materials utilized in blast loading applications are generally foam, due to its ability to compress and withstand highly transient loadings. However, this foam core lacks the ability to maintain structural integrity. In recent years, with its ability to improve structural performance and damage resistance of structures, as well as effectively dissipate blast energy, the application of polyurea to sandwich structures has become a new area of interest

The numerical investigation by Apetre et al. [4] on the impact damage of sandwich structures with a graded core (density) has shown that a reasonable core design can effectively reduce the shear forces and strains within the structures. Consequently, they can mitigate or completely prevent impact damage on sandwich composites. Li et al. [5] examined the impact response of layered and graded metal-ceramic structures numerically. He found that the choice of gradation has a great significance on the impact applications and the particular design can exhibit better energy dissipation properties. In their previous work, the authors experimentally investigated the blast resistance of sandwich composites with stepwise graded foam cores [6]. Two types of core configurations were studied and the sandwich composites were layered / graded based on the densities of the given foams, i.e. monotonically and non-monotonically. The results indicated that monotonically increasing the wave impedance of the foam core, thus reducing the wave impedance mismatch between successive foam layers, will introduce a stepwise core compression, greatly enhancing the overall blast resistance of sandwich composites.
Although the behavior of polyurea has been studied [7-10], there have been no results past or present regarding the dynamic behavior of functionally graded core with a polyurea interlayer. Tekalur et al. [11] experimentally studied the blast resistance and response of polyurea based layered composite materials subjected to blast loading. Results indicated that sandwich materials prepared by sandwiching the polyurea between two composite skins had the best blast resistance compared to the EVE composite and polyurea layered plates. Dvorak et al.

T. Proulx (ed.), *Dynamic Behavior of Materials, Volume 1*, Conference Proceedings of the Society for Experimental Mechanics Series,
DOI 10.1007/978-1-4419-8228-5_30, © The Society for Experimental Mechanics, Inc. 2011

[12] experimentally and numerically investigated the blast resistance of sandwich plates with a polyurea interlayer under blast loading. Their results suggest that separating the composite face sheet from the foam core by a thin interlayer of polyurea can be very beneficial in comparison to the conventional sandwich plate design.

The present study focuses on the blast response of sandwich composites with a functionally graded core and a polyurea (PU) interlayer. Two different core layer configurations were investigated, with the only difference arising in the location of the polyurea (PU) interlayer. The results will help to better understand the overall blast performance of sandwich composites with a functionally graded core system and PU interlayer under shock wave loading and provide a guideline for an optimal core design. The quasi-static and dynamic constitutive behaviors of the foam core materials, as well as the polyurea, were first studied using a modified SHPB device with a hollow transmitted bar. The sandwich composites were then fabricated and subjected to shock wave loading generated by a shock tube. All of the sandwich composites have an identical core thickness, overall specimen geometry and areal densities, but different locations of the polyurea interlayer. The shock pressure profiles, real time deflection images, and post mortem images were carefully analyzed to reveal the mechanisms of dynamic failure of these sandwich composites. Digital Image Correlation (DIC) analysis was implemented to investigate the real time deflection, strain, and particle velocity. The energy redistribution in the system was investigated and the results showed that the energy related behavior of these two types of sandwich composites are almost identical.

2. MATERIAL AND SPECIMEN

2.1 SKIN AND CORE MATERIAL

The skin materials utilized in this study are E-Glass Vinyl Ester (EVE) composites comprised of 18oz. E-glass fiber and a vinyl-ester matrix. The plain weave and the woven roving E-glass fibers of the skin material were placed in a quasi-isotropic layout $[0/45/90/-45]_S$.

The core materials used in the present study are Corecell^{TM} A series styrene foams manufactured by Gurit SP Technologies and a polyurea elastomer manufactured by Specialty Products Incorporated (SPI). The three types of Corecell^{TM} A foam were A300, A500, and A800 with density 58.5, 92 and 150 kg/ m^3 respectively. The cell structures for the three foams are very similar and the only difference appears in the cell wall thickness and node sizes, which accounts for the different densities of the foams. The PU elastomer was Dragonshield-HT with an elongation percentage of 620% and density of 1000 kg/ m^3

2.2 SANDWICH PANELS WITH STEPWISE GRADED CORE

The sandwich panels were produced by VARTM-fabricated process. The panels were 102 mm (4 in) wide, 254 mm (10 in) long with 5 mm (.2 in) front and back skins. The core consisted of three layers of foam and a PU interlayer. The first two layers of the foam core were 12.7 mm (.5 in), while the third layer was 6.35 mm (.25 in) and the PU layer was 6.35 mm (.25 in) respectively. Fig. 1 shows the two core layer configurations and the shock wave loading direction. Configuration 1 consisted of a core gradation of PU/A300/A500/ A800 and configuration 2 consisted of a core gradation of A300/A500/A800/PU.

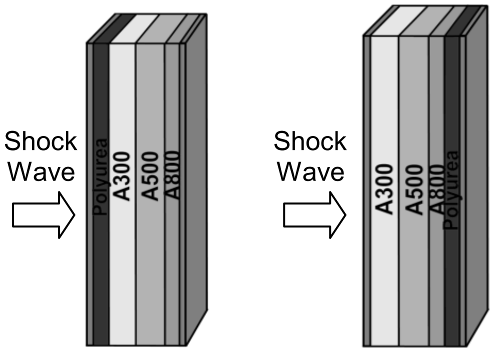

(a) Configuration1 (b) Configuration2

Fig. 1 Specimen Configurations and loading direction

3. EXPERIMENT SETUP AND PROCEDURE

3.1 MODIFIED SPLIT HOPKINSON PRESS BARS WITH HOLLOW TRANSMITTER BAR

Due to the low wave impedance of Corecell^{TM} foam materials, core materials tests were performed by a modified SHPB device with a hollow transmission bar. It has a 304.8 mm (12 in)-long striker, 1600 mm (63 in)-long incident bar and 1447 mm (57 in)-long transmitter bar. All of the bars are made of a 6061 aluminum alloy. The nominal outer diameters of the solid incident bar and hollow transmission bar are 19.05 mm (0.75 in). The hollow transmission bar has a 16.51 mm (0.65 in) inner diameter. At the head and at the end of the hollow transmission bar, end caps made of the same material as the bar were press fitted into the hollow tube. By applying pulse shapers, the effect of the end caps on the stress waves can be minimized. The details of the analysis and derivation of equations can be found in ref[13]. The cylinderical specimens with a dimension Φ10.2mm (0.4 in) X 3.8mm (0.15 in) were used for test.

3.2 SHOCK TUBE

Fig. 2 shows the shock tube apparatus with muzzle detail, which was utilized to obtain a controlled blast loading. When the diaphragms located between the high pressure and low pressure areas rupture, the rapid release of gas creates a shock wave that travels down the tube to impart dynamic loading on the specimen located in front of the muzzle. The final muzzle diameter is 76.2 mm (3 in). Two pressure transducers (PCB102A) are mounted at the end of the muzzle section 160 mm apart. The support fixtures ensure simply supported boundary conditions with a 0.1524 m (6 in) span.

In the present study, a diaphragm of 5 plies of 10 mm thick mylar sheets was utilized to generate an impulse loading on the specimen with an incident overpressure of approximately 1 MPa. For each configuration, at least three samples were tested. A high-speed side-view camera system along with a high-speed back-view Digital Image Correlation (DIC) system was utilized to capture the real time deformation process as well as mechanisms of failure. Both camera systems had an interframe time of 50 μs.

3.3 DIGITAL IMAGE CORRELATION (DIC)

Digital Image Correlation (DIC) was utilized to obtain the real time response of the sandwich composites. A speckle pattern was placed on the back face sheet of the specimens. Two high speed digital cameras, Photron SA1, were placed behind the shock tube to capture the real time deformation and displacement of the sandwich composite, along with the speckle pattern. During the blast loading event, as the specimen bends, the cameras track the individual speckles on the back face sheet. Once the event is over, a graphical user interface was utilized to correlate the images from the two cameras and generate real time strains (in plane and out of plane), deflection and particle velocity. A schematic of the set-up is shown in Fig. 4.

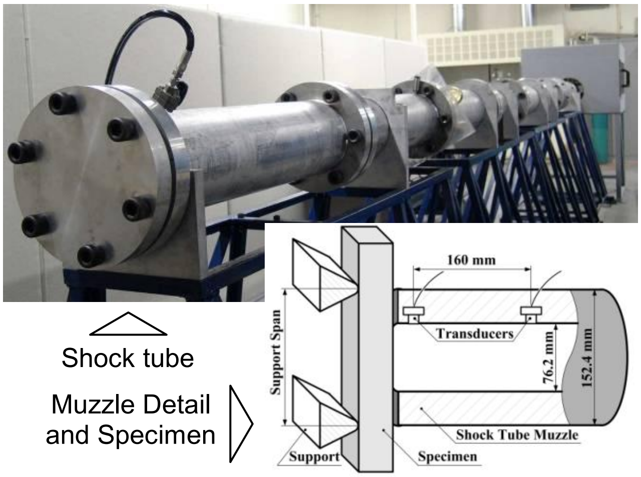

Fig. 2 Shock tube apparatus

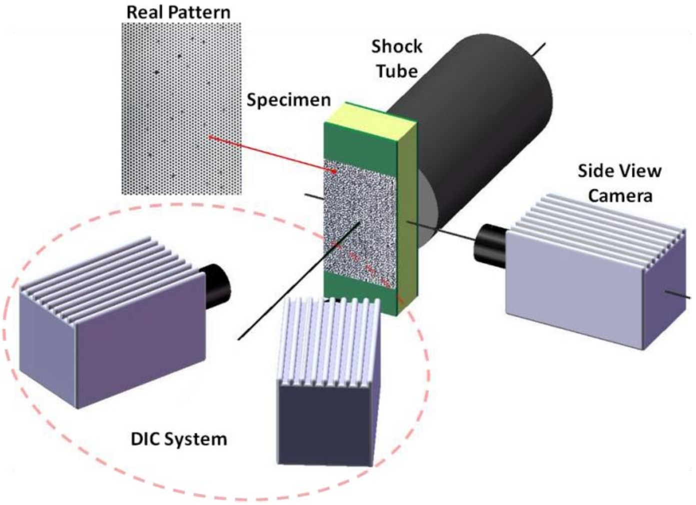

Fig. 3 Digital Image Correlation (DIC) Set-up

4. EXPERIMENTAL RESULTS AND DISCUSSION

4.1 DYNAMIC CONSTITUTIVE BEHAVIOR OF CORE MATERIALS

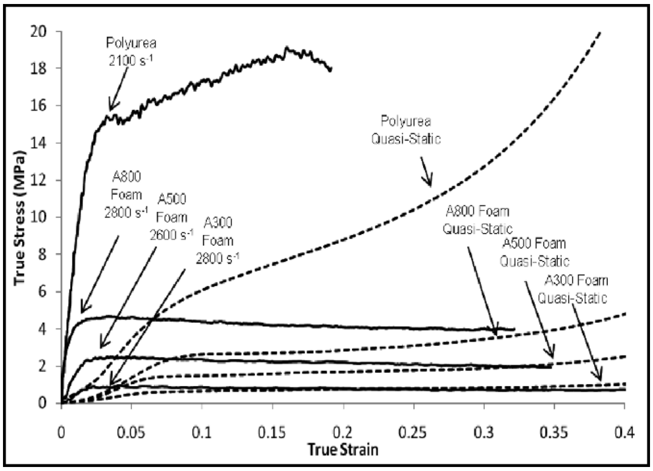

Fig. 4 Quasi-static and high strain-rate behaviors of different types of Corecell^{TM} A Foams and Dragonshield –HT Polyurea

Table1. Yield strength of core materials

Core Layer	A300	A500	A800	PU
Quasi-Static Yield Stresses (MPa)	0.60	1.35	2.46	5.28
High Strain-Rate Yield Stresses (MPa)	0.91	2.47	4.62	15.48

Fig.4 shows the quasi-static and high strain-rate behavior of the different types of Corecell^{TM} A foams and Dragonshield-HT polyurea. The quasi-static and dynamic stress-strain responses have an obvious trend for the different types of foams. Lower density foam has a lower strength and stiffness, as well as a larger strain range for the plateau stress. The high strain-rate yield stresses and plateau stresses are much higher than the quasi-static ones for the same type of foams. The dynamic strength of A500 and A800 increases approximately 100% in comparison to their quasi-static strength, while A300 increases approximately 50%. Also it can be observed that the high strain-rate yield stress of Dragonshield-HT polyurea is much higher than its quasi-static yield stress. The dynamic strength increases 200% in comparison to its quasi-static strength. The improvement of the mechanical behavior from quasi-static to high strain-rates for all core materials used in the present study signifies their ability to absorb more energy under high strain-rate dynamic loading. Table 1 shows the quasi-static and high strain-rate yield stresses respectively.

4.2 RESPONSE OF SANDWICH COMPOSITES WITH GRADED CORES

4.2.1 REAL TIME DEFORMATION

The real time side view deformation image series of configuration 1 (PU/A300/A500/A800) and configuration 2 (A300/A500/ A800/PU) under shock wave loading are shown in fig.5 respectively. The shock wave propagates from the right side of the image to the left side and some detailed deformation mechanisms are pointed out in the figures.

For configuration 1, the first core layer subjected to the shock wave loading is the polyurea (PU) interlayer. The core layer arrangement consists of a PU interlayer followed by the graded foam core. It can be observed that at t = 150 μs indentation failure has initiated. This is followed by delamination of the PU layer from the foam core at the bottom of the composite at t = 400 μs. At t = 550 μs delamination can be observed again at the top between the PU layer and foam core as well as core cracking. Also minimal core compression in the first foam core layer (A300) can be observed at this time. By t = 1150 μs, large core compression in the A300 foam is evident. Along with this compression, heavy core cracking propagating from the back face sheet towards the front face sheet as well as heavy interface delamination is visible. By t = 1800 μs heavy core cracking and interface delamination, are visible, along with compression in the core (A300 only).

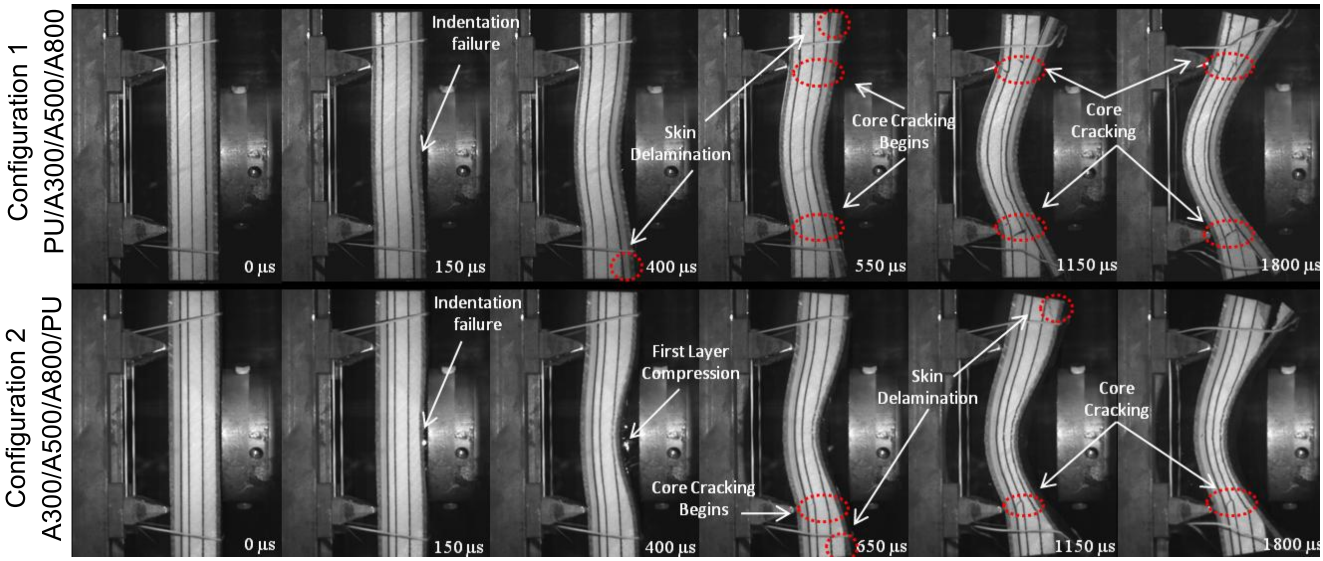
Configuration 1
PU/A300/A500/A800
Indentation failure
Skin Delamination
Core Cracking Begins
Core Cracking
0 μs
150 μs
400 μs
550 μs
1150 μs
1800 μs
Configuration 2
A300/A500/A800/PU
Indentation failure
First Layer Compression
Core Cracking Begins
Skin Delamination
Core Cracking
0 μs
150 μs
400 μs
650 μs
1150 μs
1800 μs

Fig. 5 Real Time side-view deformation of sandwich composites under shock wave loading

In configuration 2, the first core layer that is subjected to the shock wave loading is the A300 foam layer. The core layer arrangement consists of the graded foam core followed by the PU interlayer. Indentation failure in configuration 2 is evident at t = 150 μs. Indentation failure is the followed by a stepwise compression of the core. The first core layer (A300) has completely compressed by t = 400 μs, By t = 650 μs, compression has moved into the second core layer (A500) and core cracking has initiated. Also at this time skin delamination between the front face sheet and first core layer is visible. At t = 1150 μs minimal delamination is visible at the top of the composite between the first and second (A300 and A500) foam core layer. Heavy core compression can be seen in the second foam core layer (A500). By t = 1800 μs heavy core compression can be observed (A300 and A500), along with very minimal core cracking and delamination.

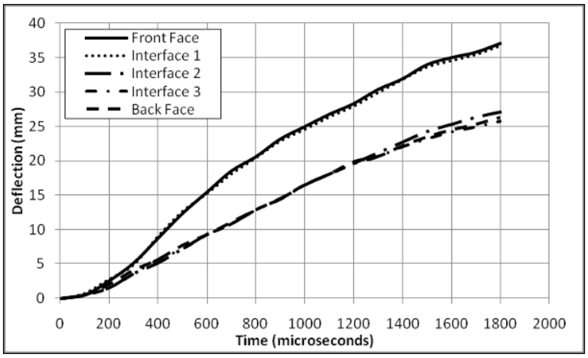

(a) Configuration 1

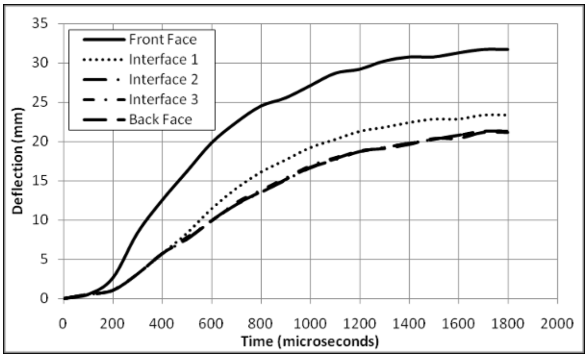

(b) Configuration 2

Fig. 6 Mid-point deflection curves for Configuration 1 and Configuration 2 (a typical response)

Both configurations exhibited a double-winged deformation shape which means both configurations were under shear loading. Unlike configuration 1 where the progression of damage was core cracking followed by interface delamination, the progression of damage in configuration 2 was core compression followed by core cracking. The difference between the two configurations and damage progression arises in the location of the PU interlayer. For configuration 2 the PU interlayer is located after the foam core, and thus the entire core, foam and PU respectively, is monotonically graded based on increasing wave impedance and therefore a stepwise core compression is visible. With the PU interlayer located in the front of the foam core (configuration 1), the core is non-monotonically graded, and thus the stepwise compression is not observed, instead heavy core cracking is evident.

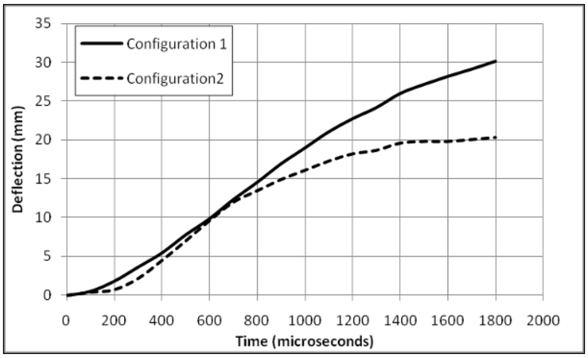

Fig. 7 Comparison of the back face deflection (averaged)

The mid-point deflections of the front face (front skin), interface 1 (between first and second core layer), interface 2 (between second and third core layer), interface 3 (between third and fourth core layer), and the back face (back skin) for both configurations, directly measured from the real – time side –view images, are shown in fig. 6 respectively. A comparison between the back face deflections for both configurations can be seen in fig. 7. It can be observed in fig. 6 that for both configurations the first core layer (A300) compresses 80% of its original thickness (10 mm compression). For configuration 1, A300 is located between interface 1 and interface 2, while in configuration 2 A300 is located between the front face and interface 1.The major difference in deflection for the two configurations can be observed in the A500 layer. For configuration 1 (between interface 2 and interface 3), it follows the same trend as interface 2, interface 3, and the back face which means there was minimal compression in the core layer. Unlike configuration 1, A500 in configuration 2 (between interface 2 and interface 3) compresses 25% of its original thickness (3.5 mm of compression). With its ability to compress in a stepwise manner, configuration 2 has the ability to weaken the shock wave by the time it has reaches the back face of the specimen and thus reduces back face deflections. This phenomenon is evident in fig. 7. It is clear from the figure that configuration 2 exhibits 33% less back face deflection than configuration 1.

4.2.2 DIGITAL IMAGE CORRELATION (DIC)

The real time response of the sandwich composites was generated using Digital Image Correlation and the results are shown in fig 8 - fig. 10. Through DIC analysis using the inspection of a single point in the center of the back face sheet , the data for mid-point deflection, in plane strain and particle velocity during the entire blast loading event was extracted. The results of the in plane strain and particle velocity shown in fig. 8 and fig. 9 respectively. Note the data in the figures is averaged amongst samples tested.

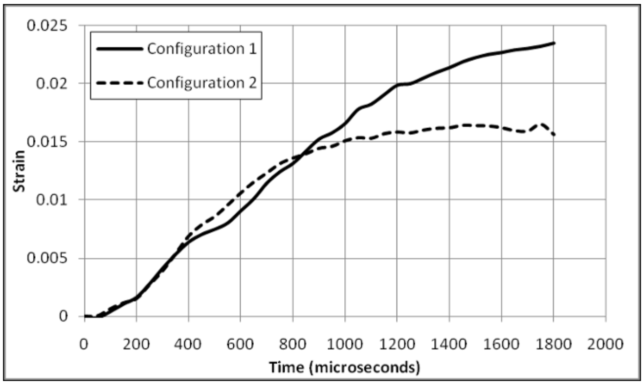

Fig. 8 In-plane strain for both configurations

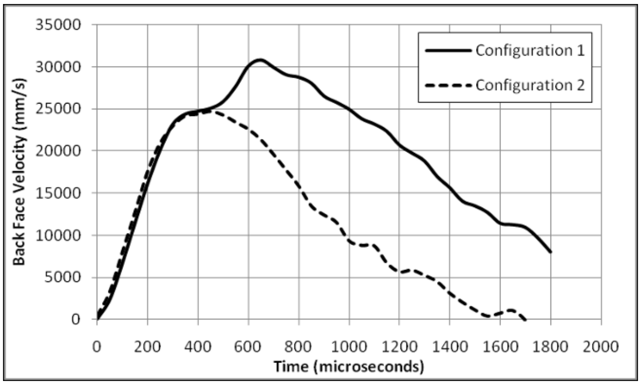

Fig. 9 Back face particle velocity

Fig. 8 shows the in plane strain of both configurations. It can be seen that configuration 1 exhibits 25% strain, while configuration 2 only exhibits only 15% strain. The back face particle velocity can be observed in fig. 9. The back face reaches a maximum mid-point particle velocity of 30,000 mm/s, while configuration 2 reaches a maximum back face particle velocity of only 25,000 mm/s. Therefore, configuration 2 reduces back face particle velocity by 15%.

Fig. 10 shows the full-field back-view deflection of configuration 2. By t= 1800 μs, the deflection in the center of the back face sheet is 21 mm. It is evident from the figure that both point inspection and full-field analysis provide great confidence in our results.

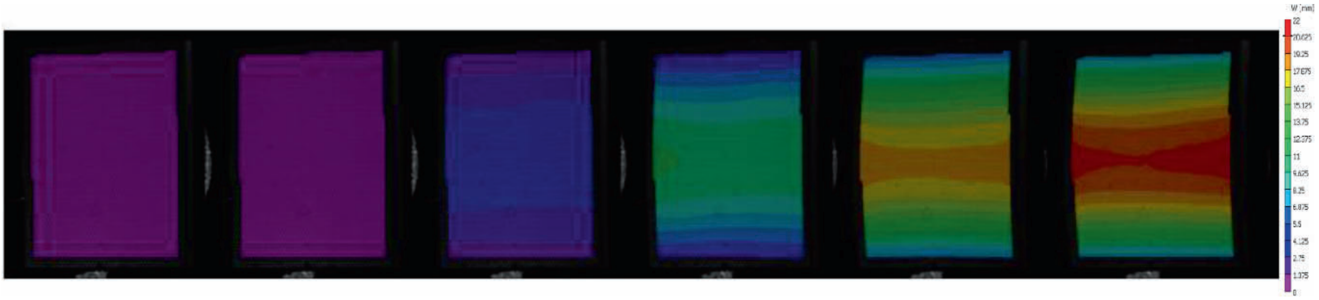

Fig. 10 Full field back view deflection of Configuration 2

4.2.3 POST MORTEM ANALYS

After the shock event occurred, the damage patterns in the sandwich composites with a functionally graded foam core and PU interlayer were visually examined and recorded using a high resolution digital camera and are shown in fig.11. For configuration 1, there were two main cracks located at the support position. Delamination is visible between the PU layer and first layer of foam core, as well as between the bottom layer of foam core and back face sheet. Also compression was only observed in the A300 core layer. Unlike configuration 1, configuration 2 showed minimal core cracking and delamination. Configuration 2 also exhibited more compression in the core, especially in the first two layers of foam (A300 and A500). This means that configuration 2 is more flexible than configuration and therefore it showed much less permanent deformation

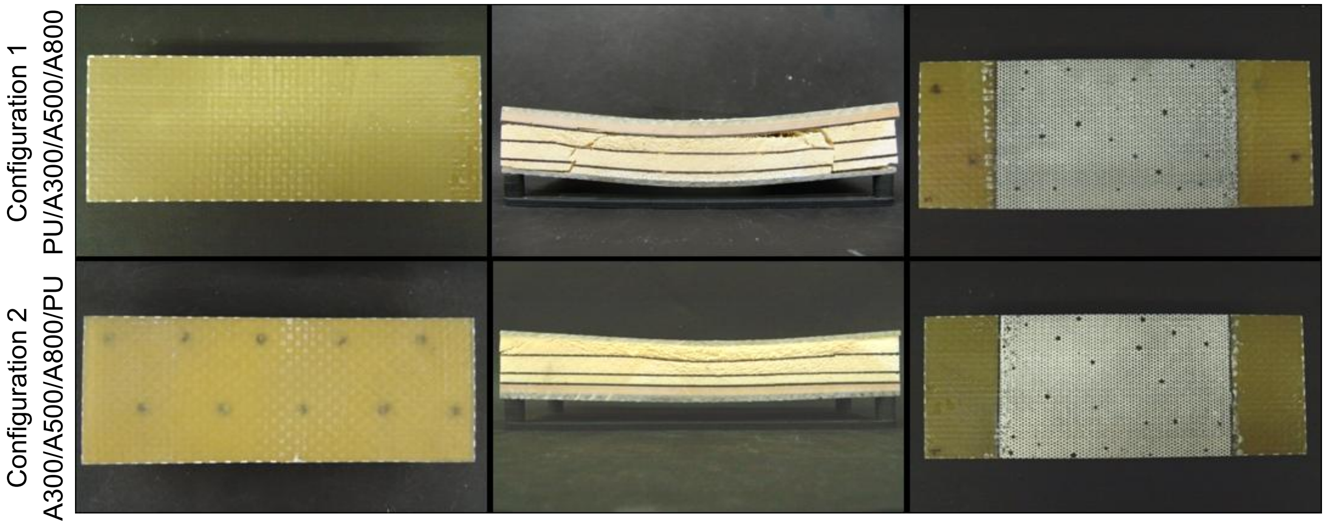

(a) Front face sheet (blast side) (b) Foam and PU core (c) Back face sheet

Fig. 11 Visual examination of sandwich composites
after being subjected to high intensity blast load

4.2.3 ENERGY EVALUATION

The energy redistribution behavior of both configurations was thoroughly analyzed using the methods described in the authors previous work [12] and are shown in fig. 12 and fig. 13. Fig. 12 shows the estimated energies for configuration 1 and configuration 2 while fig. 13 shows a comparison of the remaining energy in both configurations. It can be observed from the figure that both configurations have the same amount of energy remaining in the system after the shock loading event has occurred. Since both configurations were subjected to the same initial pressure (incident energy), and the remaining energy was the same, it can be concluded that both configurations exhibit similar energy absorbing capabilities.

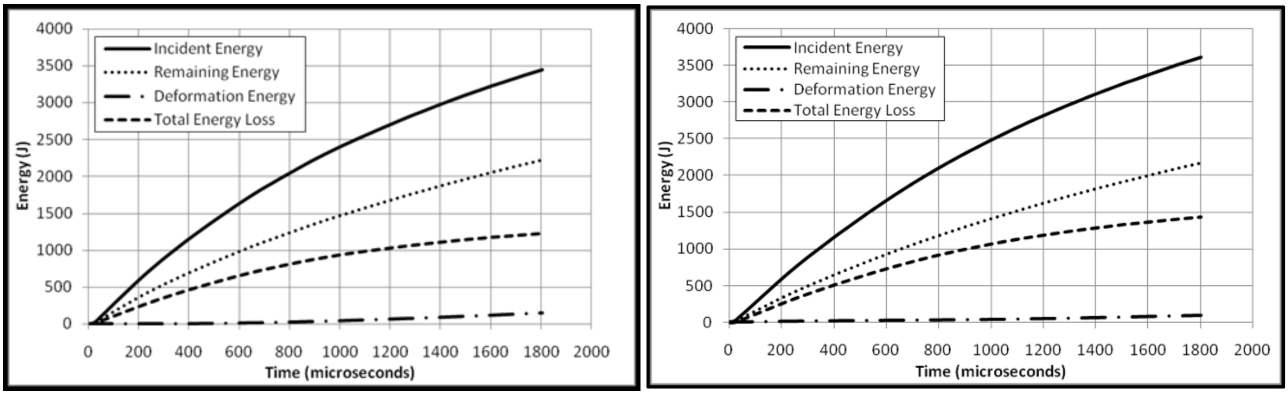

(a) Configuration 1

(b) Configuration 2

Fig. 12 Energy redistribution behavior for both configurations

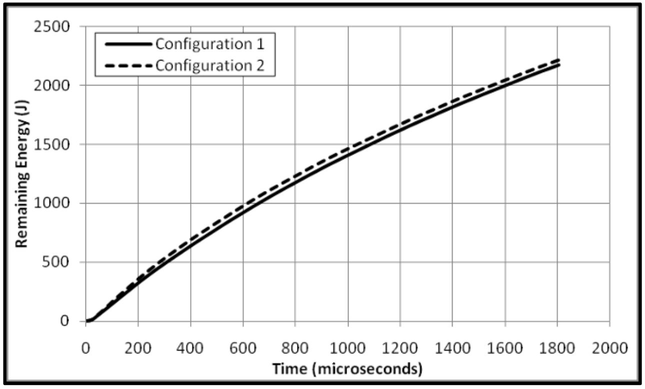

Fig. 13 Comparison of the total energy loss for both configurations

6. Summary

The following is the summary of the investigation:

(1) The dynamic stress-strain response is significantly higher than the quasi-static response for every type of Corecell^{TM} A foam studied. Both quasi-static and dynamic constitutive behaviors of Corecell^{TM} A series foams (A300, A500, and A800) and polyurea interlayer show an increasing trend.

(2) Sandwich composites with different core arrangements, configuration 1 (PU/A300/A500/A800) and configuration 2 (A300/A500/A800/PU), were subjected to shock wave loading. The overall performance of configuration 2 is better than that of configuration 1. With the application of polyurea behind the foam core and in front of the back face sheet this core layer arrangement allows for stepwise core compression. Much larger compression is visible in the A300 and A500 core layers in this configuration than visible in configuration 1. This compression reduces the shock wave by the time it reaches the back face sheet and thus the overall deflection, in-plane strain, and velocity are reduced.

(3) The methods used to evaluate the energy as described in the author's previous work [6] were implemented and the results analyzed. It was observed that both configurations had the same amount of energy remaining in the system after the shock loading event occurred. Since both configurations were subjected to the same initial pressure (incident energy), and the remaining energy was the same, both configurations exhibited similar energy absorbing capabilities.

Acknowledgement

The authors kindly acknowledge the financial support provided by Dr. Yapa D. S. Rajapakse, under Office of Naval Research (ONR) Grant No. N00014-04-1-0268. The authors acknowledge the support provided by the Department of Homeland Security (DHS) under Cooperative Agreement No. 2008-ST-061-ED0002. Authors thank Gurit SP Technology and Specialty Products Incorporated (SPI) for providing the material as well as Dr. Stephen Nolet and TPI Composites for providing the facility for creating the composites used in this study.

References

[1] Xue, Z. and Hutchinson, J.W., Preliminary assessment of sandwich plates subject to blast loads. International Journal of Mechanical Sciences, 45, 687-705, 2003.

[2] Fleck, N.A., Deshpande, V.S., The resistance of clamped sandwich beams to shock loading. Journal of Applied Mechanics, 71, 386-401, 2004.

[3] Dharmasena, K.P., Wadley, H.N.G., Xue, Z. and Hutchinson, J.W., Mechanical response of metallic honeycomb sandwich panel structures to high-intensity dynamic loading. International Journal of Impact Engineering, 35 (9), 1063-1074, 2008.

[4] Apetre, N.A., Sankar, B.V. and Ambur, D.R., Low-velocity impact response of sandwich beams with functionally graded core. International Journal of Solids and Structures, 43(9), 2479-2496, 2006.

[5] Li, Y., Ramesh, K.T. and Chin, E.S.C., Dynamic characterization of layered and graded structures under impulsive loading. International Journal of Solids and Structures, 38(34-35), 6045-6061, 2001.

[6] Wang, E. Gardner, N. and Shukla, A., The blast resistance of sandwich composites with stepwise graded cores. International Journal of Solids and Structures, 46, 3492-3502, 2009.

[7] Yi, J., Boyce, M.C., Lee, G.F., and Balizer, E. Large deformation rate-dependent stress-strain behavior of polyurea and polyurethanes. Polymer, 47(1), 319-329, 2005.

[8] Amirkhizi, A.V., Isaacs, J., McGee, J., Nemat-Nasser, S. An experimentally-based constitutive model for polyurea, including pressure and temperature effects. Philosophical Magazine, 86 (36), 5847-5866, 2006.

[9] Fatt, M.S. Hoo, Ouyang, X., Dinan, R.J., Blast response of walls retrofitted with elastomer coatings. Structural Materials, 15, 129-138, 2004.

[10] Roland, C.M., Twigg, J.N., Vu, Y., Mott, P.H. High strain rate mechanical behavior of polyurea. Polymer, 48(2), 574-578, 2006.

[11] Tekalur, S. A., Shukla, A., and Shivakumar, K. Blast resistance of polyurea based layered composite materials. Composite Structures, 84, 271-281, 2008.

[12] Bahei-Ed-Din, Y. A., Dvorak, G.J., Fredricksen, O.J. A blast-tolerant sandwich plate design with a polyurea interlayer. International Journal of Solids and Structures. 43, 7644-7658, 2006.

Proceedings of the SEM Annual Conference
June 7-10, 2010 Indianapolis, Indiana USA
©2010 Society for Experimental Mechanics Inc.

The Blast Response of Sandwich Composites with In-Plane Pre-Loading

Erheng Wang, and Arun Shukla
Dynamic Photomechanics Lab, Dept. of Mechanical, Industrial and Systems Engineering
The University of Rhode Island, 92 Upper College Road, Kingston, RI 02881, USA
wange@egr.uri.edu

ABSTRACT

The in-plane pre-loading in the ship hull structures during their service life will likely change the dynamic behavior of these structures under transverse blast loading. In the present study, the dynamic behavior of E-glass Vinyl Ester composite face sheet / foam core sandwich panels with in-plane pre-loading is investigated under shock wave loading. A special test fixture was designed which enables the application of uni-axial in-plane compressive loading when the panels are subjected to transverse blast loading. Blast tests are carried out under two levels of pre-loading and with no pre-loading using a shock tube apparatus. A high-speed side-view camera system and a high-speed back-view Digital Image Correlation (DIC) system are utilized to acquire the real time deformation of the sandwich panels. The results show that the in-plane pre-loading induced buckling and failure in the front face sheet. This mechanism greatly reduced the blast resistance of the sandwich composites. The back face deflections, back face in-plane strains, and mitigated energies were also experimentally quantified.

INTRODUCTION

Ship hull structures always undergo longitudinal compressive loading and their longitudinal strength is the most fundamental and important strength to ensure the safety of a ship structure [1]. When these pre-loaded structures are subjected to transverse blast loading, the coupling of the in-plane pre-load and transverse blast loading will likely reduce the blast resistance of the structures. Composite materials, such as sandwich structures, have important applications in such ship structures due to their advantages, such as high strength/weight ratio and high stiffness/weight ratio. Unfortunately, the most recent research focuses on the blast resistance of composite structures without an in-plane pre-load [2-4]. To date, no experimental investigations on pre-loaded structures under blast load have been done.

The dynamic responses of in-plane pre-stressed composite structures under low-velocity transverse impact have been studied. Heimbs et al.[5] tested carbon-fiber/epoxy laminated plates under an in-plane compressive pre-load. An increased deflection and energy absorption was observed under a pre-load of 80% of the buckling load. Sun et al. [6] and Choi [7] analytically investigated the effects of pre-stress on the dynamic response of composite laminates. They found that the initial in-plane tensile load increased the peak contact force while reducing the total contact duration and deflection. The compressive load reacted oppositely. However, contact impact loading will induce localized damage, which is different with blast loading. Thus, these results cannot be extended to the blast response of composite structures. The absence of experimental data of pre-stressed structures under blast loading also makes it impossible to verify the numerical models. Therefore, there is an urgent need to investigate the pre-loading effect on the dynamic behavior of composite materials under blast loading.

The present paper experimentally studies the dynamic behavior of pre-loaded sandwich composites under blast loading. The sandwich panels are composed of E-glass Vinyl Ester composite face-sheets and Corecell P600 Foam core. A fixture was designed in order to enable different static in-plane compression loadings on the sandwich panels prior to transverse blast loading. Two levels of pre-loading and zero pre-loading cases were chosen to study the effect of the pre-loading on the dynamic response of the sandwich composites. A high-speed photography system with three cameras is utilized to capture real-time motion images. Digital Image Correlation (DIC) techniques will be utilized to obtain the details of the deformation of the sandwich panels during the events. Post mortem visual observations of the test samples will provide more evidence to indentify the failure modes. These results were used to analyze the mechanism of dynamic failure of the pre-loaded sandwich composites.

T. Proulx (ed.), *Dynamic Behavior of Materials, Volume 1*, Conference Proceedings of the Society for Experimental Mechanics Series,
DOI 10.1007/978-1-4419-8228-5_31, © The Society for Experimental Mechanics, Inc. 2011

2. MATERIAL AND SPECIMEN

The skin materials that were utilized in this study are E-Glass Vinyl Ester (EVE) composites. The woven roving E-glass fibers of the skin material were placed in a quasi-isotropic layout $[0/45/90/-45]_s$. The fibers were made of the 18 oz/yd^2 area density plain weave. The resin system used was Ashland Derakane Momentum 8084 and the front skin and the back skin consisted of identical layup and materials. The core material used in the present study was Corecell^{TM} P600 styrene foams, which is manufactured by Gurit SP Technologies specifically for blast defence applications. Table 1 lists important material properties of this foam from the manufacturer's data [8].

Table1. Material properties of the foam core [8]

Foam Type	Nominal Density (kg/m^3)	Compression Modulus (MPa)	Compression Strength (MPa)	Shear Elongation %
Corecell P600	122	125	1.81	67%

The VARTM procedure was carried out to fabricate sandwich composite panels. The overall dimensions for the specimen were 102 mm wide, 254 mm long and 33 mm thick. The foam core itself was 25.4 mm thick, while the skin thickness was 3.8 mm. The average areal density of the samples was 17.15 kg/m^2. Fig. 1 shows a real image of a specimen and its dimensions.

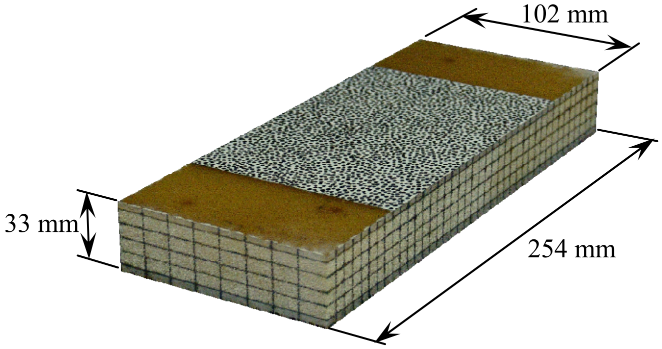

Fig. 1 Real specimen and its dimensions

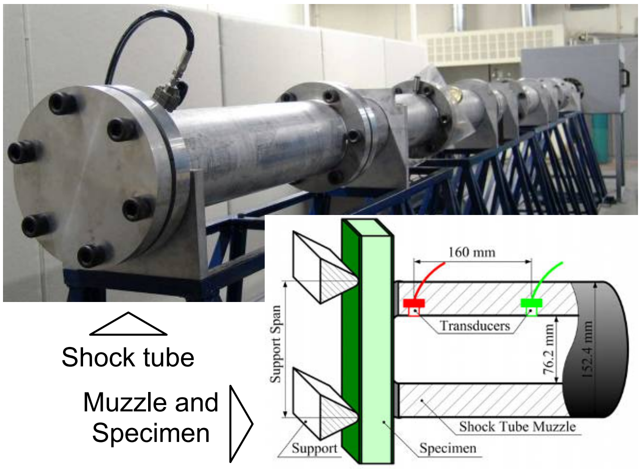

Fig. 2 Shock tube apparatus

3. EXPERIMENT SETUP AND PROCEDURE

3.1 SHOCK TUBE

The shock tube apparatus was utilized in present study to obtain the controlled blast loading. The detail of this apparatus can be found in Ref.[4]. Fig. 2 shows the shock tube apparatus with muzzle detail. The final muzzle diameter is 76.2 mm. Two pressure transducers (PCB102A) are mounted at the end of the muzzle section with a distance 160 mm. The support fixtures ensure simply supported boundary conditions with a 152.4 mm span.

3.2 IN-PLANE PRE-LOADING FIXTURE

Fig. 3 shows the fixture used to apply the in-plane static compression loading on the sandwich composite panels. The loading head is connected to a hydraulic loading cylinder, which is mounted on the frame. An aluminum cylinder with an outer-diameter Ø50.8 mm and an inner-diameter Ø38.1 mm is positioned between two plates.

Two strain gages, which are attached on this aluminum cylinder, measure the deformation of this cylinder and then calculates the load applied on the specimen. The support fixture and in-plane pre-loading fixture are all securely fastened inside a dump tank.

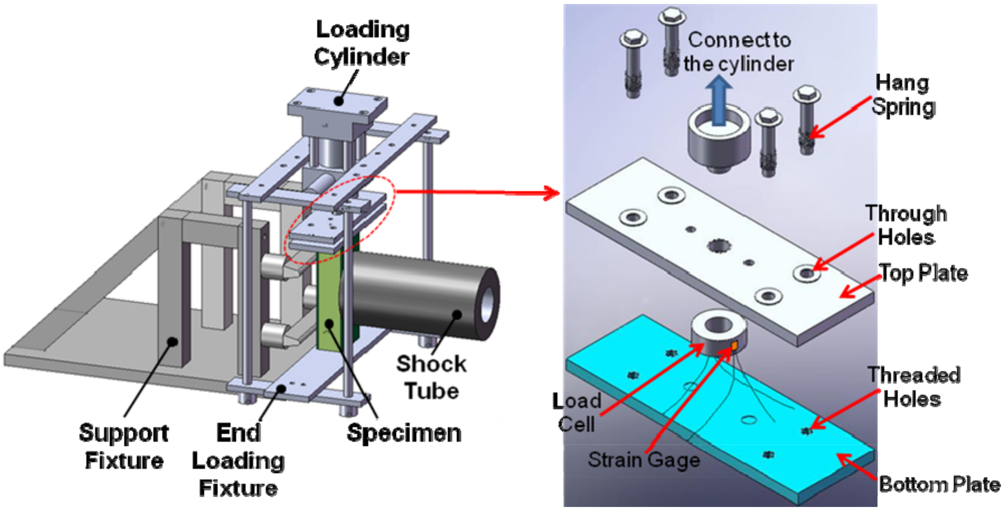
Loading Cylinder
Shock Tube
Support Fixture
End Loading Fixture
Specimen
Connect to the cylinder
Hang Spring
Through Holes
Top Plate
Load Cell
Strain Gage
Threaded Holes
Bottom Plate

(a) Fixture assembling (b) Load head

Fig. 3 In-plane pre-loading fixture

3.3 HIGH-SPEED PHOTOGRAPHY SYSTEMS

Two high-speed photography systems were utilized to capture the real-time 3-D deformation data of the specimen. Fig. 4 shows the experimental setup. It consisted of a back-view 3-D Digital Image Correlation (DIC) system with two cameras and a side-view camera system with one camera. All cameras are Photron SA1 high-speed digital camera, which have an ability to capture images at a frame-rate of 20,000 fps with an image resolution of 512×512 pixels for a 1 second time duration. These cameras were synchronized to make sure that the images and data can be correlated and compared.

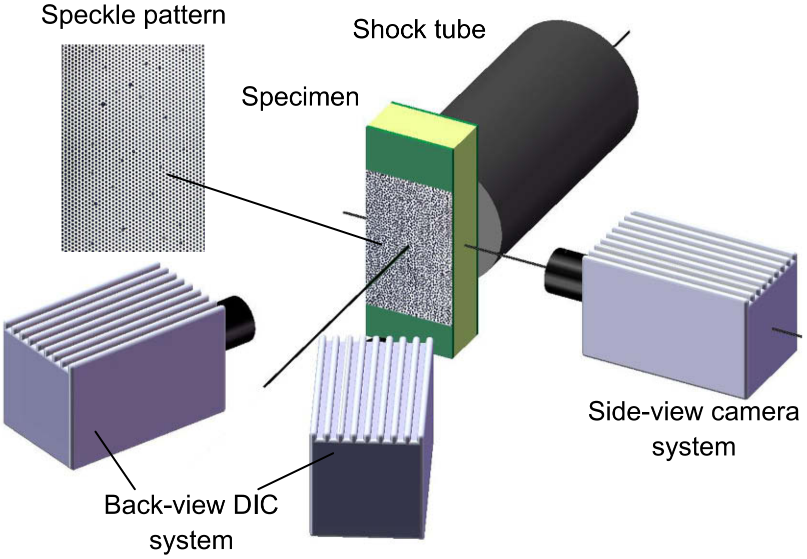
Speckle pattern
Shock tube
Specimen
Side-view camera system
Back-view DIC system

Fig. 4 High-speed photography systems

The 3-D DIC technique is one of the most recent non-contact methods for analyzing full-field shape, motion and deformation. Two cameras capture two images from different angles at the same time. By correlating these two images, one can obtain the three dimensional shape of the surface. Correlating this deformed shape to a reference (zero-load) shape gives full-field in-plane and out-of-plane deformations. To ensure good image quality, a speckle pattern with good contrast was put on the specimen prior to experiments.

3.4 EXPERIMENTAL PROCEDURE

In the present study, the shock wave loading has an incident peak pressure of approximately 1 MPa and a wave velocity of approximately 1030 m/s. The in-plane compression loading was applied on the specimen and held at a constant level until the specimen is subjected to the transverse shock wave loading. Three levels of static compression loading were chosen: 0 kN, 15 kN, 25kN. For each compression loading, at least two samples were tested. When the shock wave was released, the computer and high-speed photography system were triggered to record the pressure data and deformation images.

4. EXPERIMENTAL RESULTS AND DISCUSSION

4.1 REAL TIME DEFORMATION

4.1.1 SIDE-VIEW IMAGES

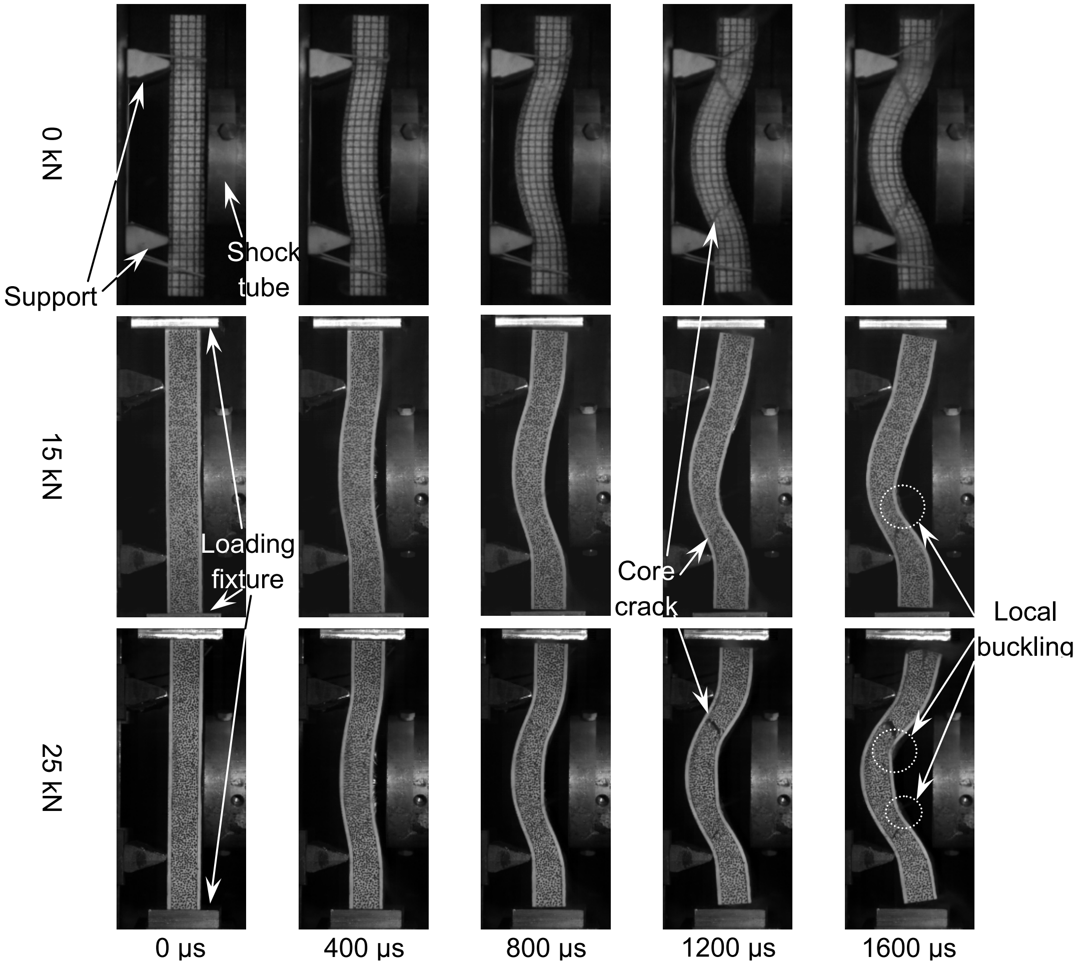

Fig. 5 Real time side-view deformation of sandwich composites with pre-loadings

Fig. 5 shows the real time side-view images of sandwich composites with different levels of compression pre-loading. The shock wave propagates from the right side of the image to the left side. Some deformation details are pointed out in the images.

From the images, it can be clearly seen that the initial deformation modes (prior to 400 μs) for the sandwich composite with different levels of pre-loading are very similar. They all show global bending with a typical double wing shape, which means that the core is under intense shear loading. Then, the sandwich composite without pre-loading (0 kN) continues bending symmetrically. The front face-sheet shows a profile with a smooth curvature. This means there is no local buckling in the front face. For the sandwich composite with 15 kN pre-loading, the initial deformation with a symmetric profile shifts to an asymmetric mode. The section of the front face-sheet close to the lower support exhibits more curvature than the section close to the upper support. This asymmetrical phenomenon indicates that there is local buckling at the lower section of the front face-sheet. At approximately 1600 µs, the fiber debonding of the front face-sheet shows clearly that local buckling is evident (shown in the white circle). For the sandwich composite with 25 kN pre-loading, there are two obvious kinks in the front face-sheet. The middle section between these two kinks shows a flat profile, which means that no moment is applied on this section. It indicates that there are two failure hinges, such as local buckling, happened at the kink positions.

Fig. 6 shows the back face out-of-plane deflection contours of sandwich composites with different levels of compression pre-loading from DIC technique. It can be seen that the deflections of the points through the width of the panels are almost same. The deflections of the panels with 0 and 15kN pre-loading are very similar. The panel with 25 kN pre-loading has higher deflection.

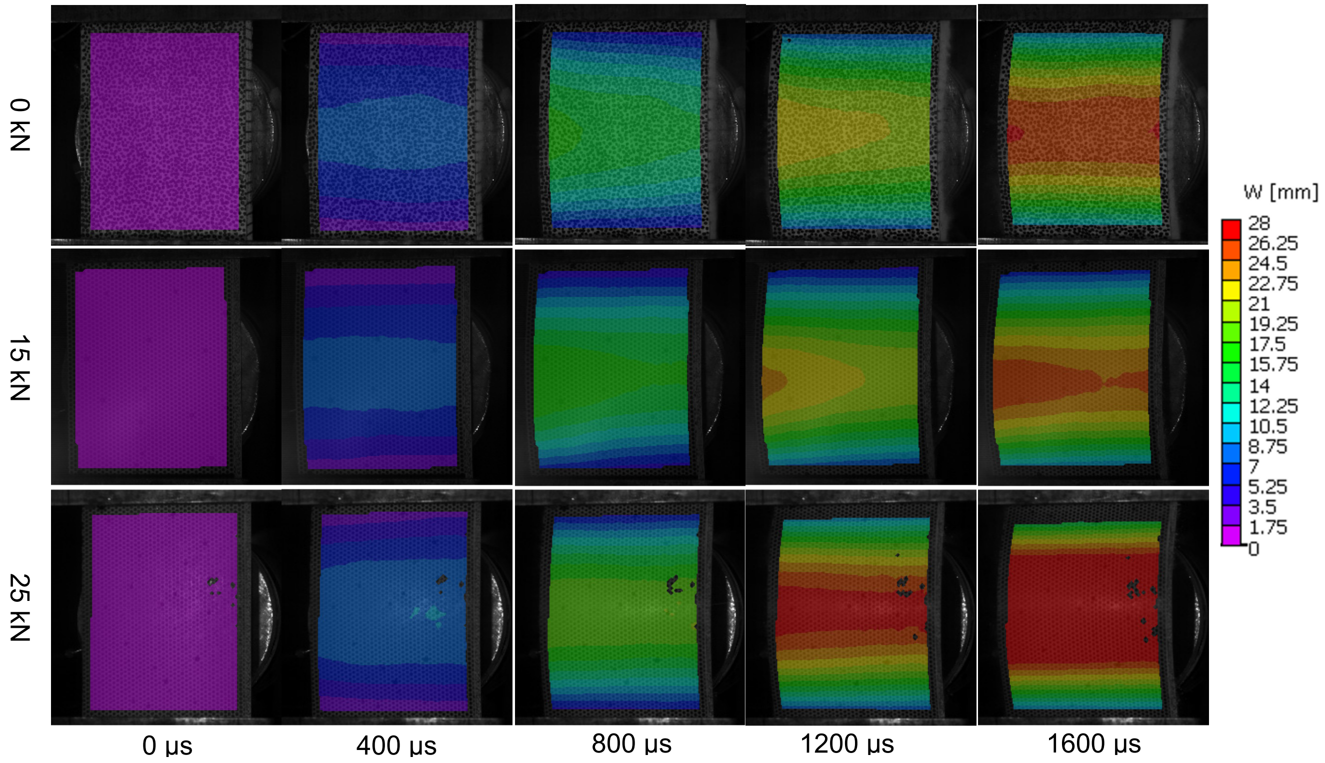

Fig. 6 Out-of-plane deflection contour of sandwich composites with pre-loadings

4.1.2 DEFLECTION AND IN-PLANE STRAIN OF THE FACE-SHEET

Fig. 7 shows the deflections of the middle point located on the front and back faces from the side-view high-speed images. From the plots, the defections of the front and back faces for each panel are almost overlapped. This means that there is no core compression in the core thickness direction. The panels with 0 and 15kN pre-loading have similar deflections while the deflection of the panel with 25 kN pre-loading is higher. This is evident in fig. 6.

Fig. 8 shows the in-plane strain eyy of the middle point of the back face from the DIC technique. Here, the vertical direction is y axis. It can be see clearly that the trend of the in-plane strains is much different from that of the out-of-plane deflections. Though the deflections are almost identical, the back-face in-plane strain of the panel with 15 kN pre-loading is much higher than that with 0 kN pre-loading. This shows that the in-plane pre-loading reduces the blast resistance of the sandwich composites. It can also be seen that the in-plane strains are almost identical for all levels of pre-loading prior to 400 μs, which means that the deformation mechanisms are very similar. This is also evident in the side-view high-speed images (Fig. 5).

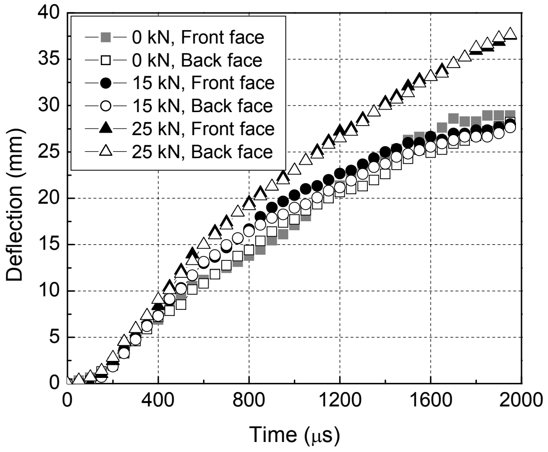

Fig. 7 Deflections of middle point at back and front faces

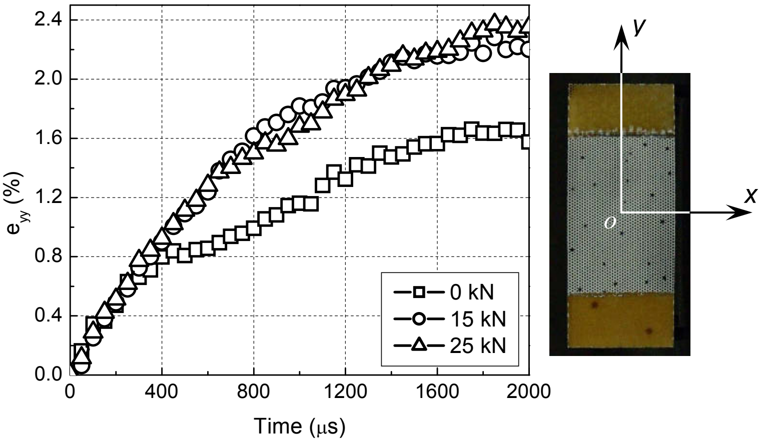

Fig. 8 In-plane strain on the back face

4.2 POST MORTEM ANALYSIS

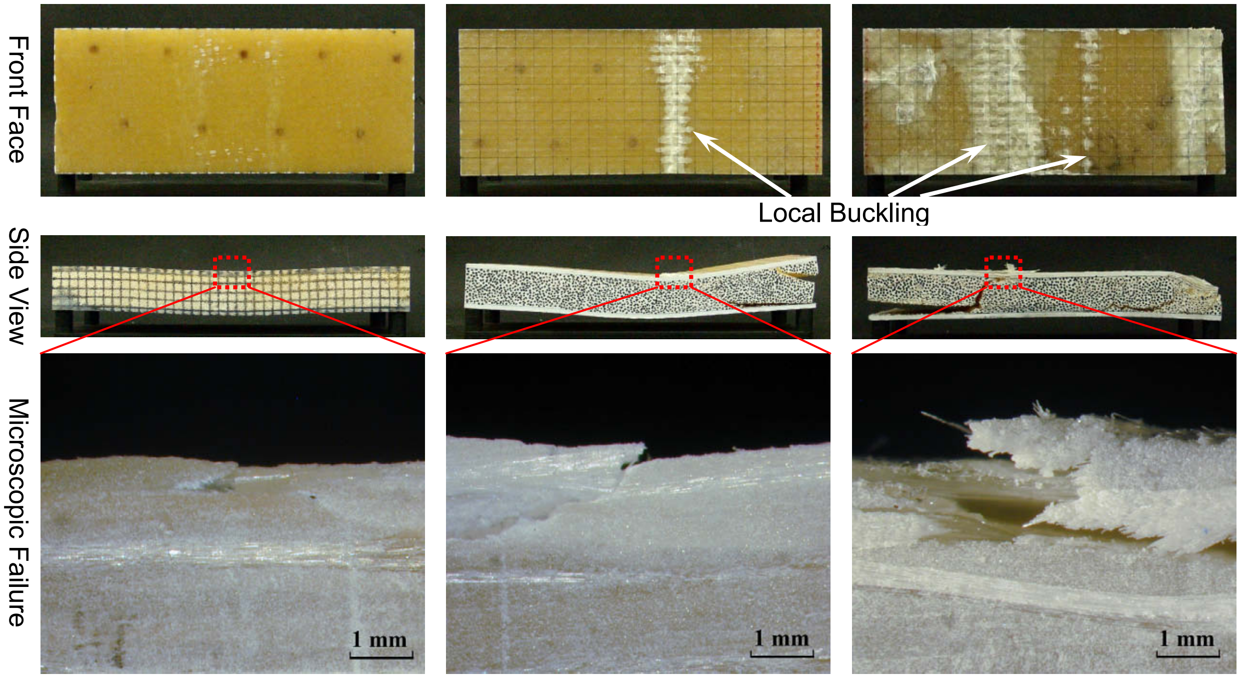

0 kN 15 kN 25 kN

Fig. 9 Post mortem images of sandwich composite with different pre-loading

The damage patterns of the sandwich panels after the shock event occurred were visually examined and recorded using a high resolution digital camera and are shown in Fig.9. Since the back face sheets don't show any change after the experiments, we don't show them here. From the front face-sheet images, the local buckling positions demonstrate an apparent trend. Note the yellow color is the original color of the specimen and the white color signifies fiber delamination and face-sheet buckling. For the panel with 0 kN pre-loading, there is no buckling on the front face. For the panel with 15 kN pre-loading, the buckling only occurred at one position, which is correlated to the section with large curvature in the side-view high-speed image. For the panel with 25 kN pre-loading, buckling occurred at two positions beside the center of the specimen, which are correlated to the two kinks in the side-view high-speed image. Those white areas at the end of the specimen are not due to local buckling induced by the pre-loading. It is due to the collision between the specimen and shock tube during the blast loading process. From the side view images, the core crack and delamination between the core and face sheets also increase with the increase of the in-plane pre-loading.

Microscopic analysis of the buckling region observed in the sandwich panels was done using a Nikon SMZ microscope. These micro images, also shown in Fig. 9, make apparent an obvious trend. For the panel with 0 kN pre-loading, there is almost no crack in the front face. For the panel with 15 kN pre-loading, the crack crossed the first two fiber layers of the front face sheet. For the panel with 25 kN pre-loading, the crack was totally opened and propagated more deeply into the face sheet. The edge of the crack shows the evidence of tearing.

5. CONCLUSIONS

Sandwich composites, with E-glass Vinyl Ester composite face sheet and CoreCell^{TM} P600 foam core, were put under an in-plane pre-load prior to being subjected to a transverse shock wave loading. Three levels of pre-loading were chosen to study the effect of pre-stresses on the dynamic behavior of the sandwich composites. A high-speed photography system and the Digital Image Correlation (DIC) technique were utilized to obtain full-field 3-D deformation data. The results show that the in-plane pre-loading induced local buckling in the front face sheet of the sandwich composites during the blast loading process. This mechanism changed the deformation mode of the sandwich composites. It is clear that higher levels of pre-loading caused more damage in the front face sheet, larger out-of-plane deflection, and higher in-plane strain on the back face sheet. Consequently, the over-all blast resistance of sandwich composites was significantly reduced.

ACKNOWLEDGEMENT

The authors kindly acknowledge the financial support provided by Dr. Yapa D. S. Rajapakse, under Office of Naval Research (ONR) Grant No. N00014-04-1-0268. The authors acknowledge the support provided by the Department of Homeland Security (DHS) under Cooperative Agreement No. 2008-ST-061-ED0002. Authors also thank Dr. Stephen Nolet and TPI Composites for providing the facility for fabricating the materials used in this study.

REFERENCES

[1] Yao, T., Hull girder strength, Marine Structures, 16,1-13, 2003.

[2] Turkmen, H.S. and Mecitoglu, Z., Dynamic response of a stiffened laminated composite plate subjected to blast load, Journal of Sound and Vibration, 221(2), 371-389, 1999.

[3] Batra, R.C. and Hassan, N.M., Blast resistance of unidirectional fiber reinforced composites, Composites Part B-Engineering, 39(3), 427-433, 2005.

[4] Wang, E., Gardner, N. and Shukla, A., The blast resistance of sandwich composites with stepwise graded cores, International Journal of Solid and Structures, 46, 3492-3502, 2009.

[5] Heimbs, S., Heller, S., Middendorf, P., Hahnel, F. and Weiße, J., Low velocity impact on CFRP plates with compressive preload: Test and modeling, International Journal of Impact Engineering, 36, 1182-1193, 2009.

[6] Sun, C.T. amd Chen, J.K., On the impact of initially stressed composite laminates, Journal of Composite Materials, 19, 490-504, 1985.

[7] Choi, I.H., low-velocity impact analysis of composite laminates under initial in-plane load, Composite Structures, 86, 251-257, 2008.

[8] http://www.gurit.com

Proceedings of the SEM Annual Conference
June 7-10, 2010 Indianapolis, Indiana USA
©2010 Society for Experimental Mechanics Inc.

Laboratory Blast Simulator for Composite Materials Characterization

Guojing Li and Dahsin Liu
Dept. of Mechanical Engineering, Michigan State University, East Lansing, MI 48824

ABSTRACT

Blasts and explosives have raised serious concerns in recent years due to the fatal injury and catastrophic damage they have caused in the combat zones and due to industrial accidents. Owing to their lightweight and complex damage process, fiber-reinforced composite materials have been found to have higher energy absorption capability and to be able to generate less lethal debris than conventional metals when subjected to impact loading. In order to characterize the blast resistance of composite materials, a piston-assisted shock tube has been modified for simulating blast tests in the laboratory due to its high safety, repeatability, accessibility and low cost. Although real blasts can be simulated relatively easily by using TNT or other chemicals, they, however, cannot be performed in general laboratories like many materials and structures testing due to their potential danger and restriction, hence hindering the design of new materials with high blast resistance. By carefully adjusting the individual components, piston-assisted shock tube has been shown to be able to produce blast waves for characterizing composite materials.

1. INTRODUCTION

In order to simulate blast waves in a general laboratory, high-pressure pressure waves may be used. However, it is imperatively important that the primary characteristics of blast waves, i.e. a blunt shock wave front followed by a trailing wave with an exponential decay, must be closely resembled in the simulated blast waves. Figure 1 shows a typical blast wave profile. It consists of a shock wave and a decayed trailing wave.

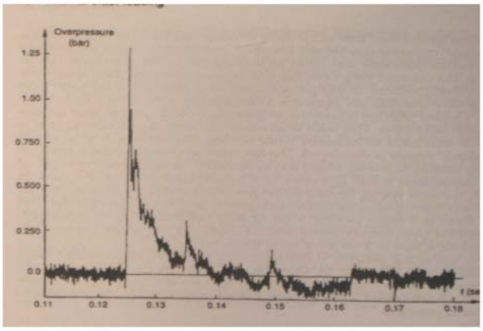

Figure 1 – A typical pressure history from a real blast.

T. Proulx (ed.), *Dynamic Behavior of Materials, Volume 1*, Conference Proceedings of the Society for Experimental Mechanics Series, DOI 10.1007/978-1-4419-8228-5_32, © The Society for Experimental Mechanics, Inc. 2011

Among the facilities capable of generating shock waves, shock tube [1-4] is perhaps the most commonly available. The shock tube was originally developed as a supersonic wind tunnel. Figure 2 shows a three-section, piston-assisted shock tube and a testing chamber. Details of the shock tube can be found in Reference [5,6]. Figure 3 shows a typical pressure history generated from the shock tube without the piston. Clearly, there is a shock wave right in the beginning. The high pressure of the shock wave lasts a long duration of 6ms. It is because of this extended long range of constant pressure at high speed, approximately 5 Mach, the shock tube is useful for supersonic aerodynamic investigations.

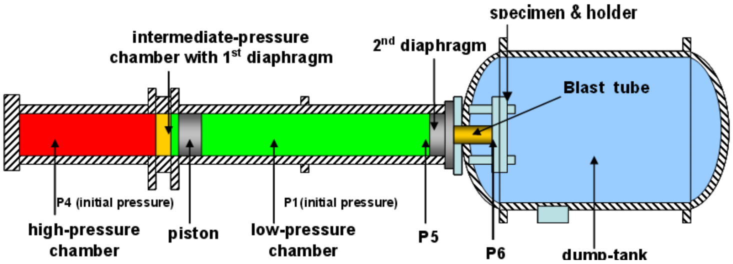
specimen & holder
intermediate-pressure chamber with 1st diaphragm
2nd diaphragm
Blast tube
P4 (initial pressure)
P1(initial pressure)
high-pressure chamber
piston
low-pressure chamber
P5
P6
dump-tank

Figure 2 – Schematic of a piston-assisted shock tube and the associated blast tube and testing chamber.

Although a shock tube can provide a shock wave, its pressure level may not be high enough for simulating blast waves which usually have ultra-high pressure levels. When compared with the real blast wave shown in Figure 1, the profile of the pressure waves generated from the shock tube is also lack of an exponential decay immediately after the shock wave. In order to increase the pressure up to a useful level, a piston may be inserted in the shock tube, as also shown in Figure 1, to increase the pressure level significantly. Figure 4 shows a typical pressure history from the shock tube with a piston. The pressure peak is now significantly higher than that generated without a piston due to the compression of the gas located in front of the piston by the piston. And the pressure wave has a rapid decay right after the peak.

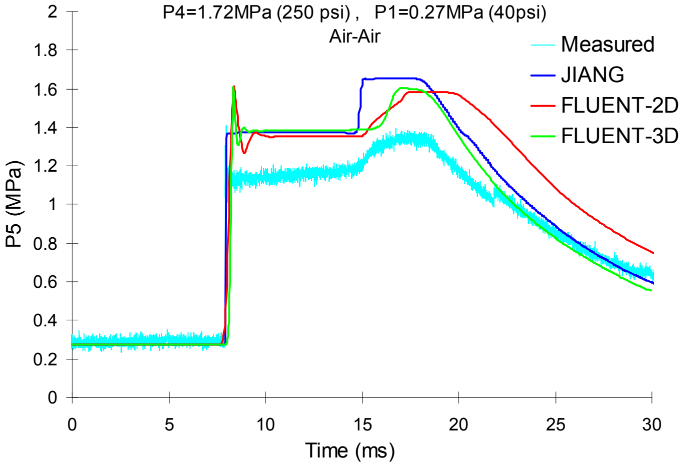

Figure 3 – Typical pressure histories from both experimental measurement and computational analyses by FLUENT.

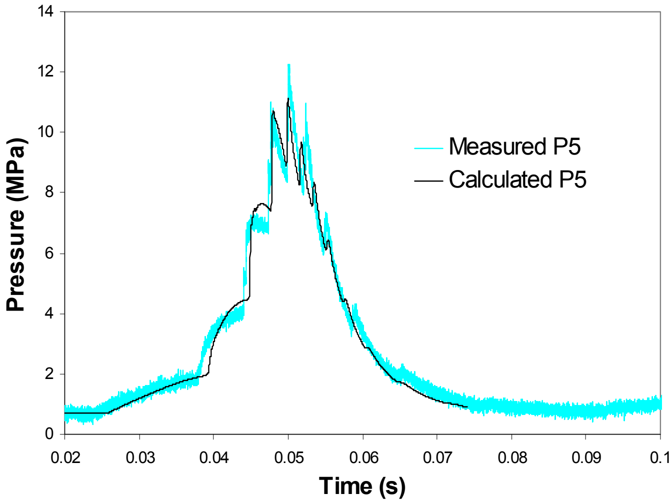

Figure 4 – Typical pressure history generated from a piston-assisted shock wave.

The major defect of the pressure wave generated from the piston-assisted shock tube is the loss of the shock wave. As shown in Figure 4, the pressure increases step by step as the piston is driven toward the right end of the shock tube. The steps are likely formed due to the high driving pressure left to the piston and the low pressure waves reflecting from the right end of the shock tube. In order to modify the pressure wave to resemble a blast wave, i.e. a high-pressure shock wave with an exponentially decayed trailing wave immediately right after it, a diaphragm is required. When the pressure level is approaching the peak, the diaphragm, which is usually made of a metal artificial defect, will be ruptured instantaneously. Accordingly, a truncated wave front like the blunt wave front of a shock wave can be formed. And a simulated blast wave can be achieved.

2. BLAST SIMULATION FACILITY

Figure 2 shows a schematic of a shock tube and a testing chamber. The tube has an inner diameter of 8cm and a length of 610cm. It is divided into three sections. The high-pressure section is 200cm long and located on the left side of the shock tube. The low-pressure section is 400cm long and located on the right side of the shock tube. The intermediate-pressure section is situated between the high-pressure section and the low-pressure section and has a length of 10cm. Two diaphragms are used to separate the tube into three sections, one on each end of the intermediate-pressure section. Depending on the pressure levels in the sections, different metals and thicknesses are chosen for the diaphragms. In addition, the diaphragms are introduced with defects so they can be ruptured instantaneously to form a shock wave. As mentioned earlier, a piston is used to largely increase the pressure level of the pressure wave. It has a mass of 2kg.

In order to transform the generated pressure wave into a blast wave, which has a shock wave with a blunt wave front immediately followed by a rapidly decayed trailing wave, a small tube, so-called blast tube, is added to the end of the shock tube. The blast tube has an inner diameter of 1.25cm and a length of 15cm. Right at the boundary between the shock tube and the blast tube, there is another diaphragm. It is used to hold the pressure wave up to a pre-determined level. Once the diaphragm is ruptured instantaneously, a shock wave will be formed in the beginning of the blast wave. Figure 5 shows the profile of a blast wave coming out of the blast tube. It is calculated based on the computational fluid dynamic program (CFD)

FLUENT and has a spherical shape.

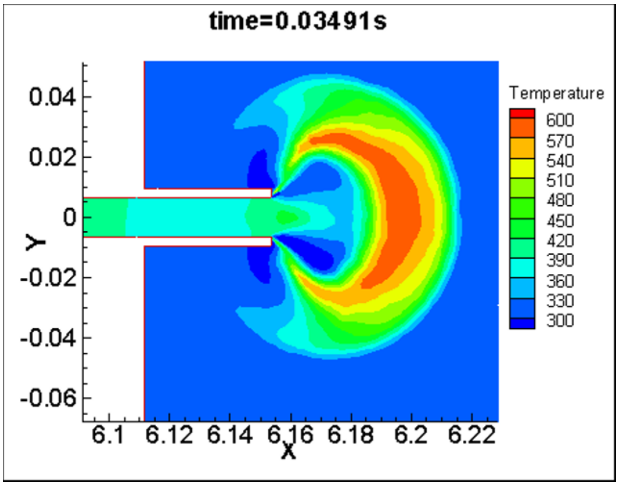

Figure 5 – Spherical shape of a blast wave based on FLUENT simulation.

3. BLAST TESTING

For blast testing, a specimen should be solidly held in front of the blast tube with or without a distance from the blast tube depending on the simulation condition. Since the blast wave coming out of the blast tube expands spherically and its pressure level drops rapidly as it moves away from the blast tube, a large specimen with a testing zone of 12.5cm in diameter and bolted around the circumference may be used. On the contrary, if a specimen is held against the blast tube, only a small zone slightly greater than the 1.25cm diameter of the blast tube will be significantly affected. Hence, a specimen with a testing zone of 3.8cm in diameter and bolted around the circumference should be sufficiently large.

Besides the plate specimens mentioned above, beam specimens can also be tested using the blast simulation facility. For example, specimens of 30cm x 10cm can be held at two locations, e.g. each is held at 5cm from each end, and loaded in the middle section, resulting in a three-point-bend type of testing. In this type of testing, a blast tube of 8cm identical to the shock tube can be used. It is also possible to use a blast tube with 8cm in diameter at one end to match with the shock tube and transforming into a vertical slit of 8cm x 1.25cm at the other end. With each type of blast tube, the specimen being tested should be held against the blast tube.

4. TESTING RESULTS

Glass/epoxy composite plate specimens with a thickness of 0.32cm were trimmed to have dimensions of 10cm x 10cm. Each specimen was then clamped by two steel ring holders with eight bolts equally spaced along a circumference of a 7.5cm diameter. A circular opening of a diameter of 3.8cm was left for blast testing. The reason for choosing these dimensions for specimens and specimen holder was because of the advantage of maximizing the use of the pressure waves produced by the shock tube based blast testing facility to identify the composite's resistance to pressure loading. In other words, the pressure waves were concentrated to damage the composite rather than to deform the specimens. Figure 6 shows the image of a damaged specimen. There was a perforation zone in the middle of the specimen surround by delamination and burnout of composite.

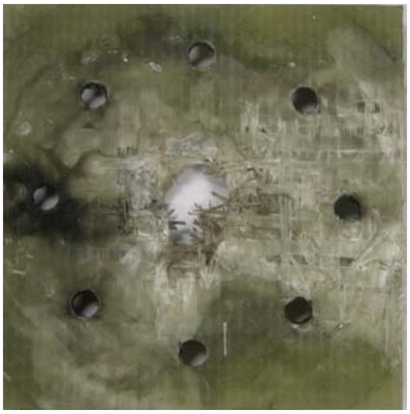

Figure 6 – Damaged glass/epoxy composite plate.

In beam testing, each specimen, also of 0.32cm thick was trimmed to be 30cm long and 10cm wide. During the testing, each specimen was simply-supported by two strips. Each strip had a radius of curvature of 0.32cm for supporting the specimens. The distance between the apexes of the curvatures of the two plates, i.e. the span of simply-supported boundary, was 21.3cm.

Each simply-supported specimen was loaded with a pressure wave at the center of its span. The pressure wave had a diameter of 8cm and a maximum pressure around 9.5MPa. Since the simply-supported specimens had a width of 10cm, which was close to the diameter of the blast waves 8cm, the pressure wave leaked out of the specimens when bending occurred. Experimental results for simply-supported specimens subjected to pressure waves are shown in Figures 7.

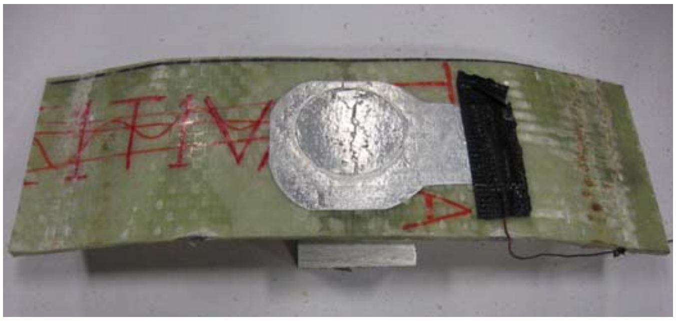

(a)

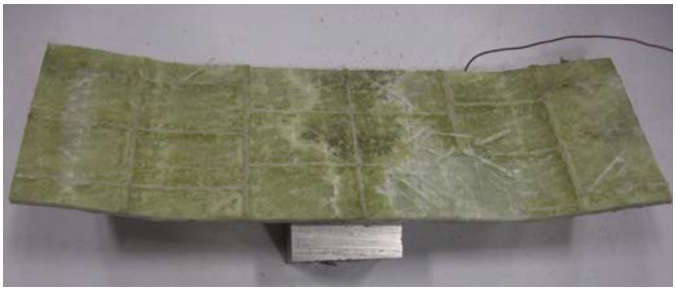

(b)

Figure 7 – Damaged glass/epoxy composite beam (a) measured side and (b) loaded side.

5. SUMMARY

The blast testing technique and procedures presented in this study is suitable for screening the blast resistance of potential armor materials. It is a highly repeatable, controllable, accessible and safe technique and can be operated by trained engineers in ordinary laboratories. The cost of running a test has also been demonstrated to be much lower than corresponding real blasts.

The fidelity of the blast testing technique, as compared with the corresponding real blasts, can be concluded based on the similarity between the characteristics of real blast waves and those of simulated blast waves. The characteristics of waves include (1) the blunt shock wave front, (2) the rapid decay right after the shock wave and (3) the spherical wave profile. The damaged morphology of the glass/epoxy specimens due to simulated blast loading was also found to be qualitatively the same as those due to real blasts.

The loading condition, boundary condition and specimen geometry and dimensions can be modified to suit individual testing needs. Measuring techniques for recording pressure, temperature, velocity and deformation of the specimens need to be further developed to identify the fundamental parameters involved in the highly dynamic blast testing.

ACKNOWLEDGEMENTS

The authors wish to express their sincere thanks to the U.S. Army TACOM for financial support and Drs. Doug Templeton and Basavaraju Raju of TARDEC, Warren, Michigan.

REFERENCES

[1] Itoh, K., “Improvement of a Free Piston Driver for a High-Enthalpy Shock Tunnel”, *Shock Waves*, Vol. 8, No. 4, 1998, pp. 215-233.

[2] Zhao, W., “Performance of a Detonation Driven Shock Tunnel”, *Shock Waves,* Vol. 14, No. 1-2, 2005, pp. 53-59.

[3] Marrion, M. C., “The gas-dynamic effects of a hemisphere-cylinder obstacle in a shock-tube driver”, *Experiments in Fluids,* Vol. 38, 2005, pp. 319-327.

[4] Aizawa, k., Yshino, S., Mogi, T., Shiina, H., Ogata, Y., Wada, Y. and Koichi, A., “Study on Detonation Initiation in Hydrogen/Air Flow”, Proceedings of 21st ICDERS, Poitiers, France, 2007.

[5] Li, Q., Liu, D., Templeton, D.W. and Raju, B.B., “A Shock Tube-Based Impact Testing Facility,” *Experimental Techniques*, 31(4), 25-28, 2007.

[6] Li, G., Li, Q., Liu, D., Raju, B.B. and Templeton, D.W., “Designing Composite Vehicles against Blast Attack,” SAE 2007 World Congress, Detroit, MI, April 16-19, 2007, Paper 2007-01-0137.

Proceedings of the SEM Annual Conference
June 7-10, 2010 Indianapolis, Indiana USA
©2010 Society for Experimental Mechanics Inc.

Experimental Characterization of Composite Structures Subjected to Underwater Impulsive Loadings

F. Latourte, D. Grégoire, H.D. Espinosa*
Northwestern University, Department of Mechanical Engineering, 2145 Sheridan Road,
Evanston IL 60201, USA
* Corresponding author: espinosa@northwestern.edu

ABSTRACT

The use of composite materials in the construction of marine vessels and aircrafts is increasing and motivated by low weight advantages. These structures have to offer blast resistance, which is critical for a wide range of transportation applications. In this context, we present an investigation of the performance of composite monolithic and sandwich panels subjected to underwater impulsive loadings. A fluid-structure interaction experimental setup allows monitoring the real time deflection of composite panels exposed to blast loadings, by means of a shadow moiré technique. The performance of these panels is compared to solid and sandwich steel structures having a similar areal mass. Both non-destructive and destructive post mortem analysis are conducted to evaluate the extent and the type of damage induced by the dynamic event. This characterization is performed at different locations of the specimens and for different impulse intensities. The experimental results will be correlated to numerical predictions obtained from finite element analysis in a second presentation.

Introduction

The construction of marine vessels, wind turbines, and civilian transportation system is on demand for high strength to weight ratio materials like glass reinforced plastics (GRP) composites. Moreover, these materials possess a low magnetic signature that is of importance to minesweeping vessels, and stealth applications [1].

Laboratory scale experiments have been conducted to study the dynamic response of composite sandwich beams subjected to projectile impacts [2, 3], the ballistic resistance of 2D and 3D woven sandwich composites [4], and the impact response of sandwich panels [5, 6] with optimized nanophased cores [7, 8]. Several experimental studies specific to marine composites subjected to impulsive loadings are also reported in [9].

In the present work, a fluid-structure interaction experimental apparatus is utilized to apply underwater impulsive loadings to composite solid and sandwich panels. This experimental apparatus, originally introduced in [10] has previously allowed the characterization of monolithic steel plates [10] and sandwich steel constructions [11, 12]. This scaled down apparatus enables testing panels of gage radius L=76.2 mm that can be easily manufactured using layups consistent with marine hulls in terms of stacking sequence and number of plies. The relatively small thickness of the plate specimens (ranging from 6 to 19 mm) is advantageous in term of post mortem evaluation by ultrasonic or microscopy techniques. Furthermore, the setup is highly instrumented and allows recording of deflection profile histories over the entire span of the panels, for a well defined impulse.

The objective is here to characterize composite panel performance in terms of impulse-deflection, using the norm already introduced in [10] that was used to characterize different steel plates as well as steel sandwiches of various core topologies [10-12]. Failure modes, damage mechanisms and their distributions will be discussed for composite monolithic and sandwich panels subjected to underwater impulsive loading.

Experimental results

Two main different types of panels have been investigated in this work: a solid and a sandwich construction. Composite solid panels consist of nine composite fabrics giving a total thickness of 5.8 mm. Composite

T. Proulx (ed.), *Dynamic Behavior of Materials, Volume 1*, Conference Proceedings of the Society for Experimental Mechanics Series,
DOI 10.1007/978-1-4419-8228-5_33, © The Society for Experimental Mechanics, Inc. 2011

sandwiches consist in six composite fabrics separated by a foam core resulting in a total thickness of 19mm. For the so-called symmetrical sandwiches, one third of the weight is distributed in each facesheet and in the core. Non-symmetrical design was also manufactured, using a heavier airside facesheet.

The composite facesheets are made from quasi-isotropic glass-fiber non-crimp fabric. The layup is infiltrated with vinylester resin and the sandwich panels encompass a 15 mm thick H250 divinycell PVC foam core. The manufacturing was performed in collaboration with Dan Zenkert (KTH-Royal Institute of Technology, Sweden).

Solid and sandwich panels were tested for impulses ranging from 1500 to 5500 and 3200 to 7000 Pa·s, respectively. The dynamic mechanical performance of the panels will be evaluated by means of time histories of deflection profiles together with normalized impulse to normalized deflection plots. Using this metric, GRP panels will be compared to solid and sandwich steel panels characterized in [10-12]. A complementary understanding of the performance of composite material comes from the damage assessment and its distribution within the panel structure. That characterization was experimentally conducted by first a non destructive ultrasonic pulse echo technique and then by cross sectioning the panels to enable macro and micro photography throughout the gage part.

From these observations, the relative importance of fiber breakage, matrix cracking and delamination will be analyzed at different level of impulses and for different constructions. For example, while delamination was extensive in solid panels even at the smallest impulses, it was mostly prevented in sandwich panels. Matrix cracking will be interpreted in terms of stiffness reduction, in order to compare damage distributions at different impulse levels.

References

[1] Mouritz AP, Gellert E, Burchill P, Challis K. *Review of advanced composite structures for naval ships and submarines*. Composite Structures 2001;53(1):21-42.

[2] Johnson HE, Louca LA, Mouring S, Fallah AS. *Modelling impact damage in marine composite panels. International* Journal of Impact Engineering 2009;36(1):25-39.

[3] Tagarielli VL, Deshpande VS, Fleck NA. *The dynamic response of composite sandwich beams to transverse impact. International Journal of Solids and Structures* 2007;44(7-8):2442-2457.

[4] Grogan J, Tekalur SA, Shukla A, Bogdanovich A, Coffelt RA. *Ballistic resistance of 2D and 3D woven sandwich composites*. Journal of Sandwich Structures & Materials 2007;9(3):283-302.

[5] Schubel PM, Luo JJ, Daniel IM. *Low velocity impact behavior of composite sandwich panels*. Composites Part a-Applied Science and Manufacturing 2005;36(10):1389-1396.

[6] Tekalur SA, Shivakumar K, Shukla A. *Mechanical behavior and damage evolution in E-glass vinyl ester and carbon composites subjected to static and blast loads*. Composites Part B-Engineering 2008;39(1):57-65.

[7] Bhuiyan MA, Hosur MV, Jeelani S. *Low-velocity impact response of sandwich composites with nanophased foam core and biaxial (+/- 45 degrees) braided face sheets*. Composites Part B-Engineering 2009;40(6):561-571.

[8] Hosur MV, Mohammed AA, Zainuddin S, Jeelam S. *Processing of nanoclay filled sandwich composites and their response to low-velocity impact loading*. Composite Structures 2008;82(1):101-116.

[9] Porfiri M, Gupta N. *A Review of Research on Impulsive Loading of Marine Composites. In: Major Accomplishments in Composite Materials and Sandwich Structures*, 2009, pp. 169-194.

[10] Espinosa H, Lee S, Moldovan N. *A Novel Fluid Structure Interaction Experiment to Investigate Deformation of Structural Elements Subjected to Impulsive Loading*. Experimental Mechanics 2006;46(6):805-824.

[11] Mori LF, Lee S, Xue ZY, Vaziri A, Queheillalt DT, Dharmasena KP, Wadley HNG, Hutchinson JW, Espinosa HD. *Deformation and fracture modes of sandwich structures subjected to underwater impulsive loads*. Journal Of Mechanics Of Materials And Structures 2007;2(10):1981--2006.

[12] Mori LF, Queheillalt DT, Wadley HNG, Espinosa HD. *Deformation and Failure Modes of I-Core Sandwich Structures Subjected to Underwater Impulsive Loads*. Experimental Mechanics 2009;49(2):257--275.

Proceedings of the SEM Annual Conference
June 7-10, 2010 Indianapolis, Indiana USA
©2010 Society for Experimental Mechanics Inc.

Controlling wave propagation in solids using spatially variable elastic anisotropy

Aref Tehranian, Alireza Amirkhizi, and Sia Nemat-Nasser*

Department of Mechanical and Aerospace Engineering
Center of Excellence for Advanced Materials, University of California San Diego
9500 Gilman Drive, La Jolla, CA 92093-0416 USA

Abstract

Stress wave propagation in solids may be controlled through spatially variable anisotropy. Recently, there have been significant efforts to guide the incident stress waves in desired trajectories in order to protect a sensitive region within the material. Here we present our work on a composite material in which stress waves are guided through smoothly varying elastic anisotropy, while keeping the mass density homogeneous. The axis of anisotropy corresponds to fiber orientation in fiber reinforced composites. In order to guide the stress waves, the axis of anisotropy should smoothly change direction to convey the energy of incident waves.

Keywords: stress wave, anisotropy, composite material, and guide.

Introduction

In transversely isotropic material, the axis of anisotropy (fiber direction in fiber-reinforced composites) can be adjusted to guide the energy of an incident quasi-longitudinal wave along a given trajectory [1-3]. If the wave vector deviates only slightly from the fiber direction, then quasi-longitudinal waves will travel more or less in the fiber direction [4-5]. Now, if the material anisotropy direction changes slightly, the group velocity will follow the same variation and change accordingly. If the wave vector initially coincides with the material's principal direction which undergoes smooth changes, then the acoustic wave energy packet would follow a similar path. Thus, it is possible to control the elastic stress-wave trajectory by proper design of material anisotropy. This is illustrated both numerically and experimentally.

Numerical Modeling

The fabricated material has isotropic mass density and is considered homogeneous at the scale of the considered wave-lengths, even though microscopically it is highly heterogeneous. Therefore, in numerical calculation, the material is modeled as a homogeneous transversely isotropic material with constant elastic moduli in material principal directions. In finite element models, the material direction for each element is specified as a function of position in accordance with the fabricated composite.

Numerical modeling of the experimental sample II in Figure 1 is performed using LS-DYNA. The model is subjected to a single 1MHz sinusoidal pulse of 100N force acting normal to the material surface over a set of nodes centered at point M. The rest of the boundary, including the central cavity is stress-free. In order to solve the problem in plain strain, out-of-plane degrees of freedom are constrained for all the solid elements. As the acoustic wave propagates in the model, it follows the smoothly varying direction of highest stiffness. The wave packet splits into two parts near the central cavity and travels parallel to the surface of the cavity that coincides with the curved direction of highest stiffness (fiber direction). Acoustic waves travelling on the two sides of the opening then join together and finally follow the constant direction of anisotropy at the end.

---

* sia@ucsd.edu Phone: 858 534 4914 Fax: 858 534 2727

T. Proulx (ed.), *Dynamic Behavior of Materials, Volume 1*, Conference Proceedings of the Society for Experimental Mechanics Series, DOI 10.1007/978-1-4419-8228-5_34, © The Society for Experimental Mechanics, Inc. 2011

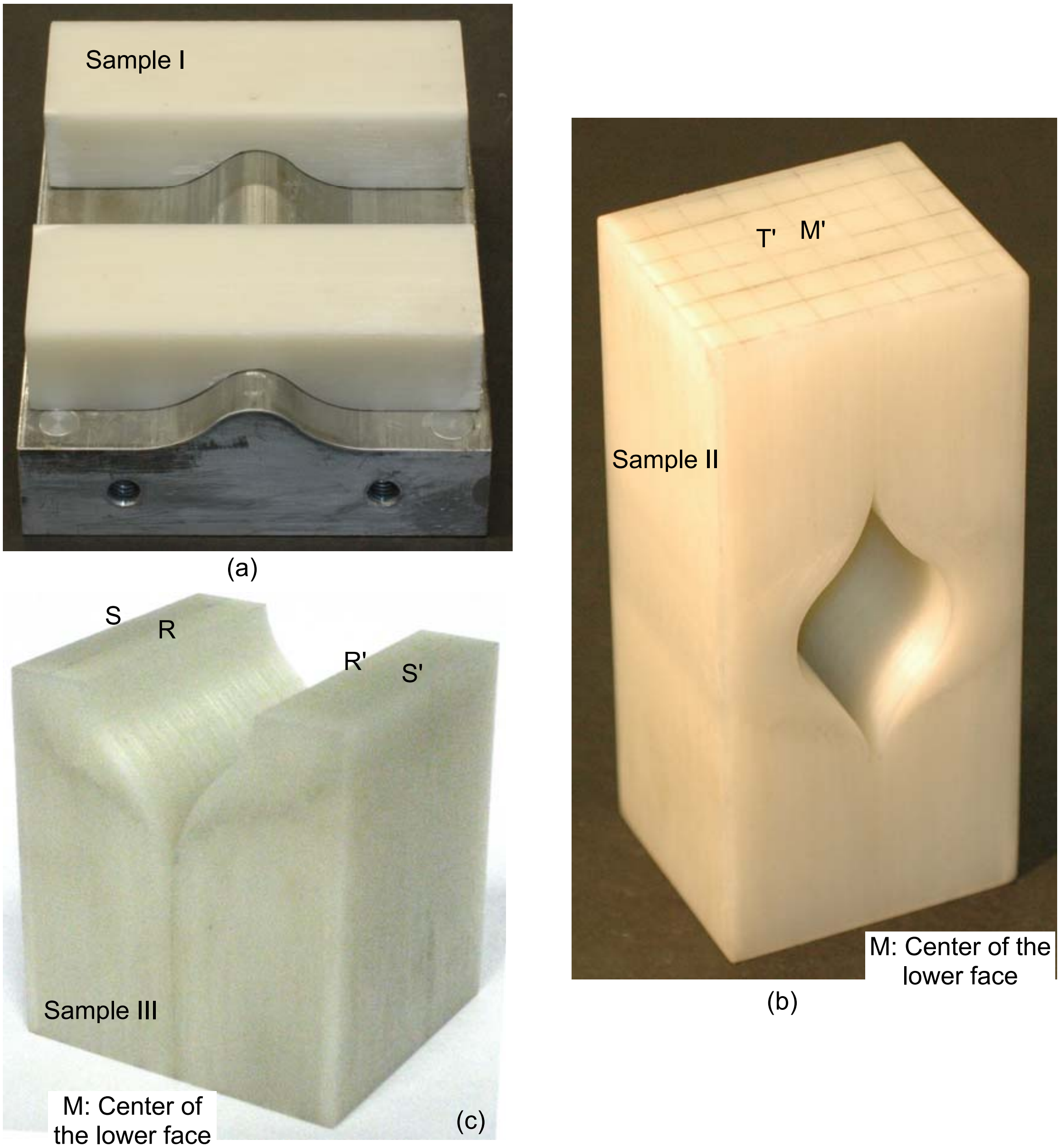

Figure 1: Fabricated fiber reinforced composite material and the designed aluminum mold. (b) Sample II is made of two pieces of composite materials (sample I) glued together with epoxy. A grid is drawn on each side of the sample to measure ultrasonic excitations. (c) Sample III is used to measure the excitation caused by acoustic waves as they cross a plane normal to the fibers, half-way through the length of the sample II.

Experiments and Results

Unidirectional glass/epoxy prepreg sheets of suitable lengths are stacked on the aluminum mold in a pre-calculated sequence to ensure that the fiber content of the resulting composite sample would be essentially uniform throughout the sample (Figure 1). Since the smallest thickness of the sample I is half its greatest thickness, every other pregreg sheet is continuous while in between layers consisted of two equal-length sheets, cut to a size to ensure the uniform glass-fiber density. The prepreg layup was then cured under recommended temperature and pressure cycles [6]. The result is cut lengthwise into three equal pieces (Sample I). Two identical pieces like sample I are glued together using epoxy to fabricate sample II. Sample III is made by cutting sample I in half across its width and then gluing the two pieces together with epoxy.

Ultrasonic measurements are performed on samples I and II. A transducer is placed on the center of lower face (point M) in Figure 1b. The amplitude of transmitted pulse is measured over a grid on the opposite face shown in Figure 1. A similar procedure is performed on sample III. Experimental results demonstrate that the measured transmitted signal is maximum at the center of the opposite sample-face (M'), although a straight line from this point to the actuating transducer (M) passes through the central cavity of the sample. The maximum amplitude in sample III is measured at points R and R' very close to the surface of cavity. This supports the numerical results that predicted the energy of acoustic waves will travel along the varying axis of anisotropy. Thus it is possible to control the stress wave propagation in a solid by designing a material with a smoothly varying anisotropy.

ACKNOWLEDGEMENTS

This work has been conducted at the Center of Excellence for Advanced Materials, CEAM, Department of Mechanical and Aerospace Engineering, University of California San Diego and it has been supported by the Office of Naval Research grant number ONR N00014-09-1-0547.

REFERENCES

[1] Amirkhizi, A. V., Tehranian, A. and Nemat-Nasser, S. “Stress-wave Energy Management through Material Anisotropy,” Wave Motion, (In Press)
[2] Tehranian, A., Amirkhizi, A. V., Irion, J., Isaacs, J. and Nemat-Nasser, S. “Controlling Acoustic-wave Propagation through Material Anisotropy,” Proceedings of Health Monitoring of Structural and Biological Systems III, SPIE 16th Annual International Conference on Smart Structures and Materials & NDE and Health Monitoring, Vol. 7295, San Diego, California, March 9-12, 2009.
[3] Tehranian, A., Amirkhizi, A. V. and Nemat-Nasser, S. “Acoustic Wave-energy Management in Composite Materials,” Proceedings of the SEM Annual Conference, Albuquerque, New Mexico, June 1-4, 2009.
[4] Auld, B. A. “Acoustic fields and waves in solids,” John Wiley & Sons (1973).
[5] Nemat-Nasser, S. and Hori, M., “Micromechanics: overall properties of heterogeneous materials,” Elsevier (1999).
[6] Schaaf, K. L., “Composite materials with integrated embedded sensing networks,” thesis (PhD), University of California San Diego, 20-25, (2008).

Proceedings of the SEM Annual Conference
June 7-10, 2010 Indianapolis, Indiana USA
©2010 Society for Experimental Mechanics Inc.

Constitutive Characterization of Multi-Constituent Particulate Composites

Dr. Jennifer L. Jordan, AFRL/RWME, 2306 Perimeter Road, Eglin AFB, FL 32542,
jennifer.jordan@eglin.af.mil
Dr. Jonathan E Spowart, AFRL/RXLMD, Wright-Patterson AFB, OH
Mr. D. Wayne Richards, AFRL/RWME, Eglin AFB, FL 32542

Abstract

Multi-constituent epoxy-based particulate composites consisting of individual particles of aluminum and a second phase (copper, nickel or tungsten) have been synthesized. The mechanical and physical properties of the composite depend on the mechanical and physical properties of the individual components; their loading density; the shape and size of the particles; the interfacial adhesion; residual stresses; and matrix porosity. These multi-phase particulate composites have been generated to investigate the deformation of aluminum in the presence of the second phase. Quasi-static and dynamic compression experiments have been performed to characterize the materials. The microstructures of the quasi-statically and dynamically deformed samples have been quantified to determine the amount of deformation in the aluminum particles, as a function of their proximity (i.e. near or far) from the second phase particles.

Introduction

Particulate composite materials composed of one or more varieties of particles in a polymer binder are widely used in military and civilian applications. They can be tailored for desired mechanical properties with appropriate choices of materials, particle sizes and loading densities. Several studies on similar epoxy-based composites have been reported and have shown that particle size [1,2], shape [3], and concentration [4] and properties of the constituents can affect the properties of particulate composites. In composites of Al_2O_3 particles in epoxy, increasing the particle concentration and decreasing the particle size were found to increase the stress at 4% strain [5]. A study of aluminum-filled epoxy found adding a small amount of filler (~ 5 vol.%) increased the compressive yield stress, but additional amounts of filler decreased the compressive yield stress [6]. However, tests on glass bead/epoxy composites found that increasing the volume percent of glass bead filler increased the yield stress and fracture toughness of the material [7,8].

Several multi-phase particulate composites have been generated to investigate the deformation of aluminum particles in the presence of a second metallic phase. In this paper, single phase (aluminum and epoxy) and multi-phase (aluminum-metal-epoxy, where metal is copper, nickel, or tungsten) have been prepared. The samples have been deformed at quasi-static and dynamic strain rates and the deformed microstructures have been examined to determine the strain in the particulates.

Experimental Procedure

Five materials were prepared for this study – two composites containing only aluminum and epoxy, with two different volume fractions of aluminum, and three composites containing an additional second metallic phase, at a fixed volume fraction. The manufacturer and average particle size for the powders are given in Table 1. The appropriate volume fractions of powder for each composite were blended into Epon 826 and cured with diethanolamine (DEA). The composite mixture was cast into blocks and appropriate samples were machined. The density of each composite was measured using pyncnometry. The sample names with corresponding volume fractions of metal powders and the measured density are reported in Table 2.

Compression experiments at quasi-static strain rates were conducted with an MTS 810 testing system with a 100 KN test frame. Care was taken to center the samples on the platens prior to testing. MTS software was used to conduct constant displacement rates tests at a strain rate of $9.4 \times 10^{-4} s^{-1}$. A thin layer of PTFE tape was used to lubricate the surfaces of the platen in contact with the test specimen. It was found that this provided better lubrication than a film of Boron Nitride (BN) with a layer of Molybdenum disilicide ($MOSi_2$) on top that was used in

T. Proulx (ed.), *Dynamic Behavior of Materials, Volume 1*, Conference Proceedings of the Society for Experimental Mechanics Series,
DOI 10.1007/978-1-4419-8228-5_35, © The Society for Experimental Mechanics, Inc. 2011

previous studies [9]. In addition to the MTS system recording the loads and displacement of the frame, interfacing software between the test frame and a video extensometer system (VIC Gauge 2.0 from Correlated Solutions Inc.) read input voltages for both the load and displacement. Additionally, this software interfaces with a video system, which allows the user to place virtual displacement gages on the specimen that are tracked as testing takes place. Multiple virtual displacement gages were used for comparison and to enable the test to continue in the event that one gage failed. Samples were loaded to, nominally, 10%, 20% and 30% strain. The samples were then used for post-mortem analysis.

Table 1: Precursor powder characteristics

Powder	Supplier	Average Particle Size (µm)
Aluminum (X81)	Toyal	27
Copper	Atlantic Equipment Engineers	37
Nickel	Atlantic Equipment Engineers	44
Tungsten	H.C. Starck (Kulite)	37

Table 2: Material compositions and measured densities used in this study.

Material	Density (g/cm^3)	Al Vol%	Cu Vol%	Ni Vol%	W Vol%	Epoxy Vol%
Epoxy-35Al	1.725	35				65
Epoxy-45Al	1.875	45				55
Epoxy-Al-Cu	2.475	35	10			
Epoxy-Al-Ni	2.513	35		10		
Epoxy-Al-W	3.652	35			10	

Compression experiments at intermediate strain rates (approximately $1x10^3$ and $5x10^3$ s^{-1}) were conducted using a split Hopkinson pressure bar (SHPB) system [10]. The experiments were conducted using the SHPB system located at AFRL/RWME, Eglin AFB, FL, which is comprised of 1524 mm long, 12.7 mm diameter incident and transmitted bars of 6061-T6 aluminum. The striker is 610 mm long and made of the same material as the other bars. The samples, which were nominally 8 mm diameter by 3.5 mm thick and 5 mm diameter by 2.5 mm thick, are positioned between the incident and transmitted bars. The bar faces were lightly lubricated with grease to reduce friction.

After quasi-static or dynamic testing, representative samples of each material were sliced along the centerline of the specimen, such that a longitudinal section containing the loading direction was visible. This face was mounted, polished, and examined using Scanning Electron Microscopy (SEM). In order to ensure statistical rigor, several images of each sample were obtained, thereby providing metallographic sections of ~100 particles for each of the conditions that were analyzed – (i) aluminum particles in close proximity to second phase particles; (ii) aluminum particles positioned away from second phase particles and; (iii) second phase particles positioned away from aluminum particles.

A deforming particle can be used as a local strain gauge. Assuming that the particle volume is conserved during deformation and that a spheroidal particle with an initial aspect ratio of 1 will deform as an oblate spheroid with its minor axis oriented along the deformation axis in the material, then any longitudinal 2-D section through the particle will have an aspect ratio, γ, directly related to the particle strain, $\bar{\varepsilon}$, by

$$\bar{\varepsilon} = -\frac{2}{3} ln(\bar{\gamma}). \tag{1}$$

In single phase samples, the aspect ratios of ~100 aluminum particles were measured to determine the average strain. In the multi-phase particulate composites, aluminum particles positioned “near” to second phase particles – i.e. those aluminum particles which had a second phase particle as a nearest neighbor – were measured along with aluminum particles that were positioned “far” from any second phase particle, i.e. those that had several particle diameters between themselves and the second phase. Additionally, the aspect ratios of the second phase particles (copper, nickel, or tungsten) were also measured.

Results and Discussion

Stress-strain curves from the five composites that were studied are presented in Figure 1. There is very little difference in the stress-strain responses of the different composites. Since the stress-strain behavior is generally dependant on the volume fraction of particles, small variation is expected in these materials having comparable volume fractions. At strains above 0.05, each of the multi-phase composites show higher flow stresses than the aluminum-containing composites, which rank according to volume fraction of aluminum. At strains below 0.05, The lower volume fraction aluminum composite (Epoxy-35Al) appears to have higher strength than the higher volume fraction composite (Epoxy-45Al) in the quasi-static regime. White, et al. have shown the presence of a percolation threshold in similar composites at a similar level of loading [11], which may account for this difference. This discrepancy is not seen in the dynamic data, where yield and flow stresses all rank according to volume fraction and presence of 2nd-phase particles.

The primary focus of this work is analysis of the strain measured in the particles themselves compared with the global strain measured on the sample. For the quasi-static experiments, these measurements were taken at three levels of strain (0.1, 0.2, and 0.3) and the results are shown in Figure 2. For the dynamic experiments, the level of strain is a result of the sample dimensions and is not as controllable as in the quasi-static experiments, but nevertheless ranges from ~0.3 – 0.45. The results from the dynamic experiments are given in Figure 3.

Figures 2 (a) and 3 (a) compare the strain in aluminum particles positioned “far” from second phase particles in the multi-phase composites and the strain measured in the aluminum particles in the aluminum-epoxy composites, for the quasi-static and dynamic experiments, respectively. In the quasi-static experiments, where the global true strain is precisely controlled, the strain in the aluminum particles tends to cluster above the global true strain, indicating efficient load transfer between the epoxy matrix and the stiffer reinforcement. In addition, the strains measured in the aluminum particles in the multi-phase composites tend to be lower than the strains in the aluminum composites without the second-phase particles, suggesting a stiffening of the matrix (effectively shielding the aluminum particles) by the addition of the second phase. This is consistent with the trends for flow stress shown in Figure 1. In the dynamic experiments, the strain in the aluminum-epoxy composites and in the aluminum particles far from the second phase seems to compare with the global true strain in the sample indicating that these particles are deforming with the epoxy matrix in a homogeneous manner. The difference between the quasi-static experiments and the dynamic experiments may result from load transfer across the

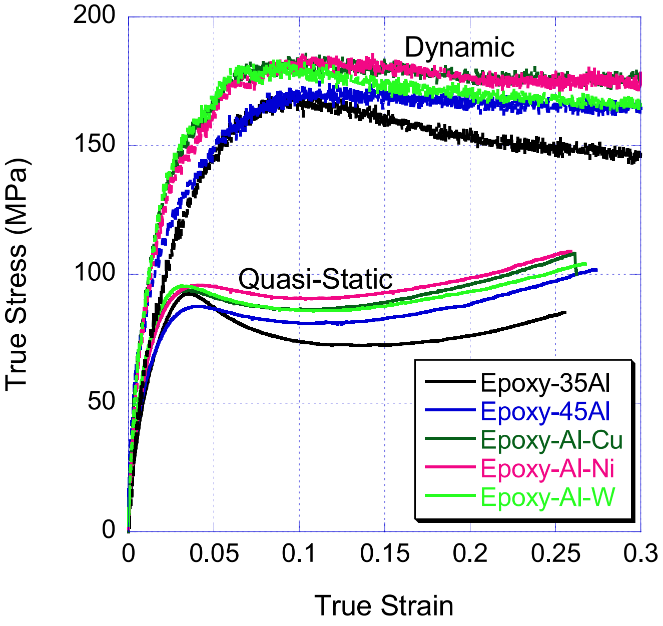

Figure 1: Stress-strain curves for each composite at quasi-static (9×10^{-4} /s) and dynamic (~1.7×10^{3} /s) strain rates.

interface between matrix and particle, which may be less efficient at higher loading rates, leading to lower overall strains in the particles. Moreover, the increased dynamic stiffness of the epoxy matrix may play a key role in reducing the apparent load partitioning between the matrix and reinforcement. In this case, the addition of the stiffer tungsten particles would have a greater effect than either the addition of copper or nickel, which is observed.

In both the quasi-static and dynamic experiments, the aluminum particles positioned “near” to second phase particles showed increased strain over those particles that were positioned “far” from the second phase particles, as shown in Figures 2 (b) and 3 (b). In the quasi-static experiments, where measurements were made at different levels of strain, the strains in the aluminum particles near to the second phase particles are consistently higher than the strains measured in aluminum particles far from the second phase particles, *at all strain levels.* In every case, the aluminum particles strain to a greater extent than predicted by the global true strain, indicating efficient load transfer between matrix and particle. However, the measured strains in the second phase particles appear to be independent of the global strain imposed on the composite. This may suggest that the stiffer (and stronger) second phase particles do not deform as readily as the aluminum particles, and simply move as rigid-bodies while the epoxy matrix and the aluminum particles undergo deformation. The enhanced deformation in the aluminum particles in close proximity to second phase particles suggests that the second phase particles act as either hammers or anvils in encouraging the aluminum particles to deform. Clearly, in spatially-heterogeneous composite microstructures such as these, local effects of microstructure, including locally high volume fractions of second phase particles would be expected to play an active role during deformation, beyond simply stiffening the epoxy matrix. In the dynamic loading regime, the strains measured in aluminum particles near to second phase particles are again consistently higher than strains measured in aluminum particles far from second phase particles, although the overall levels of strain are reduced, consistent with the load-sharing arguments presented above. In all cases, the second phase particles show the lowest strains, however, there is a clearer trend of increasing particle strain with increasing global true strain than was observed in the quasi-static data. This may indicate that the dynamically-stiffened matrix imparts sufficient load to the second phase particles to get them to deform. However, it should also be noted that even at the lowest applied strains, under quasi-static loading, there is an apparent ‘residual strain’ in the second phase particles, between 0.15 – 0.20. This may indicate an initial ‘non-sphericity’ of the particles, in the starting powders, which translates into systematic error in the strain measurements at all strain levels. Further examination of the starting powders and/or measurements on undeformed specimens are necessary in order to rule out this effect.

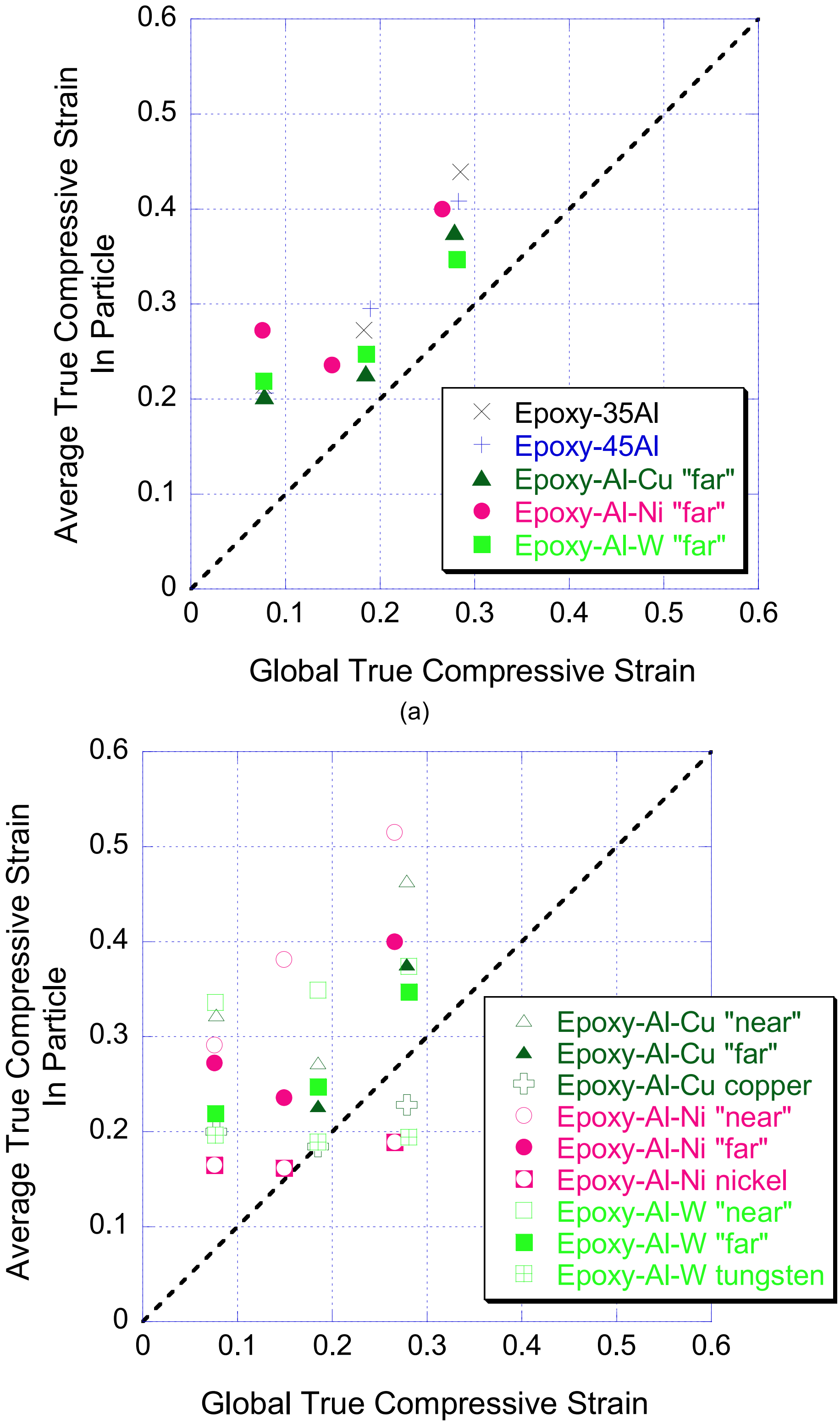

(a)

(b)

Figure 2: Quasi-static global true compressive strain versus average true compressive strain for (a) single phase (Al only) particulate composites and two-phase particulate composites with Al particles far from the second phase and (b) two-phase particulate composites, with Al and Cu, Ni or W particulates, where near indicates Al particles close to the second phase, far indicates Al particles far from the second phase.

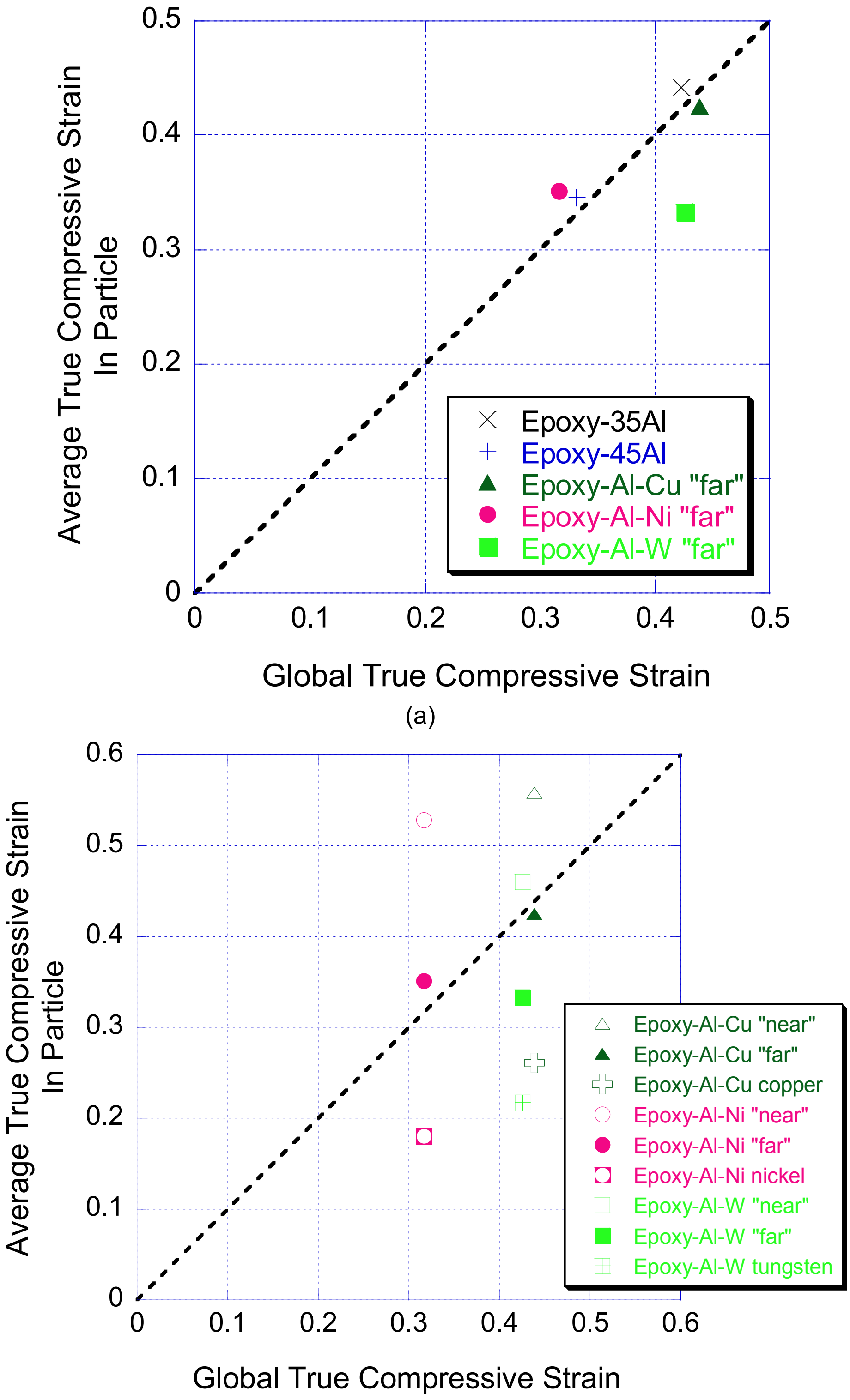

(a)

(b)

Figure 3: Dynamic global true compressive strain versus average true compressive strain for (a) single phase (Al only) particulate composites and two-phase particulate composites with Al particles far from the second phase and (b) two-phase particulate composites, with Al and Cu, Ni or W particulates, where near indicates Al particles close to the second phase, far indicates Al particles far from the second phase.

Summary

Multi-constituent epoxy-based particulate composites consisting of individual particles of aluminum and a second phase (copper, nickel or tungsten) have been synthesized to investigate the deformation of aluminum in the presence of the second phase. Quasi-static and dynamic compression experiments have been performed to characterize the materials. The microstructures of the quasi-statically and dynamically deformed samples have been quantified to determine the amount of deformation in the aluminum particles, as a function of their proximity to the second phase particles. In both the quasi-static and dynamic experiments, the aluminum particles that were close to the second phase particles showed increased strain over those that were far from the second phase particles. Furthermore, decreased load partitioning between matrix and particle was observed in the dynamic experiments.

Acknowledgements

This research was sponsored by the Air Force Research Laboratory, Munitions and Materials Directorates.

Opinions, interpretations, conclusions and recommendations are those of the authors and are not necessarily endorsed by the United States Air Force.

References

1. Martin, M., S. Hanagud, and N.N. Thadhani, *Mechanical behavior of nickel + aluminum powder-reinforced epoxy composites.* Materials Science and Engineering: A, 2007. **443**(1-2): p. 209-218.
2. Ferranti, L. and N.N. Thadhani, *Dynamic mechanical behavior characterization of epoxy-cast Al + Fe2O3 thermite mixture composites.* Metallurgical and Materials Transactions A, 2007. **38A**(11): p. 2697-2715.
3. Ramsteiner, F. and R. Theysohn, *On the tensile behaviour of filled composites.* Composites, 1984. **15**(2): p. 121-128.
4. Ferranti, J.L., N.N. Thadhani, and J.W. House, *Dynamic Mechanical Behavior Characterization of Epoxy-Cast Al +* Fe_2O_3 *Mixtures.* AIP Conference Proceedings, 2006. **845**(1): p. 805-808.
5. Oline, L.W. and R. Johnson, *Strain rate effects in particulate-filled epoxy.* ASCE J Eng Mech Div, 1971. **97**(EM4): p. 1159-1172.
6. Goyanes, S., et al., *Yield and internal stresses in aluminum filled epoxy resin. A compression test and positron annihilation analysis.* Polymer, 2003. **44**(11): p. 3193-3199.
7. Kawaguchi, T. and R.A. Pearson, *The effect of particle-matrix adhesion on the mechanical behavior of glass filled epoxies: Part 1. A study on yield behavior and cohesive strength.* Polymer, 2003. **44**(15): p. 4229-4238.
8. Kawaguchi, T. and R.A. Pearson, *The effect of particle-matrix adhesion on the mechanical behavior of glass filled epoxies. Part 2. A study on fracture toughness.* Polymer, 2003. **44**(15): p. 4239-4247.
9. Jordan, J.L., J.E. Spowart, B. White, N.N. Thadhani, and D.W. Richards, *Multifuctional particulate composites for structural applications.* Society for Experimental Mechanics - 11th International Congress and Exhibition on Experimental and Applied Mechanics, 2008. **1**: p. 67-75.
10. Gray III, G.T., *Classic split-Hopkinson pressure bar testing*, in *ASM Handbook Vol 8: Mechanical Testing and Evaluation*, H. Kuhn and D. Medlin, Editors. 2002, ASM International: Materials Park. p. 462-476.
11. White, B.W., N.N. Thadhani, J.L. Jordan, and J.E. Spowart, *The Effect of Particle Reinforcement on the Dynamic Deformation of Epoxy-Matrix Compsites.* AIP Conference Proceedings, 2009. **1195**(1): p. 1245-1248.

Proceedings of the SEM Annual Conference
June 7-10, 2010 Indianapolis, Indiana USA
©2010 Society for Experimental Mechanics Inc.

Dynamic Strain Rate Response with Changing Temperatures for Wax-Coated Granular Composites

J. W. Bridge[1,2,3]
M. L. Peterson[2,3]
C. W. McIlwraith[4]
[1]Associate Professor, Dept. of Engineering, Maine Maritime Academy, Castine, Maine 04420
john.bridge@mma.edu
[2]Department of Mechanical Engineering, University of Maine, Orono, ME 04469
[3]Racetrack Surfaces Testing Laboratory, Orono, ME 04473
[4]Gail Holmes Equine Orthopaedic Research Center, Department of Clinical Sciences,
Colorado State University, Fort Collins, CO 80523

ABSTRACT

Triaxial tests were conducted at varying load rates and temperatures for a wax-coated granular composite material. This material is used as a surface for Thoroughbred horse racing. The purpose of the test is to examine how the shear strength of a synthetic track responds to changing strain rates. The temperatures used correspond to the temperatures of the surfaces during operations. These same temperatures have been shown using differential scanning calorimetry to correspond to thermal transition regions for the wax used to coat the sand in these surfaces. Preliminary results show that these tracks are sensitive to both an increase in the rate of loading and the temperature. However there may be an upper strain rate limit where temperature effects diminish. At low strain rates, temperature affects the dynamic strengthening response, while at higher strain rates; the dynamic load governs the strength response.

KEYWORDS: granular composites, dynamic strain rate, triaxial shear strength, paraffin and microcrystalline wax, synthetic horse tracks

INTRODUCTION

Synthetic granular composite materials are being used in many Thoroughbred horse race tracks in the United States and other parts of the world. In one case, their use was mandated by the state of California in 2007 due to testimony that these tracks were significantly safer than traditional dirt tracks [1]. One of the California synthetic tracks showed a 75% reduction in catastrophic horse injuries during the first year as compared to the previous year racing on a dirt track [2]. There are several vendors of the synthetic track materials used in the U.S. with track compositions generally consisting of silica sand (>70%), polymer fibers (<5%), and rubber particles (0-15%) all coated with a paraffin-based, high oil content wax [3,4]. The oil content in a recent study of several synthetic race tracks, to include the track location in this study, ranged from 34 to over 44% by mass [5].

Previous work investigated the composition and thermal transition characteristics of the wax coating as well as the static shear strength of actual track samples tested at operational temperatures [5,6]. Operational temperatures during the summer at one synthetic track surface in Southern California had been observed to range from 18°C to over 50°C over a 4-day period [7]. These earlier tests demonstrated that the wax-coatings have a definitive effect on the material properties of the track surfaces as the thermal transitions of the wax are

T. Proulx (ed.), *Dynamic Behavior of Materials, Volume 1*, Conference Proceedings of the Society for Experimental Mechanics Series,
DOI 10.1007/978-1-4419-8228-5_36, © The Society for Experimental Mechanics, Inc. 2011

encountered. This effect has also been shown through a correlation of 6-furlong (201 m) race times and temperatures [8]. For example, there is an increase in the track static shear strength as the wax in the materials experience melting during temperatures between 20 and 50°C [5]. This temperature range, well within racing operational limits, encompassed the first differential scanning calorimetry (DSC) thermal transition region for the extracted track waxes analyzed in the previous study. Figure 1 shows the DSC curve for one operational synthetic track sampled in March 2009, Figure 2 shows the corresponding quasi-static shear strengths that correspond to the transition temperatures in the DSC curve. Note that during the first DSC thermal transition region, the shear strength increases from 16.4 to 18.7°C, resulting in a peak strength increase of over 12%. The strength decreases as the end of the first transition region is reached but increases again as the second transition region is encountered.

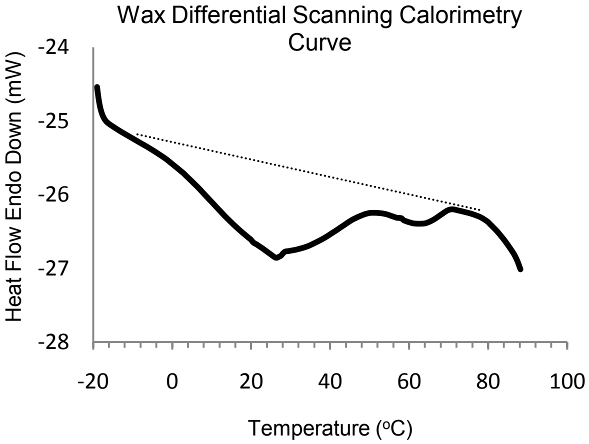

Fig. 1 DSC of extracted wax, Arlington Park, Arlington Heights, Illinois, 3-9-09.

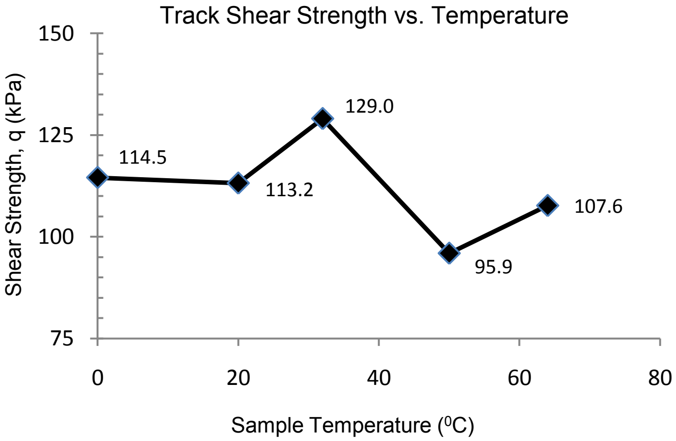

Fig. 2 Triaxial shear strength for Arlington Park, Arlington Heights, Illinois, 3-9-09.

The current study examines the effect of increasing the rate of loading on one operational synthetic race track surface at two potential operating temperatures.

MATERIALS AND METHODS

Track samples were taken from Arlington Park race track in Arlington Park, Arlington Heights, Illinois on September 27, 2009. The track had been in continual use for over 2 years. The samples were removed from the top 76.2 mm (3 in) of the track using a 75 mm-diameter sampling probe. The wax was extracted from a portion of the samples. The oil content of the wax was determined and gas chromatography (GC) and DSC tests were performed on the wax (with oil) to characterize the wax molecular carbon number distribution and thermal response. Dynamic shear strength tests were conducted on the remainder of the original track samples.

Wax Extraction and Oil Content Determination

The wax content by mass percent for each original wax-coated sample was determined using a high-purity iso-octane solvent extraction procedure described in an earlier paper [6]. Oil extraction tests were performed to measure the amount of oil present in the wax extracted from the Arlington Park race track. Tests were performed in accordance with ASTM D 3235 [9] using toluene and methyl ethyl ketone solvent extraction.

Gas Chromatography

Gas chromatography analyses of the extracted wax (with oil) were performed based on ASTM D 5442 [10] using a Hewlett Packard 5890 Series II Gas Chromatograph with flame ionization detector. Hydrogen was used as the carrier gas. The column used was a J&W Scientific capillary column DB-1HT, 30 m, with 0.32 mm inner diameter and 0.1-micron film thickness. Detector gasses employed were hydrogen at 30 ml/min and air at 400-450 ml/min. These tests give general carbon number distributions of petroleum waxes from C17 through C44 and higher. Normal and non-normal (isomer) hydrocarbon molecule mass percents are reported and results are used to help interpret DSC thermal behavior and to make comparisons between waxes.

Differential Scanning Calorimetry

Differential scanning calorimetry of the extracted wax was performed in a PerkinElmer Pyris1 with power compensation under nitrogen flow (ml/min). Two samples (9-11 mg weighed to 0.1 mg precision) of each wax were prepared in aluminum sample pans and heated from 20 to 93.3°C, 93.3 to -30°C, then -30 to 93.3°C. The thermal sequence of the tests used was consistent with the standards for DSC wax testing ASTM D 4419 [11]. Transition ranges and melting temperatures were taken from the second heating run and are plotted with thermal endotherms pointing downwards. The endotherms indicate the melting enthalpies of the wax samples as heat is absorbed during melting.

Triaxial Shear Compression Tests

Triaxial shear tests were performed to acquire track shear strength values at varying strain rates and temperatures. The tests were conducted with a screw type universal testing machine (Instron 4465, Norwood, MA, USA) based on the procedures outlined in ASTM D4767 used to characterize cohesive soils under foundations or structures. This test was modified to address the characteristics of a synthetic granular composite [12]. A consolidated, drained condition was incorporated as well as a temperature-controlled system to simulate the track operational conditions. Test confining pressures were also chosen to correspond to the depth of the critical stress field in the track. These pressures are based on the general maintenance conditions of a granular composite racetrack and the dynamic loads imposed by the forelegs of a galloping Thoroughbred horse [13]. The strength parameters involved and equation describing interactions of the sand internal friction angle and cohesion are explained in a previous paper [5]. The test setup is show in Figure 3 with accompanying component diagram.

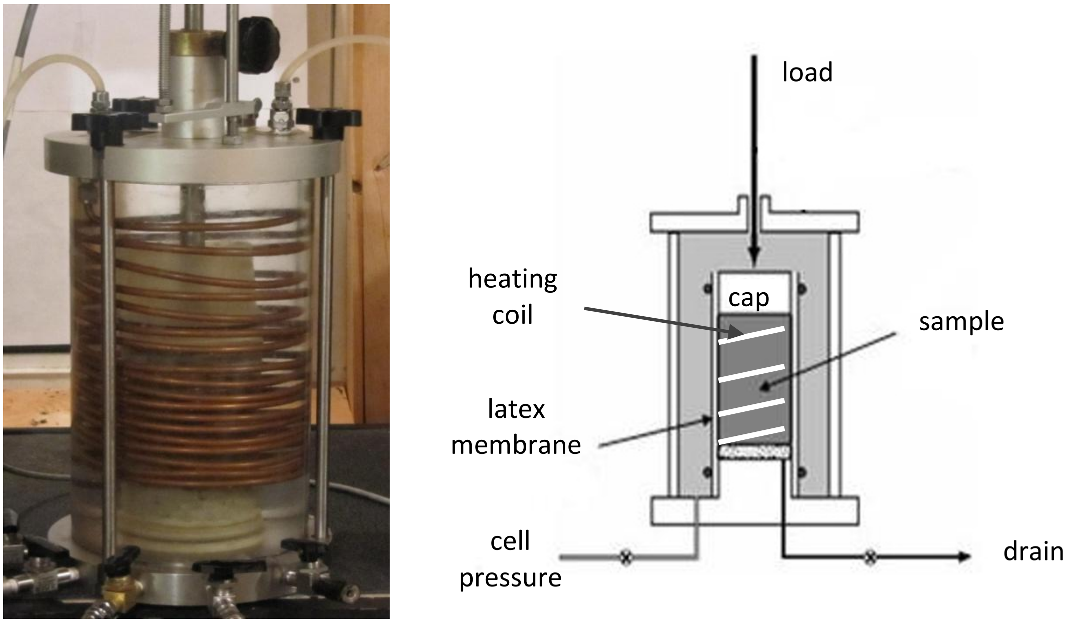

Fig. 3 Triaxial shear test setup showing sample within pressurized, temperature-controlled water test cell.

Samples to be tested were initially dried for a minimum of 24 hours prior to adding 4% moisture by mass. The 4% moisture is typical of the operating moisture content for synthetic tracks. Samples 70 mm in diameter were tightly packed in 25.4 mm compacted layer increments to a sample height of 152 mm. The tests were performed at 0.853, 10 and 100 mm/min loading rates under confining pressures of 35, 70, and 103 Pa (5, 10 and 15 psi).

The 0.853 mm/min strain rate chosen corresponds to the quasi-static load rate previously used when regularly reporting quasi-static synthetic track shear strengths[1]. The confining pressure used to report shear strength data is 103 Pa. The test temperatures selected were 20 and 50°C and based on the range of the first thermal transition region exhibited in the DSC curve. Temperature was controlled using a 0 to 100°C refrigerated water bath (Thermo Fisher Scientific, model RTE-17, Newington, NH, USA) that cycled water through the triaxial cell via a copper coil.

Results and Discussion

The wax extracted from the Arlington Park track material was found to be 9.24 % by mass and oil content was calculated at 41% by mass. The GC and DSC results with endothermic peaks are depicted in Figures 4 and 5. The GC has a bimodal isomer carbon number distribution (CND) and a very spread out normal CND. The mass percents of the normal and isomeric hydrocarbon molecules are 17.8 and 82.2 % respectively. The first DSC thermal transition begins at approximately 0^{o}C and ends at 49^{o}C. The second transition region begins at 53^{o}C and ends at 66^{o}C. The DSC nominal transition peak temperatures for each transition region are located at approximately 30 and 60^{o}C respectively.

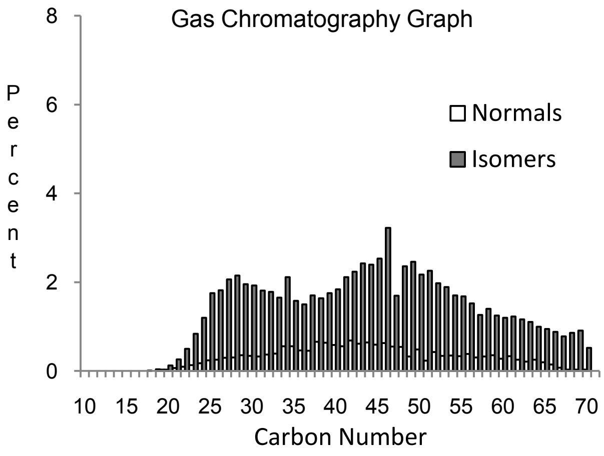

Fig. 4 GC graph of Arlington Park extracted Wax, 9-27-09.

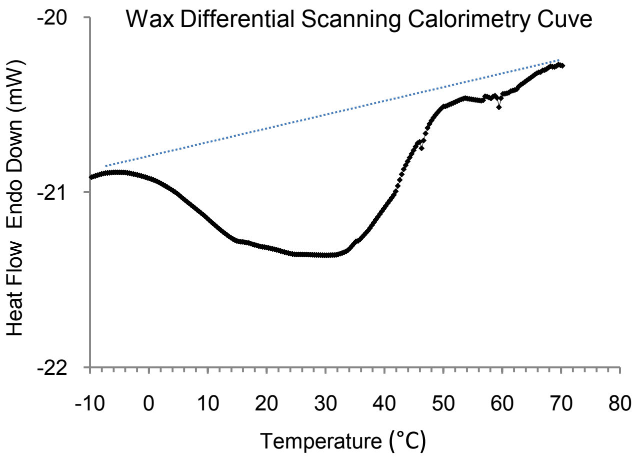

Fig. 5 DSC curve for Arlington Park extracted Wax, 9-27-09.

The results of the dynamic triaxial shear tests are shown in Figure 6. The data was extracted from Mohr-Coulomb p-q trend lines and strength envelopes as outlined in ASTM D 4767 [12]. The p-q trend lines had very high coefficient of determination r^2 values (0.999 average). There was a gradual increase in shear strength at both 20 and 50^{o}C testing temperatures as load rates increased.

[1] Testing results obtained at the Race Track Surfaces Laboratory, Orono, Maine, Mar 2009 - Dec 2009.

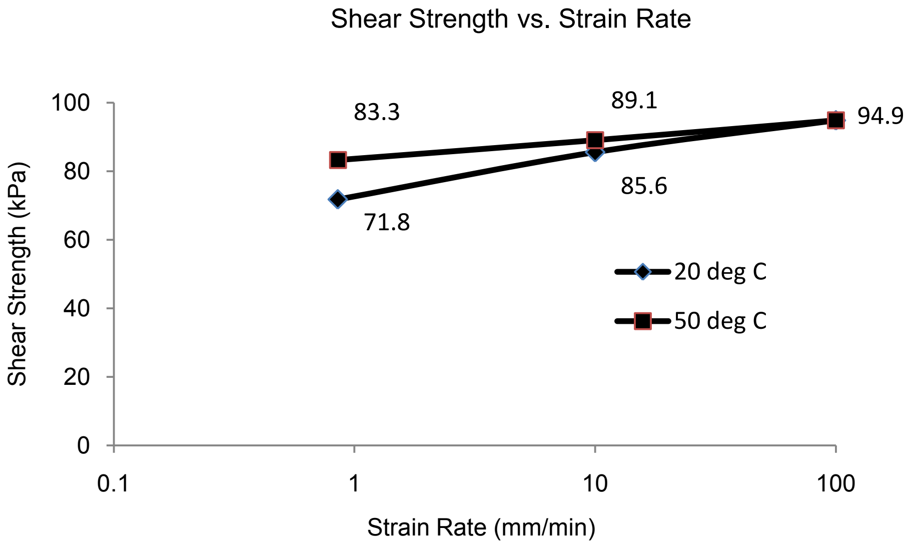

Fig. 6 Triaxial shear strength versus strain rate for Arlington Park track samples at 20 and 50°C.

The wax percent and high oil content reported are consistent with amounts found in earlier track synthetic wax studies and contribute to the wide GC carbon number distributions and DSC thermal transition regions. The GC bimodal CNDs suggest a blend of two waxes in the Arlington Park track samples. The high GC isomer percentage, coupled with CNDs extending beyond C60 (11% by mass), confirm the high-oil content in addition to the presence of complex, higher molecular weight hydrocarbon solids such as microcrystalline wax [14]. The DSC shows the largest fraction of wax undergoing complete melting at approximately 30°C and the remaining smaller fraction melting at 60°C. This melting behavior translates to a cumulative softening of the race track as these temperatures are approached.

The melting of the wax coating also contributes to a track strengthening effect at a range of temperatures as shown in the triaxial shear strengths in Figure 6. The 13.7% increase in strength between samples at the 0.853 mm/min strain rate is consistent with previously reported results for another Arlington Park sample at these temperatures [5]. As the strain rates increase from 0.853 mm/min to 10 mm/min, the 20°C samples show a 16.1 % increase in strength while the 50°C samples only shows a 4.8% increase. From 10 to 100 mm/min, the percent increase in strength narrows with shear strengths reaching almost the same levels (85.6 vs. 89.1 kPa). At the 100 mm/min strain rate, the shear strengths are identical for both temperatures (94.9 kPa). At the 20°C temperature, there is a total dynamic strengthening effect of 24.1% from 0.853 to 100 mm/min, while at 50°C the total dynamic strengthening is only 12.1%. However, the temperature only appears to affect the shear strength at low strain rates (less than 1 mm/min); the strength levels at the two temperatures quickly converge at the 10 and 100 mm/min strain rates. This suggests that at very low strain rates, increasing temperature has a greater effect as the wax-coated material becomes more fluid and coats the track constituents - enabling them to compact more easily under load. At lower temperatures under low strain rate conditions, a smaller percentage of the wax is melted and there is more time for particles to rearrange and subsequently, lower strength is exhibited. However, this temperature-induced viscoelastic response at lower strain rates diminishes with increasing dynamic load where the strain rate now governs the shear strength response.

The results of this work show that there is a complex relationship between the strain rate and the temperature of the material. This relationship is not surprising because of the well-established time temperature superposition effects in polymers [15]. From this understanding it is expected that the increase in temperature is equivalent to a decrease in time interval. This effect is clear from the results. The implications of this effect are also profound for interpretation of the biomechanical impacts of the surface on the horse. Different loading rates are experienced in the front and rear legs of the horse, since the deceleration of the center of mass of the horse occurs in the front with propulsion primarily in the hind limbs. As a result, the strain rate applied to the surface may be higher in the front limbs than in the rear. Thus, the length of the stride and relative support provided by the surface in the front and rear may be affected by temperature. This suggests that an improved understanding of the hoof landing and loading rates will need to be investigated as a part of the development of safer racing surfaces.

The strain rates tested in this study are considerably lower than those which occur in the surface when a horse gallops across it. However, this study clearly shows that strain rate effects cannot be neglected. The fact that temperature does not affect the material at the higher strain rates tested is not relevant based on previous race time data collected. Temperature has been clearly demonstrated to be an important factor in the speed of the horses and thus, has an effect on the material as well [8].

Conclusions

The dynamic shear strength of synthetic, wax-coated track materials appears to be influenced by temperature and the rate of loads imposed upon them. For the synthetic samples investigated, at the intermediate and post-melting temperatures tested, the shear strength increased with increasing strain rate. The higher temperature caused a change in shear strength only at the lowest strain rate applied (quasi-static) while at the higher strain rates (1 and 2 orders of magnitude higher), temperature effects diminished. It can be anticipated that for even higher strain rates, such as those caused by a Thoroughbred race horse, shear stresses will be much higher due to the higher strain rates. This will affect the biomechanical characteristics of a horse’s leg impacting the surface. Future work will need to consider both accurate rates of loading and an improved understanding of the physiologically appropriate rates of loading. Higher strain rates (approaching 1000 mm/min) will be conducted as well as tests at additional thermal transition temperatures to confirm the material trends of the current study. The effects of differing strain rates on the material cohesion will also be examined. While this study is far from conclusive, it demonstrates that strain rate effects in these materials are significant and that further work is needed.

Acknowledgements

This work as been primarily funded by the Churchill Downs “Safety from Start to Finish” initiative. Additional support has come from the Grayson-Jockey Club Research Foundation for funding of the basic research as well as from Sean McColl of International Group Incorporated for gas chromatography tests. Work was performed at the non-profit Racing Surfaces Testing Laboratory which is supported by a coalition of Thoroughbred racing tracks and industry organizations.

References

[1] Allison, R., “Thoroughbred Racetracks Installing Synthetic Surfaces”, JAVMA News [Online] April 1, 2007, http://www.avma.org/onlnews/javma’apr07/0070401o.asp (assessed Feb, 15, 2009).
[2] Shulman, L., *The Blood Horse*, 83, 2007, pp. 6975-6982.
[3] Polytrack® Product Information, [Online] 2010, http://www.polytrack.com/(accessed Jan 1,2010).
[4] Cushion Track Product Information, [Online] 2010, http://www.cushiontrackfooting.com/(accessed Mar 6, 2010).
[5] Bridge, J.W., Peterson, M.L., “Triaxial Effects on Triaxial Shear Strength of Granular Composites Sport Surfaces” (submitted to Journal of ASTM International, March 2010).
[6] Bridge, J. W., Peterson, M. L., Radford, D. W. and McIlwraith, C. W., “Thermal Transitions in High Oil Content Petroleum-Based Wax Blends used in Granular Sport Surfaces”, Thermochim. Acta 498, pp. 106-108, 2010.
[7] Kuo, P., “Measurement of Modulus Changes with Temperature of Synthetic Track Materials”, Masters Thesis, University of Maine, p. 17, 2008.
[8] Peterson, M. L., McIlwraith, C. W., “The Effect of Temperature on 6-Furlong Times on a Synthetic Racing Surface”, Equine Vet. J., 2009.
[9] ASTM Standard D3235: Standard Test Method for Solvent Extractables in Petroleum Waxes, Annual Book of ASTM Standards, ASTM International, West Conshohocken, PA, 2002.
[10] ASTM Standard D5442: Standard Test Method for Analysis of Petroleum Waxes by Gas Chromatography, Annual Book of ASTM Standards, ASTM International, West Conshohocken, PA, 2008.
[11] ASTM Standard D4419: Standard Test Method for Measurement of Transition Temperatures of Petroleum Waxes by Differential Scanning Calorimetry (DSC), Annual Book of ASTM Standards, ASTM International, West Conshohocken, PA, 2005.
[12] ASTM Standard D4767: Standard Test Method for Consolidated Undrained Triaxial Compression Test for Cohesive Soils, Annual Book of ASTM Standards, ASTM International, West Conshohocken, PA, 2002.

[13] Wong, J. Y., Theory of Ground Vehicles, 2nd Ed., John Wiley & Sons, NY, 1995.
[14] The International Group Inc., Wax Overview [Online] 2006, www.igiwax.com/resource/Wax_Overview (accessed Nov, 2008).
[15] Ferry, J. D., Viscoelastic Properties of Polymers, Wiley, New York, 1980.

Proceedings of the SEM Annual Conference
June 7-10, 2010 Indianapolis, Indiana USA
©2010 Society for Experimental Mechanics Inc.

Strain solitary waves in polymeric nanocomposites

I.V.Semenova, G.V.Dreiden, A.M.Samsonov

Ioffe Physical Technical Institute of the Russian Academy of Sciences,
26, Polytekhnicheskaya st., St.Petersburg, 194021, Russia
Irina.Semen@mail.ioffe.ru

ABSTRACT

Our recent theoretical and experimental investigations demonstrated the physical possibility of generation and further propagation of bulk strain solitary waves in waveguides made of nonlinearly elastic materials, namely glassy polymers: polystyrene and polymethylmethacrylate. These materials are widely used as matrices for polymeric nanocomposite materials, with an addition of a wide range of fillers that can drastically change the resulting elastic characteristics of a nanocomposite. Mechanical properties of nanocomposites depend, among other parameters, upon the filler content as well as upon an adhesion of its particles to the matrix. Here we present first experimental results on bulk strain soliton generation in a waveguide made of polymeric nanocomposite.

INTRODUCTION

Since the first observation of solitary waves on shallow water surfaces by J. Scott Russel in 1834, the most intriguing property of them was an absence of decay when propagating along a remarkable distance, even miles [1]. Many natural phenomena were described afterwards via different realizations of the non-linear wave (soliton) theory [2].

Recently we demonstrated the physical possibility of generation and propagation of bulk strain solitary waves in waveguides made of nonlinearly elastic materials (e.g. [3-5]). In general, strain soliton is a localized wave that can transport elastic energy for long distances without considerable losses.

The propagation of long nonlinear longitudinal bulk elastic waves in a uniform bar of rectangular cross section is governed by a doubly dispersive equation, written in the following dimensional form for a component $U_x = u$ of the gradient of the longitudinal displacement U, that is called as 'strain' for brevity (see [6]):

$$u_{tt} - c^2 u_{xx} = \left[\frac{\beta}{2\rho} u^2 + \frac{2a^2\nu^2}{3} \left(u_{tt} - c_1^{\,2} u_{xx} \right) \right]_{xx} \qquad (1)$$

Here t is time, a is the square side in a cross section, c and c_1 are the linear longitudinal and transversal sound velocities in a bar, respectively, ρ is the material density, $\beta \equiv 3E + 2l(1-2\nu)^3 + 4m(1+\nu)^2(1-2\nu) + 6n\nu^2$ is the nonlinearity coefficient, depending upon the Young modulus E, and the Murnaghan moduli (l,m,n) of the 3rd order. Lower indices denote derivatives in time t and space variable x, which is determined along the rod axis. An explicit dependence of the wave type on the sign of the nonlinearity coefficient and the analysis allows us to obtain the solitary wave solution to (1), having a well known bell shape:

T. Proulx (ed.), *Dynamic Behavior of Materials, Volume 1*, Conference Proceedings of the Society for Experimental Mechanics Series,
DOI 10.1007/978-1-4419-8228-5_37, © The Society for Experimental Mechanics, Inc. 2011

$$u = A\cosh^{-2}\left\{\frac{1}{L(A)}\left[x \pm V(A)t\right]\right\} \tag{2}$$

along with the constraints for a solitary wave velocity *V(A)* and the pulse width *L(A)*, under which it may exist:

$$V^2 = c^2 + \frac{A\beta}{3\rho}; \qquad L^2 = \frac{8a^2\nu^2}{3}\left[1 + \frac{3E}{A\beta}\cdot\frac{1+2\nu}{2(1-\nu)}\right]. \tag{3}$$

The amplitude and the width of the solitary wave depend on physical and geometrical properties of a waveguide.

Experimental setup shown in Figure 1 was used to record wave patterns inside and outside optically transparent waveguides by means of holographic interferometry. A system of straight equidistant carrier fringes is formed by an insertion of a wedge into the path of the object beam between two interferogram exposures. Density variations induced by the strain wave cause shifts of these carrier fringes on the resulting interferograms. Both generation and recording of the bulk compression waves were performed using Q-switched pulsed ruby lasers (20 ns, 0.5 J). Laser pulses were synchronized by means of the delayed pulse generator allowing us to vary the time interval between two pulses in a wide range and providing the accuracy of about 1 μs. A soliton was generated from an initial shock wave produced in water via laser ablation of an aluminum coated foil placed nearby the waveguide input. The laser pulse power density was controlled by the energy meter and kept close to constant ($2.3 \cdot 10^8$ W/cm^2) during the experiments in order to ensure the repeatability of soliton parameters and avoid inelastic strains in the specimen material.

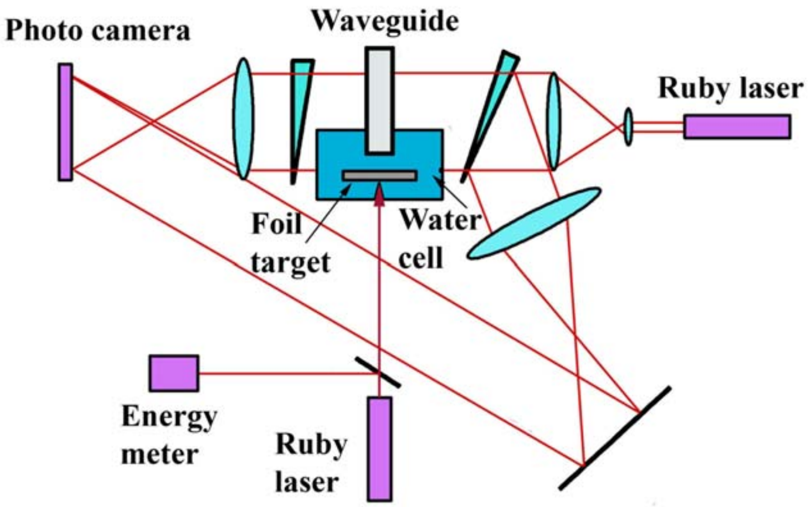

Figure. 1: Experimental set-up used for the laser induced generation of an incident compression solitary wave with subsequent recording of the wave pattern by means of holographic interferometry.

We have shown in experiments (see e.g.[1]), that the strain solitary wave, indeed, can propagate in a uniform waveguide for long distances, keeping its shape nearly constant and having no long wave of opposite sign behind. The experimentally measured decay rate for strain solitons is 30-40 times lower than that for bulk linear waves (see Table 1). Figure 2 presents the typical holographic interferogram of the formed strain soliton in a polymethylmethacrylate (PMMA) bar. Figure 3 shows transformations of soliton shape and amplitude during its propagation in a lengthy PMMA bar.

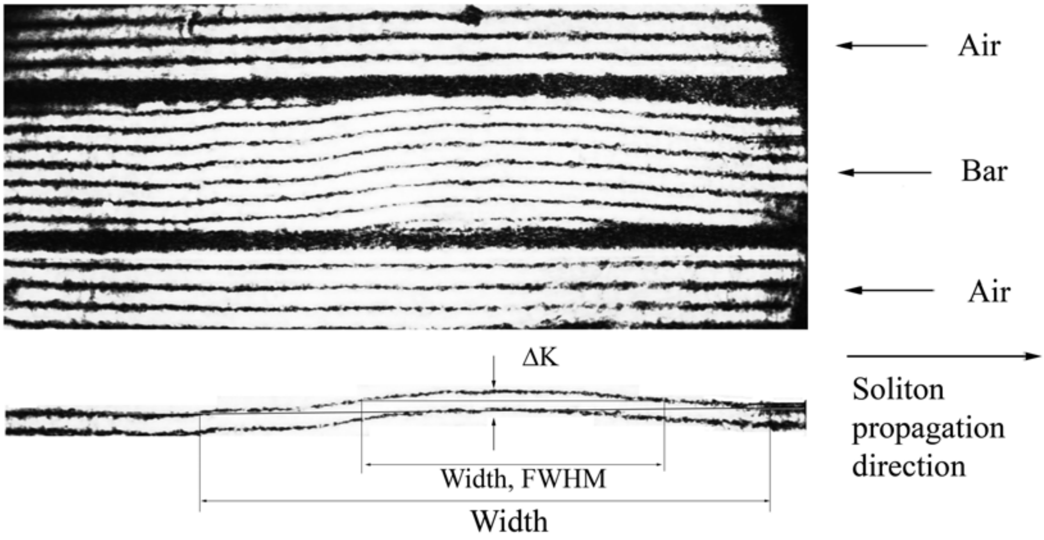
Air
Bar
Air
ΔK
Soliton propagation direction
Width, FWHM
Width

Figure 2. Holographic interferogram of the strain soliton in the PMMA bar, 10x10 mm in cross section.

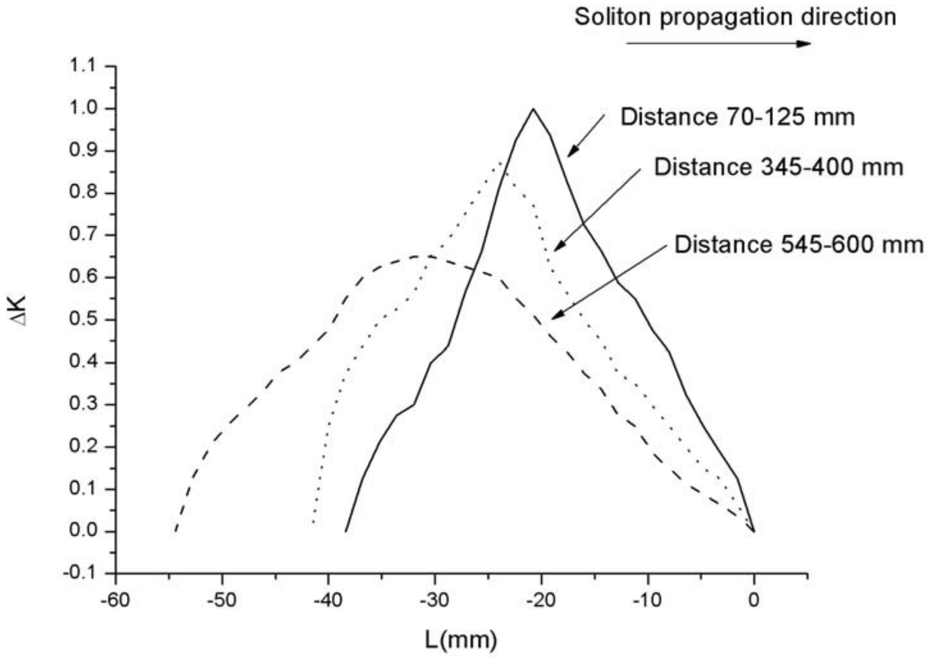

Figure 3. The shape variation of strain soliton, propagating along the PMMA bar, at specified distances from the bar input.

In our previous research we used waveguides made of two polymeric materials having significant nonlinear elasticity, namely, polystyrene (PS) and PMMA. Elastic parameters of these materials available in literature are summarized in Table 1. These materials are widely used as matrices for polymeric nanocomposite materials, with an addition of a wide range of fillers, such as carbon nanotubes, nanoclays, nanoparticles, nanoflakes etc. It is well known that these nanofillers can change drastically the resulting elastic characteristics of nanocomposite material. Specific elastic parameters (Young modulus, strength, toughness) of nanocomposites may be noticeably higher than those of pure polymeric materials used as matrices. Mechanical properties of nanocomposites depend also upon the filler content as well as upon an adhesion of its particles to the matrix.

Table 1. Elastic properties of polymeric materials

	Density	**Young modulus**	**Poisson ratio**	**Elastic moduli, 3rd order (Murnaghan)**			**Sound velocity in a rod**	**Decay rate**	
	ρ, g/cm^3	**E, N/m^2 $\cdot 10^{10}$**	**ν**	**l N/m^2 $\cdot 10^{10}$**	**m N/m^2 $\cdot 10^{10}$**	**n N/m^2 $\cdot 10^{10}$**	**C_l m/s**	**α_0 (lin) cm^{-1}**	**α (sol) cm^{-1}**
PS	1.06	0.37	0.34	-1.89	-1.33	-1	1870	0.17	0.005
PMMA	1.16	0.5	0.34	-1.09	0.77	-0.14	2080	0.25	0.009

Thus, nanocomposites are nonuniform materials in which mean magnitudes of elastic characteristics differ considerably from those of pure polymers. However, for long waves (such as bulk strain solitons having the width of the order of tens of millimeters) a nanocomposite may be considered as a basic material, having some portion of defects of a negligible size. Recently we studied ([3]) the soliton behavior in layered PMMA waveguides bonded with two types of adhesives: glassy ethyl cyanocrylate (CA) and polyurethane rubber (PU) adhesives, exhibiting quite different elastic characteristics. It was shown that even such *macro* defects as longitudinal layers of adhesive of a micrometer thickness do not cause abrupt changes of the soliton parameters. The decay rate of a longitudinal strain solitary wave propagating along a layered structure strongly depends on the type of an adhesive bonding between the layers. For two- and three-layered bars, the decay was considerably higher when layers were bonded by the rubber-like PU-based adhesive, as compared to the case when layers were bonded using the CA-based adhesive. In the latter case, the decay rate was close to that in the uniform bar. Note that the lack of an adhesive (delamination) results in the soliton fission, i.e. the formation of a soliton train from a single incident soliton ([4]).

By now all polymeric nanocomposites available to us were not transparent that made impossible the direct holographic recording of wave patterns inside a waveguide. To study the soliton behavior in such opaque materials we used layered waveguides, in which one of the layers was made of transparent PMMA and the other – of an opaque material. The schematic of a waveguide structure is shown in Figure 4. Note that in all waveguides the soliton is first generated in the uniform part (a rod, 50 mm long), and then propagates into a layered bar, bonded to the rod by a thin layer of the CA adhesive. This part is necessary since the soliton is formed from an initial weak shock wave at some distance (approximately 50 mm) from the waveguide input. This uniform part ensures that at the input of the layered structure we have a well formed soliton and its further transformations depend only on mechanical characteristics of this layered structure.

To prove the feasibility of this approach we performed experiments on soliton propagation in such two-layered waveguides made of two different transparent polymers: PMMA and PS. Figure 5 shows a wave pattern in a structure where layers are not bonded. In this case soliton from a rod enters two separate layers of PS and PMMA and then propagates through them independently. Due to the difference in velocities (see Table 1) the soliton in the upper layer (PS) lags behind the soliton in the lower layer (PMMA). The soliton amplitude in the PS layer is noticeably lower than that in the PMMA layer. The wave pattern in Figure 6, where the PS and PMMA layers are bonded together with the CA adhesive, is quite different – the wave pattern presents a combined solitary wave propagating in a bonded structure with the same velocity, amplitude and shape.

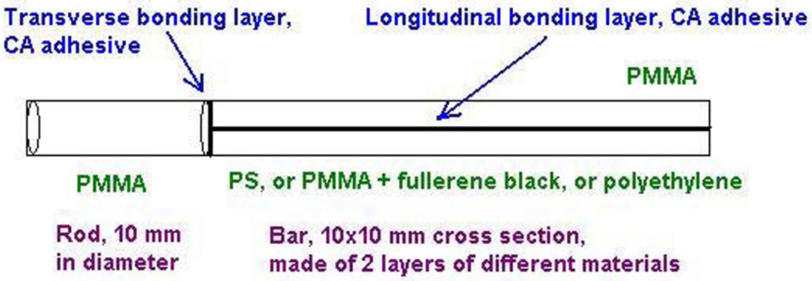
Transverse bonding layer, CA adhesive
Longitudinal bonding layer, CA adhesive
PMMA
PMMA
PS, or PMMA + fullerene black, or polyethylene
Rod, 10 mm in diameter
Bar, 10x10 mm cross section, made of 2 layers of different materials

Figure 4. Schematic of waveguides used in experiments.

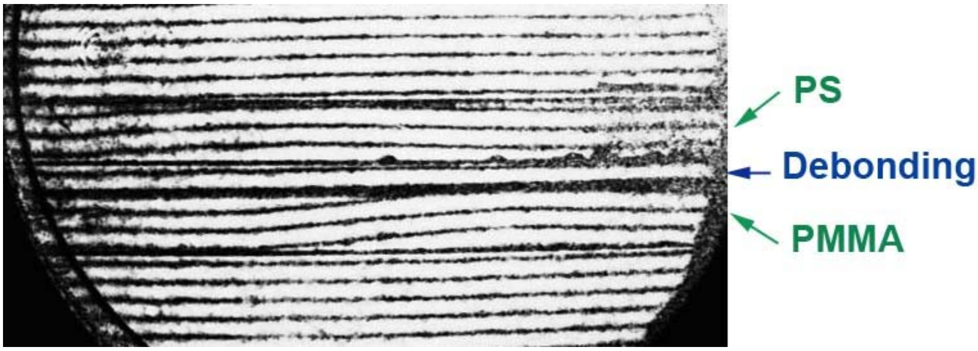
PS
Debonding
PMMA

Figure 5. Wave pattern in a bar made of PS and PMMA layers clenched together, at the distance 70-120 mm from the layered structure input

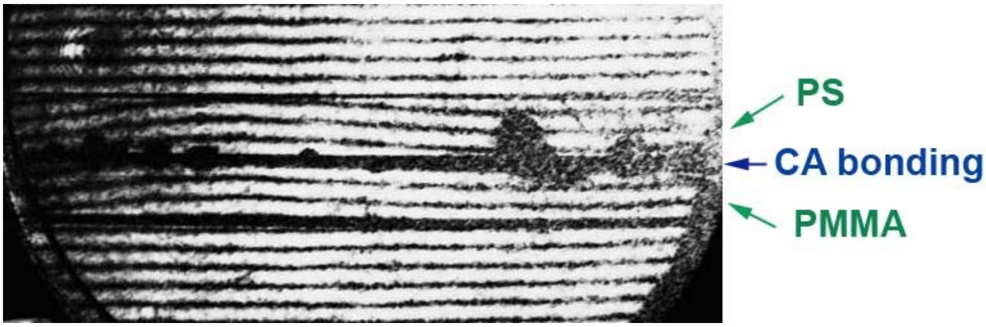
PS
CA bonding
PMMA

Figure 6. Wave pattern in a bar made of PS and PMMA layers bonded by the CA adhesive, at the distance 70-120 mm from the layered structure input

The results obtained allow to conclude that in bonded layered waveguides made of different materials strain solitons propagate as combined waves having characteristics depending upon mechanical parameters of materials and initial wave characteristics. This phenomenon may be used to develop a method of indirect evaluation of strain soliton parameters in opaque materials by means of recording of a wave pattern in an adjacent transparent material. More detailed research on this topic will be published elsewhere.

Figure 7 presents strain soliton in the bar made of PMMA and PMMA + fullerene black (1% wt) layers. Obviously the strain soliton has almost the same amplitude and shape as in the 2-layered PMMA bar. That proves, at least qualitatively, the potential existence of strain solitary waves in this modified polymeric material.

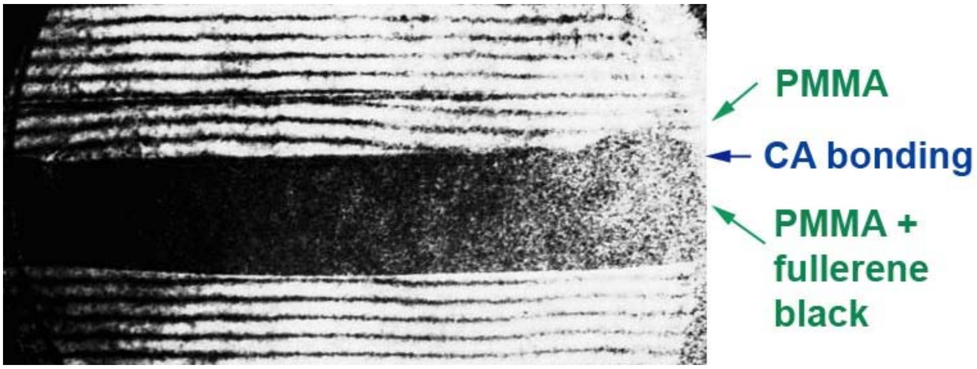

Figure 7. Wave pattern in a two-layered bar made of PMMA and PMMA + fullerene black, bonded by the CA adhesive, at the distance 70-120 mm from the layered structure input

Note that in the layered structure made of PMMA and polyethylene (the material where strain solitons cannot exist) the soliton propagating in the PMMA layer vanishes at the distance of about 70 mm from the layered part input.

The adhesion of filler components to the polymer matrix is of a crucial importance to mechanical behavior of a composite. It was demonstrated in numerous publications that poor adhesion may even cause degradation of mechanical properties of a composite compared to that of the pure polymer. It was recently shown also that adhesion may be destroyed by a shock impact applied to the composite material, that allows us to suggest that a strain soliton of sufficient amplitude may also become a source of fracture.

Thus the potential generation and subsequent behaviour of long nonlinear bulk strain solitary waves in polymeric nanocomposite materials are of a considerable interest both from a fundamental and applied points of view.

CONCLUSIONS

We report first, although indirect, demonstration of strain soliton existence in a polymeric nanocomposite. The solitary wave shape and velocity in a polymeric bar are remarkably stable in comparison with parameters of any conventional (linear or shock) elastic waves in polymers (see Table 1 where decay rates of linear and solitary waves are given). The possibility of strain soliton generation in polymeric nanocomposites should be taken into account in engineering applications of nanocomposite materials.

.

ACKNOWLEDGEMENTS

We are very grateful to Dr. A.I. Lyashkov from Ioffe Institute who provided us a sample of PMMA doped with the fullerene black.

REFERENCES

1. Editorial: soliton wave receives crowd of admirers *Nature*, **376**, 373, 1995.
2. R.K.Dodd, J.C.Eilbeck, J.D.Gibbon, H.C.Morris. “Solitons and non-linear wave equations”, Academic press, London, 1984.
3. I.V.Semenova, G.V.Dreiden, A.M.Samsonov. “On nonlinear wave dissipation in polymers”, *Proceedings SPIE*, 5880, 32-39, 2005.
4. G.V.Dreiden, K.R.Khusnutdinova, A.M.Samsonov, I.V.Semenova. “Comparison of the effect of cyanoacrylate- and polyurethane-based adhesives on a longitudinal strain solitary wave in layered PMMA waveguides”. *J. Appl. Phys.* **104**, 086108, 2008.
5. G.V.Dreiden, K.R.Khusnutdinova, A.M.Samsonov, I.V.Semenova. “Splitting Induced Generation of Soliton Trains in Layered Waveguides”. *J. Appl. Phys.*, **107**, 034909, 2010..
6. A.M.Samsonov. “Strain solitons in solids and how to construct them”. Chapman&Hall/CRC Press, 248 pp., 2001

Proceedings of the SEM Annual Conference
June 7-10, 2010 Indianapolis, Indiana USA
©2010 Society for Experimental Mechanics Inc.

Measurement of High-Strain-Rate Strength of a Metal-Matrix Composite Conductor

Peter J. Joyce[1], Lloyd P. Brown[1]
Dwight Landen[2], Sikhanda Satapathy[2]

1, U.S. Naval Academy
Mechanical Engineering Dept.
590 Holloway Rd
Annapolis, MD 21402

2. Institute for Advanced Technology
3600 Braker Lane
Austin, Texas 78759
pjoyce@usna.edu

ABSTRACT

Castings of metal matrix composites are of potential interest as high strength, high wear resistance conductors. This paper examines the high-strain-rate strength of a tungsten-carbide (WC) filled aluminum bronze alloy (C95400) selected for its good combination of good electrical and thermal conductivity and high mechanical strength, toughness, and wear resistance. A functionally graded material with high wear resistance at the surface was fabricated by centrifugal casting which uses a rotating mold to deposit the high density WC particles at the outer surface while retaining the bulk electrical and thermal conductivity of the bronze alloy for conducting applications.

In this paper we evaluate the effects of the WC particles on the dynamic material behavior of the material in the range 500 s^{-1} to 5000 s^{-1}. The electromagnetic ring expansion technique was used to obtain a nearly uniform uniaxial tensile stress in a thin ring specimen. The dynamic stress-strain response was evaluated as a function of WC particle content. The technique worked satisfactorily in the pure bronze region of the casting but in the WC filled region near the surface the conductivity was too low to effectively launch the ring specimens.

1. INTRODUCTION

The design of conductors for use in high current applications with switching present can result in large magnitude forces that are of electromagnetic (EM) origin. Conductors may achieve temperatures at an appreciable fraction of their melt temperature due to Joule heating. Traditional conductors such as high purity copper may experience a degradation of material properties due to this heating, but quantification of material behavior under conditions of high strain rate and rapid heating is a difficult experiment to conduct. Traditional high strain rate testing frequently uses heating techniques over a time scale orders of magnitude longer than the time scale associated with switching operations, and thus the material under test may degrade due to thermal effects that would not be present in actual conditions. This paper presents results of testing of a high strength conductor under conditions of rapid heating (adiabatic conditions) on a time scale of 25 µs. The testing was two-fold: a) to investigate a

T. Proulx (ed.), *Dynamic Behavior of Materials, Volume 1*, Conference Proceedings of the Society for Experimental Mechanics Series,
DOI 10.1007/978-1-4419-8228-5_38, © The Society for Experimental Mechanics, Inc. 2011

prototype metal matrix conductor that has higher strength than copper and b), perform the tests at adiabatic conditions to prevent thermal degradation of specimen material properties.

Of particular interest was an aluminum bronze alloy metal matrix composite (MMC.) Aluminum bronzes have a wide range of uses: ranging from pump and valve components to propellers and propellers hubs, they are also widely used in bearings, wear rings, and bushings. C95400 is an aluminum bronze ternary alloy: 85% Cu, 11% Al, and 4% Fe, as such it is one of the strongest copper alloys available, plus it has hardness comparable to stainless steel and electrical conductivity ten times better than stainless steel. Conductors fabricated as MMC of bronze filled with tungsten carbide (WC) are of potential interest if the reinforcing particles can mitigate some of the damage mechanisms observed in commonly used low strength, low wear resistance conductors such as C11000 copper. For this study an aluminum bronze alloy (C95400), (σ_y = 29.7ksi, %IACS = 12.96%) was selected as the base matrix, with tungsten carbide (WC), (σ_u = 49.9ksi, %IACS = 3.25-2.16%) as the strengthening material. C95400 has a significantly better yield strength when compared to that of electrolytic tough pitch copper (C11000 copper: (σ_y = 10.0ksi, %IACS = 97.96%)), however, it has a conductivity approximately one eighth that of C11000. The presence of WC within C95400 was expected to improve strength and reduce conductivity, but had not been formally quantified.

A functionally graded metal matrix composite is made through a process called centrifugal casting. Matrix material is placed in a centrifuge within an induction heater, after melting the matrix alloy, high melt temperature strengthening material is added in the form of small (typically on the micron scale) particles to the matrix. Depending on density, the particles will migrate due to centripetal force either to the outside or inside of the MMC, resulting in a MMC with significantly different physical and material properties depending on radial location. This migration of particles creates a composite which has different properties on the inside and outside radii, hence the phrase “functionally graded composite” is sometimes used to describe this type of material. Desired properties could be a function of the concentration gradient of the strengthening additive. Due to the inherent complexity of trying to analytically predict the material properties of MMCs, it is necessary to determine properties experimentally.

Solid bronze alloy (C95400) was placed in a vertically orientated centrifuge within an induction heater, after melting the bronze, WC particles were added. The denser WC particles migrated due to centripetal force to the outside mold wall of the MMC, leaving mostly bronze on the inside of the mold. Figure 1 illustrates the resulting casting process used at the Naval Surface Warfare Center (NSWC) – Carderock.

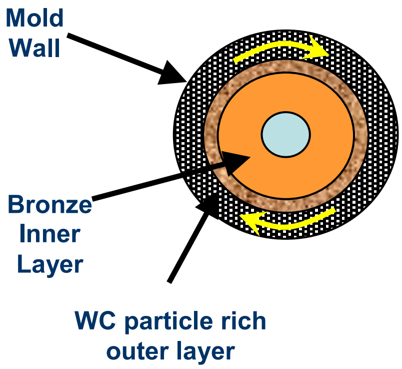

Figure 1: Sketch of the overhead view of the centrifugal mold.

Vertical centrifugal casting also experiences a gravitational effect that tends to pulls the WC particles towards the bottom of the casting. This effect results in an increased thickness of the WC region in the lower region of the casting, thus the location of the transition region has to be carefully determined when removing specimens from the castings.

2. EXPERIMENTATION

Prior to any other test and characterization, the casting was sectioned and surveyed using a microhardness test. This provided an overview of the material properties from the inner radius to outer radius of the centrifugal casting. Based on the microhardness testing results, pinpointing of the transition region between the particle filled volume of WC and the volume of relatively particle free bronze was accomplished, Figure 2 provides an image of the transition region. With the transition region located, the determination of the strain rate dependence of material tensile strength as a function of radial position within the casting was performed.

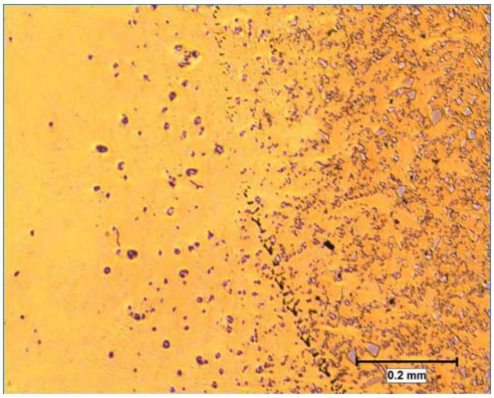

Figure 2: Micrograph of transition region within relatively pure bronze region (left) and particle rich region (right) of C95400 WC metal matrix composite.

The expanding ring test, originally proposed by [1] and refined by [2] and [3], creates much higher rates of strain than possible with traditional load frames, and matches or exceeds strain rates achieved with Split Hopkinson Pressure Bars (SHPB), with the added advantage when compared to the SHPB, of creating a tensile stress state in an adiabatic fashion. This measurement was accomplished using techniques and an apparatus described in [4] and [5]. The electromagnetically driven expanding ring (EDER) test device expands in tension a cylindrically shaped specimen, henceforth termed a “ring”, via electromagnetic (EM) forces. Figure 3 is a schematic of the EDER device used at the Institute of Advanced Technology (IAT) located in Austin, TX.

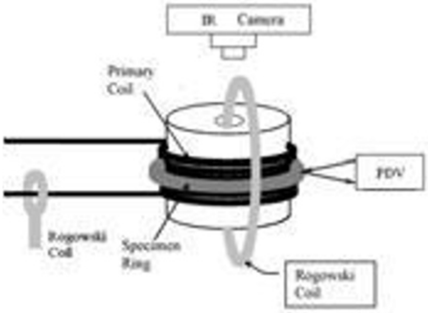

Figure 3: Schematic of EDER. The main experimental components are a solenoid powered by a capacitor bank and the ring sample placed around the solenoid. A Pearson’s coil and a Rogowski coil measure currents. Photonic doppler velocimetry (PDV) measures coil expansion and an infrared (IR) camera measures temperature.

Test specimens were fabricated as thin rings (31 mm dia, 0.50 mm thickness, 1.0 mm height) using Electro-Discharge Machining (EDM). Specimens were cut sequentially from the inner region of the casting to the outer surface of the casting on approximately 1 mm increments such that material properties could be determined as a function of radial position and particle volume fraction. Figure 4 provides an image of the specimen location in the casting and of a single ring specimen prior to testing.

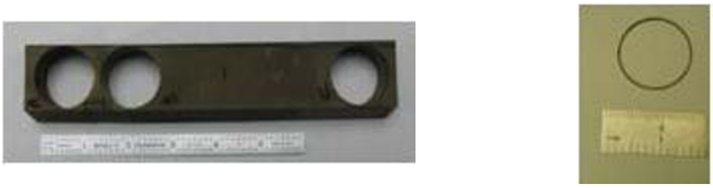

Figure 4: View of specimen location within casting (left image) and single ring specimen (right)

3. TEST DEVICE THEORY OF OPERATION

A capacitor bank is used to pulse a current through the primary windings of the solenoid coil of Figure 3. The ring specimen, placed adjacent to the solenoid windings, acts as a secondary winding. Preheating of the specimen is first accomplished using a portion of the capacitor bank and a switching network. Once desired ring temperature is achieved as measured by the IR camera, the pre-heating portion of the capacitor bank is switched off and the electromagnetic induced stress is then applied to the ring using the other portion of the capacitor bank. The discharge of the EM stress portion of the capacitor bank can be fully accomplished within 50 µs, causing additional heating of the ring and an EM tensile force in the radial direction throughout the ring. The measure of current flow into the primary winding of the solenoid (Pearson coil of Figure 3), along with measurement of the induced current in the ring and solenoid (Rogowski coil of Figure 3), is used to calculate force placed on the ring. The difference in measured currents is the current within the ring itself, this value is used to determine ring force. Ring geometry allows for subsequent determination of stress values within the ring. PDV measurement of ring expansion velocity is used to determine strain rate. For specific details of calculations, see [5].

4. TEST RESULTS

4.1 Currents

EDER experiments rely on three basic measurements to compute strength and temperature: the solenoid current, the ring current and the velocity of the ring sample. The Pearson coil measures current directly, the ring current is found by taking the difference between the Rogowski coil and Pearson coil values. Note that subsequent figures legends refer to “Bronze” and “Bronze WC”, with “Bronze WC” as the label for C95400 Bronze with Tungsten Carbide (WC) MMC ring specimens. Figure 5 shows current behavior for the solenoid and ring. Note that the duration of the experiment is approximately 30 - 35 µs. The speed of the experiment is essential for maintaining adiabatic conditions. Solenoid current has a positive peak and ring currents have a negative peak. Three sets of data were collected for predominantly bronze specimens, at strain rates of 3000, 4000 and 5000 s-^{1}. Two sets of MMC data were collected, in an attempt to match strain rates achieved with the bronze specimens. Discussion on the success of this attempt follows later.

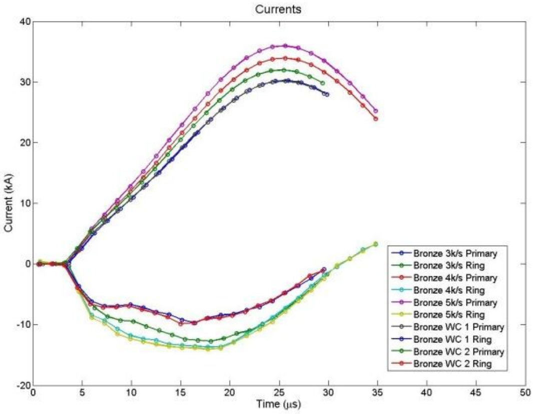

Figure 5: Average current data for solenoid and ring specimens. Current pulses are supplied by a capacitive discharge pulsed power supply. Capacitor voltage determines peak value of current.

4.2 Specimen Velocity

Displacement of the ring specimen was measured using Photonic doppler velocimetry (PDV) techniques, details concerning specific equipment type can be found in [5]. PDV provided a high resolution, low noise measurement that enabled determination of velocity. Strain and strain rate are determined using the following equations:

$$\epsilon = \ln\left(\frac{r}{r_o}\right) \; ; \; \dot{\epsilon} = \frac{v}{r} \qquad (1)$$

$$\text{where } r = r_o + \int v dt \qquad (2)$$

r_o is the initial radius of the ring and v is velocity. Figure 6 provides displacement velocity values for both bronze and MMC ring specimens. When comparing solenoid current as shown in Figure 5, note that velocity slightly lags current in the time domain. The EM force (F_{EM}) that accelerates the ring specimen is a function of solenoid current, so the velocity behavior of the bronze specimens is as expected and as seen with copper specimens previously tested and discussed in [4] and [5]. The velocity of the bronze WC MMC ring specimens were limited by the lower conductivity of the rings. Although not discussed in detail in this paper, the presence of WC particles reduces conductivity by approximately 25% when compared to C95400 bronze. This and other findings regarding physical properties will be presented in [6]. With lower conductivity, the MMC ring has less induced current and thus less F_{EM}.

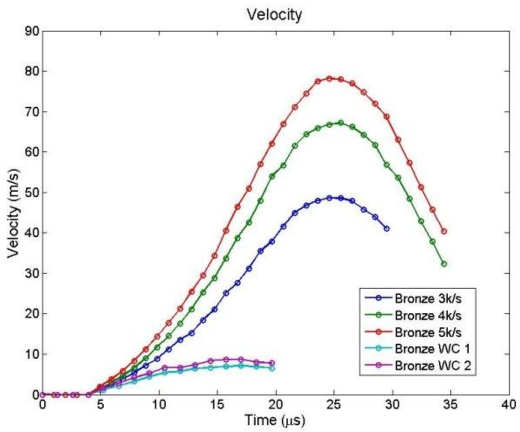

Figure 6: Plots of velocity versus time for both bronze and MMC ring specimens.

4.3 Strain Rate and Stress Determination

Equations (1) and (2) were used to determine strain and strain rate, respectively. Figure 7 provides a plot of three different magnitudes of strain rate tests performed on bronze rings and two strain rate tests performed on bronze MMC specimens. Test device failure precluded further testing of the MMC rings. The experiment was conducted in an attempt to match strain rates achieved earlier with C11000 copper rings (3000, 4000 and 5000 s^{-1}) [4] and to then match strain rates between the bronze rings and the MMC rings. As seen in Figure 7, the desired strain rates for bronze were achieved, but not for MMC rings. As discussed earlier, the relatively low conductivity of the MMC rings limited the magnitude of induced current within the ring, thus preventing attaining the desired strain rate. The maximum strain rate achieved for the MMC rings was approximately 550 s^{-1} before EDER failure stopped further experimentation.

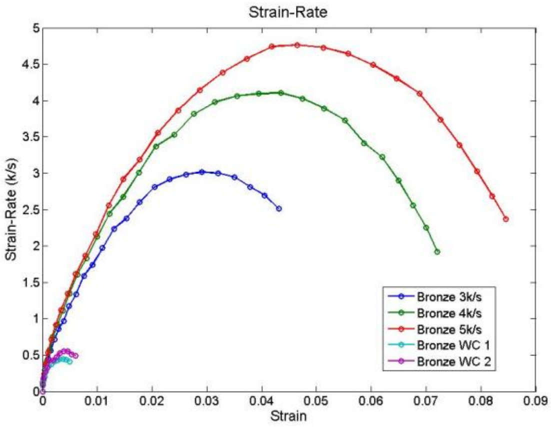

Figure 7: Strain rate versus strain values for both bronze and bronze MMC rings.

True stress values were calculated using the PDV determined specimen velocities, ring geometry and the polar coordinate equation for hoop stress based on the equation of motion (EOM). The hoop stress equation is based on assumptions presented in [2] and is as shown:

$$\sigma_H(r) = r(\frac{F_{EM}(r)}{V} - \rho a) \tag{3}$$

where r is ring radius, V is ring volume, a is acceleration and ρ is density. The value of F_{EM} is calculated from measured current through the solenoid and induced in the ring and the ring inductance. The determination of inductance and use of currents to find F_{EM} is detailed in [5] but is considered beyond the scope of this paper. Figure 8 presents true stress data versus strain for the rings tested. The behaviors of the bronze rings were as expected, with a definite trend of strain rate dependency for tensile strength. The maximum tensile stress for the 5000 s^{-1} case was approximately 33% greater than for the case of 3000 s^{-1}. The results for the bronze WC MMC were disappointing. No improvement in tensile strength was noted, in fact, the tensile strength was less than that of the bronze rings, although WC particles were added to strengthen the alloy. Note that in Figure 8, the results for the two tests conducted were almost the same, with a maximum tensile stress of almost 650 MPa, although there was a small (approximately 10%) increase in strain rate between the two tests. Two factors are postulated for this behavior. Firstly, the MMC rings had a volume fraction of almost 45% WC, which significantly increased the hardness of the material, and in turn brittleness. The shape of the MMC curve in Figure 8 also implies a significant loss of plasticity when compared to that of the bronze rings. This leads to the second postulation, in that the MMC rings are believed to behave much more like a ceramic than a metal. The MMC rings suffered catastrophic failure in tension, fragmenting into many small pieces, while on the other hands the bronze rings remained intact after plastic deformation. Figure 9 shows the residue of an MMC ring after testing.

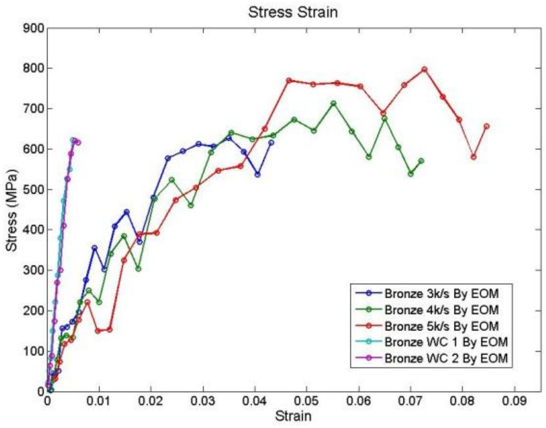

Figure 8: True stress data for bronze and MMC rings.

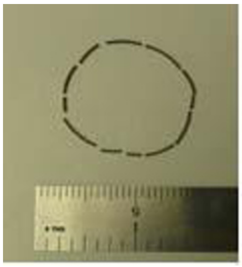

Figure 9: Post test MMC ring debris. Note large number of ring shards. Fracture surfaces were flat and granular, implying brittle failure.

4.4 Temperature Measurement

The significant and attractive feature of the EDER test is to be able to adiabatically heat the specimen via currents in a short time scale. Earlier tests to determine material properties at elevated temperatures showed that the relatively long time required for heating the specimens for quasi-static testing degraded material properties due to changes in the grain structure. This led to doubts concerning the effect if any, on material properties when rapid heating occurred in an adiabatic fashion, as might occur in switching conductors. Figure 10 shows the measured temperature behavior of the ring specimens used in this series of tests. Temperature measurement device details are found in [5]. In the MMC cases, note that the temperature quickly rises due to induced current flow, than rapidly decays away once current flow ceases. The MMC specimens display a shorter heating cycle as the catastrophic failure of the ring specimen early in the test removed induced currents much earlier than occurred in the bronze rings. Bronze rings achieved a higher temperature as more current flowed for a longer period of time, this coupled with a higher heat capacity value, resulted in a higher magnitude of temperature, coupled with a longer dwell time.

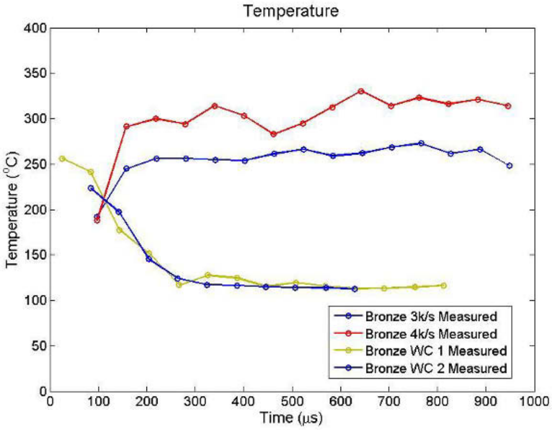

Figure 10: Temperature behavior as measured using IR camera.

5. CONCLUSIONS AND RECOMMENDATIONS

The ability to test a material other than highly conductive metals such as pure copper and aluminum alloys using the EDER has been demonstrated. Although the conductivity of C95400 bronze limits the achievable strain rate when compared to that of electrolytic tough pitch copper, 6061 and 7075 aluminum as demonstrated in [4] and [5], the feasibility of testing a metal matrix composite has been established. Additionally, the high strain rate testing of a MMC has been performed using this technique, perhaps for the first time. This particular MMC displayed brittle behavior more in keeping with that of a ceramic than that of a metal, which can be attributed to the relatively high concentration of WC particles in those specimens. Tensile strength of the MMC was approximately 650 MPa prior to catastrophic failure, with almost no plastic deformation. Although not part of the scope of this paper, much higher strength in compression has been observed using SHPB test techniques [7].

EDER results disappointingly show little to no improvement in tensile strength of the MMC over that of the C95400 aluminum-bronze matrix material.

These preliminary results must be investigated further. Failure of the expansion ring mounting section caused in part by the large amount of current required due to the low conductivity of the MMC specimens limited the number of tests that could be conducted. Methods to improve the applicability of the EDER to materials of low conductivity are being pursued, following the recommendations of [8], including the use of an electrodynamically driven pusher ring to expand the test specimens. Reducing the volume content of WC particles would probably improve the plastic behavior of the MMC. A discussion of physical properties of the MMC will be presented in a separate venue [6].

6. ACKNOWLEDGEMENTS

The authors wish to acknowledge the support of staff metallurgist Dr. A. P. “Dave” Divecha, of Naval Surface Warfare Center, Carderock, who graciously provided both samples and technical advice concerning fabrication of metal matrix composites. The following United Stated Naval Academy technical staff members are acknowledged for specimen preparation and data collection: Mr. Cort Lillard, Mr. Derek Baker, and Mr. Steve Crutchley.

7. REFERENCES

1. Walling, H., Forrestal, M., “Elastic-Plastic Expansion of 6061-T6 Aluminum Rings”, AIAA Journal, Vol. 11, 1973, p 1196-1198.
2. Gourdin, W., “Analysis and Assessment of Electromagnetic Ring Expansion as a High-Strain-Rate Test”, Journal of Applied Physics, 65 (2), January 1989, pp 411 – 422.
3. Grady, D., Benson, D., “Fragmentation of Metal Rings by Electromagnetic Loading”, Vol. 23, No. 4, December 1983, pp 393 – 400.
4. Landen, D., Satapathy, S. “Measurement of High-Strain-Rate Adiabatic Strength of Conductors”, IEEE Transactions on Magnetics, Vol. 43, No.1, January 2007, pp 349 – 354.
5. Landen, D., Wetz, D, Satapathy, S., Levinson, Scott, “Electromagnetically Driven Expanding Ring With Preheating”, IEEE Transactions on Magnetics, Vol. 45, No.1, January 2009, pp 598 – 603.
6. Joyce, P., Brown, L., Lazzaro, A., “Physical and Mechanical Characterization of a Metal-Matrix Composite Conductor”, SAMPE 2010 Fall Technical Conference, Salt Lake City, UT, October 2010 (abstract submitted.)
7. Brown, L., Joyce, P. Lazzaro, A., “Physical and Mechanical Properties of Metal-Matrix Composite Conductors”, 56th Holm Conference, Charleston, SC, October 2010 (paper accepted).
8. Gourdin, W., Weinland, S., and Boling, R., “Development of the Electromagnetically Launched Expanding Ring as a High-Strain-Rate Test Technique”, Rev. Sci. Instrumen., 60 (3), March 1989.

Proceedings of the SEM Annual Conference
June 7-10, 2010 Indianapolis, Indiana USA
©2010 Society for Experimental Mechanics Inc.

A Revisit to High-rate Mode-II Fracture Characterization of Composites with Kolsky Bar Techniques

Wei-Yang Lu, Bo Song, Helena Jin

Sandia National Laboratories, Livermore, CA 94551-0969, USA

Nowadays composite materials have been extensively utilized in many military and industrial applications. For example, the newest Boeing 787 uses 50% composite (mostly carbon fiber reinforced plastic) in production. However, the weak delamination strength of fiber reinforced composites, when subjected to external impact such as ballistic impact, has been always potential serious threats to the safety of passengers. Dynamic fracture toughness is a critical indicator of the performance from delamination in such impact events. Quasi-static experimental techniques for fracture toughness have been well developed. For example, end notched flexure (ENF) technique, which is illustrated in Fig. 1, has become a typical method to determined mode-II fracture toughness for composites under quasi-static loading conditions. However, dynamic fracture characterization of composites has been challenging. This has resulted in conflictive and confusing conclusions in regard to strain rate effects on fracture toughness of composites [1].

Currently the quasi-static ENF technique has been implemented to high-rate testing, i.e., Kolsky bar technique. In quasi-static ENF characterization, the forces applied to both sides of the specimen are balanced, $P = F_1 = 2F_2 = 2F_3$, so that the mode-II fracture toughness can be calculated with the common force, P, [2]. However, when the ENF specimen is subjected to impact loading, the force may not be equilibrated due to inertia (or stress wave propagation) effect in such a relatively large scale specimen. The validity of loading condition in dynamic characterization needs to be carefully verified. In this study, we employed a Kolsky bar with highly sensitive polyvinylidene fluoride (PVDF) force transducers to check the forces on the front wedge and back spans. High rate digital image correlation (DIC) was also conducted to investigate the stress wave propagation during the dynamic loading. The specimen material is glass fiber reinforced epoxy composite. A thin Teflon film was inserted into the composite during manufacturing process, leaving a precrack in the specimen.

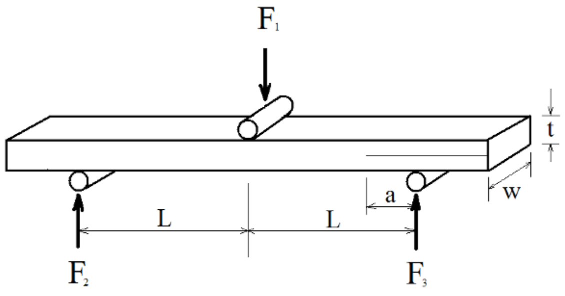

Fig. 1. Typical ENF specimen

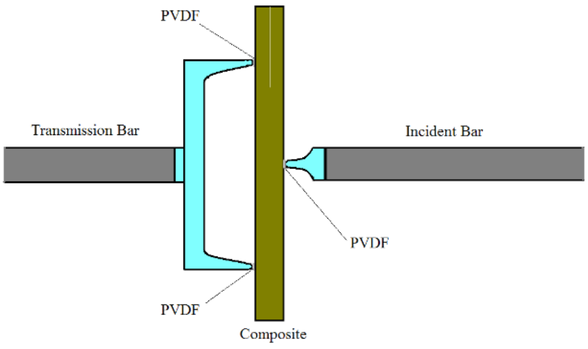

Fig. 2. The ENF specimen with PVDF transducers in Kolsky bar experiment

T. Proulx (ed.), *Dynamic Behavior of Materials, Volume 1*, Conference Proceedings of the Society for Experimental Mechanics Series, DOI 10.1007/978-1-4419-8228-5_39, © The Society for Experimental Mechanics, Inc. 2011

The PVDF is a kind of piezoelectric film force transducer with high sensitivity, even though the sensitivity is nonlinear to the applied force. After careful calibration, the PVDF film transducer was made into small square pieces that are embedded on the front wedge and back spans, as shown in Fig. 2. Figure 3 shows typical outputs from the three PVDF transducers as well as the strain gage on the transmission bar which is approximately 494 mm from the specimen back surface. In Fig. 3, the green strain gage signal has been synchronized to the specimen back surface based on conventional calculation of the distance divided by the bar longitudinal wave speed of 4900 m/s. Figure 3 clearly shows that the forces applied on the specimen are not balanced. Particularly for the first 60 microseconds, $F_1 >> F_2 + F_3$. Furthermore, the forces at both back spans are not the same, $F_2 > F_3$. The force signal from the strain gages is observed to lag behind the PVDF signals. This might be because it takes much longer for the stress signal to travel from the spans to the bar end. During this stage, transverse wave is involved, the wave speed of which is much slower than longitudinal wave. Since the forces are not equilibrated, the quasi-static analysis is no longer valid to calculate the fracture toughness.

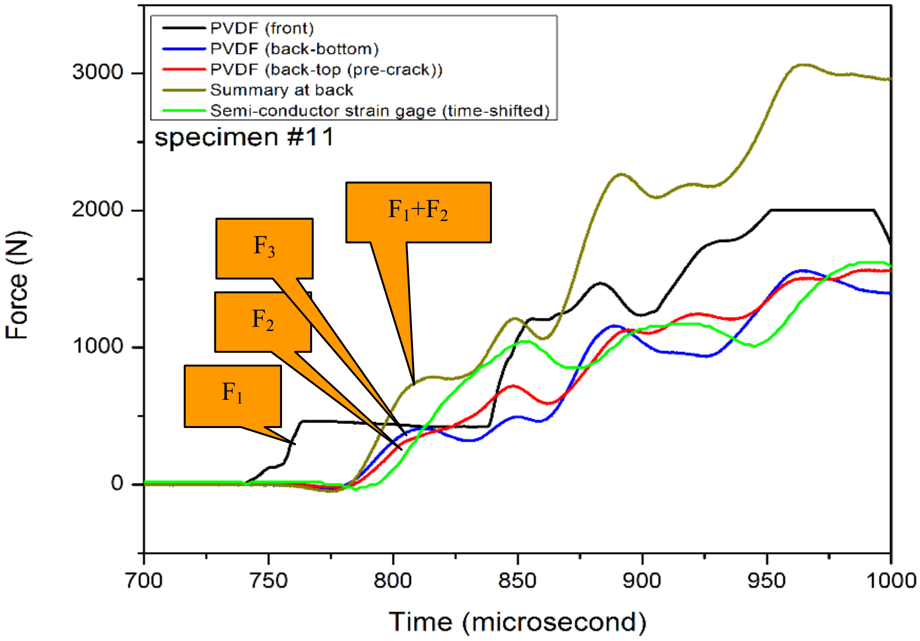

Fig. 3 The force histories in the ENF composite specimen

The non-equilibrated forces during dynamic experiment are due to relatively large specimen scale and slow transverse stress wave. When the wedge on the incident bar end starts to impact on the composite beam, a transverse wave is generated and then propagates from the center outward the top and bottom simultaneously. DIC method was used to monitor the real-time propagation of the transverse wave, the results of which are shown in Fig. 4. The time interval between the images is 5 microsecond. The pre-crack tip locates at the 3/5 between the upper span and the wedge, as shown with the black line in Fig. 4. Figure 4 shows the transverse wave front (yellow zone) propagates from the wedge towards the span. Only first two images were taken before the transverse wave arrived to the crack tip. The transverse wave speed is calculated as 1237 m/s from the two images. When the transverse wave arrived at the crack tip, the wave speed significantly reduced to 338 m/s because of drastically reduced flexural modulus due to the crack. However, the transverse wave propagates downward to the lower span at a nearly constant speed of 1237 m/s because there is no crack on the other half portion of the specimen. This may be the reason why the forces at the upper and lower spans are different.

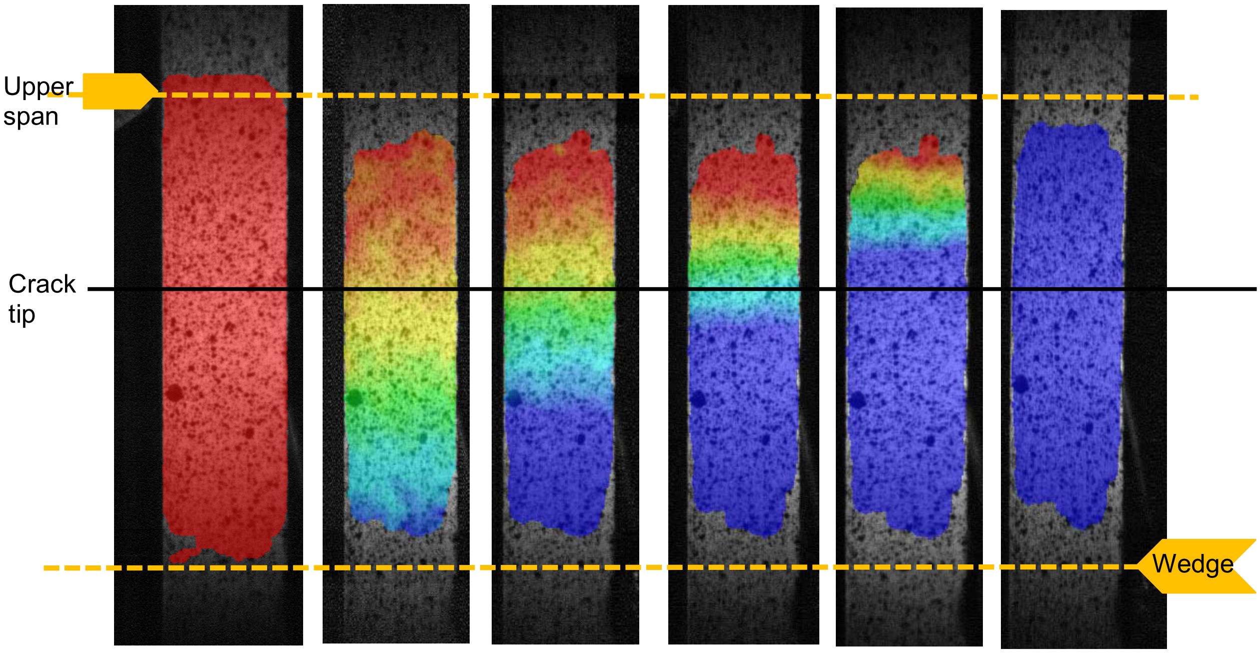

Fig. 4. Transverse wave propagation

It is calculated that the transverse wave takes nearly 45 microseconds to travel from the wedge to the upper span. Due to the large specimen size and relatively low transverse wave speed, the forces at the front wedge and back span surfaces are difficult to be balanced over the entire loading duration in a Kolsky bar experiment. Therefore, the quasi-static analysis for mode-II fracture toughness cannot be used for such a dynamic experiment. Instead, numerical simulation, such as finite element analysis, should be implemented together with the dynamic experimental data to determine the mode-II fracture toughness.

ACKNOWLEDGEMENTS

Sandia is a multiprogram laboratory operated by Sandia Corporation, a Lockheed Martin Company, for the United States Department of Energy under Contract DE-ACO4-94AL85000.

REFERENCES

1. Jacob, G. C., Starbuck, J. M., Fellers, J. F., Simunovic, S., Boeman, R. G., 2005, “The effect of loading rate on the fracture toughness of fiber reinforced polymer composites,” Journal of Applied Polymer Science, 96:899-904.
2. Yang, Z., and Sun, C. T., 2000, “Interlaminar fracture toughness of a graphite/epoxy multidirectional composite,” Transactions of the ASME, Journal of Engineering Materials and Technology, 22:428-433.

Proceedings of the SEM Annual Conference
June 7-10, 2010 Indianapolis, Indiana USA
©2010 Society for Experimental Mechanics Inc.

The Influences of Residual Stress in Epoxy Carbon-fiber Composites under High Strain-rate

Hongchueh Lee, Shih-Han Wang, Chia-Chin Chiang, Liren Tsai*
Mechanical Engineering Department, National Kaohsiung University of Applied Sciences
*415 Chien Kung Road, Kaohsiung 807, Taiwan, liren@cc.kuas.edu.tw

ABSTRACT

Epoxy carbon-fiber composite (FRP) has been widely regarded as premium construction material in automobile and leisure sporting good industries. In this research, the formation of residual strain in epoxy carbon fiber composites during curing was monitored using Fiber Bragg Gratings (FBG). Carbon-fiber composites were prepared under steady temperature gradient and the FBGs were embedded during FRP preparation process along axial fiber layout direction. The effect of residual stress to the dynamic tensile stress in these FBG imbedded carbon fiber composites was examined using modified Split Hopkinson Tensile Bar (SHTB). The relationship between residual stress and dynamic tensile stress in the FRP under a high strain rate ranging from 500 to 1000 s^{-1} was thus studied.

1. Introduction

Carbon fiber composites have been widely considered as the optimal replacement material for various industrial products, such as bicycle, racket, ski, pressure vessel, yacht, aircraft, wind vane, etc.. Despite its high cost, the high strength/weight ratio of carbon fiber composites made it utterly popularly. However, for composite materials, the inherent defects could greatly hamper the reliability and durability of the resultant products. These defects, either form during production or generated by improper handling (drop, indent, impact…etc.) could eventually determine the dynamic strength of the finishing products. In this research, a novel Fiber Bragg Grating (FBG) technology was implanted along with the Split Hopkinson Tensile Bar (SHTB) facility to study the effect of inherent residual strain to the dynamic tensile strength of epoxy carbon fiber composites.

FBG possess great compatibility with Fiber Reinforced Polymer Composites (FRP) [1]. By embedded FBG inside carbon fiber composites, the residual strain of the carbon fiber composites during production could be easily monitored. The wavelength of the embedded FBG changed before and after the FRP curing process, and the residual strain of the FRP could be determined accordingly [2]. To verify the effect of residual stress to the dynamic tensile strength of FRP, a reverse-striking SHTB in Kaohsiung University of Applied Sciences was utilized [3]. The

T. Proulx (ed.), *Dynamic Behavior of Materials, Volume 1*, Conference Proceedings of the Society for Experimental Mechanics Series,
DOI 10.1007/978-1-4419-8228-5_40, © The Society for Experimental Mechanics, Inc. 2011

SHTB was able to generate tensile pulse up to 1000 s^{-1} inside the prepared FRP and ultimately break the specimens. The results could be used to better understand the role of residual stress to the dynamic tensile strength of epoxy carbon fiber composites.

2. Experimental Configuration and Setup

2.1 Split Hopkinson Tensile Bar (SHTB)

The Split Hopkinson Tensile Bar, Fig. 1, is an adaptation of the device developed by Kolsky [4]. It consists of a gas gun system, an incident bar, a transmitted bar and a specimen assembly. A projectile fired from a gas gun impacts one end of the incident bar and generates a tensile stress pulse propagating down the bar into the specimen. This pulse reverberates within the specimen, sending a transmitted pulse into the transmitted bar and a reflected pulse back into the incident bar. The bars are designed to remain elastic throughout the test so that the complete displacement time and stress-time histories at the interfaces between the specimen and the bars can be determined from measurements of the incident, reflected and transmitted pulses [5]. The incident and transmitted bars of the SHTB were made by 20mm diameter SUS304 stainless steel.

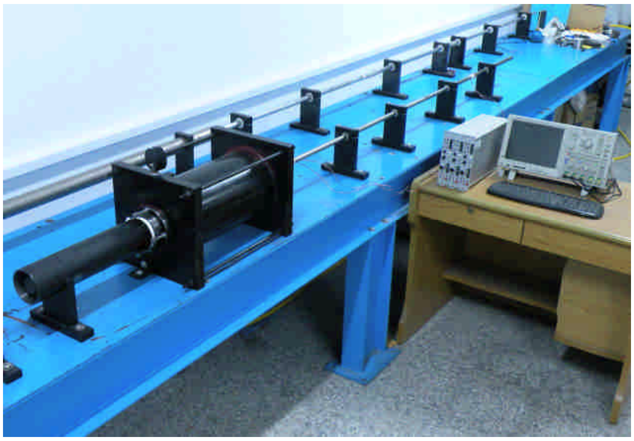

Fig.1 The SHTB facility in KUAS.

2.2 Fiber Bragg Grating sensors (FBG)

The FBG involved was fabricated from single cladding photosensitive fiber using the side writing method. The photosensitive fiber was produced by Fibercore Co. Ltd.(PS1250/1550). The FBGs are photoimprinted in photosensitive optical fiber by 248-nm UV radiation from a KrF Excimer laser. The impulse frequency of laser is 10 Hz. To avoid burning the phase mask, the laser power should be <500 mJ/cm^2. Along the fiber core, the FBG has a periodic refractive index modulation with a period of 1.05~1.08 μm, obtained by using phase masks (Lasiris Co. Ltd.) with different periods. This resulted in a peak Bragg reflecting wavelength of 1540~1564 nm. The reflectivity of the resulting FBG was about 99% and the FWHM (Full width Half Maximum) of the FBG is about 0.175 nm [1]. Light source export energy to the carbon fiber composite with FBG by coupler, and the energy change was then recorded and analyzed by oscilloscope. The residual strain of imbedded carbon fiber composites could be determined by comparing the wavelength difference in the FBG before and after curing process using by Eq.(1):

$$\frac{\Delta\lambda}{\lambda} = (1 - P_e)\varepsilon + (\alpha + \zeta)\Delta T \tag{1}$$

Where λ and Δλ represent the original and variation wavelength of optical fiber, and P_e indicates the light elastic constant. α and ζ represent the coefficient of thermal expansion and thermo-optic coefficient of the optical fiber, respectively. Fig. 2 shows the experimental arrangement of the proposed FBG plus SHTB system.

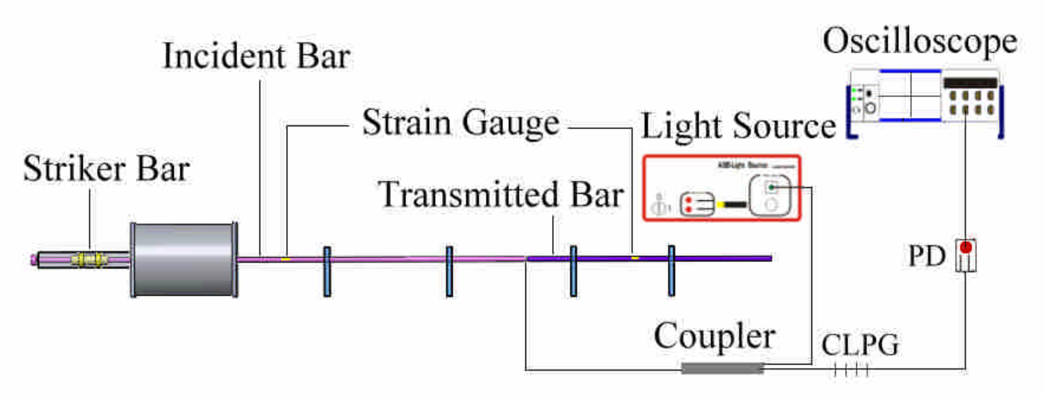

Fig.2 SHTB plus FBG experimental configurations.

3. Specimen Assembly

3.1 Materials and Specimen Preparation

Prepregs from Advanced International Multitech (batch number: B10037K) was utilized to compose the epoxy carbon fiber specimens. A series of 0^{o} specimens was prepared: (1) fold the carbon laminate with ten ply (about 1 millimeter) by 0^{O}; (2) put the Fiber Bragg Grating (FBG) on the center of aminate plane [5]; (3) let the optical fiber out from lateral direction, and then take another ten ply of 0^{o} prepreg laminate to cover the FBG, totally 20 carbon fiber ply.

3.2 Dog-Bone Shaped Specimens

After the specimens were cured properly, each assembly was then sent machined to dog-bone shape for better tensile stress distribution, as shown in Fig.3. The effective section for each specimen was located at the center with crosssection area approximately 3mm x 2mm. A stainless steel fixer was designed to hold the carbon-fiber specimens. The fixer provides axial support during the experiments, and it also offered the required clearance for better aligning the SHTB incident and transmitted bars, Fig. 3(a). Fig. 3(b) shows the finished specimen assembly of a FBG embedded carbon fiber composite.

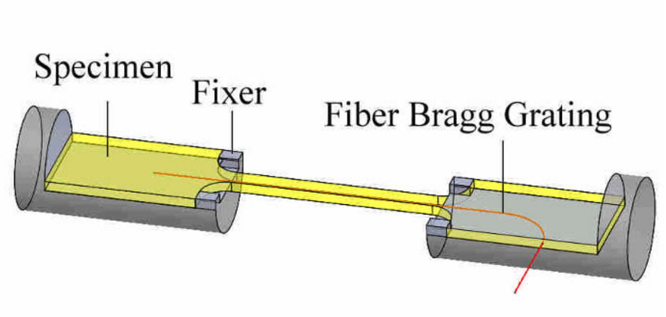

(a)

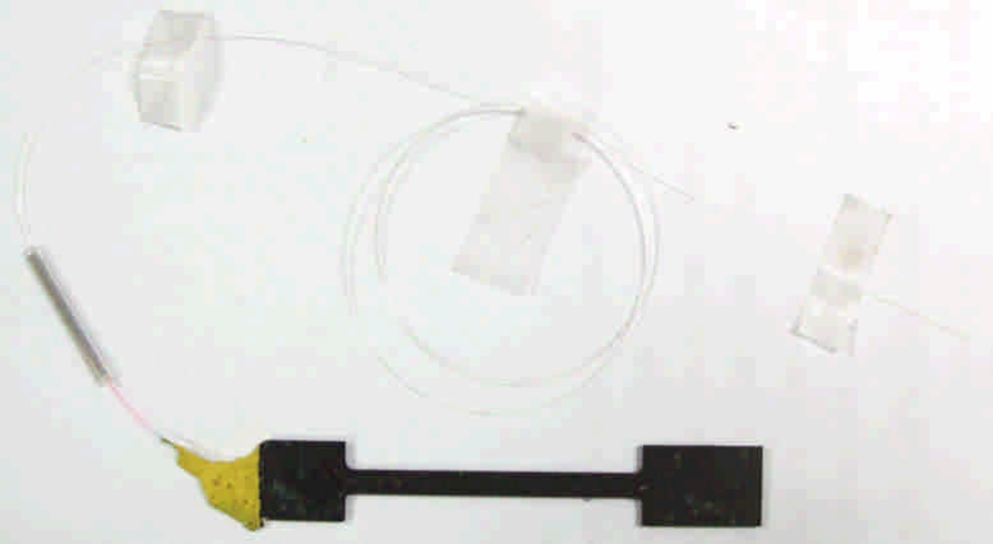

(b)

Fig.3 (a) Illustration of specimen assembly; (b) CF06 specimen for experiment.

4. Preliminary Results and Discussion

In the present study, several FBG embedded FRP specimens were prepared to determine the relation between residual stresses to the dynamic tensile strength of the proposed carbon fiber composites. The changes of FBG wave length during the curing process for each specimen were monitored, as shown in figure 4. The wavelength of specimen CF06 showed clear increment with increasing temperature. After the specimens are cooled down to atmosphere temperature, the wavelength of each specimen was also recorded. Figure 5 showed the wavelength of specimen CF03 before and after curing, and from the wavelength difference, the residual strain was determined to be 0.015%. In Fig. 6, the dynamic tensile stress vs. strain relationship of two specimen assemblies, CF01 and CF02, were presented. The specimen with higher residual stress, CF01 (residual strain 0.015%), possesses a more oscillatory stress vs. strain relationship, while the specimen with lower residual stress, CF02 (with residual strain 0.011%) has a much more smooth stress vs. strain relationship, Fig. 6. It also seems that specimen CF02 has a higher tensile strength between the two. However, the specimens were under different tensile loading strain rates, so the tensile strength difference could be contributed from the strain rates difference. The tensile strength of the FRPs at higher strain rates should be further studied to ensure the relationship between residual stress and tensile strength at severe engineering application conditions.

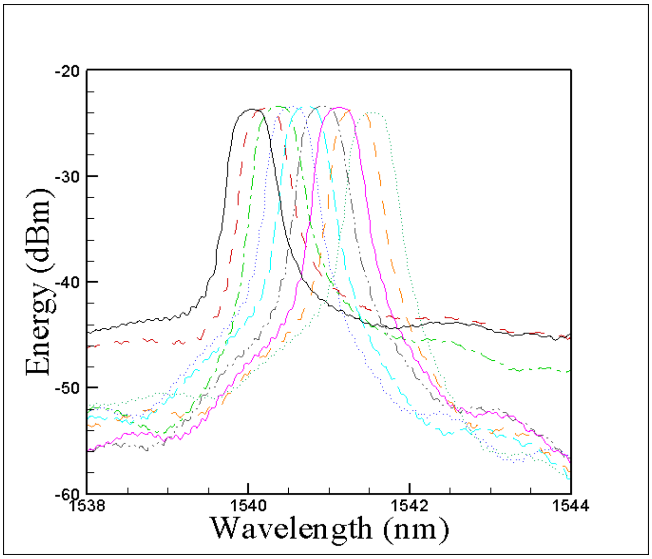

Fig.4 Difference of wavelength of specimen recorded by FBG till 180°C for experiment CF06.

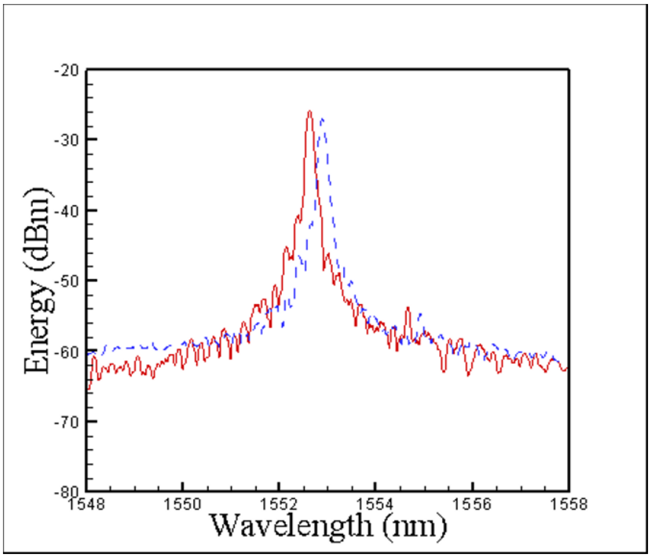

Fig.5 Difference of wavelength of specimen CF03 recorded by FBG before and after curing. The calculated residual strain was 0.015%.

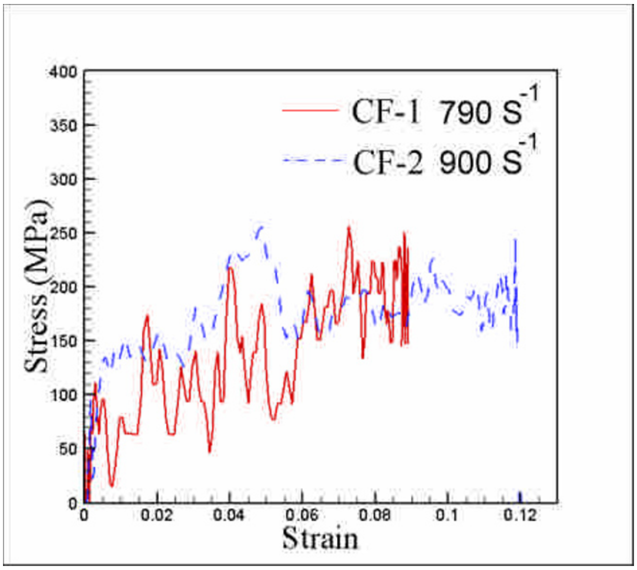

Fig. 6 Stress vs. Strain curves from SHTB experiments.

5. Summary

FBGs were embedded inside FRP specimens to exam the relationship between residual stress and dynamic tensile strength of layered carbon fiber composites. The residual strain was able to be monitored during curing procedure and the residual strain was recorded for each specimens. The SHTB experiments showed that the residual stress in the FRP mainly affects the stress vs. strain profile of the examined FRP but provide no obvious evidence for its influence to the dynamic tensile strength. This characteristic at higher strain rates remained to be determined.

Acknowledgements

This work is funded by The National Science Council (grant number NSC-97-2221-E-151-019). The author wants to give special thanks to Mr. Chien-chang Huang. Without his kind help, the experiments won't be able to carry on smoothly.

References

[1] Tsai L., Cheng T. C., Lin C. L. and Chiang C. C., Application of the embedded Optical Fiber Bragg Grating sensors in curing monitoring of Gr/Epoxy laminated composites, Proceedings of SPIE, 2009

[2] Mandal J., Bragg grating tuned fiber laser system for measurement of wider range temperature and strain, Optics Communications, 2005

[3] Tsai L., Chiang C. C., Wang S. H., and Lin H. R., Dynamic Response of Low Friction, High Strength Hydrogels, 25th Annual Conference of Chinese Society of Mechanical Engineering, 2009

[4] Bailey J. A., Mechanical Testing and Evaluation, ASM Vol.8

[5] Taniguchi N., Tensile strength of unidirectional CFRP laminate under high strain rate, Adv. Composite Mater., Vol. 16, No. 2, pp. 167–180, 2007

Proceedings of the SEM Annual Conference
June 7-10, 2010 Indianapolis, Indiana USA
©2010 Society for Experimental Mechanics Inc.

Strain rate-dependent and temperature- dependent compressive properties of 2DC$_f$/SiC Composite

Yingchun **Wang *, Shukui Li , Jinxu Liu**
School of Materials Science & Engineering, Beijing Institute of Technology,
Beijing 100081, P.R. China
*Corresponding author. E-mail address: wangyc@bit.edu.cn

ABSTRACT

Effects of strain rate and temperature on dynamic behaviors of 2DC$_f$/SiC composite were investigated by improved Split Hopkinson Pressure Bars (SHPB) using pulse shaper. Results show that the shape of incident wave changes from rectangle to triangle after using pulse shaper in SHPB testing. The dynamic compressive strength of the composite increases with strain rate increasing from 500s^{-1} to 1700s^{-1}, while shows decreasing tendency with strain rate rising from 1700s^{-1} to 2750s^{-1}, indicating a maximum dynamic strength at strain rate of about 1700s^{-1}. The 2DC$_f$/SiC composite exhibits higher strength and better ductility at elevated temperature in the range of 460℃～500℃ compared with that at room temperature.

Keywords: C$_f$/SiC composite; SHPB ; stain-rate sensitivity

1. Introduction

Carbon-fiber-reinforced SiC-matrix (C$_f$/S$_i$C) composites have such advantages as low density, high ratios of stiffness/weight and strength /weight, and failure stress that can sustain under high temperature conditions, all of which enable them considered as desirable high temperature structure materials, especially in aerospace field[1].

Referring to C$_f$/S$_i$C composites, there are several methods to fabricate them, including chemical vapor infiltration (CVI), slurry infiltration combined with hot-pressing and polymer-infiltration-pyrolysis (PIP)[2-4]. The PIP route is being actively developed recently because it has many potential advantages, such as low-processing temperature, controllable ceramic compositions, and near-net-shape technology [5].

Many researchers have studied on the mechanical properties of two-dimensional carbon fiber cloth reinforced

T. Proulx (ed.), *Dynamic Behavior of Materials, Volume 1*, Conference Proceedings of the Society for Experimental Mechanics Series, DOI 10.1007/978-1-4419-8228-5_41, © The Society for Experimental Mechanics, Inc. 2011

silicon carbide (2DC$_f$/SiC) composites. However, most of them are focus on their static properties, and a little literatures are available regarding dynamic behaviors of C$_f$/S$_i$C composites. The SHPB technology developed by Kolsky, has been widely used to determine the high strain rate response of materials under tension, compression and torsional loading. M.S.Liu et. al. [6] investigated dynamic compressive properties at strain rates ranging from 10^{-4} s^{-1} to 2.8×10^{3} s^{-1} of 2DC$_f$/S$_i$C composites fabricated by CVI method using SHPB. They found the dynamic compressive stress-strain curves are non-liner and the failure strain reduces with strain rate increasing. Y.L.Li et.al. [7] summarized that the strain rate has slight influence on the dynamic compression strength of 3D needle-punched C/S$_i$C composite.

Due to extensive application in aeronautic and aerospace fields, thermal shock resistance, and high-temperature static properties of C/S$_i$C composites are studied by some researchers [8]. However, the dynamic behaviors of C$_f$/S$_i$C composites at elevated temperature have not yet been reported to our knowledge. When C$_f$/S$_i$C composites are used at aerospace field, structures may be subjected to high temperature and impulse loading such as the impact of debris [9,10]. To accurately predict material behaviors in these conditions, dynamic mechanical properties of these type of materials under a wide range of strain rates and at elevated temperatures should be investigated.

In this paper, the dynamic responses of 2DC$_f$/S$_i$C composite fabricated by PIP route were performed under impulse loading at room temperature and at elevated temperatures of 460℃~500℃ by using a SHPB apparatus.

2. Experimental

2.1. Material selection and specimen fabrication

Plain weave carbon cloth of type HS of 3K PAN base fibers was used as the reinforcement of 2DC$_f$/S$_i$C composite. The tensile strength and elastic modulus of the fibers were about 3000 MPa and 210GPa, respectively. The 2DC$_f$/S$_i$C composite was prepared by PIP route with polycarbosilane and divinylbenzene used as the precursor of S$_i$C matrix. The volume fraction of carbon fibers in 2DC$_f$/S$_i$C composite specimens was about 38%.

The cylindrical specimens for dynamic compression with a diameter of 5mm and a length of 5mm were cut from a 2DC$_f$/S$_i$C composite plate to ensure the axial direction of specimens is vertical to the carbon cloth plain.

2.2. Experimental techniques

The dynamic compressive experiments were tested by the improved SHPB apparatus as shown in Fig.1. The loading strain rates were controlled by changing the gas pressure and the size of pulse shaper.

The specimen was sandwiched between the input and output bars. The striker bar propelled by pressured gas impacted against the input bar, and a compressive stress pulse was generated in the striker and the input bars. The duration of the loading pulse was equal to the time for the stress wave to traverse back and forth once in the striker bar. When the compressive stress pulse impinged on the specimen, parts of the incident pulse was reflected back into the input bar and the other part of it was transmitted through the specimen into the output bar.

Ravichandran G. [11] found that the stress pulse need to reflect back and forth more than three times to get to a constant strain rate. So it is difficult to ensure that a nearly constant strain rate at the early period of the test duration was gained by using the conventional SHPB. For the fracture strain of C_f/S_iC composites is small, the specimens fracture in a very short time. Consequentially, it can't be ensured to obtain a constant strain rate in the short time using the conventional SHPB with an incident pulse wave shape of rectangle. Under this test condition the dynamic properties of C_f/S_iC composites is incredible. To solve the problem, a hard copper cushion, also called pulse shaper was placed at the impact end of the incident bar to introduce a monotonically increasing ramplike stress pulse in the incident bar [12]. Fig.2 shows the shape of incident wave changes from rectangle to triangle after using pulse shaper in SHPB testing properties of $2DC_f/S_iC$ composites which causes the time of reaching a constant strain rate to reduce from 35μs to 15μs. Thus most of stress is gained at a certain constant strain rate during dynamic loading process. The sizes of pulse shapers were cylinders with diameters of 3mm and 6mm, thicknesses of 0.8mm,1,2mm and 1.6mm, respectively.

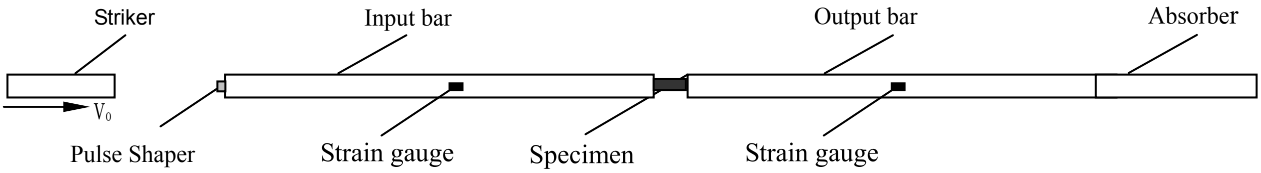

Fig.1. Schematic illustration of the improved SHPB

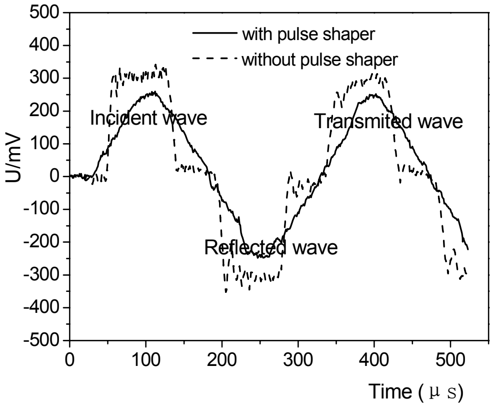

Fig.2. Comparison of incident waves with or without pulse shaper

Based on the theory of one-dimensional elastic wave propagation, the stress (σ_s). Strain rate ($\dot{\varepsilon}_s$) and strain (ε_s) can be evaluated as

$$\sigma_s = E(\frac{A_b}{A_s})\varepsilon_T(t) \qquad (1)$$

$$\varepsilon_s = -\frac{2C_o}{l_s}\int_0^t \varepsilon_R(t)dt \qquad (2)$$

$$\dot{\varepsilon}_s = -\frac{2C_o}{l_s}\varepsilon_R \qquad (3)$$

Where $\varepsilon_T(t)$ and $\varepsilon_R(t)$ are the transmitted and reflected strain pulses, respectively, E, A_b, C_0 denote the Young's modules, cross-sectional area and longitudinal wave speed of the bars. l_s and A_s are the length and cross-section area of the specimen.

The effects of strain rates on dynamic behaviors were determined at room temperature. Dynamic responses of $2DC_f/S_iC$ at elevated temperatures ranging from 460℃ to 500℃ at strain rate of about $1000s^{-1}$ were conducted by using a SHPB, with a tube heating furnace which can heat the specimens before and during the test. The specimen was heated to a certain elevated temperature and kept the temperature for 20 minutes before testing.

After the dynamic experiment, fracture surfaces of these specimens were observed using a scanning electron microscope (SEM).

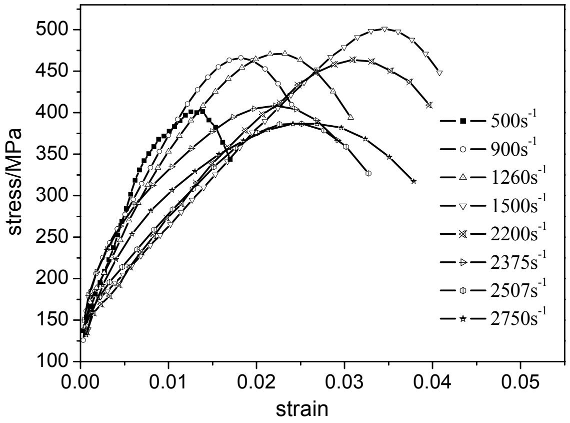

Fig.3. The stress vs.strain curves of the 2DCf/SiC composite under dynamic compression at room temperature

3. Results and discussion

3.1. Dynamic responses at different strain rates

Strain rates varied from $500s^{-1}$ to $2750\ s^{-1}$ obtained by changing the gas pressure and the size of shaper during the dynamic compression process of $2DC_f/S_iC$ composites. Fig.3 shows the stress vs. strain curves of samples at a wide range of strain rates at room temperature. It can be observed that the dynamic compressive strength changes with strain rate increasing. For further recognizing the principle of strain rate-dependent compression properties of $2DC_f/S_iC$, The fracture strengths vs. strain rates of $2DC_f/S_iC$ composite at strain rates in the range of $500s^{-1}$~$2750s^{-1}$ are shown in Fig.4. It can be seen clearly that at strain rates in the range of $500s^{-1}$~$1700s^{-1}$ the dynamic compression strength goes up with strain rates increasing from about 400MPa to 583MPa. Then it declines from 583 MPa to 350MPa with the strain rates rising in the range of $1700s^{-1}$~$2750s^{-1}$, indicating a maximum strength at strain rate of $1700s^{-1}$. The trend of fracture stain changing with strain rate increasing in the Fig.3 is similar as that of the dynamic compression strength.

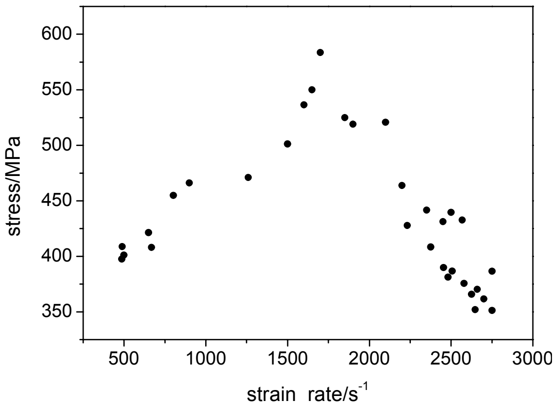

Fig.4. The fracture strength of 2DC$_f$/S$_i$C composite at strain rates in the range of 500s^{-1}~2750s^{-1}

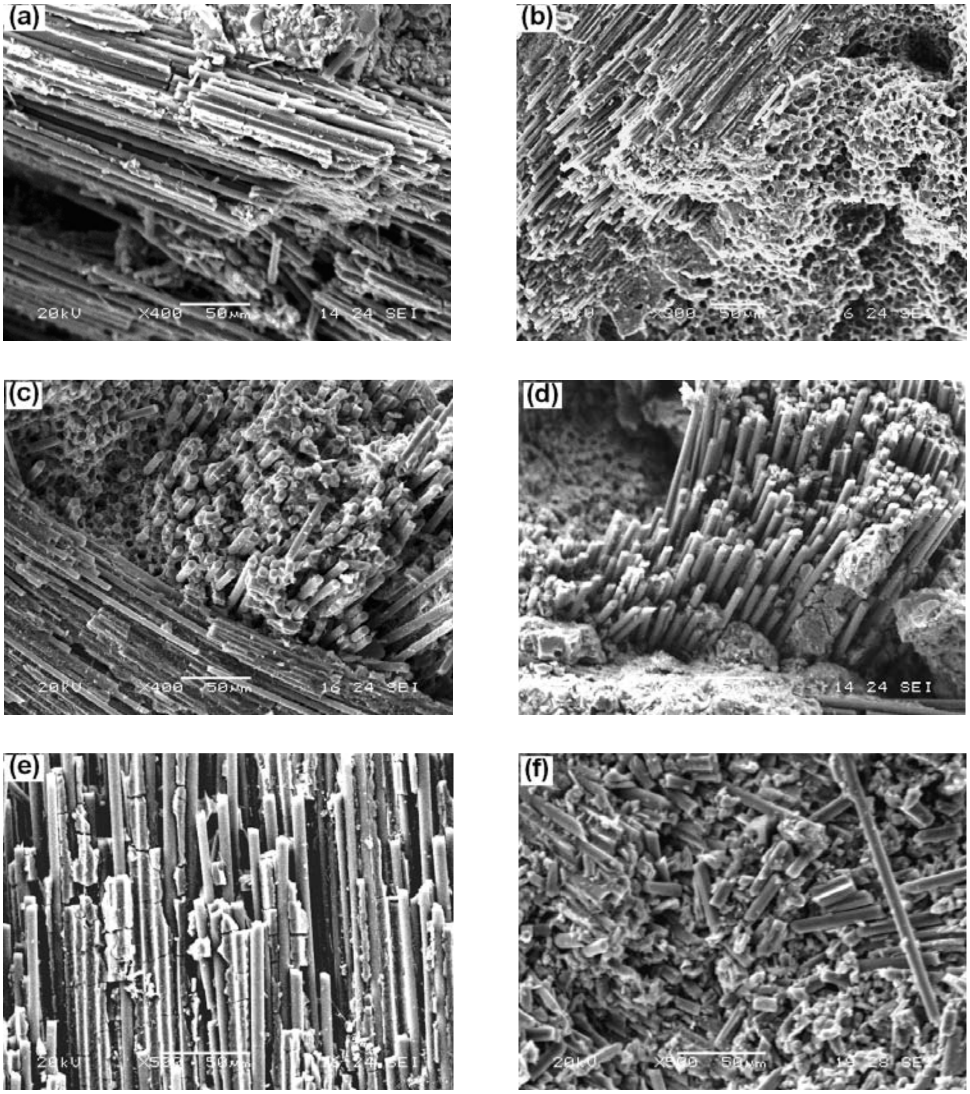
(a)
20kU X400 50µm 14 24 SEI
(b)
(c)
20kU X400 50µm 16 24 SEI
(d)
14 24 SEI
(e)
(f)

Fig.5. Scanning electron micrographs of 2DC$_f$/SiC samples tested at room temperature at stain rates of （a）500s^{-1},（b）600 s^{-1}, （c）850 s^{-1}, （d）1200 s^{-1}, （e）2000s^{-1}, (f) 2500s^{-1}

Scanning electron micrographs of representative samples tested at a wide range of strain rates are shown in Fig.5. We can observe that fiber/matrix debonding is mainly responsible for facture of samples at strain rates of 500s^{-1}

and 600s^{-1}(Fig.5.a and Fig.5.b). The fracture surface can be seen extensive fiber pullout at strain rates of 850s^{-1} and 1200s^{-1}(Fig.5.c Fig.5.d), which exhibits the good effect of fiber reinforcing matrix. When strain rates are over 2000s^{-1} the samples almost break into many small fragments. Many cracks in the fibers and matrix were observed on those larger fragments surface (Fig5.e), and there are a large amount of cracked fibers and matrix on the surface of composites at strain rate of 2500s^{-1} (Fig.5.f). So many fracture fragments of the composites means much more surface occurrence, which constituted important energy absorption mechanism at higher strain rates of over 2000s^{-1} under experimental condition.

Combining the data of dynamic compression properties and fracture surface features by SEM observation at strain rates in the range of 500s^{-1}~2750s^{-1}, it was reasonable for us to definite the strain rate of 1700s^{-1} as a critical strain rate, under which the compressive strength is positively strain-rate dependent. By contrast, over the strain rate of 1700s^{-1} the compressive strength is negative strain-rate dependent. At strain rate ranging of 500s^{-1}～1700s^{-1}, the strain rate sensitivity of samples is attributive to inertia-dominated dynamic crack growth from pre-existing flaws. And, those pores are compressed to close. The carbon fibers pullout causes the strength and toughness of 2DC$_f$/S$_i$C composite increase at the same time with the strain rate increasing. However, when the strain rate is over the critical strain rate, the impact energy is so large that it overtakes matrix loading capability and loading transform from matrix to fiber. As a result, matrix and fiber is fractured and fiber is cracked. Furthermore, the samples are crushed catastrophically.

3.2. Dynamic responses at elevated temperature

To accurately predict 2DC$_f$/S$_i$C composite dynamic responses at elevated temperatures, the dynamic compressive properties at temperatures rang of 460℃～500℃ was carried out. Fig.6. clearly shows that the deformation capability of samples before fracture increases obviously, and the dynamic compressive strength also has a slightly rise at temperature ranging of 460℃-500℃ compared with unheated samples subjected to the similar strain rate of 1000s^{-1}. That the fracture surface of sample (Fig.7.) at temperature of 460℃ shows much less fractured fibers, indicating that the carbon fibers is more flexible at elevated temperature, which leads to the ductility increase. Furthermore, the increase in ductility delays the onset and progression of damage, thus resulting in strength a rise to some extent.

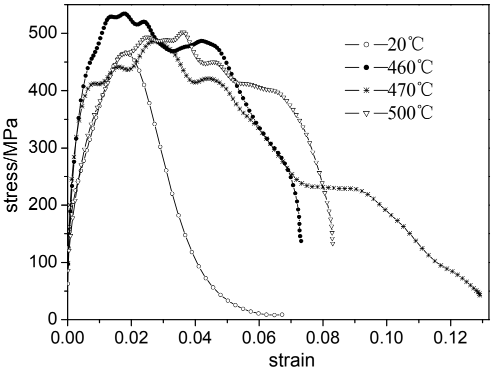

Fig.6. The stress vs. strain curves of the 2DC$_f$/S$_i$C composite at stain rate of 1000s^{-1} under dynamic compression at elevated temperature

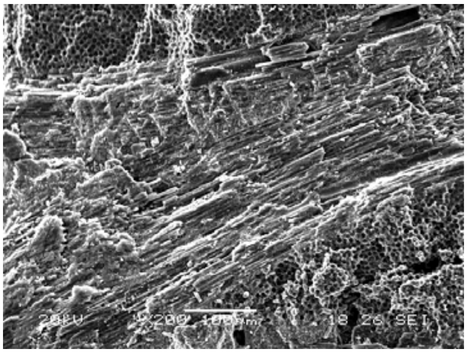

Fig.7. Scanning electron micrograph of 2DC$_f$/SiC sample tested at elevated temperature of 460℃ at stain rates of 1000s^{-1}

From above research, it indicates that the 2DC$_f$/S$_i$C composite exhibit better ductility and higher strength at elevated temperature under the dynamic compressive loading than that at room temperature. Therefore the results will help designers to design C$_f$/S$_i$C composite as structure materials used under severe conditions.

4. Conclusions

The dynamic compressive properties of the 2DC$_f$/S$_i$C composite prepared by PIP route at strain rates in the range of 500s^{-1}～2750s^{-1} at room temperature and at elevated temperature in the range of 460℃～500℃ at strain rate of 1000s^{-1} have already studied. The fracture surfaces of those samples have been observed. The following conclusions could be drawn from the present investigations.

(1) The shape of incident wave changes from rectangle to triangle after using pulse shaper in SHPB testing which can ensure the stress of the 2DC$_f$/S$_i$C composite obtained at a certain constant strain rate.

(2) The dynamic compressive strength of the 2DC$_f$/S$_i$C composite increases with strain rate going up from 500s^{-1} to 1700s^{-1}, while shows decreasing tendency with strain rate increasing from 1700s^{-1} to 2750s^{-1}, indicating a maximum dynamic strength at strain rate of 1700s^{-1}.

(3) The 2DC$_f$/SiC composite exhibits higher strength and better ductility at elevated temperature range of 460℃～500℃ compared with that at room temperature.

Acknowledgements

This work was supported by the Key Laboratory Fund of National Defense Technology. The 2D C$_f$/S$_i$C composite was provided by Key Laboratory of Advanced Ceramic Fibers & Composites, National University of Defense Technology.

References

[1] X.G.Zhou, Y. You, C.R. Zhang, B.Y. Huang, X.Y. Liu, Effect of carbon fiber pre-heat-treatment on the microstructure and properties of Cf/SiC composites[J], Mater. Sci. Eng. A 433 (2006) 104–107.

[2] J. Suo, Z. Chen, J. Xiao, W. Zheng, Influence of an initial hot-press processing step on the mechanical properties of 3D-C/SiC composites fabricated via PIP[J], Ceram. Int. 31 (2005) 447–452.
[3] Q.S. Ma, Z.H. Chen, W.W. Zheng, H.F. Hu, Processing and characterization of three-dimensional carbon fiber- reinforced Si-O-C composites via precursor pyrolysis[J], Mater. Sci. Eng. A352 (1/2) (2003) 212–216.
[4] Z.F. Xie, Z.H. Chen, J.Y. Xiao, Application of active filler in preparation of fiber reinforced ceramic matrix composites by polymer-infiltration-pyrolysis II - Preparation and performance test of composites[J], Acta Mater. Compos. Sin, (China),. 20(2003) 27-32.
[5] K. Jian, Z.H.Chen, Q.S. Ma, Effects of pyrolysis temperatures on the microstructure and mechanical properties of 2D-Cf/SiC composites using polycarbosilane[J], Ceram. Int. 33 (2007) 73–76.
[6] M.S. Liu, Y.L. Li, F.Xu, Z.J. Xu, L.F. Cheng, Dynamic compressive mechanical properties and a new constitutive model of 2D-C/SiC composites[J], Mater. Sci. Eng. A 489 (2008) 120–126.
[7] Y.L.Li, T. Suo, M.S.Liu, Influence of the strain rate on the mechanical behavior of the 3D needle-punched C/SiC composite[J], Mater. Sci. Eng. A 507 (2009) 6–12.
[8] J. S. Lee*, T. Yano, Fabrication of short-fiber-reinforced SiC composites by polycarbosilane infiltration[J], J. Eur. Ceram. Soc., 24 (2004) 25–31.
[9] T. Gomez-del Rıo, E. Barbero, R. Zaera, C. Navarro, Dynamic tensile behaviour at low temperature of CFRP using a split Hopkinson pressure bar[J], Compos. Sci. Technol.65 (2005) 61–72.
[10] K. Fujii, E. Yasuda, T. Akatsu, Y. Tanabe, Effect of characteristics of materials on fracture behavior and modeling using graphite-related materials with a high-velocity steel sphere[J], Int. J. Impact Eng. 28 (2003) 985–999.
[11] Ravichandran G，Subhash G. , Critical Appraisal of Limiting Strain Rates for Compression Testing of Ceramics in a Split Hopkinson Pressure Bar[J], Am. Ceram. Soc.，1994; 77(1):263-267.
[12] Frew D.J, Forrestal M.J, W. Chen, Pulse Shaping Techniques for Testing Brittle Materials with a Split Hopkinson Pressure Bar[J]，Exp. Mech., 2002; 42(1):93-106.

Proceedings of the SEM Annual Conference
June 7-10, 2010 Indianapolis, Indiana USA
©2010 Society for Experimental Mechanics Inc.

Compression Behavior of Near-UFG AZ31 Mg-Alloy at High Strain Rates

Mikko Hokka[1,2], Jeremy Seidt[2], Thomas Matrka[2], Amos Gilat[2], Veli-Tapani Kuokkala[1], Juha Nykänen[1], Sören Müller[3]

[1]Tampere University of Technology
P.O.B. 589, 33101 Tampere, Finland
mikko.hokka@tut.fi
[2]The Ohio State University, Department of Mechanical Engineering
[3]Technische Universität Berlin, Extrusion Research and Development Center

ABSTRACT

The superior specific strength of magnesium alloys makes them very attractive for several applications, especially in transportation, aviation, and space industries. Usually the properties of most metals, including magnesium alloys, can be enhanced by reducing the average grain size, which leads to increasing strength without decreasing the ductility of the material too much. One of the methods used today to decrease the grain size is the severe plastic deformation (spd), where the grain size is decreased by applying a very high shear strain under high hydrostatic pressure, leading to the accumulation of dislocations and eventually forming new smaller grains. Usually the amount of material that can be processed at one time is very limited, making most of the severe plastic deformation techniques less suitable for industrial production. One of the interesting techniques that allows larger batch sizes to be processed at one time is called reciprocating extrusion. In this work, the compression properties of the reciprocating extrusion processed standard magnesium alloy AZ31 were studied in a wide range of strain rates. The results show that the strength of AZ31 is significantly higher after reciprocating extrusion as compared to squeeze cast AZ31, and at the same level as for the hot rolled and ECAP processed AZ31. The compression tests were also monitored using digital cameras, and the surface strain distributions on the specimen were calculated using digital image correlation. The strains on the surfaces of the specimens were fairly homogeneous and no significant barreling was observed. The failure of the specimens occurred at a 45 degree angle in all tests, preceded by a rapid formation of a shear band.

INTRODUCTION

Magnesium alloys are one of the lightest constructional metals that are used for special applications in the aerospace and transportation industries, mainly due to their high specific strength and stiffness. Most magnesium alloys are used as castings, but also forged components are manufactured for mechanically more demanding applications. Generally magnesium alloys have moderate strength and limited formability due to their hexagonal crystal structure. The strength of most alloys can, however, be improved by increasing the alloying, by using heat treatments, or by reducing the grain size of the metal. The latter can be done, for example, by alloying, by thermomechanical treatments, or by subjecting the material to severe plastic deformation. Severe plastic deformation (spd) basically increases the dislocation density of the material until the dense dislocation walls become high angle grain boundaries and the average grain size of the material is significantly reduced. For metals with good formability, such as aluminum and copper, the severe plastic deformation processing can usually be done at room temperature, but for metals with limited formability, such as magnesium alloys, the processing is usually carried out at elevated temperatures that limits the achievable grain sizes.

Crystalline metals can be distinguished into coarse grained materials with grain sizes larger than 1 μm, ultrafine grained (UFG) materials with grain sizes between 1 μm and 0.1 μm, and nanocrystalline materials with grain sizes less than 0.1 μm. Most metals respond positively to severe plastic deformation processing and the grain sizes can be reduced to ultrafine or even nanocrystal levels. Grain refinement by severe plastic deformation has received considerable attention in the past decade due to its strength enhancing capabilities. However, magnesium alloys

T. Proulx (ed.), *Dynamic Behavior of Materials, Volume 1*, Conference Proceedings of the Society for Experimental Mechanics Series,
DOI 10.1007/978-1-4419-8228-5_42, © The Society for Experimental Mechanics, Inc. 2011

have not been the most studied material, and more effort has gone to studying other more deformable metals such as aluminum, copper, and titanium. The magnesium alloys offer great weight reduction potential for the transportation and aviation industries, where heavier materials may be replaced with these alloys. The magnesium alloys, however, have some drawbacks, e.g., lower ductility and strong textural effects, which have hindered their implementation in the past.

One of the aims of the severe plastic deformation processing is to increase the strength of the material without expensive alloying and heat treatments, and without decreasing the ductility too much. However, according to the literature, increasing the strength of magnesium alloys is not as straightforward as for some other commonly used construction metals. Zúberová et al. [4] studied the compression behavior of the magnesium alloy AZ31 with different grain sizes. They found that the yield strength of the equal-channel angular pressed (ECAP) AZ31 was significantly higher than that of the squeeze cast AZ31 but not much higher than the strength of the hot rolled AZ31. The fracture strength was actually higher for the hot rolled material. At higher temperatures the yield strength of the ECAP processed AZ31 decreased very rapidly, and at 200 °C the yield strength of the hot rolled material exceeded the yield strength of the ECAP processed material. Kang et al. [2] studied AZ31 magnesium alloy and were able to decrease the grain size of the material down to less than 3 μm by warm ECAP, but the strength of the material decreased with decreasing grain size, whereas the micro hardness and elongation increased with decreasing grain size. Li et al. [3] were able to decrease the grain size of a ZK60 magnesium alloy to about 0.8 μm by ECAP at 473 K. However, this particular alloy is an age hardening alloy, and the ECAP processing under high hydrostatic stress changed the morphology of the precipitates and the strength of the material actually decreased by over 200 MPa. Also, due to their hexagonal structure, magnesium alloys can show a distinctively different behavior in tension and in compression, and the strength properties can be generally very anisotropic. Müller et al. [1] studied the strength differential effect (SDE) in magnesium alloys and found that the SDE is significantly reduced when the grain size of the material is reduced.

In this work, the compression behavior of the reciprocating extrusion processed AZ31 magnesium alloy was studied in a wide range of strain rates using a conventional hydraulic materials testing machine and a Hopkinson Split Bar device. Usually the strain is measured using extensometers at low strain rates and calculated from the displacements of the ends of the pressure bars in the Hopkinson Spit Bar methods. In this study, the strain in the specimen is measured directly from the surface of the specimen using high speed photography and digital image correlation (DIC). DIC enables measuring of the strain with the same method at low and high strain rates, thus improving the comparison of the results obtained at different strain rate regimes.

EXPERIMENTAL

The material studied in this work was a standard magnesium alloy AZ31, which was SPD processed using the reciprocating extrusion. The material was SPD processed with and without prior extrusion, and both grades were studied. The reciprocating extrusion processing was performed by extruding the billet five times back and forth through the extrusion (kneeding) die, which is basically a narrower collar in the extrusion channel (see Fig. 1). The inner diameter of the extrusion die was 30 mm, while the diameter of the collar was 24 mm. Back pressure was applied to force the billet back into its original thickness after passing the collar, and the process was repeated several times before the billet was extruded to a round bar with a 10 mm diameter. The temperature of the die and the specimen was 300 °C, and after the final extrusion the material was air cooled. The microstructures of both grades were very similar, consisting mainly of very small grains and a few larger grains with an average grain size between 6-8 micrometers. The alloy processed in the extruded state had a more equiaxed grain structure, whereas the microstructure of the alloy processed without prior deformation contained more deformed and elongated grains. The material was prepared at the Technische Universität Berlin.

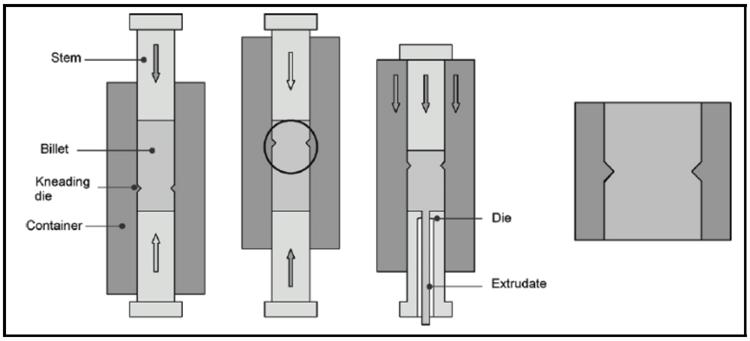

Figure 1: Schematics of the reciprocating extrusion device used to process the AZ31 alloy [after 1].

The materials were tested in compression at various strain rates. The tests were performed using a servohydraulic materials testing machine at low rates ($\dot{\varepsilon}$ <1 s^{-1}) and a Hopkinson Split Bar device at high rates ($\dot{\varepsilon}$ >500 s^{-1}). The conventional Hopkinson Split bar equipment that was used in this study has high strength titanium bars with ½ inch diameter. The stress in the specimen was measured using strain gages bonded on the surface of the transmitted bar.

The compression tests were monitored by two digital cameras looking at the specimen at different angles. At low strain rates, two Point Gray Research Grasshopper cameras with 2 megapixel resolution were used to obtain the image pairs, and at strain rates of 1 s^{-1} and above, two Photron Fastcam SA1.1 high speed cameras were used. The specimens and short sections of the bars or anvils were painted with a base coat, over which a high contrast speckle pattern was applied. For low rate experiments, a white base coat with black speckles were used, whereas at high strain rates the colors were reversed due to the increased need of illumination at higher frame rates, which lead to excess glare when using the white base coat. Spatial Lagrange strains in the specimen were calculated from the displacements on the surface of the specimen by tracking the movement of small image subsets. Average engineering strain over the surface of the specimen was calculated from the spatial Lagrange strains using Equation 1, where E_{11} is the Lagrange strain in the axial direction of the specimen. For a good overview of the digital image correlation techniques with examples see, e.g., ref. [6].

$$\varepsilon_E = \frac{\sum_{i=1}^{N} \sqrt{1+2E_{11}^{i}} - 1}{N} \tag{1}$$

RESULTS AND DISCUSSION

Figure 2 shows the compression true stress vs. true strain curves measured at room temperature at different strain rates. The fracture strain in the tests varies between 0.15 and 0.22. The yield strength of the AZ31, which was cast and SPD processed (Fig 2b) is slightly higher than that of the AZ31, which was extruded before SPD processing (Fig. 2a). At low strain rates, the strength of both materials continuously increases after the yield point. At high strain rates, however, the strain hardening rate in the beginning of the test is significantly lower but then increases rapidly after about 3% of strain. Such high strain hardening rates are typical for magnesium alloys, and the concave shape of the curve is normally attributed to the mechanical twinning [5], which is enhanced at higher strain rates and leads to an increasing strain hardening rate with increasing strain rate.

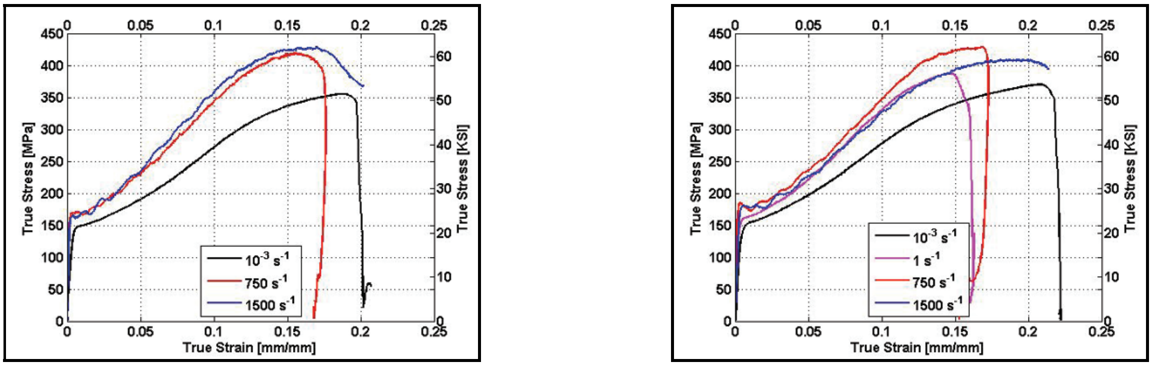

a) b)

Figure 2: True stress vs. true strain curves for the studied AZ31 alloy: a) cast, extruded and SPD processed and b) cast and SPD processed material.

The yield strength of both materials clearly increases with strain rate, which can be seen even better in Figure 3a, which shows the yield strength, flow stress at 10% of plastic strain, and the fracture strength as a function of logarithmic strain rate. From the figure it is, however, clear that the strain rate sensitivities for both grades of AZ31 are not very high. For the yield strength, the increase is only from about 150 MPa at the strain rate of 10^{-3} s^{-1} to 175 MPa at 1000 s^{-1}, and for the fracture strength from about 360 MPa to ca. 400 MPa.

In Figure 3b, the results of this work are compared with the results of Zúberová et al. [4], who studied the compression behavior of AZ31 alloy in squeeze cast, hot rolled, and ECAP processed states. The yield strength of the AZ31 processed with the reciprocating extrusion is about 60 MPa higher (or 50%) than that of the squeeze cast AZ31, whereas the strength of the hot rolled material lies just below the ECAP processed and reciprocating extrusion processed materials. The squeeze cast material has a very coarse microstructure compared to all other grades of the same material. However, it is interesting to notice that ECAP processing does not provide any significant increase in the yield strength compared to hot rolling or reciprocating extrusion processing. Also, Müller at al. [1] studied the reciprocating extrusion processed AZ31, and they measured yield strengths exceeding 200 MPa for the same alloy as studied in this work. However, the problem with the reciprocating extrusion is the gradient microstructure and increasing grain size towards the center of the bar axis. In this study, the specimens were machined from the extruded10 mm bars so that and the outer layers of the bars were removed by turning. The outer regions are most likely the most deformed areas during the reciprocating extrusion and therefore have the smallest grain sizes and highest strength. Removing these regions to fabricate the compression specimens will most likely influence the measured strength values.

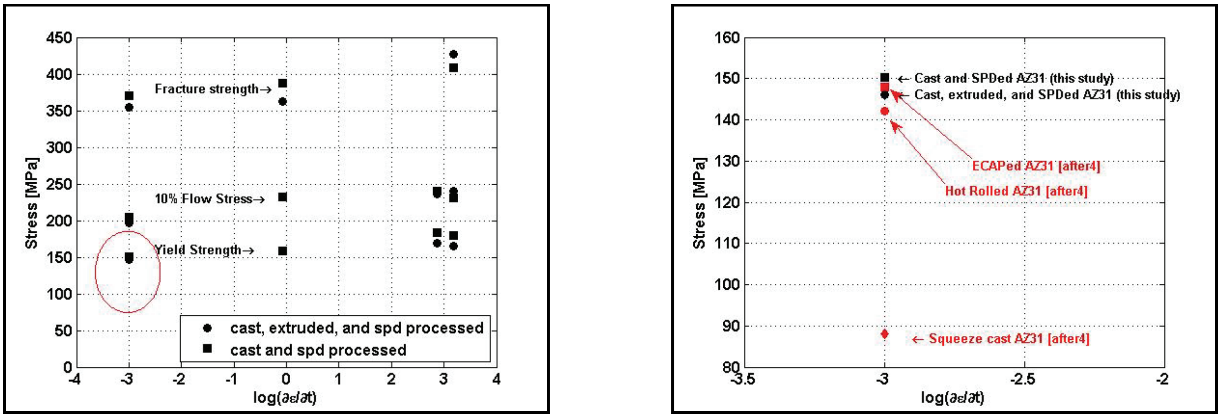

a) b)

Figure 3: Results of the compression tests at a wide range of strain rates, a) yield strength, flow stress at 10% of plastic strain, and fracture strength, and b) comparison of the results of this study to the ones presented by Zúberová et al. [4].

The strains on the surfaces of the specimens were calculated from the image pairs acquired with the two digital cameras. The difference between the maximum and minimum axial strains was of the order of 5 to 8 %, as shown in Figure 4, where the strain distributions on the surface of the specimen along the compression axis are shown together with average strains (dashed lines) for different stages of deformation. The strain distributions appeared to be somewhat asymmetric with respect to position in all tests, but the amount of strain increased quite uniformly with deformation. The degree of asymmetry was also different in each test for reasons that are not completely understood. The evolution of strain with time was very similar for both materials and independent of strain rate. The distribution of strains remains fairly uniform until the localization of strain and the formation of the shear band at a 45 degree angle with respect to the loading axis. The shear band forms very rapidly just before the final fracture. In all tests, the maximum compressive strains were found somewhere near the middle of the gage section, not at either end of the specimen. The overall deformation was fairly uniform and the specimens did not barrel much during the deformation, which is probably due to the low maximum strains and adequate lubrication of the specimen and bar interfaces.

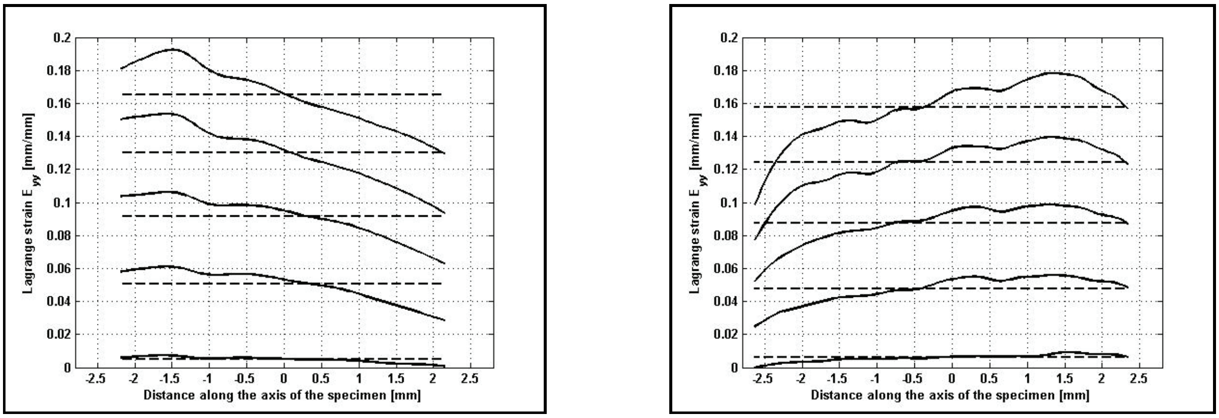

a) b)

Figure 4: The axial strain along the gage section of the specimen for the a) cast, extruded and SPD processed AZ31, and b) cast and SPD processed AZ31.

Figure 5 shows the last frame before the fracture, overlaid with the Lagrange strain on the surface in the transverse direction (Fig. 5a) and in the axial direction (Fig. 5b) for the cast and SPD processed AZ31 tested at the strain rate of 1000 s^{-1}. The specimen fractured no more than 10 μs (~0.015 in strain) after these images were obtained. In both images, the formation of the shear band is very clearly seen and the strain localization is very strong. In the transverse direction, the Lagrange strain in the shear band exceeds 0.3, whereas the strain elsewhere in the gage area varies from 0.12 to 0.18. In the axial direction, the maximum Lagrange strains are around 0.24, and the strain elsewhere in the specimen is less than 0.2. The shear strain component in the xy-plane was very low.

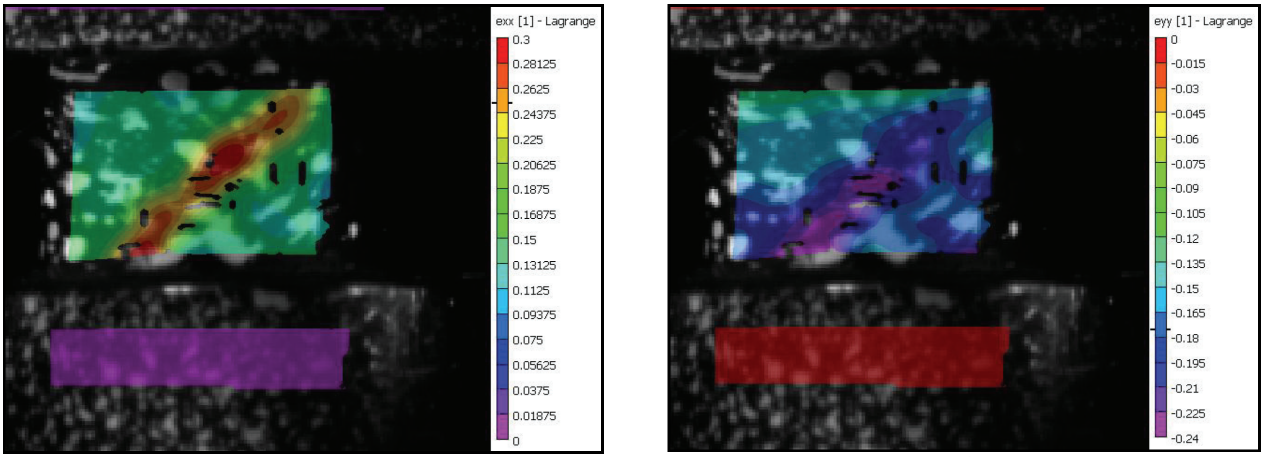

a) b)

Figure 5: Last frame before fracture for the cast and SPD processed AZ31 alloy at a strain rate of 1000 s^{-1}, a) Lagrange ε_{xx} (transverse strains) and b) Lagrange ε_{yy} (axial strains).

SUMMARY

The mechanical behavior of a reciprocating extrusion processed AZ31 magnesium alloy was studied in compression at a wide range of strain rates. The tests were monitored using digital cameras, and from the acquired image pairs the strains on the surface of the specimens were calculated using digital image correlation. This method enables non-contact measurement of strains directly from the specimen at a very wide strain rate range, where typically several techniques are needed to measure the strain. Also, the DIC technique was shown to be able to capture the formation of a shear band even at very high strain rates.

The results of the mechanical tests show that the strength of the SPD processed AZ31 increases with strain rate and that the fracture strength increases more than the yield strength or the flow stress at low strains. The strain hardening rate of AZ31 also increases strongly with increasing strain rate and the stress strain curves show an upward concave appearance, which are both typical for twinning and slip controlled deformation due to the increased incidence of twinning at high strain rates. The yield strengths of the studied SPD processed AZ31 are significantly higher than those of the squeeze cast AZ31 but comparable to the yield strengths of the hot rolled and ECAP processed AZ31 [4].

The final failure of the specimen occurs by a 45 degree shear fracture along a shear band that develops very rapidly just before the fracture. After the formation of the shear band, most of the strain localizes into the narrow region around the band, which rapidly leads to the final failure of the specimen.

ACKNOWLEDGEMENTS

This work was partly funded by the Academy of Finland under the grant no. 130780 and the Finnish Agency for Technology and Innovation (MIVA project). The support from the Finnish Foundation for Technology Promotion is also acknowledged.

REFERENCES

1. K. Müller, S. Müller, Severe plastic deformation of the magnesium alloy AZ31, Journal of Materials Processing Technology, 187-188, 2007.
2. S. H. Kang, Y. S. Lee, J. H. Lee, Effect of grain refinement of magnesium alloy AZ31 by severe plastic deformation on material characteristics. Journal of Materials Processing Technology, 201, 2008.
3. B. Li, S. Joshi, K. Azevedo, E. Ma, K.T. Ramesh, R.B. Figueiredo, T.G. Langdon, Dynamic testing at high strain rates of an ultrafine-grained magnesium alloy processed by ECAP. Materials Science and Engineering A, 517, 2009.

4. Z. Zúberová, Y. Estrin, T. T. Lamark, M. Janecek, R. J. Hellmig, M. Krieger, Effect of equal channel angular pressing on the deformation behavior of magnesium alloy AZ31 under uniaxial compression. Journal of Materials Processing, 184, 2007.
5. J. Jiang, A. Godfrey, W. Liu, Q. Liu, Microtexture evolution via deformation twinning and slip during compression of magnesium alloy AZ31. Materials Science and Engineering A, 483-484, 2008.
6. M. Sutton, J. Orteu, H. Schreier, Image Correlation for Shape, Motion and Deformation Measurements. Springer Science, 2009.

Proceedings of the SEM Annual Conference
June 7-10, 2010 Indianapolis, Indiana USA
©2010 Society for Experimental Mechanics Inc.

Dynamic Torsion Properties of Ultrafine Grained Aluminum

Mikko Hokka[1,2], Jari Kokkonen[1], Jeremy Seidt[2], Thomas Matrka[2], Amos Gilat[2], Veli-Tapani Kuokkala[1]

[1]Tampere University of Technology, Department of Materials Science
P.O.B. 589, 33101 Tampere, Finland
mikko.hokka@tut.fi
[2]The Ohio State University, Department of Mechanical Engineering

ABSTRACT

Mechanical properties of most metallic materials can be improved by reducing their grain size. One of the methods used to reduce the grain size even to the nanometer level is the severe plastic deformation processing. Equal Channel Angular Pressing (ECAP) is one of the most promising severe plastic deformation processes for nanocrystallization of ductile metals. Nanocrystalline and ultrafine grained metals usually have significantly higher strength properties but lower tensile ductility compared to the coarse grained metals. In this work, the torsion properties of ECAP processed ultrafine grained pure 1070 aluminum were studied in a wide range of strain rates using both servohydraulic materials testing machines and Hopkinson Split Bar techniques. The material exhibits extremely high ductility in torsion and the specimens did not fail even after 300% of strain. Pronounced yield point behavior was observed at strain rates 500 s^{-1} and higher, whereas at lower strain rates the yielding was continuous. The material showed slight strain softening at the strain rate of 10^{-4} s^{-1}, almost ideally plastic behavior at strain rates between 10^{-3} s^{-1} and 500 s^{-1}, and slight but increasing strain hardening at strain rates higher than that. The tests were monitored using digital cameras, and the strain distributions on the surface of the specimens were calculated using digital image correlation. The strain in the specimen localized very rapidly after yielding at all strain rates, and the localization lead to the development of a shear band. At high strain rates the shear band developed faster than at low strain rates.

INTRODUCTION

Metallic materials can be distinguished into coarse grained, fine grained, ultrafine grained, and nanocrystalline depending on the average grain size. If the average grain size is larger than 1 µm, the material is either fine grained or coarse grained, the transition between these two being somewhere around 10 µm. Between 100 nm and 1 µm, the material is called ultrafine grained, and when the grain size is less than 100 nm, it is classified as a nanocrystalline material. Nanocrystalline and ultrafine grain size metals have many excellent properties compared to the coarse grained materials with the same chemical composition. For example, most metals with grain sizes in the nanocrystalline range show excellent strength, hardness, and fatigue properties as well as improved wear and corrosion resistance, in some cases combined with increased toughness even at low temperatures. Potential applicability of these materials is also wide, including aerospace applications, transportation, health care equipment and components, defense applications, and even implant technology due to the possible high purity of the materials (i.e., even pure metals can exhibit substantial strength values when the grain size is small enough).

There are basically two main techniques to produce metals with grain sizes less than one micrometer; consolidating and sintering of metal powders, and severe plastic deformation. Sintering of metal powders, however, often produces porous microstructures with higher impurity content. Severe plastic deformation, on the other hand, can be used to produce nanocrystalline or ultrafine grain size metals from virtually any metal by simply applying extreme plastic strains on the existing coarse grained bulk material. One of the severe plastic deformation processes that have been successfully used to produce nanocrystalline and ultrafine grained metals is the Equal Channel Angular Pressing (ECAP). In the traditional ECAP, the material billet is pressed several times through the channels in the ECAP die. The ECAP die consists of input and output channels, which meet at an angle usually close to 90°. The material undergoes simple shear as the billet is pushed through the die and the

T. Proulx (ed.), *Dynamic Behavior of Materials, Volume 1*, Conference Proceedings of the Society for Experimental Mechanics Series,
DOI 10.1007/978-1-4419-8228-5_43, © The Society for Experimental Mechanics, Inc. 2011

strain accumulates during consecutive passes. Eventually, the high plastic shear strains will lead to refined microstructure and texture. Different kind of microstructures and textures can be manufactured by using different processing “routes”, in which the billet is rotated between consecutive passes. In route C, the billet is rotated 180° between passes, whereas alternating 90° rotation between clockwise and counter-clockwise directions is called route B_a, and 90° rotation in the same direction route B_c. In route A, the billet is not rotated at all. Route B_c has been found to produce the most equiaxed grain structure with the highest ratio of high-angle boundaries [3]. For a good review of the ECAP processes, see for example ref. [10].

The mechanical properties and behavior of most materials are strongly affected by the applied strain rate, temperature, and type of loading. For coarse grained metals, the strength usually increases with increasing strain rate, especially at strain rates around 10^3 s^{-1}, where a rapid increase in strength is often observed. At quasi-static and intermediate strain rates (<~500 s^{-1}), the deformation behavior of crystalline materials, such as coarse grained metals, is readily explained by the thermally activated dislocation motion. At higher strain rates (>~1000 s^{-1}), the dislocation drag mechanisms start to control the deformation behavior, and usually the strength of the material increases dramatically as the mechanism changes. However, when the crystal size is decreased to nanometer scale, the movement of dislocations becomes increasingly difficult. At the moment, however, the strain rate dependent deformation and hardening mechanisms of nanocrystalline metals are not properly understood yet. May [1] et al. studied the strain rate sensitivity of coarse grained and ECAP processed ultrafine grained aluminum (AA1050) and found that the strain rate sensitivity in compression for the ultrafine grained aluminum is about 3.5 times higher than that for the coarse grained material. The effect was even more clear at elevated temperatures, where the strain rate sensitivity factor, $m=\log(\sigma)/\log(\dot{\varepsilon})$, was as high as 0.25, which is ten times higher than that for the same coarse grained material. Also the strain hardening rate, $\theta=d\sigma/d\varepsilon$, is different for the ultrafine grained metals when compared to large grained metals. Kokkonen et al. [4] performed tension and compression tests at various strain rates and temperatures for ECAP processed AA1070 and found that the strain softening observed at low strain rates changes to strain hardening at high strain rates and/or low temperatures. The strain softening in ECAP processed aluminum alloys at low strain rates has generally been attributed to dynamic recovery, which is reduced at low temperatures [2-3].

Some materials such as the ECAP processed metals can show fairly poor ductility in tension, which is due to the low strain hardening capability and plastic instability of the material that occurs rapidly after the yielding. However, the material can still flow significantly in tension after the necking and the fracture strains can be fairly high. Therefore, the formability of ultrafine grained materials can still be very good as was shown by Sirivaraman and Chakkingal [12], who studied the deformability of ultrafine grained commercial purity aluminum by upsetting tests. Also, the instability and fracture that is observed in tension does not necessarily occur in the same way in shear, and the torsion deformation can continue to much higher strains before the final fracture of the material. Therefore, the torsion behavior often describes the overall formability of the material better than the results of a simple tension test, which are influenced also by the structural response of the specimen. In this work, the torsion properties and behavior of ECAP processed 1070 aluminum were studied at a wide range of strain rates. The tests were also monitored by high speed digital cameras, and the strain distributions were calculated from the acquired images using digital image correlation.

MATERIALS AND EXPERIMENTS

The material studied in this work was pure AA1070 (99.7 wt-% Al) aluminum. The material was processed at the Warsaw University of Technology by forcing 25*25*115 mm^3 billets through a two-turn ECAP die four times and rotating the billet by 90° between the passes. The channels in the two-turn die make two 90° turns, so one pass effectively corresponds to two passes in a single turn die following the route C, and when the billets are rotated 90° between the passes, the route becomes C + B_c. The die design is shown in Fig. 1. The total accumulated strain after the ECAP processing was equivalent to about 9.4, leading to the average grain size around 750 nm. The grain size was determined from transmission electron micrographs in a previous study [4]. The die construction, numerical simulations used for the optimization of the design, and the actual ECAP processing are presented in more details in refs. [5,6]. In addition to the ultrafine grained AA1070 aluminum, some tests were also performed on a standard AA7075-T6 aluminum alloy for comparison.

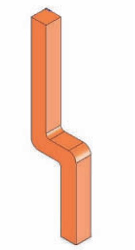

Figure 1: Equal channel angular pressing die used for producing the ultrafine grained structure.

The behavior of this material at different strain rates and temperatures has been previously characterized in tension and in compression [4, 8-9]. In this study, the material properties were characterized in torsion using both a servohydraulic materials testing machine and a torsion Split Hopkinson Pressure Bar (SHPB) device with a pre-torque clamp-release system. The device used in this work is described in details in ref. [8].The SHPB device consists of 7/8 inch diameter aluminum alloy incident and transmitted bars, between which the thin walled tube specimen is glued. The incident torsion pulse is generated by releasing a pre-stored torsion load from the free end of the incident bar. The pre-torque is applied by a hydraulic pulley and stored by clamping the incident bar at a suitable distance from the pulley. The clamp is held by a brittle(ish) aluminum pin, which can be rapidly broken by a second hydraulic press. When the pin is broken, the torsion pulse is released to propagate in the bar towards both the specimen and the pre-torque pulley. As the wave reaches the pulley, it is reflected back as a torsion wave with equal magnitude but opposite sign, which cancels the original pulse creating an incident pulse with a length equal to twice the distance from the clamp to the hydraulic pulley. As the incident wave reaches the specimen, part of the wave is reflected back as a wave of torsion with a sign opposite to the incident wave, and part of the incident wave is transmitted through the specimen into the transmitted bar deforming the specimen at a high rate. The time resolved load and strain history of the specimen can be calculated from the incident, reflected, and transmitted shear stress pulses. In this study, however, the strains and strain rates were calculated from the image analysis results.

The high rate torsion tests were monitored using two Photron Fastcam SA1.1 high speed cameras, whereas two Point Gray Research Grasshopper cameras with 2 megapixel resolution were used to monitor the low rate experiments. The cameras were viewing the specimen at different angles and synchronized to take images at the same time. VIC 3D image correlation software was used to calculate the full field strain distributions on the surface of the specimens as well as the displacements of the grip sections of the specimen, from which the average shear strain can also be calculated. The cameras were acquiring images at the frame rate of 125.000 s^{-1} in the high rate experiments and at frame rates between 0.1..19 s^{-1} in the low rate experiments, yielding about 150 to 400 image pairs for each test.

The thin walled torsion specimens were machined from rectangular bars for the ultrafine grained aluminum and from a standard 0.5 inch diameter round bar for the 7075-T6 aluminum alloy. The gage length of the specimens was 5.08 mm (0.2 in), the outer diameter 9.65 mm (0.38 in), and the wall thickness 0.38 mm (0.015 in) for the 7075 alloy. The dimensions were the same for the ultrafine grained specimens except for the wall thickness that was increased to 0.76 mm (0.03 in). The specimens were further connected to adaptors, and the whole specimen adaptor assembly was glued to the ends of the stress bars of the Hopkinson Bar device or fixed to the hydraulic clamps of the servohydraulic materials testing machine. The contrast pattern for photography was first applied by painting the gage section of the specimens and the adaptors with black base color, over which white speckles were hand painted for maximum contrast. However, it was soon noticed that the hand painted dots were too thick and broke off from the surface at fairly low strains. Even though white base color and spray painted black contrast pattern were found to have better adhesion to the surface, it still broke off at shear strains around 60-90%. Therefore, the average strain on the specimen was at the end calculated from the 3D displacements of the ends of the bars using Equation 1.

$$\gamma = \frac{r_s \theta}{l_s} = \frac{r_s}{l_s} \arccos\left(\frac{\overline{a} \bullet \overline{b}}{\| a \| * \| b \|}\right) \tag{1}$$

where r_s and l_s are the average radius and gage length of the specimen, θ is the angle of twist between the opposite ends of the specimen, and $\overline{a}$ and $\overline{b}$ are vectors from the centerline to the surface of the specimen at the opposite ends of the gage section.

RESULTS AND DISCUSSION

Figure 2a shows the shear stress *vs.* shear strain curves at different strain rates for the ultrafine grained 1070 aluminum and Figure 2b the corresponding curves for the 7075-T6 aluminum alloy. The strength levels for the 7075 alloy are naturally significantly higher than those measured for the ultrafine grained 1070 pure aluminum. However, the maximum strains are rather low for the 7075 aluminum, whereas none of the ultrafine grained 1070 specimens failed in any of the tests, and shear strains of more than 300% were measured without fracture. At strain rate 10^{-4} s^{-1}, the ultrafine grained material clearly softens with increasing strain, but when the strain rate is increased by a factor of ten, the strain softening is already reduced significantly. At the strain rates of 10^{-3} s^{-1} to 10^{-2} s^{-1} the material softens in the beginning of the test, but above 20% of strain the material is almost ideally plastic. At the strain rate 0.5 s^{-1}, the behavior of the material is virtually ideally plastic without the previously seen softening in the beginning of the test. At higher strain rates, the yielding of the specimen is clearly different from that observed at low strain rates. At the strain rate of 500 s^{-1}, the yield point is clearly pronounced, and the at strain rate of 2000 s^{-1}, the peak is more than 10 MPa higher than the subsequent flow stress after a few percent of plastic strain. Also, the material slightly hardens with strain at the strain rate of 2000 s^{-1} and shows a maximum stress at around 80-100% of shear strain, after which the strength slightly decreases. The observed behavior resembles the behavior found for this material also in compression [4]. The strain softening at very low strain rates is most likely due to the dynamic recovery, which is significantly reduced at higher strain rates and lower temperatures [2,3], leading to slightly increasing strain hardening of the material. The pronounced yielding behavior, on the other hand, is most likely explained by the lack of sufficient mobile dislocations in the initially heavily deformed material, leading to the observed increasing yield peak with increasing strain rates.

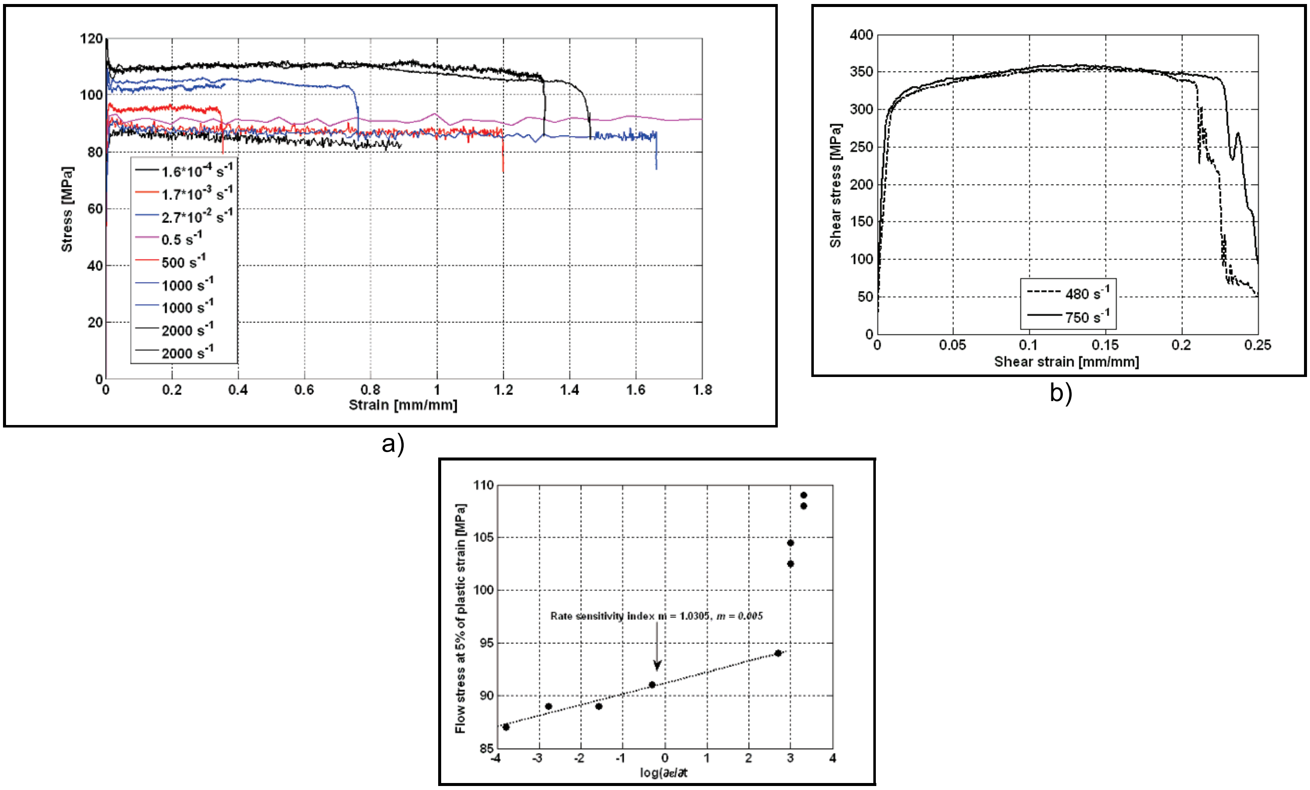

a)

b)

c)

Figure 2: Results from the torsion tests: a) stress strain curves for the ultrafine grained pure 1070 aluminum, b) stress strain curves for the 7075-T6 aluminum alloy, and c) flow stress at 5% of plastic strain for the ultrafine grained aluminum as a function of logarithmic strain rate.

Figure 2c shows the flow stress at 5% of plastic strain for the ultrafine grained 1070 aluminum. In the low strain rate region, the flow stress steadily increases from 87 MPa to 94 MPa, and the absolute strain rate sensitivity factor, $m=\Delta\sigma/\Delta\log(\dot{\varepsilon})$, and the relative strain rate sensitivity factor, $m = \Delta\log(\sigma)/\Delta\log(\dot{\varepsilon})$, have values of 1.0305 MPa and 0.005, respectively. The values measured in this study for torsion are somewhat lower than those presented by Kokkonen et al. [11] and Kuokkala et al. [9] in compression and tension for similar ultrafine grained 1070 aluminum. However, the differences are small and can most likely be explained by slight differences in the grain size refinement procedures and therefore slightly different microstructures.

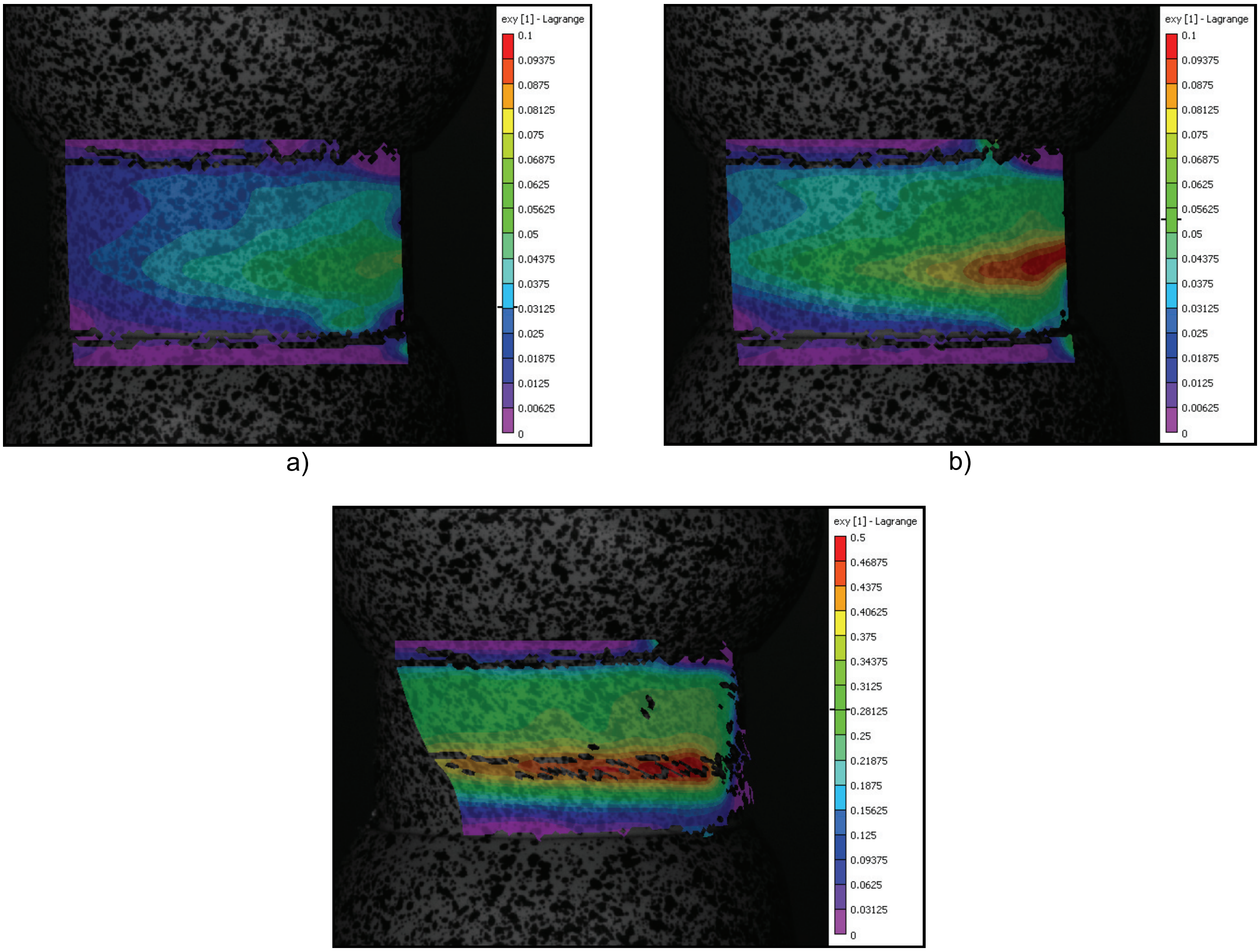
exy [1] - Lagrange
0.1
0.09375
0.0875
0.08125
0.075
0.06875
0.0625
0.05625
0.05
0.04375
0.0375
0.03125
0.025
0.01875
0.0125
0.00625
0
exy [1] - Lagrange
0.1
0.09375
0.0875
0.08125
0.075
0.06875
0.0625
0.05625
0.05
0.04375
0.0375
0.03125
0.025
0.01875
0.0125
0.00625
0
exy [1] - Lagrange
0.5
0.46875
0.4375
0.40625
0.375
0.34375
0.3125
0.28125
0.25
0.21875
0.1875
0.15625
0.125
0.09375
0.0625
0.03125
0

a)

b)

c)

Figure 3: Localization of strain in a torsion test at the strain rate of 1.6 10^{-4} s^{-1}: a) strains just after yielding, b) a developing shear band, and c) a fully developed shear band.

Figure 3 shows the image correlation results for the torsion test of an ultrafine grained 1070 aluminum sample at the strain rate of 1.6 10^{-4} s^{-1}. In the very early stages of the test (Figure 3a), both ends of the specimen are nearly undeformed and the yielding starts rather uniformly in the middle of the gage section, but then rapidly localizes to the right side of the gage section. The maximum strain is around 6% of Lagrange shear strain ($\varepsilon_{xy}=½*\gamma$), whereas most of the gage section is still at around 2-3% of Lagrange shear strain. In Figure 3b, the localization is more clearly visible, showing a maximum Lagrange shear strain of 10%, while the surrounding regions still remain at about 6-7% of Lagrange shear strain. However, the shear band does not extend over the whole gage section until at much higher strains. Figure 3c shows the fully developed shear band in the middle of the gage section with a maximum Lagrange shear strain around 50%, while the surrounding areas remain closer to 35%. The behavior does not change much in the low rate experiments, which can be seen in Figure 4, where similar pictures taken from a test performed at the strain rate of 0.5 s^{-1} are shown. The yielding starts this time from the left hand side and localizes rapidly only after a few percent of strain. The shear band develops, and in Fig 4b it already extends across the whole gage section but still shows a clear maximum on the left hand side with strains up to 10%. The right hand side is still at only 5% of strain, and the regions outside the shear band at about 2-3 % of strain. At later stages, the shear band develops further and the strain increases more rapidly within the shear band, while other regions experience much less strain. Figure 4c shows a fully developed shear band with twice as much strain compared to the surrounding regions.

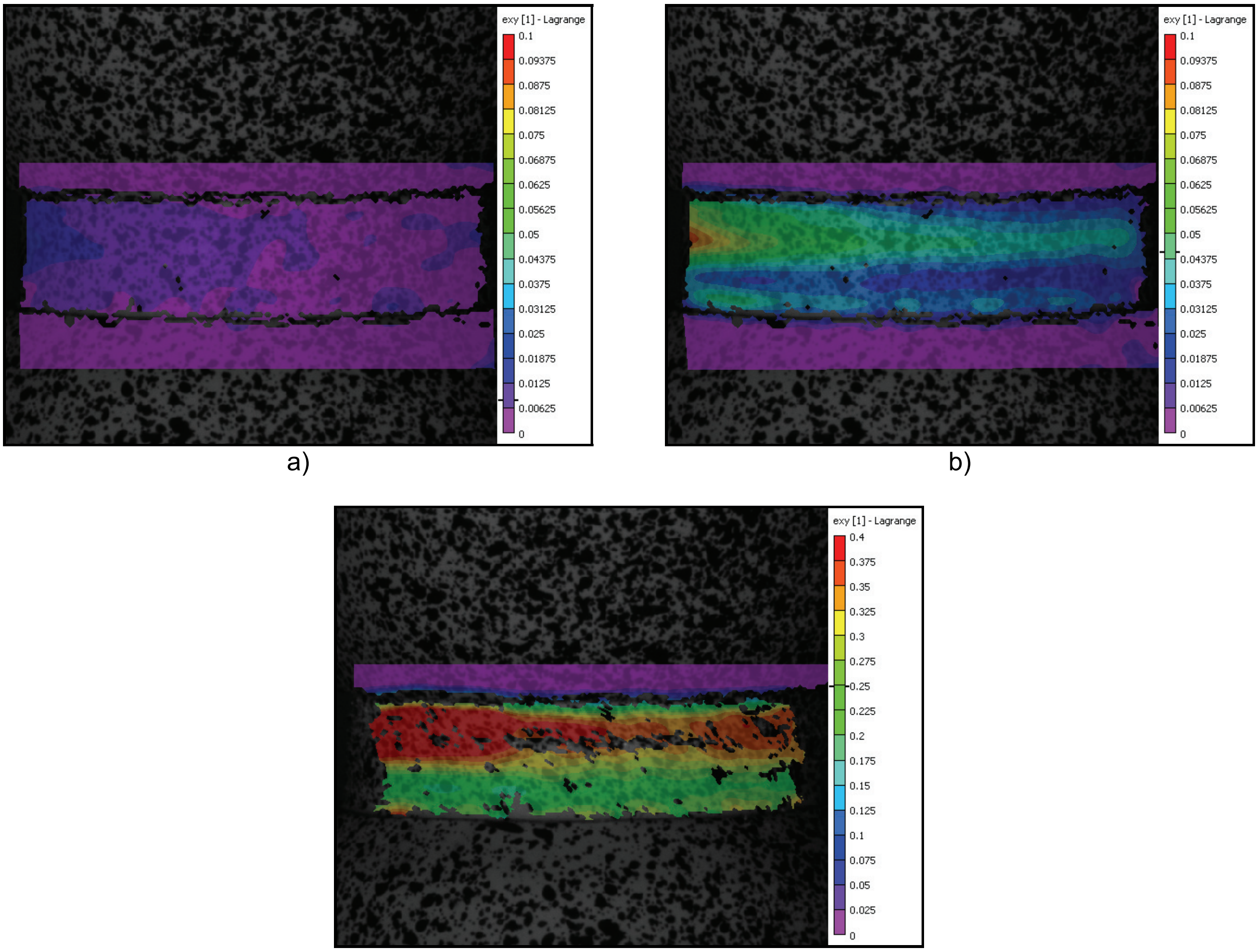
exy [1] - Lagrange
0.1
0.09375
0.0875
0.08125
0.075
0.06875
0.0625
0.05625
0.05
0.04375
0.0375
0.03125
0.025
0.01875
0.0125
0.00625
0
exy [1] - Lagrange
0.1
0.09375
0.0875
0.08125
0.075
0.06875
0.0625
0.05625
0.05
0.04375
0.0375
0.03125
0.025
0.01875
0.0125
0.00625
0
exy [1] - Lagrange
0.4
0.375
0.35
0.325
0.3
0.275
0.25
0.225
0.2
0.175
0.15
0.125
0.1
0.075
0.05
0.025
0

a)

b)

c)

Figure 4: Localization of strain in a torsion test at the strain rate of 0.5 s^{-1}: a) strains just after yielding, b) a developing shear band, and c) a fully developed shear band.

The development of the shear band clearly changes when the strain rate is further increased. Figure 5 shows the development of the shear band at the strain rate of 1000 s^{-1}. Also at high strain rates, the strain localizes already after the first few percents of Lagrange shear strain, but at this strain rate the localization zone is much narrower and extends through the gage section already at very low strains. Fig. 5a shows the early stages of the test, where the strain has already localized and the shear band extends through the entire gage section. The strain in the localized region is around 3-4%, whereas in the surrounding regions it is only 0-2%. The shear band develops fast and the localization continues throughout the test, as shown in Figures 5b and 5c.This type of behavior was observed in all high strain rate tests. It should be noted, however, that despite the localization of strain and the development of the shear band, the strain also increases in the surrounding regions throughout the test at all strain rates. This means that the material in the shear band must have a positive strain hardening rate at all strain rates and that it is high enough to compensate for the thermal softening taking place in the shear band, which at high strain rates and high strains can be quite significant.

The more rapid development of the shear band at high strain rates could simply be explained by the adiabatic heating and consequent thermal softening of the material. However, the shear band extends through the gage section almost immediately after yielding, and therefore the thermal softening alone cannot contribute enough to the development of the shear band. The faster development of the shear band is most likely related to the different yielding behavior of the material at higher strain rates. The pronounced yielding of utrafine grained metals is usually explained by the lack of mobile dislocations that causes the remaining free dislocation to move faster in the beginning of the test [1], thus requiring a higher stress. Therefore it is possible that the avalanche of gliding dislocations that follows the break-up of pinned dislocations causes faster localization of strain due to the very high local deformation rates and consequent thermal softening.

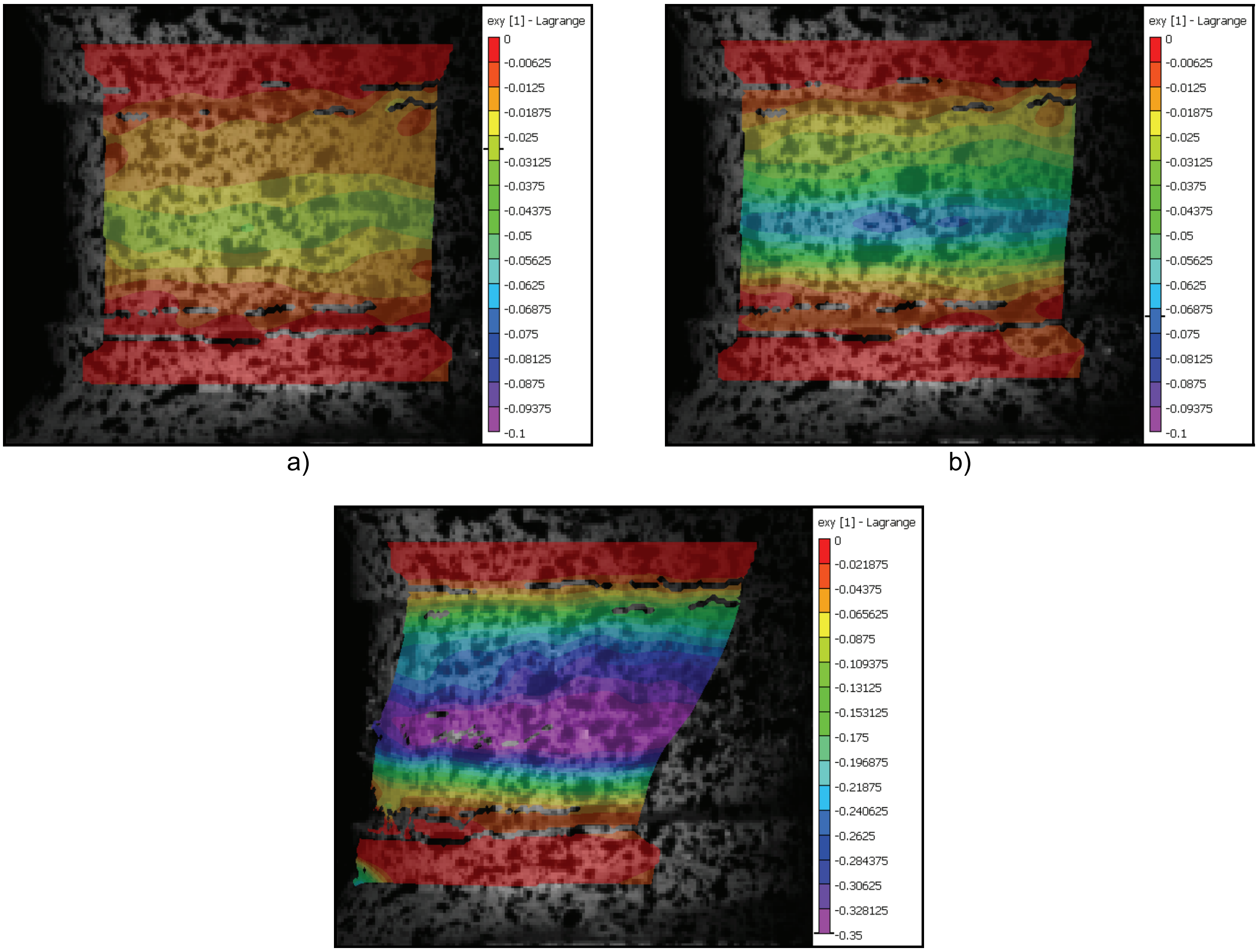

a) b)

c)

Figure 5: Localization of strain in a torsion test at the strain rate of 1000 s^{-1}: a) strains just after yielding, b) a developing shear band, and c) a fully developed shear band.

From the digital image correlation results it is very clear that the average strain calculated from the displacements of the ends of the bars does not represent the behavior of the material very well. The strain localizes very rapidly during the first few percents of deformation. The maximum strain in the shear band can be more than twice as high as in the surrounding regions of the gage section. However, the problems with the adhesion of the contrast pattern currently limit the usable range of digital image correlation to about 60-100 % of shear strain.

SUMMARY

The behavior and properties of pure 1070 aluminum were characterized in a wide range of strain rates in torsion. Thin walled tube specimens were machined from ECAP processed 1070 aluminum and tested using a conventional servohydraulic materials testing machine at low strain rates and the Hopkinson Split Bar technique at high strain rates. A pronounced yielding behavior was observed at strain rates 500 s^{-1} and above. At low strain rates the material showed either slight strain softening or almost ideally plastic behavior. At higher strain rates the strain hardening rate showed an increase with increasing strain rate. The material was found to be well deformable in torsion, exhibiting shear strains over 300% without failure.

The tests were also monitored using digital cameras to facilitate the calculation of strains on the surface of the specimen during deformation. During the tests, deformation localized very rapidly and a shear band formed across the gage section of the specimen. At low strain rates, however, the development of the shear band was slower and the band nucleated and grew from one side of the specimen and only then propagated through the gage section. At higher strain rates, the formation of the shear band was much faster and it extended over the whole gage section almost immediately after yielding.

ACKNOWLEDGEMENTS

Special thanks are due to Dr. Rosochowski and Dr. Oljenik for providing the ultrafine grained material. This work was partly funded by the Academy of Finland under the grant No. 130780 and by the Finnish Agency for Technology and Innovation (MIVA project). The support from the Finnish Foundation for Technology Promotion is also acknowledged.

REFERENCES

1. May J. Höppel H., Göken M., Strain rate sensitivity of ultrafine-grained aluminum processed by severe plastic deformation. Scripta Materialia, 53, pp. 189-194, 2005.
2. El-Danaf E. Mechanical properties and microstructure evolution of 1050 aluminum severely processed by ECAP to 16 passes. Materials Science and Engineering A, 487, pp 189-200, 2008.
3. El-Danaf E., Soliman M. Almajid A., El-Rayes M., Enhancement of mechanical properties and grain size refinement of commercial purity aluminum 1050 processed by ECAP. Materials Science and Engineering A, 458, pp 226-234, 2007.
4. Kokkonen J. Kuokkala V.-T., Lech Olejnik, Andrzej Rosochowski, Dynamic behavior of ECAP processed aluminum at room and sub-zero temperatures. In the proceedings of the annual SEM conference, Orlando Fl, 2008.
5. Rosochowski A., Olejnik L. Numerical and Physical modeling of plastic deformation in 2-turn equal angular extrusion. Journal of Materials Processing Technology, 125-126, pp. 309-316, 2002.
6. Olejnik L. Rosochowski A., Methods of fabrication metals from nano-technology. Bulletin of the Polish Academy of Sciences, Technical Sciences, 53, pp. 413-423, 2005.
7. Gilat A., Torsional Kolsky bar testing. ASM Handbook, 8, Materials Park, Ohio, USA, 2000.
8. Kokkonen J., Kuokkala V.-T., Seidt J., Walker A., Gilat A., Olejnik L., Rosochowski A. High strain rate deformation analysis of UFG aluminum sheet samples. In the proceedings of the annual SEM conference, Albuquerque NM, 2009.
9. Kuokkala V.-T., Kokkonen J., Song B., Chen W., Olejnik L., Rosochowski A., Dynamic responce of severe plastic deformation processed 1070 aluminum at various temperatures. In the proceedings of the Dymat Technical Meeting, Bourges, France, 2008.
10. Valiev R., Langdon T. Principles of equal-channel angular pressing as a processing tool for grain refinement. Progress in Materials Science, 51, pp 881-981, 2006.
11. Kokkonen J., Kuokkala V.-T., Isakov M., Dynamic behavior of UFG aluminum at a wide range of strain rates and temperatures in compression and tension. Journal de Physique IV, 1, pp. 647-653, 2009.
12. Sivaraman A., Chakkingal U., Investigations on workability of commercial purity aluminum processed by equal channel angular pressing. Journal of Materials Processing Technology, 202, pp. 543-548, 2008.

Proceedings of the SEM Annual Conference
June 7-10, 2010 Indianapolis, Indiana USA
©2010 Society for Experimental Mechanics Inc.

Effect of aging treatment on dynamic behavior of Mg-Gd-Y Alloy

Lin Wang, Qiao-yun Qin, Cheng-wen Tan, Fan Zhang, Shu-kui Li
School of Materials Science & Engineering, Beijing Institute of Technology
5 South Zhongguancun Street, Haidian District, Beijing 100081, P. R. China
Corresponding author: Lin Wang, Lindawang_bit@bit.edu.cn

ABSTRACT: Magnesium alloy is very attractive in many industrial applications due to its low density. The structure-property relationships of the magnesium alloy under quasi-static loading have been extensively investigated. However, the dynamic behavior, particularly the mechanism of high-rate plastic deformation, of the magnesium alloy requires more in-depth investigations. In this paper, the effect of aging treatment on the quasi-static and dynamic properties of a typical rare earth Mg-Gd-Y magnesium alloy is investigated. In particular, the plastic deformation mechanism under dynamic compression loading is discussed. Split Hopkinson Pressure Bar (SHPB) was used to carry out dynamic compression tests with controllable plastic deformation by using stopper rings. The experimental results demonstrate that both static and dynamic properties of the Mg-Gd-Y alloy vary under various aging treatment conditions (under-aged, peak-aged and over-aged conditions), due to two different kinds of second phases: remnant micro size phase from solid solution treatment and nano precipitation from aging treatment. The results of microstructure characterization and statistic analysis of the metallographic phase are presented. The area fraction of the twinned grains increases due to aging treatment and dynamic loading. The main plastic deformation mechanism of the rare earth Mg-Gd-Y magnesium alloy is dislocation slip, rather than twinning for the conventional AZ31 magnesium alloy under high strain rate loading.

Introduction

Magnesium alloy is widely used in many industrial applications due to its low density and relatively high strength. Rare earth Mg-Gd-Y magnesium alloy is newly developed magnesium alloy with such distinct characteristics as high strength compared with conventional magnesium alloys. The addition of rare earth element of Gd and Y can improve obviously the strength and anti-creep properties of this rare earth magnesium alloy [1-5]. The structure-properties relationships of Mg-Gd-Y under static loading condition have been widely investigated.

Peng et al.[6] pointed out that the precipitation series of Mg-Gd-Y-Zr alloy is Mg(SSSS)→β''(DO19) →β'（bcc）→β_1（fcc）→β(bcc)，and β'' and β' coexist at peak-aged condition, with size of 10nm and 20nm respectively. In over-aged condition, β' evolutes and partly change into nano size needle shape second phase β_1. Gao and other researchers have indicated that β phase precipitate during solid solution and keep intact during following aging process [7-11]. Nie [12,13] had investigated the precipitation process of WE54 alloy under 220°C aging

T. Proulx (ed.), *Dynamic Behavior of Materials, Volume 1*, Conference Proceedings of the Society for Experimental Mechanics Series,
DOI 10.1007/978-1-4419-8228-5_44, © The Society for Experimental Mechanics, Inc. 2011

and no precipitation occurred in solid solution process. The higher strength of rare earth magneiusm alloys compared with conventional AZ31 alloy is due to the second phases precipitation. As the rare earth magnesium alloys have been used in dynamic loading conditions, but relatively less researches on the dynamic behaviors of this typical rare-earth magnesium alloy, therefore the dynamic behaviors require more in-depth investigation. The plastic deformation mechanism of magnesium alloy under room temperature is usually twinning, while under some certain loading and high temperature conditions, such as hot rolling, the plastic deformation is slipping. Wang et al. have investigated that the plastic deformation mechanism of conventional AZ31 magnesium alloy is twin, under the loading condition of $2300s^{-1}$ strain rate with 4.6% deformation [14]. While for the rare earth magnesium alloy, the different alloying principle may influence the mechanical behavior, and further influence the plastic deformation mechanism.

In this paper, the effects of aging on the formations of second phase in various aging processes and on both static and dynamic properties of Mg-Gd-Y alloy were investigated, particularly, the plastic deformation mechanism under dynamic loading was discussed.

2 Experimental procedures

The chosen experimental material was Mg-Gd-Y alloy, with as-received hot rolled plate condition. The chemical composition is as follows: Gd 11.9wt%, Y0.8 wt%, Zr 0.44wt%, Mg the rest. In order to obtain second phases, aging treatment was carried out at 225℃, with various soaking times from 2 hours to 192 hours, then air cooling. Different aging stages were determined with micro Vickers hardness measurement. XRD measurement was conducted to evaluate the different second phases. Under-aged condition of 6 hours, peak-aged condition of 10 hours and over-aged condition of 192 hours were chosen for in-depth investigations. The as-received samples were also included for comparison.

Static compression properties were measured by means of universal material testing machine. Split Hopkinson Pressure Bar (SHPB) was used to conduct the dynamic compression experiments, with the strain rates of $1600s^{-1}$ and $2600s^{-1}$. The static sample was φ6×15mm and dynamic sample φ8×8mm cylinder, machined along the thickness direction of rolling plate. After the static and dynamic experiments, the recovered samples were sectioned along the axis direction and prepared with standard metallography method for optical microscope(OM) and scanning electronic microscope(SEM) observations. Statistics measurement was carried out with Image-Pro Plus software for grain size and area fraction of twined grain and area fraction of twin calculation. The magnifying power was 300 times and total 494 pictures were included. The effect of aging treatment on the dynamic behavior and plastic mechanism of Mg-Gd-Y alloy were discussed.

3 Results and discussions

3.1 Second phase precipitation in aging treatment

The microstructure of as-received hot rolled Mg-Gd-Y alloy plate is shown in Fig. 1(a), (b). The grain size is about 15μm. There are two micro size remnant second phases existed: square second phase rich with Gd and Y and round second phase rich with Zr. After aging treatment, grain sizes change little after short or long time aging treatments. The main microstructure evolution is the precipitation of nano size second phase β′,according to XRD measurement results, as shown in Fig. 1 (c) and (d). From 6 hours under-aged to10 hours peak-aged samples, the number of β′ phase increases and the size grow with aging time, although still within nano size range. For 192 hours over-aged sample, the β′ phase change from round to needle shape.

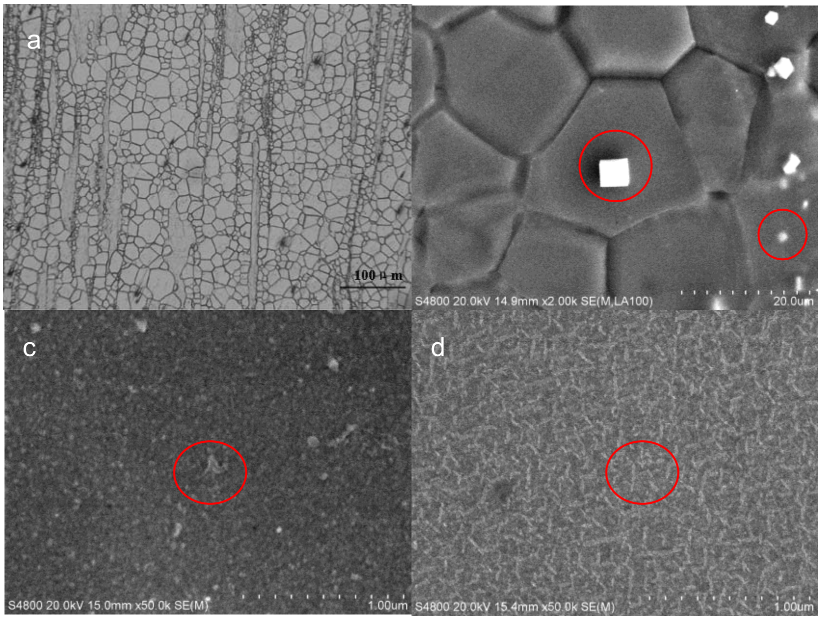
a
100 μ m
S4800 20.0kV 14.9mm x2.00k SE(M,LA100)
20.0um
c
S4800 20.0kV 15.0mm x50.0k SE(M)
1.00um
d
S4800 20.0kV 15.4mm x50.0k SE(M)
1.00um

Fig.1. SEM observation of Mg-Gd-Y alloy before and after aging treatment

(a) low power observation of as-received alloy; (b) square and round remnant phases in as-received material; (c) nano second phase β′ at peak-aged of 10h; (d) nano second phase at over-aged of 192h

3.2 Static and dynamic mechanical properties of Mg-Gd-Y alloy with and without aging treatment

The static and dynamic compression experiments were conducted and true stress-true strain curves obtained, as shown in Fig. 2. Under static compression, the strengths increase and reach maximum at the peak-aged and then decrease at over-aged stage with prolonging aging time. The peak-aged samples exhibit the highest values and the as-received samples show the lowest strength under all strain rates loading.

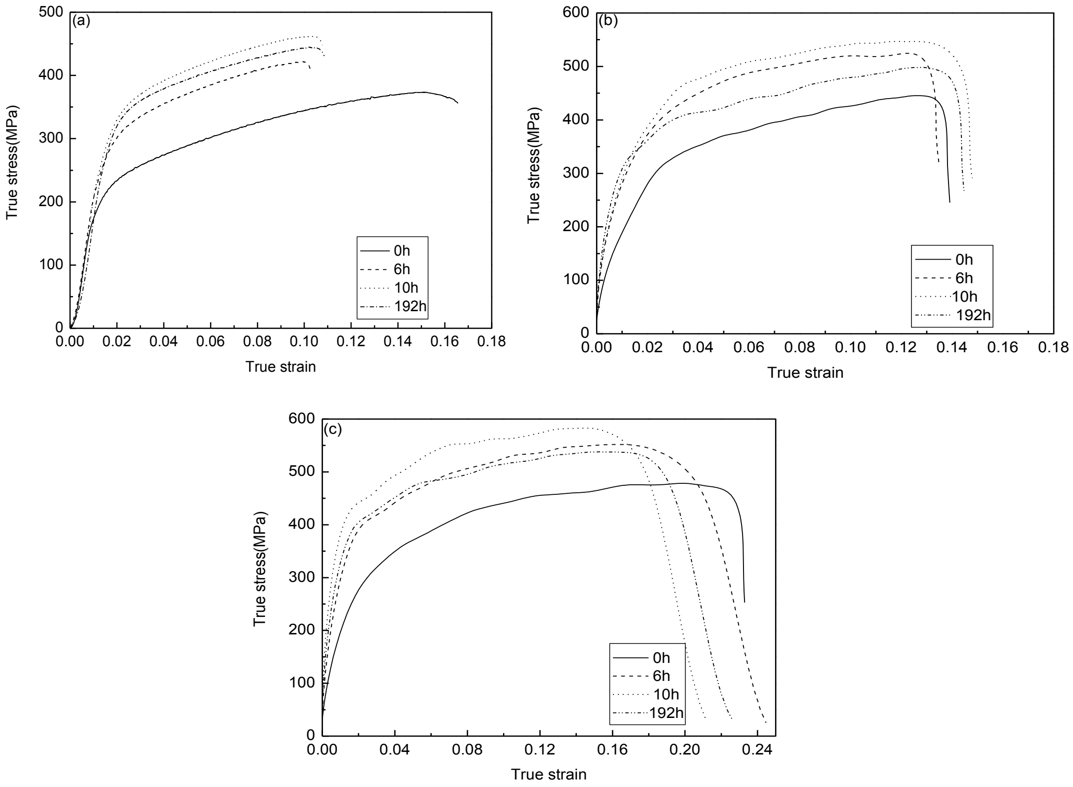

Fig.2 True stress-true strain curves of Mg-Gd-Y alloy at various ageing times

(a) 10^{-3} s^{-1} (b) $1600s^{-1}$ (c) $2600s^{-1}$

The dynamic stress-strain curves at 1600s^{-1} are similar with those under static loading conditions, except that the stress of 6 hours under-aged sample lie above that of 192 hours over aged sample. The stress of peak-aged sample exhibits highest values among all samples. The stress of 6 hours under-aged sample shows a little lower than the peak-aged sample. The stress-strain curves at 2600s^{-1} show the same trend as those at 1600s^{-1}, while both the stresses and strain values are higher than those at 1600s^{-1}.

The stress developments for different aged condition under three strain rates are possibly the contribution of nano size second phase β′. Before aging, there are micro remnant second phase exist. During aging treatment, the precipitation of β′ phase contribute to the increasing of the hardness and strength. At under-aged condition, the number of β′ phase is relatively less and their shapes are mainly round and lath, which have weak nailing effects on the movement of dislocation. When peak aged, the number of β′ phase increase and the shapes change from round into needle or plate which indicates a stronger pinning function on dislocation and hence the material exhibit higher strength value. The over-aged samples have relatively lower strength than peak-aged one is that the size of β′ phase grow, which weaken the strengthen effect of nano second phase β′. Therefore, among all un-aged and aged samples, the as-received samples exhibit the lowest strength under both static and dynamic loading conditions.

3.3 Twin statistics of Mg-Gd-Y alloy with and without different aging treatment

Twinning statistics were conducted under two strain rates, 10^{-3}s^{-1} and 2600s^{-1}, both with the certain deformation amount of 4.0%. Dynamic compression tests were performed with SHPB with controllable plastic deformation by using stopper rings to obtain 4.0% strain. Some typical pictures with 4.37mm^2 visual area are shown in Fig. 3.

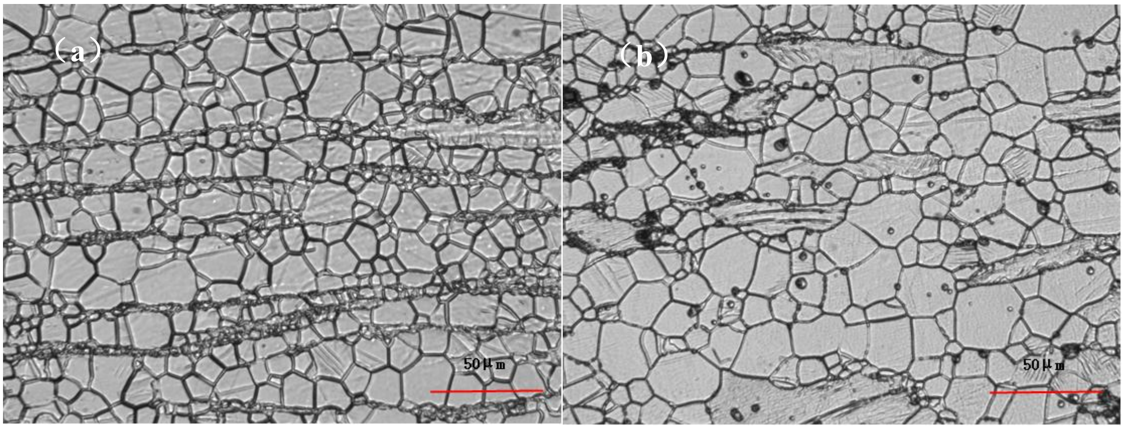

Fig. 3 Typical microstructure of Mg-Gd-Y alloy for statistic calculation (a) 10^{-3}s^{-1} (b) 2600s^{-1}

Two parameters were calculated, area fraction of twinned grain and area fracture of twin, as shown in Fig.4. For the parameter of area fraction of twinned grain, the highest value is about 8%. When under static loading, the value of lack-aged and peak-aged samples are higher than those of as-received and over-aged treatment. When under dynamic loading, these values in each samples are higher than those under static loading conditions. For the parameter of area fraction of twin, although there are some bit differences among different aging samples and under different loading conditions. All values are lower than 2%. The 6h lack aged sample exhibits noticeable higher values under dynamic loading than that under static loading.

The two statistics results have shown that Mg-Gd-Y alloy after aging treatment exhibit higher values of area fraction of twinned grain and fraction of twin, compared with the un-aged rolling samples. Most different aged treatment condition materials exhibit higher area fraction of twinned grain under dynamic loading conditions than those under static loading condition, while the area fraction of the twin vary a bit.

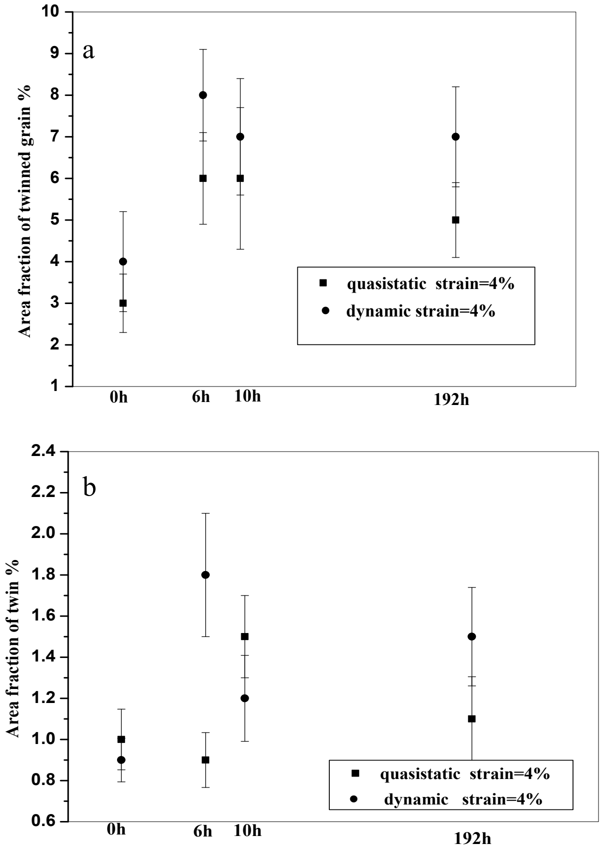

Fig. 4 Statistic results of twinned grain and twin in Mg-Gd-Y alloy
(a) area fraction of twinned grain (b) area fraction of twin

Our twin statistic calculation results are much different with that of AZ31 magnesium alloy carried out by Wang [14]. Wang had investigated that the plastic deformation mechanism of AZ31 magnesium alloy under high strain rate by using statistics calculation. His experiments had showed that the fraction of twin is as high as 35%, much higher than our experimental results and then deduced that the main plastic deformation mechanism of AZ31 under dynamic loading is twin. Therefore, the plastic deformation mechanisms of Mg-Gd-Y alloy must be different with the conventional magnesium alloy.

In Mg-Gd-Y alloy, Gd, Y elements are replacing elements with the element percent of 2.3%. While in AZ31 alloy, Al and Zn percentage is 3%, which is more than the alloying element of Mg-Gd-Y alloy. The increasing amount of alloying element will lead to the decreasing of stacking energy and increasing the plastic deformation ability of easier going of twinning. The axis ratio change with the increasing of alloying elements. The axis ratios of AZ31 and Mg-Gd-Y are 1.624 and 1.618 respectively. The higher axis ratio means that the symmetry of the rare earth magnesium alloy increase and twin is more likely occurring in AZ31 alloy. Therefore, different from the plastic deformation of twin in AZ31 magnesium alloy, the main plastic deformation of Mg-Gd-Y is most possibly dislocation slipping. Further TEM confirmation is needed.

In Mg-Gd-Y alloy, after aging treatment, the precipitation of second phase including Gd and Y results in the largely decreasing of Gd, Y element in the matrix. With the decreasing of alloying elements in matrix after aging treatment, the magnesium alloy are prone to twining compared with the as-received un-aged sample, therefore area fraction of twinned grain and fraction of twin increase at peak-aged and over-aged conditions, compared with that of the as-received one. The different behavior of Mg-Gd-Y alloy under dynamic and static loading is that the twinning stress is very sensitive to strain rate. The area fraction of twinned grain and twin of sample undergo dynamic loading is generally higher than those under static loading. With the increasing strain rates, the tendency of twinning increase. However, as shown in Fig. 4(a), the area fraction of twinned grain of as-received rolling plate under dynamic loading do not change obviously, which is the result of element concentration in original solid solution is high and can prevent twin from occurring. With 10 hours peak-aged and 192 over-aged treatment and the precipitation of nano second phase β′ , the solution atoms reduced obviously which might contribute to the increasing of area fraction of the twinned grain. But due to many precipitating second phases restraining the twinning, the area fraction of the twinned grain is similar with those under static loading condition. For the case of 6 hours under-aged sample, the less precipitation second phase reduce the solid solution element amount, but is not enough to restrain the twinning, therefore the area fraction of twinned grain improve obviously compared with those of static loading condition.

5. Conclusion

The purpose of this paper was to investigate the effect of aging treatment on dynamic behavior of rare earth Mg-Gd-Y magnesium alloy. The under-aged, peak-aged and over-aged conditions, as well as the as-received hot rolling condition, of Mg-Gd-Y magnesium alloy were subjected to static compression and Hopkinson bar compression testing of cylindrical samples. The conclusions are as follows:

(1) Both static and dynamic properties of the Mg-Gd-Y alloy vary under various aging treatment conditions (under-aged, peak-aged and over-aged conditions). With prolonging aging time, the strengths increase and reach maximum at the peak-aged and then decrease at over-aged stage. The peak-aged sample also exhibits the highest values under all strain rate loading. The as-received rolling sample shows the lowest strength.

(2) The difference strengths between the as-received sample and aged ones are due to two different kinds of second phases: remnant micro size phase from solid solution treatment and nano precipitation second phase from aging treatment.

(3) According to statistic results of area fraction of twinned grain and fraction of twin at controlled strain of 4%, area fractions of twinned grain increased at both aging and dynamic loading and reach the maximum of 8% for the peak-aged condition. Area fractions of twin are less than 2% for all kinds of samples at both quasi-static and dynamic loading. The much difference twin statistic results between Mg-Gd-Y alloy and AZ31 indicate the main plastic deformation mechanism of the rare earth Mg-Gd-Y magnesium alloy is dislocation slip, rather than twinning for the conventional AZ31 magnesium alloy under high strain rate loading.

References

[1] Rokhlin L L. Advance light alloys and composites. In: Proceedings of NATO Advanced Study Institute[M]. Kluwer; 443, 1998

[2] Drits M E. Effect of alloying on properties of Mg-Gd alloys[J].Metal Science and Heat Treatment,

21(11):62-64,1979

[3] Anyanwu I A. Aging characteristics and high temperature tensile properties of Mg-Gd-Y-Zr alloys [J]. Materials Transactions, 42(7): 1206-1211,2001

[4] Shigeru I. Age hardening characteristics and high temperature tensile properties of Mg-Gd and Mg-Dy alloys [J]. Journal of Japan Institute of Light Metals, 44(1): 3-8, 1994

[5] Anyanwu I A. Aging characteristics and high temperature tensile properties of Mg-Gd-Y-Zr alloys [J]. Materials Transactions, 42(7): 1206-1211,2001

[6] Peng L M, Zeng X Q, Yuan G Y,et al. Effects of solid solution treatments on microstructure and mechanical properties of AM60B magnesium alloys with RE addition[J].Materials Science Forum,2003,153:419-422.

[7] Gao Y, Wang Q D. Behavior of Mg–15Gd–5Y–0.5Zr alloy during solution heat treatment from 500 to 540 ◦C [J].Materials Science and Engineering A, (459):117-123,2007

[8] Shigeru I. Age hardening characteristics and high temperature tensile properties of Mg-Gd and Mg-Dy alloys [J]. Journal of Japan Institute of Light Metals, 44(1): 3-8, 1994

[9] Kawabata T. HRTEM observation of the precipitates in Mg-Gd-Y-Zr alloy [J]. Materials Science Forum, 419 (422): 303-306,2003,

[10] Shigeharu K. High temperature deformation characteristics and forge ability of Mg-heavy rare earth element-Zr alloys [J]. Journal of Japan Institute of Light Metals, 48(4): 168-173,1998

[11] He S M.Percipitation in a Mg–10Gd–3Y–0.4Zr(wt%)alloy during isothermal aging at 250℃[J].Journal of Alloys and Compounds, (421):309-313,2006

[12] Nie J F. Effects of precipitate shape and orientation on dispersion strengthening in magnesium alloys [J].Scripta Materialia, (48):1009-1015, 2003

[13] Nie J F, Effects of precipitate shape and orientation on dispersion strengthening in magnesium alloys [J]. Scripta Materialia, (48): 1009, 2003

[14] Wang J T, Yin D L. Effect of grain size on mechanical property of Mg-3Al-1Zn alloy [J]. Scripta Materialia, (59)63-66,2008

Proceedings of the SEM Annual Conference
June 7-10, 2010 Indianapolis, Indiana USA
©2010 Society for Experimental Mechanics Inc.

Plasticity Under Pressure Using a Windowed Pressure-Shear Impact Experiment

J.N. Florando*[1], T. Jiao[2], S. E. Grunschel[2,3], R.J. Clifton[2], D. H. Lassila[1], L. Ferranti[1], R. C. Becker[1,3], R.W. Minich[1], and G. Bazan[1]

[1] Lawrence Livermore National Laboratory, [2]Division of Engineering, Brown University,
[3]U.S. Army Research Laboratory
* Corresponding Author: 7000 East Ave., M/S L-340, Livermore, CA 94550. florando1@lln.gov

Many experimental techniques have been developed to determine the compressive strength or flow stress of a material under high strain rate or shock loading conditions [1-3]. In addition, pressure-shear techniques have been developed that allow for the measurement of the shearing response of materials under pressure [4-6]. The technique described is similar to the traditional pressure-shear plate-impact experiments except that window interferometry is used to measure both the normal and transverse particle velocities at a sample-window interface. The velocities are measured using the normal displacement interferometer (NDI) for the normal velocity, and the transverse displacement interferometer (TDI) for the transverse velocity [7].

A schematic of the experiment is shown in Figure 1. For our experiment, the diameters of the impactor, sample and window are 31.75 mm. A 3 mm thick Ta-10W flyer is used for all the experiments, and the window material is a 10 mm thick c-cut sapphire. Two types of samples, both polycrystalline Cu and V have been tested and have a nominal thickness of 1.5 mm. For the TDI measurement a 1200 lines/mm grating is etched in the sapphire and a thin (~120 nm) metallic film is deposited over the grating. The sample attached to the film side of the window by application of glue at several locations on the outer circumference of the sample.

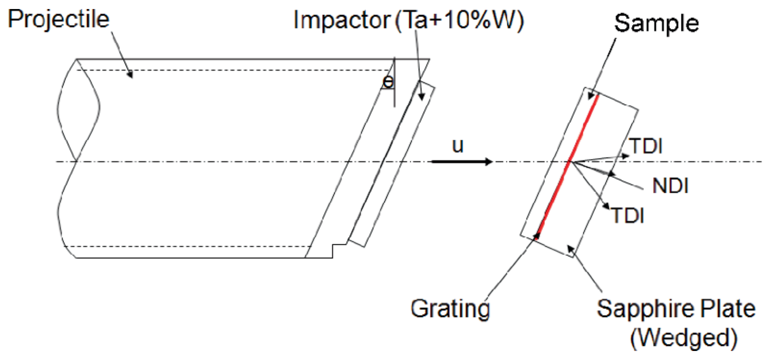

Figure 1. Schematic of the experiment

T. Proulx (ed.), *Dynamic Behavior of Materials, Volume 1*, Conference Proceedings of the Society for Experimental Mechanics Series,
DOI 10.1007/978-1-4419-8228-5_45, © The Society for Experimental Mechanics, Inc. 2011

The experimental result for a Cu experiment is shown in figure 2. Figure 2a shows an example of the interferomentric data from the NDI and TDI measurement taken at the sample/window interface. For the TDI measurement (pink) each fringe is equivalent to a the transverse displacement of 416 nm. The velocity is calculated by taking the derivative as a function of time, and the experimental velocity data are shown in Figure 2b. The flow stress of the material is extracted by using a LLNL hydrodynamics code, ALE3D, and an appropriate strength model. For the Cu experiments, the Mechanical Threshold Model (MTS) [8] is used and can be matched to the transverse velocity profile with parameters that calculate a flow stress of 180 MPa. Similar experiments have also been performed on polycrystalline V and calculate a flow stress of approximately 600 MPa [9].

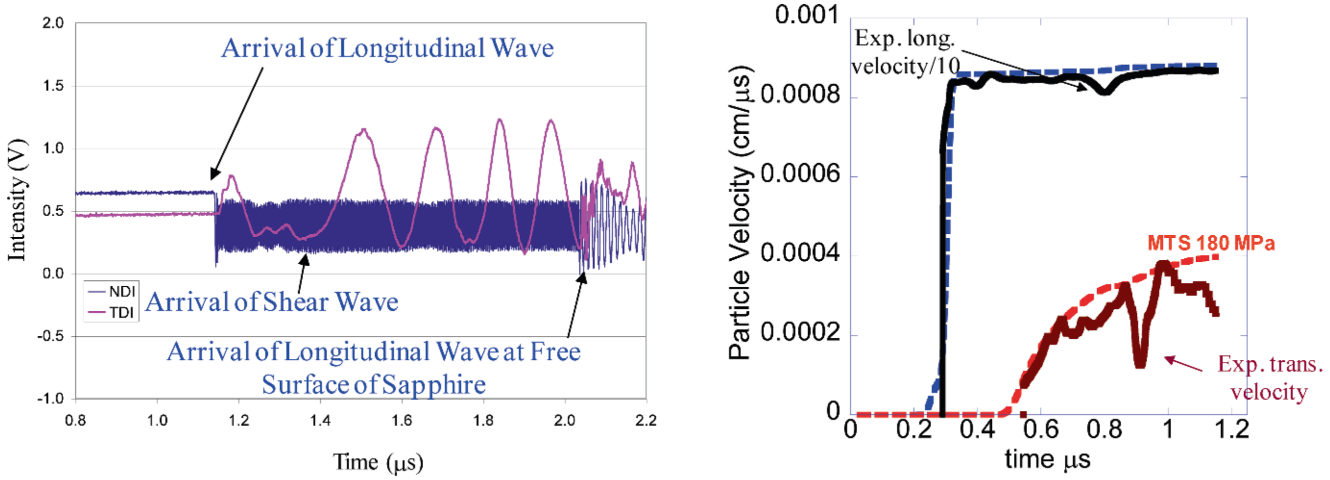

a) b)

Figure 2- a) NDI and TDI record measured at the Cu/sapphire interface. b) Experimental longitudinal and transverse particle velocities compared with hydrodynamics simulations. The MTS model predicts a flow stress for the Cu of 180 MPa.

Acknowledgments

Funding was provided by the LLNL Laboratory Directed Research and Development and the WCI “Dynamics of Metals” programs. This work was performed under the auspices of the U.S. Department of Energy by Lawrence Livermore National Laboratory under Contract DE-AC52-07NA27344.

References

1. Asay, J.R. and Lipkin, J., "A Self Consistent Technique for Estimating the Dynamic Yield Strength of a Shock Loaded Material", J. of Applied Physics 49, 4242, 1978.
2. Barker, LM, Lundergan, CD and Herrmann, W, "Dynamic Response of Aluminum", J. of Applied Physics 35, 1203, 1964.
3. Fowles, GR, "Shock Wave Compression of Hardened and Annealed 2024 Aluminum", J. of Applied Physics 32, 1475, 1961.
4. Clifton, R.J., Klopp, R.W. and Student, G., "Pressure-Shear Plate Impact Testing", ASM Handbook 230, 1985.
5. Yuan, G., Feng, R. and Gupta, Y.M., "Compression and Shear Wave Measurements to Characterize the Shocked State in Silicon Carbide", J. of Applied Physics 89, 5372, 2001.
6. Espinosa, H.D., "Dynamic Compression-Shear Loading with in-Material Interferometric Measurements", Rev. of Scientific Instruments 67, 3931-3939, 1996.
7. Kim, K.S., Clifton, R.J. and Kumar, P., "A Combined Normal and Transverse Displacement Interferometer with an Application to Impact of Y Cut Quartz", J. of Applied Physics 48, 4132, 1977.
8. Follansbee P.S., and Kocks, U.F., "A Constitutive Description of the Deformation of Copper Based on the Use of the Mechanical Threshold Stress as an Internal State Variable", Acta Metall. 36, 81, 1988.
9. Florando, J.N., et al., "High Rate Plasticity Under Pressure Using a Windowed Pressure-Shear Impact Experiment", Proc. Shock Comp of Cond. Matter. 1195, 723, 2010.

Proceedings of the SEM Annual Conference
June 7-10, 2010 Indianapolis, Indiana USA
©2010 Society for Experimental Mechanics Inc.

The Effect of Tungsten Additions on the Shock Response of Tantalum

J.C.F. Millett, M. Cotton, S.M. Stirk, N.K. Bourne, N.T. Park

AWE, Aldermaston, Reading, RG7 4PR. United Kingdom.
email – Jeremy.Millett@awe.co.uk

ABSTRACT

The behaviour of tantalum under shock loading conditions has received significant attention due to its use as a penetrator material by the military. In common with other body centred cubic materials such a tungsten and tungsten heavy alloy (WHA), it has been shown to display a significant drop in shear strength behind the shock front before release waves bring the material back to ambient conditions. Microstructural examination of recovered samples has shown that deformation is achieved largely by the motion of existing dislocations rather than dislocation generation. As dislocation motion can be considered to be a stress relief mechanism, the observed decrease in shear strength is in agreement with microstructural results. We now extend these shear strength measurements to Ta-2.5wt% W to examine the effects of simple alloying on tantalum.

INTRODUCTION

The mechanical response (including shock loading) of metallic materials is controlled by a number of factors such as grain size, additional phase size and distribution and cold work amongst others. Perhaps the simplest way to manipulate properties is through dilute alloying, whereby small additions of a second element are added such that they remain in solid solution. In the case of face centred cubic (fcc) metals, this can have a profound effect. In the case of copper-aluminium alloys (up to 6%Al). Rohatgi *et al.*[1-3] showed that during shock loading, deformation shifted from the generation of dislocation cells in pure copper, to one where twinning was the dominant mechanism at higher aluminium concentrations. Shock experiments in nickel and a nickel-cobalt alloy [4] also showed a change in the evolution of shear strength behind the shock front. In the case of nickel, shear strength increased for a period of *ca*. 500 ns before reaching a constant level. This was in agreement with earlier microstructural work which showed that dislocation cells took a similar time to reach their final confirmation [5]. In contrast, shear strength in nickel-60% cobalt, continued to increase for pulse widths of 1 μs. This was explained in terms of the lower stacking fault energy (SFE-γ) increasing the separation of partial dislocations, thus reducing their mobility. In the case of the alloy, this promoted the formation of deformation twins in the early stages of deformation, delaying the formation and slowing the motion of dislocations. In contrast, tantalum [6], tungsten [7] and a tungsten heavy alloy (WHA) [8] show the opposite response, whereby shear strength decreases somewhat behind the shock front. In the case of tantalum at least, this was correlated with a deformation microstructure that was largely dependent upon the motion of existing dislocations rather than their generation [9]. As dislocation motion can be considered a stress relief mechanism, the reduction in shear strength behind the shock front would appear consistent with these observations. It was speculated that similar behaviour occurred in tungsten, although one dimensional recovery work showed that the material was brittle when shocked at room temperature [10]. However, it was also suggested that brittle failure may also play a part in the reduction in shear strength [7]. The reduced ability to generate additional dislocation line length in these metals was ascribed to the high Peierls (lattice friction) stress. However, in very recent work, similar measurements in niobium [11] and molybdenum [12] (second period transition element analogues of tantalum and tungsten), no such reduction in shear strength was observed. In the case of niobium, the calculated Peierls stress was observed to be very low, in fact similar to that of nickel, suggesting that dislocation generation could occur at a level whereby apparent shear strength reductions could be negated. Indeed, much earlier, Huang and Gray [13], in examining shock loaded niobium via transition electron microscopy (TEM) showed a dense distribution of dislocation tangles, rather than the long straight screw segments observed in tantalum. The situation with molybdenum is not so clear cut. The high Peierls stress would suggest that dislocation generation would be difficult, giving a response similar to that of

T. Proulx (ed.), *Dynamic Behavior of Materials, Volume 1*, Conference Proceedings of the Society for Experimental Mechanics Series,
DOI 10.1007/978-1-4419-8228-5_46, © The Society for Experimental Mechanics, Inc. 2011

tantalum or tungsten. However, previous microstructural work showed that a high dislocation density could be sufficient to trigger extra dislocation generation [14]. In addition, twinning has also been observed, although it appears that there is no agreement as to the thresholds where they appear [15]. As yet, these issues are yet to be resolved, but in this work, we know turn our attention to the effects of alloying. As previously discussed, simple alloying in fcc metals such as nickel has been shown to have a profound effect upon the shock response. We now examine how small (2.5% by weight) additions of tungsten effect the behaviour of tantalum (referenced hence forth in this article as TaW) during shock loading.

EXPERIMENTAL PROCEDURE

All shots were performed on a 50 mm bore, 5 m long single stage gas gun [16]. 65 mm diameter by 11 mm thick targets were machined from plate stock such they were flat and parallel to ± 5 μm. Each target was sectioned in half, and a manganin stress gauge (MicroMeasurements type J2M-SS-580SF-025) introduced 2 mm from the impact face. In this orientation, the gauge would be sensitive to the lateral component of stress (σ_y), and hence the shear strength (τ) could be determined through the well known relation,

$$2\tau = \sigma_x - \sigma_y \,. \tag{1}$$

Impact (longitudinal - σ_x) stresses in the range 2.5 – 11.8 GPa were induced by impacting dural (aluminium 6082-T6) and copper flyers at velocities of 200 to 498 m s^{-1}. These experimental conditions were chosen to mimic a previous programme on pure tantalum [6], and hence a direct like for like comparison between the pure metal and the alloy could be made. Lateral stresses were determined from the raw voltage data using the methods of Rosenberg and Partom [17], with a modified analysis that requires no prior knowledge of the impact conditions [18]. Finally, it has also been shown that the shape of the gauge can also effect the final result at low stresses which must be accounted for [19]. Longitudinal stresses were not measured since previous experience has shown that closely related alloys have near identical equations of state.

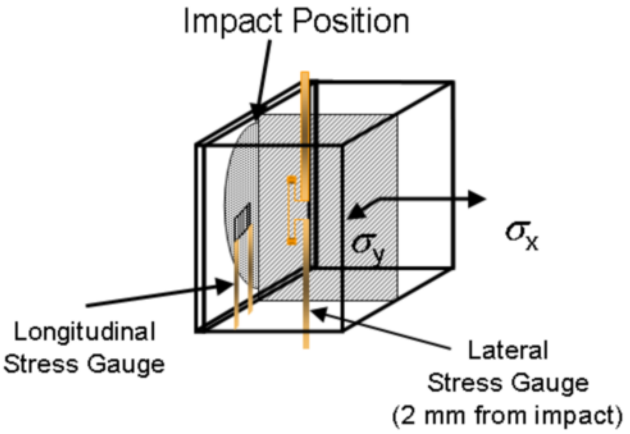
Impact Position
σ_y
σ_x
Longitudinal Stress Gauge
Lateral Stress Gauge (2 mm from impact)

Figure 1. Schematic diagram of specimen configuration and gauge placement.

MATERIALS

Table 1. Elastic properties of TaW. Pure tantalum is included for comparison.

	c_L (mm μs^{-1})	c_s (mm μs^{-1})	ρ_0 (g cm^{-3})	ν
TaW	4.12±0.05	2.11±0.05	16.78±0.02	0.322
Ta [6]	4.13±0.05	2.04±0.05	16.58±0.02	0.339

c_L – longitudinal sound speed
c_S – shear sound speed
ρ_0 - ambient density
ν - Poisson's ratio

The alloy was cold rolled from *ca*. 300 mm to 11 mm in a number of stages, with an intermediate annealing treatment of 1100°C for one hour between rolling passes.

RESULTS

In figure 2, we present lateral stress histories from Ta-2.5%W. As a comparison, we also show the equivalent traces from pure tantalum from a previous investigation.

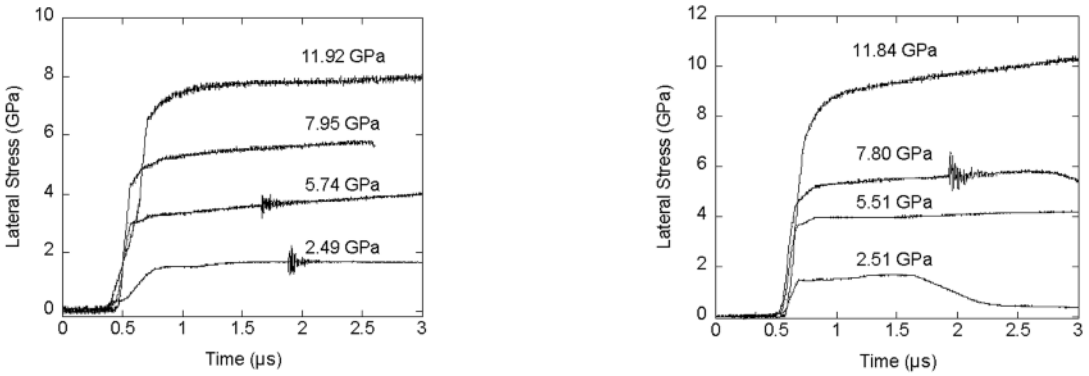

a. Ta-2.5%W. b. Pure tantalum [6].

Figure 2. Lateral stress traces from shock loaded tantalum alloys.

As can be seen, the lateral stress response in TaW is qualitatively similar to that of pure tantalum [6], consisting of a sharp rise with the arrival of the main shock, followed by a shallower increase in lateral stress behind the shock front. From equation 1, this implies that both materials lose shear strength behind the shock front. Similar behaviour has been observed in tungsten [7] and a WHA [8], but not in either niobium [11] or molybdenum [12], which both possess the bcc structure. Shear strengths have been determined using equation 1, using the lateral stress behind the shock front where the stress rises at a constant gradient. We have also assumed that the Hugoniot stress of TaW is the same as tantalum [20]. We have done so since the Hugoniots of pure metals and their dilute alloy systems (for example iron and mild steel [21], aluminium alloys [20] and tungsten and alloys [8]) have been shown to near identical. The results are presented in figure 3, with those of pure tantalum [6] as a comparison.

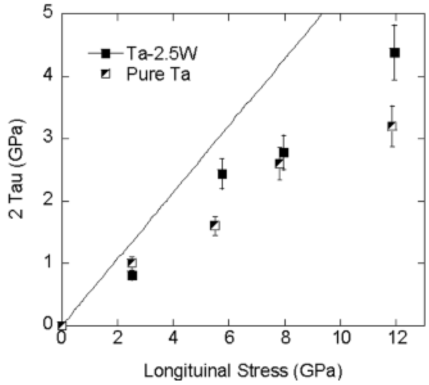

Figure 3. Shear strengths of TaW and Ta [6]. The straight line fit assumes a purely elastic response, based on equation 2.

The straight line is the calculated elastic response for TaW, using the Poisson's ratio (ν) measured ultrasonically,

$$2\tau = \frac{(1-2\nu)}{(1-\nu)}\sigma_x \, . \qquad (2).$$

Both materials lie below the elastic calculation, indicating that they are responding plastically. It can also be observed that as a general trend, TaW is somewhat stronger that pure tantalum, as would be expected from an alloy system.

Finally, in figure 4, we examine the increase in lateral stress (and hence the reduction in shear strength) behind the shock front, both from TaW and pure tantalum [6].

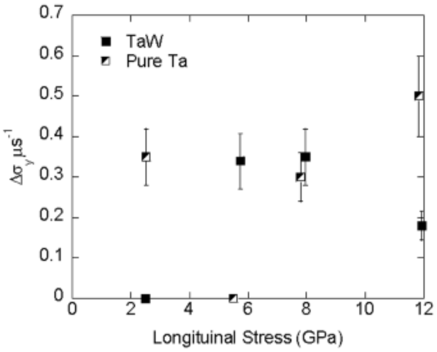

Figure 4. Lateral stress gradient behind the shock front for TaW and pure tantalum [6].

Although there is a degree of scatter in the data, it would be apparent that the behaviour of both materials is similar.

DISCUSSION

The use of lateral stress gauges to determine the shear strength of materials behind the shock front has been proven to be a useful tool, in addition with microstructural examination, in the identification of deformation mechanisms during such events. In fcc materials such as nickel and it's alloys, a reduction in stacking fault energy has been shown to result in a shift in deformation processes from one dominated by dislocation motion and generation, forming a well defined cell structure in the high SFE nickel [22] to one dominated by twin formation in the lower stacking fault energy alloys Ni-60Co and stainless steel 304L [4, 23]. Correspondingly, lateral stresses have been shown to decrease behind the shock front in pure nickel, whilst being near constant in SS304L, suggesting a hardening response in the former, whilst little change occurs in the latter. In bcc metals, the available evidence to elucidate similar processes during shock loading is not so advanced. Previous work in tantalum [6], tungsten and alloys [7,8] showed an increase in lateral stress behind the shock front (see figures 2 and 4), indicating a *reduction* in shear strength. Microstructural observations showed rather than the generation of new dislocation line length, deformation was achieved largely by the motion of dislocations already present within the microstructure, with the possibility of a small amount of twin formation as well. As has already been mentioned, dislocation motion on it's own can be considered a stress relief process, and hence the reductions in strength behind the shock front would appear to be in agreement with such observations. Whilst it was assumed that such behaviour was typical of bcc metals, subsequent work on niobium [11] and molybdenum [12], both of which show a near constant shear strength behind the shock front, indicates this is not the case. In the case of the former, it was suggested that a low lattice friction or Peierls stress (τ_{PN}) encouraged the formation of dislocations during shock loading, confirmed by work by Huang and Gray [13]. In table 2, we have tabulated the Peierls stresses for a number of bcc metals (plus nickel for comparison), calculated through the following relation [24] –

$$\tau_{PN} = \frac{2G}{1-\nu} Exp\left(\frac{-2\pi w}{b}\right); w = \frac{a}{1-\nu}, \qquad (3)$$

where G is the shear modulus, b the lattice parameter, a the interplanar spacing and w the dislocation width. It should be noted that these values of Peierls stress can only be taken as order of magnitude calculations as they do not account for the pressure dependence of the various parameters. However, in the case of TaW, it appears to have a somewhat higher Peierls stress than pure tantalum, suggesting that dislocation generation is if anything even more difficult.

Table 2. Peierls stress for five metals.

Metal	*G* (GPa)	ν	*b* (nm)	τ_{PN} (MPa)
Nb	36.3	0.403	0.330	70
Mo	121.5	0.296	0.315	629
Ta	69.0	0.339	0.331	252
W	160.2	0.279	0.316	940
Ni	81.7	0.315	0.352	85
TaW	74.71	0.322	0.311	315

CONCLUSIONS

The shock response of the alloy tantalum – 2.5 weight% tungsten, has been observed in terms of the lateral stress and development of shear strength behind the shock front. It has been noted that there is an increase in lateral stress behind the shock front, prior to arrival of release waves, indicating that there is a corresponding reduction in shear strength. Such behaviour has been observed previously in other body centred cubic metals such as tungsten and it’s alloys and more significantly, pure tantalum, although not in materials such as niobium or molybdenum. Calculation of the Peierls (lattice friction) stress has been shown to be high, indicating that deformation is controlled largely by the motion of dislocations already present within the microstructure rather than generation of further dislocation line length. Shear strengths themselves have been observed to be slightly higher than the corresponding values for pure tantalum, as might be expected for a dilute substitutional alloy. Further work is underway to determine equation of state, Hugoniot Elastic Limit and spall (dynamic tensile) strength.

ACKNOWLEDGMENTS

The authors would like to thank Gareth Appleby-Thomas and Andy Roberts of Cranfield Defence and Security for their help in performing the shock loading experiments in this article. We also acknowledge Geoff Shrimpton (AWE) for supplying the material and many useful discussions.

British Crown Copyright MoD/2010

REFERENCES

1. A. Rohatgi, K.S. Vecchio and G.T. Gray III, Acta Mater., **49**, (2001), 427-438.
2. A. Rohatgi, K.S. Vecchio and G.T. Gray III, Met. Mat. Trans. A., **32A**, (2001), 135-145.
3. A. Rohatig and K.S. Vecchio, Mater. Sc. Engng., **A328**, (2002), 256-266.
4. J.C.F. Millett, N.K. Bourne and G.T. Gray III, Met. Mat. Trans., **39A**, (2008), 322-334.
5. L.E. Murr and D. Kuhlmann-Wilsdorf, Acta Metall., **26**, (1978), 847-857.
6. G.T. Gray III, N.K. Bourne and J.C.F. Millett, J. Appl. Phys., **94**, (2003), 6430-6436.
7. J.C.F. Millett, G.T. Gray III and N.K. Bourne, J. Appl. Phys., **101**, (2007), 033520.
8. J.C.F. Millett, N.K. Bourne, Z. Rosenberg and J.E. Field, J. Appl. Phys. **86**, (1999) 6707-6709.
9. G.T. Gray III and K.S. Vecchio, Met. Mat. Trans. A. **26A**, (1995), 2555-2563.
10. D.H. Lassila and G.T. Gray III, J. Phys. IV. **4**, (1994), 349-354.
11. A. Workman, J.C.F. Millett, S.M. Stirk, N.K. Bourne, G. Whiteman and N.T. Park, in "Shock Compression of Condensed Matter - 2009", edited by M.L. Elert, W.T. Buttler, M. D. Furnish and W.G. Proud (AIP Press, Melville, NY, 2010), p. 1019-1022.
12. S.M. Stirk, J.C.F. Millett, N.K. Bourne, G. Whiteman and N.T. Park, in "Shock Compression of Condensed Matter - 2009", edited by M.L. Elert, W.T. Buttler, M. D. Furnish and W.G. Proud (AIP Press, Melville, NY, 2010), p. 1123-1126.
13. J.C. Huang and G.T. Gray III, Mater. Sci. Engng., **A103**, (1988), 241-255.
14. S. Mahajan and A.F. Bartlett, Acta Metall., **19**, (1971), 1111-1119.
15. L.E. Murr, O.T. Inal and A.A. Morales, Acta Metall., **24**, (1976), 261-270.
16. N.K. Bourne, Meas. Sci. Technol., **14,** (2003), 273-278.
17. Z. Rosenberg and Y. Partom, J. Appl. Phys., **58**, (1985), 3072-3076.
18. J. C. F. Millett, N. K. Bourne and Z. Rosenberg, J. Phys. D. Applied Physics, **29**, (1996), 2466-2472.
19. Z. Rosenberg, N. K. Bourne and J. C. F. Millett, Meas. Sci. Technol., **18**, (2007), 1843-1847.
20. S. P. Marsh, LASL Shock Hugoniot data, University of California Press, Los Angeles, 1980.
21. N. Bourne and J. Millett, Scripta Mater., **43**, (2000), 541-546.

22. P.S. Follensbee and G.T. Gray III, Int. J. Plast., **7**, (1991), 651-660.
23. J.C.F. Millett, G. Whiteman and N.K. Bourne, J. Appl. Phys. **105**, (2009), 033515.
24. R.E. Smallman, “Modern Physical Metallurgy”, Butterworths, London, (1985).

Proceedings of the SEM Annual Conference
June 7-10, 2010 Indianapolis, Indiana USA
©2010 Society for Experimental Mechanics Inc.

Stress Perturbations Caused by Longitudinal Stress Gauges

R E Winter and P T Keightley, Hydrodynamics Division, AWE, Aldermaston, Reading, Berkshire, RG4 7PR, UK

In general, the diagnostics used to evaluate the shock state parameters in samples loaded by stress waves perturb the fields they are measuring. For example the insulating layers in which stress gauges have to be mounted in a conducting sample usually result in impedance mismatched interfaces. Similarly, velocity interferometry inevitable requires the wave to interact with a mismatch interface. In such situations wavelets generated by the parts of the wave that arrive early at the mismatch interface reflect back into the sample and interfere with the later-arriving parts of the wave. In principle, high resolution hydrocodes may be used to compute, and thereby potentially, take account of, the perturbations caused by intrusive diagnostics. For example Winter and Harris computed the perturbing effect of lateral stress gauges [1] and Huang and Assay [2] computed the effect of a mismatch boundary on velocimetry records. The confidence with which fine-mesh hydrocodes may be used to correct diagnostic records to their "in-situ" wave forms depends, of course, on the accuracy of the codes which, in turn, depends on factors such as the mesh size used and on the constitutive models of the materials in the configuration under investigation.

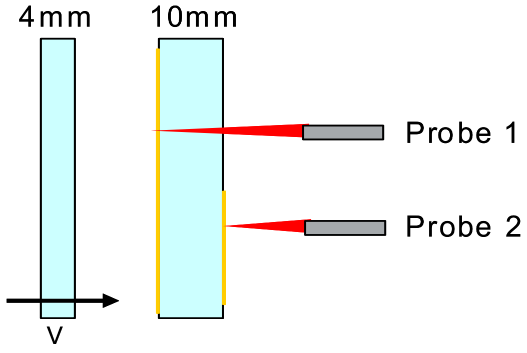

Figure 1

Figure 1 shows one of a series of experiments in which sapphire targets were impacted by sapphire projectiles. The Impact velocities were chosen to keep the sapphire in its elastic range. Velocimetry was used to obtain data from which the constitutive model of the sapphire was estimated. The constitutive model was then used to deduce the expected wave profiles. As shown in figure 2, which corresponds to the configuration shown in figure 1, the computed wave profile matched the observed profiles very closely, thereby confirming that the constitutive model was valid.

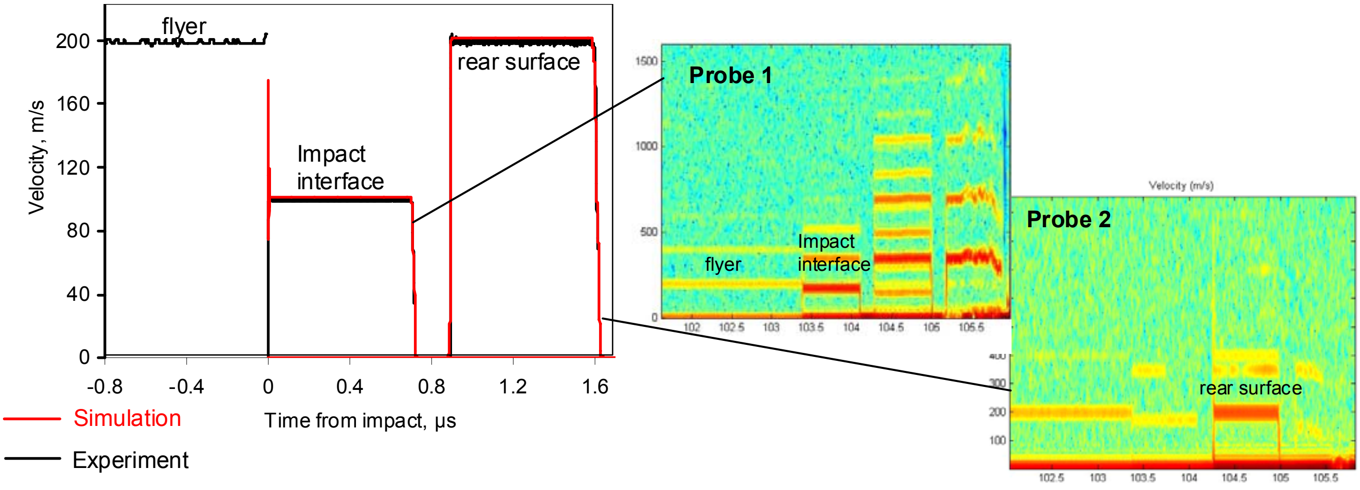

Figure 2

Then experiments were conducted in which manganin stress gauges were mounted in sapphire targets. Figure 3 shows distance times plots and and predicted velocity profiles generated using the AWE Lagrangian code "CORVUS". The mesh size was 10μm. It is seen that including the gauge makes a substantial difference to the predicted profiles at the front and back (free surface) faces of the sapphire target.

Finally, figure 4 shows the experimentally-determined free-surface velocity profile compared with the simulation. The insets show the raw signal together with the derived profile for comparison with the two velocity pulses from the lower right of figure 3. The main graph shows the first pulse in detail. It is seen that even the fine detail of the experimental trace is reproduced by the simulation.

T. Proulx (ed.), *Dynamic Behavior of Materials, Volume 1*, Conference Proceedings of the Society for Experimental Mechanics Series, DOI 10.1007/978-1-4419-8228-5_47, © The Society for Experimental Mechanics, Inc. 2011

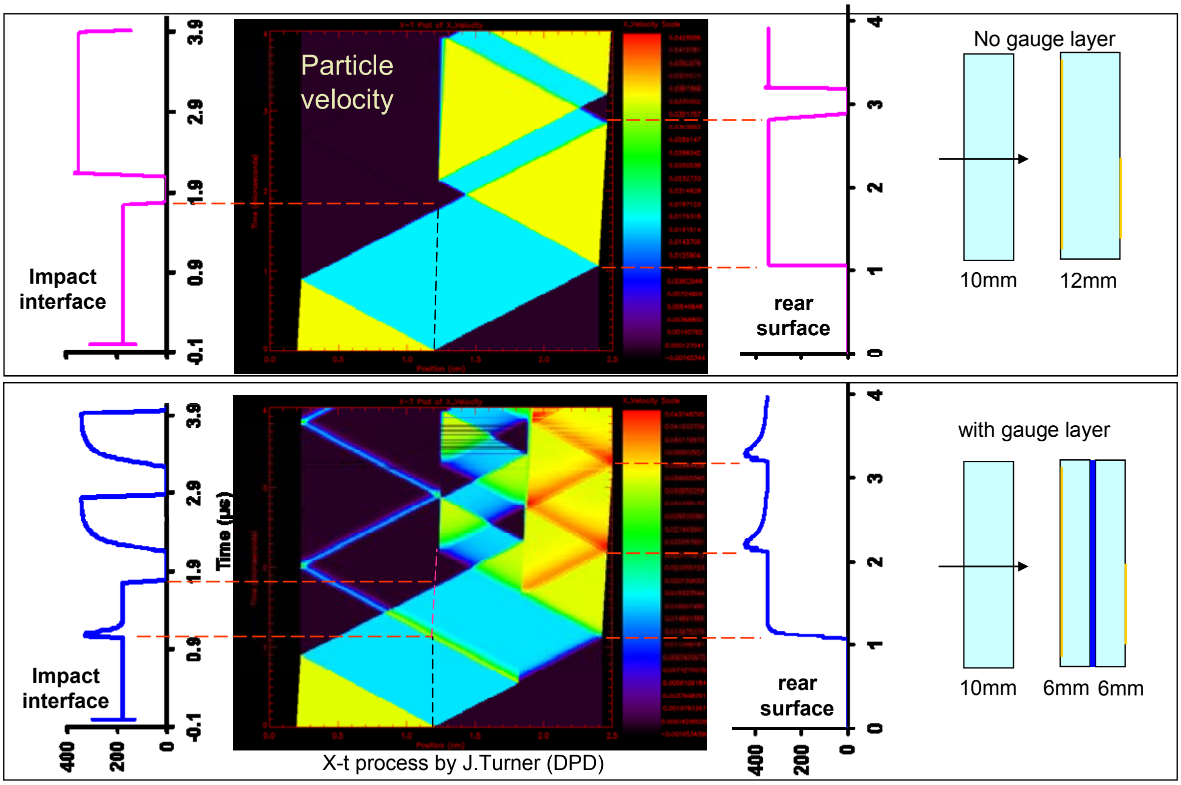

Figure 3

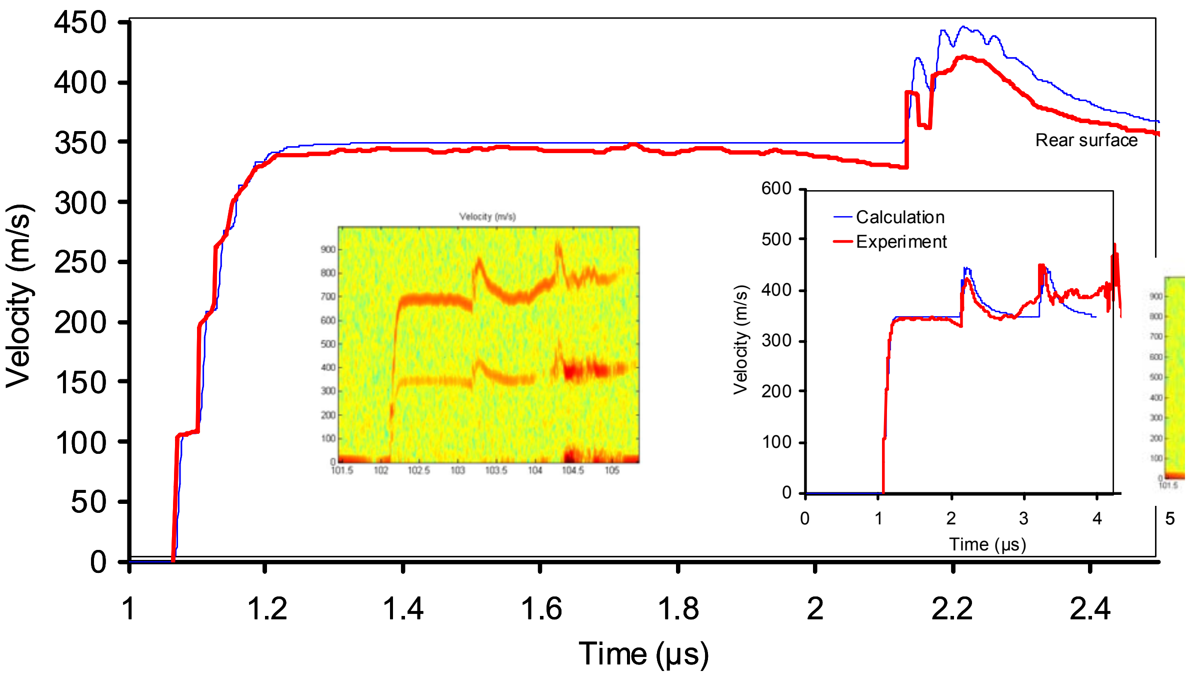

Figure 4

It has been shown a) that the longitudinal gauge significantly affects the wave which passes through it and b) that the CORVUS simulation closely reproduces the observed free surface profile. We conclude that, in situations where the measurement technique has an effect on the time-dependant field it is measuring, there are good prospects that the hydrocode may be used to determine the corresponding “in situ” field.

1. Winter R E and Harris E J 2008 J. Phys. D.: Appl. Phys. **41** 035503
2. Huang H and Asay J R 2005 J. Appl. Phys. **98** 033524

Proceedings of the SEM Annual Conference
June 7-10, 2010 Indianapolis, Indiana USA
©2010 Society for Experimental Mechanics Inc.

Measuring Strength at Ultrahigh Strain Rates

Tracy J. Vogler
Sandia National Laboratories
7011 East Ave.
M.S. 9042
Livermore, CA 94550
tjvogle@sandia.gov

Abstract

The use of uniaxial strain ramp loading experiments to measure strength at extremely high strain rates is discussed. The technique is outlined and issues associated with it are examined. Results for 6061-T6 aluminum are presented that differ from the conventional view of strain rate sensitivity in aluminum alloys.

Introduction

Strain rate sensitivity is measured through a combination of quasistatic, Hopkinson bar, and pressure-shear experiments [1]. The pressure-shear technique has largely been limited to strain rates of order 10^6 s^{-1}. Strengths from shock experiments have not, in general, been successfully related to these engineering experiments [1]. However, recent advances in laser and magnetically driven ramp loading have made it possible to achieve significantly higher rates, 10^5 - 10^8 s^{-1}, under uniaxial strain compression. Strengths determined at these rates can provide a more complete picture of the strain rate sensitivity of materials.

Strength Measurements under Uniaxial Strain Ramp Loading

A variety of techniques can be used to create uniaxial strain ramp loading in materials including graded density impactors [2], magnetic loading [3,4], and indirect laser drive [5]. Because shocks do not occur in these experiments, they are commonly referred to as isentropic or, more properly, quasi-isentropic loading. Velocity histories are measured for multiple samples of different thickness that have the same input conditions as shown in Fig. 1a. Lagrangian analysis or characteristics techniques [6] and other techniques can be utilized to infer the loading response of the material as shown in Fig. 1b. Because of the nature of the loading and the governing equations (conservation of mass and momentum), though, only one component of the stress tensor, σ_x, can be determined. Shear components are zero by symmetry, but the lateral stress, $\sigma_y = \sigma_z$, is unknown. However, by

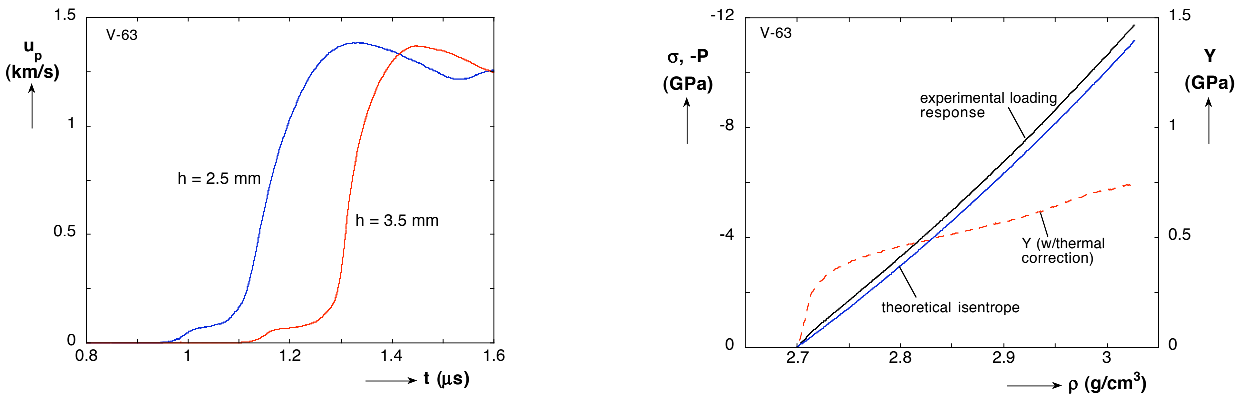

(a)

(b)

Figure 1 Ramp loading results from a magnetically driven experiment [4] on 6061-T6 aluminum: (a) free-surface velocity histories for two samples of different thickness and (b) loading response, pressure-density response from a theoretical equation of state [8], and calculated flow stress *Y*.

T. Proulx (ed.), *Dynamic Behavior of Materials, Volume 1*, Conference Proceedings of the Society for Experimental Mechanics Series, DOI 10.1007/978-1-4419-8228-5_48, © The Society for Experimental Mechanics, Inc. 2011

comparison to the pressure-volume response of the material [7], the flow stress *Y* can be determined from

$$Y = \frac{3}{2}\left(-\sigma_x - P\right), \tag{1}$$

where *P* is the thermodynamic pressure and both terms on the right of the equation are evaluated at the same density and temperature. The flow stress calculated in this manner is also shown in Fig. 1b. A well-established equation of state (EOS) for aluminum [8] was used in order to determine the pressure used in Eq. 1 for a given density and temperature. The equation of state is not sufficient, though, since heating due to plastic work must also be taken into account [9]. For the data shown in Fig. 1, the correction at the peak stress level is approximately 10%, with the correct strength being that much lower than if plastic work is not considered. It should also be pointed out that developing an EOS that is accurate over a wide range of pressures and temperatures is a challenging endeavor. Although the EOS used here is considered very good, relatively small uncertainties in the EOS result in relatively large uncertainties in *Y* because Eq. 1 involves the difference of two numbers of comparable size.

Strain Rate Sensitivity

Strengths obtained from ramp loading [2-5] are compared to quasi-static and intermediate rate data [1,10-12] in Fig. 2a. All data are shown for an equivalent plastic strain of 6%, which corresponds to a compressive strain of 9% for uniaxial compression. It should be pointed out that the data at the highest strain rate [5] were not obtained for 6061-T6 aluminum alloy but on a relatively pure aluminum. Nevertheless, the new ramp loading data are consistent with the Hopkinson bar and pressure-shear data from the literature, showing a significant rise in strength above strain rates of about 10^5 s^{-1}.

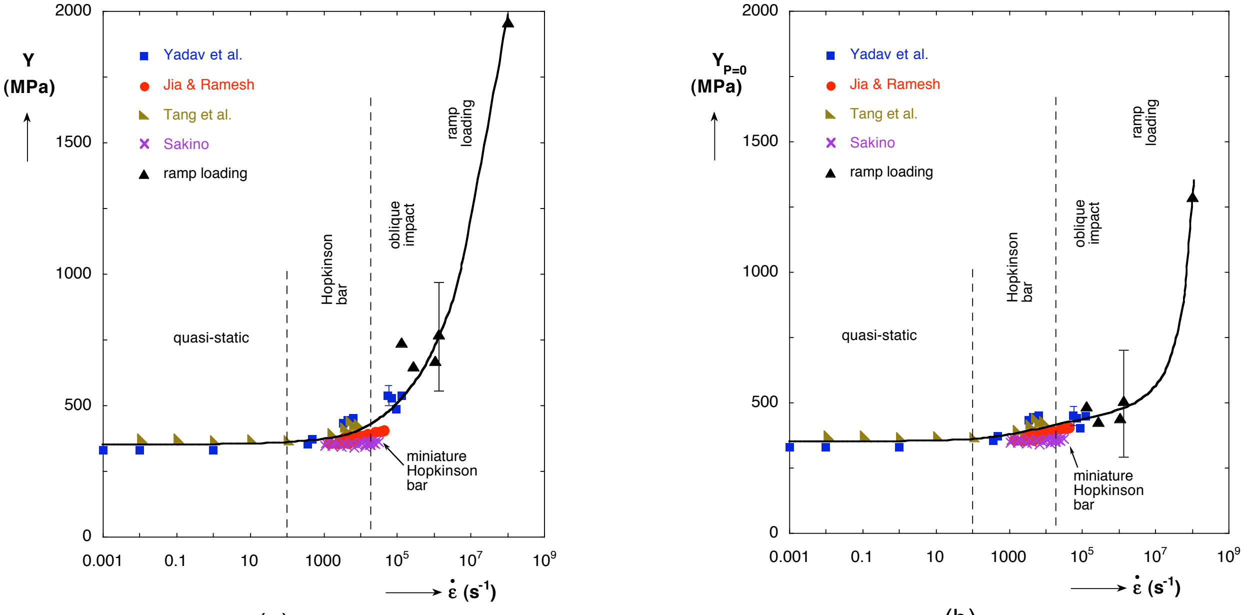

(a) (b)

Figure 2 Strain rate sensitivity for 6061-T6 aluminum (a) including ramp loading results and (b) correcting for the pressure sensitivity of the flow stress.

The ramp loading data, however, were obtained at a mean stress (pressure) level of approximately 9 GPa, while the quasi-static and Hopkinson bar data were taken at a pressure level of essentially zero. Theoretical arguments [13] suggest that strength scales with pressure, and this is a key feature of most constitutive models intended for regimes of high pressure. Scaling *Y* according to

$$Y_{P=0} = \frac{G_o}{G(P)} Y(P), \tag{2}$$

where G_o is the ambient shear modulus, $G(P)$ is the shear modulus at the pressure level corresponding to the test conditions. Correcting for the 9 GPa pressure in ramp loading experiment using Eq. 2 lowers the strength by about 34%, while correcting for the ~3 GPa pressure in the pressure-shear experiments lowers them by about 17%. When the strengths from ramp loading and pressure-shear are corrected in this manner as shown in Fig. 2b, the results are quite different than before. Now, only modest strain rate sensitivity is seen at rates of 10^6 s^{-1}, and the onset of strong rate sensitivity has been shifted by at least two decades. The significant difference in rates for magnetically driven [3] and laser driven [5] experiments makes it impossible to determine this more accurately, though.

Additional experimental data are needed to verify that the strain rate sensitivity shown in Fig. 2b is accurate, since it represents the simplest correction for pressure possible. Some data [14] suggest that BCC materials respond quite differently to pressure. Also, additional data between the magnetic and laser experiments are needed to better understand the rate sensitivity and gain confidence in the results in this regime.

Conclusions

Uniaxial strain ramp loading can extend strength measurements to strain rates above those in pressure-shear experiments. However, great care must be taken in doing so, particularly in ensuring the accuracy of the quasi-isentrope to which the experimental data are compared and in accounting for pressure dependence of strength. New ramp loading results suggest the strain rate dependence of 6061-T6 aluminum does not become significant until approximately 10^7 s^{-1}, approximately two orders of magnitude higher than reported previously.

Acknowledgements

Sandia is a multiprogram laboratory operated by Sandia Corporation, a Lockheed Martin Company, for the United States Department of Energy's National Nuclear Security Administration under contract DE-AC04-94AL85000.

References

[1] Yadav, S., Chichili, D.R. and Ramesh, K.T., "The mechanical response of a 6061-T6 Al/Al_2O_3 metal matrix composite at high rates of deformation." *Acta Metallurgica et Materialia* **43**: 4453-4464 (1995).

[2] Barker, L.M., “High-pressure quasi-isentropic impact experiments.” *Shock Waves in Condensed Matter*, Elsevier Science, pp. 217-224 (1984).

[3] Davis, J.-P., "Experimental measurement of the principal isentrope for aluminum 6061-T6 to 240 GPa." *Journal of Applied Physics* **99**: 103512 (2006).

[4] Ao, T., J.R. *et al.*, "A compact strip line pulsed power generator for isentropic compression experiments." *Review of Scientific Instruments* **79**: 013903 (2008).

[5] Smith, R.F., *et al.*, "Stiff response of aluminum under ultra-fast shockless compression to 110 GPa." *Physical Review Letters* **98**: 065701 (2007).

[6] Rothman, S.D., Davis, J.-P., Maw, J., Robinson, C.M. Parker, K., and Palmer, J., "Measurement of the principal isentropes of lead and lead-antimony alloy to ~400 kbar by quasi-isentropic compression." *Journal of Physics D: Applied Physics* **38**: 733-740 (2005).

[7] Fowles, G.R., "Shock wave compression of hardened and annealed 2024 aluminum." *Journal of Applied Physics* **32**: 1475-1487 (1961).

[8] Kerley, G.I., "Theoretical equation of state for aluminum." *International Journal of Impact Engineering* **5**: 441-449 (1987).

[9] Vogler, T.J., "On measuring the strength of metals at ultrahigh strain rates." *Journal of Applied Physics* **106**: 053530 (2009).

[10] Jia, D., and Ramesh, K.T., "A rigorous assessment of the benefits of miniturization in the Kolsky bar system," *Exp. Mech.* **44**, 445-454 (2004).

[11] Tang, X., Prakash, V., and Lewandowski, J.J., "Dynamic deformation of aluminum 6061 in two different heat-treatments," in *Proceedings of the 2005 SEM Annual Conference and Exposition*, Society for Experimental Mechanics, Paper #323, S.7 (2005).

[12] Sakino, K., "Strain rate dependence of dynamic flow stress considering viscous drag for 6061 aluminium alloy at high strain rates," *J. Phys. IV* **134**, 183-189 (2006).

[13] Kelly, A. and Macmillan, N.H., *Strong Solids*. Oxford, U.K., Clarendon Press (1986).

[14] Becker, R., Arsenlis, A., Marian, J., Rhee, M., Tang, M., and Yang, L.. “Continuum level formulation and implementation of a multi-scale model for vanadium.” Lawrence Livermore National Laboratory report LLNL-TR-416095 (2009).

Proceedings of the SEM Annual Conference
June 7-10, 2010 Indianapolis, Indiana USA
©2010 Society for Experimental Mechanics Inc.

Shear Stress Measurements in Stainless Steel 2169 Under 1D Shock Loading

G. Whiteman and J. C. F. Millett

[1]AWE, Aldermaston, Reading, RG7 4PR, United Kingdom
email – glenn.whiteman@awe.co.uk

ABSTRACT

The material addressed in this research is stainless steel 2169, a 200 series stainless steel which has so far found applications in aviation, demolition, motor-vehicle design and nuclear reactor containment. Longitudinal and lateral stresses during the shock loading of 2169 have been measured using manganin stress gauges. The shear strength has been shown to increase with impact stress and it is seen that when compared with another common austenitic stainless steel (304L) the initial HEL is greater, but that 2169 has a lesser degree of hardening with increased impact stress. The results are discussed in terms of structure and degree of alloying.

INTRODUCTION

200 series steels have a rapidly growing market share largely due to the relatively low costs of the manganese and nitrogen used to replace nickel content in the more common alloys. As such there is a need to investigate the dynamic strength behaviour of these materials which can be required to withstand high-rate loading when used in applications such as aircraft engine parts or reactor containment.

This paper focuses on the shear strength properties of stainless steel 2169 (SS-2169), however, other shock experiments have been undertaken by the present authors to determine its Hugoniot, Hugoniot Elastic Limit (HEL) and dynamic spall strength [1-2]. Other relevant uni-axial stress and uni-axial strain deformation experiments on SS-2169 and related materials include those by Maulik *et al.* [3], who investigated structural changes in SS-2169 through low temperature quasi-static (QS) deformation. They saw that a densely faulted structure is produced leading to the formation of deformation twins, which are the major post test constituent of the microstructure. Kassner and Breipthaupt [4] performed spilt Hopkinson pressure bar (SHPB) and QS tensile tests on SS-2169 over a range of temperatures (293 to 1023 K) and strain-rates (10^{-4}, 10^{2} and 10^{4} s^{-1}), showing an approximately constant strain-rate sensitivity of flow stress over the range of strain-rates suggesting that the mechanism of plastic flow at high and low rates is similar. Follansbee [5] also performed SHPB and QS experiments on SS-2169 over the same strain-rate regime although he showed that there was increased rate sensitivity as low as 10^{2} s^{-1}, which was attributed to the rate sensitivity of structural evolution rather than changing deformation mechanism. Gu *et al.* [6] measured the dynamic tensile strength and HEL of a similar nitronic steel (HR-2) over an initial temperature range of 300 to 1000 K at a shock stress of ~ 8 *G*Pa. Huang *et al.* [7] and Wise and Mikkola [8] undertook plate impact experiments on SS-2169 determining Hugoniot parameters in the 8 to 20 *G*Pa range. Gust *et al.* [9] performed experiments to determine Hugoniot parameters up to 320 *G*Pa for AMS 5656C, a similar nitronic steel. Brusso *et al.* [10] performed exploding foil plate shock experiments in the 20 to 53 *G*Pa range with 10 to 70 *n*s load durations, studying dislocation generation and twinning in recovered specimens to support the concept of a finite rate plastic process.

In this paper a series of one dimensional (1D) strain, plate impact experiments performed on SS-2169 are presented. Lateral and longitudinal stresses were measured over a range of impact stresses from *ca.* 1 to 18 *G*Pa in order to quantify the dynamic shear strength, a significant indicator of a material's resistance to shear localisation, fragmentation, and ballistic attack [11].

MATERIAL

The material investigated in this research is a hot-rolled, nitrogen-strengthened austenitic stainless steel. The composition supplied by the manufacturer is (in weight %): Cr - 19.56, Mn - 8.56, Ni - 6.62, Si - 0.35, N - 0.31,

T. Proulx (ed.), *Dynamic Behavior of Materials, Volume 1*, Conference Proceedings of the Society for Experimental Mechanics Series, DOI 10.1007/978-1-4419-8228-5_49, © The Society for Experimental Mechanics, Inc. 2011

P - 0.023, C - 0.02, S - 0.003, with the balance Fe. The mean density (ρ_0) is 7.75 ± 0.01 g cm^{-3}. Ultrasonic measurements give mean values of longitudinal (c_L) and shear (c_S) wave speeds of 5.69 and 3.15 ± 0.01 mm μs^{-1} respectively. The resultant mean value of the Poisson's ratio (v) is 0.279. Characterisation by electron back-scatter diffraction showed that the initial material has little crystallographic texture, an approximately equiaxed grain structure and that the mean grain size is 90 ± 40 μm. As the material has a low stacking fault energy (SFE ≈ 41 *m*J m^{-2} [12]) and has been hot-rolled, there are annealing twins in approximately 70 % of the grains.

THEORY AND EXPERIMENTS

The consequences of isotropy and elastic-perfectly plastic behaviour imply that applied longitudinal shock stress (σ_x) has hydrostatic (P) and deviatoric (τ) components, thus, $\sigma_x = P + 4\,\tau/3$. Under the same assumptions in 1D strain, P is the average of the three orthogonal components of stress, P = $(\sigma_x + \sigma_y + \sigma_z)/3$. Due to the radial symmetry of the 1D strain field, the two lateral stress components (σ_y and σ_z) are equal (assuming that the material is isotropic). Combining the two equations yields a relation for shear strength, $2\tau = \sigma_x - \sigma_y$. It is therefore seen that the shear strength can be determined by measuring both components of stress, using manganin stress gauges mounted in the appropriate orientations. The technique to measure lateral stress has been developed and discussed in detail previously [13-16] and is now used routinely to monitor the shock response of many materials.

These experiments were carried out on gas gun facilities at the Cavendish Laboratory, Cambridge University and at AWE. Manganin stress gauges, MicroMeasurements types LM-SS-125CH-048 and J2M-SS-580SF-025, were mounted in orientations that made them sensitive to measuring σ_x and σ_y respectively. For electrical insulation all gauges were mounted between two layers of mylar sheet (25 μm thick) using low viscosity epoxy resin. Longitudinal gauges were calibrated according to Rosenberg *et al.* [17]. Lateral gauges were calibrated, and voltage data converted to stress, using the methods of Rosenberg and Partom [18] with a modified analysis that does not require prior knowledge of the impact conditions [15]. Finally, the shape of the gauge itself was also taken into account as that may affect the final result [19].

Figure 1 shows the experimental configuration for the experiments measuring σ_x in the steel targets using two embedded gauges to determine the Equation of State (EoS) of the material in terms of the shock Hugoniot. Varied impact velocities of 6 mm copper flyer plates were used between *ca.* 230 to 900 m s^{-1} to generate impact stresses in the range *ca.* 4 to 18 *G*Pa. For EoS experiments 1 to 5 the targets consisted of three disks cut such that the loading direction was along the axis of the original bar stock with a rear mounted PMMA window and centrally (± 5 mm) focussed VISAR interferometry [20-21] to record the interface particle velocity. EoS experiment 6 consisted of a copper front plate and two 60 mm diameter disks of SS-2169. Further experimental details are shown in Table 1. Figure 2 shows the experimental configuration for the lateral gauge (LG) experiments measuring σ_y in the steel targets. Varied impact velocities of 6 mm copper, aluminium and PMMA flyer plates were used to obtain impact stresses in the range *ca.* 1 to 18 *G*Pa. The targets each consisted of two blocks of SS-2169 with a gauge layer between them, the gauges were mounted such that the sensitive element was approximately 4 mm from the impact face. The blocks were cut such that the loading direction was along the radial direction of the original bar stock. On one experiment (LG 6) laser Heterodyne velocimetry (HetV) [22-23] was fielded on the rear surface of the steel to measure particle velocity. Further experimental details are shown in Table 2. The alignment of the samples and flyer plates in all of these experiments were planar to within 1 *m*rad.

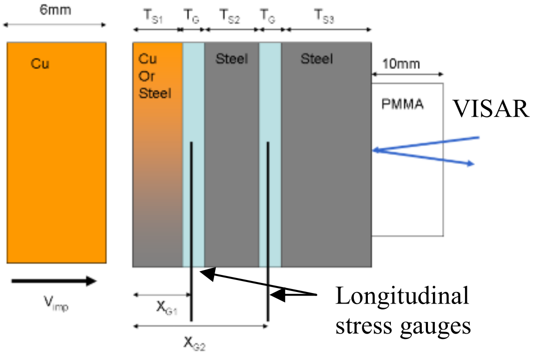

Figure 1. Schematic target design for EoS experiments. Front target plates were SS-2169 except for experiment EoS 6 which was copper. No VISAR was fielded on EoS 6.

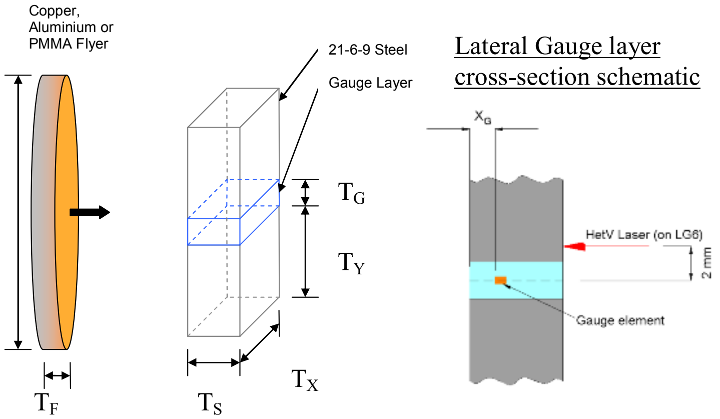

Figure 2. Schematic target design for LG experiments. T_S = 9.95 mm, T_F = 6.00 mm, T_X = 55 mm and T_Y = 15 mm.

Exp. No.	**V_{imp} (m s^{-1})** ± 0.5 %	**T_{S1} (mm)** ± 0.01	**T_{S2} (mm)** ± 0.01	**T_{S3} (mm)** ± 0.01	**T_G (µm)** ± 10	**X_{G1} & X_{G2} (mm)**
EoS 1	403	Steel 3.94	Steel 3.95	Steel 5.97	155	4.020 8.125
EoS 2	600 *	Steel 3.94	Steel 3.95	Steel 5.95	155	4.020 8.125
EoS 3	230	Steel 3.96	Steel 3.95	Steel 5.95	155	4.040 8.145
EoS 4	802	Steel 3.96	Steel 3.94	Steel 5.93	155	4.040 8.135
EoS 5	898	Steel 3.94	Steel 3.93	Steel 5.94	155	4.020 8.105
EoS 6	692	Cu 3.00	Steel 4.98	Steel 10.02	100	3.050 8.130

Table 1. Details of EoS experiments undertaken. X_G values quoted are the distance from the target front face to the front of the gauge element. * Velocity measurement for EoS 2 is only accurate to 5% due to failure of velocity pins.

Exp. No.	**Flyer Mat.**	**V_{imp} (m s^{-1})** ± 0.5 %	**T_G (µm)** ± 10	**X_G (mm)** ± 0.1	**σ_y immediately after shock (GPa)**	**σ_y 1 µs after shock (GPa)**	**σ_x (GPa)**
LG 1	Cu	219	120	4.1	2.35 ± 0.05	2.27 ± 0.05	3.90 ± 0.08
LG 2	Cu	396	120	3.8	5.86 ± 0.12	5.08 ± 0.12	7.30 ± 0.15
LG 3	Cu	592	120	3.7	9.32 ± 0.19	8.87 ± 0.18	11.33 ± 0.23
LG 4	Cu	896	120	3.7	13.89* ± 1.39	N/A	18.09 ± 0.36
LG 6 i)	Al	253	110	4.0	1.39 ± 0.03	1.36 ± 0.03	2.68 ± 0.06
ii)					1.39 ± 0.03	1.36 ± 0.03	2.48 ± 0.11
LG 8	PMMA	256	110	4.0	0.30 ± 0.01	0.30 ± 0.01	0.69 ± 0.02

* Peak value reached – gauge fails before likely maximum stress is achieved.

Table 2. Lateral gauge experiments and results. Errors in stress are 2 % for manganin gauge data [17], 4 % for longitudinal stress in LG 6 i) (as this was derived from velocimetry results) and 10 % for lateral stress in LG 4 (early gauge failure).

RESULTS

In figure 3 are presented typical longitudinal and lateral gauge results converted to stress, from the *ca.* 220 m s^{-1} impacts of 6 mm copper flyers on SS-2169 targets plates. The VISAR rear surface velocity trace is also included. Most of the stress histories show a steady rise without a distinct separation of elastic and plastic waves before reaching an approximately constant value. The features interrupting the flat tops of the longitudinal stress pulses are reflections from the other embedded gauge. The lateral gauge histories all show a steady rise and also appear to show some degree of reduction in stress with time behind the shock front.

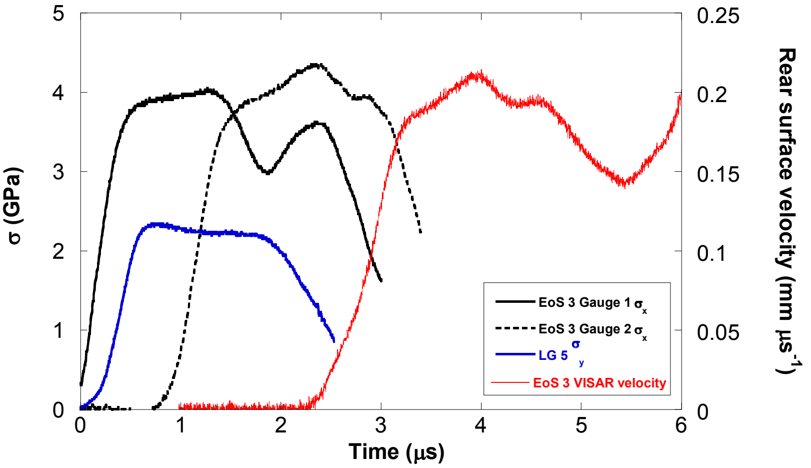

Figure 3. Gauge stress profile for experiment LG1 and gauge and VISAR records for EoS 3.

The timings of the two longitudinal gauges and rear surface velocimetry in the EoS experiments allow a direct measurement of shock velocity (U_s). Longitudinal stress in the steel is directly measured by the gauges and the in-steel particle velocity (u_p) has been measured by converting the interface velocity of the window and target using knowledge of the flyer and window material densities and Hugoniots [24-25] and assuming negligible difference between this and the release adiabat at these stresses. These measurements allow two points on the shock Hugoniot to be determined from each experiment. The shock Hugoniot states derived from this research are plotted on figure 4 in the U_s - u_p and σ_x - u_p planes together with lower shock stress experiments on the same material discussed elsewhere [1-2] and data from other researchers on similar alloys [9, 7-8]. Figure 4 indicates that the data correlates closely with that from the previous researchers despite small differences in the material compositions and conditions used. Assuming the linear relationship, $U_s = c_0 + S.u_p$, gives c_0 as 4.43 mm μs^{-1} and S as 1.43.

The HEL determined from these and previous experiments on the same steel [1] is 1.27 ± 0.64 *G*Pa. Previous research on a similar steel where targets of sufficient thickness were used to account for pre-cursor decay give a comparable HEL of 1.32 *G*Pa for a SS-2169 with a grain size of 44 *µ*m [7]. The lateral stress results are summarised in Table 2. The table shows σ_y both at the peak and 1 *µ*s after the plateau. The longitudinal stress shown is that determined from the intercept of flyer and target Hugoniots (except LG 6i which is the value determined from the velocimetry). Figure 5 shows the shear stress derived from these experiments as a function of impact stress. Also plotted are the HEL and a straight line representing the calculated elastic response for an isotropic material relating strength to impact stress thus, $2\tau = \sigma_x.(1-2\nu)/(1-\nu)$. For comparison, equivalent data for mild steel [26] and stainless steel 304L [27] have been included.

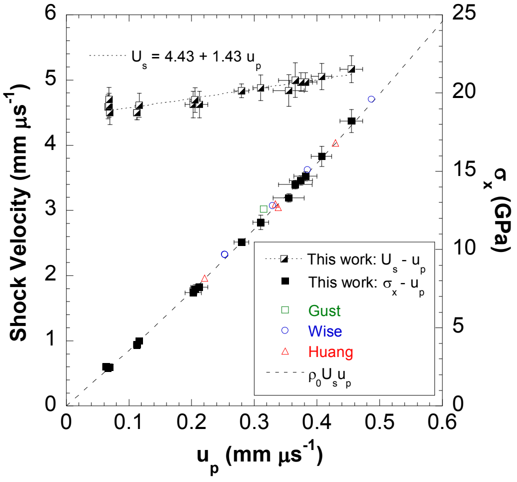

Figure 4. Hugoniot data in σ_x - u_p & U_s - u_p planes. Data from other researchers also shown. Linear fit to U_s data used to plot line through σ_x data. Error in u_p for points derived from VISAR is 2% and for those using gauges is 2 to 5 %.

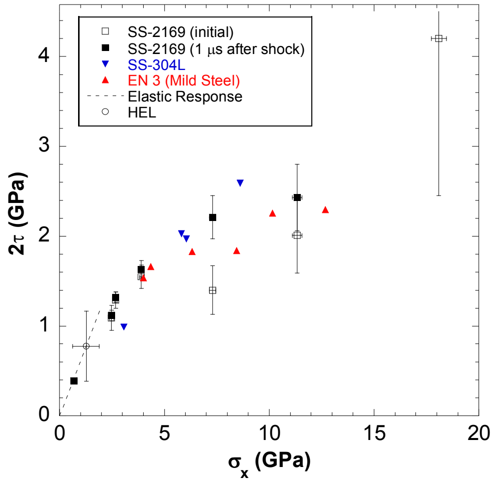

Figure 5. Plot of 2τ versus σ_x for LG experiments. Data collected from just behind the shock and 1 *µ*s after the peak is shown. HEL and elastic response are also shown along with data for stainless steel 304L and mild steel.

DISCUSSION

Figure 4 shows clearly that the shock Hugoniot of SS-2169 can be reasonably represented by a straight line in the U_s - u_p plane and that the data matches that of the previous research on similar steels as would be expected given the minor differences in alloying and grain structure. The determined HEL has a large range as the elasto-plastic wave separation was not well defined in any of the experiments. This could be explained as a result of the variation of grain sizes in this material as well as the manifestation of iterative increases in pressure caused by interaction of elasto-plastic waves and the free surface.

The results in figure 5 show the shear stress derived from experiment LG 8 which had σ_x at the lower end of the HEL range fits closely on the theoretical elastic line lending confidence to the results. At the onset of plastic deformation the mild steel is stronger than both of SS-2169 and 304L probably due to the hard iron carbide (cementite) phase acting as a barrier to dislocation motion. Both the stainless steels then have a greater hardening effect with longitudinal stress than mild steel due to their low SFE (41 *m*J m^{-2} for SS-2169 and 18 *m*J m^{-2} for 304L [12]). Low SFE means deformation via twinning mechanisms is preferred over dislocation formation and motion. The numerous deformation twins evident in almost every grain can be seen when comparing figure 6 (a), the pristine microstructure, with figure 6 (b), the recovered and sectioned target from experiment EoS 5. The hardening effect with longitudinal stress occurs because less energy is converted to dislocation motion making the material resist more permanent shape change. The effect of variation in SFE is also seen when comparing the two stainless steels as although SS-2169 has a higher HEL than 304L it shows lesser degree of hardening.

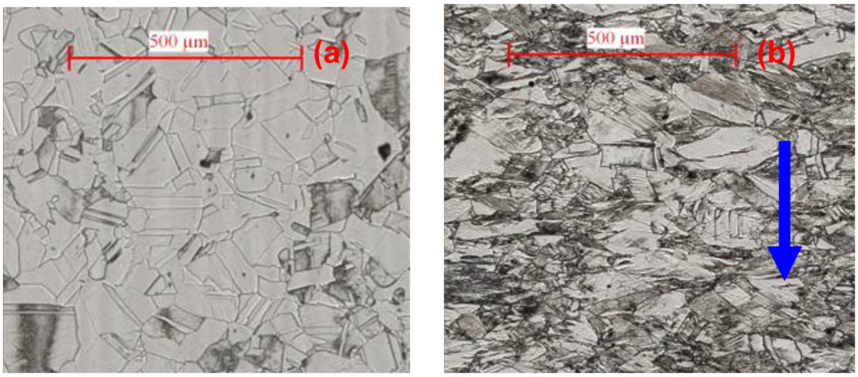

Figure 6. **(a)** Optical micrograph of pristine SS-2169 showing equiaxed grain structure with a large number of annealing twins. **(b)** Optical micrograph from recovered sectioned target from EoS 5, the shock direction is indicated by the arrow. This type of recovery does not constitute genuine 1D strain recovery although it does offer qualitative deformation information.

From the lateral gauge trace (figure 3) and the shear strength data in figure 5, it would appear that there is a degree of strengthening behind the shock front in 2169. Hydrocode modelling [28] has suggested that this is an artefact resulting from the low impedance gauge layer for experiments with σ_x up to ~ 11 *G*Pa. However, in pure nickel this apparent strengthening has also been correlated with increases in dislocation density with increasing pulse duration [29], and hence it would appear that such behaviour is a genuine material response. Additionally, such behaviour in fcc metals has also been observed to change with SFE. In Ni-60Co, where SFE was reduced to 20 – 80 *m*J m^{-2} from *ca*. 200 *m*J m^{-2} in pure nickel, this strengthening behind the shock front was seen to extend over the entire pulse duration, compared to pure nickel where strengthening was seen to be complete after *ca.* 500 *n*s [29]. It was suggested that in the alloy, initial deformation was accommodated by twinning, thereby slowing, but not stopping the contribution of dislocation based mechanisms, allowing them to operate over a longer time period. Where SFE was reduced even further, in this case 304L (16.8 *m*J m^{-2}), dislocation mobility is reduced sufficiently that twinning becomes the dominant deformation mechanism. In this case, little hardening can occur behind the shock front, and hence the lateral stress traces appear flat [30]. The SFE of SS-2169, at *ca.* 41 *m*J m-2, indicates a response more akin to that of Ni-60Co, and hence the degree of strengthening behind the shock front (figures 3 and 5) would appear to support this hypothesis. This is an example which shows that crystal structure and not necessarily constituent materials should be considered as paramount when attempting to investigate the physics of deformation mechanisms.

CONCLUSIONS

The 1D shock response of SS-2169 has been investigated to determine its Hugoniot and dynamic shear strength in the 1 to 18 *G*Pa impact stress range. A shock Hugoniot has been measured which is consistent with previous research on similar grades of steel. The shear stress has been measured and shown to increase with applied stress. SS-2169 is an fcc material of similar engineering properties to the commonly used 304L, thus 304L was chosen as a comparison, whilst bcc mild steel was compared as a common engineering steel. It has been shown that the SS-2169 is stronger than 304L. Further, it has a higher but similar hardening rate with impact stress as mild steel but lower than that of 304L. This is believed to be explainable due to the SFEs in the materials leading to an increase in twinning and dislocation interactions with resultant increase in hardening for lower SFE materials. The experiments presented here have provided useful data on this specific alloy of stainless steel and further have provided data for the increased understanding of shock response of low SFE fcc metals. Further research such as 1D strain recovery experiments are required to elucidate active material deformation mechanisms more clearly. Comparisons of these compressive strength experiments with dynamic tensile strength experiments could also prove informative.

REFERENCES

[1] Whiteman, G., *MPhil Dissertation, Cambridge University: Studies of SS 21-6-9 Varied Strain-Rates* 2007.

[2] Whiteman, G.*, et al. Spall Experiments on Stainless Steel 21-6-9 Varying Pulse Lengths and Longitudinal Stress*. in *Proceedings of the SCCM Conference*. 2009: American Institute of Physics.

[3] Maulik, P.*, et al.*, *Structural Changes in 21-6-9 Stainless Steel on Low-Temperature Deformation.* Scripta Metallurgica, 1983. **17**(2): p. 233-236.

[4] Kassner, M.E.*, et al.*, *Yield stress of type 21-6-9 stainless steel over a wide range of strain rates (10^{-5} -10^{4} s^{-1}) and temperatures.* Mechanical Properties at High Rates of Strain, 1984: p. 47-54.

[5] Follansbee, P.S., *High-Strain-Rate Deformation of FCC Metals and Alloys.* International Conference on Metallurgical Applications of Shock-Wave and High-Strain-Rate Phenomena, 1985. **28**: p. 451-479.

[6] Gu, Z.*, et al.*, *Shock response of stainless steel at high temperature.* J. Mat. Sci., 2000. **35**(9): p. 2347-51.

[7] Huang, S.*, et al. Experimental measurements of 2169 stainless steel under dynamic loading*. in *Proceedings of the SCCM Conference*. 1994: American Institute of Physics.

[8] Wise, J.L.*, et al. Hugoniot and wave-profile measurements on shock-loaded stainless steel (21Cr-6Ni-9Mn)*. in *Proceedings of the SCCM Conference*. 1987: American Institute of Physicss.

[9] Gust, W.H.*, et al.*, *Hugoniot parameters to 320 GPa for 3 types of steel.* High Temp. High Pres., 1979. **11**.

[10] Brusso, J.A.*, et al. Use of electric gun experiments to study the shock deformation behaviour of 21-6-9 stainless steel*. in *Proceedings of the SCCM Conference*. 1987: American Institute of Physics.

[11] Meyer, L.W.*, et al. Interdependencies between the dynamic mechanical properties and the ballistic behavior of materials*. in *12th Int. Symp. Ballistics 1990*. 1990. San Antonio, Texas.

[12] Schramm, R.E.*, et al.*, *Stacking fault energies of seven commercial austenitic stainless steels.* Metallurgical and Materials Transactions A, 1975. **6**(8): p. 1345-1351.

[13] Feng, R.*, et al.*, *Material strength and inelastic deformation of silicon carbide under shock wave compression.* J. App. Phys. , 1998. **83**: p. 79.

[14] Gupta, S.C.*, et al.*, *Piezoresistance response of longitudinally and laterally oriented ytterbium foils subjected to impact and quasi-static loading.* J. App. Phys., 1985. **57**: p. 2464.

[15] Millett, J.C.F.*, et al.*, *On the analysis of transverse stress gauge data from shock loading experiments.* J. Phys. D: Appl. Phys., 1996. **29**(9): p. 2466-2472.

[16] Rosenberg, Z.*, et al.*, *Longitudinal dynamic stress measurements with in-material piezoresistive gauges.* J. App. Phys. , 1985. **58**: p. 1814.

[17] Rosenberg, Z.*, et al.*, *Calibration of foil-like manganin gauges in planar shock wave experiments.* J. App. Phys. , 1980. **51**: p. 3702-3705.

[18] Rosenberg, Z.*, et al.*, *Lateral stress measurement in shock-loaded targets with transverse piezoresistance gauges.* J. App. Phys. , 1985. **58**: p. 3072.

[19] Rosenberg, Z.*, et al.* in *Proceedings of the SCCM Conference*. 2005: American Institute of Physics.

[20] Barker, L.M.*, et al.*, *Laser interferometer for measuring high velocities of any reflecting surface.* J. App. Phys. , 1972. **43**: p. 4669.

[21] Barker, L.M.*, et al.*, *Interferometer Technique for Measuring the Dynamic Mechanical Properties of Materials.* Review of Scientific Instruments, 1965. **36**: p. 1617.

[22] Strand, O.T., *Compact system for high-speed velocimetry using heterodyne techniques, .* Rev. Sci. Instrum. , 2006. **77**: p. 083018.

[23] Strand, O.T., Whitworth, T. L. *Using the Heterodyne Method to Measure Velocities on Shock Physics Experiments*. in *Proceedings of the SCCM Conference*. 2007: American Institute of Physics.

[24] Barker, L.M.*, et al.*, *Shock-Wave Studies of PMMA, Fused Silica, and Sapphire.* J. App. Phys. , 1970. **41**(10): p. 4208.

[25] Marsh, S.P., *LASL Shock Hugoniot Data*. 1980: University of California Press.

[26] Millett, J.C.F.*, et al.*, *Shear stress measurements in copper, iron, and mild steel under shock loading conditions.* J. App. Phys. , 1997. **81**: p. 2579.

[27] Whiteman, G.*, et al. Longitudinal and Lateral Stress Measurements in Stainless Steel 304 Under 1D Shock Loading*. in *Proceedings of the SCCM Conference*. 2007: American Institute of Physics.

[28] Winter, R.E.*, et al.*, *Measurement of stress perturbations caused by lateral gauges.* J. Phys. D., 2008. **41**.

[29] Millett, J.C.F.*, et al.*, *The Behavior of Ni, Ni-60Co, and Ni$_3$Al during One-Dimensional Shock Loading.* Metallurgical and Materials Transactions A, 2008. **39A**: p. 322 - 334.

[30] Millett, J.C.F.*, et al.*, *Lateral stress and shear strength behind the shock front in three face centred cubic metals.* J. App. Phys, 2009. **105**.

© British Crown Copyright 2009/MOD

Proceedings of the SEM Annual Conference
June 7-10, 2010 Indianapolis, Indiana USA
©2010 Society for Experimental Mechanics Inc.

Spall Strength of AS800 Silicon Nitride Under Combined Compression and Shear Impact Loading

Vikas Prakash, David Nathenson and Fuping Yuan

[1]Department of Mechanical & Aerospace Engineering
Case Western Reserve University
Cleveland, OH 44106-7222 USA
Email: vikas.prakash@case.edu, din@case.edu, fuping.yuan@case.edu

ABSTRACT

Plane shock wave experiments inducing compression and simultaneous compression and shear were performed on an AS800 grade silicon nitride ceramic, to measure dependence of its dynamic tensile, or spall, strength on shock induced compressive and shear stresses. The experiments were conducted using the 82.5 mm single-stage gas gun facility at Case. A multi-beam VALYN VISAR^{TM} was used to obtain the free surface velocity time profiles. The nature of the failure front and the observed variation in the measured spall strength of silicon nitride are discussed.

INTRODUCTION

Ceramic materials are being considered for use in aircraft engine components because they can surpass the thermal limitations of nickel based superalloys and other current engine materials. Ceramics exhibit higher melting temperatures, better creep resistance, and higher strength retention at elevated temperatures as compared to these materials. However, the brittle nature of ceramics can lead to premature damage and catastrophic failure due to foreign object impacts during normal and abnormal operations. AS800 grade silicon nitride is a fourth generation material with better particle impact resistance than many other ceramics [1]. In order for the strength of the material to be further quantitatively characterized however, the behavior of the material must be studied under conditions where the dynamic uniaxial material response can be discerned.

Shock compression testing yields valuable insights into the dynamic behavior of materials. The high strain rates upon impact enable the stress wave behavior to be studied. It is stress waves that cause damage to the material distinct from that of quasi-static damage. The stress wave behavior of planar shock compression impacts is predictable using one dimensional wave analysis. The Hugoniot state that exists following passage of the stress wave yields information about the shock and particle velocities as well as the dynamic stress and strain. Through the use of highly controlled planar impact conditions, material properties such as the Hugoniot elastic limit and the dynamic tensile, or spall, strength can be examined.

In shock compression testing, the material is subjected to an initial loading. This stress level, if high enough may cause the material to reach a limiting point where the deformation ceases to be elastic and becomes irreversible. This is known as the Hugoniot elastic limit, or the HEL of the material. This property is experimentally observed in the material, and it may vary according to specimen thickness and loading condition [2]. The HEL can also be related to the dynamic yield stress [3].

The compressive shock reflection from the free surfaces of the flyer and specimen generates rarefaction waves that, if the geometry is correct, intersect in the specimen to produce tensile stress. A material may exhibit spallation due to the interaction of the rarefaction waves at this point. The material's resistance to dynamic failure is dependent upon the spall strength, which is an important dynamic tensile property. The spall strength can vary with impact stress and pulse duration, and other experimental parameters.

In order to examine the dynamic behavior of AS800 grade silicon nitride under shock compression and shock compression-shear loading conditions, the 82.5 mm bore diameter single-stage gas gun facility at Case Western Reserve University was employed. Using this system, specimens were subjected to shock compression, creating one dimensional wave propagation conditions within the test specimen. Measurements of the rear surface particle velocity were then performed using a VISAR^{TM} interferometer. This particle velocity was directly related to the internal material stress state. Tests were employed under a variety of conditions, generating pure compressive stresses up to 11 GPa and compression-shear up to a normal stress of 6.9

T. Proulx (ed.), *Dynamic Behavior of Materials, Volume 1*, Conference Proceedings of the Society for Experimental Mechanics Series,
DOI 10.1007/978-1-4419-8228-5_50, © The Society for Experimental Mechanics, Inc. 2011

GPa at a fixed skew angle of 12 degrees. From these tests, the elastic shock compression, elastic-plastic shock compression and elastic shock compression-shear behavior of the material were examined.

MATERIALS

Experiments were performed on AS800 grade silicon nitride manufactured by Honeywell. These samples came in disk form with 50 mm diameter and thickness of 5.5 mm and 8 mm. The silicon nitride had a longitudinal wave speed, C_T, of 10.9 km/s and an initial density, ρ_T, of 3.27 g/cm^3 with a mechanical impedance ($Z_T=\rho_T C_T$) of 35.5 MPa/(m/s). Tungsten carbide flyers were employed to increase the attainable stress level. The tungsten carbide flyer disks were 50 mm in diameter and 2.83 mm thick. They were made by General Carbide and were of GC103 grade, which had 3.7 wt% cobalt as a binder. The disks had a longitudinal wave speed, C_F, of 6.99 km/s and an initial density, ρ_F, of 15.2 g/cm^3, which resulted in an impedance, Z_F, of 106 MPa/(m/s). The Hugoniot curve of tungsten carbide is also known [4]. A low impedance window material, PMMA was employed in the pressure-shear experiments to prevent premature failure in shear. PMMA has an elastic material impedance, Z_W, of 2.38*10^6 Pa/(m/s). These elastic impedances and wave speeds were employed in the calculation of the material behavior.

EXPERMENTIAL METHODS

A total of thirteen experiments were conducted on the silicon nitride specimens using the single-stage gas gun. These included six shock compression experiments with 5.5 mm thick silicon nitride flyers and 8 mm thick silicon nitride specimens and three shock compression experiments with 2.83 mm thick tungsten carbide flyers and 8 mm thick silicon nitride specimens. Also performed were four shock compression-shear impact experiments with 2.83 mm thick tungsten carbide flyers and 5.5 mm thick silicon nitride specimens. The impact velocities varied from 65 m/s to 528 m/s. The free surface particle velocity was raised to a maximum of 792 m/s by the impedance mismatch between the tungsten carbide and the silicon nitride. The velocity profiles of the free surface were examined to enable the determination of the material stress states.

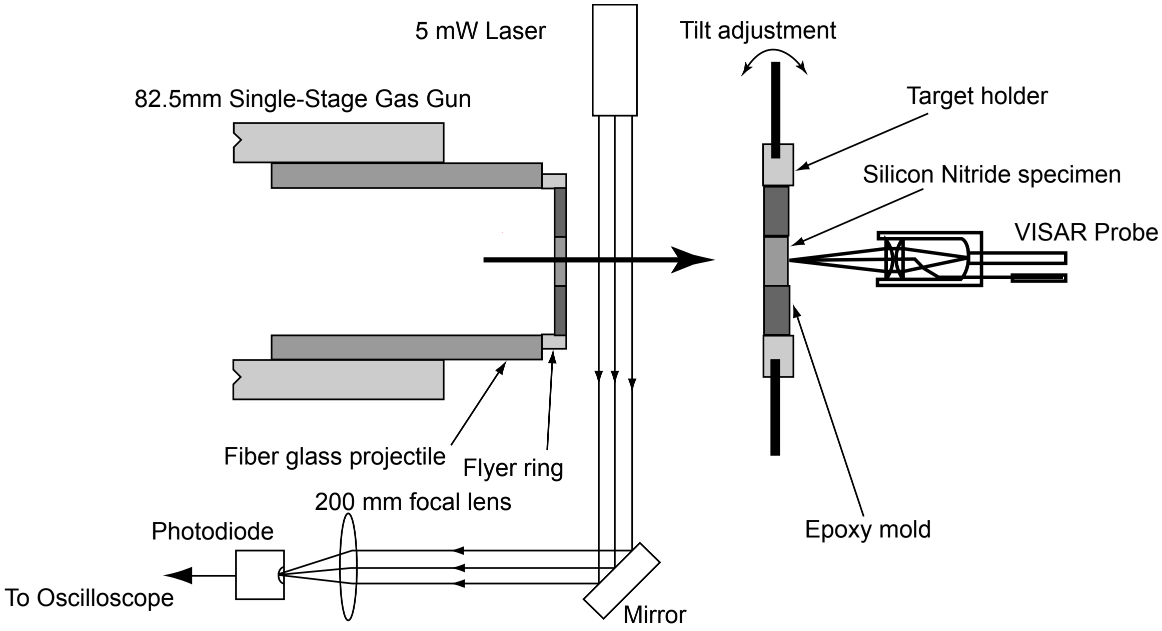

Figure 1: Experimental configuration showing gun barrel, projectile, specimen, and measurement systems.

The 82.5 mm diameter bore single-stage gas gun uses compressed air or helium to accelerate a projectile down a 4.57 meter barrel with speeds up to about 550 m/s (Figure 1). The fiberglass projectile supports the flyer of silicon nitride or tungsten carbide and assures its alignment with the silicon nitride specimen. The flyer is oriented either normal to the impact direction or at twelve degrees to the normal. The flyer and specimen plates were aligned using an autocollimator, establishing parallelism between the surfaces of 5x10^{-4} radians or better. The grounding of four isolated pins flush with the specimen surface enable the measurement of the relative tilt during the experiment. The projectile is prevented from rotating by means of an attached teflon key that fits into a key-way which traverses the length of the barrel. The impact is conducted at a vacuum level less than 50 μm of Hg to avoid the effects of air shock waves. Impact velocity is recorded using multiple laser beams, generated by a UNIPHASE Helium-Neon 5 mW laser (Model 1125p), that cut the path of the projectile and are then collimated into a high speed photo-diode (Figure 1).

Free surface particle velocity measurements are taken on the rear surface of the specimen by means of a Valyn VISAR^{TM} interferometer [5]. The rear surface of the specimen is coated with a 100 nm layer of aluminum to produce a reflective surface for the VISAR^{TM} probe. A COHERENT VERDI 5 Watt solid-state diode-pumped frequency doubled Nd:YVO$_4$ CW laser with wavelength of 532 nm is utilized for this measurement. The recorded and analyzed data produces a free surface velocity vs. time profile from which material behavior including the Hugoniot state, the HEL, and the spall strength can be calculated.

ANALYSIS AND RESULTS

Each experimental series contributed to the picture of silicon nitride behavior that is being developed. The shock compression with silicon nitride flyers was used to establish a baseline for the elastic behavior with increasing velocity. The corresponding Hugoniot elastic and hydrodynamic stresses and strains in the material are determined from the free surface particle velocities and the shock velocities (Figures 2 and 3). It is apparent from the data that the material spall strength varies with velocity (Figure 6a). The tungsten carbide flyers were used to examine the material behavior in the region of the HEL at the initiation of plastic deformation. The plastic spallation behavior of the material differs from the elastic trend. Finally, the shock compression-shear experiments were designed to measure the detriment to the material strength due to the fixed twelve degree skew angle. As will be seen below, the difference in the spall strength is distinct. The analysis will examine first the determination of the HEL and then the variation in spall strength due to various factors.

Stress vs. Strain and Shock vs. Particle Velocity

The behavior of materials under shock compression is well defined by one dimensional wave theory when edge effects can be neglected. In this case, the propagation of waves from the point of impact of a flyer and a specimen can be determined by knowing the material's shock properties and its rear surface particle velocity. The stress, strain, and particle velocity states inside the material can then be determined. The wave propagation distance vs. time profile and the stress vs. particle velocity profile enable the material behavior to be determined from these factors. These diagrams can be produced for the shock compression experiments (Figure 2) and the shock compression-shear experiments (Figure 3).

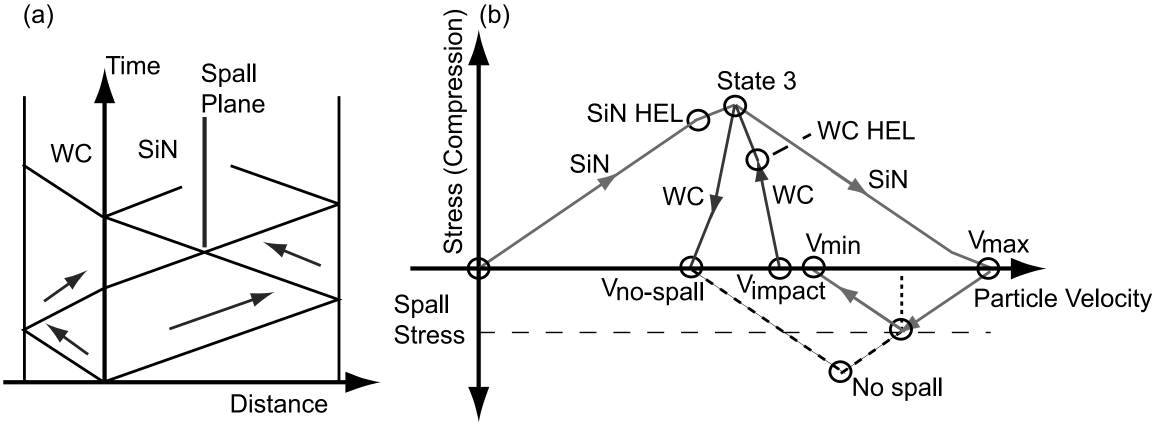

Figure 2: Stress wave propagation in a pure compression WC flyer and SiN specimen experiment: (a) Time vs. distance diagram, (b) Stress vs. particle velocity diagram.

The material shock velocity can be plotted versus the particle velocity in state 3, u_P. Particle velocity is directly obtained from the experiment. For all cases, the loading and unloading of the specimen is symmetric and the particle velocity is simply one half of the particle velocity measured at the free surface, V_4.

$$u_P = V_4/2 \,. \tag{1}$$

The shock velocity, U_S, is computed by measuring the thickness of the specimen prior to impact, T, doubling it, and dividing this by the time between the impact and the start of the wave, $t_{arrival}$, as measured on the rear surface.

$$U_S = 2T/t_{arrival} \,. \tag{2}$$

The values for each experiment are provided in Table 1. These two values are then compared to each other (Figure 4a). From this, the shock velocity can be seen to be unchanging within the elastic region. In fact, the average of the shock velocities is around 10.7 km/s, which is within 1.8 % of the elastic wave speed of 10.9 km/s. This is as expected since the shock velocity should be equivalent to the longitudinal wave speed in the elastic regime. A limited number of experiments could be conducted above the HEL due to velocity limitations of the gas gun. However, in the highest stress experiment (SC-8), the shock velocity dropped to 8.57 km/s suggesting a downward trend with increasing inelastic deformation.

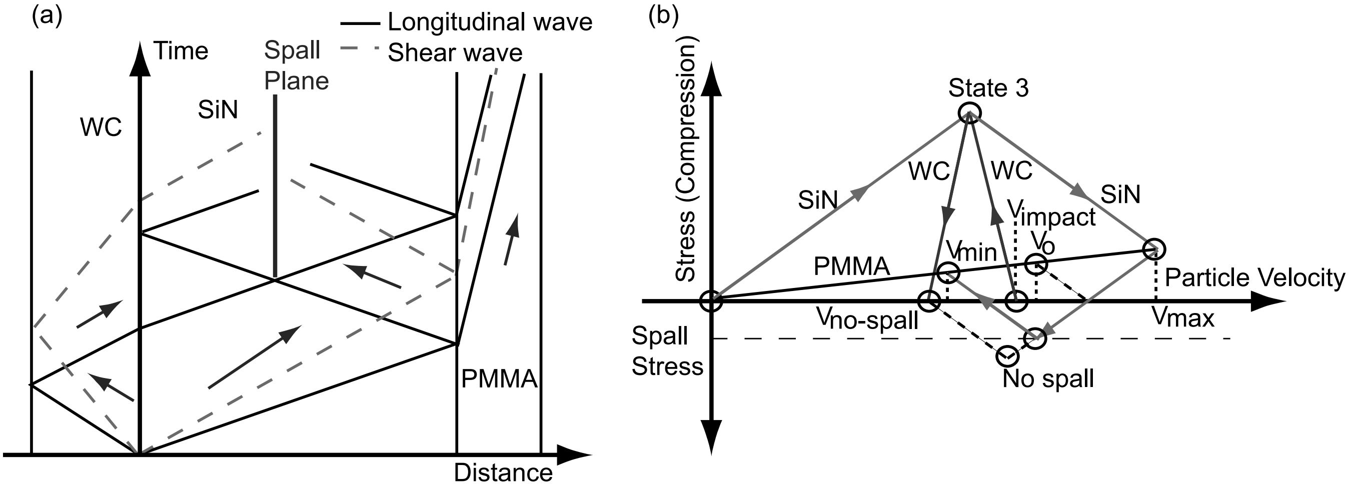

Figure 3: Stress wave propagation in a compression-shear WC flyer and SiN specimen experiment. (a) Stress vs. particle velocity diagram. (b) Time vs. distance diagram.

The Hugoniot state, which is state 3 in the above diagrams, has stress and strain levels that can be computed for each experiment, using the shock and particle velocities for that experiment. These values allow for the computation of both the elastic and hydrodynamic curves, which represent the material behavior under dynamic conditions. The elastic stress, σ_E, can be found from the elastic impedance of the material:

$$\sigma_E = \rho_O C_T u_P = Z_T u_P \, . \qquad (3)$$

The elastic strain, ε_E, is simply the particle velocity divided by the elastic wave speed:

$$\varepsilon_E = u_P / C_T \, . \qquad (4)$$

In the shocked state, a material's stress and strain can be found using hydrodynamic equations. The hydrodynamic stress, σ_H, can be computed from the shock and particle velocities using:

$$\sigma_H = \rho_O U_S u_P \, . \qquad (5)$$

The corresponding hydrodynamic strain, ε_H, can be determined by:

$$\varepsilon_H = U_S / u_P \, . \qquad (6)$$

These values are listed in Table 1. Once these values have been computed, the stress versus strain curves are plotted and indicate the dynamic behavior of the material within the elastic regime and in the beginning of the plastic regime (Figure 4b). Based on the equations for elastic stress and strain, a linear fit is drawn which represents the elastic portion of the dynamic response of the silicon nitride due to the relationship that can be obtained by combining Equations (3) and (4):

$$\sigma_E = \rho_O C_T^2 \varepsilon_E = 386 \varepsilon_E \ \text{(GPa)}. \qquad (7)$$

Additionally, an linear equation from the behavior of all of the points under the hydrodynamic calculations was:

$$\sigma_H = 191 \varepsilon_H + 1.71 \ \text{(GPa)}. \qquad (8)$$

This had an R^2 value of 0.712.

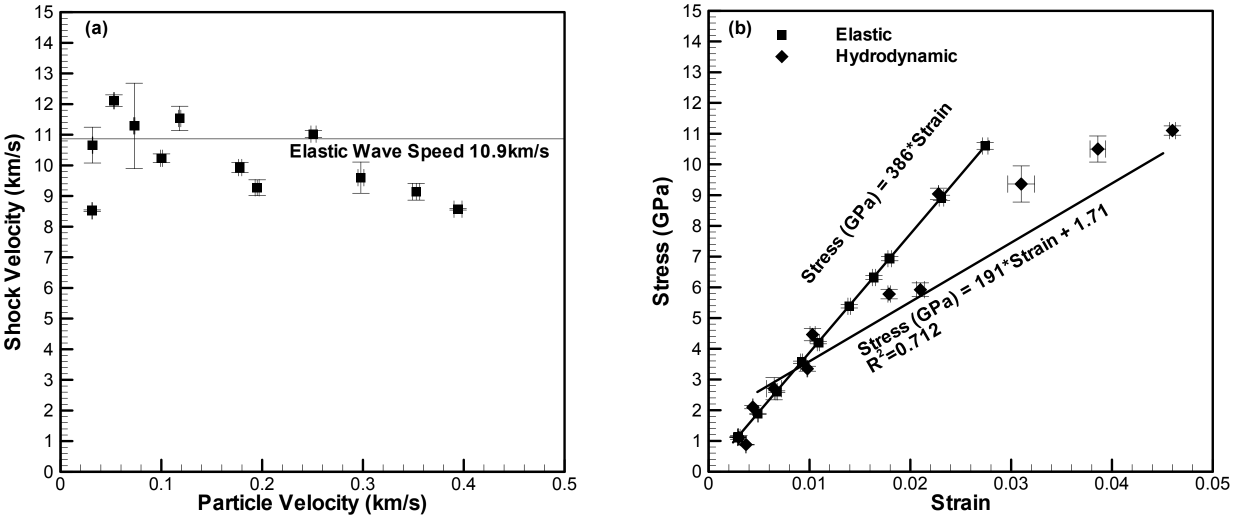

Figure 4: (a) Shock versus Hugoniot state particle velocity for all experiments. (b) Elastic and hydrodynamic stress vs. strain.

The Hugoniot Elastic Limit

The HEL is defined as the onset of inelastic deformation under dynamic loading. This point is experimentally determined by examining a sudden decrease in slope of the stress profile as it jumps from the initial state to state 3 in Figure 2b. The loading shock also has a change of slope on the S-V diagram at a point defined by the HEL velocity and stress (Figure 2b). This point is measured from the rear surface velocity history as, $V_{4\text{-}HEL}$. When plotted, the velocity profiles show the increase to the maximum compressive stresses is linear and thus elastic in all except the two highest velocity experiments (Figure 5a). The HEL is calculated according to Equation (9) as:

$$\sigma_{HEL} = \frac{Z_T V_{4-HEL}}{2} \,. \tag{9}$$

The material's plastic behavior is shown both in experiment SC-6 and to a lesser extent in experiment SC-7. From the plot of experiment SC-6 (Figure 5b), where a decrease in the slope is clearly visible at about 692 m/s, the HEL can be observed to be around 12 GPa, as expected from the literature [6]. In one case, the calculated HEL is 12.1 GPa for material with a density of 3.16 g/cm^3 and a wave speed of 10.7 km/s [6]. This characterization enables the material deformation to be broken down into two regimes, the elastic and elastic-plastic regimes. The changing deformation condition will also have an effect on the spall strength.

From the HEL estimate, the dynamic yield stress, Y_O, can be estimated. Based on plane strain assumptions, this transformation is necessary because the measured HEL stress is only the normal component of the stress within the material. According to a well established formula [7], the dynamic yield stress is related to the HEL by a factor of Poisson's ratio, ν:

$$Y_O = \sigma_{HEL} \frac{1-2\nu}{1-\nu} \,. \tag{10}$$

The dynamic yield stress of the material is therefore approximately 7.6 GPa.

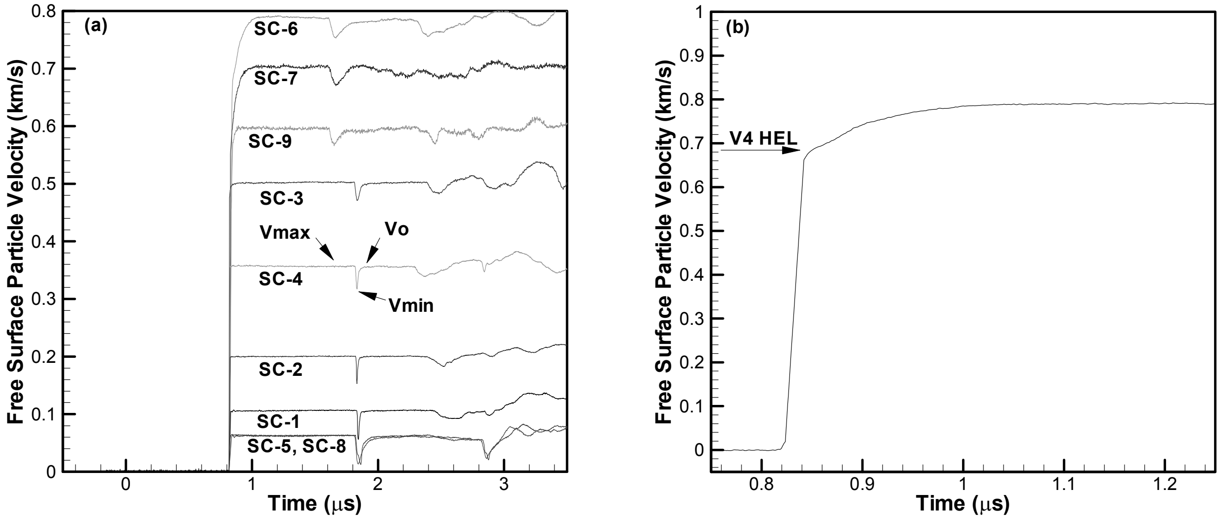

Figure 5: (a) Free surface velocity versus time profiles for the shock compression experiments. (b) In this close view of the rising pulse of experiment SC-6, the reduction in slope that corresponds to the onset of plastic deformation at the HEL can be clearly seen.

The Spall Strength Under Shock Compression

The resistance of the material to internal spallation due to the intersection of two rarefaction waves is known as the spall strength. This spall strength is a critical parameter for dynamic impacts because it represents the limiting factor for material failure. The catastrophic nature of spallation drives the necessity for the measurement of the strength of the material's resistance.

The spall strength of the material can be determined by means of free surface particle velocity measurements. Inspecting the velocity vs. time profiles of the shock compression experiments (Figure 5a), a dip can be seen that corresponds to the time at which the effect of the intersection of the two release waves reaches the rear surface. Upon the stress wave reaching the rear surface, the free surface particle velocity is at its maximum point, V_{max}. The waves created by the spall process first reduce the rear surface velocity to, V_{min}, a minimum value. This corresponds to the bottom of the dip. As the spall progresses, the rear surface velocity accelerates again to another value, V_o.

The pull back time represents the rise time from the minimum velocity, V_{min}, to the steady state velocity after the spall, V_O. At 65 m/s, experiment SC-5, the pull back time is about 0.09 microseconds, representing insufficient stress to cause an immediate brittle fracture (Figure 5a). In experiment SC-1 at 107 m/s the pull back time is 0.03 microseconds. Over most of the elastic range the pull back time slowly increases from this value. This shorter pull back time represents a sudden brittle fracture. At 502 m/s experiment SC-3, which employed the silicon nitride flyer, shows that an elongation in the pullback time to 0.09 microseconds is present. This increasing time suggests a slower accumulation of damage rather than an immediate brittle fracture. The change to the tungsten carbide flyer, which caused a shorter stress pulse width also increases the pull back time, resulting in a more lengthy damage accumulation. In experiment SC-6, which has the highest stress level, the pull back time is about 0.13 microseconds. The spall dip represents the surface de-acceleration and re-acceleration due to the material being fractured internally along the spall plane. This dip therefore is indicative of the spall strength which can be found:

$$\sigma_{Spall} = \frac{1}{2} Z_T \left(V_o - V_{\min} \right) . \tag{11}$$

This equation produces the spall strength for the normal shock experiments (Table 1). The resultant spall strengths clearly vary linearly with velocity. The spall stress resulting from increasing velocities is seen to decrease to 63% of its lower velocity value in the elastic range. That is, the spall strength drops from 895 MPa at 65 m/s free surface particle velocity, averaging the results from experiments SC-5 and SC-8, to 564 MPa at 599 m/s in experiment SC-9 (Figure 6a). This decrease indicates that as the maximum compressive stress becomes more severe, that the material resistance to spallation drops.

A linear fit was employed in order to approximate the elastic regime spall degradation. The linear fit yielded the following equation for the spall strength as a function of free surface particle velocity (km/s):

$$\sigma_{spall} = \text{-}733 V_4 + 958 \ \text{(MPa)}. \tag{12}$$

This line had a correlation coefficient of $R^2 = 0.974$. If the impact velocity is low enough, the material should not spall. However, spallation was observed in all the experiments, even at as low as 65 m/s (SC-5, SC-8) so no lower limit could be established.

Under plastic loading conditions in the two highest velocity experiments, the spall strength does not continue to drop. Instead, the spall strength measurements are near constant, being within 18 MPa of each other (Table 1). Specifically, the spall strength is 640 MPa at 708 m/s free surface particle velocity, experiment SC-7, and drops to 622 MPa at 792 m/s, experiment SC-6. The stabilization of the spall strength is most likely due to the effect of plastic deformation during shock induced compression prior to the spall. This has the effect of increasing the spall strength over what an extrapolation of the elastic trend would indicate.

The Spall Strength Under Shock Compression-Shear

The addition of shear stresses due to the 12 degree skew angle impact caused a reduction in the material spall strength. The tungsten carbide flyer plates, the same as used in the shock compression experiments above were employed here. These plates enabled higher impact stresses to be generated than is possible using silicon nitride flyers. The state of pure shear produces a component of tensile stress which, following reflection of the compressive wave from the free surface can generate material failure prior to spall if the impact velocity is high enough (Figure 3).

The state of stress inside the sample was analyzed to determine the range of velocities for which failure would occur due to tensile spall, but failure in shear prior to spallation would not. The maximum velocity for which this condition held true was found to be around 300 m/s impact speed, or 412 m/s free surface particle velocity, for the tungsten carbide flyers when a PMMA window was employed to prevent the state following the reflection of the compressive wave from being a state of zero compressive stress. The resulting experiments were carried out in the elastic regime only for the target so as not to exceed the critical parameter of premature fragmentation.

The stress wave profile due to the PMMA results in the velocity dip due to spall not recovering to the pre-dip velocity (Figure 6b). This creates a distinction between the pre-dip peak velocity, V_{max}, and the post-dip peak velocity, V_o, which was not evident in the pure compression experiments. To find the spall strength, a formula that examines the recovery portion of the dip and includes the target impedance, Z_T, window impedance, Z_W, V_o, and, V_{min}, is employed:

$$\sigma_{Spall} = \frac{1}{2}\left(Z_T + Z_W\right)\left(V_o - V_{\min}\right) . \qquad (13)$$

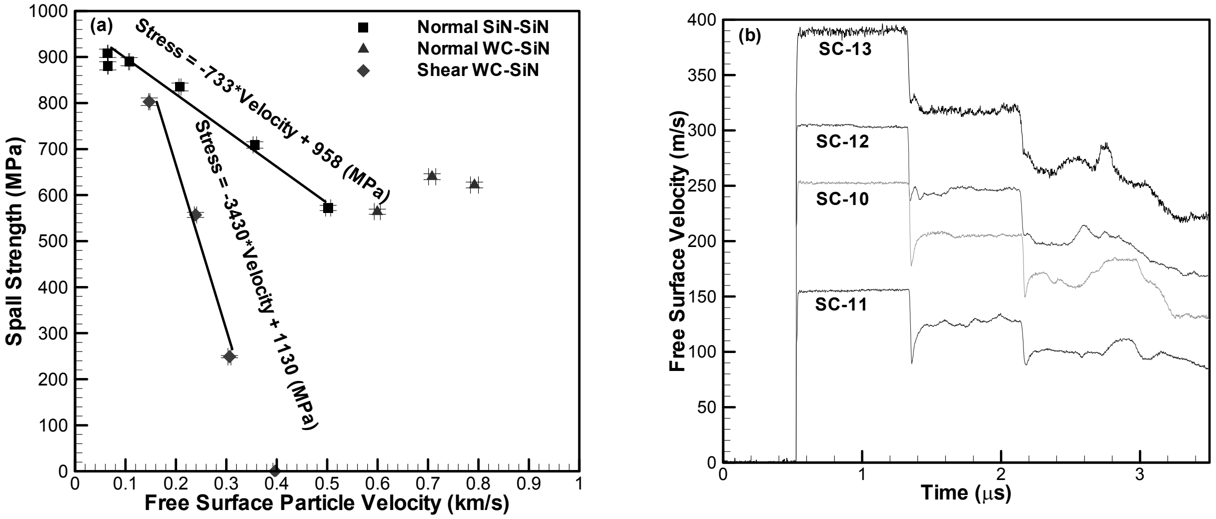

Figure 6: (a) Spall strength plotted versus the free surface velocity. Here, the effects of plastic deformation and of added shear stress at twelve degrees can be clearly seen. (b) Free surface velocity versus time profiles for the shock compression-shear experiments.

In the shock compression-shear experiments, the spall stress can be seen to drop more rapidly than the pure compressive experiments. The spall strength reduces from 803 MPa at 147 m/s free surface particle velocity to 249 MPa at 306 m/s (Figure 6a). The strength at the higher velocity is just 31% of that at the lower velocity. This steeper drop in shear indicates that the off normal loading creates a severe degradation of the spall strength even at a mild impact angle of twelve degrees.

As in the elastic compression regime, a linear fit was employed to provide a quantitative trend for the experiments. Here, the fit for the three higher spall stress points produced the following equation of spall strength as a function of free surface particle velocity (km/s):

$$\sigma_{spall} = -3430V_4 + 1330 \text{ (MPa)}. \tag{14}$$

The zero spall stress point is not used in this calculation, due to uncertainty about the velocity where the spall strength disappears. The correlation coefficient for this fit was $R^2 = 0.977$. The slope of this line is steeper by almost five times than that for the pure compressive experiments.

Because the silicon nitride HEL is never exceeded in this set of experiments, no plastic deformation occurs to retard crack growth. The shear stress enhances brittle crack growth well before the spall occurs. This shear stress causes breaking up of the material, but does not cause failure. However, it does significantly reduce the amount of stress needed to create material spall. This effect becomes more pronounced with increasing velocity. It is this process that accounts for the difference in spall strength between the shock pressure-shear and normal shock compression experiments.

Table 1: Experimental Results for Spall Stress, Shock and Particle Velocities, and Hugoniot Stress and Strain

Experiment Number	Impact Velocity	Flyer Type	θ	Spall Stress	U_S	u_P	σ_E	ε_E	σ_H	ε_H
SC-1	107 m/s	SiN	0°	908 MPa	1.21 km/s	53.1 m/s	1.88 GPa	4.89E-3	2.10 GPa	4.38E-3
SC-2	208 m/s	SiN	0°	881 MPa	1.02 km/s	100 m/s	3.56 GPa	9.22E-3	3.35 GPa	9.79E-3
SC-3	528 m/s	SiN	0°	890 MPa	1.10 km/s	251 m/s	8.91 GPa	2.31E-2	9.04 GPa	2.28E-2
SC-4	355 m/s	SiN	0°	835 MPa	9.93 km/s	178 m/s	6.32 GPa	1.64E-2	5.78 GPa	1.79E-2
SC-5	66.0 m/s	SiN	0°	709 MPa	8.52 km/s	31.5 m/s	1.12 GPa	2.90E-3	0.88 GPa	3.70E-3
SC-6	546 m/s	SiN	0°	572 MPa	8.57 km/s	394 m/s	plastic	plastic	11.1 GPa	4.60E-2
SC-7	494 m/s	WC	0°	564 MPa	9.14 km/s	353 m/s	plastic	plastic	10.5 GPa	3.86E-2
SC-8	64.9 m/s	WC	0°	640 MPa	1.07 km/s	31.8 m/s	1.13 GPa	2.93E-3	1.11 GPa	2.99E-3
SC-9	417 m/s	WC	0°	622 MPa	9.60 km/s	298 m/s	10.5 GPa	2.74E-2	9.36 GPa	3.10E-2
SC-10	186 m/s	WC	12°	803 MPa	1.15 km/s	118 m/s	4.20 GPa	1.09E-2	4.46 GPa	1.03E-2
SC-11	115 m/s	WC	12°	557 MPa	1.13 km/s	73.2 m/s	2.60 GPa	6.74E-3	2.70 GPa	6.49E-3
SC-12	233 m/s	WC	12°	249 MPa	1.74 km/s	152 m/s	5.38 GPa	1.39E-2	8.63 GPa	8.71E-3
SC-13	299 m/s	WC	12°	0 MPa	9.27 km/s	195 m/s	6.93 GPa	1.80E-2	5.92 GPa	2.10E-2

DISCUSSION AND CONCLUSIONS

The dynamic material response of silicon nitride under shock compression conditions results in information on the material's HEL and its spall strength. The HEL of the material is determined from the elastic-plastic nature of the highest level shock compression experiments. The dynamic compressive yield strength is found from the HEL. The spall strength of the material changes linearly with impact velocity. The effects of inelastic shock compressive deformation and shock compression-shear loading on the spall strength are also studied. Also, the elastic relations between the shock and particle velocity and elastic and hydrodynamic relations between the Hugoniot stress and strain are examined.

The relationship between the measured shock and particle velocities for state 3 represents the material equation of state. In this study, only the elastic regime has been covered in sufficient detail to determine the behavior. The average shock velocity corresponds within 1.8% to the longitudinal wave speed. The elastic stress vs. strain relationship, otherwise known as the Hugoniot curve exhibits similar behavior to the hydrodynamic relationship in the elastic regime. However, divergence between the two estimates occurs as the material begins to plastically deform.

In these experiments, the Hugoniot Elastic Limit indicates the beginning of plastic behavior under shock compression. In two of the normal impact experiments using tungsten carbide flyers, the material exceeded this limit. From the resulting free surface particle velocity histories, the material HEL is observed to be 12 GPa. This limit correlates well with other experimental findings for silicon nitrides. A resulting estimate of the dynamic compressive yield strength is 7.6 GPa.

The spall is the dynamic failure of the material due to the intersection of two rarefaction waves. Under shock compressive loading, the spall strength is found to decrease with increasing maximum compressive stress. The spall under elastic conditions is found to decrease by 37% from the maximum measured value, 895 MPa at 65 m/s free surface particle velocity, to the minimum measured value, 564 MPa at 599 m/s. This trend indicates a drop in the resistance to spall at higher velocities. Under plastic deformation however, the material appears to have a near constant spall strength. This indicates that the permanent material deformation under high shock compressive loads acts to counteract the reduced spall strength.

Shock compression-shear experimentation was conducted to determine the detriment of off normal impacts. In observing the impacts at 12 degrees it is apparent that the degradation in spall strength with increasing velocity occurs more swiftly than in normal impact. In fact, the spall strength decreases by 69% of its 147 m/s free surface particle velocity value, 803 MPa, by 306 m/s, where it is 249 MPa. The slope of the linear fit line is almost five times as steep as the pure compression impacts. This decreased spall strength is due to brittle mode damage caused by the shear stresses. No plasticity is present to increase the spall strength in these experiments. Thus, the material fails more easily, and above 306 m/s free surface particle velocity has almost no spall strength.

As can be seen from the experiments above, there is significant loss of spall strength both from increasing velocity and from the addition of shear loading under shock compression. The strength degradation is offset by plastic deformation under shock compression at very high velocities, where the compressive stress in the material exceeds the HEL of 12 GPa. The addition of shear stress reduces the spall strength dramatically as the impact velocity increases. The effects on spallation of these factors are of importance when determining the suitability of the material for aerospace applications.

ACKNOWLEDGMENTS

The authors would like to acknowledge financial and technical support from NASA's advanced aero-propulsion research program through grant No. NAG 3-2677 and the Case Prime Fellowship for financial support.

REFERENCES

1. Choi, S. R., J. M. Pereira, L. A. Janosik, and R. T. Bhatt. Foreign Object Damage Behavior of Two Gas-Turbine Grade Silicon Nitrides by Steel Ball Projectiles at Ambient Temperature. NASA/TM-2002-211821. 2002.

2. Graham, R. A. In: High-Pressure Shock Compression of Solids. J. R. Asay & M. Shahinpoor Ed., 75-114. 1993.

3. Meyers, M. A. In: Dynamic Behavior of Materials. John Wiley & Sons: New York. 182. 1994.

4. Dandekar, D. P. Spall Strength of Tungsten Carbide. U.S. Army Research Laboratory, ARL –TR-3335. 2004.

5. Barker L.M, Barker V.J., Barker Z.B. Valyn VISAR User's Handbook. Albuquerque, New Mexico, USA. 2000.

6. Nahme, V. Hohler, A. Stilp. Determination of the Dynamic Material Properties of Shock Loaded Silicon-Nitride. American Institute of Physics. 765-768. 1994.

7. Reinhart, W. D., & L. C. Chhabildas. Strength Properties of Coors AD995 Alumina in the Shocked State. Sandia National Laboratories. 2002.

Proceedings of the SEM Annual Conference
June 7-10, 2010 Indianapolis, Indiana USA
©2010 Society for Experimental Mechanics Inc.

Spallation of 1100-O aluminum under plate impact loading

C. Williams[a,b,*], D. Dandekar[a], and K. T. Ramesh[b]

[a] U. S. Army Research Laboratory, Aberdeen Proving Ground, MD 21005-5066

[b] The Johns Hopkins University, Baltimore, MD 21218-2681

*cwilliams@arl.army.mil

Abstract

Spallation is a failure mode that is of great importance in the understanding of a number of impact problems associated with both defense and geophysical applications. Plate impact experiments are usually conducted to study the spall behavior of materials. Spall occurs when rarefaction waves interact to generate tensile stresses that are greater than the threshold stress required for damage initiation. Damage involves the initiation, growth, and coalescence of microcracks or microvoids during tensile loading. In this work, plate impact experiments are conducted to study the effects of peak stress, pulse duration, and loading rate on the spall behavior of 1100-O aluminum. The free surface velocity and resulting pullback velocity are measured and analyzed for each experiment.

Currently, it is generally accepted that the spall strength of a material is dependent on the peak compressive shock pressure, pulse duration, and loading rate [1-7]. A review of the literature has shown the spall strength dependence on peak compressive shock pressure to vary. In general, increasing the peak pressure increases the dislocation density, stacking fault density, and number of deformation twins [8]. Stevens and Tuler [9] have shown that the peak compressive stress does not have significant effects on the spall strength of 1020 steel and 6061-T6 aluminum. Similarly, Kanel et al. [10] and Boteler and Dandekar [11] have shown respectively that the spall strengths of AD1 (1100-O aluminum) and 5083-H131 aluminum do not depend on peak compressive shock pressure. However, Chen et al. [12] and Ogorodnivov et al. [13] have observed a strong spall strength dependence on compressive shock pressure for aluminum (pure and 6061), iron, and copper. The effect of pulse duration on the mechanical response and dislocation substructure is not fully understood, but generally, increasing the pulse duration has been found to increase the post yield strength, hardness, and change the deformation substructure [6].

A total of 13 experiments were conducted to study the effect of peak pressure, pulse duration, and loading rate on the spall strength of 1100-O aluminum. Aluminum 1100-O was used for both the flyer and target material except for the case where the peak pressure was ~4 GPa, for which case the flyer material was X-cut quartz. The following properties were measured for Al 1100-O: density, ρ = 2710 kg/m^3, longitudinal wave speed, C_L = 6470 m/s, and shear wave speed, C_S = 3132 m/s. From these and other data, the following properties were calculated: bulk sound speed, C_o = 5364 m/s, shear modulus, μ = 27 GPa, Lame's modulus, λ = 60 GPa, elastic modulus, E = 72 GPa, and bulk modulus, K = 78 GPa. All shock experiments for this program were conducted using both

T. Proulx (ed.), *Dynamic Behavior of Materials, Volume 1*, Conference Proceedings of the Society for Experimental Mechanics Series, DOI 10.1007/978-1-4419-8228-5_51, © The Society for Experimental Mechanics, Inc. 2011

single stage 51 mm diameter (for velocities greater than 700 m/s) and 102 mm diameter (for velocities less than 700 m/s) gas guns at the shock physics facility at the Army Research Laboratory (ARL), Aberdeen Proving Ground (APG) . The results obtained from this work show an increase in spall strength between 4 GPa and 8.4 GPa, followed by a decrease up to 11.5 GPa. A similar trend was observed by Chen et al. [11] using 1060 aluminum with the reversal in spall strength occurring at 13.5 GPa. Further, the spall strength was observed to decrease when the pulse duration was varied from 0.31 μs to 1.55 μs. This result is in agreement with the general literature. Finally, the spall strength was found to increase as the tensile loading rate was varied from 3.61 GPa/μs to 6.30 GPa/μs and then approaches saturation at approximately 10.15 GPa/μs. The overall conclusion from this work is that recovery experiments are required to further probe the deformation mechanisms involved during the increasing and decreasing phase of the spall strength as the peak compressive pressure is varied.

Reference

[1] Johnson, J. N., Gray III, G. T., and Bourne, N. K., J. Appl. Phys. 86, 4892 (1999).

[2] Trivedi, P. B., Asay, J. R., Gupta, Y., and Field, D. P., J. Appl. Phys. 102, 083513 (2007).

[3] Murr, L. E., Shock Waves and High-Strain-Rate Phenomena in Metals (edited by M. A. Meyers and L. E. Murr), Plenum, New York, 1981, p.753.

[4] Gray III, G. T. and Follansbee, P. S., Shock Waves in Condensed Matter (edited by S. C. Schmidt and N. C. Holmes), Elsevier Science Publishers, 1988, p.339.

[5] Gray III, G. T. and Morris, C. E., Sixth World Conference on Titanium (edited by P. Lacombe, T. Tricot, and G. Beranger), Les Edition de Physique, France, 1989, p.269.

[6] Gray III, G. T. and Follansbee, P. S., Impact Loading and Dynamic Behavior of Materials (edited by C. Y. Chiem, H. D. Kuntz, and L. W. Meyer), Deutsche Gesellschaft fuer Metallkunde, Germany, 1988, p.541.

[7] Antoun, T., Seaman, L., Curran, D. R., Kanel, G. I., Razorenov, S. V., and Utkin, A. V., Spall Fracture, High-Pressure Shock Compression of Condensed Matter, edited by Lee Davidson and Yasuyuki Horie, 2003.

[8] Gray III, G. T., High-Pressure Shock Compression of Solids, edited by J. R. Asay and M. Shahinpoor (Springer-Verlag, New York, 1993), p. 186-215.

[9] Stevens, A. L. and Tuler, F. R., J. Appl. Phys. 86, 4892 (1971).

[10] Kanel, G. I., Razorenov, S. V., Bogatch, A., Utkin, A. V., Fortov, V. E., and Grady, D. E., J. Appl. Phys. 79, 8310 (1996).

[11] Boteler, J. M. and Dandekar, D. P., CP955 Shock Compression of Condensed Matter (edited by M. Elert, M. D. Furnish, R. Chau, N. Holmes, and J. Nguyen), American Institute of Physics, 2007, p.481.

[12] Chen, X., Asay, J. R., Dwivedi, S. K., and Field, D. P., J. Appl. Phys. 99, 023528 (2006).

[13] Ogorodnivov, V. A., Ivanov, A. G., and Tyun'kin, E. S., Fiz. Goreniya, Vzryva, 94, (1992).

Proceedings of the SEM Annual Conference
June 7-10, 2010 Indianapolis, Indiana USA
©2010 Society for Experimental Mechanics Inc.

Line VISAR and Post-Shot Metallography Comparisons for Spall Analysis

M.D. Furnish, Sandia National Laboratories[1]
G.T. Gray, III and J.F. Bingert, Los Alamos National Laboratory

Abstract: Key to understanding spallation phenomena is determining the spatial and temporal distribution of failure nucleation. We have conducted a series of spallation experiments on copper and tantalum using a line-imaging VISAR (LIV), which measures the velocity histories at a continuous series of points in a dynamic experiment. In these experiments on carefully characterized copper and tantalum, we attempted to produce an incipient spall condition while monitoring with LIV. Pre-shot sample characterization included spatially resolved mapping of grain locations and orientations by electron backscatter diffraction (EBSD). The samples were then soft-recovered and sectioned along the same line as monitored by the LIV. We sought to determine whether the sample distension inferred from the LIV data agree with that measured in the sectioned post-shot samples, and whether the spatial variations in the LIV data correspond more closely to failure structure on the spall plane or to near-surface grain structure (and consequent wave processing). Two experiments yielded ~1 mm spall separation; the other two are close to incipient spall conditions.

Point velocimetry has been routinely used in a wide variety of dynamic experiments since the 1971 development of VISAR [1], and in recent years methods such as PDV [2] have become important as well. However, spatially resolved velocimetry, such as the line-imaging VISAR (LIV) [3, 4], is available. However, LIV is more difficult to deploy than point velocimetry, and less commonly used. This instrument operates by illuminating a line on a target surface or interface of interest, then imaging the returned light through a VISAR (delaying one leg relative to the other, then recombining), and recording the resultant spatially resolved fringe pattern with a streak camera. For each point on the line, the streak image thus contains a fringe record providing a velocity history.

Through its ability to record velocity along a line, continuous both in time and position, LIV can provide information on the dynamic evolution of voids, joints [5] and spallation phenomena [6]. In particular, it potentially can provide enough information to deduce the evolution in time and space of nucleating and coalescing voids in a metal undergoing spallation.

Several key questions must be answered before concluding that the LIV method can definitely provide *useful* time-and-space information on the spallation process. (1) Can the position-and-time-dependent sample distension deduced from LIV be corroborated by post-shot analysis of recovered samples? The recovered samples represent the $t \rightarrow \infty$ case. (2) Are surface motion details dominated by events at the spall plane, or by near-surface grain structures? (3) What is the meaningful spatial resolution? Finally, (4) can void growth directly beneath the line be distinguished from void growth elsewhere? By the last, we mean that if the line is along the x-axis, and the surface of the sample is the x-y plane, is it possible to constrain the y-coordinate of an apparent void affecting the velocity history along the line?

The present work is designed to begin answering these four questions. Two samples each of copper and tantalum were mounted into spall rings, polished, etched, and scribed to provide landmarks for correlating the LIV-monitored line with later metallographic analyses. The samples were then carefully characterized by electron backscatter diffraction (EBSD) mapping of the crystals at the surface in the region between the scribe marks. The tantalum is from a stock obtained as commercially pure, triple electron-beam melted and annealed 10.2 mm thick plate from Cabot Corporation [7]. The average grain size was 33 - 42 μm. The copper was fully annealed oxygen free high conductivity (OFHC) copper, with 40 μm equiaxed grains following annealing at 600 ºC for 1 hour.

---

[1] Mailing Address: Sandia National Laboratories, MS 1195, Albuquerque NM 87185; email mdfurni@sandia.gov

T. Proulx (ed.), *Dynamic Behavior of Materials, Volume 1*, Conference Proceedings of the Society for Experimental Mechanics Series, DOI 10.1007/978-1-4419-8228-5_52, © The Society for Experimental Mechanics, Inc. 2011

Next the samples were assembled into targets for use in a compressed gas gun. Impactors of tantalum or copper were prepared to match the respective samples, and were half the thickness of those samples to cause mid-sample spallation. For these experiments, a soft-recovery system was built (Fig. 1), which utilizes a pellicle (breakable plastic membrane) as the terminal optical element in the line VISAR path, a spall ring stripper, and soft recovery materials. Impact conditions were chosen to give rise to incipient spall conditions with symmetric impacts: Cu-1 (144 m/s, 2.60 GPa), Ta-1 (248 m/s, 7.34 GPa), Cu-2 (116 m/s, 2.08 GPa), and Ta-2 (221 m/s, 6.51 GPa). Typical LIV results are shown in Fig. 2. Cu-1 and Ta-1 were spalled by ~1 mm; others were incipient.

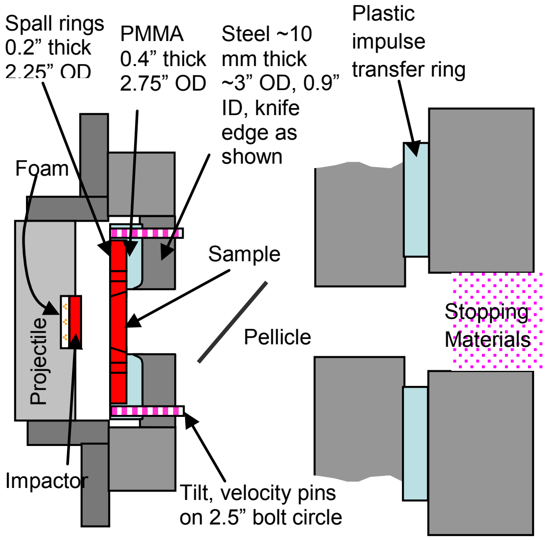
Spall rings 0.2" thick 2.25" OD
PMMA 0.4" thick 2.75" OD
Steel ~10 mm thick ~3" OD, 0.9" ID, knife edge as shown
Plastic impulse transfer ring
Foam
Sample
Pellicle
Stopping Materials
Projectile
Impactor
Tilt, velocity pins on 2.5" bolt circle

Figure 1. Shot configuration.

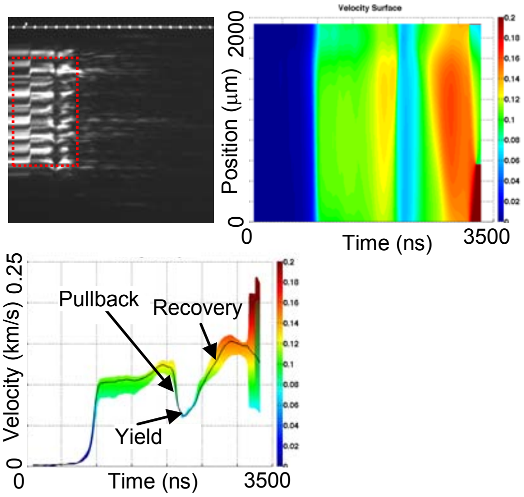

Figure 2. LIV results for Cu-1. (a) Raw streak camera record; (b) Inferred velocity surface; (c) Spatial average of velocity.

Finally, the recovered samples were analyzed for the introduction of surface defects, then prepared for a bisection along the line defined by the scribe marks for correlation with the line VISAR images. This effort is underway.

There are several areas of concern: (1) Positioning the LIV relative to landmarks on sample (using projections of the sample surface carried back to the streak camera input slit) was difficult. (2) The streak camera image had wide point-to-point intensity variations due to the sample surface and the small f-number of the system. As well, intensities varied with time, probably due to a strong dependence on sample surface tilt. (3) Recovering the sample intact was successful for all but Cu-2, in which the spall ring did not separate.

Nevertheless, it is hoped that these experiments will begin to answer the questions posed earlier determining whether LIV is useful for studying spallation mechanisms.

Acknowledgments: This work was conducted at Los Alamos and Sandia National Laboratories. Sandia is a multiprogram laboratory operated by Sandia Corporation, a Lockheed Martin company, for the United State Department of Energy's National Nuclear Security Administration under Contract DE-AC04-94AL85000.

References:
[1] Barker, L.M. and Hollenbach, R.E, J. Appl. Phys. **43**, 4669 (1972).
[2] Strand, O.T., Goosman, D.R., Martinez, C., and Whitworth, T.L., Rev. Sci. Instrum. **77**, 83108 (2006)
[3] Hemsing, W.F., Matthews,A.R., Warnes, R. H., George, M.J., Whittemore, G.R., pp. 767-70 in Shock Compression of Condensed Matter – 1991, AIP Press, 1992.
[4] Trott, W.M. and Asay, J.R., pp. 837-840 in Shock Compression of Condensed Matter – 1997, AIP Press, 1998.
[5] Furnish, M.D., Trott, W.M. et al, pp. 1159-1162 in Shock Compression of Condensed Matter – 2003, AIP Press, 2004.
[6] Furnish, M.D., Chhabildas, L.C., Reinhart, W.D. Trott, W.M. and Vogler, T.J., Int. J. Plasticity **25**, 587-602, 2009.
[7] Gray, G. T. III, N. K. Bourne and J. C. F. Millett, J. App. Phys., 94, 6430 – 6436, 2003.

Proceedings of the SEM Annual Conference
June 7-10, 2010 Indianapolis, Indiana USA
©2010 Society for Experimental Mechanics Inc.

Failure of firefighter escape rope under dynamic loading and elevated temperatures

G.P. Horn, P. Kurath
Department of Mechanical Science and Engineering, University of Illinois at Urbana-Champaign
1206 W. Green St. Urbana, IL 61801

ABSTRACT

Fire Service escape rope systems are a firefighter's last resort for a controlled exit from elevated floors of a burning structure when conditions rapidly deteriorate. The escape rope is likely to be deployed from a room that is at least partially involved with fire and must support a fully loaded firefighter making a hasty exit, resulting in dynamic loading. These dynamic loads are accompanied by elevated temperatures, which will affect the strength and stiffness of the rope. Current standards only require that escape rope systems be tested at room temperature and under quasi-static loading in order to be certified as a personal escape rope. A pilot study will be presented that provides the first experimental quantification of the decline in rope strength and stiffness at elevated temperatures. These data are interpreted with a simple kinetics model for the dynamic loading of rope for various escape scenarios, suggesting that the "factor of safety" that is assumed in current escape rope standards is quickly eliminated by the dynamic forces during escape and temperature dependent strength deterioration. Suggestions and guidelines for an improved certification protocol are forwarded.

I. INTRODUCTION

Emergency escapes from burning buildings require firefighters to have complete confidence in their equipment, especially in the likely scenario when it must be deployed from a room fully involved with fire. In these scenarios, escape efforts require the use of rope systems as life-critical components. The Fire Service has been faced with several high profile incidents in recent years where line of duty fatalities have occurred in scenarios where escape ropes have not been available or could not be deployed safely. One of the most high profile incidents occurred on January 2005 in New York City where two firefighters were fatally injured and four others were critically injured [1].

Escape rope systems consist of a length of rope, usually 50 to 75 feet long, and typically a device to control the rate of descent and a method of attaching the rope to the body and to an anchor. The only part that is required of any system is the escape rope itself. These ropes are designed to allow the firefighter to make an emergency egress and descend 3-4 stories to reach the ground or a floor below the fire. The total time to anchor the rope, make a controlled descent, and possible enter a lower floor can require several minutes even for the most seasoned firefighter. In recent years, there have been significant advances in anchoring and descent control device design and rope materials. Anchors and descent control devices are typically made from metals that can withstand the temperatures in an involved room. On the other hand, escape rope is made from polymeric materials with a much lower thermal capacity; the rope still must have enough strength and stiffness to hold the firefighter, but not be too stiff or it will cause the escaping firefighter severe injury.

When a firefighter must escape a structure fire from an elevated floor during an emergency scenario, dynamic loading of the rope system will invariably occur. The firefighter will be facing no other escape options and rapidly deteriorating conditions within the structure. He or she will be loaded with heavy and restrictive firefighting equipment and may likely be fatigue from suppression or search activities and possibly burned. Anchoring the rope in these conditions will commonly result in an excess amount of rope being paid out resulting in slack line. The rapid exit scenario may then result in a free fall condition causing dynamic loading on the rope.

The most common benchmark for the design and performance standards for rope and rope equipment that is used by fire and rescue services is *NFPA 1983: Standard on Fire Service Life Safety Rope and System Components* [2]. The minimum breaking strength (MBS) of virgin rope (tested at room temperature) is required to be 13.5 kN and rope material must have a minimum melting temperature of 200°C for the rope to qualify by the

T. Proulx (ed.), *Dynamic Behavior of Materials, Volume 1*, Conference Proceedings of the Society for Experimental Mechanics Series,
DOI 10.1007/978-1-4419-8228-5_53, © The Society for Experimental Mechanics, Inc. 2011

NFPA standard as “escape rope”. However, it is important to note that these standards do not attempt to quantify the effect that realistic service temperature might have on escape rope performance if deployed from an involved room. The reliability of escape rope systems is often directly related to its strength and stiffness, and these systems are often deployed at temperatures that are known to degrade the properties of rope. The magnitude of this degradation has not been completely documented.

This study presents the design of and initial results from a series of experiments to study the cause of strength or stiffness degradation of firefighting escape ropes in service conditions to allow estimation of dynamic loads that may be encountered when deploying the escape systems in emergency scenarios. Where possible, existing NFPA standards were followed to provide a straightforward comparison to previous data and potentially an avenue toward expanding the scope of current standards. This study considers only temperature effects but other service factors (e.g. rope bending/kinking, knot tying, and abrasions) will be studied to determine the most damaging combination of conditions for escape rope failure. For this initial study, a single brand of NFPA certified nylon escape rope was employed.

II. MODEL OF FIREFIGHTER DYNAMIC LOADING

To model the impact forces applied to a firefighter during an emergency escape, a simplified kinetics description of the rope deployment and dynamic loading scenario will be employed, Figure 1. It is assumed that the rope acts like a linear spring. Even though the load displacement plots are not entirely linear, the initial stiffness reported in Table 1 will be employed as an approximation. The firefighter will be modeled as a solid mass that does not deform and the anchor is assumed to be completely rigid. In most situations, the anchor will deflect slightly to help absorb a small amount of energy, though not as much as for sport climbers who can use the friction of carabiners and a belayer to significantly reduce the loads. These assumptions provide a worst case scenario, but one that is realistic.

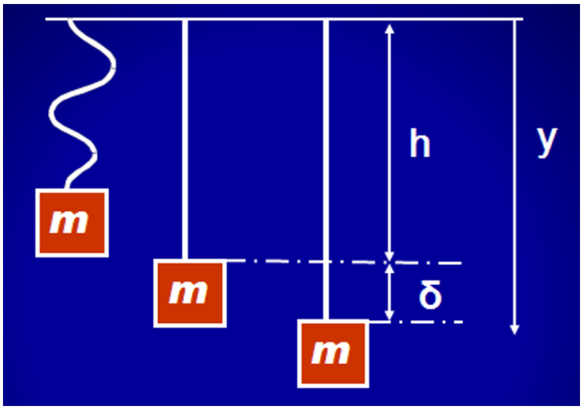

Figure 1. Simplified model of dynamic loading of rope.

A kinematics description of the scenario is provided below:

$$m\ddot{y} = mg \qquad y \le h$$
$$m\ddot{y} = -k(y-h) + mg \qquad y > h \tag{1}$$

where m is the mass of the firefighter and k is the rope stiffness. The solution to this set of equations is:

$$y = \left[\left(\frac{mg}{k}\right)^2 + \frac{2mgh}{k}\right]^{\frac{1}{2}} \cos\left[\left(\frac{k}{m}\right)t' - \phi\right] + h + \frac{mg}{k}. \tag{2}$$

For this study, we are most interested in maximum forces generated by the rope, which occurs at the point of the maximum deflection:

$$\delta_{\max} = y - h = \frac{mg}{k} + \frac{mg}{k}\sqrt{1 + \frac{2hk}{mg}} \tag{3}$$

$$F_{\max} = k\delta_{\max} = mg + mg\sqrt{1 + \frac{2hk}{mg}} \tag{4}$$

Important to the accurate utilization of this simple model is the experimental determination of the rope stiffness, k, for the conditions in which the escape rope system will be deployed. For the axial loading scenario of interest here,

$$k = \frac{AE}{L} = \frac{M}{L} = \frac{M}{L_p + L_s}, \tag{5}$$

where M is the “rope modulus”, L_p is the pay out length of the rope (between the anchoring point and exit from the building), and L_s is the length of slack in the rope that may lead to a fall outside of the exit point of the same distance. The units of rope modulus require experimental collection of load-strain data from the rope test, which presents a particular challenge in rope testing experiments due to the extensive slippage with standard rope fixtures and particularly when only a portion of the rope is maintained at elevated temperatures. Thus a new experimental protocol was developed as outlined in the next section. The rope pay out length will depend on the anchoring scenarios

There are three anchoring scenarios that we will consider with this model. The first method requires the firefighter to anchor the rope at the window sill. From anecdotal evidence, once a firefighter has made their way to the window, they are not likely to go back into the room to find an anchor, thus this may be the most common location to anchor the rope. It also results in the least amount of rope being paid out (and thus less rope available to absorb energy). The second scenario is one where an anchor is available at the bottom of the wall under the window, such as a radiator. In this case, approximately 2 feet of rope will be paid out prior to the exit location at the window sill. In the final scenario, the firefighter has anchored the rope to some remote location in the room and thus can pay out between 5 and 10 feet of rope before bailing out of the window. This scenario provides the most rope length for energy absorption, but also increases the risk of rope burn through, reduces the length available to make a safe descent to the ground, and may require a significant amount of time to access the window due to the large frictional forces required to pay out the rope over such long distances.

Equation (4) can also be derived using an energy balance approach using appropriate assumptions and has been utilized to study the effect of falls during sport climbing [4,5]. Due to the incredibly stiff ropes utilized in the Fire Service, including the direct anchoring scenarios required and the lack of a belayer (individual who plays out rope to minimize impact forces in sport climbing) in this application, many of the assumptions that bring these models into question for the climbing application are not as significant in this case.

III. EXPERIMENTAL PROCEDURES

For the elevated temperature testing of escape rope, a Riehle screw driven test frame (Figure 2) with a 44.5 kN load range was employed. Rope loading fixtures were designed and built to the NFPA 1983 standards. A furnace was designed and fabricated such that a uniform controlled temperature could be applied over a 9 inch section of rope while the test was being conducted. An extensometer was devised that utilizes a linear variable displacement transducer (LVDT) to collect deformation data in the heated section.

For these initial experiments, a 9mm Nylon kernmantle NFPA 1983 certified escape rope was tested at room temperature, 100 °C and 200 °C . Five repeats of each test were performed in accordance with NFPA 1983.To set up the tests, the rope was wrapped three times around the top fixture, and then the extensometer was attached to the gage section. This assembly was then passed through the rope furnace. Next, the rope was pretensioned around the lower fixture and then wrapped three times prior to final attachment to a cleat to minimize rope slippage. The rope was then cycled from 0.4 to 1.3 kN (10% of required MBS) multiple times until the rope had settled into the grips. The rope samples were then loaded until failure. For elevated temperature tests, the oven was ramped up to the maximum temperature in about 30 minutes and was then held at maximum temperature for approximately 30 minutes before testing to ensure a uniform temperature in the

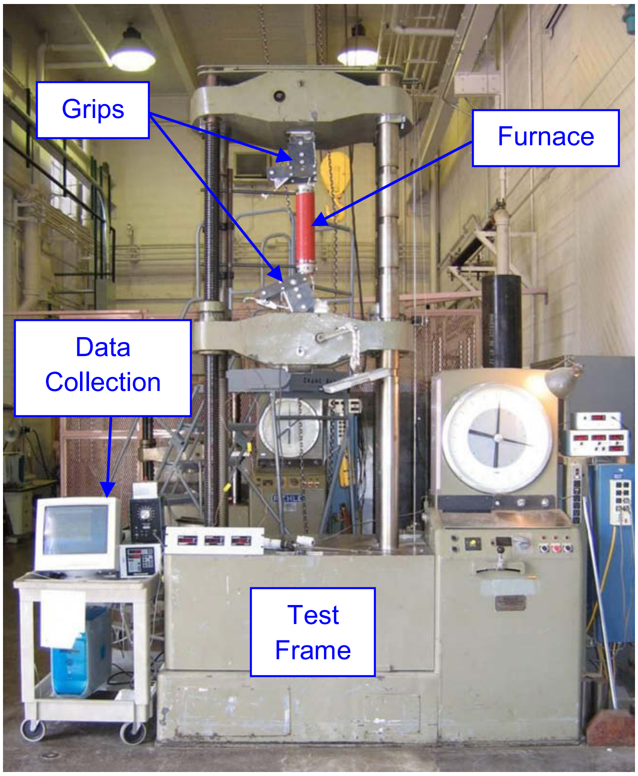

Figure 2. Experimental high temperature escape rope testing apparatus.

gage length of the rope. This procedure was established using multiple thermocouple temperature measurements along the gage length of the rope. No significant elongation or drop in load was observed during the heating or hold time.

IV. HIGH TEMPERATURE EXPERIMENTAL RESULTS AND DISCUSSION

Experimental rope strength and stiffness data is summarized in Figure 3 and Table 1. In Figure 3, a representative curve from each of the temperatures tested is provided. As Table 1 indicates the average failure strength of the rope decreases from over 21 kN at room temperature to just under 13 kN at 200°C. The standard deviation of each of the repeated tests is less than 2%, demonstrating excellent repeatability of the experiments.

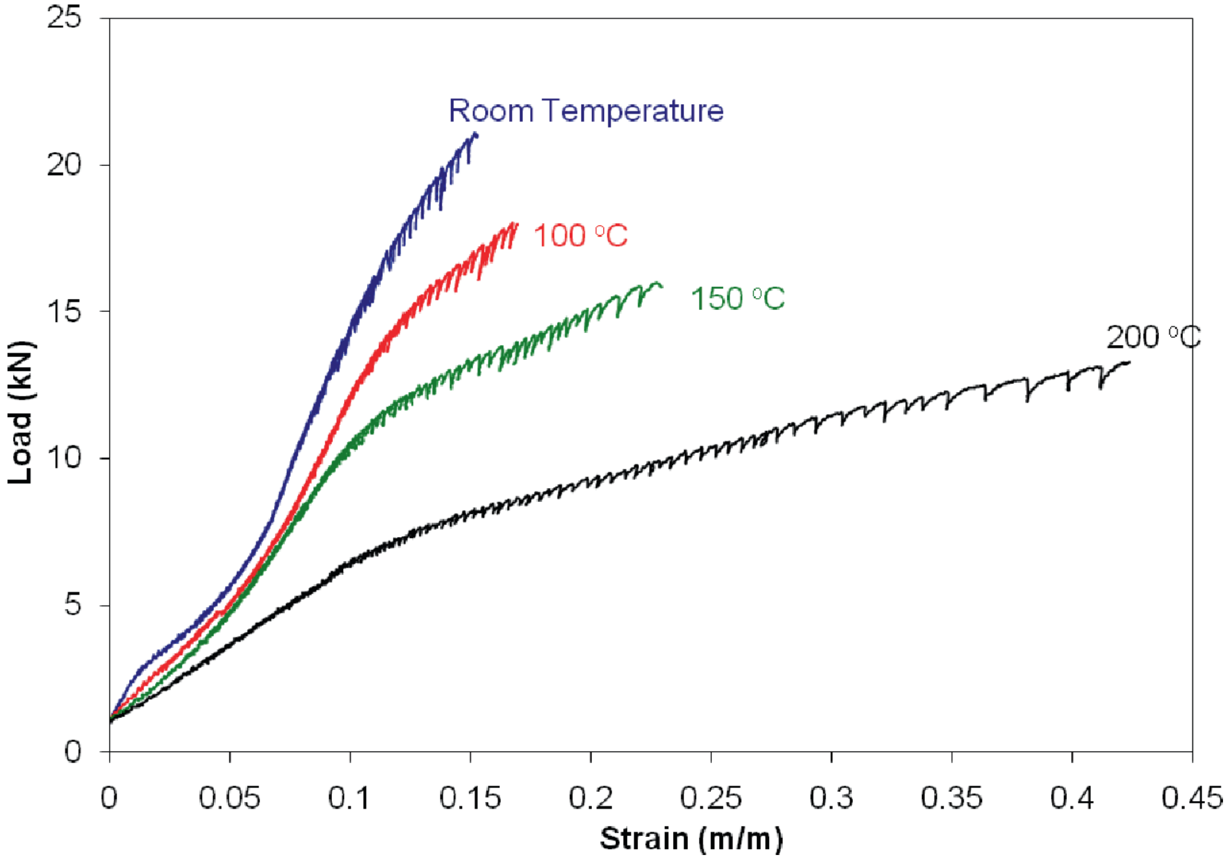

Figure 3. Escape rope load-strain behavior at various temperatures.

Following NFPA 1983 standard, the minimum breaking strength (MBS) was calculated as the average of the mean failure load minus three times the standard deviation. MBS decreases from 20.0 kN at room temperature - which satisfies the NFPA standard requirement - to 11.7 kN at 200°C - which is significantly below the required value. This tested rope is significantly stronger than required (certified at 19.3 kN at room temperature) and has a larger diameter than other available NFPA certified escape ropes. For lower rated, smaller diameter ropes that are manufactured with similar materials, the temperature at which the strength drops below the NFPA standard is likely to be even lower. The temperatures tested here are well below the windowsill level temperatures recorded during Grieff's escape rope testing [6] and thus may underestimate strength loss that could be encountered in an actual structural fire. These results are somewhat encouraging in that this rope maintained some strength at the NFPA mandated minimum melting temperature (~200°C) because nylon has a much higher melting point than required. However, they are discouraging from the perspective that conservative estimates of service temperature cause a nearly 40% drop in the breaking strength.

Table 1. Failure load and stiffness data for 9 mm nylon kernmantle escape rope.

Temp (°C)	Failure Load (kN)			Structural Stiffness (kN/m/m)
	Average	Standard Deviation	MBS	Average
20	21.4	0.5	20.0	142.5
100	17.9	0.3	17.2	118.4
200	12.9	0.4	11.7	55.7

It is apparent that as the temperature is raised from 75 to 200 °C, the rope becomes significantly more compliant. Table 1 summarizes the approximately 60% drop in initial stiffness from room temperature testing to 200 °C. This reduction in stiffness can be beneficial when the rope is subjected to dynamic loading as long as these dynamic forces do not exceed the reduced strength of the rope.

V. DYNAMIC LOADING DISCUSSION

Reviewing the functional form of equation (4), it is apparent that even an $L = 0$ m distance fall – load is applied suddenly to the rope, but no fall takes place - results in dynamic loads that are twice the static weight of the firefighter. A firefighter bailing out of a burning building in an emergency scenario will likely experience some amount of freefall due to the slack in the rope that must be taken up before the rope starts to carry some weight and these dynamic loads increase dramatically.

Figure 4a displays the results from this model for various different rope lengths assuming the static firefighter weight is 1.3 kN. It is important to note that the individual making this emergency exit will be in full firefighting bunker gear (approximately 90-110 N) and wearing a self contained breathing apparatus (minimum 110 N) in addition to other equipment and tools that they will be carrying. Thus, the static weight of the individual is significantly more than just their body weight. The horizontal lines on these figures represent the MBS of the tested rope at 20 and 200 °C. As can be seen by the four dynamic loading curves, forces on the rope increase as the fall distance increases. At the same time, the forces increase as less rope is paid out prior to the emergency exit. As Figure 4b indicates, rope at elevated temperatures generates less force than one at room temperature due to its reduced stiffness. From the perspective of dynamic loading, a decrease in stiffness is advantageous, yet one can see that even for relatively small free falls that may reasonably be expected in service, the forces in the rope may approach or exceed the MBS at these elevated temperatures.

While the strength of the rope may be sufficient to withstand 9+ kN dynamic loads, this same force will be transmitted to the firefighter through a harness (in an ideal scenario), ladder belt, or, in a worst case scenario, directly from the rope. Loads of this magnitude could cause severe bone and skin injuries as well as potential internal organ trauma. Furthermore, if an anchor is not properly set into a solid material or structure, it can pull out or fail under this level of loading.

Dynamic loading becomes increasingly important when one considers using a stiff aramid escape rope. For instance, Technora ropes have been introduced as a high strength, low weight option that does an excellent job retaining strength properties at elevated temperatures. Unfortunately, these systems also have a structural stiffness that is almost an order of magnitude stiffer than similar strength nylon ropes. If a 1.3 kN firefighter takes a 0.6 m fall on Technora rope with a 0.6 m payout($L_p = 0.6$ m, $L_s = 0.6$ m), the dynamic load would be 37.6 kN (compared to 15.2 kN for the tested nylon rope at room temperature). As a result of these forces, it is highly recommended that escape ropes, and especially Technora ropes, be employed with a device that assists in absorbing dynamic loading to minimize impact force on the rope and body.

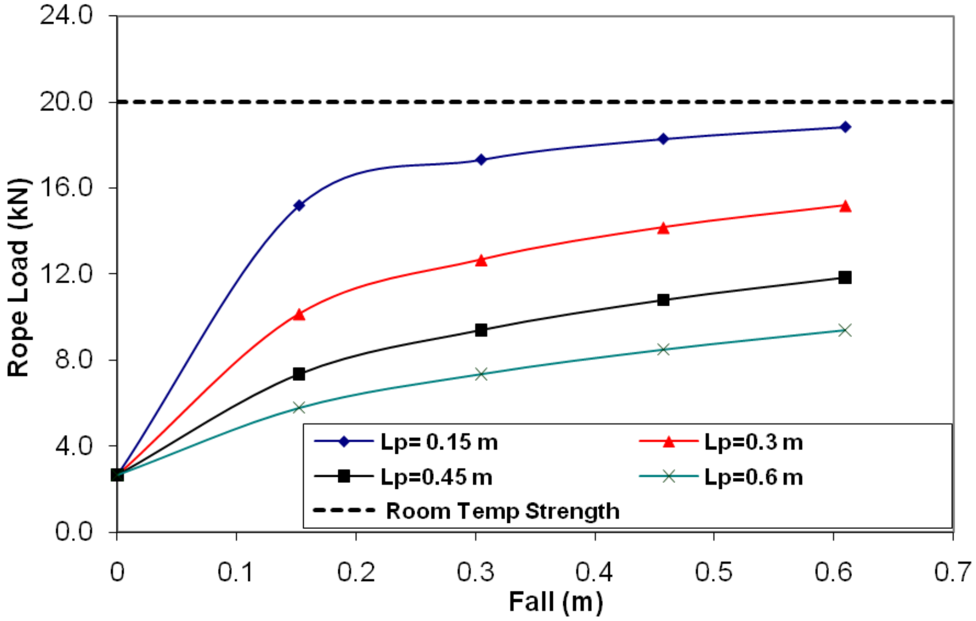
(a) 1.3 kN Firefighter on 9.0 mm Nylon at Room Temp

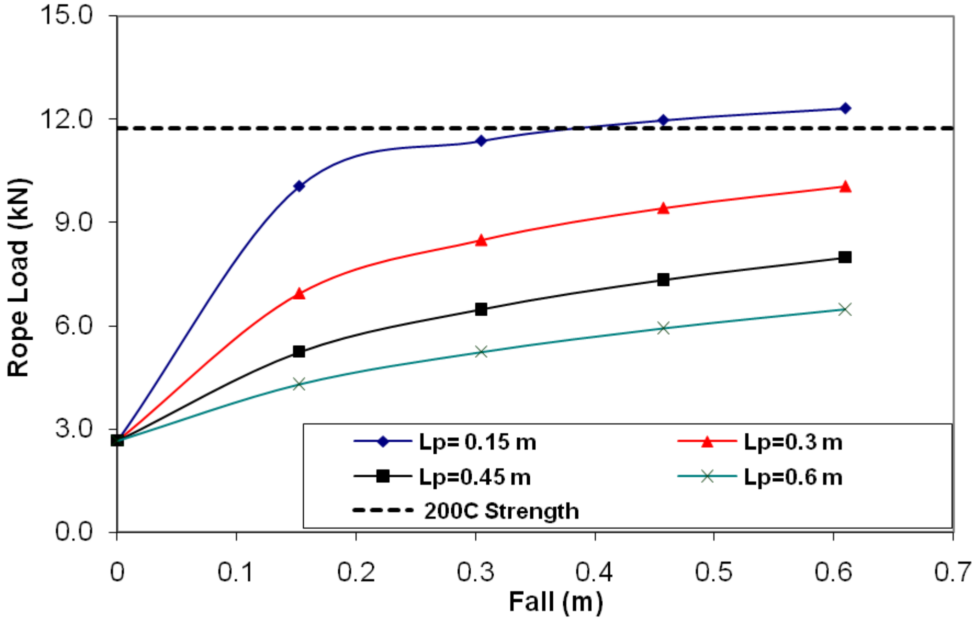
(b) 1.3 kN Firefighter on 9.0 mm Nylon at 200 °C

Figure 4. Dynamic loads on a rope for various fall lengths (L) and pay outlengths (L_p), for a 1.3 kN firefighter at room temperature and 200°C.

Finally, a longer anchor length (L_p) relative to the fall distance will significantly reduce the forces in the rope. Though not always practical, it may be possible to anchor the escape rope further from the exit point; potentially across the room from an escape window. If, for example, the attachment length could be increased, the maximum force encountered by the rope for the 1.3 kN firefighter taking the same fall distance (L = 0.6 m) is reduced from 15.2 kN (L_p = 0.6 m) to 9.4 kN (L_p = 3.0 m) at room temperature for the rope tested in this program.

V. CONCLUSIONS

A basic study of the effect of dynamic loading was presented in conjunction with the development of a high temperature rope testing apparatus. The experiments have allowed the first quantification of strength and stiffness of rope systems at elevated temperatures. The relatively small increase from 20 ºC to 200 ºC results in a nearly 40% reduction in strength and 60% reduction in stiffness. The rope tested in this initial study was nearly 50% stronger than the NFPA standard requirement at room temperature and yet when tested at 200 ºC, its strength was below NFPA 1983 minimum.

Using a kinetics description of the fall event, the dynamic loads that may be experience due to a fall on this type of rope were estimated. Even for relatively small free falls that may reasonably be expected in service, the forces in the rope may exceed the minimum breaking strength of the rope. This simple model also provides some helpful hints for deploying escape rope systems. If operationally feasible, minimize rope slack and free falls to reduce the risk of escape rope failure. Even if the rope does not break, the large forces generated by dynamic loading highlight the need for training in exit strategies and rope anchoring procedures to reduce injuries. Techniques for exiting windows that significantly reduce or eliminate dynamic loads should be taught and employed whenever possible. Dynamic forces can be significantly reduced by employing a descent device or technique that allows friction to absorbs a significant portion of the impact from these falls. It is also possible that an additional energy absorption device between the firefighter and the rope can be employed to reduce these loads. The issue of high impact loads is magnified when dealing with higher stiffness escape ropes such as Technora systems. Appropriate placement and fastening of the rope anchor is critical for surviving even small falls without injury. Finally, while not always practical, fall loads can be significantly reduced if it is possible to anchor a greater distance from the point of exit.

Testing rope properties at elevated temperatures is an important process that NFPA may want to consider for future editions of NFPA 1983 standard for escape ropes. Collection of both strength and stiffness data is recommended as it allows a more detailed analysis of the damage caused by elevated temperatures. For the nylon rope tested here, the significant reduction in stiffness resulted in lower forces from dynamic loads, which somewhat mitigated the effect of reduced strength at 200 °C. The only way to measure changes in these rope properties at elevated temperatures is to develop a standardized test procedure.

ACKNOWLEDGEMENTS

The authors thank Ernie Timmons for his assistance in building the furnace for elevated temperature rope testing.

REFERENCES

1. O'Donnell, M., "City Firefighters Build Their Own Escape System", *The New York Times*, June 6, 2005. http://www.nytimes.com/2005/06/06/nyregion/06ropes.html?ex=1153022400&en=1a9c55bc589e5d0b&ei=5070
2. *NFPA 1983: Standard for Life Safety Rope and System Components, 2001 Edition*. National Fire Protection Association, Quincy, MA.
3. *Firefighter's Handbook: Essentials of Firefighting and Emergency Response*, 2nd Edition, Delmar Thomson Learning, Clifton Park, NY, 2004
4. Vogwell, J., and Minguez, J.M., "The safety of rock climbing protection devices under falling loads", *Engineering Failure Analysis*, **14**, 1114-1123, 2007.
5. Pavier, M., "Experimental and theoretical simulations of climbing falls", *Sport Engineering*, **1**, 79-91, 1998.
6. Greiff, J.S., "Performance Tests of personal escape rope systems", *Fire Engineering*, 45-60, 2001.
7. McKently, J., Parker, B., and Smith, C., *Escape line bake off* , presented at ITRS, 2003

Proceedings of the SEM Annual Conference
June 7-10, 2010 Indianapolis, Indiana USA
©2010 Society for Experimental Mechanics Inc.

Determination of True Stress−True Strain Curves of Auto-body Plastics

Chunghee Park[1)]·Jinsung Kim[1)]· Hoon Huh[*1)]·Changnam Ahn[2)]

[1)] School of Mechanical, Aerospace and Systems Engineering, KAIST, 335 Gwahak-ro,

Yuseong-gu, Daejeon 305-701, Republic of Korea

[2)] Hyundai & Kia Corporate Research & Development Division, 772-1 Jangduk-dong,

Hwaseong-si, Gyeonggi-do 445-706, Republic of Korea

chungheepark@kaist.ac.kr, soitgoes@kaist.ac.kr, hhuh@kaist.ac.kr

and fedummy@hyundai.com

ABSTRACT

This paper is concerned with tensile characteristics of auto-body plastics at various strain rates ranging from 0.001/sec to 100/sec. Tensile characteristics at the high strain rate are important in prediction of deformation modes of plastic components which undergo the high-speed deformation during car crash. Uniaxial tensile tests at the quasi-static strain rate were conducted at strain rates ranging from 0.001/sec to 0.01/sec by using a tensile testing machine, INTRON 5583. Uniaxial tensile tests at intermediate strain rates were conducted at strain rates ranging from 0.1/sec to 100/sec by using a high-speed material testing machine developed. Since the deformation of plastics is accompanied with localized deformation and a conventional extensometry method(CEM) is no longer valid for strain measurement, a force equilibrium grid method(FEGM) is newly proposed in order to acquire accurate true stress−true strain curves of plastics. FEGM is utilized with image capture of non-uniform distribution of deformation at each elongation stage from a high speed camera in aids of grid methods. The relation between true stress and true strain at the designated strain rate and increment were obtained by collecting the load data by the equilibrium and the deformation images.

1. Introduction

The plastic has been widely used in the interior of an automobile such as a dashboard and an airbag module. It also has been utilized in the exterior such as a bumper. The interior parts of an automobile directly influence the safety of passengers with the fracture of the plastic component. Therefore, tensile properties of the plastic should be fully identified to predict damages of passengers. Tensile properties of the plastic at the high strain rate have to be applied to the design of the vehicle in case the vehicle undergoes high-speed deformation such as car crash. Especially, tensile properties of the plastic at intermediate strain rates are important since the range of the strain

T. Proulx (ed.), *Dynamic Behavior of Materials, Volume 1*, Conference Proceedings of the Society for Experimental Mechanics Series,
DOI 10.1007/978-1-4419-8228-5_54, © The Society for Experimental Mechanics, Inc. 2011

rate is several tens to hundreds per second in a real auto-body crash.

Static tensile properties of the plastic are well known by a standard tensile testing method using a standard specimen. However, it is difficult to obtain tensile properties of the plastic at the high strain rate influenced by the strain rate because testing methods and conditions are complicated and are not specified in the standard yet. Engineering stress−engineering strain curves are acquired by uniaxial tensile tests at the quasi-static and intermediate strain rates. True stress−true strain curves converted from engineering stress−engineering strain curves are required for finite element crash analysis of those plastics. In metallic materials, the gauge section deforms uniformly during uniaxial tensile tests so that the conventional extensometry method(CEM) has been used to acquire true stress−true strain curves. However, in plastic materials, the strain is non-uniformly concentrated due to the localized deformation in the gauge section. Thus, a new converting method is required to acquire accurate true stress−true strain curves of the plastics.

There are many researches dealt with the strain rate effect of the plastic. Walley et al. [1] studied on the deformation behavior of various polymers in terms of the strain rate. Cook et al. [2] investigated the effect of the strain rate and the composition for epoxy-resin. CEM is used in order to acquire true stress−true strain curves of general metallic materials which undergo uniform deformation in the gauge section [3-6]. However, stress and strain concentrations happen with non-uniform deformation after the necking in auto-body plastics. Consequently, CEM is no longer valid for auto-body plastics. Solving this problem, several researches were conducted. Marquez̃Lucero el al. [7] observed a propagation of the necking of circular plate specimen, and Parsons el al. [8] measured strain of three axes simultaneously during uniaxial tensile tests. Kim el al. [9] introduced optimization method using the finite element method in order to predict true stress−true strain curves of polypropylene.

In this paper, uniaxial tensile tests at the quasi-static and intermediate strain rates are conducted to acquire tensile properties of auto-body plastics with the variation of the strain rate. There exist so many different kinds of plastics and material properties are also different in accordance with kinds of plastics. Hence, the deformation behavior should be analyzed for each kind of plastics in order to acquire accurate true stress−true strain curves. A force equilibrium grid method(FEGM) is newly proposed as a method to analyze the deformation behavior accurately at the strain rates to acquire accurate true stress−true strain curves. Flow stresses are obtained grid-wise with the use of the equilibrium of each grid under applied tensile force. The accuracy of the proposed method was evaluated with finite element analysis which simulates uniaxial tensile tests of the specimen at intermediate strain rates using acquired tensile properties of the plastics.

2. Uniaxial tensile tests of auto-body plastics

2.1. Experimental conditions

Tensile specimens for the standard test are specified in the regulation of ASTM IV as shown in Figure 1.a. However, this regulation is valid for the quasi-static test and does not include the high-speed tensile testing method and the corresponding specimens. A modified ASTM IV standard specimen with an extended grip section is used for uniaxial tensile tests for intermediate strain rates in order to realize the desired tensile velocity. The length of the gauge section is 33 mm, the width is 6 mm and the thickness is 2 mm. Grids are marked with an interval of 1 mm in order to observe the non-uniform deformation behavior and measure the instantaneous strain conveniently. A tensile test specimen with grid marks is shown in Figure 1.b. Material used in uniaxial tensile tests is acrylonitrile butadiene styrene(ABS). Uniaxial tensile tests at the quasi-static strain rate are conducted at strain rates ranging from 0.001/sec to 0.01/sec by using the tensile testing machine (INSTRON 5583) and uniaxial tensile tests at intermediate strain rates are conducted at strain rates ranging from 0.1/sec to 100/sec by using a high-speed material testing machine(HSMTM) developed.

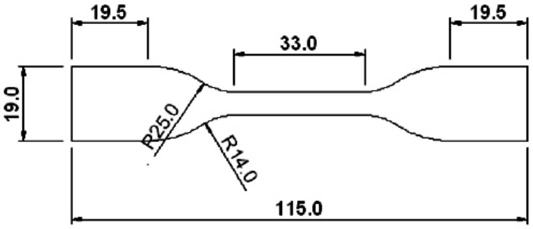

1.a. ASTM IV standard specimen.

1.b. Tensile test specimen with grid marks.

2.2. Experimental results

Engineering stress−engineering strain curves acquired from uniaxial tensile tests at the quasi-static and intermediate strain rates are shown in Figure 1.c. The results show that the flow stress increases as the strain rate increases. A converting process from engineering stress−engineering strain curves to true stress−true strain curves is required for accurate structural analysis at high strain rates. A CEM usually applied to general metallic materials is valid when the specimen deforms uniformly in the entire gauge section. However, the deformation of the plastic is localized on a small portion of the gauge section as shown in Figure 1.d. and a CEM is not applicable to measure the elongation corresponding to the flow stress. In order to measure accurate strain correctly, localized deformation in a small portion of the gauge section has to be carefully evaluated with the corresponding flow stress. A new analysis method has to be developed to convert engineering stress−engineering strain curves to true stress−true strain curves.

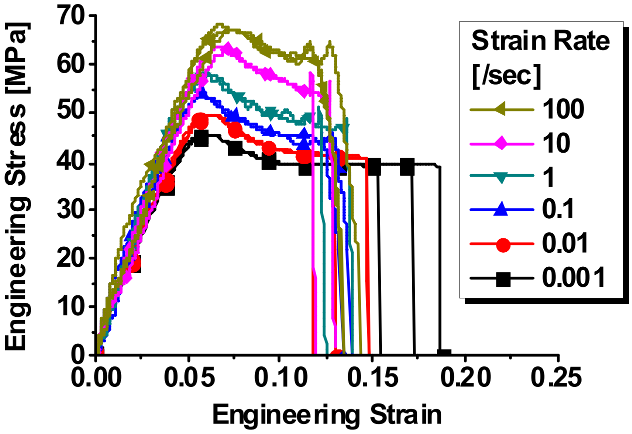

1.c. Engineering stress−engineering strain curves with the variation of the designated strain rate.

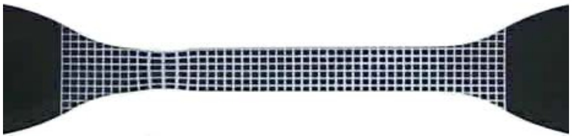

1.d. A deformed shape of an auto-body plastic during a uniaxial tensile test.

3. Force equilibrium grid method(FEGM)

3.1. Basic concept of FEGM

A force equilibrium grid method is proposed to convert engineering stress−engineering strain curves to true stress−true strain curves. Figure 2.a. demonstrates the deformation behavior of a plastic specimen during a uniaxial tensile test. In order to calculate a correct flow stress at each deformation stage, a concept of the force equilibrium is utilized in each grid system. A free-body diagram of three grid elements marked in the Figure 2.a.(1) shows that the applied forces of each grid element, F_1, F_2 and F_3, are equal to each other along the axial direction. From the force equilibrium condition, the relation among these forces is expressed below:

$$F_1 = F_2 = F_3 \tag{1}$$

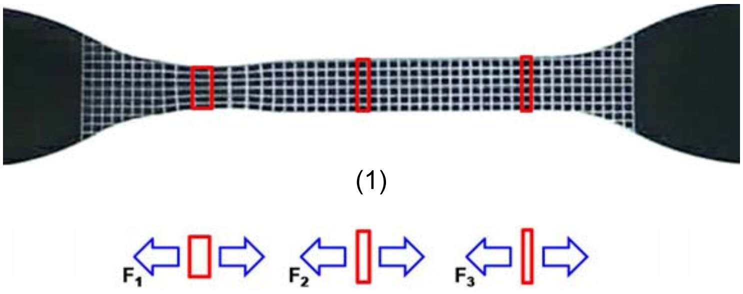

(1)

(2)

2.a.(1) Deformed shape of three grid elements during a uniaxial tensile test;
(2) free-body diagram of three grid elements.

Using this basic concept, the true stress can be obtained from applied forces and the true strain can be obtained from measuring amount of the deformation of a grid at each time increment of a uniaxial tensile test. This new converting method can measure the true strain and calculate the true stress using captured images with a high-speed camera and force data during a uniaxial tensile test. It should be noticed that this method requires several specimens with tensile tests at different strain rates for a true stress−true strain curve at the designated strain rate since the strain rate is different from point to point within the gauge section due to non-uniform deformation.

3.2. The relation between true stress and true strain

Deformation images obtained from a uniaxial tensile test were analyzed in order to collect the relation between true stress and true strain at each grid element for the specific strain and strain rate. Comparing the two grid elements with the constant time increment, the strain and strain rate can be calculated simultaneously. This process is carried out at each time increment, *i*-th step, until the last *n*-th step. The true strain increment of the single grid element along the axial direction after the constant time increment, *dt*, can be represented as below:

$$d\varepsilon_{true} = \ln\left(1 + d\varepsilon_{eng.}\right) = \ln\left(1 + \frac{l' - l}{l}\right) = \ln\frac{l'}{l} \tag{2}$$

The true strain is calculated from the integration of the true strain increment as below:

$$\varepsilon = \sum_{i=1}^{n} \left(d\varepsilon\right)_i \tag{3}$$

Assuming the incompressible condition of the material, a cress-sectional area can be obtained from the length of the element using a formula below:

$$l_0 A_0 = l_0 w_0 t_0 = lwt = lA \quad \text{or} \quad A = \frac{l_0}{l} A_0 \tag{4}$$

Finally, the true stress can be calculated using the load data at the instant and the cross-sectional area as below:

$$\sigma = \frac{F}{A} = \frac{F}{wt} \tag{5}$$

In this way, the relation between true stress and true strain at each deformation increment are obtained for grid elements in the gauge section. In order to collect different data for true stress−true strain, six elements from three regions which have remarkably different deformation behavior were chosen as shown in Figure 2.b. Obviously, the true stress−true strain data obtained from the three regions are different from each other in terms of stress, strain and strain rate.

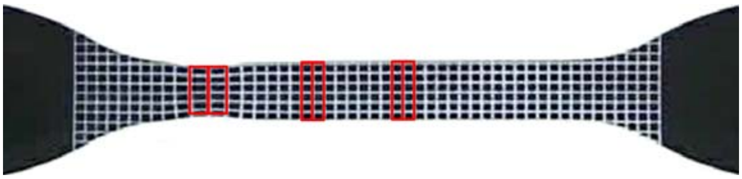

2.b. Three regions which have different deformation behavior.

3.3. Examination of actual strain rates

The true strain with respect to time is measured and shown in Figure 2.c. The true strain varies in accordance with deformation behaviors of specimens. Even in the same grid element, the true strain varies with respect to time. Since the strain rate of grid elements does not correspond to the designated strain rate of uniaxial tensile tests, a calculating process of the actual strain rate is required through observation of deformation behaviors of grid elements.

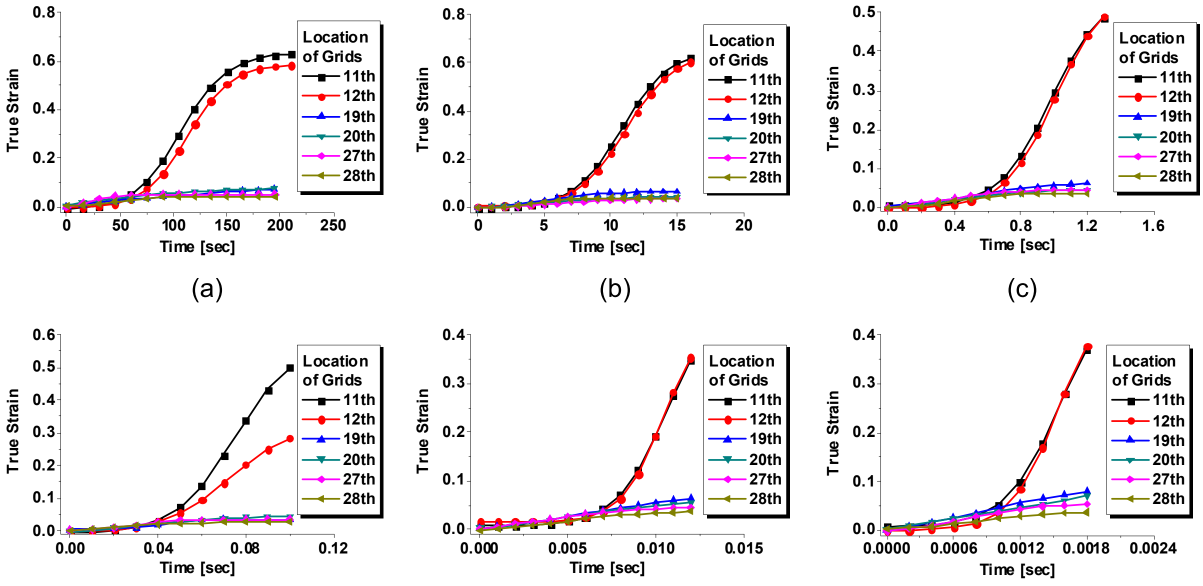

(a) (b) (c)

(d) (e) (f)

2.c. Variation of the true strain with respect to time at various designated strain rates:
(a) 0.001/sec; (b) 0.01/sec; (c) 0.1/sec; (d) 1/sec; (e) 10/sec; (f) 100/sec.

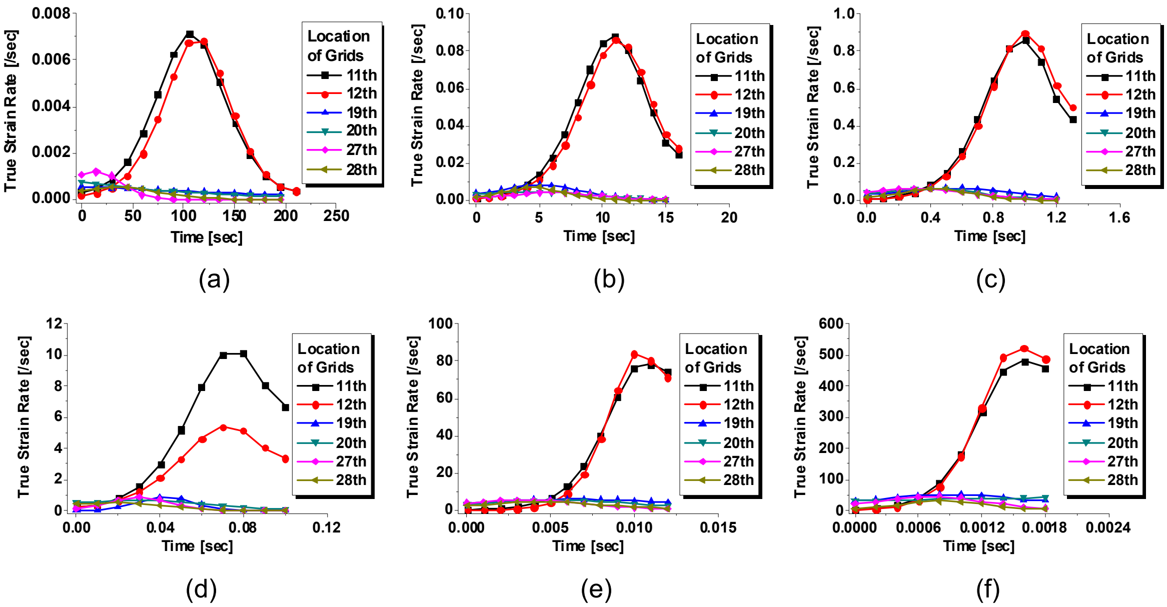

(a) (b) (c)

(d) (e) (f)

2.d. Variation of the actual strain rate with respect to time at various designated strain rates:
(a) 0.001/sec; (b) 0.01/sec; (c) 0.1/sec; (d) 1/sec; (e) 10/sec; (f) 100/sec.

In order to calculate the actual strain rate, the true strain with respect to time was utilized. The actual strain rate can be obtained from first derivatives of the true strain with respect to time. The actual strain rate obtained at each grid element is shown in Figure 2.d. Though the uniaxial tensile tests were conducted with constant speeds, the actual strain rate obtained at each grid element as well as the true strain varies in accordance with deformation behaviors of specimens and time. That is, the tensile characteristics at various strain rates are represented not by the designated strain rate of the uniaxial tensile tests but by the actual strain rate acquired from FEGM. The relation between true stress and true strain calculated in previous section can be correlated with the actual strain rate acquired from FEGM, hence, the relation between true stress and true strain at the actual strain rate corresponded to the real deformation behavior can be obtained.

3.4. True stress−true strain curves with the variation of the actual strain rate

Correlating a true stress and a true strain at the actual strain rate, the relation between true stress and true strain with the variation of the actual strain rate is obtained to construct a true stress−true strain curve. The relation between true stress and true strain with the variation of the actual strain rate is obtained by using proposed method and are represented in Figure 2.e. In these figures, groups of points plotted with same symbols indicate true stress−true strain relationship at a certain range of the actual strain rate. Supposing that there are curves which go through between points of adjacent symbols, they indicate a true stress−true strain curve of the material in accordance with a representative strain rate such as 0.001, 0.01, 0.1, 1, 10, 100/sec. These curves are described in Figure 2.f. The equation of these curves is expressed below and the coefficients of the equation are tabulated in Table 1.

$$\sigma = \sigma(\varepsilon) + \sigma(\dot{\varepsilon}) = \left\{A + B \cdot e^{(\varepsilon/n)}\right\} + \left\{C \cdot \ln\left(\frac{\dot{\varepsilon}}{\dot{\varepsilon}_0}\right)\right\},\ \dot{\varepsilon}_0 = 0.001/\sec \tag{6}$$

Table 1 Coefficients of equation (6).

Material	Form	A	B	n	C
ABS	Additional	27.554	20.046	0.655	1.902

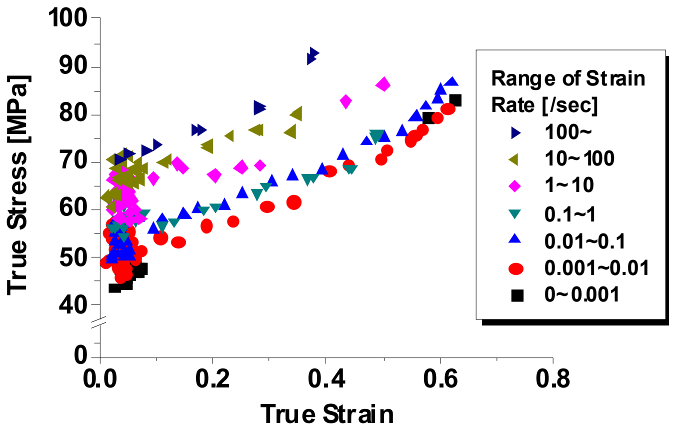

2.e. Data points to relate true stress to true strain with the variation of the strain rate.

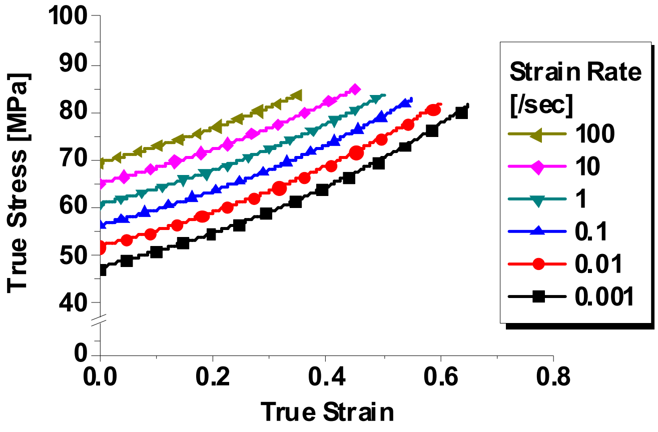

2.f. True stress−true strain curves with the variation of the strain rate.

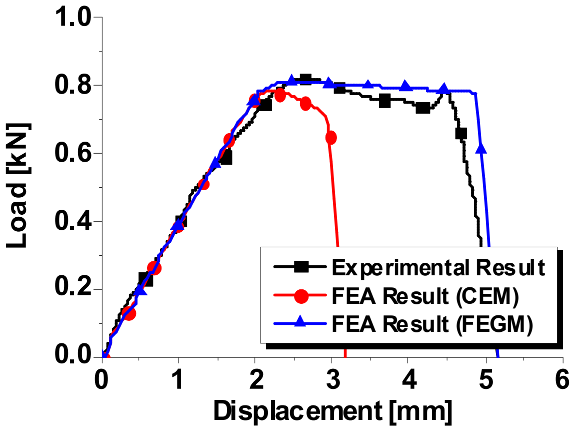

2.g. Comparison of experimental result with finite element analysis results.

3.5. Numerical verification of FEGM

The material properties of the true stress−true strain curve at various strain rates acquired from FEGM were evaluated with finite element analysis of uniaxial tensile tests. The commercial software, LS-DYNA 3D, v.971, were used for finite element analysis. Three−dimensional solid elements were utilized and a half model was adopted for the sake of symmetry of uniaxial tensile tests. The tensile speed is chosen to be 3.3 m/sec which corresponds to a nominal strain rate of 100/sec. The FE system has been constructed with 7488 elements and 9891 nodes. The material properties at various strain rates acquired from FEGM and CEM were applied to finite element analysis as piecewise linear data for comparison and evaluation. The finite element analysis results using the given material properties acquired from FEGM were compared with those acquired from CEM in order to check the validity of FEGM. Load−displacement graphs obtained from experiment and numerical analyses are shown in Figure 2.g. The finite element analysis result with the material properties acquired from FEGM shows good agreement with the experimental result, while that with the material properties acquired from CEM fails to correctly describe the real deformation behavior.

4. Conclusion

In this paper, a data analysis method named force equilibrium grid method(FEGM) is newly proposed. This method can convert engineering stress−engineering strain curves to true stress−true strain curves correctly and acquire accurate true stress−true strain curves with the variation of the strain rate for materials that have severe localized deformation. The contribution of this paper has been summarized below:

(1) Uniaxial tensile tests at quasi-static and intermediate strain rates ranging from 0.001/sec to 100/sec are conducted for various auto-body plastics. It is noticed as a general concept the flow stress increases, as the strain rate increases.
(2) Using FEGM, the true stress and true strain can be directly calculated at each grid element. FEGM can obtain the actual strain rate which corresponds to the real deformation behavior of the specimen.
(3) The true stress−true strain curves at each actual strain rate are acquired from FEGM.
(4) The true stress−true strain curves obtained are interpolated as flow stress curves with hardening function of an additive type.
(5) Finite element analysis results using the material properties acquired from FEGM demonstrates excellent agreement with experimental results than those using the material properties acquired from CEM.

References

[1] S. M. Walley, J. E. Field, P. H. Pope, N. A. Safford, "A study of the rapid deformation behaviour of a range of polymers", Phil. Trans. R. Soc. Lond. A, Vol. 328, No. 1597, pp. 1-33, 1989.
[2] A. E. Mayr, W. D. Cook, G. H. Edward, "Yielding behaviour in model epoxy thermosets - I. Effect of strain rate and composition", Polymer, Vol. 39, No. 16, pp. 3719-3724, 1998.
[3] H. Huh, S. B. Kim, J. H. Song and J. H. Lim, “Dynamic tensile characteristics of TRIP-type and DP-type steel sheets for an auto-body”, International Journal of Mechanical Sciences, Vol. 50, No. 5, pp. 918-931, 2008.
[4] H. Huh, J. H. Lim and S. H. Park, “High speed tensile test of steel sheet for the stress−strain curve at the intermediate strain rate”, International Journal of Automotive Technology, Vol. 10, No. 2, pp. 195-204, 2009.
[5] A. Marquez-Lucero, C. G'Sell, K. W. Neale, "Experimental investigation of neck propagation in polymers", Polymer, Vol. 30, No. 4, pp. 636-642, 1989.
[6] E. M. Parsons, M. C. Boyce, D. M. Parks, M. Weinberg, "Three-dimensional large-strain tensile deformation of neat and calcium carbonate-filled high-density polyethylene", Polymer, Vol. 46, No. 7, pp. 2257-2265, 2005.
[7] J. S. Kim, H. Huh, K. W. Lee, D. Y. Ha, T. J. Yeo, S. J. Park, "Evaluation of dynamic tensile characteristics of polypropylene with temperature variation", International Journal of Automotive Technology, Vol. 7, No. 5, pp. 571-577, 2006.
[8] J. S. Kim, H. Huh and K. W. Lee, “Evaluation of dynamic tensile characteristics of polypropylene composites with temperature variation”, Journal of Composite Materials, Vol. 43, No. 23, pp. 2831-2853, 2009.

Proceedings of the SEM Annual Conference
June 7-10, 2010 Indianapolis, Indiana USA
©2010 Society for Experimental Mechanics Inc.

Elasto-viscoplasticity behaviour of a structural adhesive under compression loadings

D. MORIN[a,b,c], G. HAUGOU[a,b,c], F. LAURO[a,b,c], B. BENNANI[a,b,c]

[a]Univ Lille Nord de France, F-59000 Lille, France

[b]UVHC, LAMIH, F-59313 Valenciennes, France

[c]CNRS, FRE 3304, FR-59313 Valenciennes, France

Corresponding author: gregory.haugou@univ-valenciennes.fr

ABSTRACT

Improvement of automotives' crashworthiness is of high interest for governments prior to objectives focused on the reduction of passengers' injuries. In these recent years, steel industries have studied the dynamic behaviour of tapered side rails so as to increase the capacities of energy absorption combined with light-weight aspects. On the basis of the global mass' reduction of cars, bonded techniques have been tested with respect to the reduction of the mass/energy's ratio. In this study, a test programme has been performed on a structural adhesive under a very large range of strain rates, thus [0.1;5000] /s. For that, a split Hopkinson bars device made of PA66 has been used so as to access to materials responses in the upper domain of strain rates, thus [500;5000] /s. To complete the expected domain of strain rates, compression tests have been done using a high-speed hydraulic machine on the same geometry from 0.1 up to 50 /s. A special mould has been machined and 2 sheets have prepared (thickness: 4 and 6 mm) in order to consider the effect of the pressure during the curing process. Water jet technique has been used to extract cylindrical samples from the sheet with accurate dimensions.

I) Context

The introduction of high strength adhesives in structural parts of transportation cars is of high interest for designers and engineers. This assembly technique gives the possibility to join any sort of material whatever configuration with particular interest regarding mass and cost reduction opportunities proposed on new generation of cars. But, non negligeable stress concentration levels can be attended after bonding processes. Here are defended crashworthiness issues considering bonding techniques introduced in framework of cars. Recently, a new generation of adhesives has been developed by the chemical industry in order to improve the performance of adhesives prior to shear strength level. These adhesives are based on an epoxy matrix which is modified by addition of polymer nodules affecting plasticity and other mechanical properties such as visco-elasticity, visco-plasticity, Bauschinger effect, damage evolution during plasticity [1, 2]. In the present study, the identification of the BETAMATE 1496V^{TM} adhesive is lead.

In order to describe these mechanical responses of adhesives, different tests devices have been suggested, and the scientific literature has highlighted two strategies:

T. Proulx (ed.), *Dynamic Behavior of Materials, Volume 1*, Conference Proceedings of the Society for Experimental Mechanics Series, DOI 10.1007/978-1-4419-8228-5_55, © The Society for Experimental Mechanics, Inc. 2011

- experimental tests programmes based on elementary assemblies (butt joint for tensile/compressive loadings, single or double lap joint for shear loading and scarf joints for mixed loadings [3-5]. These tests are mostly proposed by the scientific review [6, 7], but a non-uniform stress distribution inside the bonded joints is generally discussed.
- experimental tests programmes on bulk specimens available on condition that the behaviour of the adhesive has no dependency regarding the thickness of the samples [2].

The authors have performed an extended tests programme based on bulk specimens extracted from plates obtained with two pressure levels. One objective is to establish if this parameter has modified significantly the material responses with prior to the chemical theory of adhesion which considers that no effect of thickness can be observed. A large range of strain rates has been investigated from 0.1 up to 5000 /s using Split Hopkinson pressure bars technique (high strain rates) and a high speed machine (low and medium strain rates) associated with electro-optical extensometer as well as 3D Digital Image Correlation techniques. Compression tests have been firstly explored nevertheless tensile tests have been also performed. The present paper provides results on stress-strain responses associated with strain rate so that Finite Element modeling is then initiated for the considered adhesive.

II) Identification of mechanical properties

F.E. modeling of transportation frameworks under dynamic loadings requires the identification of physical parameters describing the evolution of the behaviour model in function of total strains and rates of strain. Here, the behaviour model is fitted up to 0.5 in plastic strain for the BETAMATE 1496V^{TM} adhesive determined using an innovative identification technique. This technique is based on the calculation of full-field strain at the surface of the samples using 3D Digital Image Correlation techniques [8].

II-a) Description of the experimental devices

The material responses of the considered adhesive have obtained using two experimental devices : a high speed machine (Instron VHS 65/20 – capacities : load : 65 kN, speed range : 1 mm/s to 20 m/s) has been arranged to perform compression tests using special patterns designed for reduced size of samples (see fig.1b). A set of two piezo-electrical load cells (see fig.1b – Kistler 9343) has been mounted on the compression set-up with a calibrated measurement range close to 7 kN and an electro-optical extensometer (see fig.1 – Rudolph XR200 – bandwidth 250 kHz) has been prepared so as to ensure the measurement of the current shortening of the specimen up to large strains (measurement range: 25 mm). Here, the description of the high-speed machine is omitted due the well knowledge of this device where natural frequencies disturbances have be widely underlined in the literature. For the present compression tests, a maximum velocity close to 0.3 m/s has been applied to limit inertia effects on the samples and natural disturbances of the set patterns/load cell at the upper part of the device.

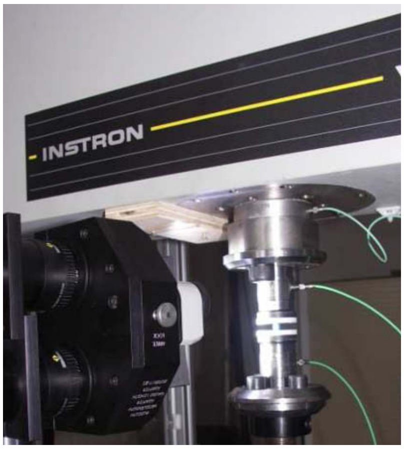

Fig1a).: High speed machine and measurement devices (Load and displacement).

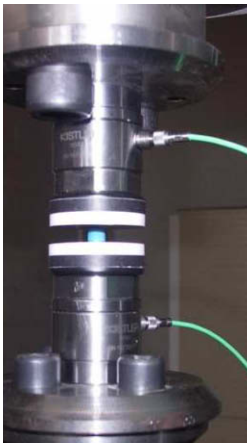

Fig 1b):Location of the adhesive's sample between plates.

For the upper range of strain rates, a set of PA66 cylindrical bars has been developed assuming elastic pulses separation along finite cylindrical bars. The calculation of the material responses is done using full strain bridges placed at strategic locations along input and output bars so that no superposition of the elastic incident and reflected pulses can occur during the test. For that, a Lagrangian diagram is needed in order to confirm the dimension of the bars in function of the length of the projectile and the wave's speed of the elastic pulses. The Split Hopkinson pressure bars device is here composed of a set of bars with a diameter close to 40 mm and a total length of each bar close to 3 m. The measurement bars are aligned along a rigid frame made of aluminum so as to confer good parallelism conditions at the location of the sample located at the interface of the two bars (see fig.2b).

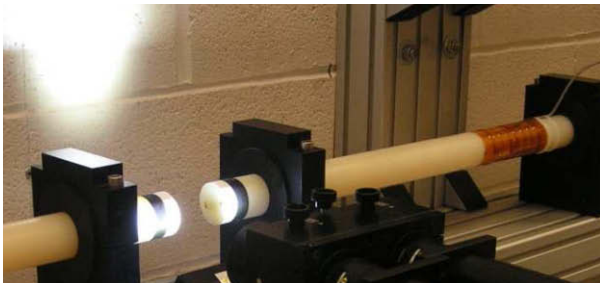

Fig.2a: PA66 bars for dynamic compression tests.

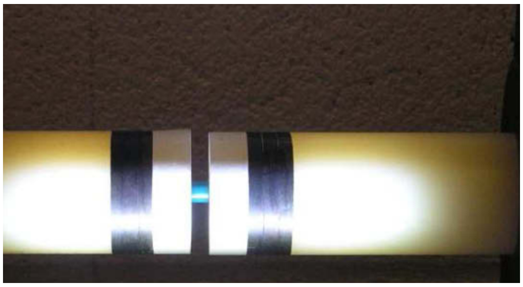

Fig.2b: Location of the adhesive's sample.

For many applications on Hopkinson bars devices, the material as well as the diameter of the bars are chosen so as to access to signals with acceptable amplitudes depending on the properties of the sample (natural amplifications are preferred compared to electrical amplifications applied on ampli-conditioning sytems). The length of the projectile is close to 1 m generating a duration time close to 1.2 ms. In these conditions, the material response with total strains over 0.6 can be obtained up to 500 /s. As a visco-elastic material is used for the cylindrical bars, special calculations are required in order to consider correction of dispersions along the bars as well as viscoelasticity of the constitutive material of the measurement bars [9]. The governing equations – needed to access to the nominal stress-strain responses after the test – are here reminded (equations (1) to (4) expressed according the elastic formulation [10]), and used in the DAVID software developed by Gary [11]:

$$\varepsilon_N(t) = \frac{v_{IN}(t) - v_{OUT}(t)}{l_S} \tag{1}$$

where $v_{IN}(t)$ and $v_{OUT}(t)$ are respectively the input and output bars' speed and l_S is the intial length of the sample.

$$v_{IN}(t) = C_{IN} \cdot (\varepsilon_{INC}(t) - \varepsilon_{REF}(t)) \tag{2}$$

where $\varepsilon_{INC}(t)$ and $\varepsilon_{REF}(t)$ are respectively the amplitude of the incident and reflected pulses propagatin in the input and bar. C_{IN} is the wave's speed of the incident and reflected pulses propagating in the input bar.

$$v_{OUT}(t) = C_{OUT} \cdot \varepsilon_{TRA}(t) \tag{3}$$

where $\varepsilon_{TRA}(t)$ is the amplitude of the transmitted pulse and C_{OUT} is the wave's speed of the transmitted pulse propagating in the output bar.

$$\sigma_N(t) = \frac{S_{OUT} \cdot E_{OUT}}{S_S} \cdot \varepsilon_{TRA}(t) \tag{4}$$

where S_{OUT} and S_S are respectively the cross section of the output bar and the sample. E_{OUT} is the elastic modulus of the output bar. $\sigma(t)$ is the current stress calculated in the sample

Finally, a set of two high speed camera (Photron APX RS 3000) have been oriented with an angle close to 30° and data acquisitions have been done at 50 f/s with a resolution of 1024×1024 pixels to access to qualitative and quantitative data (see fig.3).

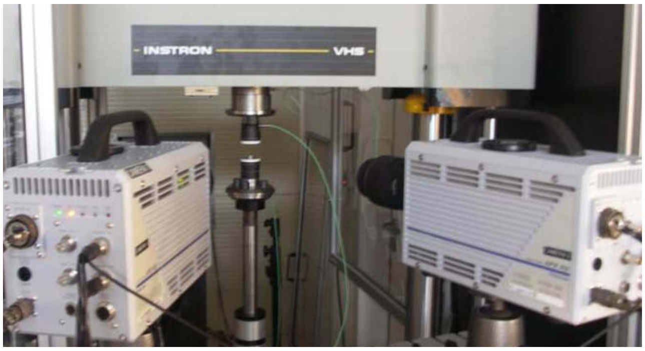

Fig.3: configuration of the set of high speed cameras.

II-b) Preparation of the samples

The preparation of bulk specimens has lead the authors to define a special forming process so that plates of pure adhesive can be obtained. The authors have designed an aluminum mold with a rectangular form. Teflon has been spread firstly to avoid adhesions between the mold and the fresh adhesive stored in a cartridge. Mechanical properties of adhesives can be significantly affected by temperature and time of curing [4] but also by the pressure applied during the curing process [12]. For that, the authors have decided to control these parameters applied on the different plates with a heating press. Two pressure levels have been imposed on the plates during the curing phase, thus 1 and 4 MPa. Despite the high caution level during the preparation of the plates, it remains difficult to obtain pore-free samples. The authors have then controlled the porosity with lightening through the plates. They have also quantified the size of pores which cannot be detected easily using the X-ray µCT technique. The pore size has been estimated close to 80 µm, these values will be considered as initial void for further FE simulations. After these controls, specimens have been machined using water jet cutting in the adhesive plates. This technique gives the opportunity to reduce the heating of small size samples as well as crack initiation during the machining.

The geometry proposed here for the compression tests is in accordance with the NF-ISO-604 norm (see fig.4a and 4b).

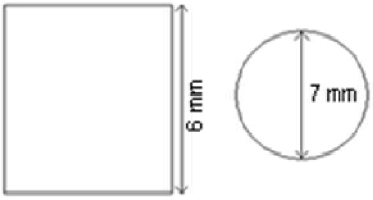

Fig 4a : samples from plate with 4 MPa pressure.

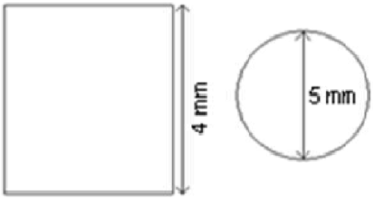

Fig 4b : samples from plate with 1 MPa pressure.

This norm is based on equation 5 where a critical plastic strain is calculated in function of the ratio between height and radius of the sample. Here, different radii of the samples are defined according to a value close to 0.5 in plastic strain and the expected range of strain rates.

$$\varepsilon_C \leq 0.4 \cdot (\frac{x}{h})^2 \tag{5}$$

where ε_C is the critical strain, x the radius of the cylindrical sample and h the height of the initial sample.

Fig.5: Geometry of the compression samples.

III) Main results

A set of 6 samples has been tested using the high speed machine with the mentioned dimensions. The range of velocity was equal to 1 and 300 mm/s providing mean strain rates close to 0.15 and 50 /s respectively. To complete the material responses, a set of 9 samples has been testing using the Split Hopkinson pressure bars (SHPB) device described previously under 3 different velocities. A second range of strain rates has been reached on condition that forces' equilibrium is achieved, thus here:

- 600 up to 2500 /s for samples with 6 mm thick,
- 1400 up to 5000 /s for samples with 4 mm thick.

Figure 6 illustrates initial and post mortem samples; the authors have previously lubricated each face of the sample using a water-based lubricant so as to reduce friction effects, ensure homogenous strains and prevent from buckling troubles.

500 /s

1200 /s

Fig.6: Geometry of the compression specimens before and after the test.

III-a) Validation of the stress-strain relations' computation

As stress computation formula depends on the longitudinal strain, the validity of the strain calculated after the test has to be checked. The longitudinal strain is only valid on condition that no buckling troubles occur during the test. In these conditions, the current shape of the cylindrical samples has been controlled using 3D Digital Image Correlation with tests performed on the high-speed machine. As shown in figure 7, the shape of the specimen has revealed a cylindrical shape up to high plastic strains without global or local buckling.

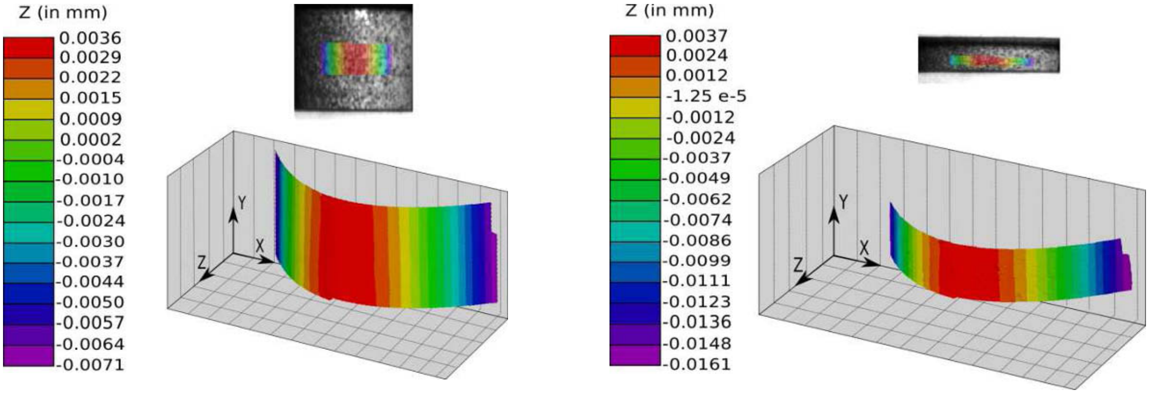

Fig.7: initial (left) and deformed (right) shape of the cylindrical sample.

Once the calculation of the longitudinal strain is reached, the computation of the current stress is then validated for the tests at medium and high strain rates. For the computation of the current stress on the Hopkinson bars' tests, an additional step is needed. Longitudinal strain is not extracted directly from a global measurement but from the elastic waves' system (equations 1 and 2, [10]). For these reasons, a comparison between total strains calculated from governing equations related to Hopkinson tests and measurements from an electro-optical extensometer. Figure 8 has illustrated a good correlation between both techniques regarding the displacement/time responses at the input (IB) and output (OB) bars as well as the current shortening of the sample. The current stress computed from the Hopkinson bars measurement is then acceptable.

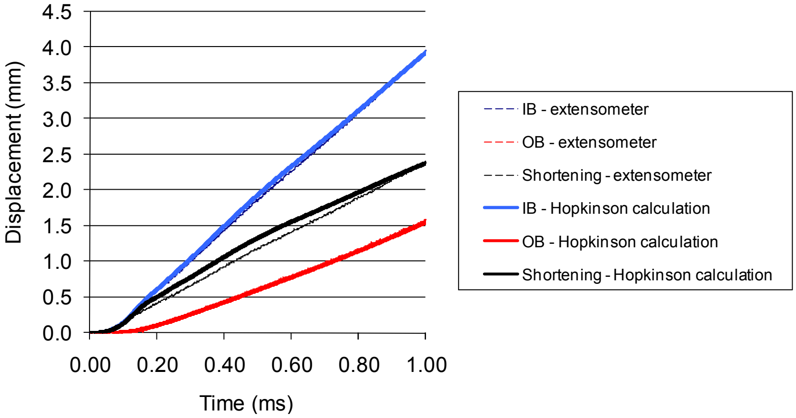

Fig.8: Comparison of the displacements' calculation (500 /s): electro-optical extensometer (dotted line) and Hopkinson formulas (thick line).

III-b) Presentation of the behaviour laws - Comments

Figure 9 illustrates behaviour laws at 50 /s approximately based on samples extracted from plates curing under 1 MPa and 4 MPa pressure, respectively. Obviously, the curing process has revealed difference in stress level between the two series of samples at a similar strain.Figure 10 has underlined a high visco-plastic behaviour, and a saturation effect around 2000 /s for the highest pressure level. On the 1 MPa pressure level's specimens, the materials responses have shown stress-strain relations where the saturation effect was not put clearly into evidence, and may be due to the difference of pressure applied on the plates during the curing phase. The mentioned relations have also revealed a hook at the beginning of the plastic stress-strain relations pronounced under dynamic loadings. But, this hook is not observed for the compression relations established for the tests performed on the samples extracted from the 1 MPa pressure plates. Whatever, both stress-strain relations have underlined a structural hardening around 0.4 in true plastic strain.

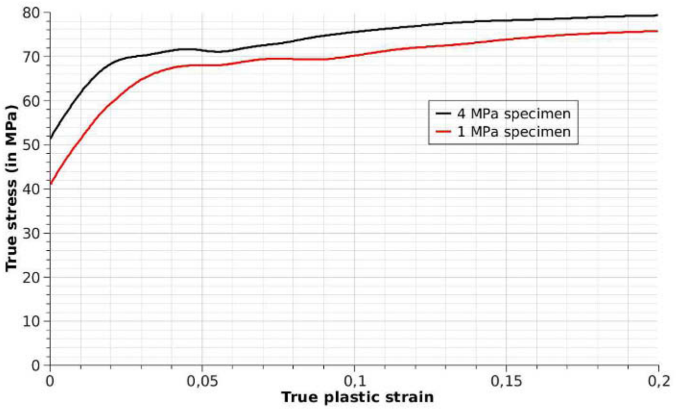

Fig.9 : Comparison of stress-strain relations for a set of samples tested at 53 /s.

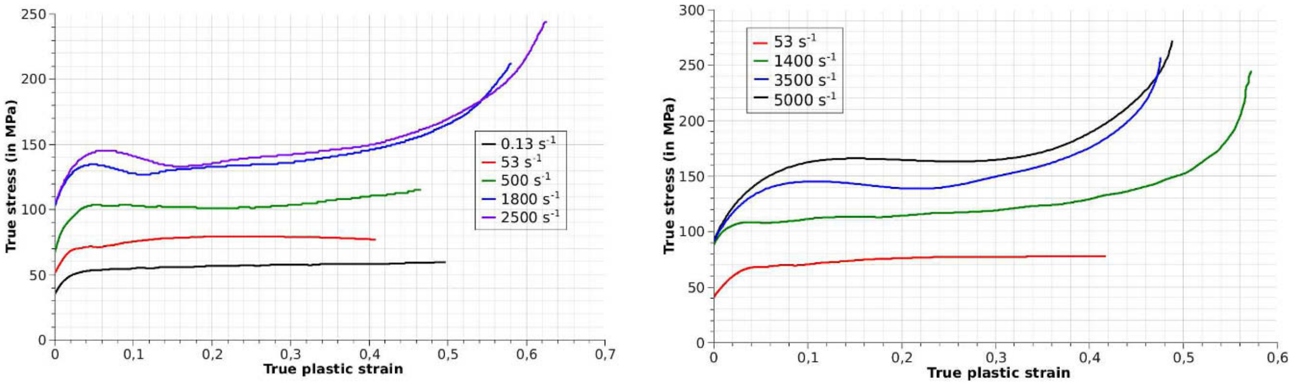

Fig.10 : Behaviour laws of 4 MPa (left) and 1 MPa (right) pressure samples – Compression loading.

III-c) Behaviour laws modeling

Plastic behaviour of structural adhesives can be implemented in Finite element codes with tabulated behaviour laws or using a mathematical model. In terms of mathematical models, visco-plasticity is generally modeled in commercial Finite Element codes using Johnson-Cook or Cowper-Symmonds models. These models do not describe correctly the viscous phenomenon due to their multiplicative formulation. An example of visco-plastic behaviour law is then proposed on the 1 MPa material responses (see fig.11). This model is based on a modified G'Sell behaviour law generally used for the description of polymer plasticity [13]. All parameters have to be strain rate dependent with objective to describe correctly the viscoplasticity of the considered material.

$$\sigma = \sigma_Y(\varepsilon) + K(\varepsilon)\cdot[1 + h_1(\varepsilon)\cdot\varepsilon_P + h_2(\varepsilon)\cdot{\varepsilon_P}^2 + h_3(\varepsilon)\cdot{\varepsilon_P}^2]\cdot[1 - e^{-W(\varepsilon)\cdot\varepsilon}] \tag{6}$$

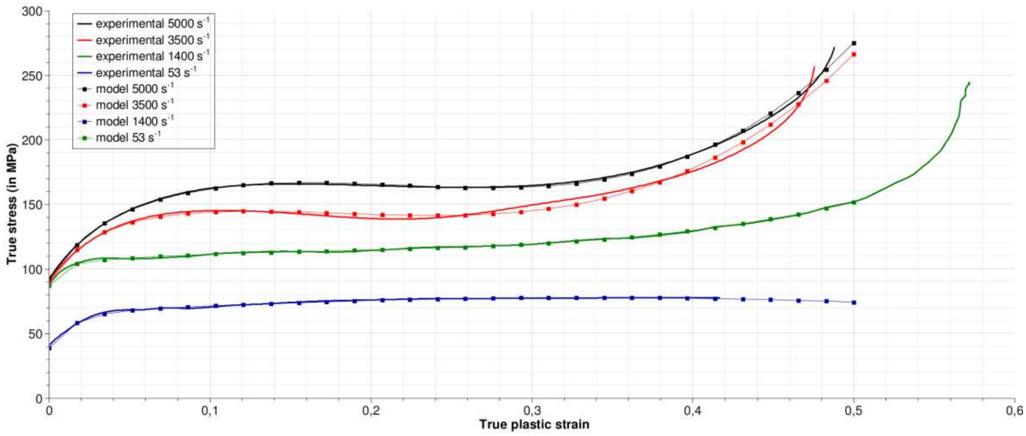

Fig.11 : Example of visco-plastic model identification on the 1 MPa specimens.

IV) Conclusions

The various applications of high-strength adhesives in transportation industries has lead the scientific community to identify mechanical properties of these materials in particular case of crashworthiness and impact. Non-contact measurement techniques have given the opportunity to obtain stress-strain relations from quasi-static to dynamic loadings up to the very large strains. The present works provides a complete description of the evolution of the BETAMATE 1496V^{TM} adhesive for energy capabilities of automotive frameworks under dynamic loadings for mass reduction aspects. The curing pressure has revealed to be a sensitive parameter on the materials responses on bulk samples. This work has highlighted Finite Elements modeling opportunities of joint laps from quasi-static to dynamic loadings.

REFERENCES

[1] Duncan B., Dean G. Measurement and models for design with modern adhesives, International Journal of Adhesion and Adhesives, 23, 141-149, 2003.

[2] Goglio L., Peroni L., Peroni M., Rossetto M., High strain rate compressive and tension behaviour of an epoxy bi-component adhesive, International Journal of Adhesion and Adhesives, 28, 329-339, 2008.

[3] Berry N.G., d'Almeida J.R.M., The influence of circular centered defects on the performance of carbonepoxy single lap joints, Polymer testing, 21, 373-379, 2002.

[4] Bed A., Malvade I., Biswas P., Schroeder J., An experimental and analytical study of the mechanical behavior of adhesively bonded joints for variable extension rates and temperatures, International Journal of Adhesion and Adhesives, 23, 1-15, 2007.

[5] You M., Yan Z., Zheng X., Yu H., Li Z., A numerical and experimental study of gap length on adhesively bonded aluminium double-lap joint, International Journal of Adhesion and Adhesives, 27, 696-702, 2007.

[6] de Morais A.B., Pereira A.B., Teixeira J.P., Cavaleiro N.C., Strength of epoxy adhesive-bonded stainless steel joints, International Journal of Adhesion and Adhesives, 27, 679-686, 2007.

[7] Derewonko A., Godzimirski J., Kosiuczenko K., Niezgoda T., Kiczko A., Strength assessment adhesive-bonded joints, Computational materials science, 2007.

[8] Lauro F., Bennani B., Morin D., Epee A., The SEE method for determination of behaviour laws for strain rate dependent material – Application to polymer material, international Journal of Impact Engineering, 37, 715-722, 2010.

[9] Zhao H., Gary G., Klepaczko J.R., On the use of the viscoelastic Split Hopkinson Pressure bars, International of Journal of Impact Engineering, 19, 319-330, 1997 .

[10] Gary G., Some aspects of dynamic testing with wave-guides, New experimental methods in Materials dynamic and impact, Warsaw 1, Poland, 179-222, 2001.

[11] Gary G. Degreef V., DAVID, Users manual version, Labview version, LMS Polytechnique, Palaiseau, 2008

[12] Mengel R., Häberle J., Schlimmer M., Mechanical properties of hub/shaft joints adhesively bonded and cured under hydrostatic pressure, International Journal of Adhesion and Adhesives, 27, 568-573, 2007.

[13] G'Sell C., Marquez-Lucero A., Determination of the intrinsic stress/strain equation of thin polymer films from stretching experiments under plane-strain tension, Polymer, 34, 2740-2749, 1993.

Proceedings of the SEM Annual Conference
June 7-10, 2010 Indianapolis, Indiana USA
©2010 Society for Experimental Mechanics Inc.

Dynamic behaviors of fiber reinforced aerogel and Mg/aerogel composites

Shukui Li, Jinxu Liu*, Jie Yang, Yingchun Wang, Lili Yan
School of Materials Science and Engineering, Beijing Institute of Technology, Beijing 100081, People's Republic of China
- *Corresponding author. E-mail address: liujinxu@bit.edu.cn

ABSTRACT

The dynamic behaviors of glass fiber reinforced silica aerogel and the Mg/aerogel composites are experimentally investigated using spilt Hopkinson pressure bars. For the purpose of comparison，dynamic responses of hydrogel are also investigated. Incident wave shaping experiments are designed to investigate the shaping effects of aerogel and Mg/aerogel structures. Results show that the fiber reinforced aerogel exhibits significant strain rate strengthening and strain hardening behavior. The strength of the investigated aerogel exhibits evidently size effect: strength of aerogel shows an increasing tendency with the size of sample due to the special nano-porous network structure of aerogel. The incident wave shaped by the composite structure of Mg/aerogel is obviously weaker than that of single magnesium alloy or aerogel, indicating a better protective capacity of Mg/aerogel composite structures.

Keywords*:* Dynamic behaviors; Glass fiber reinforced aerogel; Microstructural analysis; Incident wave shaping.

1 Introduction

Aerogels are ultra-lightweight open-celled mesoporous materials. They display an interconnected network structure which is composed of nanoparticles and nanopores[1]. As a kind of function materials, aerogels are widely used in thermal insulation, nuclear particle detection, optic and light-guides, electronic device and shock absorption et al. [2]. So far, aerogels are commonly not considered to be used as structural materials due to their low yield strength and brittleness. Currently, attention is focused on improving the mechanical properties of aerogels without sacrificing other unique properties [3]. In order to improve the mechanical properties especially strength and ductility of aerogels, epoxy resin [4], polyvinyl butyral [5], ceramic fiber [6] and glass fiber [7] are often added into aerogel as reinforcements. Glass fiber reinforced silica aerogel is one kind of inorganic aerogels with fibers as the reinforcements. In glass fiber reinforced aerogel, silica colloidal particles connect with each other to form the nano-porous network structure. Glass fibers connect firmly with the surrounding aerogel matrix. To a certain degree, the reinforcements have improved the mechanical properties of aerogels.

Recent studies have focused on the compressive behaviors of aerogels, which are of interest for force protection under impact. Atul Katti [8] found that during the quasi-static compression, isocyanate cross-linked amine-modified aerogels show linearly elastic at small strain and then exhibited yield behavior, followed by densification and inelastic hardening. Luo [9] found that the isocyanate-crosslinked silica aerogel became stiffer with the increase of strain rate under impact. Moreover, Luo[10] have proved that at high strain rate, the specific energy absorption for isocyanate-crosslinked vanadia aerogels is higher than that of polymethacrylimide or Rohacell foam, which are often used in engineering applications. Thus, due to the ultra-lightweight and good energy absorption capacity, aerogel have potentials to be used for force protection. However, the dynamic behaviors of aerogels under high strain rate are not very clear so far. Further testing is needed to determine the energy absorption capacity and protection capacity of aerogel, which is of great importance to protection applications of aerogels.

T. Proulx (ed.), *Dynamic Behavior of Materials, Volume 1*, Conference Proceedings of the Society for Experimental Mechanics Series,
DOI 10.1007/978-1-4419-8228-5_56, © The Society for Experimental Mechanics, Inc. 2011

In the present study, we study the dynamic behaviors of glass fiber reinforced silica aerogel and Mg/aerogel composites using a large-sized split Hopkinson pressure bar (SHPB). The buffering capacity and energy absorption characteristic of both aerogel and Mg/aerogel composites are investigated using incident wave shaping technique. The aerogel and Mg/aerogel shows good protection capacity under high speed impact, which exhibit the applications prospect of aerogel in protection field and light-composite armor field.

2 Experimental

2.1 Materials

Glass fiber reinforced silica hydrogel were prepared via a sol–gel process with a TEOS–water–ethanol mixture catalyzed by ammonia. Glass fibers were dispersed in the mixture. The gel was aged in the solution for three days. This aging process strengthened the gel. Finally, the glass fiber reinforced silica hydrogel was supercritically dried to form the glass fiber reinforced silica aerogel. The density of this aerogel is $0.2g/cm^3$. The mass percentage of glass fiber is 50%. Fig. 1 shows the SEM images of fiber reinforced aerogel. The glass fiber connect firmly with the aerogel matrix (Fig. 1a), and gel particles connect with each other to form the nano-porous network structure (Fig. 1b).

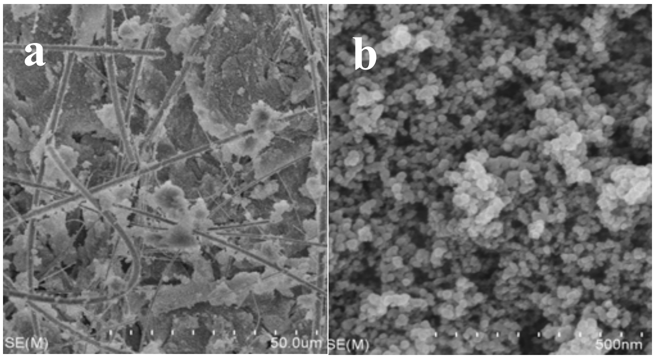

Fig.1 SEM image of fiber reinforced aerogel
(a) ×1000 (b) ×100000

2.2 Dynamic compression experiments

The dynamic compressive of aerogel and hydrogel were performed by a large-sized SHPB with the samples having a diameter of 37mm and a length of 4mm. The bars of SHPB facility were made of hard aluminum alloy with Young's modulus of 70.25GPa, density of 2.81 g/cm^3 and wave speed of 5000m/s. The diameter of all bars is 37mm. The lengths of the incident bar, transmission bar and striker bar are 2000mm, 2000mm and 800mm, respectively. The duration of the incident wave is 320μs. In the dynamic experiment, a resistance strain gauge was stuck on the incident bar to measure the incident wave signal. Because aerogel has much lower strength and impedance compared with the bars, the initial stage of transmitted wave signal is too weak to be captured by resistance strain gauge. In order to capture the weak signal on the transmission bar effectively, a semiconductor strain gauge was stuck on the transmission bar to measure the transmitted wave signal. Since the sensitivity coefficient of the semiconductor strain gauge is 100, which is about 50 times greater than that of the resistance strain gauge, thus the signal-to-noise ratio of the signal measured by the semiconductor strain gauge is about 50 times greater than that measured by the resistance strain gauge, providing accurate wave signal on the transmission bar. Dynamic stress-strain curves of the aerogel samples were obtained by computing the incident, reflected and transmitted wave [11]. In order to studying the stain rate sensitivity of aerogel, the quasi-static compression experiments were conducted by computer controlled electronic universal testing machine.

2.3 Incident wave shaping using fiber reinforced aerogel and Mg/aerogel composites

For the purpose of studying protection capacity of aerogel and Mg/aerogel composites, incident wave shaping experiments were conducted on the SHPB facility. The length of the striker bar was 200mm, generating pulse duration of 80μs. Aerogel and Mg/aerogel composites were attached in front of the incident bar as wave shapers. Then, the striker bar was launched at the same velocity, and the incident wave signals were measured be strain gauge attached on the incident bar. The original incident wave without shaping by aerogel was also measured under same impact velocity for comparison. In accordance with the comparation and analysis of the incident waves shaping by aerogel and Mg/aerogel, the protection capacity against high speed impact of aerogel and Mg/aerogel composites were discussed.

3 Results and discussion

3.1 The dynamic mechanical properties of aerogel

Fig. 2 shows the dynamic and quasi-static compressive stress-strain curves of fiber reinforced aerogel at different strain rates. The stress-strain curves can be divided into three stages: initial linear elastic stage (ε<0.3), yield stage and densification stage. In the initial linear elastic stage, all the stress-strain curves exhibit the same elastic modulus of about 0.5MPa, indicating the elastic modulus has no obvious relation with loading rate. In the yield stage, the nanopores of aerogel collapse under axial compression, followed by compaction of nanopaticles in the densification stage. Fig. 3 shows the micro-features of the aerogel after dynamic loading. The original glass fibers were crushed to pieces (see Fig. 3(a)), and the enlarged micrograph shows compact texture in which nanopores disappeared and nanopaticles contact closely with each other (see Fig. 3(b)). Due to the strengthening and toughening effect of fiber, the fiber reinforced aerogels show higher yield stress and better ductility than pure aerogel. However, the strength of fiber reinforced aerogels is still at a low level. Another important observation from Fig. 2 is that the fiber reinforced aerogel exhibits significant strain rate strengthening and strain strengthening behavior in yield stage and densification stage. The strengths of aerogels show an obviously increasing tendency with strain rate. When loading at strain rates 0.0034^{-1}, 0.017^{-1}, 4000^{-1}, and $6000s^{-1}$, the strengths of aerogels are 1.5 MPa, 1.8 MPa, 4.0 MPa and 6.8MPa at the stain of 0.7, respectively.

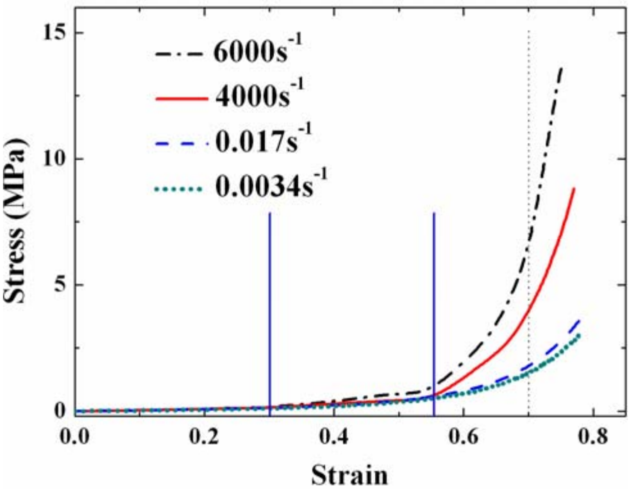

Fig. 2 Stress-strain curves of aerogel at different strain-rates

The effect of strain rate on the mechanical property of porous material can be characterized by strain rate sensitivity *m* [12]:

$$m = \frac{\ln(\sigma_2 / \sigma_1)}{\ln(\dot{\varepsilon}_2 / \dot{\varepsilon}_1)} \tag{1}$$

where $\dot{\varepsilon}_1$ and $\dot{\varepsilon}_2$ are the strain rates; σ_2 and σ_1 are the stresses at strain rates of $\dot{\varepsilon}_1$ and $\dot{\varepsilon}_2$ respectively. Fig. 4 shows the strain rate sensitivity of aerogel at different strain rates and strains. It can be observed that the strain rate sensitivity of aerogel show an obviously increasing tendency with both strain and strain rate. Thus, it can be see that the fiber reinforced aerogel exhibit a higher strength when subjected to high stain rate loading, indicating that the aerogel may have a better buffering capacity and energy absorption capacity.

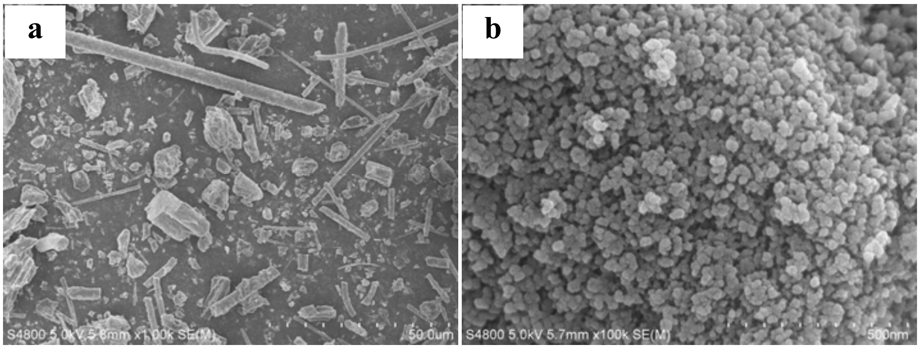

Fig.3 SEM showing images of aerogel after dynamic compression
(a) ×1000 (b) ×100000

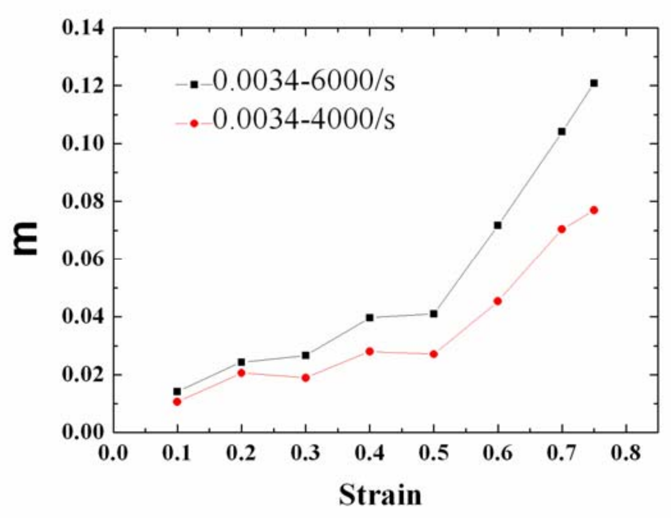

Fig.4 Strain rate sensitivity of aerogel at different strain rates and strains

The absorption energy per unit volume (W) for aerogel can be evaluated by integrating the area under the stress-strain curve, namely:

$$W = \int_0^{\varepsilon_m} \sigma(\varepsilon) d\varepsilon \qquad (2)$$

where σ is the flow stress and ε_m is the strain of aerogel. The calculated absorption energy per unit volume of aerogel at a strain of 75% for the strain rates of $0.017s^{-1}$ and 6000^{-1} are 0.41 and 1.07 MJ/m^3, respectively. It can be seen that the value of absorption energy at strain rate 6000 is about 160% higher than that of quasi-static. The evidently improved energy absorption capacity of aerogel at high strain rate indicates a better buffering capacity and protection capacity under high-speed impact, which is significant for the ballistic protection application.

For permeable material with average pore diameter of d, the permeability follows [14]:

$$K = Ad^2(1-\rho_f/\rho_s)^{3/2} \qquad (3)$$

where A is a constant, d is the average pore diameter of permeable material, ρ_f and ρ_s are mass density of foam and monolithic material, respectively, and ($1-\rho_f/\rho_s$) is the porosity of permeable material. Due to the special nano-scale pores of the aerogel, the permeability of aerogel is very poor. When subjected to high strain rate deformation, the gas in the nano-scale pores can not permeate outwards in a very short time. During this process the gas can bear some stress, resulting in an increase of strength. However, during the quasi-static compression process, the gas has enough time to permeate outwards in a long time, thus it will not lead to the increase of internal pressure. Under dynamic compression, the stress contribution of the fluid in the nano-scale pores can be calculated as follows [15]:

$$\Delta\sigma = \frac{cl^2\mu\dot{\varepsilon}}{d^2(1-\frac{\rho_f}{\rho_s})^{\frac{3}{2}}} \tag{4}$$

where c is a constant, l^2 is the basal area of samples, $\dot{\varepsilon}$ is the strain rate and μ is the viscosity of the fluid in pores. From Eq. (4), it can be seen that the stress contribution of the gas in the nano-scale pores relate to strain rate and strain. The stress contribution of the gas in the nano-scale pores is proportional to strain rate. Because the average pore diameter is decreased with increasing of strain, the stress contribution of gas increased with strain. So it is understandable that fiber reinforced aerogel exhibits significant strain rate strengthening and strain hardening behavior.

Fig. 5 shows the stress-strain curves of fiber reinforced aerogel samples with different basal area at the same strain rate of 4000s^{-1}. It can be seen that the strength of the investigated aerogel shows obviously size effect: the flow stress shows an increasing tendency with the size of sample. As discuss before, the gas in aerogel is hard to permeate outwards in a short time due to the special nano-porous network structure of aerogel. With the increased basal area of aerogel sample, the gas in the nanoscale pores need to move a farther distance to escape from aerogel, which lead to the gas being harder to permeate outwards, and thus generate a greater contribution to increased strength.

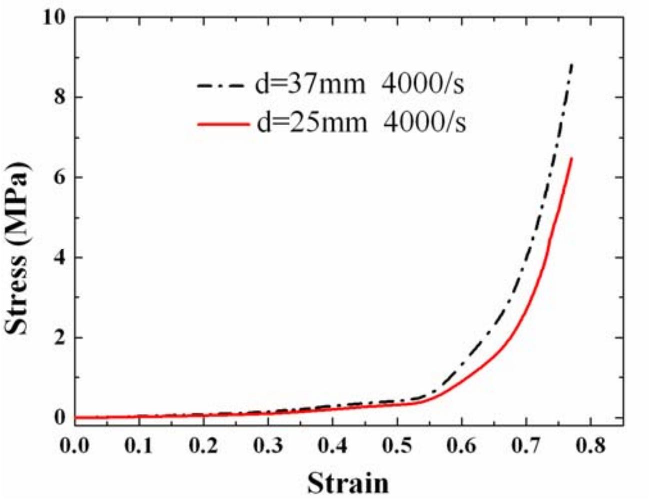

Fig. 5 Compressive stress-strain curves for aerogel samples of different basal area at the same strain rate

The dynamic compressive properties of aerogel saturated with water (hydrogel) were also investigated for comparison. Fig. 6 displayed the stress–strain curves of dry (aerogel) and water-saturated aerogel samples (hydrogel) at high strain rates. Obviously, hydrogel shows higher strength and smaller failure strain that aerogel. When the strain rates are of 6×10^3 and 4×10^3 s^{-1}, the compressive strengths of water-saturated aerogel are 26.1 and 18.2MPa respectively, indicating that the dynamic compressive strength is positive proportional to the strain rate. This is consistent with Equation (4). The viscosity of water is 1×10^{-3}Ns/m^2, while the viscosity of gas is 1.85×10^{-5}Ns/m^2. Since water is incompressible fluid, and the viscosity of the water is about 54 times greater than that of gas. According to Equation (4), the stress contribution of water is much greater than that of gas. The load capability of water makes a great contribution to improvement of compressive strength of hydrogel. Thus, the water-saturated aerogel shows stiffened behavior at high strain rates compared with aerogel. At high strain rate, the internal stress in water-saturated aerogel is much higher than that of aerogel, and the stress increased more rapidly than that of aerogel due to the incompressibility of water. When the internal stress in pores of hydrogel increases rapidly to a certain value, the failure of water-saturated hydrogel occurred earlier than that of aerogel, and the dynamic failure strain of water-saturated aerogel is small than that of aerogel.

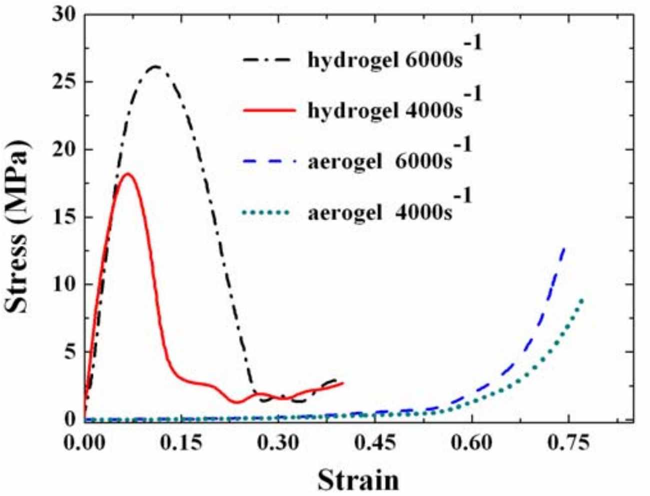

Fig. 6 Compressive stress-strain curves for both dry and water-saturated aerogel at high strain rates.

3.2 Analysis of buffering capacity and energy absorption characteristic

The incident wave (stress-time curves) shaping by aerogel and hydrogel are shown in Fig. 7, and the original stress-time curve without shaping by aerogel and hydrogel is displayed for comparison. It can be observed that the stress-time curves shaping by hydrogel and aerogel change from rectangle to triangle with the maximum value of stress obviously decreased while the pulse duration is prolonged. For the incident wave which shaping by aerogel with a thickness of 12mm, the maximum stress on the incident bar decreased from 700MPa to 311MPa, and the duration time of the wave increased from 80μs to 210μs. The significant decreased stress level obviously indicates a good protection capacity of aerogel against high speed impacts. Besides, it can be seen from Fig. 7 that, the stress-time curves shaping by hydrogel show a lower stress level than that of hydrogel, indicating a better protection capacity of aerogel than that of hydrogel. In addition, the stress level shaping by hydrogel and aerogel show an obviously decreasing tendency with increasing of sample thickness, indicating that the protection capacity of aerogel increased with increasing of thickness. Aerogel plays a buffer role when the striker impact on it, which decreased the stress level effectively. However, the incident wave doesn't have significant difference after wave shaping by hydrogel and the stress level is still high, indicating a poor shaping effect of hydrogel. The most likely reason for this is that the hydrogel failures immediately when subjected to high speed impacts, thus the hydrogel loses protection capacity in a short time. Although hydrogel has high strength than aerogel under high strain rate, aerogel exhibits better protection capacity against high speed impact, thus it can be seen that strength may not direct proportional with protection capacity.

The incident waves shaping by aerogel, Mg and composite structures of Mg/aerogel are shown in Fig. 8. All the pulse shapers have the same thickness of 12mm. The Mg/aerogel composite structures are composed of 4mm magnesium alloy combined with 8 mm aerogel or 8mm magnesium alloy combined with 4mm aerogel. It can be observed from Fig. 8 that the stress-time curves shaping by Mg/aerogel composite structures show obviously low stress level and short pulse duration than that of individual Mg and aerogel at same thickness, indicating the best protection capacity of Mg/aerogel composite.

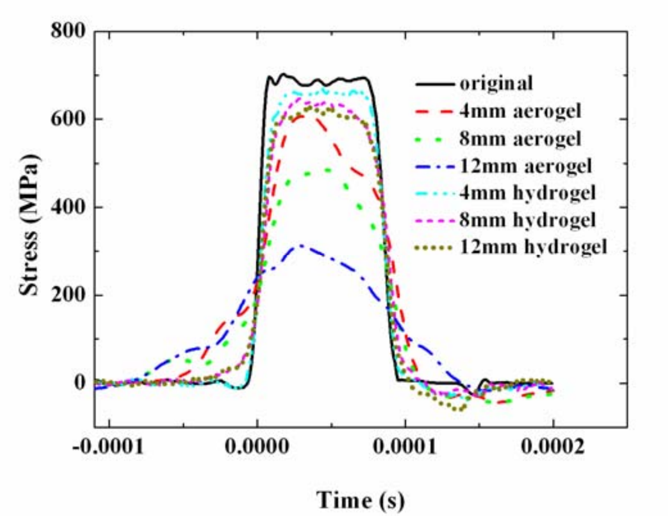

Fig. 7 Stress-time curves on the incident bar before and after incident wave shaping using aerogel and hydrogel

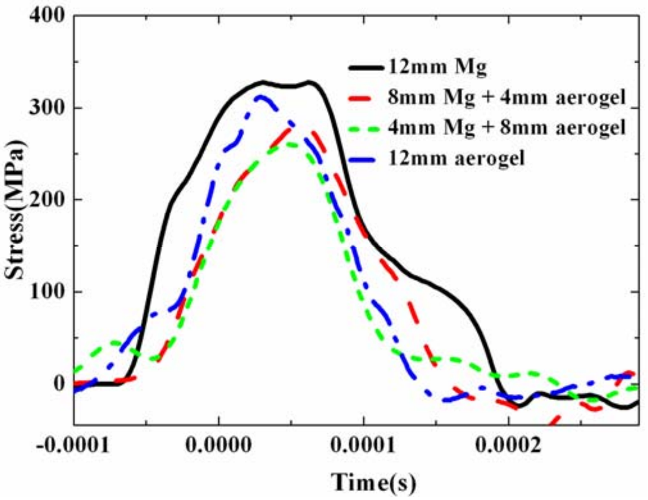

Fig.8 Incident waves shaped by aerogel, Mg and composite structures of Mg/aerogel

It is well known that aerogels are ultra-lightweight materials. However aerogel have relatively low strength, thus it is almost has never been considered for use as protection and armor materials. In the present study, both the fiber reinforced aerogel and Mg/aerogel composites exhibit good protection capacity against high speed impacts. The results strongly suggest that the fiber reinforced aerogel and Mg/aerogel composites have bright application prospect in protection field and light-composite armor material.

4 Conclusions

The dynamic compressive properties of glass fiber reinforced aerogel were investigated using spilt Hopkinson pressure bars. The protection capacity of aerogel and Mg/aerogel composites were investigated using incident wave shaping technique. Results show that the fiber reinforced aerogel exhibits significant strain rate strengthening and strain hardening behavior. The strength of the investigated aerogel exhibits obviously size effect:

strength of aerogel shows an increasing tendency with the size of sample due to the special nano-porous network structure of aerogel. Although hydrogel shows higher strength than that of aerogel under high strain rate deformation, the aerogel exhibits better protection capacity against high speed impact than that of hydrogel. The stress-time curves shaping by aerogel change from rectangle to triangle with the maximum value of stress obviously decreased. The stress-time curves shaping by Mg/aerogel composite structures show obviously low stress level and short pulse duration than that of individual Mg and aerogel at same thickness, indicating a better protection capacity of Mg/aerogel composite.

Reference

[1]A. Soleimani Dorcheh, M.H. Abbasi, Silica aerogel; synthesis, properties and characterization, Journal of Materials Processing Technology, 199,10-26, 2008.

[2] Hrubesh.L. W., Aerogel applications, Journal of Non-Crystalline Solids, 225, 335-342, 1998.

[3] Kelly E. Parmenter, Frederick Milstein, Mechanical Properties of Silica Aerogels, Journal of Non-Crystalline Solid, 223, 179-189, 1998.

[4] Nikhil Gupta, William Ricci, Processing and compressive properties of aerogel/epoxy composites, Journal of Materials Processing Technology, 198, 178–182, 2008.

[5] G. S. KIM, S. H. HYUN, Effect of mixing on thermal and mechanical properties of aerogel-PVB composites, Journal of Materials Science, 38, 1961-1966, 2003.

[6] Deng Zhongsheng, Wang Jue, Wu Aimei, Shen Jun, Zhou Bin. High strength SiO_2 aerogel insulation, Journal of Non-Crystalline Solids, 225, 101-104, 1998.

[7] Chang-Yeoul Kim, Jong-Kyu Lee, Byung-Ik Kim, Synthesis and pore analysis of aerogel-glass fiber composites by ambient drying method, Colloids and Surfaces A: Physicochemical and Engineering Aspects, 313-314, 179-182, 2008.

[8] Atul Katti, Nilesh Shimpi, Samit Roy, Chemical, physical, and mechanical characterization of isocyanate cross-Linked amine-modified silica aerogels, Chemistry of Materials, 18, 285-296, 2006.

[9] Luo H., Lu H., Leventis, The compressive behavior of isocyanate-crosslinked silica aerogel at high strain rates, Mechanics of Time-Dependent Materials, 6, 83-111, 2006.

[10] Luo. H, Churu. G., E. F. Fabrizio, Synthesis and characterization of the physical, chemical and mechanical properties of isocyanate-crosslinked vanadia aerogels, Journal of Sol-Gel Science and Technology, 48, 113-134, 2008.

[11] J. F. Liu, Z. D. Wang, S. S. Hu, Chin, J. Exp. Mech, 13, 218-223, 1998.

[12] Blaz L., Evangelista E., Strain rate sensitivity of hot deformed Al and AlMgSi alloy, Materials Science and Engineering A, 207, 195-201, 1996.

[13] Mukai T , Kanahashi H , Miyoshi T., Experimental study of energy absorption in a closed-celled aluminum foam under dynamic loading, Scripta Materialia, 40, 921-927, 1999.

[14] W. F. Brace, J. Geophys. Res. 82, 3343-3349, 1977.

[15] L. J. Gibson, M. F. Ashby, Cellular Solids: Structure and Properties, second ed., Cambridge University Press, Cambridge, 1997.

Proceedings of the SEM Annual Conference
June 7-10, 2010 Indianapolis, Indiana USA
©2010 Society for Experimental Mechanics Inc.

Mechanisms of Slip Weakening and Healing in Glass at Co-Seismic Slip Rates

Vikas Prakash, Fuping Yuan and Nirav Parikh
Department of Mechanical and Aerospace Engineering
Case Western Reserve University, Cleveland, OH 44106-7222
Email: vikas.prakash@case.edu; fxy11@case.edu; nirav.parikh@case.edu

ABSTRACT

The determination of co-seismic slip resistance in earth faults is critical for understanding the magnitude of shear stress reduction and hence the near-fault acceleration that can occur during earthquakes. Knowledge of shear resistance dependency on slip velocity, slip distance, normal stress, and surface roughness is fundamental information for understanding earthquake physics and the energy released during such events. In the present study plate-impact pressure-shear friction experiments were employed to investigate the frictional resistance in soda-lime glass at relevant normal pressures and co-seismic slip rates. Detailed atomic force microscopy (AFM) and scanning electron microscopy (SEM) studies were carried out to understand the microstructures formed during the sliding process.

The results of the experiments indicate that a wide range of frictional slip conditions exist at the slip interface. These slip conditions range from no-slip followed by slip weakening, strengthening, and then seizure for the case of glass-on-glass experiments. The first-weakening (μ ~ 0.2) is most likely due to the thermal weakening induced by flash heating and incipient melting at asperity junctions, while the second-strengthening (μ ~0.4 to 1.0) is understood to be caused by coalescence and solidification of melt patches. These results can be used to provide an understanding of mechanisms during dynamic fault weakening, and also to establish the constitutive description for the slip behavior in geological materials that can be used in dynamic models of earthquake rupture.

Keywords: slip weakening; shear resistance; rocks and rock-analog materials; plate-impact pressure-shear friction experiments; modified torsional Kolsky-bar friction experiments

1. Introduction

The determination of co-seismic slip resistance in earth faults is critical for understanding the magnitude of shear stress reduction and hence the near-fault acceleration that can occur during earthquakes. Friction stresses at constant normal pressure and sliding speeds less than 1 mm/s have been well studied for a wide range of materials [1-7], experimental data suggest that frictional

T. Proulx (ed.), *Dynamic Behavior of Materials, Volume 1*, Conference Proceedings of the Society for Experimental Mechanics Series,
DOI 10.1007/978-1-4419-8228-5_57, © The Society for Experimental Mechanics, Inc. 2011

resistance in geo-materials at slip speeds ≤ 1 mm/s, slip distance < 1mm is quite high (μ ~ 0.6 to 0.85) [8-9]. The characterization of these results in terms of rate and state variable friction has allowed a better understanding of a wide variety of aspects of the mechanics of earthquakes, including, for example, what to expect in terms of premonitory slip and Omori's Law for aftershock decay [6]. However, seismic inversions provide evidence that frictional resistance of major faults at co-seismic slip speeds (~1-2 m/s) may be quite low [10]. Moreover, very little data exist for the simultaneously high slip rates and large slip displacements characteristic of co-seismic slip, and the data that do exist suggest that the behavior at these slip speeds is dramatically different and the dynamic slip weakening occurs [11-15].

Earthquake occurs because fault strength falls down with increasing slip or slip rate, so the understanding of dynamic fault weakening during the nucleation and the propagation of a seismic rupture is a major task for researchers involved with fault and earthquake physics. Rice [16] recently has summarized two primary thermal weakening mechanisms which are assumed to act in combination during fault events: (1) Thermal pressurization of pore fluid within the fault core by frictional heating which assumes the presence of water within shallow crustal fault zones such that the effective normal stress $\bar{\sigma}_n$ ($\bar{\sigma}_n = \sigma_n - p$, where σ_n is the compressive normal stress on the fault and p is pore fluid pressure) controls frictional strength, and which reduces the effective normal stress and hence reduces the shear strength associated with any given friction coefficient [15,17-24]; (2) Flash heating and consequent weakening at highly stressed asperity contacts during rapid slip which reduces the friction coefficient, a process studied for many years as the key of understanding the slip rate dependence of dry friction in metals at high slip rates [25-28], and which has also been considered recently in seismology as a mechanism that could be active in controlling fault friction during seismic slip in the range before macroscopic melting [12, 29-32].

These two mechanisms are expected to become important immediately after seismic slip initiates, but as large slip develops thermal power generated during the solid-on-solid slip overwhelms the ability of thermal conduction to carry the heat away from the slip interface, macroscopic melting may occur too for sufficiently large combinations of slip and effective normal stress [33]. In this regime, the slip resistance is expected to be primarily controlled by the shear-strain rate, the thickness and viscosity of molten layers [12, 33-34]. Molten layers have a low viscosity and may lubricate faults reducing dynamic friction. However, melting is not a simple weakening mechanism for rock and analog materials. Hirose et al. [12] conducted a series of experiments on Indian gabbro at slip rates of 0.85-1.49 m/s and normal stresses of 1.2-2.4 MPa by using a rotary-shear apparatus. The experiments on gabbro have revealed two stages of slip weakening separated by a marked strengthening regime. By examination of microstructures of simulated fault zone under SEM at different total displacements, they proposed that the first slip weakening is due to the thermal weakening induced by flash heating at asperity contacts and early stage of melting, slip strengthening is caused by the coalescence of melt patches into a thin molten layer, while the growth of molten layer during friction melting is the primary cause of the second slip weakening.

Another weakening mechanism by silica gel formation has been identified by Toro et al. [14]. They studied the slip resistance of Arkansas Novaculite rock at a slip rate of 0.03 m/s and a normal stress of 5 MPa by using a servo-controlled compression-torsion apparatus. They proposed that the observed slip weakening is due to formation of silica gel, and the time-dependent recovery of shear strength is due to thixotropic behavior of the gel. Although different physical processes such as flash heating at asperity contacts, formation of silica gel, thermal pressurization of pore fluid, and frictional melting have been proposed that could lower shear resistance during fast co-seismic slip, these mechanisms and/or their applicability to earthquakes are still poorly understood; thus the slip resistance during earthquakes is still unknown.

In addition to the paucity of friction data and/or constitutive descriptions for large and rapid sliding on a fault at constant normal stress, there is not much knowledge of the effect on frictional resistance during sudden changes in normal stress. This is important, since during seismic slip there can be abrupt changes in both normal and shear stresses. Data exist at low slip speeds showing that a simple Coulomb representation for the effect of normal stress is inadequate and that there are memory effects following a change in normal stress [35-37], but few data exist at high slip velocity [38-40]. Theoretical studies of slip at dissimilar material interfaces [41-42] have shown that spatially inhomogeneous slip causes an alteration of normal stress, so this, as well as effects from non-planar faults and interactions between nearby faults, can cause changes in normal stress. Reductions of normal stress can reduce frictional resistance and thus lead to possible destabilization of slip [43-47].

Nevertheless, the current state of knowledge is so insufficient that all of the processes responsible for frictional resistance during co-seismic slip are not yet known, nor any reliable constitutive description of the behavior that can be used in dynamic models of earthquake rupture. In the present study plate-impact pressure-shear friction experiments were employed to investigate frictional resistance in soda-lime glass at co-seismic slip rates. The results of these experiments can be used to provide insights into the mechanisms of dynamic fault weakening and also the constitutive description of the slip behavior that can be used in dynamic models of earthquake rupture. Both atomic force microscopy (AFM) and scanning electron microscopy (SEM) studies were conducted to understand the effect of high speed friction on the morphology of surface layer formed during the sliding process.

2. Plate-impact Pressure-shear Friction Experiment

2.1 Experimental Configuration

The plate-impact pressure-shear friction experiments were conducted using the 82.5 mm bore single stage gas gun facility at Case Western Reserve University. The schematic of the experimental configuration is shown in Figure 1. A fiberglass projectile carrying the flyer plate is accelerated down the gun barrel by means of compressed air. The rear end of the projectile has sealing O-ring and a Teflon key that slides in a key-way inside the gun barrel to prevent any rotation of the projectile. In order to reduce the possibility of an air cushion between the flyer and target plates, impact takes place in a target chamber that has been evacuated to 50 μm of Hg prior to impact. To ensure the generation of plane waves with wave-front sufficiently parallel to the impact face, the flyer and the target plates are carefully aligned to be parallel to within 2×10^{-5} radians by using an optical alignment scheme developed by Kim et al. [48]. The actual tilt between the two plates is measured by recording the times at which four, isolated, voltage-biased pins, that are flush with the surface of the target plate, are shorted to ground. Impact takes place at an angle θ relative to the direction of approach. This results in pressure-shear loading at the flyer-target (tribo-pair) interface. By controlling the skew angle θ, the impact velocity, a variety of friction states with normal stress varying from 200 MPa to 1 GPa and slip speeds from no slip to 50 m/s can be obtained. During the experiment both normal and transverse particle velocity histories of the rear surface of the target plate are measured by laser interferometer. These measurements are used to infer the normal and shear tractions, slip-velocity and temperature at the tribo-pair interface. Also, all measurements of the particle velocity are made before the arrival of the release waves from the lateral boundary of the specimen. In view of this, and during the time interval of interest, the flyer and target plates can be considered to be essentially infinite in their spatial dimensions and the tribo-pair to be modeled as a semi-infinite half plane sliding on another. This simplification in the tribo-pair geometry allows one-dimensional wave theory to be used in the interpretation of the experimental results. Other details regarding the design, execution and data analysis of the experiments can be found elsewhere [49].

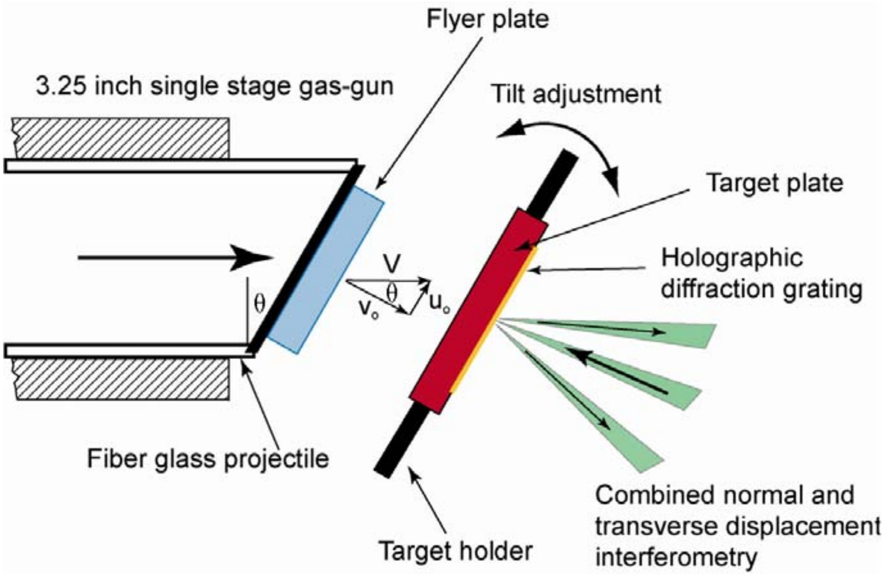
Flyer plate
3.25 inch single stage gas-gun
Tilt adjustment
Target plate
Holographic diffraction grating
V
θ
θ
V₀
u₀
Fiber glass projectile
Target holder
Combined normal and transverse displacement interferometry

Figure 1: Schematic of the plate-impact pressure-shear friction experiment.

2.2 Tribo-pair Materials and Design of the Pressure-shear Experiments

The first series of experiments were conducted on soda-lime glass. The choice of glass is dictated by a number of previous studies [50-52] which have shown that the frictional behavior of glass is almost identical to that of rock. In the present study, the flyer and target plates comprise Ti-6Al-4V and CH tool-steel plates with thin films of soda-lime glass (5 μm in thickness) deposited on the impacting faces by Thin-Films Research, Inc. in Westford, MA (Figure 2a). The impact speed is chosen such that the flyer and target plates remain elastic and the measured shear stress will essentially represent the sliding resistance of glass-on-glass. Also, given the relatively high wave speed in glass, the 5 μm thickness of the soda-lime glass film is not expected to lead to any significant wave dispersion effects. The impedance mismatch between the flyer and target plates will introduce abrupt drop in normal stress at the interface when the release wave reflects back from free surface. Thus, two distinct dynamic friction states are obtained in the experiment; the first state (State 1) allows the investigation of the dynamic frictional resistance of interface under constant normal pressure, while the second state (State 2) allows the investigation due to abrupt changes in normal pressure. The wave propagation in the flyer and target plates is illustrated as a time-distance diagram in Figure 2b. The abscissa represents the spatial position of the wave front at a particular time while the ordinate represents the temporal location of the wave front. When the flyer plate impacts the target plate, both longitudinal and shear waves are generated in the flyer and the target plates. The solid lines represent the longitudinal wave fronts while the dashed lines represent the shear wave fronts. The slopes of the solid and the dashed lines represent the inverse of the longitudinal wave speed C_L and shear wave speed C_s, respectively.

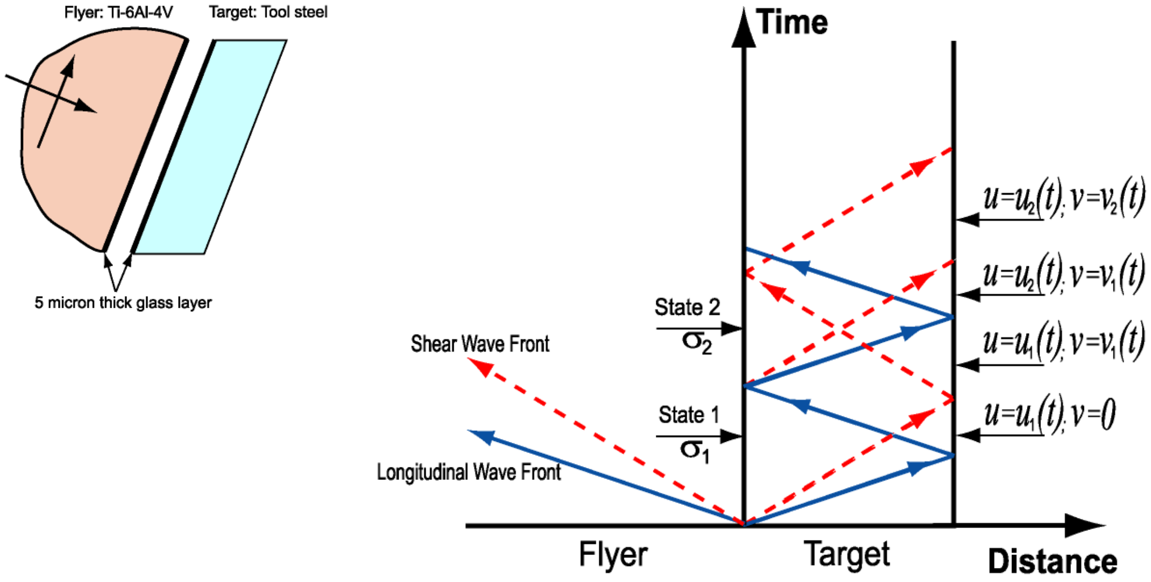

(a) (b)

Figure 2: (a) Plate-impact configurations for soda-lime glass, (b) Wave propagation in flyer and target plates: time-distance diagram.

2.3 Wave Analysis of Pressure-shear Friction Experiments: Calculation of Interfacial Tractions, Slip Velocity, Slip Distance and Temperature

Prior to impact the flyer is accelerated to a known velocity V_0. Then, the initial normal and transverse components of the particle velocity of the flyer plate are, u_0 and v_0 respectively. These velocities can be expressed in terms of the skew angle θ and the impact velocity V_0, as

$$u_0 = V_0 \cos\theta \quad \text{and} \quad v_0 = V_0 \sin\theta \tag{1}$$

When the flyer impacts the target, both the normal and transverse components of particle velocity are imposed on the impact face of the target plate. Using the method of characteristics for 1-D hyperbolic wave equations the normal and transverse components of interfacial traction and slip velocity can be related to the normal and transverse components of particle velocity of the free surface of the target plate, $u_{fs}(t)$ and $v_{fs}(t)$, respectively.

State 1

The components of traction at the interface between the flyer and the target can be expressed as:

$$\tau_1(t) = \frac{(\rho C_s)_t}{2} v_{1fs}(t) \tag{2}$$

$$\sigma_1(t) = -\frac{(\rho C_L)_t}{2} u_{1fs}(t) \tag{3}$$

In (2) and (3), ρ is the mass density, C_L and C_s are the longitudinal and shear wave-speeds respectively, v_{1fs} and u_{1fs} are the transverse and the normal components of particle velocity at the rear surface of the target plate, and the subscripts f and t refer to the flyer and target plates, respectively. From the knowledge of the impact velocity V_0, skew angle θ, the shear impedances of the flyer and the target plates, and the measured free-surface transverse velocity v_{1fs}, the slip velocity in state 1 can be expressed as:

$$V_1^{slip} = V_0 \sin\theta - \left[\frac{(\rho C_s)_t + (\rho C_s)_f}{2(\rho C_s)_f} \right] v_{1fs}(t) \tag{3}$$

State 2

When the compressive longitudinal wave reflects from the free surface of the target plate it reduces the compressive normal stress at the interface from σ_1 to σ_2:

$$\sigma_2 = \frac{\left[(\rho C_L)_f - (\rho C_L)_t \right]}{\left[(\rho C_L)_f + (\rho C_L)_t \right]} \sigma_1 \tag{5}$$

For the 7075-T5 Al alloy/CH tool-steel tribo-pair employed in the present experiments the ratio $\sigma_2 / \sigma_1 = 0.245$. The friction stress and slip velocity can be obtained by solving the characteristic relations for State 2 as:

$$\tau_2(t) = \frac{(\rho C_s)_t}{2} v_{2fs}(t) \tag{6}$$

$$V_2^{slip} = V_0 \sin\theta - \left[\frac{(\rho C_s)_t + (\rho C_s)_f}{2(\rho C_s)_f} \right] v_{2fs}(t) \tag{7}$$

Bulk Temperature at the Tribo-pair Interface

The temperature rise in the vicinity of the tribo-pair interface is estimated by solving the following one-dimensional transient heat conduction [53] to yield

$$T(x,t) = \frac{1}{k} \int_0^t \dot{q}(\xi) \frac{\sqrt{\alpha}}{\sqrt{\pi (t-\xi)}} \exp\left(\frac{-x^2}{4\alpha (t-\xi)} \right) d\xi \tag{8}$$

In Eq. (8), T is the temperature rise, t is time, k is the thermal conductivity, α is the thermal diffusivity, $\dot{q}(t)$ is the heat source and x is the distance perpendicular to the interface.

In order to calculate the temperature distribution in the tribo-pair materials, an estimate for the heat source $\dot{q}(t)$ is required. Using the experimentally measured friction stress τ, and slip velocity V^{slip}, the frictional power can be written as

$$\dot{q}_{glass}(t) = 0.5\tau(t)V^{slip}(t) \quad (9)$$

3. Experimental Results

3.1 Plate-impact Pressure-shear Friction Experiment

Figure 3(a) shows history of the interfacial slip velocity and coefficient of kinetic friction for glass-on-glass slip. At such high slip speed (~20m/s), soda-lime glass shows no-slip initially, followed by slip weakening, strengthening, and then seizure. The mechanism of those phenomena will be discussed later. At the instant of pressure drop, a state of slip results again at the frictional interface. It is interesting to note that the coefficient of kinetic friction is observed to be as high as 1.4 at the instant of pressure drop, then reduces to about 0.8. This is understood to be due to memory effects following a change in normal stress mentioned in previous research [40]. Moreover, it is interesting to note that value of μ in State 2 is higher than that observed in State 1. This can be attributed to the higher level of accumulated plastic strains in State 2 as compared to during State 1, which leads to larger effective area of contact. By assuming that slip is occurring between two semi-infinite glass blocks, the average temperature rise at the tribo-pair interface is estimated by solving the one-dimensional transient heat conduction equation [53] and shown in Figure 3(b). It is interesting to note that the estimated interfacial temperature rise is close to the melting point of glass at these high shear stresses and slip velocities. Figure 4 represents AFM scans of the glass surface before and after the experiment. Glass layer is intact before experiment (Figure 4(a)), while molten glass can be clearly seen smeared on the sliding surface of deformed glass layer shown in Figure 4(b).

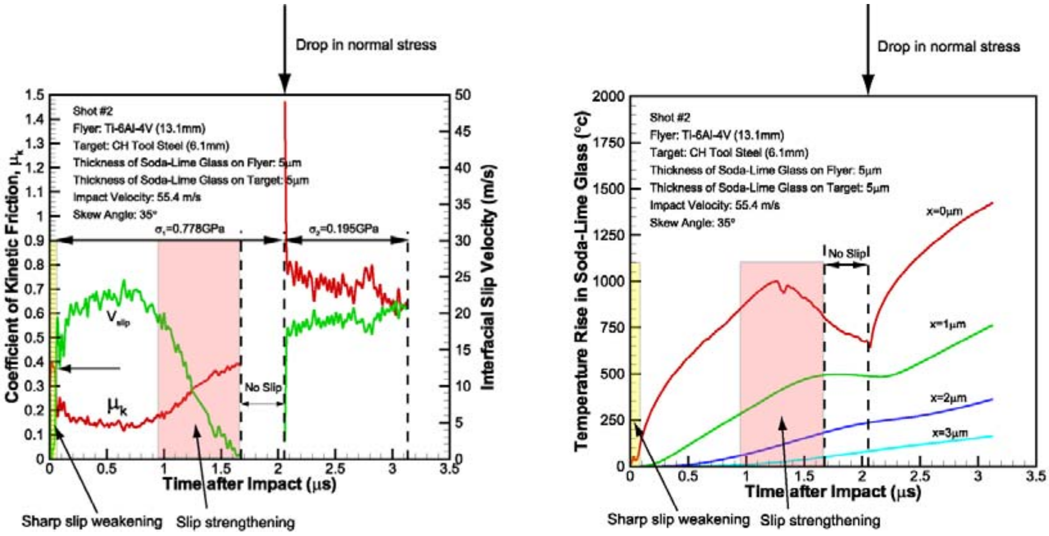

(a) (b)

Figure 3: Plate-impact pressure-shear experiment for glass-on-glass: (a) History of slip velocity and coefficient of kinetic friction, (b) Estimated temperature rise at tribo-pair interface.

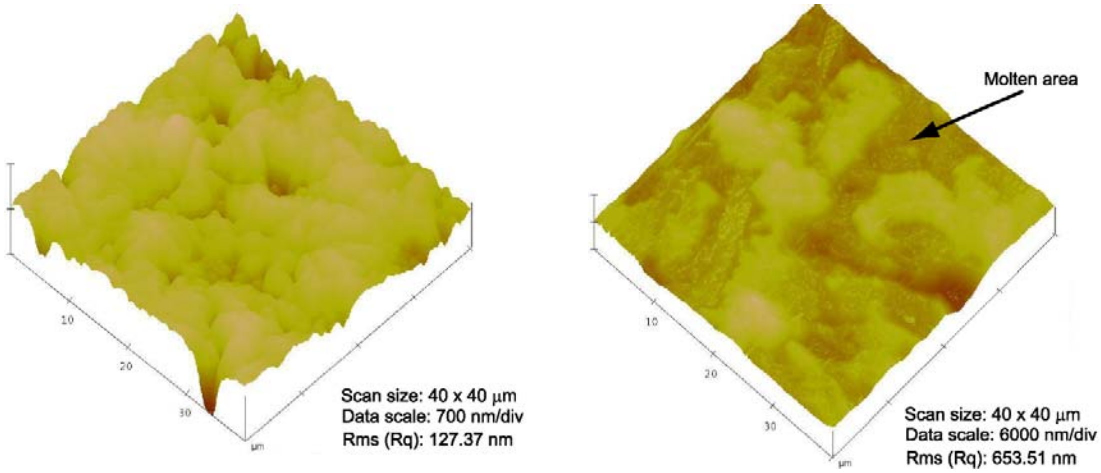

(a) (b)

Figure 4: AFM scans of soda-lime glass film: (a) before test, (b) after test.

Summary and Discussions

In the present study, the pressure-shear friction experiments on both soda-lime glass and Arkansas Nocaculite rock show slip weakening followed by slip strengthening, and the modified torsional Kolsky-bar friction experiments on soda-lime glass show much lower friction coefficients than those obtained at quasi-static slip rates (≤ 1 mm/s). The above mechanical and morphological data have to be integrated to elucidate the physical processing during high speed slip on rocks and analog materials.

Recent measurements of contact area and contact indentation strength σ_C in transparent materials by light scattering [54-55], including quartz, confirmed earlier suggestions [56] that the shear strength τ_C is very high (estimated to be of order 10% of the shear modulus *G*) at asperities contacts in typical rock systems, and thus when forced to shear, they generate intense but highly localized heating during their life time. The local shear strength τ_C of the asperity contact will presumably degrade continuously with increasing flash temperature T_a. An elementary model considering flash heating at asperity contacts had been proposed recently by Rice [16, 29]. The model considers contacts of uniform size L, and hence lifetime L/V where L is the slip needed to renew the asperity contact population, and V is slip rate; and assumes that their shear strength remains at the low-temperature value τ_C until temperature has reached a critical value T_{crit} above which the weakened shear strength τ_W is assumed to has a negligibly small value compared to its lower temperature value τ_C (Figure 5). Their temperature rise is estimated from a simple one-dimensional transient heat conduction equation, with heating power $\tau_C V$ per unit area at the sliding contact surface. Beeler and Tullis [30] and Tullis and Goldsby [31] observed that a better fit of Rice's model to data showing strong rate-weakening of friction was to assume to small but non-negligible τ_W for $T_a > T_{crit}$. The model thus defines a critical slip rate V_{crit} such that there is no weakening if $V < V_{crit}$, but strong weakening if $V > V_{crit}$. That is, the friction coefficient μ, which has the value μ_0 at low slip rates and μ_W at high slip rates, is given in this simple model by:

$$\mu = \mu_0 \ \mathit{if}\ V < V_{crit},\ \ \mu = (\mu_0 - \mu_W)\frac{V_{crit}}{V} + \mu_W \ \mathit{if}\ V > V_{crit}; \qquad (18)$$

where $V_{crit} = \alpha \dfrac{\pi}{L}\left[\dfrac{\rho c\left(T_{crit} - T_{bulk}\right)}{\tau_C}\right]^2,$ (19)

and α is thermal diffusivity, ρc is heat capacity per unit volume.

$V_{crit} = 0.12$ m/s has been estimated to be onset of severe thermal weakening for glass and geo-materials, when it is recognized that $L = 5\ \mu m$, $\tau_C = 3.0$ GPa and temperature range from ambient up to ~900 ^{0}C. Recent laboratory studies [11-14] and our results imposing rapid slip on geological and analog materials are indeed consistent with such an expected friction reduction at higher slip rates. The results suggest that friction coefficient is about 0.2 to 0.4 at average seismic slip rates for geo-materials.

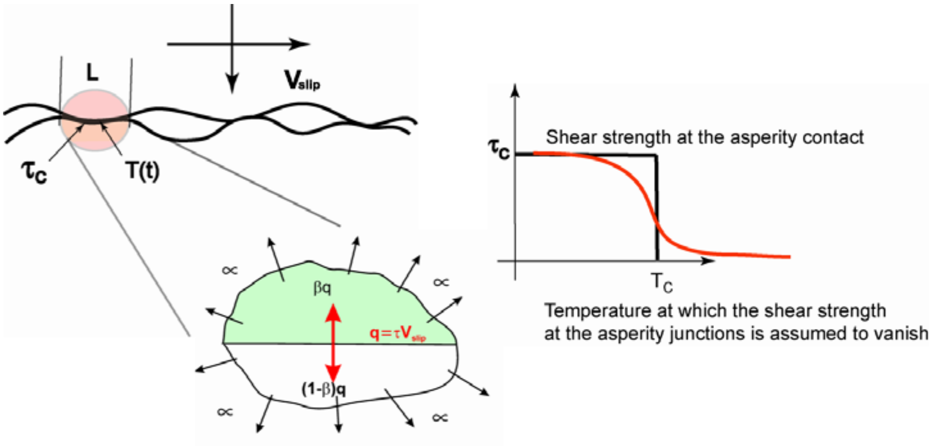
L
V_slip
τc
T(t)
∝
βq
q=τV_slip
(1-β)q
τc
Shear strength at the asperity contact
Tc
Temperature at which the shear strength
at the asperity junctions is assumed to vanish

Figure 5: Flash heating at asperity contacts

Based on the above model, we conclude that the first slip-weakening for soda-lime glass is most likely due to the thermal weakening induced by flash heating and incipient melting at asperity contacts, while the second-strengthening is caused by coalescence and solidification of melt patches.

Low values of μ for rocks and analog materials obtained in current experiments may explain fault weakening during seismic slips. The large decrease in μ at higher slip rates is also consistent with rupture propagating as a self-healing slip pulse [57]. Moreover, the experimental results for rocks and analog materials at such high slip rates (0~20 m/s) will help to establish the constitutive description of the behavior that can be used in dynamic models of earthquake rupture.

ACKNOWLEDGEMENTS

The authors would like to acknowledge the financial support of South California Earthquake Center and NSF EARTH #08100183.

REFERENCES

1. Dieterich, J. H., Modeling of rock friction: I, experimental results and constitutive equations. Journal of Geophysical Research 84(B5), 2161-2168, 1979.
2. Dieterich, J. H., Constitutive properties of faults with simulated gouge. Mechanical Behavior of Crustal Rocks. American Geophysical Union, Washington, D.C., Vol. 24, PP. 103-120, 1981.
3. Ruina, A., Slip stability and state variable friction laws. Journal of Geophysical Research 88(B12), 10359-10370, 1983.
4. Tullis, T. E. and Weeks, J. D., Constitutive behavior and stability of frictional sliding of granite. Pure Applied Geophysics 124, 383-414, 1986.
5. Marone, C., Laboratory-derived friction laws and their application to seismic faulting. Annual Review Earth and Planetary Science 26, 643-696, 1998.
6. Scholz, C. H., Earthquakes and friction laws. Nature, Vol. 391, 37-42, 1998.
7. Marone C., The effect of loading rate on static friction and the rate of fault healing during the earthquake cycle. Nature, Vol. 391, 69-72, 1998.

8. Byerlee, J. D., Friction of rocks. Pure Applied Geophysics, 116, 615-626, 1978.
9. Dieterich, J. H., Time-dependent friction and the mechanics of stick slip. Pure Applied Geophysics, 116, 790-806, 1978.
10. Heaton, T. H., Evidence for and implications of self-healing pulses of slip in earthquake rupture. Physics of the Earth and Planetary Interiors, 64, 1-20, 1990.
11. Tsutsumi, A. and Shimamoto, T., High-velocity frictional properties of gabbro. Geophysical Research Letters 24, 699-702, 1997.
12. Hirose, T. and Shimamoto, T., Growth of molten zone as a mechanism of slip weakening of simulated faults in gabbro during frictional melting. J. Geophys. Res., 110 (B5), Art. No.B05202, doi: 10.1029/2004JB003207, 2005.
13. Goldsby, D. L. and Tullis, T. E., Low frictional strength of quartz rocks at sub-seismic slip rates. Geophysical Research Letters 29(17), Art. No. 1844, 2002.
14. Toro, G. D., Goldsby, D. L. and Tullis, T. E., Friction falls towards zero in quartz rock as slip velocity approaches seismic rates. Nature, Vol. 427, 436-439, 2004.
15. Sibson, R. H., Interaction between temperature and pore-fluid pressure during earthquake faulting – A mechanism for partial or total stress relief, Nature, 243, 66-68, 1973.
16. Rice, J. R., Heating and weakening of faults during earthquake slip. Submitted to Journal of Geophysical Research, 2005.
17. Lachenbruch, A. H., Frictional heating, fluid pressure, and the resistance to fault motion. J. Geophys. Res., 85, No. B11, 6097–6122, 1980.
18. Mase, C. W., and L. Smith., Pore–fluid pressures and frictional heating on a fault surface. Pure Appl. Geophys., 122, 583-607, 1985.
19. Mase, C. W., and L. Smith., Effects of frictional heating on the thermal, hydrologic, and mechanical response of a fault. J. Geophys. Res., 92, No. B7, 6249–6272, 1987.
20. Lee, T. C., and Delaney, P. T., Frictional heating and pore pressure rise due to a fault slip. Geophys. J. Roy. Astronom. Soc. 88 (3), 569-591, 1987.
21. Andrews, D. J., A fault constitutive relation accounting for thermal pressurization of pore fluid. J. Geophys. Res., 107, No. B12, 2363, doi: 10.1029 / 2002JB001942, ESE 15-1–15-8, 2002.
22. Wibberley, C. A. J., Hydraulic diffusivity of fault gouge zones and implications for thermal pressurization during seismic slip. Earth Planets Space, 54, 1153-1171, 2002.
23. Noda, H., and T. Shimamoto, Thermal pressurization and slip-weakening distance of a fault: An example of the Hanaore fault. Southwest Japan. Bull. Seismol. Soc. Amer., in press, 2005.
24. Sulem, J., I. Vardoulakis, H. Ouffroukh, and V. Perdikatsis, Thermo-poro-mechanical properties of the Aigion fault clayey gouge - Application to the analysis of shear heating and fluid pressurization. Soils and Foundations. 45 (2), 97-108, 2005.
25. Bowden, F. P., and P. H. Thomas, The surface temperature of sliding solids. Proc. Roy. Soc. Lond., Ser. A, 223, 29-40, 1954.
26. Archard, J.F., The Temperature of Rubbing Surfaces. Wear, 2, 438-455, 1958-1959.
27. Kuhlmann-Wilsdorf, D., Flash temperatures due to friction and joule heat at asperity contact. Wear, 105, 187-198, 1985.
28. Ashby, M.F., Abulawi J. and Kong H.S., Temperature Maps for Frictional Heating in Dry Sliding. Tribology Transactions, Volume 34, 4, 577-587, 1991.
29. Rice, J. R., Flash heating at asperity contacts and rate-dependent friction, EOS Transactions, American Geophysical Union, 80, F6811, 1999.
30. Beeler, N.M., and T.E. Tullis, Constitutive relationships for fault strength due to flashheating. USGS Open File Report, submitted, 2003.
31. Tullis, T. E., and D. L. Goldsby, Flash melting of crustal rocks at almost seismic slip rates. Eos Trans. AGU, 84(46), Fall Mtg. Suppl., Abstract S51B-05, 2003.
32. Tullis, T. E., and D. L. Goldsby, Laboratory experiments on fault shear resistance relevant to coseismic earthquake slip. SCEC Annual Progress Report for 2003.
33. Okada, M., Liou, N.-S., Prakash, V. and Miyoshi, K., Tribology of high speed metal-on-metal sliding at near-melt and fully-melt interfacial temperatures. Wear 249, 672-686, 2001.
34. Bowden, F. P., F.R.S. and Persson, P. A., Deformation, heating and melting of solids in high-speed friction. Proceeding of Royal Society of London, A260 433-458, 1960.
35. Linker, M. F. and Dieterich, J. H., Effects of variable normal stress on rock friction: observations and constitutive equations. Journal of Geophysical Research 97, 4923-4940, 1992.

36. Richardson, E. and Marone, C., Effects of normal force vibrations on friction healing. Journal of Geophysical Research 104, 28859-28878, 1999.
37. Bureau, L., Baumberger, T. and Caroli, C., Shear response of a frictional interface to a normal load modulation. Physics Review E 62, 6810-6820, 2000.
38. Irfan, M. A. and Prakash, V., Time resolved friction during dry sliding of metal on metal. International Journal of Solids and Structures 37, 2859-2882, 2000.
39. Prakash, V. and Clifton, R. J., Time Resolved Dynamic Friction Measurements in Pressure-Shear Experimental Techniques in the Dynamics of Deformable Bodies. Vol. AMD Vol. 165 ASME, New York, pp 33-47, 1993.
40. Prakash, V., Friction response of sliding interfaces subjected to time varying normal pressures. Journal of Tribology 120, 97-102, 1998.
41. Weetman, J., Unstable slippage across a fault that separates elastic media of different elastic constants. Journal of Geophysical Research 85, 1455-1461, 1980.
42. Adams, G. G., Self excited oscillations of two elastic half-spaces sliding with a constant coefficient of friction. Journal of Applied Mechanics 62, 867-872, 1995.
43. Andrews, D. J. and Ben-Zion, Y., Wrinkle-like slip pulse on a fault between different materials. Journal of Geophysical Research, 102, 553-571, 1997.
44. Simoes, F. M. F. and Martins, J. A. C., Instability and ill-posedness in some friction problems. International Journal of Engineering Science 36, 1265-1293, 1998.
45. Cochard, A. and Rice, J. R., Fault rupture between dissimilar materials: ill-posedness, regularization, and slip-pulse response. Journal of Geophysical Research 105(25), 891-907, 2000.
46. Ranjith, K. and Rice, J. R., Slip dynamics at an interface between dissimilar materials. Journal of Geophysical Research 104, 28859-28878, 2001.
47. Ben-Zion, Y., Dynamic ruptures in recent models of earthquake faults. Journal of Mechanics and Physics of Solids 49, 2209-2244, 2001.
48. Kim, K.S., Clifton, R.J., and Kumar, P., A combined normal and transverse displacement interferometer with an application to impact of Y-cut Quartz, Journal of Applied Physics, 48, 4132-4139, 1977.
49. Prakash, V., A pressure-shear plate impact experiment for investigating transient friction. Experimental Mechanics 35(4), 329-336, 1995.
50. Weeks, J. D., Beeler, N. M. and Tullis, T. E., Frictional behavior; glass is like a rock. In: Eos Transactions, Fall Meeting Abbreviations Supplement, 72. AGU, pp. 457-458, 1991.
51. Dieterich, J. H. and Kilgore, B. D., Direct observation of frictional contacts; new insights for state dependent properties. Pure Applied Geophysics 143, 283-302, 1994.
52. Dieterich, J. H. and Kilgore, B. D., Imaging surface contacts; power law contact distributions and contact stresses in quartz, calcite, glass and acrylic plastic. Tectonophysics 256, 219-239, 1996.
53. Carslaw, H. S. and Jaeger, J. C., Conduction of heat in solids. Oxford University Press, London, 1959.
54. Dieterich, J. H., and B. D. Kilgore, Direct observation of frictional contacts: New insights for state-dependent properties. Pure Appl. Geophys., 143, 283-302, 1994.
55. Dieterich, J. H., and B. D. Kilgore, Imaging surface contacts: power law contact distributions and contact stresses in quartz, calcite, glass and acrylic plastic. Tectonophysics, 256, 219-239, 1996.
56. Boitnott, G. N., R. L. Biegel, C. H. Scholz, N. Yoshioka and W. Wang, Micromechanics of rock friction 2: Quantitative modeling of initial friction with contact theory. J. Geophys. Res., 97, 8965-8978, 1992.
57. Beeler, N. M., Tullis T. E., Self-healing slip pulses in dynamic rupture models due to velocity dependent strength, Bulletin of the Seismological Society of America, 86, 1130-1148, 1996.

Proceedings of the SEM Annual Conference
June 7-10, 2010 Indianapolis, Indiana USA
©2010 Society for Experimental Mechanics Inc.

Rate dependent response and failure of a ductile epoxy and carbon fiber reinforced epoxy composite

Eric N. Brown[1], Philip J. Rae[2], Dana M. Dattelbaum[3], David Stahl[3]
[1]Los Alamos National Laboratory, ADW, Los Alamos, NM 87545 USA
[2]Los Alamos National Laboratory, MST-8, Los Alamos, NM 87545 USA
[3]Los Alamos National Laboratory, DE-9, Los Alamos, NM 87545 USA

ABSTRACT

An extensive characterization suite has been performed on the response and failure of a ductile epoxy 55A and uniaxial carbon fiber reinforced epoxy composite of IM7 fibers in 55A resin from the quasistatic to shock regime. The quasistatic and intermediate strain rate response, including elastic modulus, yield and failure have are characterized by quasistatic, SHPB, and DMA measurements as a function of fiber orientation and temperature. The high strain rate shock effect of fiber orientation in the composite and response of the pure resin are presented for plate impact experiments. It has previously been shown that at lower impact velocities the shock velocity is strongly dependent on fiber orientation but at higher impact velocity the in-plane and through thickness Hugoniots converge. The current results are compared with previous studies of the shock response of carbon fiber composites with more conventional brittle epoxy matrices. The spall response of the composite is measured and compared with quasistatic fracture toughness measurements.

DISCUSSION

The strength properties of a carbon fiber filled epoxy composite are presented. Tension, compression, and shear measurements [1] were made on the composite in three fiber orientations and on the pure epoxy. The epoxy resin was remarkably ductile for such a materil and the strength behavior was found to be senitive to both strain-rate and temperature. The mechanical properties of the composite were found to be highly dependant on the fiber orientation but lass sensitive to strain –rate and temperature. Those changes that were observed correlated closely with the changes in the properties of the epoxy matrix.

A number of gas gun-driven plate impact experiments have been performed to define a Hugoniot-based equation of state for both the resin and composite. The shock compression response of the 55A resin is in line with previous reports for related epoxies, including the widely-used EPON class of resins. The composite materials show a complex shock response, with the shock wave profiles being highly influenced by the composite nature, and varied impedance character of the composite constituents and void volume. X-ray microtomography has shown the presence of large voids within the composite that are largely unidirectional through the entirety of the sample. All of the plate impact samples were characterized by this method to allow future importation of microstructures into simulation codes. Five experiments performed to define the equation of state of the composite, with additional experiments aimed at probing dynamic tensile (spall) strength in the through thickness direction. The data are more consistent with the data of Dandekar [2] than those reported by Hixson or Millett [3,4]. The shock wave profiles recorded at the free surface of the composite in symmetric impact spall experiments indicates that the composite has a week spall strength, consistent with earlier reports [3].

ACKNOWLEDGMENTS

Los Alamos National Laboratory is operated by LANS, LLC, for the NNSA of the US Department of Energy under contract DE-AC52-06NA25396. This research was supported under the auspices of the US Department of Energy and the Joint DoD/DOE Munitions Program.

REFERENCES

1 E.N. Brown, C. Liu “Applying Digital Image Correlation to Unidirectional Composite Iosipescu Shear Test

DOI 10.1007/978-1-4419-8228-5_58, © The Society for Experimental Mechanics, Inc. 2011

Specimens” in Proceedings Of The SEM Annual Conference On Experimental Mechanics, 2007.

2 D.P. Dandekar, C.A. Hall, L.C. Chhabildas, W.D. Reinhart “Shock response of a glass-fiber-reinforced polymer composite,” *Compsoite Structures* 2003 61(1-2) 51–59.

3 R.S. Hixson, personal communication, Los Alamos, NM, 2008.

4 J.C.F. Millett, N.K. Bourne, Y.J.E. Meziere, YJE, et al. “The effect of orientation on the shock response of a carbon fibre-epoxy composite,” *Composite Science and Technology* 2007 **67**(15-16) 3253–3260.

5 P.J. Rae, E.N. Brown, B.E. Clements, D.M. Dattelbaum. “Pressure induced phase change in poly(tetrafluoroethylene) at modest impact velocities,” *Journal of Applied Physics* 2005 **98**(6)063521.

Proceedings of the SEM Annual Conference
June 7-10, 2010 Indianapolis, Indiana USA
©2010 Society for Experimental Mechanics Inc.

High Pressure Hugoniot Measurements Using Converging Shocks

J.L. Brown, G. Ravichandran
Division of Engineering and Applied Science, California Institute of Technology,
1200 E. California Blvd., Pasadena CA 91125, jlbrown@caltech.edu

ABSTRACT

Plate impact experiments are a powerful tool in equation of state development, but are inherently limited by the range of impact velocities accessible to the gun. In an effort to dramatically increase the range of pressures which can be studied with available impact velocities, a new experimental technique is being developed. The possibility of using converging shock waves to produce a high pressure Mach reflection is examined. The technique proposed uses a composite target simply consisting of two concentric cylinders, with the only requirement being the initial shock speed in the outer cylinder is greater than that in the inner cylinder. Conically converging shocks will be generated at the interface due to the impedance mismatch and axisymmetric geometry of the composite target. Upon convergence, an irregular reflection must occur, at which point the conical analog of a Mach reflection develops. Once the Mach reflection reaches a steady state, the high pressure state in the Mach disk can be measured using velocity interferometry and impedance matching techniques. Experimental results on a copper inner cylinder are in good agreement with numerical simulations and data in the literature.

1. INTRODUCTION

High pressure equation of state measurements can be determined by subjecting the material to a one dimensional plane shock wave. The resulting equilibrium state behind the shock wave can be characterized by making two experimental measurements of the jump in material properties, typically shock speed and particle velocity, and relating the rest of the thermodynamic properties with the Rankine-Hugoniot conservation equations. Shock waves of this type are usually generated by the planar impact of flat plates. Because the resulting pressure of the shock wave generated in this type of experiment is determined by the impact velocity, there has been considerable interest in finding techniques which can be used to extend the range of the impact velocities. Gun systems, for example, were traditionally limited by two-stage launcher technology to velocities of approximately 7 km/s [1] , until the development of the hypervelocity launcher [2] which utilizes a graded density impactor to produce quasi-isentropic loading of a third stage flyer to velocities of 12 km/s. Later, isentropic loading was generated magnetically using Sandia national laboratories Z accelerator [3] where flyer velocities of over 25 km/s have been obtained [4].

Significant pressure increases can also be achieved through the interaction of shock waves. The nonlinear nature of shock waves can result in irregular reflections under special conditions, a phenomenon first discovered by Ernst Mach in 1869. The subject is thoroughly reviewed in gases

T. Proulx (ed.), *Dynamic Behavior of Materials, Volume 1*, Conference Proceedings of the Society for Experimental Mechanics Series,
DOI 10.1007/978-1-4419-8228-5_59, © The Society for Experimental Mechanics, Inc. 2011

by Bleakney and Taub [5], and the first experimental observations of Mach reflections in metals were made by Al'shuler et al [6]. A few years later, Fowles and Isbell [7] produced conically converging shocks in metal cylinders by detonating the front surface of a surrounding cylinder of explosive. The resulting Mach reflection was measured with a streak camera viewing the rear surface, for which significant pressures were found in the Mach disk. Similar measurements of the Mach configuration using the same idea were made in plexiglass cylinders using a flash gap technique by Adadurov et al [8]. This method was later extending to mechanical impact testing, where composite cylinders were used to generate the converging shocks and subsequent Mach reflection for the generation of extreme pressures in recovery experiments [9].

In the present study, the feasibility of using convergent shock waves to make accurate high pressure EOS measurements is investigated. Numerical simulations are conducted to verify the technique and design the experiments. Quantitative measurements of the Mach wave are made using a velocity interferometer for any reflecting surface (VISAR) [10], and the material Hugoniot is generated using the measured velocity wave profiles and impedance matching techniques.

2. EXPERIMENTAL SETUP

The so-called Mach lens configuration utilizes the composite target shown in Figure 1. The composite consists of an inner cylinder surround by a concentric outer cylinder. Upon impact, a plane shock is generated at the front of the target, with the requirement that the shock speed in the outer cylinder is higher than that in the inner. The impedance mismatch at the cylinder interface results in a conical shock wave which converges on the axis of the inner cylinder. Upon convergence, the conical analog of a Mach reflection has been shown to occur [7-9, 11], and the stable shock configuration results in a relatively plane Mach disk for which there is a significant increase in pressure over the initial shock. After a distance in travel roughly equal to the inner cylinder diameter [9], the shock configuration becomes steady in time and the Mach disk reaches a limiting diameter. Since the configuration is steady, the velocity of the Mach disk is assumed to be the same as the shock speed in the outer cylinder. Simply speaking, the converging shocks essentially serve to increase the shock speed in the inner cylinder from its initial value to that of the outer cylinder. If the outer material and the impactor are well characterized, an accurate measurement of the impact velocity and impedance matching can be used to obtain the shock speed of the Mach wave. Since the Mach wave is assumed to be planar near the center of the target, the shocked state in the Mach disk should lie on the principle Hugoniot. Thus, a single measurement of the particle velocity behind the Mach disk provides an estimate of the inner cylinder Hugoniot.

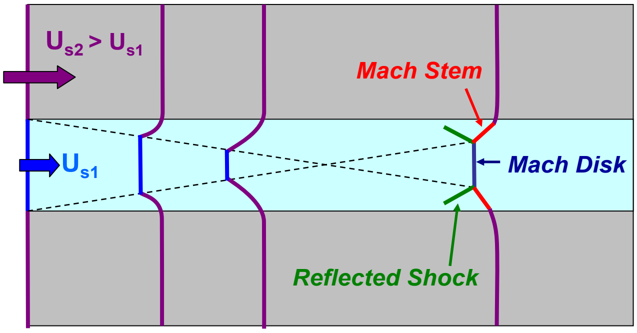

Figure 1. Mach lens target configuration. An initially plane shock is generated at impact on the left of the lens.

While the physics involved in the transient development of the Mach reflection is very complex, the resulting steady state can be completely characterized by simple impedance matching techniques. As shown in Figure 2a, there are 3 basic states associated with the Mach configuration. State 1 is simply the shocked state of the outer cylinder, and is calculated by impedance matching between the impactor and outer cylinder materials. State 2 is the shocked region in the Mach cone and is calculated by assuming the shock speed is the same as in state 1. The resulting particle velocity in state 2 can then be found from the shock-particle velocity Hugoniot. Finally, state 3 can be estimated by assuming the interface between the two materials is effectively a slip stream. That is, the pressures in states 1 and 3 are equal, but there is a discontinuity in the particle velocities. Since the change from state 2 to 3 will be isentropic, a release isentrope can be constructed, and state 3 can be calculated from the intersection of the isentrope with the pressure calculated in state 1.

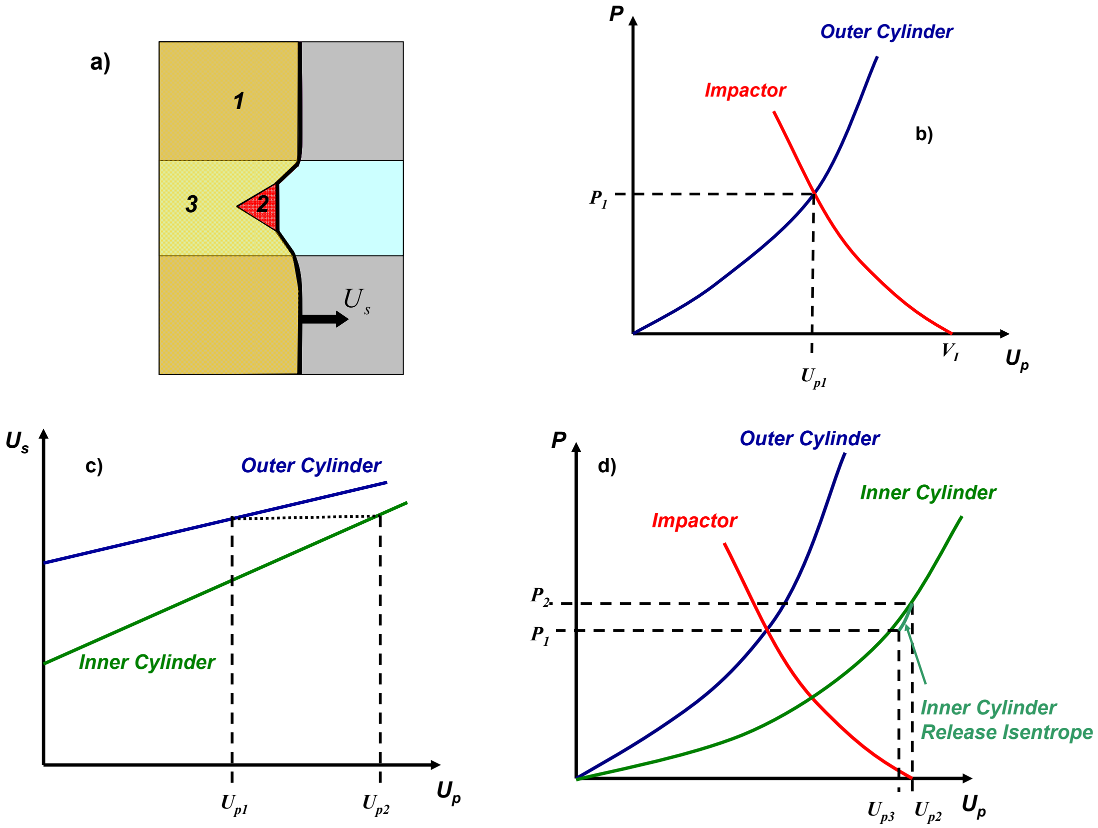

Figure 2. Impedance matching to determine the steady Mach configuration equilibrium state. a) Steady Mach configuration with the three regions of concern. b) Impedance matching between the impactor and outer cylinder determine state 1. c) State 2 is assumed to have the same shock speed as state 1. c) Isentropic release from state 2 to the pressure in state 1 determines state 3.

3. NUMERICAL SIMULATIONS

A series of simulations were conducted using the LS-DYNA finite element code. All of the simulations utilized axi-symmetric elements, an elastic perfectly plastic strength model, and the Mie-Gruneisen EOS with a linear shock-particle velocity Hugoniot. Pressure contours showing the development of the Mach configuration in a typical simulation is shown in Figure 3. In this setup, a thin copper flyer is hitting the composite target consisting of a copper inner cylinder and molybdenum outer cylinder. The simulation clearly captures many of the simple features previously assumed with this type of configuration, namely, the initial generation of conically converging shocks, an irregular Mach reflection upon convergence, and then growth of the Mach configuration into a steady state. Further, the impedance matching techniques discussed previously predict a shock velocity of 5.66 km/s with a corresponding peak Hugoniot particle velocity of 1.16 km/s in the copper. For simplicity, the Hugoniot can be used to estimate the release isentrope, which gives a steady state particle velocity of 0.59 km/s behind the Mach wave. As shown in Figure 3e the simulations agree very well with this simple theory.

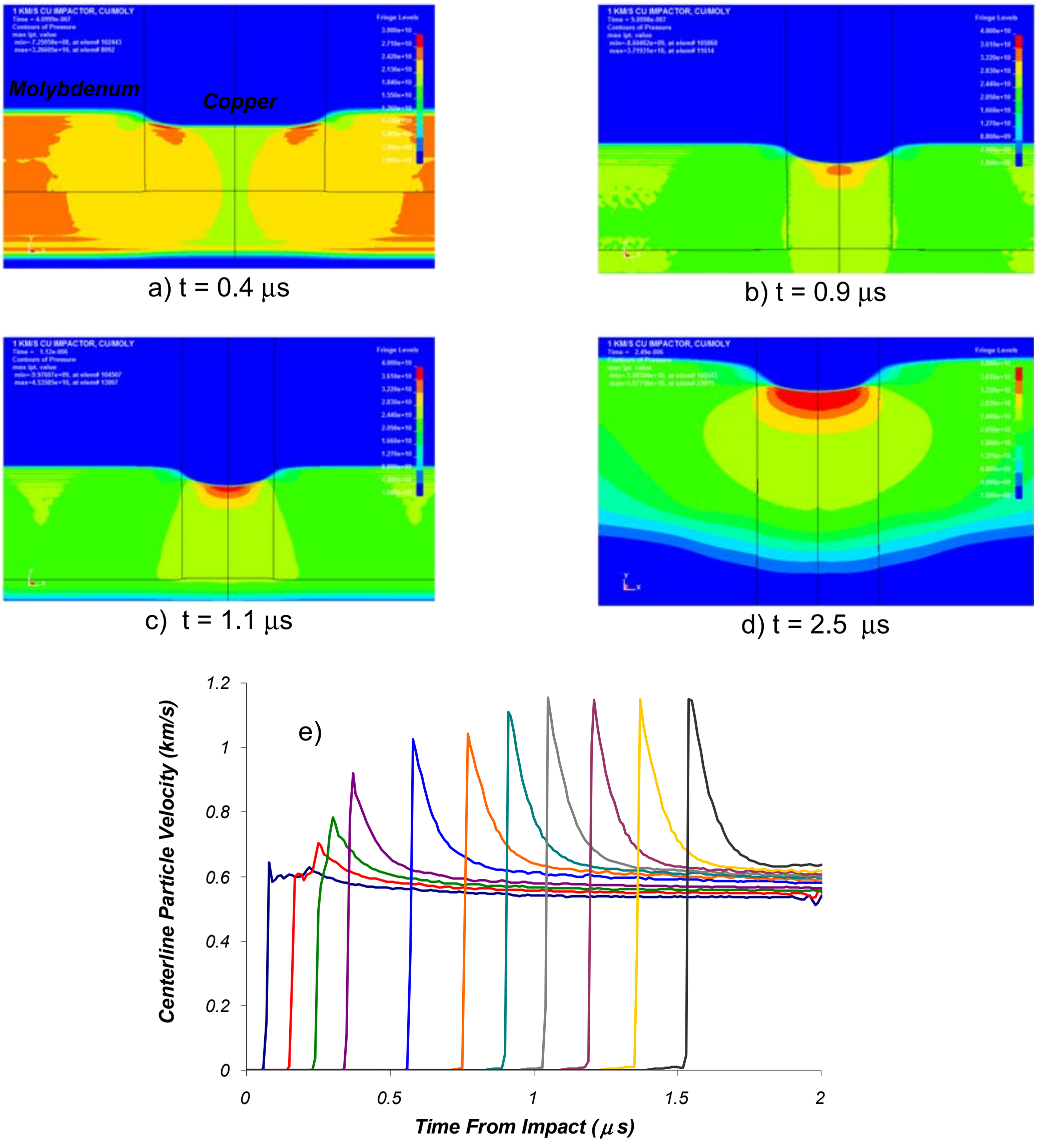

a) t = 0.4 μs

b) t = 0.9 μs

c) t = 1.1 μs

d) t = 2.5 μs

Figure 3. Simulated Mach lens experiments with a copper flyer impacting a copper and molybdenum target at 1 km/s. Pressure contours showing the formation and subsequent growth of the Mach wave are shown in a), b), c), and d). The particle velocity at Lagrangian points along the center line of the target are shown in e).

4. EXPERIMENTAL RESULTS AND DISCUSSION

Impact experiments were conducted using a 3 m long propellant gun with a 37 mm bore to velocities of 1.8 km/s using the target configuration shown in Figure 4a. The impactors were disks with a diameter of 34 mm and thickness of 3 mm. The target cylinders were 15 mm long while the diameters of the outer and inner cylinders were 34 mm and 5 mm, respectively. A small amount of low viscosity epoxy was applied to the inner cylinder and it was press fit into the outer cylinder, assuring a good interface. The dimensions were dictated by the gun bore diameter. The diameter of the inner cylinder was selected to ensure there would be no interference from edge effects due to the outer cylinder free surface, while still maintaining enough length such that the Mach configuration is steady. Numerical simulations were used to confirm each setup.

While not shown here, the simulations also suggested some asymptotic tendencies of the size of the Mach disk. This was, for the most part, a qualitative observation that as the pressures in the Mach disk and the outer cylinder become close, $P_2 \rightarrow P_1$, the Mach disk diameter approaches the inner cylinder diameter. Conversely, as the pressure difference becomes large, the Mach disk diameter becomes very small. As such, in an effort to eliminate any problems associated with measuring a small Mach disk, a material with a stiff Hugoniot and high wave speed was desired. These trends tend to run contradictory, but molybdenum seems to be an excellent outer cylinder material in this regard. Copper was selected as model inner cylinder since its response is well known and it was shown to work well in the original experiments of this type [7]. Experiments were also conducted with an aluminum outer cylinder. This was done in an attempt to maximize the gain in these experiments since aluminum has very high wave speeds for a metal.

Results from the VISAR measurements of the free surface at the rear of inner cylinder are shown in Figure 4a, such that the waveforms overlay at an arbitrary time. The initial profiles were measured using a polished rear surface, and, as shown, there seems to be movement in front of Mach front. The elastic wave speed is expected to be slower than the shock velocity in these experiments, so this is, perhaps, indicative of an instability due to imperfections in sample surfaces. Further, the loss of light contrast after the shock is believed to be the result of a loss of reflectivity as the shock breaks out at the rear surface. More recent experiments have been conducted monitoring a diffuse rear surface. These profiles do not exhibit much movement ahead of the shock, and some of the release profile is measured.

While future experiments will try to capture the entire wave profile, the primary goal at this point in the work is to make a measurement of the Hugoniot. For each experiment, the shock velocity can be found through impedance matching between the impactor and outer cylinder. The corresponding particle velocity is estimated from the measured velocity profile, where for simplicity, it is assumed to be half of the free surface velocity. The resulting Hugoniot states are shown in Figure 4b and are in good agreement with data in the literature [12]. Another look at this data set in pressure-particle velocity space is shown in Figure 4c. Here, each shot is plotted in a different color and symbol. The lower pressure point is initial shocked state, which can be viewed as the equivalent plate impact state. The higher pressure point is the state resulting from the Mach configuration, and the magnification in pressure along with the required plate impact velocity to reach this pressure is given alongside each arrow. For example, the purple data set shows the results for a steel impactor hitting a copper/aluminum Mach lens target at 1.3 km/s. The state measured is 3.5 times greater than that expected from the standard shock experiment. Further, the traditional plate impact experiment would require an impactor velocity of 3.5 km/s to reach this pressure.

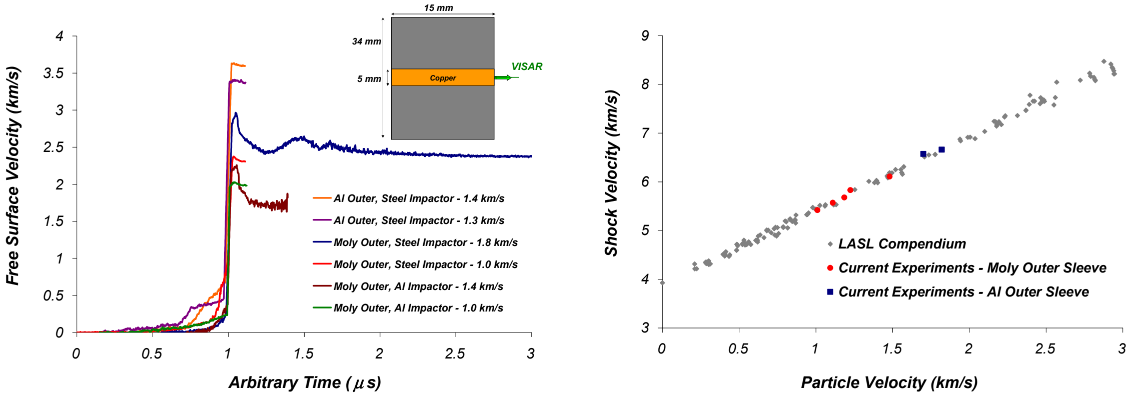

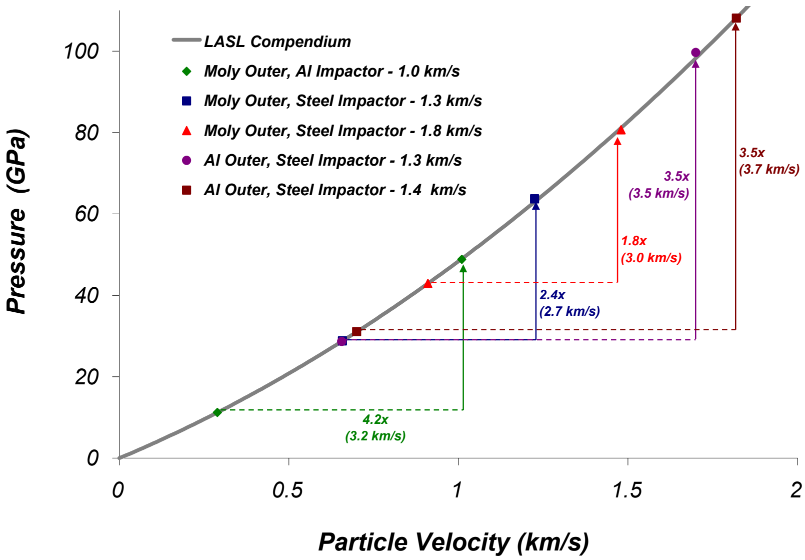

Figure 4. Mach lens target configuration. An initially plane shock is generated at impact on the left of the lens.

5. CONCLUSIONS

Previous works on conically converging shock waves suggest it is possible to make high pressure equation of state measurements from the resulting Mach reflection. The possibility is explored in this work through numerical simulations and experimental measurements of the Mach wave velocity profile. The Mach lens is a simple target assembly consisting only of two concentric cylinders. Since the shock velocity is essentially obtained for free, only a single independent measurement of the particle velocity is required to fully characterize the equilibrium state behind the Mach reflection. The Mach reflection is assumed to be locally planar where the velocity is measured, and the resulting state of uniaxial strain suggests the equilibrium state should lie on the principal Hugoniot and be in good agreement with previous measurements. This proves to be the case, as the Hugoniot measurements in this work agree very well existing data, and the resulting states are up to 4.2 times greater than the initial shock pressure. While the impact velocity of the gun is limited to 1.8 km/s, equivalent Hugoniot states of up to 3.7 km/s are measured.

6. ACKNOWLEDGEMENTS

The research support provided by the Caltech Center for the Predictive Modeling and Simulation of High-Energy Density Dynamic Response of Materials through the U.S. Department of Energy contract DE-FC52-08NA28613 is gratefully acknowledged.

7. REFERENCES

1. W. D. Crozier and W. Hume, "High-velocity, light-gas gun," *J. Appl. Phys.,* vol. 28, pp. 892-894, 1957.
2. L. C. Chhabildas, J. E. Dunn, W. D. Reinhart, and J. M. Miller, "An impact technique to accelerate flier plates to velocities over 12 km/s," *Int. J. Impact Engng.,* vol. 14, pp. 121-132, 1993.
3. C. A. Hall, M. D. Knudsen, J. R. Asay, R. Lemke, and B. Oliver, "High velocity flyer plate launch capability on the Sandia Z accelerator," *Int. J. Impact Engng.,* vol. 26, pp. 275-287, 2000.
4. M. D. Knudsen, D. L. Hanson, J. E. Bailey, C. A. Hall, and C. Deeney, "Principal Hugoniot, reverberating wave, and mechanical reshock measurements of liquid deuterium to 400 GPa using plate impact techniques," *Phys. Rev. B.,* vol. 69, 2004.
5. W. Bleakney and A. H. Taub, "Interaction of Shock Waves," *Rev. Mod. Phys.,* vol. 21, 1949.
6. L. V. Al'tshuler, S. B. Kormer, A. A. Bakanov, A. P. Petrunin, and A. I. G. Funtikov, A.A., "Irregular conditions of oblique collision of shock waves in solid bodies," *Sov. Phys. JETP,* vol. 14, 1962.
7. G. R. Fowles and W. M. Isbell, "Method for Hugoniot Equation-of-State Measurements at Extreme Pressures," *J. Appl. Phys.,* vol. 36, pp. 1377-1379, 1964.
8. G. A. Adadurov, A. N. Dremin, and G. I. Kanel, "Mach reflection parameters for plexiglass cylinders," *ZPMTF,* vol. 10, pp. 126-128, 1969.
9. Y. Syono, T. Goto, and T. Sato, "Pressure enhancement by conically convergent shocks in composite cylinders and its application to shock recovery experiments," *J. Appl. Phys.,* vol. 53, pp. 7131-7135, 1982.
10. L. M. Barker and R. E. Hollenback, "Laser inteferometer for measuring high velocities of any reflecting surface," *J. Appl. Phys.,* vol. 43, pp. 4669-4675, 1972.
11. Y. Mori and K. Nagayama, "Observation of shock wave convergence or collision induced by shaping of plane shock front in solids," *SPIE High-Speed Photography and Photonics,* vol. 1801, pp. 357-361, 1992.
12. S. P. Marsh, *LASL Shock Hugoniot Data*: University of California Press, Ltd., 1980.

Proceedings of the SEM Annual Conference
June 7-10, 2010 Indianapolis, Indiana USA
©2010 Society for Experimental Mechanics Inc.

Photonic Doppler Velocimetry Measurements of Materials Under Dynamic Compression

T. Ao and D.H. Dolan
Sandia National Laboratories, Albuquerque, NM 87185, tao@sandia.gov

Photonic Doppler velocimetry (PDV), also known as heterodyne velocimetry [1], is a compact displacement interferometer system that is rapidly becoming a standard diagnostic in dynamic compression research. A PDV system is essentially a fiber-based Michelson interferometer, utilizing recent advances in near-infrared (λ_0 = 1550 nm) detector technology and fast digitizers to record beat frequencies in the gigahertz range. Compared to the traditional shock wave diagnostic VISAR [2], some advantages of PDV include simple assembly and operation, readily available components, and the lack of an intrinsic delay time. In PDV measurements, Doppler shifted light from a moving target is combined with unshifted light, creating a beat frequency that is proportional to the target velocity ($f = 2v/\lambda_0$). For a target moving at 1 km/s, a measured PDV signal would have a beat frequency of 1.29 GHz. The frequency content of the PDV signal is typically calculated using a sliding short-time Fourier transform (STFT). Within each signal segment of time duration τ, the beat frequency is extracted from the peak of the power spectrum where the velocity resolution is defined by how well the frequency peak can be resolved.

In a typical (standard) PDV configuration, a single laser light source is used to illuminate a target and provide an unshifted reference light for interference with the target light (see Fig. 1a). When the target is stationary, no beating within the PDV signal occurs since the reflected light from the target also remains unshifted. The relationship between the time duration τ and characteristic peak width Δf follows the uncertainly product: $(\Delta f)\,\tau > (4\pi)^{-1}$. For example, to achieve a velocity precision Δv = 10 m/s, the minimum time duration needed in the STFT analysis is τ = 6 ns. For measured velocities that are reasonably large (> 1 km/s), the relative velocity precision ($\Delta v/v < 1\%$) is sufficient to investigate many dynamic material properties. However, low velocity (< 100 m/s) transients can be difficult to resolve with standard PDV since the beat period of the feature of interest may be longer than the time duration of the analysis. Also, in order to improve the poor relative velocity precision ($\Delta v/v \sim 10\%$), τ must be increased thus sacrificing time precision.

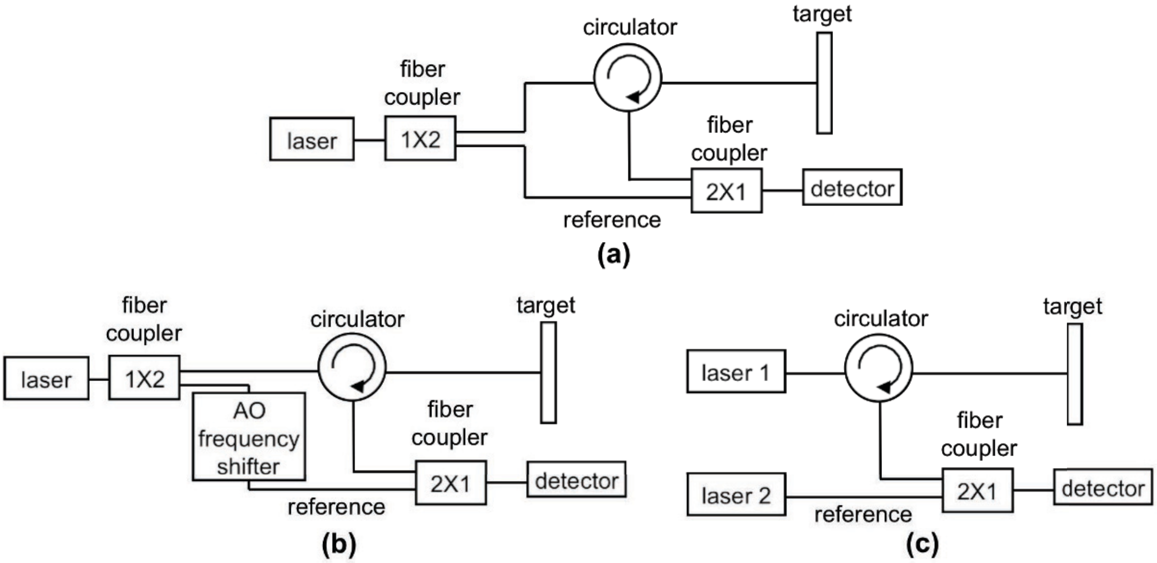

Figure 1. PDV schematic: (a) standard, (b) frequency-conversion with AO frequency shifter, and (c) frequency-conversion with 2 lasers.

T. Proulx (ed.), *Dynamic Behavior of Materials, Volume 1*, Conference Proceedings of the Society for Experimental Mechanics Series,
DOI 10.1007/978-1-4419-8228-5_60, © The Society for Experimental Mechanics, Inc. 2011

To provide optimal velocity and time precision measurements, a “frequency-conversion” PDV configuration has been developed where the reference light is preset at a slightly different frequency (wavelength) than the target light frequency. This is achieved by either using an acousto-optic (AO) frequency shifter to modify the reference light frequency (see Fig. 1b) or by using two separate laser sources at slightly different frequencies (see Fig. 1c). In this configuration, the PDV signal contains an underlying beat frequency even when the target is stationary. Thus, the low velocity features now have a shorter beat period than in the standard PDV configuration, which enables the use of a small time duration while maintaining sufficient velocity precision.

Another attractive feature of PDV is its ability to measure multiple velocities simultaneously. However, this has been shown to create some complications when measuring a dynamically loaded sample through a window [3]. For example, two shock ring-up experiments of a quartz sample sandwiched between two sapphire windows are presented in Fig. 2. The PDV measurements were made in one experiment through a bare sapphire window (see Fig. 2c), and in another experiment through an anti-reflective (AR) coated sapphire window (see Fig. 2d). When a bare sapphire window was used, a secondary reflection was clearly observed in the STFT spectrum. This secondary frequency peak perturbed the primary frequency peak, which resulted in noticeable oscillations in the extracted apparent velocity (see Fig. 2b). The use of the AR coated sapphire window significantly reduced these oscillations.

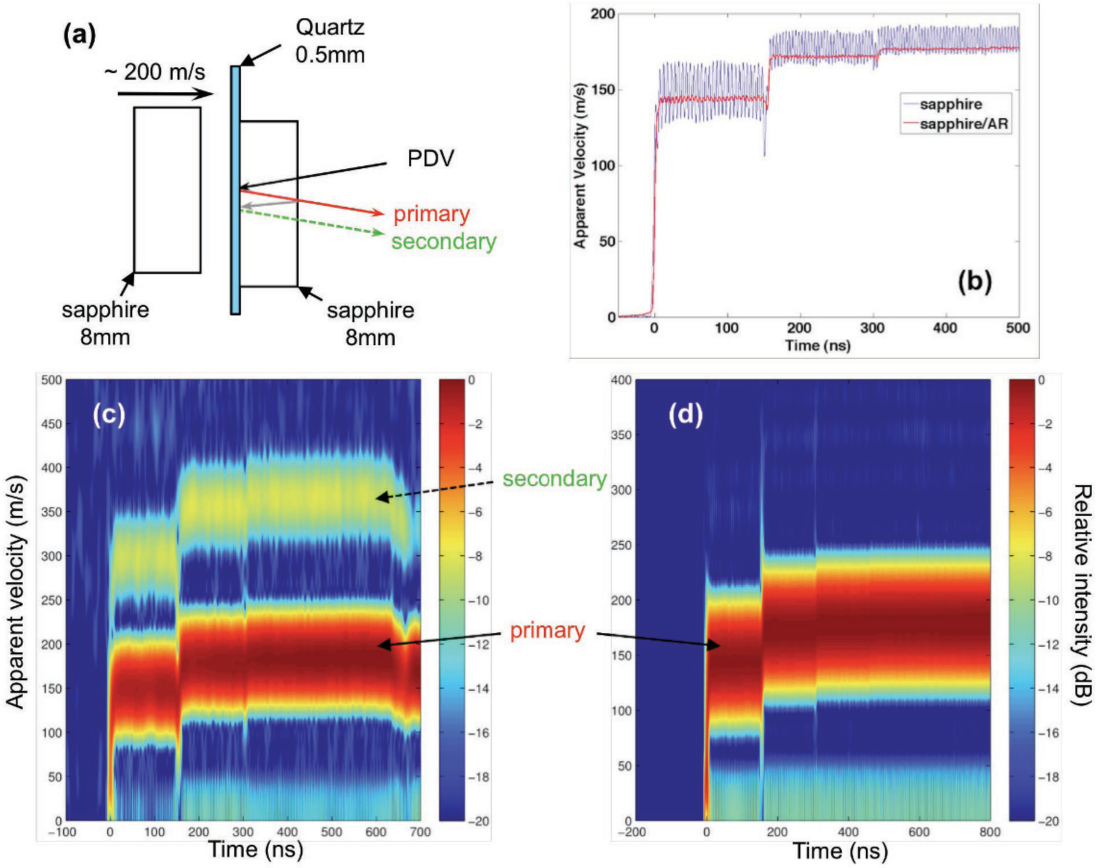

Figure 2. Shock ring-up experiments: (a) setup, (b) extracted apparent velocities with τ = 5 ns, (c) STFT spectrum with bare sapphire, and (d) STFT spectrum with AR coated sapphire.

Sandia is a multiprogram laboratory operated by Sandia Corporation, a Lockheed Martin Company, for the U.S. Department of Energy’s National Nuclear Security Administration under Contract No. DE-AC04-94AL85000.

REFERENCES

[1] Strand, O.T., Goosman, D.R., Martinez, C., and Whitworth, T.L., Rev. Sci. Instrum. **77**, 83108 (2006).
[2] Barker, L.M. and Hollenbach, R.E, J. Appl. Phys. **43**, 4669 (1972).
[3] Jensen, B.J., Holtkamp, D.B., Rigg, P.A., and Dolan, D.H., J. Appl. Phys. **101**, 013523 (2007).

Proceedings of the SEM Annual Conference
June 7-10, 2010 Indianapolis, Indiana USA
©2010 Society for Experimental Mechanics Inc.

Dynamic Equibiaxial Flexural Strength of Borosilicate Glass at High Temperatures

Xu Nie[1], Weinong Chen[1*]

[1]AAE&MSE schools, Purdue University
[*] Corresponding author: Prof. Weinong Chen, 701 W. Stadium Ave. West Lafayette, IN 47907-2045
Email: wchen@purde.edu

ABSTRACT

A novel high temperature ring-on-ring Kolsky bar technique was established in this study to investigate the dynamic equibiaxial flexural strength of borosilicate glass at elevated temperatures. The application of this technique has realized non-contact heating of the glass specimen and prevented the introduction of thermal shock upon specimen engagement. Experimental results have demonstrated a profound temperature dependence on the flexural strength. Vickers indentation has been introduced on glass surface to create controllable surface cracks. These surface cracks were then heat treated with the same thermal history as those tested in a high temperature dynamic experiment. The evolution of crack morphology at 200°C, 550°C and 650°C were examined and discussed based on the different regions on the strength-temperature chart. It was found that residual stress relaxation may have played an important role in the strengthening below 200°C, while crack healing and blunting may account for the strengthening above 500°C.

INTRODUCTION

Glass materials have seen increasing applications as transparent vehicle armor and sealants for solid oxide fuel cells where in both cases high temperatures are frequently involved. Among all the mechanical properties, the failure strength of glass materials is of critical importance to predict the lifetime performance of the components, and to evaluate the system reliability especially at elevated temperatures. Early research has identified the strength of glass materials as a function of temperature and loading rate [1, 2]. It is only until recent decades that the mechanisms for the heat treatment effect on glass strength were systematically explored. In this paper, we investigated the dynamic equibiaxial ring-on-ring flexural strength of a borosilicate glass using a modified high temperature Kolsky bar setup. Flexural strength of this borosilicate glass was reported over a large temperature range from room temperature up to 750˚C. In order to study the effect of heating process on the morphology of surface cracks, Vickers indentation technique was adopted to facilitate well defined surface cracks. The indented samples were then heat treated at 200˚C, 550˚C and 650˚C under the identical thermal histories as those being mechanically tested. Polarizing optical microscope images were taken from these samples after heat treatment. The evolution in crack morphology was discussed, and was linked to the flexural strength variation at high temperatures.

EXPERIMENTS AND RESULTS

Figure 1 shows the dynamic equibiaxial ring-on-ring flexural strength of borosilicate glass as a function of temperature. As the temperature gradually increases, this strength versus temperature chart can be literally divided into 3 regions, each having a distinct characteristic. The first region is from room temperature to around

T. Proulx (ed.), *Dynamic Behavior of Materials, Volume 1*, Conference Proceedings of the Society for Experimental Mechanics Series, DOI 10.1007/978-1-4419-8228-5_61, © The Society for Experimental Mechanics, Inc. 2011

200°C, where the flexural strength saw an uprise of approximately 50% compared to the strength at room temperature. This increase happened between 100~200°C. In the third region, the strength stepped up again to form another plateau until softening eventually took place over 650°C. Figure 2 shows the side view of a Vickers crack before and after heat treatment at 200°C. The change in contrast of cone cracks suggests the crack plane might have slightly rotated which results in a change of light deflection. Since the as-received borosilicate glass samples were mechanically ground and polished before being tested, the surface cracks were thought to be prevailing on glass surfaces and have been proven to be the strength-limiting flaws in room temperature ring-on-ring experiments. Evidences shown in Fig. 2 pointed out that the contact residual stress relaxation around the indentation cracks have taken place during the heating and soaking process, which may lead to the strength increase in region I. For the purposed of comparison, the same glass sample which has been heat treated at 200°C was further treated at 550°C and 650°C to study the evolution of the same crack at higher temperatures. The optical microscope images after heat treatment are shown in Fig.3. It is evident from the figures that the radial crack has been progressively blunted during the heat treatment above the glass transition temperature. Besides blunting mechanism, progressive crack healing is also observed in this temperature range as indicated by the arrows in Fig. 9 (b) and (c). The cone crack which intercepted the radial crack was diminishing when heat treated at 550°C, and was completely disappeared after heat treatment at 650°C. The presence of both mechanisms is beneficial to relieve stress concentration at the crack tip which would possibly lead to the increase in flexural strength in region III.

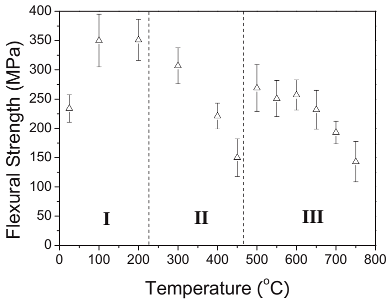

Fig. 1 Flexural strength of borosilicate glass as a function of temperature.

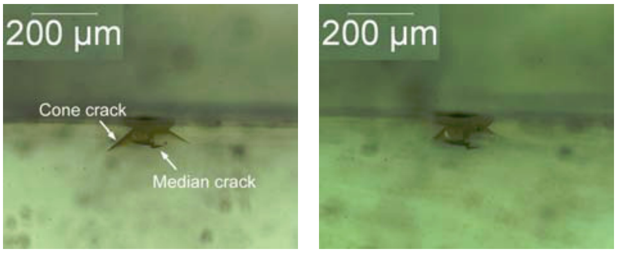

(a) (b)

Fig. 2 Stress relaxation caused by heating, (a) as-indented specimen, and (b) after heat treatment at 200°C

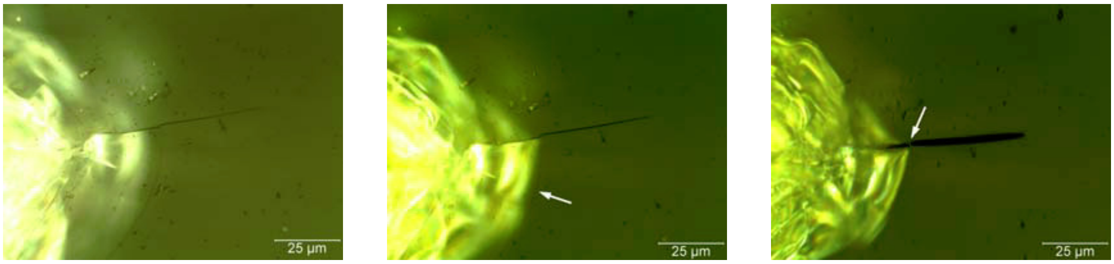

(a) (b) (c)

Fig. 3 Surface crack blunting and healing at 550°C and 650°C, (a) as-indented, (b)treated at 550°C, and (c) treated at 650°C

REFERENCE:

[1] G. O. Jones and W. E. S. Turner, “The Influence of Temperature on the Mechanical Strength of Glass”, Journal of the Society of Glass Technology, 26, 35-61 (1942)

[2] R. J. Charles, “Static Fatigue of Glass II”, Journal of Applied Physics, 29, 1554-1560 (1958)

Proceedings of the SEM Annual Conference
June 7-10, 2010 Indianapolis, Indiana USA
©2010 Society for Experimental Mechanics Inc.

Measurement of Stresses and Strains in High Rate Triaxial Experiments

Md. E. Kabir
Schools of Aeronautics and Astronautics, Purdue University
701 West Stadium Avenue, West Lafayette, IN 47907-2045, USA
Phone: 1-765-494-7419, Email: mkabir@purdue.edu

Weinong W. Chen
Schools of Aeronautics/Astronautics, and Materials Engineering, Purdue University
701 West Stadium Avenue, West Lafayette, IN 47907-2045, USA

Veli-Tapani Kuokkala
Department of Materials Science, Tampere University of Technology
P.O.Box 589, 33101 Tampere, Finland

ABSTRACT

Triaxial experiments are widely used for finding the shear properties of geo-materials such as sand, clay and rock. In many instances, these materials undergo dynamic loading where the material is subjected to high rate of deformation. To observe the material response in such condition, a high rate triaxial experimental setup has been developed recently. In the current phase of the work, novel experimental techniques are developed to measure the specimen dimensions and stresses during dynamic triaxial experiments.

INTRODUCTION

Triaxial experiments are conducted in two steps. In the first step, the specimen is loaded isotropically. The specimen is then axially loaded to generate shear. Typical triaxial test specimen is cylindrical in shape. Thus there are only two principal directions: axial and radial, which simplifies the load-deformation measurement. Specimen length and axial load in the shear phase are typically recorded outside the pressure chamber but the diameter change and pressure variation is recorded locally. The frequency response of such devices is typically only up to 20 Hz, which is in the quasi-static region of deformation rates. The shear phase of the dynamic triaxial experiment has duration of 200 μs. Most of the quasi-static measurement techniques do not have sufficient frequency response to measure the load and specimen dimensions at this rate. Therefore, new methods have been developed to accurately measure the loads and displacements in both phases. In the following sections, the new load and deformation measurement techniques are described briefly. The details of the techniques can be found elsewhere [1].

MEASUREMENT TECHNIQUE

To conduct dynamic triaxial experiments, two pressure chambers are integrated with a Kolsky bar [2]. One chamber is installed around the specimen, which is called radial chamber. The other one is at the far end of the transmission bar, called longitudinal chamber. In the isotropic pressure phase, a desired hydrostatic pressure is applied using high pressure fluid. In the shear phase, a dynamic axial load is applied by the impact of the striker on to the incident bar.

The loading in isotropic consolidation phase is quasi-static in nature. Therefore, conventional pressure and length change measurement outside the pressure chamber are sufficient to use. A line pressure gage is used for hydrostatic load measurement and an LVDT (linear variable differential transformer) to measure the length change. Strain gages are mounted on the incident and transmission bars to record the incident, reflected, and transmitted signals which analyzed using one-dimensional wave theory to measure the axial load and deformation during the shear phase [3-4].

During the dynamic phase the radial stress is measured by a manganin gage. The radial deformation in both phases of the experiment is measured by a novel capacitive transducer. The capacitive transducer is

T. Proulx (ed.), *Dynamic Behavior of Materials, Volume 1*, Conference Proceedings of the Society for Experimental Mechanics Series,
DOI 10.1007/978-1-4419-8228-5_62, © The Society for Experimental Mechanics, Inc. 2011

fabricated by placing a coiled spring around the specimen followed by a small copper tube mounted on the transmission bar specimen end. A Schering Bridge along and lock-in amplifier are used as the null detector to balance the bridge [5].

To demonstrate the feasibility of the measurement technique dynamic triaxial experiments were conducted on Quikrete #1961® sand. The specimen diameter was 19 mm with a length of 9.3 mm. The specimens are initially contained in polyolefin heat shrink tubes. The specimen is pressurized to 100 MPa, it is then dynamically compressed along the axial direction at a strain rate of 1000/s. The shear dilation of the specimen is shown in Fig. 1.

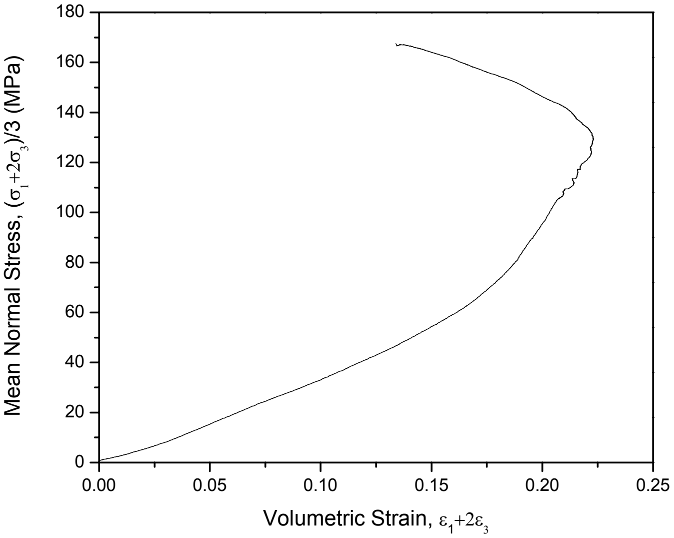

Fig. 1: Total shear dilation plot for 100 MPa and 1000 s^{-1} strain rate

This particular plot includes both the phases and requires all stresses and strains to be measured. Then all these stress-strains are converted to true forms. It is seen from the figure that the behavior of the sand resembles that of the quasi-static triaxial experiment.

ACKNOWLEDGEMENT

This research is sponsored by the Sandia National Laboratories, which is operated by Sandia Corporation, a Lockheed Martin Company, for the United States Department of Energy under Contract DE-AC04-94AL85000.

CONCLUSION

Measurement technique for the stresses and strains the dynamic triaxial experiment has been developed and demonstrated for the dynamic triaxial experiment on sand.

REFERENCES

1. Kabir, M. E. and Chen, W. W., Measurement of Stresses and Strains on the High Strain Rate Triaxial Test, Review of Scientific Instruments 80 (12), doi:10.1063/1.3271538, 2009.
2. Frew, D. J. Akers, S. A. Chen, W.W. and Green, M.L., Development of a Dynamic Triaxial Kolsky Bar, Experimental Mechanics (Submitted).
3. Kolsky, H., An Investigation of the Mechanical Properties of Materials at Very High Rates of Loading, Proc. Roy. Soc. London B, 62, 676-700, 1949.
4. Follansbee, P. S., The Hopkinson Bar, Mechanical Testing, Metals Handbook 8, 9the ed., American Society for Metals, Metals Park, OH, 198-217, 1985.
5. Bera, S.C. and Chattopadhyay, S., Measurement 33, 3-7, 2003.
6. Pilla, S., Hamida, J.A. and Sullivan, N.S., Review of Scientific Instruments 70 (10), 4055-4058, 1999.

Proceedings of the SEM Annual Conference
June 7-10, 2010 Indianapolis, Indiana USA
©2010 Society for Experimental Mechanics Inc.

A new technique for combined dynamic compression-shear test

P.D. Zhao[1], F.Y. Lu[1], R. Chen[1], G.L. Sun[2,3], Y.L. Lin[1], J.L. Li[1], L. Lu[4]*

1. College of Science, National Univ. of Defense Technology, 410073 Changsha, China
2. College of Optoelectronics Science and Engineering, National Univ. of Defense Technology, 410073 Changsha, China
3. Institute of systems and mathematics, Naval Aeronautical Engineering Institute, 264001 Yantai, China
4. College of electronic science and engineering, National Univ. of Defense Technology, 410073 Changsha, China

*Corresponding author: Zhaopengduo@163.com

Abstract: We propose a dynamic combined compressive and shear experimental technique at high strain rates (10^2-10^4 s^{-1}). The main apparatus is mainly composed of a projectile, an incident bar and two transmitter bars. The close-to-specimen end of the incident is wedge-shaped with 90 degree. In each experiment, there are two identical specimens respectively agglutinated between one side of the wedge and one of transmitter bars. When a loading impulse travels to specimens along the incident bar, because of the special geometrical shape, the interface of specimen glued with the incident bar has an axial and a transverse velocity. Thus, the specimens endure the combined pressure-shear loading at high strain rates. The compression stress and strain are obtained by strain gages located on the bars; the shear stress is measured by two piezoelectric crystals of quartz with special cut direction embedded at the end (near specimen) of transmitter bars; the shear strain is measured with a novel optical technique which is based on the luminous flux method. The feasibility of this methodology is demonstrated with the SHPSB experiments on a polymer bonded explosive (PBX). Square-shaped specimen is adopted. Experimental results show that the specimen is obviously rate-dependent. Shear and compression failure occur for the specimen.

INTRODUCTION

The combined compressive and shear deformation at high strain rates (10^2-10^4 s^{-1}) is encountered in several kinds of processing, such as grinding, machining, forming, events or processes that result in penetration. Stress wave studies, utilizing the uniaxial stress or strain condition, are commonly used to determine material response at high strain rates. Generally speaking, the mechanical response of materials subjected to complex stresses isn't consistent to the response at uniaxial condition. Studying the dynamic response of materials under combined compression-shear loading is important to get material behaviors more accurately and fully.

Koller[1] and Young[2] proposed two kinds of inclining impact test methods, where the fronts of longitudinal wave and shear wave weren't parallel. It's difficult to analyze the stress state quantitatively in these cases. Thirty years ago, Clifton and Abou-Sayed[3] designed an oblique-plate impact experiment based on gas gun, which was used to study constitutive models of materials at high pressures and strain rates ($>10^4$ s^{-1}). Compression-shear loading is attained by inclining the flyer, specimen and target plates with respect to the axis of the projectile in the same angle. Later on, many other scientists and engineers[4-11] continuously improved this technique. Pressure-shear experiments offer a unique capability for the characterizing materials under dynamic loading conditions. These experiments allow high pressures, high strain rates (10^4-10^7 s^{-1}) and finite deformations to be generated. Pressure-shear plate impact testing, however, is limited to fine-grained materials, because the grain size must be small enough compared to specimen thickness to ensure that a representative average polycrystalline response is measured. Such experiments are lengthy because of the time required for specimen preparation. Huang and Feng[12] modified the torsional Kolsky (or split-Hopkinson) bar and designed the Kolsky-bar compression-shear

T. Proulx (ed.), *Dynamic Behavior of Materials, Volume 1*, Conference Proceedings of the Society for Experimental Mechanics Series, DOI 10.1007/978-1-4419-8228-5_63, © The Society for Experimental Mechanics, Inc. 2011

experiment which could be used to study the dynamic response of materials at high strain rates (10^2-10^4). This experimental method, however, doesn't really achieve combined compression-shear loading during loading. Because the speed of shear (or distortional wave) wave isn't equal to that of longitudinal wave. The specimen endures compression loading earlier, and it is subjected by shear loading when shear wave arriving. This situation is far from the actual condition. Meanwhile, for diminishing the stress and strain gradient from inner to outer of the wall, the tube specimens require a relative thin-wall thickness and a large diameter. For some materials, it's hard to satisfy.

This paper describes a newly developed combined compression-shear loading technique, the Split Hopkinson Pressure Shear Bar (SHPSB). The experimental setup, including the modified SHPB system, measurements for compression stress and strain, an optical system for the shear strain, and the quartz crystal for the shear stress measurements are discussed in EXPERIMENT. Experimental results of a PBX specimen are presented in RESULTS AND DISCUSSION, and conclusions are summarized finally.

EXPERIMENT

The split Hopkinson pressure shear bar (SHPSB) technique is developed from the split Hopkinson pressure bar (SHPB). It is mainly consisted of a strike bar, an incident bar and two transmitter bars. The incident bar is same as the bar in SHPB at the close-to-projectile end, but the other end of the incident bar is wedge-shaped. The angle of the wedge is 90 degree as shown in Fig.1(a). The length and diameter of the incident bar is 1800 and 37mm, respectively. The length and diameter of the both transmission bars are 1000 and 20mm. In each experiment, there are two identical specimens respectively agglutinated between one side of the wedge and one of transmitter bars. When the strike bar impacts the incident bar, a loading impulse travels to specimens along the bar. Because of the special geometrical shape, interface of the specimen glued to the incident bar gets an axial and a transverse velocity. Thus, the specimens endure the combined compressive and shear loading at high strain rate.

There were three sets of strain gages located on the bars for compression-stress and strain measurements, and two quartz transducers with special cut direction (Φ20mm×0.25mm) embedded at the end of transmission bars for shear stress measurement. A novel optical apparatus was employed to measure shear strain of specimen, which was based on the luminous flux method. The schematic of SHPSB is shown in Fig.1(b).

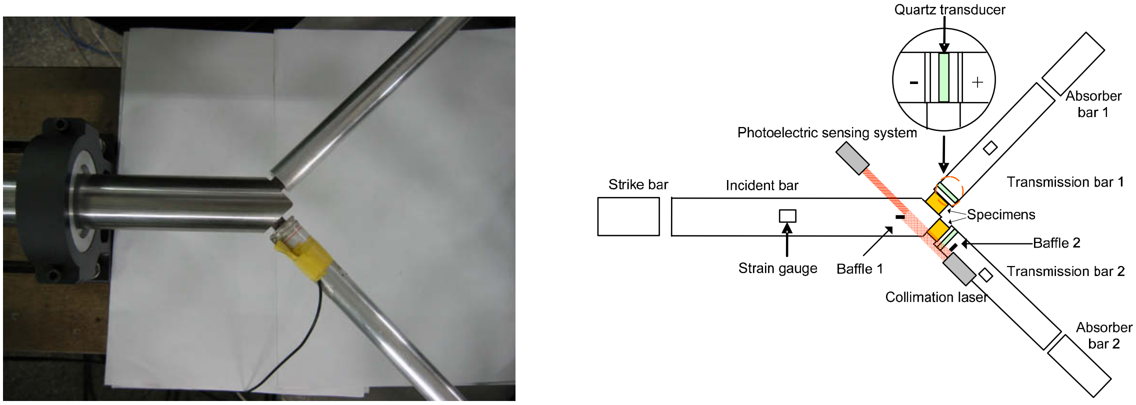

(a) (b)

Fig. 1. (a) Photo of the experimental setups; (b) Schematic of the experiment apparatus

Following propagating stress wave theory, we know that there are two kinds of waves, a longitudinal wave and a bending (or flexural) wave in bars during the experiment. The transmission bars have an axial and a transverse motion, which correspond to longitudinal and bending wave. As the transmission bars are elastic, these two waves propagate independently. Because two transmission bars are symmetrical about the axis of the incident bar, no transverse movement is in existence. Similar with SHPB, the strike bar is great longer than the specimen in SHPSB experiments. So the specimens are under pressure and shear forces equilibrium during testing.

The compression stress in specimen can be deduced by axial strain from strain gauges mounted on the transmission bars. In fact, not only longitudinal wave arouses the axial strain in the transmission bars, but also bending wave results in the change of axial strain. When bending wave propagates in a thin bar, one part is in compression, and the symmetrical part about the axis of the bar is in tension. In SHPSB experiment, a pair of strain gauges is mounted on each transmission bar at symmetrical locations. And these two strain gauges are settled at opposite arms in Wheatstone bridge. So the output voltage from bridge is a mean of the two strain gauges' voltage. Herein, the influence of bending wave to the axial strain of the bars is eliminated using the above method.

The compression stress of specimen is:

$$\sigma = \frac{A_t E \varepsilon_t}{A_s} \tag{1}$$

Where A_t, A_s are respectively cross section areas of the transmission bars and incident bar; E and ε_t are respectively elastic module and the axial strain of the bar measured by the transmission strain gauges.

Based on the theory of stress wave[13], it's clear that longitudinal wave generates one dimension stress state in thin bar, and all shear stress terms are equal to zero. The shear stress in the transmission bar of SHPSB, therefore, is caused by bending wave, which is a kind of dispersion wave. Waves with different wavelength are of different phase velocities. As an important mechanics parameter in governing equation for bending wave, shear stress is frequently changing with wave propagation. It's hard to deduce the shear stress in specimen from the history of shear stress at some fixed locations on the transmission bar, similar to the operation in case of longitudinal wave. Thus, it requires that the shear stress gauge is closer to the specimen. In SHPSB experiments, we make use of quartz with special cut direction as shear stress gauge, which is just in response to shear stress. The distance between the quartz and the specimen is 2mm. If we neglect the tiny difference between the shear force in specimen and that of the transmission bar where quartz transducers embedded, the shear stress in specimen can be expressed with:

$$\tau = \frac{A_t \tau_t}{A_s} \tag{2}$$

Where τ_t is the shear stress measured by the quartz transducer.

LS-DYNA is employed to simulate the SHPSB experiment. Numerical model is the same as the actual setup. To simplify the question, an elastic material model is chosen for the specimen. We validate the method of compression and shear stress measurement using the numerical results as shown in Fig.2.

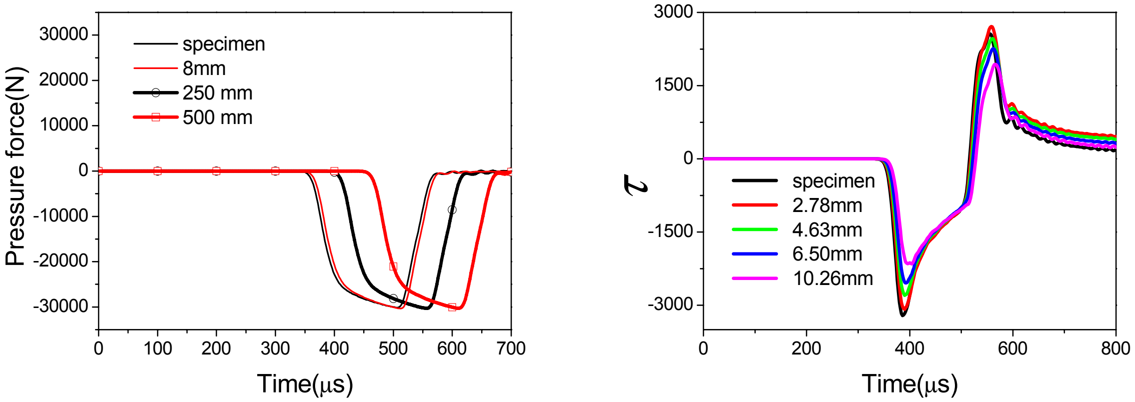

(a) (b)

Fig. 2 (a) Average pressure force in the specimen and transmitted bar; (b) Average shear force in the specimen and transmitted bar

The "specimen" curve represents the average pressure force history of specimen in Fig.2(a), and the curve "8mm" stands for the average pressure force of two elements in the transmission bar, which is symmetric about the bar's axis. And these two elements are 8mm away from the specimen. So do the curves "250mm" and "500mm". We can find that all curves are identical with each other in Fig.2(a), and it indicates that the method for measurement of the compression stress is valid. Fig.2(b) shows the shear force histories at different position. The “specimen” curve is average shear force history of the specimen. And other curves represent the average shear force histories at different cross sections of the transmitted bars, which are respectively 2.78, 4.63, 6.50 and 10.26mm away from the specimen. In the range of 2.78mm, the shear force histories are identical with that of specimen. The relative peak difference between the shear force of specimen and that of the cross section which is in 2.78mm away from specimen is less than 5%. It implies that equation (2) is reasonable.

The sketch map of velocity analysis for the specimen of SHPSB is provided in Fig.3. The particle velocity at the incident bar end v can be divided into the axial velocity v_{1p} and transverse velocity $v_{1\tau}$, similarly, there are axial velocity v_{2p} and transverse velocity $v_{2\tau}$ at the transmitter bar end. Thus, the compression and shear strain rates of the specimen are respectively:

$$\dot{\varepsilon} = \frac{v_{1p} - v_{2p}}{l} \tag{3}$$

$$\dot{\gamma} = \frac{v_{1\tau} - v_{2\tau}}{l} \tag{4}$$

Where l is thickness of the specimen. Thus if we know the history v_{1p}, v_{2p}, $v_{1\tau}$ and $v_{2\tau}$, we can calculate the compression and shear strain rates of the specimen using equation (3), (4). Furthermore, the compression and shear strain can be got by an integral operation.

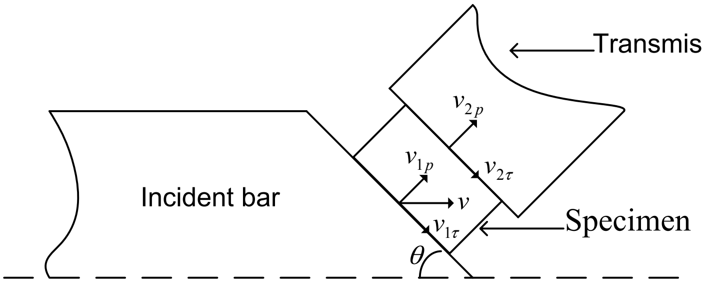

Fig. 3 Sketch map of velocity analysis for the specimen of SHPSB

For v_{1p} and v, there is relationship:

$$v_{1p} = v \sin\theta \tag{5}$$

Where θ =45° is equal to the angle between axial direction of the incident bar and the transmission bar.

For one-dimensional elastic longitudinal wave, there is equation:

$$v = c_0(\varepsilon_i + \varepsilon_r) \tag{6}$$

Because the elastic bending and longitudinal wave propagate independently in the transmission bar, thus

$$v_{2p} = c_0 \varepsilon_t \tag{7}$$

Where c_0, ε_i, ε_r and ε_t are respectively the velocity of longitudinal wave in the elastic bar, the incident strain and reflection strain measured by strain gauge mounted on the incident bar, and the transmission strain measured by the transmission strain gauge.

Substituting equation (5), (6), (7) into equation (3) yields

$$\dot{\varepsilon} = \frac{c_0}{l}\left[\frac{\sqrt{2}}{2}(\varepsilon_i + \varepsilon_r) - \varepsilon_t\right] \tag{8}$$

And the compression strain of the specimen is:

$$\varepsilon = \int_0^t \frac{c_0}{l}\left[\frac{\sqrt{2}}{2}(\varepsilon_i + \varepsilon_r) - \varepsilon_t\right]dt \tag{9}$$

For $v_{1\tau}$ and v, there is also relationship:

$$v_{1\tau} = v\cos\theta \tag{10}$$

But, it's hard to know $v_{2\tau}$ in experiments. So, we tried to get a difference of the transverse velocities or displacements at interfaces between the specimen and bars.

Ramesh and Narasimhan[14] proposed a method, known as the Laser Occlusive Radius Detector (LORD) to determine the radial deformations of specimens in SHPB experiments. Adding a collimated line head in front of the laser, Li[15] modified the LORD to measure the visco-plastic tensile strains in the SHTB (the split Hopkinson tension bar) experiments. We used a similar optical apparatus with Li to measure shear strain of the specimen.The optical setup for shear strain consists of three major components: an optical arrangement for generating a laser rectangular beam with uniform intensity per unit length, photoelectric sensing apparatus for detecting and measuring the light, the optical baffles fixed on the incident bar and transmission bar.

The optical emission system includes: a collimation laser operates at 660 nm with a 20 mW output power, which exports a collimated light beam with uniform intensity; an optical slit changes the circular light spot into the rectangular.

The photoelectric sensing part consists of a collecting lens and a photodiode light detector. The collecting lens focuses the incoming laser light into the photodiode detector, which is placed near its focus. The photodiode detector output is pre-amplified, and the optoelectronics and the preamplifier together are of 2 MHz bandwidth. The output voltage of the detector is proportional to total amount of the laser light collected. The whole system is at noise level less than 0.4 mV.

The optical baffles are respectively integrated firmly with bars by aluminum hoops. The relative displacement between optical baffles1 (on the incident bar) and optical baffles2 (on the transmission bar) is identical with that of two interfaces between the specimen and bars.

The basic ideal for measuring shear strain is very simple. The apparatus is mounted so that the light beam runs parallel with the axis of the transmission bar as shown in Fig.4(a). If the specimen and transmission bar just move along their axial direction, the width of laser beam will not change, and no signal outputs. If there is a few of relative transverse displacements of the two interfaces of the specimen with bars, optical baffles will block part of laser beam, and the changes of voltage will be recorded by oscilloscope. In other words, the optical apparatus is not sensitive to axial movement of the specimen, but very sensitive to transverse movement. Knowing the relationship of the width-change of laser beam and output voltage, we can get the transverse relative velocity ($v_{1\tau} - v_{2\tau}$) or the transverse relative displacement.

To calibrate the optical system, we use a high precision gauge to partly block the laser beam, which is perpendicular to direction of the beam as shown in Fig.4(a). The blocking width ranges from 0 to 10 mm at a step of 0.1 mm. A specific blocking width (d) corresponds to a light-blocking width Δd and a certain amount of voltage reading (ΔU) in the detector output. Fig.4(b) shows the results in two calibrating experiments, in which the locations of the high precision gauge is 4 centimeters apart. The Δd -ΔU curve exhibits a good linearity, indicating a high uniformity of the laser sheet:

$$\Delta d = k\Delta U \tag{11}$$

where k=1.79 mm/V is a calibration parameter of the optical system for the shear strain. So the shear strain is expressed with:

$$\gamma = \frac{\Delta d}{l} = \frac{k\Delta U}{l} \tag{12}$$

By differential operation, we can get the shear strain rates.

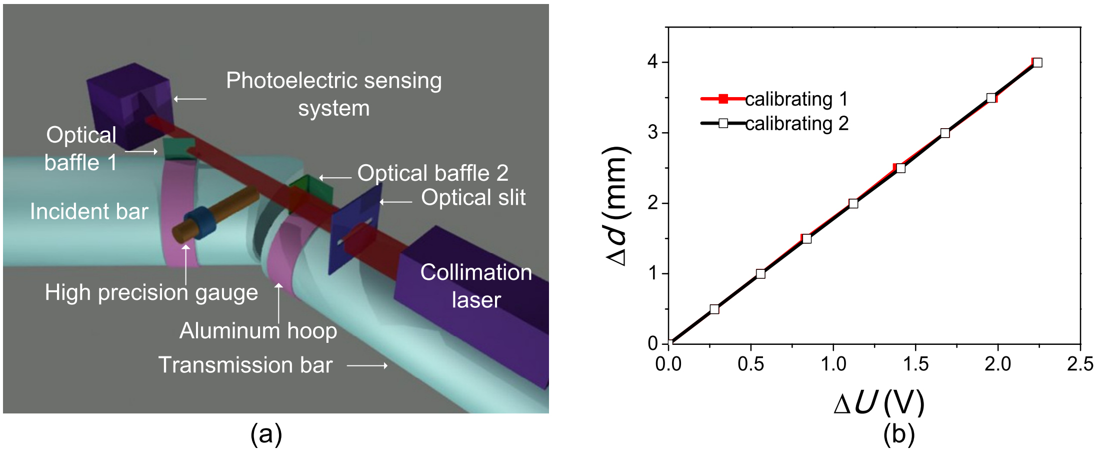

(a) (b)

Fig.4(a) Schematic of calibration for the optical apparatus; (b) Results of the calibration experiments

RESULTS AND DISCUSSION

To demonstrate the feasibility of the above technique, we have performed SHPSB tests on a polymer bonded explosives (PBX). The cubic specimens are made by molding. Size of the specimen is 13mm×13mm×5mm as shown in Fig.5(a), with mass density of 1.6g/cm^3. Fig.5(b) shows typical oscilloscope signals in the experiment. CH1 is connected to the strain gauge on the incident bar, recording the incident and the reflection longitudinal waves, CH2 is connected to the strain gauge on the transmission bar 2, recording the transmission longitudinal waves, CH3 is connected to the quartz crystal, measuring the shear force, and CH4 is connected to the optical system, monitoring the transverse motion of the specimen. The compression stress and strain of specimens are calculated by equation (1) and (9), and the shear stress and strain are calculated by equation (2) and (12).

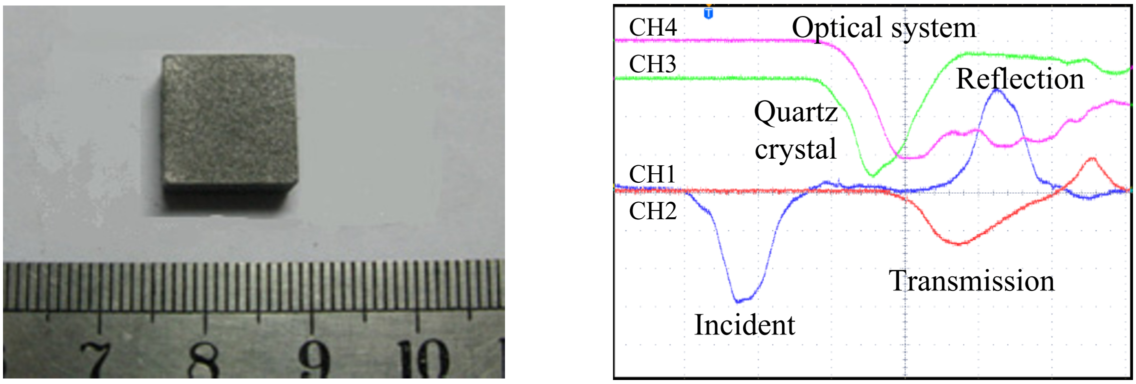

(a) (b)

Fig.5 (a) Photo of the specimen; (b) Oscilloscope signals of test

Typical compression stress-strain curves obtained at high strain rates are shown in Fig.6(a). Average pressure strain rates at three levels are 500, 540and 600s^{-1}. And corresponding shear stress-strain curves are shown at various strain rates in Fig.6(b), and the average shear strain rates are 450, 820, 750s^{-1}. In addition, the curves with the same symbol belong to one experiment in Fig.6.

From the Fig.6, we know that this PBX is sensitive to pressure strain rates, also to shear strain rates. At compression strain rates 500s^{-1}, the peak compression stress is about 12MPa, and the largest shear stress is about 1.8MPa in this experiment. In fact, these two peak values are not corresponding to each other. As shown in Fig.7(a) for a typical test, we calculate the compression stress and shear stress histories. The time corresponding to the peak of shear stress curve is earlier than the time corresponding to the peak of compression stress curve. The compression strain and shear strain histories are shown in Fig.7(b). The vertical lines in Fig.7 represent the times when the compression and shear stresses getting to the peak. Before the compression and shear strains arriving at the peak value, the shear and compression stresses reach the largest values. In other words, after reaching the peak value, the shear stress begins to drop with the strain sequentially increasing. It indicates that two kinds of failure modes (shear and compression failure) occur for the specimen, and shear failure occurs before compression failure appearing. It's identical with the fact that the shear strength is less than compression strength for this kind of material.

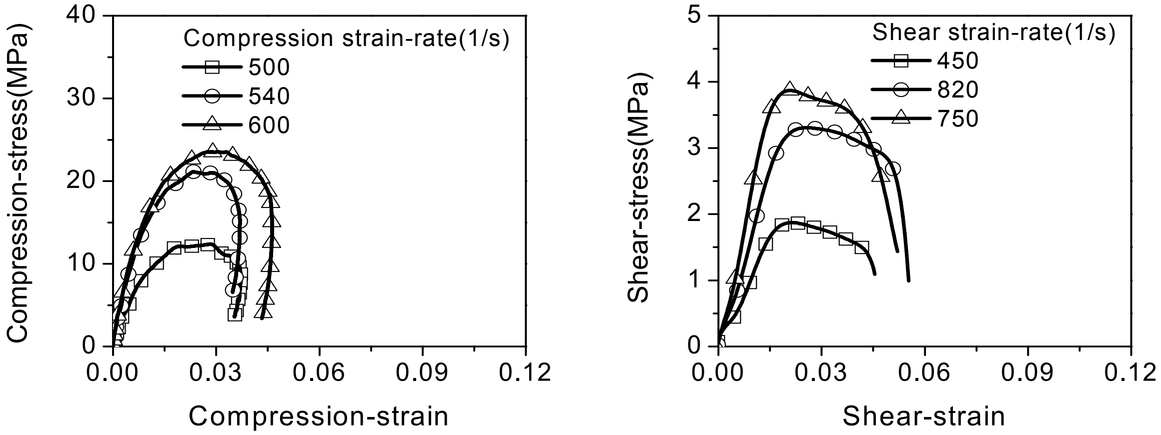

Fig. 6 (a) Engineering compression stress-strain curves; (b) Engineering shear stress-strain curves;

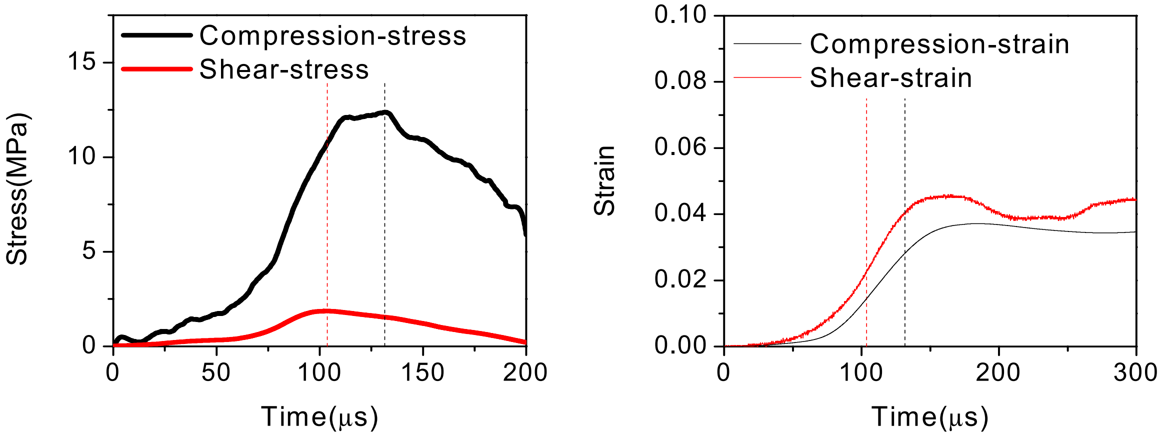

Fig. 7 (a) Compression and shear stress histories curves; (b) Compression and shear strain histories curves;

CONCLUSION

We propose a modified SHPB testing method, SHPSB technique, to measure the dynamic responses of specimens under combined compression-shear loading at high strain rates (10^2-10^4). In this method, strain gauges are employed to measure the compression stress and strain of specimens, piezoelectric force transducers are embedded in the transmitted bars in order to measure the loading shear force, and an optical apparatus based on the luminous flux method, is used to monitor the transverse motion of specimens, from which the average shear strain is deduced. The feasibility of this technique is demonstrated with the SHPSB experiments on a PBX. The experimental results show that this PBX is sensitive to strain rates, and shear and compression failure occur for the specimen, and shear failure occurs before compression failure appearing. This technique is readily implementable and can be applied to investigating dynamic-mechanics property of materials under complex stress state.

ACKNOWLEDGMENTS

This work was supported by the Natural Science Foundation of China (NSFC) through Grant No. 10672177 & 10872215 and 10902100. And we would like to acknowledge the support of National Key Laboratory Foundation under grant NO.9140C670902090 and Science Foundation of CAEP under grant NO.2009A0201008.

REFERENCES

[1] Koller L. and Fowles G., "Compression-shear waves in Arkansas novaculite", In: Timmerhaus K. Barber M., eds. High Pressure Science and Technology, Proceedings of Sixth AIRAPT Conference, Boulder CO, 1977. New York: Plenum Press, 2: 927 (1979).

[2] Young C. and Dubugnon O., "A reflected shear-wave technique for determining dynamic rock strength", Int J Rock Mech Min Sci & Geomech Abstr. 14: 247-259 (1977).

[3] Abou-Sayed A.S., Clifton R.J., and Hermann L., "The oblique-plate impact experiment", Exper Mech. 127-132 (1976).

[4] Gilat A. and Clifton R.J., "Pressure-shear waves in 6061-T6 aluminum and alpha-tianium", J Mech Phys Solids. 33: 263-284 (1985).

[5] Prakash V. and Clifton R.J., "Time resolved dynamic friction measurements in pressure-shear". in: Vol. 165 Experimental Techniques in the Dynamics of Deformable Bodies. 33-47 (1993).

[6] Machcha A.R. and Nemat-Nasser S., "Effects of geometry in pressure-shear and normal plate impact recovery experiments:Three-dimensional finite-element simulation and experimental observation", J Appl Phys. 80: 3267-3274 (1996).

[7] Tong W., "Pressure-shear stress wave analysis in plate impact experiments", int.J.Impact enging. 19: 147-164 (1997).

[8] Frutschy K.J. and Clifton R.J., "High-temperature pressure-shear plate impact experiments using pure tungsten carbide impactors", Exper Mech. 38: 116-125 (1998).

[9] Frutschy K.J. and Clifton R.J., "High-temperature pressure-shear plate impact experiments on OFHC copper", J Mech Phys Solids. 46: 1721-1743 (1998).

[10] Prakash V., "Time-resolved friction with applications to high-speed machining: Experimental observations", Tribology Transactions. 41(2): 189-198 (1998).

[11] Page N.W., Yao M., Keys S., et al., "A high-pressure shear cell for friction and abrasion measurements", Wear. 241: 186-192 (2000).

[12] Huang H. and Feng R., "A study of the dynamic tribological response of closed fracture surface pairs by Kolsky-bar compression-shear experiment", International Journal of Solids and Structures. 41(11-12): 2821-2835 (2004).

[13] Graff K., Wave motion inelastic solids, Columbus: Ohio University Press, (1975).

[14] Ramesh K.T. and Narasimhan S., "Finite deformations and the dynamic measurement of radial strains in compression Kolsky bar experiments", International Journal of Solids and Structures. 33(25): 3723-3738 (1996).

[15] Li Y. and Ramesh K.T., "An optical technique for measurement of material properties in the tension Kolsky bar", International Journal of Impact Engineering. 34: 784-798 (2007).

Proceedings of the SEM Annual Conference
June 7-10, 2010 Indianapolis, Indiana USA
©2010 Society for Experimental Mechanics Inc.

A New Compression Intermediate Strain Rate Testing Apparatus

Amos Gilat, and Thomas A. Matrka

The Ohio State University
Department of Mechanical Engineering
201 West 19th Avenue
Columbus, OH 43210 USA
gilat.1@osu.edu

ABSTRACT

A new apparatus for testing in compression at intermediate strain rates is introduced. The apparatus consists of a loading hydraulic actuator and a very long (40 m) transmitter bar. The specimen is placed with one end touching the end surface of the long bar and the other end free. The specimen is loaded by the actuator that impacts the specimen's free end directly. Once loaded, the specimen deforms between the actuator and the transmitter bar. As the specimen is loaded and deformed, a compression wave propagates into the transmitter bar. The amplitude of this wave is measured with strain gages that are placed on the transmitter bar at a distance of about five diameters from the specimen. The wave in the transmitter bar propagates all the way to the end of the bar and then reflects back toward the specimen. The experiment can continue until the reflected wave reaches the strain gages (milliseconds). The strain in the specimen (full field) is measured directly on the specimen using Digital Image Correlation with high speed cameras.

BACKGROUND

The basic mechanical properties of materials (stress strain relation and failure) are typically determined by testing material coupon specimens in tension, compression, and shear. When the effect of strain rate on these properties is investigated, the tests are done at different strain rates. Standard hydraulic testing machines are usually used for testing at quasi-static strain rates in the range from 10-5 s^{-1} up to about 2 s^{-1}. These tests are called quasi-static because the specimen and the testing machine are in static equilibrium during the test. At high strain rates, the split Hopkinson bar technique is used for testing at strain rates ranging from about 300 s^{-1} to about 5000 s^{-1}. In this technique, the specimen is short and is in a state of equilibrium (inertia effects are not considered) during most of the test (except in the very beginning of the test). The rest of the apparatus (the bars) are not in static equilibrium. The stress waves that propagate in the bars are recorded and are used for determining the history of the deformation and stress in the specimen.

Tests at strain rates between about 10 s^{-1} and 200 s^{-1}, defined here as intermediate strain rates, are difficult to conduct. They are too low to be done with the standard split Hopkinson bar technique, and as explained below, they are too high to be done with standard hydraulic machines because in this range inertia effects become significant. Many researchers have tried to conduct intermediate strain rate tests with hydraulic machines. The actuator of a typical machine can move fast enough to deform the specimen at the required strain rate. Sometimes the hydraulic machines use an open loop control with an actuator that has a slack. In this way the actuator accelerates to the required speed before it get engaged with the specimen. The results from such tests, however, are not accurate. The problem is that during the test the whole machine is not in static equilibrium and stress waves and inertia effects cannot be handled by the machine. The time scale of an intermediate strain rate test is of the same order as the time scale for the stress waves to travel in the frame of the machine and the time it takes for the various components of the machine (grips, load cell, mechanical connections) to accelerate. The records from intermediate strain rate tests done with a hydraulic machine (force measured by the load cell and strain, if measured) are typically noisy with large oscillations (referred to as ringing) [1]. The problem is that the

T. Proulx (ed.), *Dynamic Behavior of Materials, Volume 1*, Conference Proceedings of the Society for Experimental Mechanics Series, DOI 10.1007/978-1-4419-8228-5_64, © The Society for Experimental Mechanics, Inc. 2011

force that is measured by the load cell (assuming that the frequency response of the load cell itself is suitable), that is typically placed at the top of the machine, is not exactly the force that is applied to the specimen at the same instant. As the specimen is loaded, different components of the testing machines (grips, adaptors, etc.) accelerate at different rates (depending on their mass and geometry) and the reading of the load cell includes the combined inertia effect of all the components.

In many cases the noisy records from an intermediate strain rate test are smoothed by electronic or numerical means and the smoothed stress strain curves are considered to represent the property of the tested material. Attempts have been made to reduce the noise and oscillations in the records in such tests and/or to account for the inertia effects, [2-5]. For example, in addition to the machine load cell, stiff load cells (quartz based) have been placed close to the specimen. The intention is to measure the force that is actually applied to the specimen. Unfortunately, the records are still noisy with ringing due to wave reflections from different components of the machine. In other experiments, an accelerometer is attached to the grips of the specimen. The intention is to multiply the signal from the accelerometer by a constant and add it to the signal of the load cell. In some cases this can reduce the noise, but due to the complexity of inertia effects and wave reflections it still does not give good results. In a different approach the whole testing machine is modeled (including dynamic effects and waves) by assuming a constitutive relationship for the specimen that is tested. The simulation predicts the noisy record of the load cell and if it agrees with the measured record it is concluded that the assumed response of the specimen is the actual property of the material that is tested.

The present paper introduces a new apparatus for testing materials in compression at strain rates between about 10 s^{-1} and 200^{-1}. The apparatus consists of a hydraulic actuator and a long transmitter bar. Stress strain curves obtained from testing specimens made of epoxy are clean and smooth without ant evidence of oscillations or ringing.

EXPERIMENTAL TECHNIQUE

The new compression intermediate strain rate apparatus, shown schematically in Fig. 1, is made of a hydraulic actuator and a long transmitter bar. The transmitter bar and the impact face of the actuator are both made from materials that remain elastic during the test. The specimen is placed with one end touching the end surface of the long bar and the other end free. The specimen is loaded by the actuator that impacts the specimen's free end directly. Once loaded, the specimen deforms between the actuator and the transmitter bar. As the specimen is loaded and deformed, a compression wave propagates into the transmitter bar. The amplitude of this wave is measured with strain gages that are placed on the transmitter bar (at a distance of about five diameters from the specimen). The transmitted wave is used for measuring the force that is applied to the specimen (as in the compression split Hopkinson bar). The wave in the transmitter bar propagates all the way to the end of the bar and then reflects back toward the specimen. The experiment can continue until the reflected wave reaches the strain gages. Since the strain rates are relatively low, the duration of the test is relatively long (milliseconds) and the transmitter bar has to be quite long. The experiment has to be designed (cross-sectional areas of the specimen and the transmitter bar) such that the amplitude of the stress wave in the transmitter bar is relatively small. The actuator must be large enough (load capacity) such that it moves at essentially constant speed throughout the duration of the test. The strain in the specimen during the tests is measured by 3D Digital Image Correlation (DIC). The DIC is used for measuring the strain directly on the specimen, and for determining the engineering strain from measuring the difference between the displacement of the end of the transmitter bar and the face of the actuator.

The actual apparatus is shown in Figs. 2. The transmitter bar is made of 40 m long 22.23 mm diameter stainless steel bar. The hydraulic actuator was custom made for the present application, and can move at a speed of 2 m/s while applying a force of up to 22,000 N.

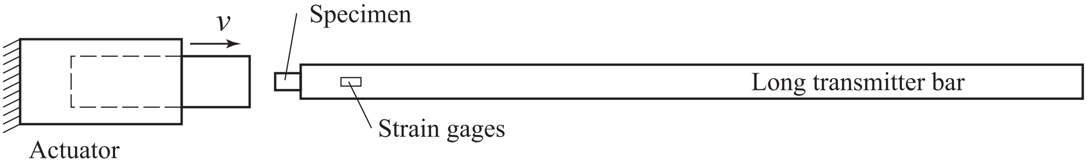

Figure 1: Schematics of the compression intermediate strain rate testing apparatus.

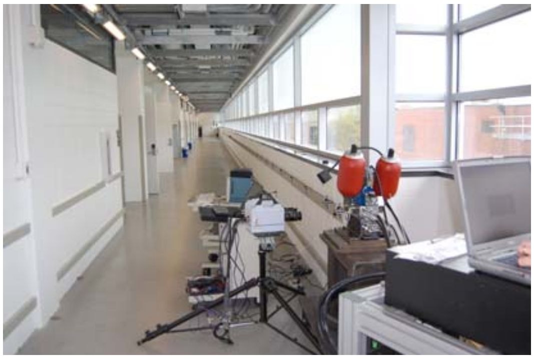

Figure 2: Overall view of the compression intermediate strain rate testing apparatus.

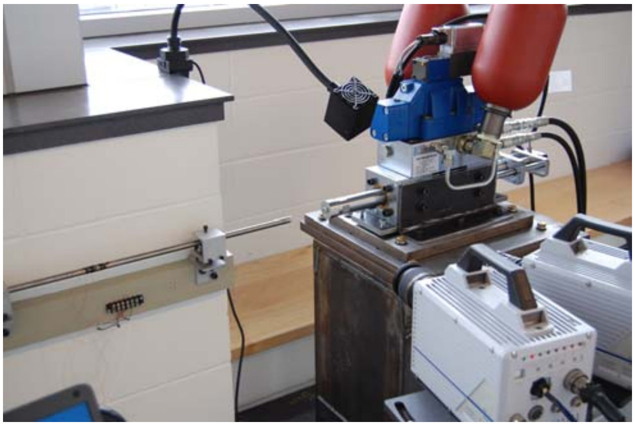

Figure 3: Hydraulic actuator and transmitter bar of the compression intermediate strain rate testing apparatus.

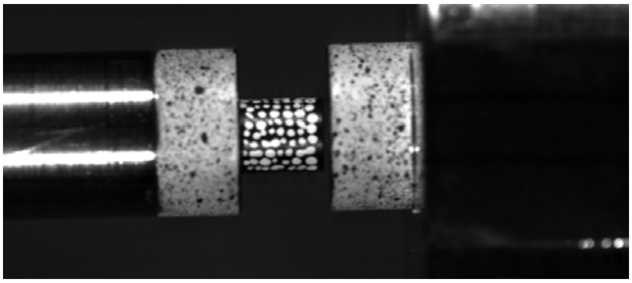

Figure 4: Specimen between the actuator and the transmitter bar.

RESULTS

Application of the new compression intermediate strain rate apparatus is shown here for testing specimens made of PR-520 epoxy. The force recorded by the strain gages on the transmitter bar during a test is shown in Fig. 5. The curve in this figure is the raw signal that was recorded (multiplied by a constant). The signal was not changed (averaged, or smoothed) by any electronic or numerical means. As can be seen, the signal is clean and smooth without any oscillations. The strain measured by the DIC system is shown in Fig. 6. The figure shows the Lagrange strain measured on the specimen directly. The strain is an average strain determined by DIC over most of the area of the specimen. Figure 6 shows also the engineering strain determined from the relative displacement between the ends of the specimen divided by the initial length of the specimen. The relative displacement is determined by applying DIC to the end of the transmitter bar where the specimen is placed and to the end of the actuator that impacts the specimen. As can be seen in Fig. 6, the strains determined by the two methods are essentially identical at small strains up to about strain of 0.1. Later on as the strains become larger the Lagrange strain is smaller than the engineering strain. The strain rate is obtained from the slope of the strain vs. time plot. From Fig. 6 the strain rate is approximately 80 s^{-1}. The stress stain curve from is test is shown in Fig. 7.

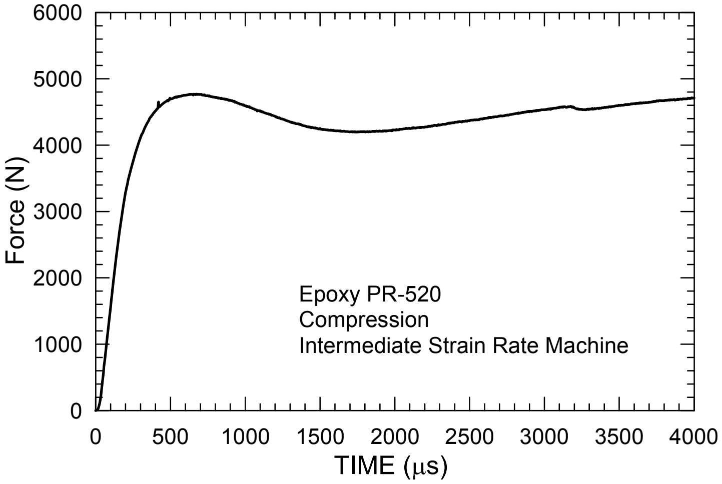

Figure 5: Force measured on the transmitter bar.

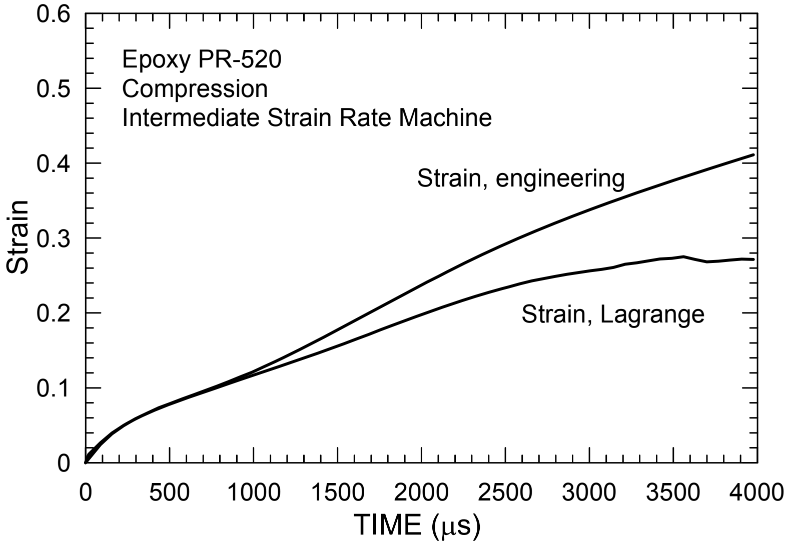

Figure 6: Strain measured using DIC.

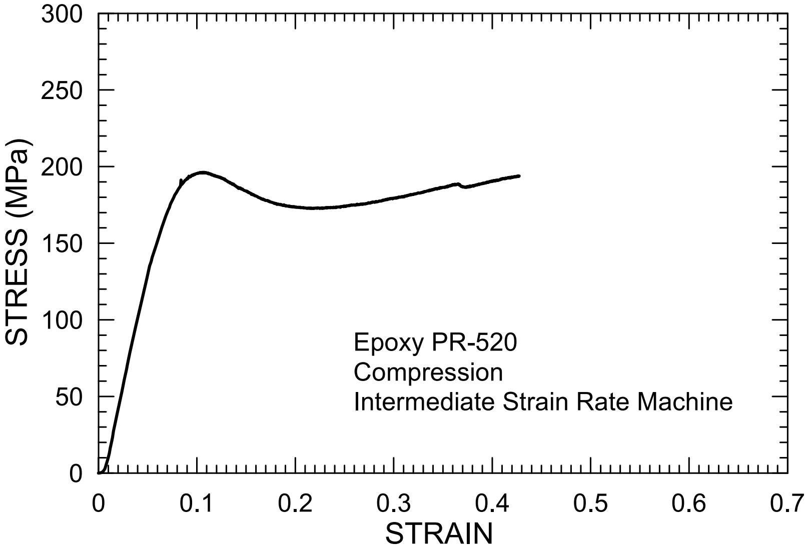

Figure 7: Engineering stress strain curve of epoxy PR-520 at strain rate of approximately 80 s^{-1}.

CONCLUSIONS

A new apparatus for compression testing at intermediate strain rates ranging from about 10 s^{-1} to 200 s^{-1} has been presented. The apparatus consists of a hydraulic actuator that presses the specimen against a long transmitter bar. The stress in the specimen is determined from the amplitude of the compression wave in the transmitter bar. The strain is measured with digital image correlation using high speed cameras. The stress strain curves that are obtained from tests with this apparatus are smooth without any oscillations (ringing) that are typical in tests at these strain rates with standard hydraulic machines.

ACKNOWLEDGEMENTS

The research reported in this paper was supported by NASA (NRA Grant NNX08AB50A). Many thanks are due to the project manager, Dr. Mike Pereira of NASA Glen Research Center.

REFERENCES

1. B.L. Boyce, M.F. Dilmore, Int. J. Impact Engineering, 36, 263 (2009)
2. H.S. Shin, H.M Lee, M.S. Kim, Int. J. Impact Engineering, 24, 571 (2000)
3. W. Bleck, I. Schael, Steel Res. 171 (5), 173 (2000)
4. S. Diot, D. Guines, A. Gavrus, E. Ragneau, J. Impact Engineering, 34, 1163 (2007)
5. R. Othman, P. Guegan, G. Challita, F. Pasco, D. LeBreton, Int. J. Impact Engineering, 36, 460 (2009)

Proceedings of the SEM Annual Conference
June 7-10, 2010 Indianapolis, Indiana USA
©2010 Society for Experimental Mechanics Inc.

A modified Kolsky bar system for testing ultra-soft materials under intermediate strain rates

R. Chen[1], S. Huang[2], K. Xia[2]*

1. National University of Defense Technology, Changsha, China, 410073
2. University of Toronto, Toronto, Ontario, Canada, M5S 1A4
*Corresponding author: kaiwen@ecf.utoronto.ca

Abstract: A 25 mm Kolsky bar made of 7075 Aluminum is modified to test ultra-soft materials under intermediate strain rates (10 to 100/s). In the modified system, an ultra-long loading pulse (5 ~ 50 ms) is generated using an 800 mm steel striker with a pulse shaper made of soft rubber. The slope of the long incident pulse thus produced is small enough to ensure both the dynamic force balance of the sample and the intermediate strain rate deformation of the sample. For such long loading pulses, the traditional data reduction scheme that is based on the strain gauge measurements is not possible. We use a laser gap gauge to measure the deformation of the sample directly and monitored the low amplitude dynamic loading forces on the sample with a pair of piezoelectric force transducers that are embedded in the bars. A commercial foam rubber is tested to demonstrate the feasibility of our modified system. Annular-shaped specimen is adopted to minimize the dynamically induce axial stress in the specimen. Experimental results show that the foam rubber is strongly rate dependent in the intermediate strain rate range.

INTRODUCTION

Strain rate dependency is one of the most important properties of ultra-soft materials such as foam rubbers. To determine material response at low strain rates ($< 10^1$ s^{-1}), one can use servo-hydraulic loading frame.[1] For measurements under strain rates higher than 10^1 s^{-1}, the diagnostic systems (load cell and linear variable differential transducer) used in loading frames can not provide sufficient frequency response for accurate force and displacement measurements. On the other hand, for intermediate to high strain rate measurement where the strain rate is larger than 10^2 s^{-1}, conventional Kolsky bar system is extensively used.[2-4] However, to test materials the intermediate strain rate range (10^1 to 10^2 s^{-1}) is very changeling, especially for ultra-soft materials. It is thus the objective of this paper to develop an experimental system that can be used to carry out accurate measurements of ultra-soft materials in this strain rate range.

Some attempts have been done to addresses the gap in strain rates. A long loading pulse (in the order of milliseconds) is needed to achieve the desired strain rate and to ensure dynamic force balance[5, 6]. Zhao and Gray developed the “slow bar” technique which can generate a long loading pulse without a duration limitation[7]. Shim et al. use a high-impedance striker to generate long pulses[8]. The data reduction in the conventional Kolsky bar test requires a clear separation between the incident pulse and the reflected pulse. The duration of the loading pulse is thus constrained by the length of the incident bar. Zhao and Gray use the 2-point strain measurements technique to separate the overlapped strain gauge signal[7]. To use a long incident bar is another way to get clear separation between the incident and reflected pulses for long loading. For example, Song et al. developed a long bar system for the intermediate strain rate characterization of soft materials[9]. However, it is not always realistic to increase the length of the incident bar. For a loading pulse with 2 ms duration, the incident and reflected pulses will unavoidably overlap if the incident bar length is shorter than 10 m assuming the strain gauge is mounted at the center of incident bar made of aluminum. Song et al. employed a high-speed digital camera to take sequential images of specimen deformation in a Kolsky bar system[10] to obtain the intermediate strain rate property. But only few points of strain can be given due to the speed limit. When testing ultra-soft materials using Kolsky bar, the tiny transmitted signal will lead to significant error if one measures the transmitted load using the traditional

T. Proulx (ed.), *Dynamic Behavior of Materials, Volume 1*, Conference Proceedings of the Society for Experimental Mechanics Series, DOI 10.1007/978-1-4419-8228-5_65, © The Society for Experimental Mechanics, Inc. 2011

strain gauges. The X-cut quartz has been shown to be much more sensitive in detecting forces in its X-direction than the strain gauge in Kolsky bar tests, with three orders of magnitude increase of sensitivity.[11]

To address the deficiencies of conventional Kolsky bar system for testing ultra-soft materials, we develop a modified Kolsky bar system in this work. To achieve the desired intermediate strain rate, a long striker and a special pulse shaper are employed to substantially extend the duration of the loading pulse, which features a slow rising front. The strain gauge measurements are abandoned in our modified system. The dynamic loading forces on both side of the specimen are monitored by a pair of piezoelectric force transducers that are buried in the incident bar and transmitted bar,[11] and the strain is monitored directly using a recently developed laser gap gauge.[12] This system is then used to test a commercially available foam rubber from McMaster-Carr at strain rate from 20 to 200 s^{-1}.

MODIFIED KOLSKY BAR SYSTEM

In this research, we modified a 25 mm Kolsky bar system to investigate the response of ultra-soft materials under intermediate strain rates. The bars are made of 7075 Aluminum alloy, with the yield strength of 455 MPa. The incident bar is 1500 mm long and the transmitted bar is 1000 mm long. The way to achieve intermediate strain rate loading is to have a long loading pulse with a slow rising front (Fig. 1).

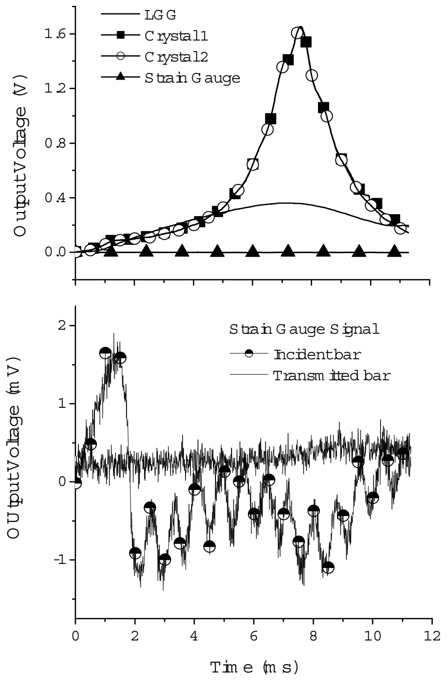

Fig. 1. Typical output signals of the modified SHPB system. (a) All outputs and (b) The enlarged strain gauge outputs.

To generate a longer loading pulse, we use an 800 mm long, 25 mm diameter maraging steel bar as the striker and a 12.5 mm diameter pulse shaper made of 2.5 mm thick rubber. When the striker impact the pulse shaper and the incident bar with a velocity of 1 m/s, an incident pulse with duration about 1 ms is generated. At the incident bar-sample interface, most of the incident pulse will be reflected as tension due to the huge mismatch between acoustic impedance of the bar and that of the specimen. The reflected pulse will be reflected one more time at the impact end of the incident bar, inducing second compression on the specimen. In our design, the incident bar is 1500 mm long, the second compression will arrive at the specimen 0.6 ms latter after the first pulse. In this way, there will be third compression, forth compression and so on due to reflection at the impact end of the incident bar. These compressive pulses add up and lead to a loading pulse with duration in the range of 5 ~ 50 ms depending on the striker velocity.

As shown in Fig1.b, the amplitudes of both strain gauge signals are very small for a typical test. The strain record from the strain gauge on the transmitted bar is essentially the white noise of the oscilloscope. The strain record from the strain gauge on the incident bar features a linear portion in the beginning, which is followed by steep decrease. This decrease of the strain is due to the superposition of the incident (compressive) pulse by the reflected wave (tensile). The initial slope of the incident wave is only about 866 MPa/s. For a typical incident wave in Kolsy bar experiments, the amplitude is around 25 MPa and the duration of the rising front is around 25 μs, this leads to a slope of 1000 GPa/s, which is about 1000 time of the slope achieved in our tests. The small slope of the incident pulse ensures the intermediate strain rates deformation of the sample as will be shown later.

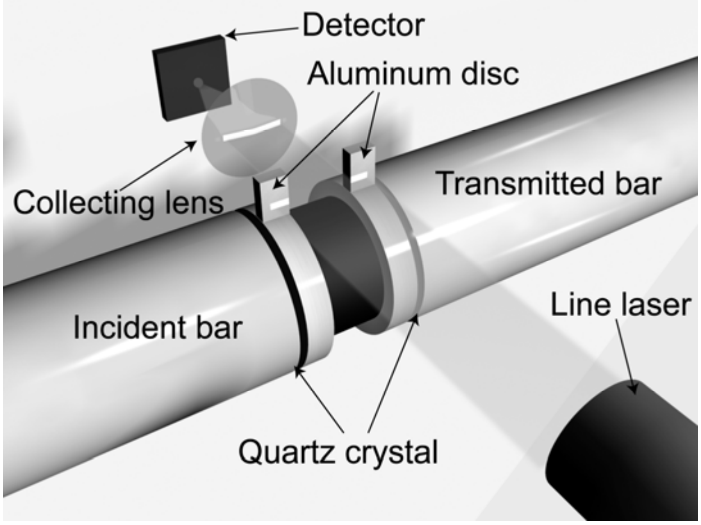

Fig. 2. Schematics of modified SPPB system.

In a conventional Kolsky bar system, two strain gauges mounted on the incident bar and transmitted bar are used to measure the stress wave profiles. A clear separation of incident and reflected waves is required for obtain the strain using the reflected strain for 1-wave analysis, or other operations for 2- and 3-wave analyses.[4] At intermediate strain rate, the loading pulse needs to be extended to as long as a few milliseconds.[6] This will lead to an overlap of incident and reflected wave (Fig. 1b). As a result of this overlap, one can not measure the deformation of the specimen with strain gauge signals. To overcome this obstacle, we used a laser gap gauge (LGG) to measure the deformation of the specimen directly (Fig. 2). The idea of using optical techniques in Kolsky bar testing was first proposed by Griffith and Martin,[13] who used a white light to monitor the displacements at the end faces of a cylindrical specimen. Ramesh and Kelkar adopted a line laser to measure the velocity history of flyer in planer impacts.[14] Later, this technique was used to measure the radial expansion of specimens in Kolsky bar tests.[15, 16] Details of our LGG system was reported elsewhere.[12]

The LGG measures the distance between the two bar-specimen interfaces, i.e., the length of the specimen. The output of the LGG is voltage (Fig. 1) and it is calibrated to obtain the sample length measurements[11]. The strain is then calculated by dividing the change of the sample length by the initial sample length.

When testing ultra-soft materials using Kolsky bar, the transmitted signal is too small due the mismatch between the acoustic impedance of the bar and that of the materials, as the strain gauge signals shown in Fig. 1b. We use two piezoelectric force transducers that are sandwiched between the specimen and two bars respectively to directly measure the dynamic loading forces. As shown in Fig.2, the quartz crystal is calibrated by the strain gauge signal. When the striker hits the incident bar without a pulse shaper, a square wave will be generated in the incident bar, which can be monitored by both the strain gauge and the quartz crystal. The stress amplitude 6.54MPa is obtained by the strain gauge. We can calculate the parameter of the crystal gauge (3.57MP/V), where as the average amplitude of the crystal signal is 1.83V. We can see that the signal to noise ratio of the quartz crystal measurements is substantially better than that of the strain gauge signal.

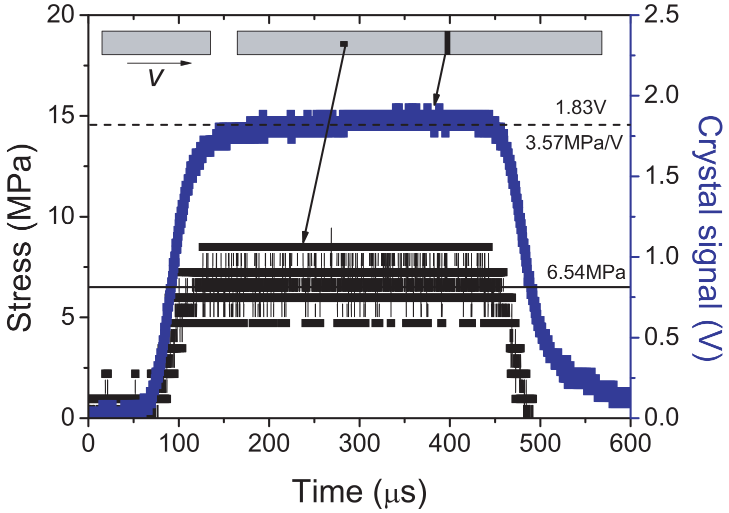

Fig. 3. The quartz crystal is calibrated by the strain gauge signal.

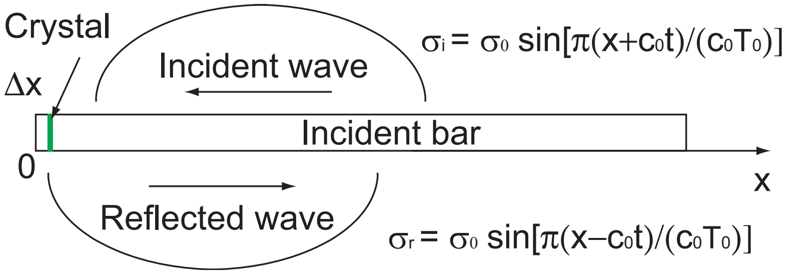

Fig. 4. Schematics of the error induced by embedding.

In our experimental design, the positive pole of the crystal is glued to the bars, and the negative pole of the crystal is glued to the aluminum disc, with the distance of Δx away from the specimen (FIG. 4). This distance could be ignored for the quasi-static test where the wave propagation effects need not to be considered. However, in the dynamic tests, the measured stress by the imbedded crystal may be different from that at the end of the incident bar. As shown in Fig.3, we assume that the incident wave has the sinusoidal form $\sigma_i = \sigma_0 \sin[\pi(c_0 t - x)/c_0 T_0]$, where σ_0 is the maximum stress of the incident wave, T_0 is the duration, c_0 is the wave velocity of the bar. The origin is chosen at the incident bar-specimen interface and the incident pulse arrives at the bar-specimen interface at time 0. We used the conversion that the compression is positive hereafter. The loading wave will be mostly reflected at the bar-specimen interface due to the huge mismatch of the acoustic impedance. Let us examine an extreme case, where 100% of the wave is reflected. The reflected wave is $\sigma_r = -\sigma_0 \sin[\pi(c_0 t + x)/c_0 T_0]$. The summation of the incident wave and the reflected wave gives:

$$\sigma = -2\sigma_0 \sin(\frac{\pi x}{c_0 T_0})\cos(\frac{\pi t}{T_0}) \tag{1}$$

From Eq. (1), the dynamic stress on the incident bar-specimen end, where $x = 0$, is always 0. However, the maximum stress measured by the imbedded crystal, which is located at $x = \Delta x$ is:

$$\Delta\sigma = 2\sigma_0 \sin(\frac{\pi \Delta x}{c_0 T_0}) \tag{2}$$

The elastic wave velocity of the bars is c_0 = 5000 m/s. In a typical Kolsky bar test, assuming the loading duration T_0 = 200 μs, and the amplitude of the incident wave σ_0 = 25 MPa, the stress error is around be 0.5 MPa if Δx =3 mm. This value is in the same order of the strength of ultra-soft materials (~0.1 MPa). In our design, a 1 mm thick aluminum shim of the same diameter as the quartz crystal is used as the negative pole between quartz crystal and specimen, the loading duration is longer than 5 ms, and the loading amplitude is around 2 MPa. Using Eq. (1), we find that the error induced by embedding is within 0.5 kPa, which is negligible even for low strength ultra-soft materials.

RESULTS AND DISSCUSTION

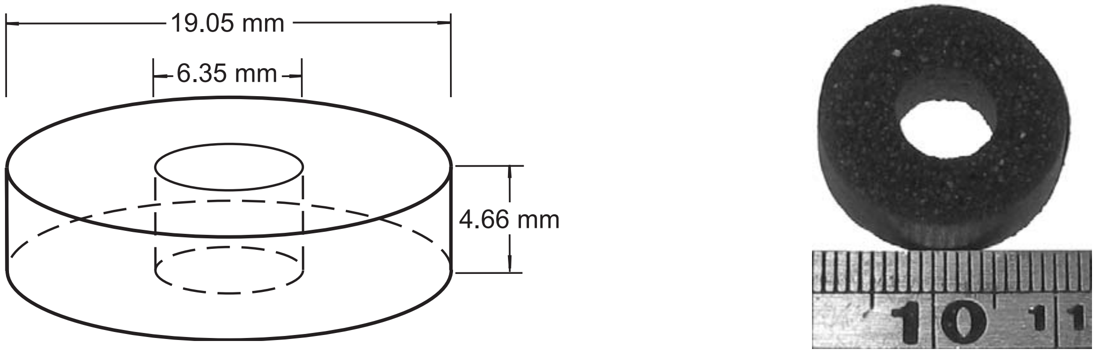

(a) (b)

Fig. 5. Schematic and photograph of a specimen used in this study.

A commercially available closed cell silicone foam rubber (from McMaster-Carr) is selected in this research. The black foam rubber with the density of 96 kg/m^3 is manufactured follow the ASTM specification (E84 25/50). It is available in the form of a tube with outer diameter of 19.05 mm and inner diameter of 6.35 mm. The tube is sliced into an annular disc with thickness of 4.66 mm. A schematic of the specimen is shown in FIG. 5a and FIG. 5b shows a photograph of an untested specimen.

The radial inertia effect in specimen in Kolsky bar experiment has been studied since it was invented [17], and was further discussed recently by Forrestal [18] and Song [19, 20]. The radial inertia in specimen leads to an extra axial stress in the cylindrical specimen. The distribution of the inertia induced axial stress σ_z^l, along the radial direction was found to be parabolic, with its maximum value reached at the center of the specimen and zero value on outer surface of the cylindrical specimen.[18] The additional axial stress averaged over the specimen cross-section is:[19]

$$\bar{\sigma}_z^l = \frac{a^2 \rho_s}{8} \ddot{\varepsilon} \tag{3}$$

where a is the radius of the specimen, ρ_s is the density of the specimen material, and $\ddot{\varepsilon}$ is the specimen's axial strain acceleration. In a typical Kolsky bar experiment, the strain acceleration at the beginning of loading is of the order of 10^8 s^{-2}. The additional stress in a specimen with a diameter of 6 mm and density of 96 kg/m^3 is estimated to be of the order of 50 kPa. This additional axial stress may be negligible when testing regular engineering materials, such as metals, rocks and glasses. However, it is in the same order of magnitude of the flow stress of foam-rubbers (~100 kPa) and will thus lead to significant error in the experimental results. The inertia-induced stress can be minimized by using an annular specimen that help decrease the axial strain acceleration in the specimen.[19, 20] A parametric study shows that the inertia-induced stress in an annular specimen decreases rapidly as the inner radius reaches about 30% of the outer radius.[19] We can also see from Eq. (3) that long loading pulses with slow rising front help decrease the dynamically induced additional axial stress.

For the typical test, the outputs are shown in Fig. 1. We can see that the dynamic forces on both sides of the sample are recorded and dynamic stress equilibrium is achieved (Fig. 6). There is a regime of approximately linear variation of strain with time for times between 1.5 ms and 5 ms in the curve of strain history in Fig. 6. The slope of this region was determined from a least squares fit as strain rate, shown as a dashed line in the figure.

Figure 7-(a) shows a typical stress-strain curve of foam rubber. Compared to the result of high speed camera,[5] our method can give detailed strain measurements and thus complete stress strain curve. The results show that the loading of the diagrams is non-linear especially at higher stresses within the range of strain rates used. At low strains, the stress-strain curve of the foam rubber features a straight line of linear elastic deformation, which is followed by a plateau of deformation at almost constant stress indicating collapsing of cells. The last deformation of the foam rubber is the plastic deformation of the densified material.[21] Figure 7-(b) shows the strain rate effect of the foam rubber from low to intermediate strain rates. The yielding strength of foam rubber increases with the strain rate. The quasi-static result obtained by an MTS machine with 10^{-2} strain rate is also shown as reference.

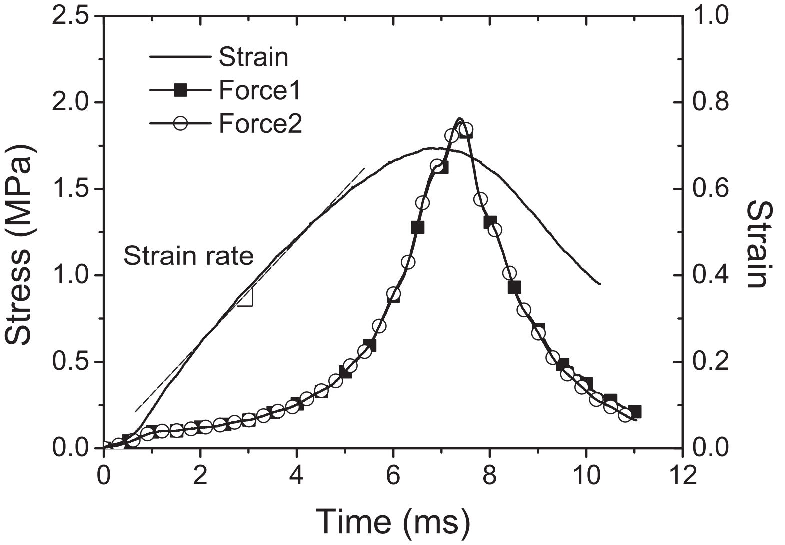

Fig. 6. Stress balance of the specimen, and the determination of strain rate.

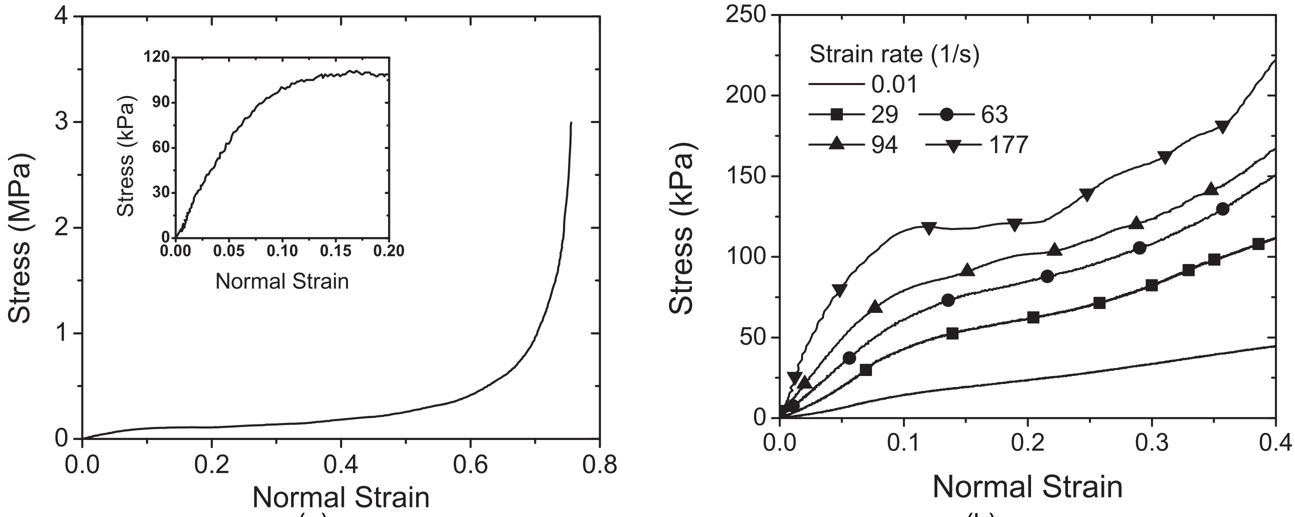

(a)

(b)

Fig. 7. (a)Typical stress-strain curve of foam rubber.(b) Strain rate effect of foam rubber.

CONCLUSIONS

In this work, we modified a 25 mm Kolsky bar made of 7075 Aluminum to test ultra-soft materials under intermediate strain rates. To achieve the desired strain rate range, we used an 800 mm steel striker with a pulse shaper made of soft rubber. The slope of the resulting ultra-long loading pulse (5 ~ 50 ms) is small enough to ensure both the dynamic force balance of the sample and the intermediate strain rate of the sample deformation. A laser gap gauge is employed to measure the deformation of the sample directly, and the low amplitude dynamic loading forces on the sample are monitored by a pair of piezoelectric force transducers that are buried in the incident and transmitted bars at ends close to the specimen. A commercial foam rubber is tested to demonstrate the feasibility of our modified system. Experimental results show that this new method is effective and reliable for determining the dynamic compressive stress-strain responses of materials with low mechanical impedance and low compressive strength.

ACKNOWLEDGMENTS

This work was supported by the Natural Science Foundation of China (NSFC) through Grant No. 10872215 & 10902100, and the Natural Sciences and Engineering Research Council of Canada (NSERC) through Discovery Grant No. 72031326.

REFERENCES

[1] Kuhn H.A., "Uniaxial Compression Testing". in: Vol. 8 ASM Handbook Vol 8, Mechanical Testing and Evaluation. 338-357 (2000).

[2] Field J.E., Walley S.M., Proud W.G., et al., "Review of experimental techniques for high rate deformation and shock studies", International Journal of Impact Engineering. 30: 725-775 (2004).

[3] Gama B.A., Lopatnikov S.L., and Gillespie Jr J.W., "Hopkinson bar experimental technique: A critical review", Applied Mechanics Review. 57(4): 223-250 (2004).

[4] Gray G.T. and Blumenthal W.R., "Split-Hopkinson Pressure Bar Testing of Soft Materials". in: Vol. 8 ASM Handbook Vol 8, Mechanical Testing and Evaluation. 1093-1114 (2000).

[5] Song B., Chen W.W., and Lu W.Y., "Mechanical characterization at intermediate strain rates for rate effects on an epoxy syntactic foam", International Journal of Mechanical Sciences. 49(12): 1336-1343 (2007).

[6] Song B., Chen W., and Lu W.Y., "Compressive mechanical response of a low-density epoxy foam at various strain rates", Journal of Materials Science. 42(17): 7502-7507 (2007).

[7] Zhao H. and Gary G., "A new method for the separation of waves. Application to the SHPB technique for an unlimited duration of measurement", Journal of the Mechanics and Physics of Solids. 45(7): 1185-1202 (1997).

[8] Shim V.P.W., Liu J.F., and Lee V.S., "A technique for dynamic tensile testing of human cervical spine ligaments", Experimental Mechanics. 46: 77-89 (2006).

[9] Song B., Syn C.J., Grupido C.L., et al., "A Long Split Hopkinson Pressure Bar (LSHPB) for Intermediate-rate Characterization of Soft Materials", Experimental Mechanics. 48: 809-815 (2008).

[10]Song B., Chen W., and Lu W.Y., "Mechanical characterization at intermediate strain rates for rate effects on an epoxy syntactic foam", International Journal of Mechanical Sciences. 49(12): 1336-1343 (2007).

[11]Chen W., Lu F., and Zhou B., "A quartz-crystal-embedded split Hopkinson pressure bar for soft materials", Experimental Mechanics. 40(1): 1-6 (2000).

[12]Chen R., Xia K., Dai F., et al., "Determination of Dynamic Fracture Parameters Using a Semi-circular Bend Technique in Split Hopkinson Pressure Bar Testing", Engineering Fracture Mechanics. doi:10.1016/j.engfracmech.2009.02.001 (2009).

[13]Griffith L.J. and Martin D.J., "Study of dynamic behavior of a carbon-fiber composite using split Hopkinson pressure bar", Journal of Physics D-Applied Physics. 7(17): 2329-2344 (1974).

[14]Ramesh K.T. and Kelkar N., "Technique for the Continuous Measurement of Projectile Velocities in Plate Impact Experiments", Review of Scientific Instruments. 66(4): 3034-3036 (1995).

[15]Ramesh K.T. and Narasimhan S., "Finite deformations and the dynamic measurement of radial strains in compression Kolsky bar experiments", International Journal of Solids and Structures. 33(25): 3723-3738 (1996).

[16]Li Y. and Ramesh K.T., "An optical technique for measurement of material properties in the tension Kolsky bar", International Journal of Impact Engineering. 34: 784-798 (2007).

[17]Kolsky H., "An investigation of the mechanical properties of materials at very high rates of loading", Proceedings of the Royal Society A-Mathematical Physical and Engineering Sciences. B62: 676-700 (1949).

[18]Forrestal M.J., Wright T.W., and Chen W., "The effect of radial inertia on brittle samples during the split Hopkinson pressure bar test", International Journal of Impact Engineering. 34(3): 405-411 (2007).

[19]Song B., Ge Y., Chen W., et al., "Radial inertia effects in kolsky bar testing of extra-soft specimens", Experimental Mechanics. 47: 659-670 (2007).

[20]Song B., Chen W., Ge Y., et al., "Dynamic and quasi-static compressive response of porcine muscle", Journal of Biomechanics. 40(13): 2999-3005 (2007).

[21]Yu J.L., Li J.R., and Hu S.S., "Strain-rate effect and micro-structural optimization of cellular metals", Mechanics of Materials. 38(1-2): 160-170 (2006).

Proceedings of the SEM Annual Conference
June 7-10, 2010 Indianapolis, Indiana USA
©2010 Society for Experimental Mechanics Inc.

Visualization and measurements of wave propagations in slurry hammers

K. Inaba, H. Takahashi, N. Kollika, and K. Kishimoto
Tokyo Institute of Technology
2-12-1 Ookayama, Meguro-ku, Tokyo, 152-8552, JAPAN
E-mail: inaba@mech.titech.ac.jp

ABSTRACT

We are studying strongly-coupled fluid-structure interaction generated by a stress wave propagating along the surface in the slurry (mixture of water and solid particles) adjacent to a thin solid shell. This is realized, experimentally, through projectile impact along the axis of a slurry-filled tube. We have tested polycarbonate tubes with 52 mm inner diameter and 4 mm wall-thicknesses. A steel impactor is accelerated to 1 m/s by gravity and strikes a polycarbonate buffer within the tube located at the top of the slurry surface. Strain gages measure hoop strains every 200 mm and pressure transducer records reflected pressure at the closed end of the specimen tube. Since we use the polycarbonate tube, we can visualize original distribution of solid particles inside the specimen tube and motions of particles due to the propagation of slurry hammer for low volume fraction cases. Wave speeds obtained in our experiments decreased as volume fraction of particles of calcium carbonate increases while theoretical wave speeds proposed by Han et al. (1998) for a slurry hammer are independent on the fraction. Reflected pressure reduces when a volume fraction of particle increases while the impulse calculated by integrating reflected pressure histories just slightly reduces with the fraction increasing.

1 Introduction

The propagation of coupled fluid and solid stress waves in liquid-filled tubes is directly relevant to the common industrial problem of water hammer [1, 2, 3]. Two failure occurred in nuclear power plants due to detonation loading inside the pipe system; Hamaoka-1 NPP in Japan, Brunsbüttel KBB in Germany [4]. In these accidents, detonable mixtures were accumulated by radiolysis and water is present near the explosion. It is quite likely that the impact-loaded water interacted with the tube wall and caused a fluid-structure interaction and escalated the damages during the explosions.

When a shock in a liquid propagates perpendicular to submerged structure, flexural waves are generated in the structure. The main wave propagation mode is flexural wave in the structure which can be closely coupled to a pressure wave in the liquid. To investigate this type of coupling, we are using projectile impact and thin-wall water-filled tubes to generate stress waves in the water that excite flexural waves in the tube wall, see Fig. 1.

We have been using this configuration to study [5, 6] elastic and plastic waves in water-filled metal and polymer tubes. The theory of water hammer and our previous studies show that the extent of fluid-solid coupling in this geometry is determined by a non-dimensional parameter.

$$\beta = \frac{KD}{Eh} \tag{1}$$

where K is the fluid bulk modulus, E is the solid Young's modulus, D is the tube diameter, and h is the wall thickness. In this case, the coupling is independent of the blast wave characteristics and only depends on the fluid and solid properties and geometry. The Korteweg waves travel at a speed (Lighthill [7])

$$c = \frac{a_f}{\sqrt{1+\beta}} \tag{2}$$

T. Proulx (ed.), *Dynamic Behavior of Materials, Volume 1*, Conference Proceedings of the Society for Experimental Mechanics Series,
DOI 10.1007/978-1-4419-8228-5_66, © The Society for Experimental Mechanics, Inc. 2011

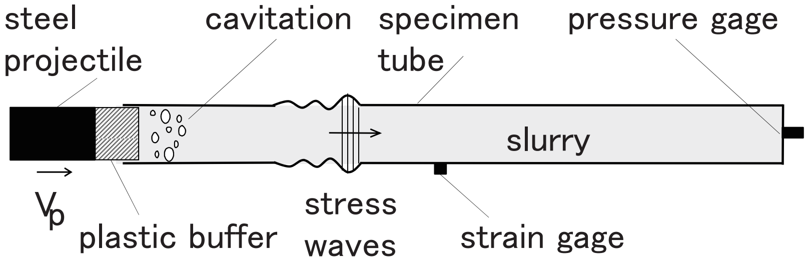
steel projectile
cavitation
specimen tube
pressure gage
slurry
V_p
plastic buffer
stress waves
strain gage

Figure 1: Schematic diagram of axi-symmetric water-in-tube configuration for generation of tube flexural waves coupled with stress waves propagating in the water.

which, depending on the magnitude of β, can be significantly less than the sound speed a_f in the fluid or the bar wave speed $\sqrt{E/\rho_s}$ in the tube. The parameter β is sufficiently large in our experiments that we obtain significant fluid-solid coupling effects. Previous experiments [8] on flexural waves excited by gaseous detonation are superficially similar to the present study but these have all been in the regime of small β.

The current study reports results for slurry-hammer as elastic wave propagation generated by low-speed impacts. The present work extends in a systematic fashion our previous studies [5, 6, 9] in which we used metal tubes or composite tubes. The dynamic interaction between solids and fluid for homogeneous slurries has been studied by several researchers [10, 11]. In their formulations, solid particles are modeled without detail observation during the wave passage. In the present study, we used polycarbonate tubes so that we can visualize particle motions inside the tube and discuss effects of particles on the wave speeds and pressure loadings.

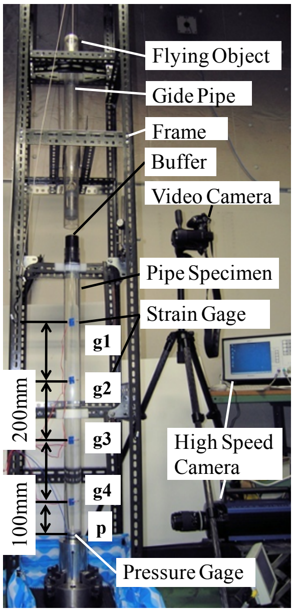
Flying Object
Gide Pipe
Frame
Buffer
Video Camera
Pipe Specimen
Strain Gage
g1
g2
g3
g4
p
200mm
100mm
High Speed Camera
Pressure Gage

Figure 2: Picture of free-fall test facility.

Experimental Methods

We built a free-fall facility to perform experiments on the fluid-structure interaction as shown in Fig. 2. The guide tube for the projectile is mounted vertically above a specimen polycarbonate tube filled with water or slurry. The 50 mm diameter and 1.5 kg steel projectile is accelerated by a gravity up to 1 m/s; reflected pressure recorded at the closed bottom end is about 0.6 MPa. A high-speed digital camera (FC100, Casio) is used to measure the projectile

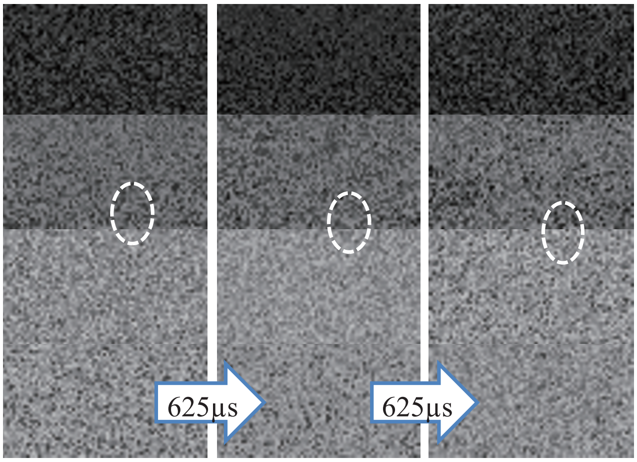

Figure 3: Particle motions after the passage of slurry hammer wave.

speed at the impact. The average projectile speed dropping from 100 mm height is 0.71 m/s. A high-speed video camera (HPV-1, Shimadzu) is used to observe the particle motions due to wave propagations and determine particle speeds just after the passage of the wave by post-processing the images (see Fig. 3). Obtained particle speed is 0.49 m/s and does not change in the range less than volume fraction of 0.2%.

The impact-generated stress waves cause the tube to deform and the resulting coupled fluid-solid motion propagates along the tube and within the water or the slurry. The deformation of the tube is measured by strain gages oriented in the hoop direction and the pressure in the water is measured by a piezoelectric transducer mounted in an aluminum fitting sealed to the bottom of the tube (Fig. 4). The specimen polycarbonate tube has 52 mm inner-diameter and 60 mm outer-diameter and 4 mm wall-thickness. Strain gages are mounted to measure the hoop strain of the polycarbonate tube at 200 mm increments. The bottom of the tube is fastened to an aluminum bar mounted in a lathe chuck that is placed directly on the floor.

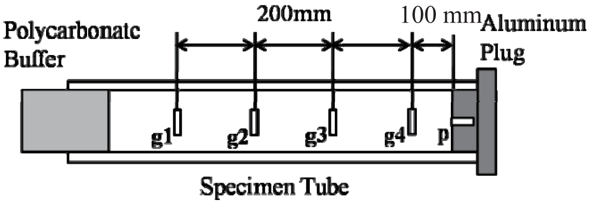

Figure 4: Schematic of test specimen tube with buffer, pressure transducer (p), and strain gages (g1-g4).

The projectile is not completely ejected from the guide tube when it impacts a polycarbonate buffer placed on the water surface. A gland seal is used to prevent water and slurry moving through the clearance space between the buffer and specimen tube. In this fashion, the stress waves due to the impact of the projectile are transmitted directly to the water surface inside the specimen tube. Slurry is prepared by mixing water and calcium carbonate particles (CaCO3, averaged diameter 6 μ m, density 2.7 g/cm^3, up to 600 g).

2 Results and discussion

Figure 5 shows hoop strain histories for a water case without particles measured at locations g1 to g4 as given in Fig. 4. The red trace in Fig. 5 is the pressure history and since this is obtained in the solid end wall, the pressure values are enhanced over those for the propagating wave due to the effects of reflection at the aluminum-water interface. In Fig. 5, the strain signal baselines are offset proportional to the distance from the buffer bottom. The blue line indicate the leading edge of the primary (main) stress wave front. The primary wave speed is 412 m/s. The subsequent reflection of the primary waves from the bottom and re-reflection from the buffer can be observed

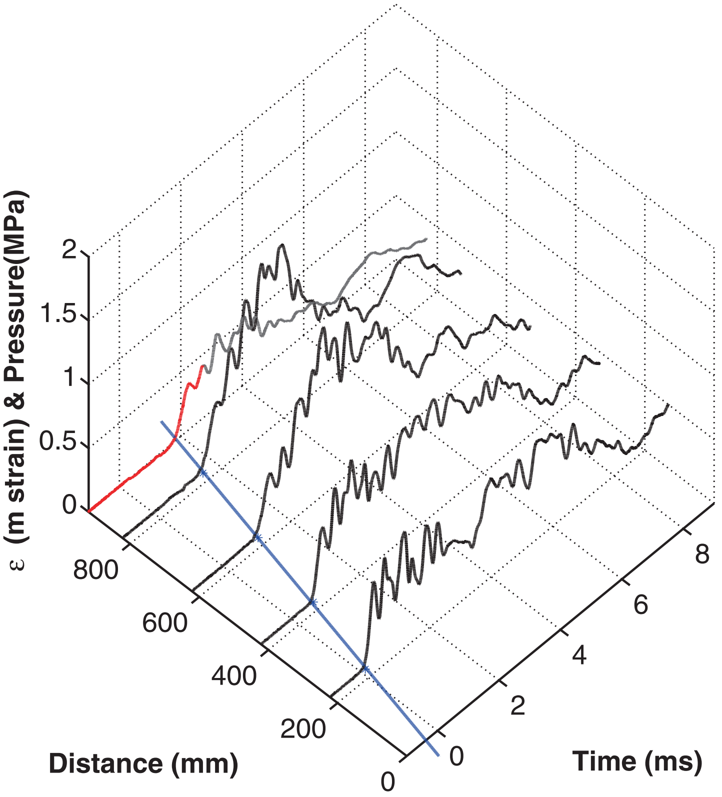

Figure 5: Strain and pressure histories for shot 062, $C_V = 0\%$, water case.

as distinct strain pulses. Peak pressure at the front is 0.57 MPa.

Hoop strain histories for a slurry case is presented in Fig. 6. This figure is drawn in the same manner as Fig. 5. Volume fraction of particles is 11.3% and total 600 g of particles are mixed in the water. Each experiment of slurry is conducted within a minute after mixing so that we can measure the slurry hammer at homogeneous conditions. The frontal wave speed is 246 m/s and is slower than that of the water case. The peak pressure is 0.40 MPa and is lower than that of the water case. We found that the tube is expanded before the arrival of the main stress wave. Since there is no expansion for the water case, this is unique for the slurry hammer case.

Figure 7 shows the relation between the slurry-hammer speed and the volume fraction of the particle. As the volume fraction increases, the speed decreases from 400 m/s to 250 m/s. Han et al. [11] proposed the equation to predict the speed of the slurry hammer for homogeneous mixture. In their equation, the slurry-hammer speed is calculated with the water and the particle speeds. We substituted the buffer and the particle speeds into their equation as the water and the particle speeds and obtained the theoretical values. The theoretical estimation is presented in the Fig. 7. With increasing the volume fraction, experimental results decreases more than theoretical estimations. First, we used the particle velocity obtained in the case for low volume fraction (0.2%) due to the limitation of the particle visualization. Therefore, there is a posibility that the particle speed dramatically changes as the volume fraction increases. The other reason for the disagreement is considered to be caused by scattering of frontal waves due the the presence of particles.

The relation between the frontal peak pressure and the volume fraction of particles is given in Fig. 8. Experimental results indicated that the peak pressure does not change by increasing the volume fraction of the particles. Theoretical results also shows the weak dependence on the volume fraction. Since there was the presence of particles near the buffer, the buffer motion was strongly affected by the particles, which results in dispersion of the peak pressure. The peak pressure can be estimated by the product of the density of slurry, wave speed, and the boundary speed

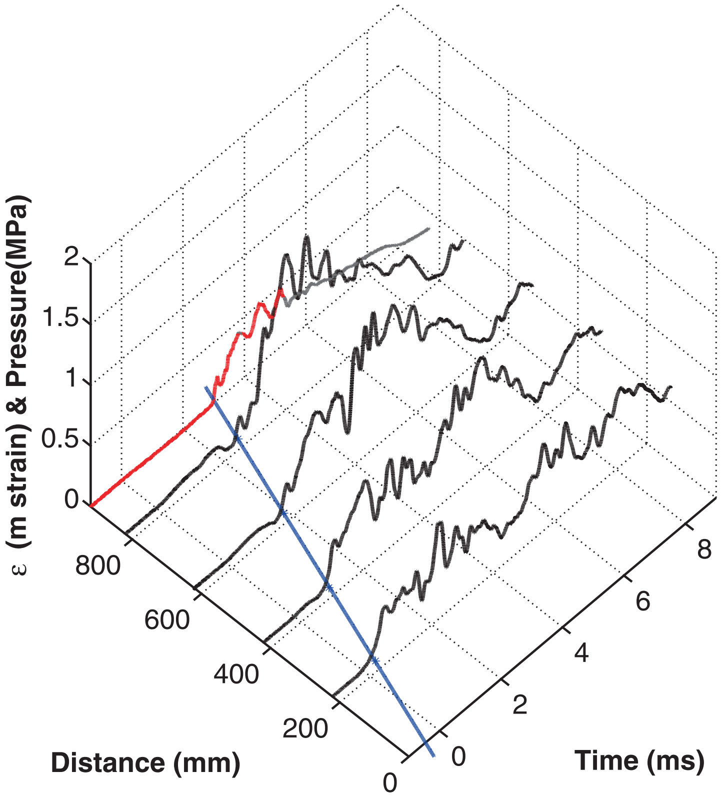

Figure 6: Strain and pressure histories for shot 062, $C_V = 11.3\%$, slurry case.

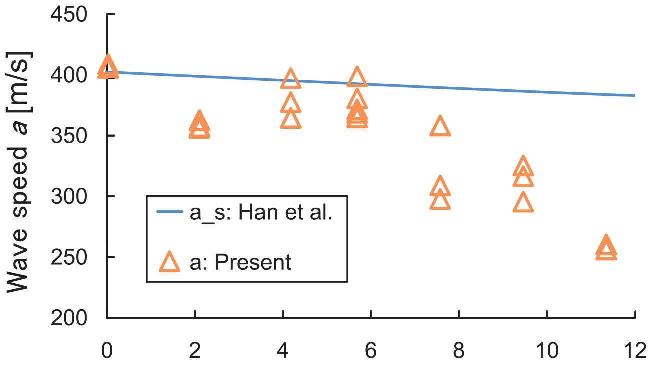

Figure 7: The relation between the slurry-hammer speed and the volume fraction of particles C_V.

(the buffer speed). Figure 9 is obtained by substituting the experimental wave speed into the equation for the peak pressure. As shown in this figure, peak pressure decreases as the volume fraction increases. If the scattering becomes dominant due to the presence of particles, it is reasonable that the peak pressure decreases as the volume fraction increases.

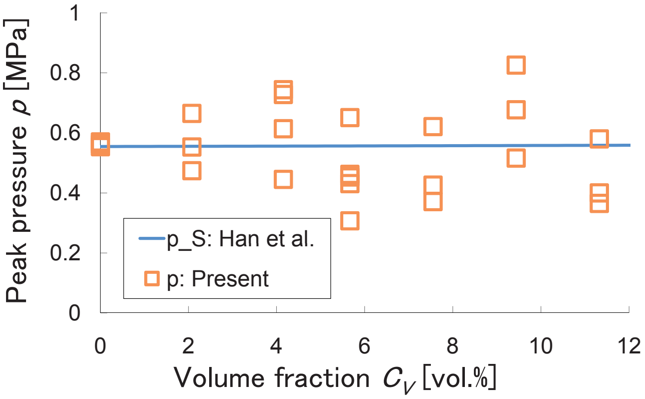

Figure 8: The relation between the peak pressure and the volume fraction of particles C_V.

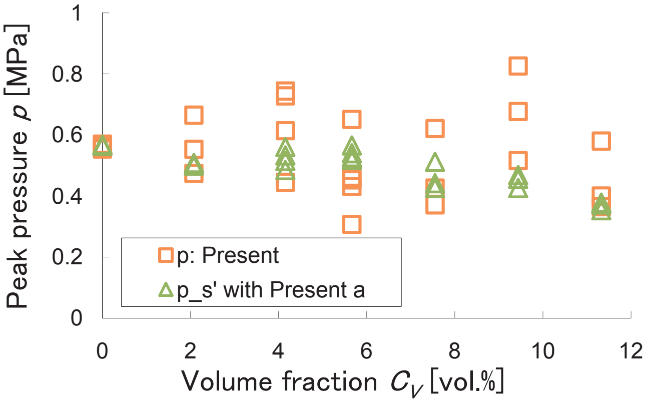

Figure 9: The relation between the peak pressure and the volume fraction of particles C_V estimated from wave speeds.

3 Summary

We used projectile impact to study the propagation of coupled structural and pressure waves in slurry-filled polycarbonate tubes. The main disturbance travels at a Korteweg speed for water case but becomes slower as the volume fraction of particle increases. The wave speeds in experiments indicated the difference from the theoretical estimations proposed by Han et al. Peak pressure in experiments shows weak dependence on the volume fraction and agree with the trend of the theoretical estimations.

References

[1] Wylie, E. B., and Streeter, V. L., 1993. *Fluid Transients in Systems.* Prentice-Hall, Inc., NJ.

[2] Tijsseling, A. S., 1996. "Fluid-structure interaction in liquid-filled pipe systems: A review". *Journal of Fluids and Structures,* **10**, pp. 109–146.

[3] Wiggert, D. C., and Tijsseling, A. S., 2001. "Fluid transients and fluid-structure interaction in flexible liquid-filled piping". *Applied Mechanics Reviews,* **54**(5), pp. 455–481.

[4] Shepherd, J. E., 2009. "Structural response of piping to internal gas detonation". *Journal of Pressure Vessel Technology,* **131**(3).

[5] Inaba, K., and Shepherd, J. E., 2008. "Flexural waves in fluid-filled tubes subject to axial impact". In Proceedings of the ASME Pressure Vessels and Piping Conference. July 27-31, Chicago, IL USA. PVP2008-61672.

[6] Inaba, K., and Shepherd, J. E., 2008. "Impact generated stress waves and coupled fluid-structure responses". In Proceedings of the SEM XI International Congress & Exposition on Experimental and Applied Mechanics. June 2-5, Orlando, FL USA. Paper 136.

[7] Lighthill, J., 1978. *Waves in Fluids*. Cambridge University Press.

[8] Shepherd, J. E., 2006. "Structural response of piping to internal gas detonation". In ASME Pressure Vessels and Piping Conference., ASME. PVP2006-ICPVT11-93670, presented July 23-27 2006 Vancouver BC Canada.

[9] Inaba, K., and Shepherd, J. E., 2009. "Fluid-structure interaction in liquid-filled composite tubes under impulsive loading". In Proceedings of the SEM XII Annual Conference & Exposition on Experimental and Applied Mechanics. June 1-4, Albuquerque, NM USA. Paper 413.

[10] Liou, C. P., 1984. "Acoustic wave speeds for slurries in pipelines". *Journal of Hydr Engng,* **110**(7), pp. 945–957.

[11] W. Han, Z. Dong, H. C., 1998. "Water hammer in pipelines with hyperconcentrated slurry flows carring solid particles". *Science in China SeriesE,* **41**(4), pp. 337–347.

Proceedings of the SEM Annual Conference
June 7-10, 2010 Indianapolis, Indiana USA
©2010 Society for Experimental Mechanics Inc.

A Newly Developed Kolsky Tension Bar

Bo Song, Bonnie R. Antoun, Kevin Connelly, John Korellis, Wei-Yang Lu

Sandia National Laboratories, Livermore, CA 94551-0969, USA

Mechanical characterization of materials requires highly precise and reliable experimental facilities. At 2009 SEM conference, we presented a newly developed Kolsky compression bar at Sandia National Laboratories, Livermore, CA. Comparing the compression bar, development of Kolsky tension bar is much more challenging. In this study, besides remedies for the Kolsky compression bar design were used for the new tension bar, the loading device facilitating tension wave was newly designed. The newly developed Kolsky tension bar was demonstrated reliable and precise for investigation of stress-strain behavior as well as damage and failure response of materials under impact loading conditions.

Figure 1 shows the photograph of the newly developed Kolsky tension bar at Sandia National Laboratories, Livermore, CA. As shown in Fig. 1, the tension bar (on right) was secured to the same optical table with the compression bar (on left) that we presented at 2009 SEM Conference. The linear bearings with interior Frelon® coating were employed to support the whole Kolsky tension bar system from the momentum trap bar, gun barrel all the way to the incident and transmission bars. The same laser based alignment system is also applicable to align the tension bar system. The detailed information regarding the optical table, linear bearings, and the laser alignment system can be found in Ref. [1].

Figure 2 shows the schematic of the Kolsky tension bar. The bars are 19.05 mm in diameter. Two bar materials, C350 maraging steel and 7075-T651 aluminum alloy, are used for mechanical characterization of hard and soft materials, respectively. The incident and transmission bars are 3560 mm and 2135 mm long, respectively. The steel gun barrel, which has an OD of 31.8 mm and ID of 19.05 mm, is 1835 mm long. The specimens are attached to both incident and transmission bars through appropriate adapters, as shown in Fig. 2.

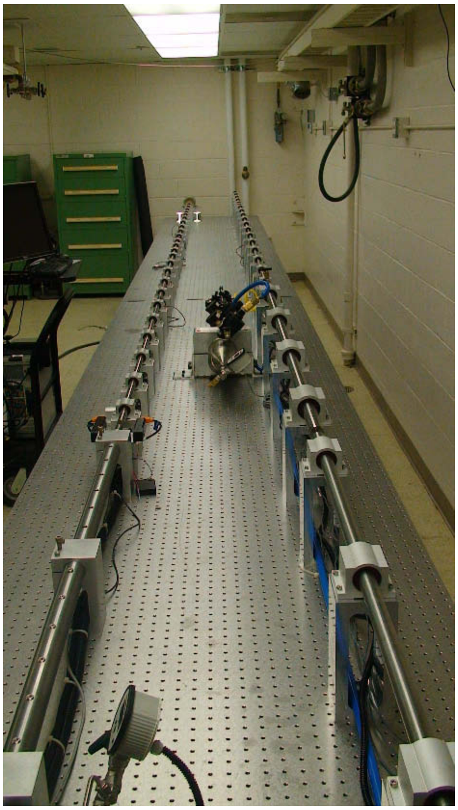

Fig. 1. Photograph of the new Kolsky tension bar

In Kolsky tension bar design, the loading method becomes challenging. Inappropriate loading method may produce distorted signals that are not usable for data reduction, or requiring more efforts in data interpretation. Many different loading methods for Kolsky tension bar have been developed in the past decades. In this study, we developed a new loading method for the Kolsky tension bar, as shown in Fig. 2. The gun barrel is directly connected to the incident bar with a coupler. The cylindrical striker set inside the gun barrel is launched by the sudden release of the compression air in the air cylinder that is connected to the gun barrel through flexible air hose. The striker impacts on the end cap that is threaded into the open end of the gun barrel, producing a tension on the gun barrel. The striker was coated with a thin layer of Teflon® to reduce the friction with the gun barrel. The gun barrel is supported with Frelon® coated linear bearings, making it free movement in the axial direction. The tension wave in the gun barrel transmits into the incident bar and then loads on the specimen installed between the incident and transmission bars. This gun design can produce very reliable and coaxial impact of the striker. Figure 3 shows a typical incident pulse produced by this new tension

T. Proulx (ed.), *Dynamic Behavior of Materials, Volume 1*, Conference Proceedings of the Society for Experimental Mechanics Series,
DOI 10.1007/978-1-4419-8228-5_67, © The Society for Experimental Mechanics, Inc. 2011

bar system without any specimen installed. The nearly perfect square pulse was produced, indicating the excellent loading and aligning conditions of the new Kolsky tension bar. Since the solid striker impacts on the flat end cap, which is similar to the loading in the compression bar, the pulse shaping technique, which has been demonstrated necessary for valid Kolsky bar experiments, can be easily applied to this tension bar system.

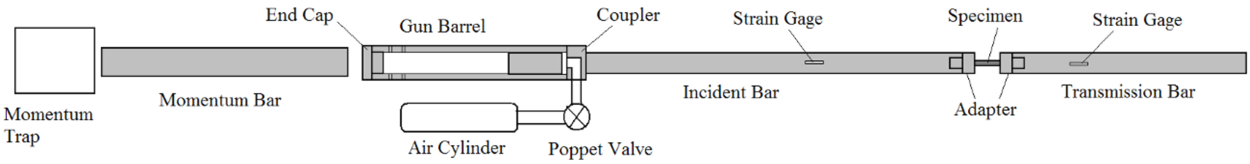

Fig. 2. A schematic of the Kolsky tension bar apparatus

Since the specimen is attached to the bars through additional adapters with threads, this leaves many free surfaces in the bar system. The stress wave propagation may be disturbed, consequently leading to erroneous measurements in specimen strain. Another issue that affects the specimen strain measurement is determination of specimen gage length. In this study, we investigated the stress wave propagation in the incident bar with artificial free surface close to the bar end. The effects of the free surfaces due to specimen installation are presented. In addition, we used different methods to determine the equivalent gage length of the specimen. Based on these investigations, dynamic tensile experiments were conducted on a 17-4 steel. Proper pulse shaping technique was applied to the tensile experiment to facilitate valid loading conditions. The dynamic tensile stress-strain curves for this material were obtained. Moreover, a high speed digital camera was employed to monitor the whole tensile deformation until necking to failure. This newly developed Kolsky tension bar has demonstrated satisfying capability to obtain reliable and precise stress-strain response of material under high rate tensile loading conditions.

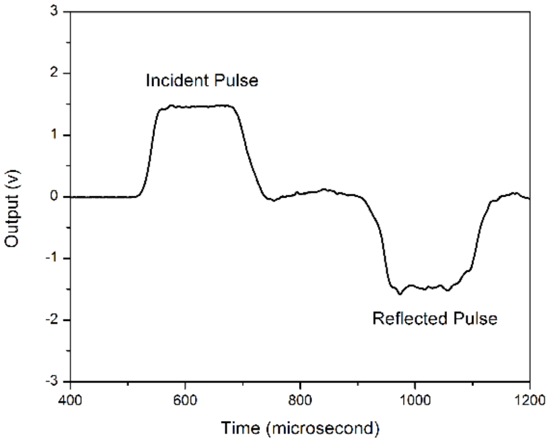

Fig. 3. Typical strain-gage signals on the incident bar

ACKNOWLEDGEMENTS

Sandia is a multiprogram laboratory operated by Sandia Corporation, a Lockheed Martin Company, for the United States Department of Energy under Contract DE-ACO4-94AL85000.

REFERENCES

1. Song, B., Connelly, K., Korellis, J., Lu, W.-Y., and Antoun, B. R., 2009, “Improved Kolsky-bar design fro mechanical characterization of materials at high strain rates,” Measurement Science and Technology, Vol. 20, 115701(1-8).

Proceedings of the SEM Annual Conference
June 7-10, 2010 Indianapolis, Indiana USA
©2010 Society for Experimental Mechanics Inc.

Evaluation of Welded Tensile Specimens in the Hopkinson Bar

Kathryn A. Dannemann, Sidney Chocron, Arthur E. Nicholls
Southwest Research Institute, San Antonio, TX

Abstract

The high strain rate behavior of a welded interface was evaluated using a split Hopkinson pressure bar (SHPB). The welds of interest are under-matched welds between identical aluminum alloys; the welds were processed using metal inert gas (MIG) welding. A direct tension bar setup was employed for the high strain rate testing. To accommodate both the weld and the heat affected zone in the gage length of the tensile specimen, it was necessary to use a longer specimen than is typically used for SHPB tensile testing. Limitations on specimen geometry and maintaining the weld bead intact were imposed to provide a specimen that was most representative of the material and application. Challenges associated with specimen design and testing in the pressure bar are discussed. Numerical simulations were employed to assist with specimen design and interpretation of the wave response. The experimental results obtained to date will be presented at the conference.

Background

Welded aluminum construction is utilized in high speed naval vessels for weight reduction. Understanding the behavior of these welded joints, especially at high strain rates, is critical for design of ship structures. Aluminum alloys used in marine applications (e.g., 5000 and 6000 series alloys) show significant strength decline when fusion welded [1,2]. The strength decline for under-matched welds in structures must be considered as plastic deformation will often localize at a weld during structural deformation [1,3]. Although the mechanical behavior of aluminum weld metals have been evaluated, testing has generally been conducted on coupons extracted from the weld (e.g., [4,5]). The effects of structural constraints on the weld are not usually considered in mechanical characterization studies of weldments. An objective of the present investigation is to evaluate the behavior of welded specimens (vs. weld metal only). The test specimens contained the weld bead and the heat affected zone (HAZ) on either side of the weld.

Materials

Two different welded aluminum alloys were evaluated: Al 5083-H116 and Al 6082-T651. Under-matched welds were processed between identical aluminum alloys using metal inert gas (MIG) welding and 5183 filler wire. For the Al 5083 alloy, 9.5-mm thick plates, machined down to 6.35 mm at the weld joint, were welded together. Thinner stock (approximately 3.8-mm) was used for the Al 6082 welds owing to differences in the material application. Both virgin and welded specimen blanks of each aluminum alloy were provided by the Naval Surface Warfare Center, Carderock Division, for testing. Although some high strain rate test data is available for the Al 5083 alloy [6], monolithic material from the same plate was tested to provide a baseline for comparison with the welded specimens. High strain rate test results for the less common Al 6082 alloy are not available in the literature.

Specimen Design

A standard tensile specimen could not be employed for the SHPB tension tests owing to the longer gage lengths (30-mm minimum) required to accommodate the weld, and HAZ material on either side of the weld, in the specimen gage section. An additional design requirement was the need to include the weld crown in the specimen to ensure that fracture occurs in a manner typical of a production weldment. Two different specimen designs were employed owing to the difference in thickness of the aluminum stock: 9.5-mm Al 5083 and 3.8-mm Al 6082. To allow direct comparison of the results, identical specimen designs were also used for tests on the corresponding virgin material.

The thickness of the Al 5083 plate was adequate for machining a threaded specimen for use in the direct tension bar setup. Several threaded cylindrical specimen designs were initially considered. The specimen design chosen

T. Proulx (ed.), *Dynamic Behavior of Materials, Volume 1*, Conference Proceedings of the Society for Experimental Mechanics Series,
DOI 10.1007/978-1-4419-8228-5_68, © The Society for Experimental Mechanics, Inc. 2011

is illustrated in Figure 1, and was selected based on numerical simulation results of the SHPB direct tension test, and initial testing trials. This flat specimen design was chosen to eliminate the need for machining near the weld. Numerical simulations were conducted to analyze the stress wave response for tensile specimens with different gage lengths.

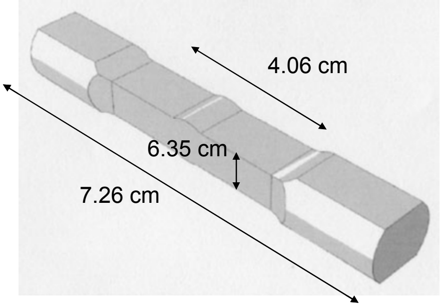

Figure 1. View of welded SHPB tensile specimen for Al 5083 prior to threading of the grip ends.

The simulation results confirmed that stress wave equilibrium is achieved in these tensile specimens with long gage lengths. This is illustrated in the force versus time plot in Figure 2. However, there was some concern whether specimen failure would occur on the first stress pulse due to the extra long specimen gage length (approximately 50-mm) needed to accommodate the weld. The numerical simulations were also used to estimate strain rates in the specimen as a function of the specimen length.

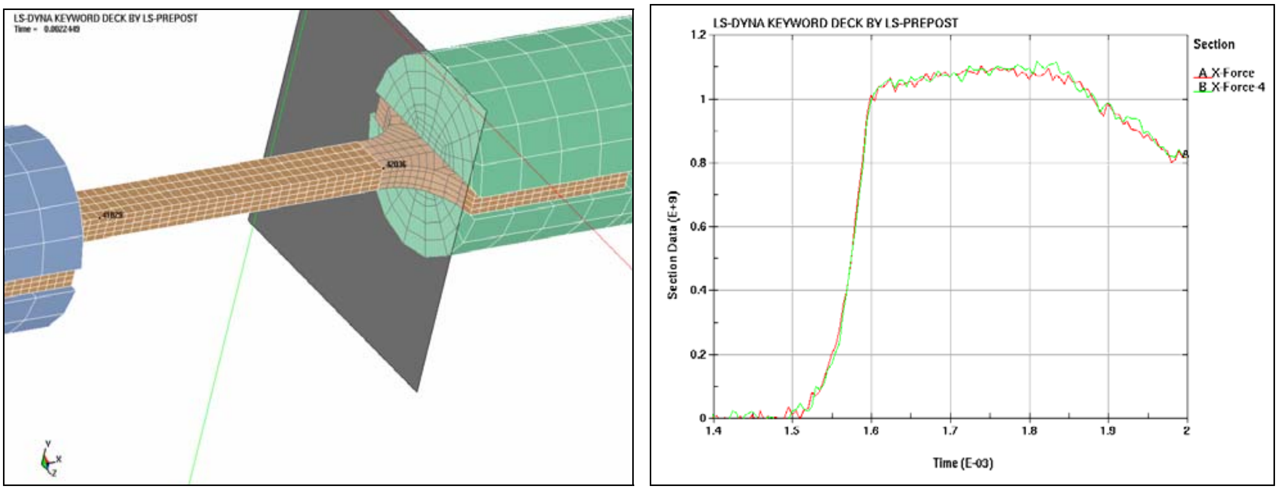

Figure 2. Numerical simulation of a SHPB direct tension test for a flat specimen design (with 50-mm long gage length). The results in the force vs. time plot show that stress equilibrium is maintained for this longer specimen. The two locations are those shown in the schematic on the left at opposite ends of the gage length.

For Al 6082, a flat specimen design was also used since the thickness of the available plate was only 2-3 mm. A specimen gage length exceeding 30-mm was also required for the Al-6082 specimens so that the weld and heat affected zone could be accommodated. A dog-bone geometry was utilized to ensure specimen failure in the gage section.

Experimental Procedure

High strain rate tension tests were conducted at SwRI using a Hopkinson bar system that allows direct tension loading of the specimen. The tensile load is applied directly to the specimen versus indirect tension systems, such as that developed by Lindholm [7]. Direct tension systems are preferred as specimen pre-damage can occur with indirect tension SHPB setups since the specimen is loaded in compression before pulling it in tension. The principle of the direct tension system is the same as for traditional SHPB systems. A projectile (30 or 60-cm long) travels down the barrel and impacts a reaction mass; the stress wave is reflected directly through the tensile specimen. The projectile, incident and transmitter bars are maraging steel; the bar diameter is 25-mm. Reduction of the data to obtain stress-strain curves is identical to the analysis for traditional SHPB systems.

The high strain rate (~10^2 s^{-1}) tests were conducted using the SwRI direct tension bar system; welded and virgin specimens were tested. The maximum strain rate achieved for the SHPB tests was approximately 800 s^{-1}, owing to the long specimen gage length. The Al 5083 specimens were threaded into the bars. A different grip was utilized for the Al 6082 specimens; the grip adapter was threaded into the bars. Low strain rate (~10^{-4} s^{-1}) tension tests were also conducted using an MTS servohydraulic machine. These tests were performed on specimens with similar geometries to allow a direct comparison with the higher strain rate test results.

To obtain an accurate strain measurement, failure of the tensile specimen must occur on the initial pulse. Estimates of the strain are possible; post-test measurements on the specimen can also provide strain estimates. Since first pass failure does not always occur, strain gages were applied to some specimens in the HAZ region on either side of the weld. This strain data was used to "calibrate" the numerical simulations used to aid in interpretation of the experiments.

Acknowledgments

The authors acknowledge the Office of Naval Research Aluminum Structural Reliability Program, under the direction of Dr. Paul Hess, for funding this work. Technical insights obtained from discussions with Dr. Ken Nahshon of the Naval Surface Warfare Center, Carderock Division, are also gratefully acknowledged. Appreciation is extended to Mr. Darryl Wagar (SwRI) for his assistance with testing and specimen design.

References

1. M.D. Collette, "The Impact of Fusion Welds on the Ultimate Strength of Aluminum Structures", 10th International Symposium on Practical Design of Ships and Other Floating Structures", Houston, TX, 2007.
2. L. Zheng, D. Petry, H. Rapp, T. Wierzbicki, "Characterization and Fracture of AA6061 Butt Weld", *Thin-Walled Structures*, Vol. 47, Issue 4, p. 431-441 (2009).
3. B.C. Simonsen, R. Tornqvist, "Experimental and Numerical Modeling of the Ductile Crack Propagation in Large-Scale Shell Structures", *Marine Structures*, Vol. 17, p. 1-27 (2004).
4. Y.J. Chao, Y. Wang and K.W. Miller, "Effect of Friction Stir Welding on Dynamic Properties of AA2024-T3 and AA7075-T7351", *Welding Research Supplement,* 196s-200s, (2001).
5. R.W. Fonda, P.S. Pao, H.N. Jones, C.R. Feng, B.J. Connolly, A.J. Davenport, "Microstructure, Mechanical Properties and Corrosion of Friction Stir Welded Al 5456", *Materials Science and Engineering A519*, p. 1-8, (2009).
6. A.H. Clausen, T. Borvik, O.S. Hopperstad, A. Benallal, "Flow and Fracture Characteristics of Aluminum Alloy AA5083-H116 as Function of Strain Rate, Temperature and Triaxiality", *Materials Science and Engineering A364*, p. 260-272, (2004).
7. U.S. Lindholm and L.M. Yeakley, "High Strain Rate Testing: Tension and Compression", *Experimental Mechanics*, Vol. 8, p.1-9, (1968).

Proceedings of the SEM Annual Conference
June 7-10, 2010 Indianapolis, Indiana USA
©2010 Society for Experimental Mechanics Inc.

Effect of Aspect Ratio of Cylindrical Pulse shapers on Force Equilibrium in Hopkinson Pressure Bar Experiments

Sandeep Abotula[1] and Vijaya Chalivendra[2*]
[1]Dynamics Photo Mechanics Laboratory, University of Rhode Island, RI 02881
[2]Department of Mechanical Engineering, University of Massachusetts Dartmouth, MA 02747
[*]Corresponding author: vchalivendra@umassd.edu, 508-910-6572

ABSTRACT

A detailed experimental study was conducted in designing cylindrical pulse shapers for testing various types of materials using split Hopkinson pressure bar (SHPB) test setup. Copper-182 alloy and annealed C11000 was used as pulse shaper materials and six different types of pulse shapers for each case with their thickness to diameter (t/d) ratios ranging from 0.23 to 0.51 were used. Six types of materials namely Aluminum 6061-T6, Acrylic (Plexiglas), Ultra High Temperature Glass-Mica Ceramic (Macor), Ultra High Molecular Weight Polyethylene (UHMWPE), polyurethane and polyurethane syntactic foam were considered for testing. Inertial effects of pulse shapers play an important role in determining stress equilibrium in the specimen. The effect of t/d ratio of the pulse shaper on the force equilibrium condition at the specimen ends for above materials at a strainrate regime of 1000-2000/s was discussed and better pulse shapers for above materials were recommended.

INTRODUCTION

Pulse shaping has been used as a prominent technique for generating force equilibrium condition between incident and transmission bars in split Hopkinson pressure bar (SHPB) experimentation for the last one decade [1-3]. Force equilibrium is difficult to achieve when metallic SHPB setup is used to test both brittle and soft materials. The pulse shaping becomes very useful technique to ramp the incident pulse and generate force equilibrium conditions while testing above materials. Duffy *et al*. [4] were probably the first authors to propose the technique of pulse shaping. They used the pulse shaper in the form of a concentric tube to smooth pulses generated by explosive loading for the torsional Hopkinson bar. Franz *et al*. [5] and Follansbee [6] discussed various techniques for shaping the pulse and minimizing the dispersion of waves in the bars. Pulse shapers they used were slightly larger than the bars with 0.1-2.0 mm thick and the materials used for pulse shapers were paper, aluminum, brass or stainless steel. After these initial studies, the pulse shaping technique has been further investigated by several researchers recently. Nemat-Nasser *et al*. [7] recommended OFHC copper as pulse shaper to achieve ramp pulses for ceramics using SHPB. Chen *et al.* [8] used a polymer disk with elastomers to lengthen the incident compressive pulses. In addition to polymer disk as a pulse shaper, they also used a thin disk of annealed or hard C11000 copper to achieve ramp in the incident pulses for brittle materials that have failure strain less than 1.0%. Also Chen *et al.* [9] designed a combination of copper and mild-steel as a pulse shaper by experimental trials. The pulse shaper consists of two disks where steel end of the pulse shaper is attached to the incident bar and the striker impacts the copper end of the pulse shaper.

It can be noticed from above studies that copper has been successfully used as a pulse shaper in shaping incident pulse and generating force equilibrium conditions. It was identified from above studies that there was no detailed study conducted to understand the effect of pulse shaper aspect ratio (thickness/diameter) on the shaping of the incident pulse and initiation time of force equilibrium conditions. Hence this paper is mainly focused on studying the effect of the different aspect ratios of the pulse shapers on force equilibrium conditions when tests are conducted for different types of materials. Six types of materials namely Aluminum 6061-T6, Acrylic (Plexiglas), Ultra High Temperature Glass-Mica Ceramic (Macor), Ultra High Molecular Weight Polyethylene (UHMWPE), polyurethane and polyurethane syntactic foam are considered for testing. Both SHPB and modified SHPB with hollow transmission bar made out of Aluminum 7075-T651 are used in conducting this study.

T. Proulx (ed.), *Dynamic Behavior of Materials, Volume 1*, Conference Proceedings of the Society for Experimental Mechanics Series, DOI 10.1007/978-1-4419-8228-5_69, © The Society for Experimental Mechanics, Inc. 2011

EXPERIMENTAL DETAILS

Table 1. Different types of pulse shapers

Pulse shaper type	Thickness (mm)	Diameter (mm)	Pulse shaper	t/d ratio
Type-1	No pulse shaper	--		--
Type-2	1.13	4.76	C182	0.237
Type-3	1.6	6.35	C182	0.251
Type-4	1.6	4.76	C182	0.336
Type-5	1.10	3.175	C 182	0.346
Type-6	3.00	6.35	C182	0.472
Type-7	1.6	3.175	C182	0.503
Type-8	1.13	4.76	C11000*	0.237
Type-9	1.6	6.35	C11000*	0.251
Type-10	1.6	4.76	C11000*	0.336
Type-11	1.10	3.175	C11000*	0.346
Type-12	3.00	6.35	C11000*	0.472
Type-13	1.6	3.175	C11000*	0.503

C11000*: Annealed C11000 alloy

Design of Pulse Shaper

Frew *et al*. [10] investigated analytically and specified a range of thickness to diameter (t/d) ratio of 0.16 to 0.5 for pulse shapers. Based on this specified range, in this study, six different types aspect ratios for both pulse shaper materials are designed as shown in Table-1. As given in Table-1, no pulse shaper is named as Type-1 and used as a reference. Type-2 to Type-13 has different t/d ratios by changing either thickness or diameter. The range of t/d ratios considered in this study is 0.237 to 0.503. High strength Copper (Alloy 182) and annealed C11000 was used as a material for pulse shapers.

Tested Materials

Six different materials namely Aluminum 6061-T6; Acrylic, also called Plexiglas; High-temperature Glass-filled Ceramic, also called Macor; Ultra-high molecular weight polyethylene (UHMWPE); Polyurethane; Polyurethane syntactic foam were considered for studying the effect of t/d ratio of the pulse shaper on the force equilibrium conditions. The above chosen materials fall in a wide spectrum of materials such as metal, brittle polymer, ceramic, ductile polymer, elastomer and foam. Identification of proper aspect ratio of pulse shapers for these materials in this study will help the researchers to choose appropriate type of pulse shaper while conducting experiments of similar type of materials. Polyurethane (supplied by Hapflex Inc., MA, USA) is thermoset polymer, which consists of two parts, part-A: resin and part-B: Hardener. Polyurethane syntactic foam is made using same above polyurethane with 30% weight fraction of gas bubbles (supplied by 3M, MA, USA). The pulse shaper for one type of material would not be same for all other types of materials due to fact that above materials do not have same impedance.

Experimental Procedure

In order to perform low-strain rate testing on all proposed materials, both traditional and modified SHPB setups are employed. Traditional SHPB consists of a striker, an incident bar and a transmission bar and they are all made of aluminum 7075-T651 as shown in Figure 1. The striker bar used in these experiments has a diameter of 12.7mm and length 203.2mm. Incident and transmission bars have the diameter of 12.7 mm and length up to 1220mm. A pulse shaper of different dimensions listed in the above section is placed using KY jelly at the impact end of the incident bar as shown in Figure 1. The specimen is sandwiched between incident bar and transmission bar. Specimen has the thickness of 3mm and diameter of 6.35mm. Molybdenum disulfide lubricant is applied between specimen and the contacting surfaces of bars to minimize the friction.

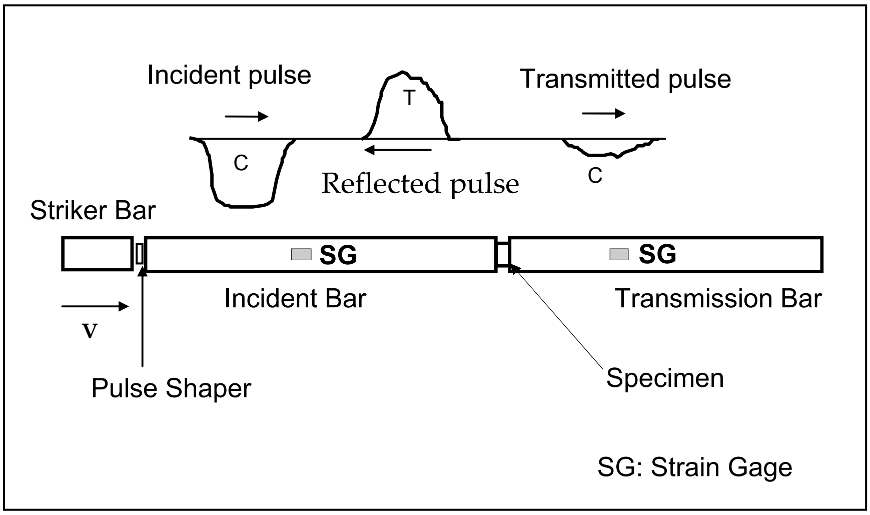

Figure 1. Experimental setup of SPHB

For characterizing low-impedance materials such as Plexiglas, Macor, UHMWPE, Polyurethane and Polyurethane foam, a modified SHPB is used. This setup has hollow transmission bar, which provides a decent compressive pulse while testing the above mentioned low impedance materials. An aluminum end cap is press fitted into the hollow tube to support the specimen at the specimen transmission bar interface. Same Aluminum 7075-T651 alloy was used for hollow transmission bar. The transmission bar has the outside diameter of 12.7mm and inside diameter of 9.5mm with incident bar (A_i) to transmission bar (A_t) area ratio of $\frac{A_i}{A_t} = 2.28$ [8].

When striker bar impacts the incident bar, an elastic compressive stress pulse, referred as incident pulse is generated. The generated pulse deforms the pulse shaper at the impact end and creates a ramp in the incident pulse which further propagates along the incident bar. When the incident pulse reaches the specimen, some part of it reflects back into the incident bar (reflected pulse) in the form of tensile pulse due to the impedance mismatch at the bar-specimen interface and the remaining part is transmitted (transmission pulse) to the transmission bar. Axial strain gauges mounted on the surfaces of the incident and transmission bar provide time-resolved measures of the elastic strain pulses in the bars.

Experiments were carried out at an strainrate regime of 1000-2000/s for all six different types of materials. Different striker lengths and pressures were used for different materials to obtain the above said strainrate.

Force equilibrium within the specimen during the wave loading is attained when forces on each face of the specimen are equal. From Nicholas [2] and Gray [11], the expressions for the forces at the specimen incident bar interface and at the specimen transmission bar interface are given equations (1) and (2) respectively.

$$F_i = A_b E_b (\varepsilon_i + \varepsilon_r) \tag{1}$$

$$F_t = A_b E_b \, \varepsilon_t \tag{2}$$

Where A_b is cross-sectional area of incident bar; E_b is Young's modulus of the bar material; ε_i, ε_r, ε_t are time-resolved strain values of the incident, reflected and transmitted pulses respectively.

When these two forces in equations (1) & (2) are equal, then the specimen is said to be in dynamic force equilibrium. The ratio of these two forces as given in equation (3) provides a measure for force equilibrium. For ideal equilibrium conditions, the ratio should be 1.0.

$$F_i \big/ F_t = (\varepsilon_i + \varepsilon_r) \big/ \varepsilon_t \qquad (3)$$

In the following experimental results section, the effect of aspect ratio of pulse shaper is discussed by plotting the force ratio given in equation (3) as function of specimen loading time. The initiation time for force equilibrium upon loading the specimen and the extent of force equilibrium during whole loading duration is discussed.

EXPERIMENTAL RESULTS

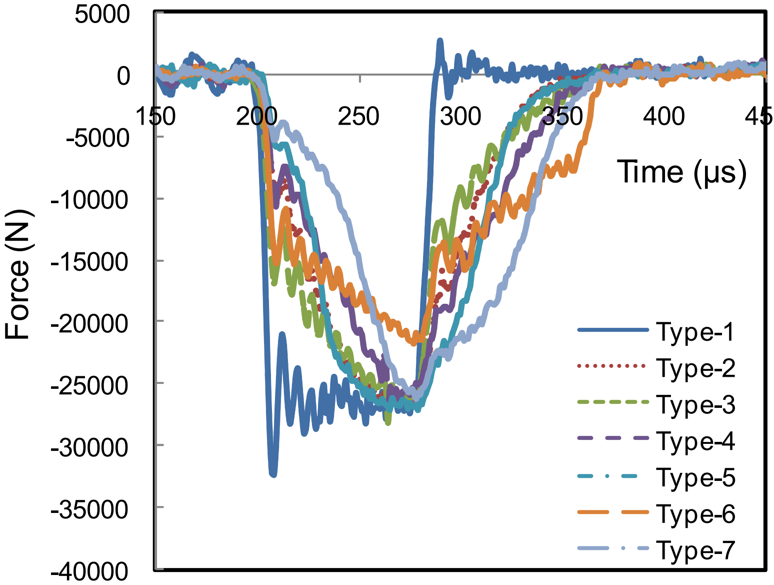

Figure 2. Typical incident pulses for different types of pulse shapers

As discussed in the above section, the pulse shaper should generate a ramped incident compressive pulse for gradual loading of the test specimen which is sandwiched between two bars. Figure 2 shows the typical incident pulses obtained from the experiments for different aspect ratios of C182 alloy pulse shaper. It can be noticed that for Type-1 which is the case for no pulse shaper, the incident pulse has no ramp and the maximum force is attained in less than 10μs, so the specimen does not have much time to reach equilibrium. For all other types of pulse shapers, it takes approximately 50μs to reach the maximum force, and thus allowing sufficient time for the specimen to be in equilibrium. It can be noticed that the length of the pulse increases with pulse shapers against the no pulse shaper (Type-1). Similar case was observed for annealed C11000 alloy pulse shaper. From Figure 2, it can be seen that, as the diameter of the pulse shaper increases, it provides very good ramp in the incident pulse. Also as the thickness of the pulse shaper increases, the rising time of the incident pulse increases. So from the designed pulse shapers, Type-5 (thickness=1.10mm, diameter = 3.175mm and t/d = 0.346) pulse shaper provided very good ramp and long rising time in the incident pulse. However, the pulse shaper with this aspect ratio may not provide good equilibrium for all the materials since the time required in reaching equilibrium is different for different materials and also it depends on the impedance mismatch between the specimen-bar interfaces. The ratio of mechanical impedance of the specimen to bars (β) is given by,

$$\beta = \frac{A\rho c}{A_0 \rho_0 c_0} \qquad (4)$$

Where A, ρ and c are the area, density and wave speed of the specimen respectively and A_0, ρ_0 and c_0 represents area, density and wave speed of the pressure bars. ρc defines mechanical impedance. As the impedance mismatch between the specimen-bar interfaces increases, the value of β decreases. The number of reverberations (*n*) required for the specimen to attain equilibrium is given by,

$$n = \frac{c * t}{L} \tag{5}$$

Where *t* represents the time required for the specimen to reach equilibrium in μs and *L* represents the length of the specimen [12]. To attain equilibrium, the loading pulse has to travel *n* times from one end to other end of the specimen.

Table 2. Ratio of impedances of different material to pressure bars

Material	β
Al 6061-T6	$\approx \frac{1}{4}$
Plexiglas	$\approx \frac{1}{30}$
Macor	$\approx \frac{1}{6} - \frac{1}{4}$
UHMWPE	$\approx \frac{1}{100}$
Polyurethane Elastomer	$\approx \frac{1}{1000}$
Polyurethane Foam	$< \frac{1}{1000}$

Table 2. shows the ratio of mechanical impedance of specimen to bar for different materials tested in this paper. From the table, it can be observed that the value of β decreases for soft materials. So it can be assumed that attaining equilibrium will be difficult for the softer (low impedance) materials.

The dimensions of the pulse shapers are also restricted. The diameter of the pulse shaper after impact cannot exceed than the bar diameter. Also if the thickness of the pulse shaper is too large, it absorbs maximum amount of energy from the striker and transmits very less energy to the incident bar. The rise time of the pulse also increases with thicker pulse shapers and this may lead to the overlapping of the pulses when tested at low strain rates. So it is not advisable to use thicker pulse shapers.

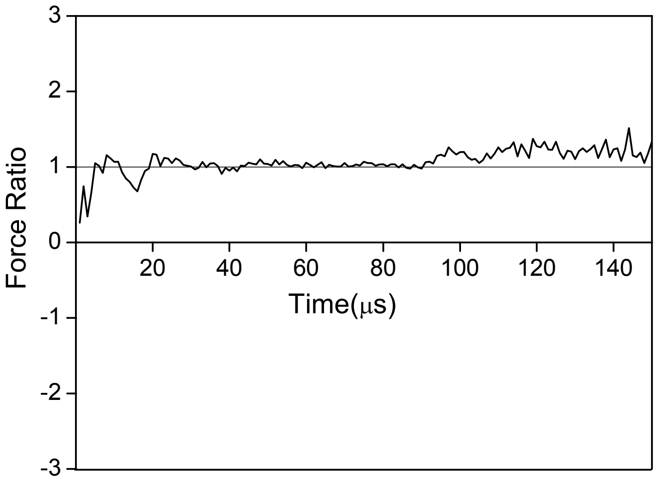

Figure 3. Force equilibrium condition of Al 6061-T6 using Type 2 pulse shaper

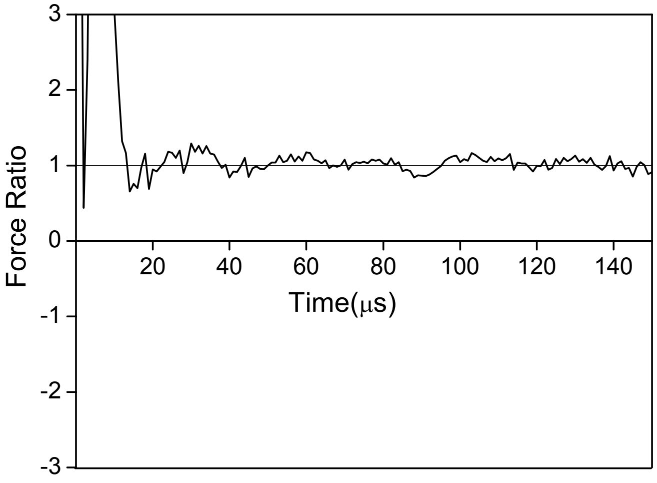

Figure 4. Force equilibrium condition of Plexiglas using Type 5 pulse shaper

For all the materials tested in this study, due to brevity of space only pulse shapers that generated the best force equilibrium condition were reported in this paper. The solid line in all the figures represents the ideal force ratio of 1.0. All the pulse shapers tested provided better equilibrium than the case of no pulse shaper but only certain aspect ratio of pulse shaper provided equilibrium for the entire loading duration. Figure 3 shows the force ratio of Al 6061-T6 using Type-2 (thickness=1.13mm, diameter=4.76mm and t/d=0.237) pulse shaper. It can be noticed from the figure that the selected pulse shaper provides the force ratio that is very close to 1.0 for most of the specimen loading time and their force equilibrium initiates at around 5μs. As Aluminum 6061-T6 is tested with Al 7075-T4 bars, the impedance mismatch between the specimen and pressure bars is very less and it helped in attaining very good equilibrium even at early stage of loading.

Figure 4 shows the force ratio for acrylic (Plexiglas) material using Type-5 (thickness=1.10mm, diameter=3.175mm and t/d=0.346) pulse shaper. Type-5 pulse shaper attains the force equilibrium at around 17μs upon starting of the loading of the specimen. Due to the significant difference in the impedance mismatch of Plexiglas (refer Table 2) with respect to pressure bars, it became difficult to get equilibrium at early stages. After the equilibrium is achieved, It maintains for rest of the loading duration.

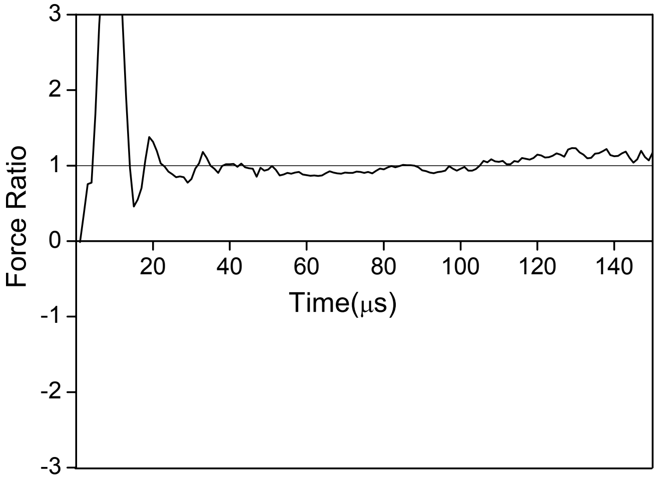

Figure 5. Force equilibrium condition of Macor using Type 5 pulse shaper

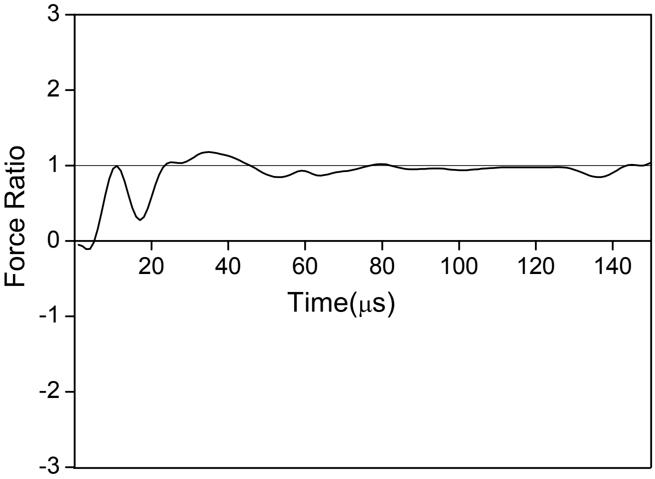

Figure 6. Force equilibrium condition of UHMWPE using Type 11 pulse shaper

Force ratio curves for ultra-high temperature glass-mica ceramic (Macor) for the pulse shaper Type-5 is shown in Figure 5. Macor is a brittle ceramic and having force equilibrium condition before the specimen breaks under dynamic loading conditions is essential for meaningful dynamic compressive strength value. Type-5 pulse shaper attains the force equilibrium at around 14μs. As in the case of Plexiglas, due to significant difference in the impedance mismatch, no equilibrium was achieved before 14μs. Macor reached equilibrium little early than Plexiglass since impedance mismatch of Macor with respect to output bars is less when compared to Plexiglas. It also maintains the equilibrium for the rest of the loading duration.

Figure 6 shows the force ratio curve for ultra high molecular weight polyurethane (UHMWPE) specimen using Type-11 (thickness = 1.10mm, diameter = 3.175mm and t/d = 0.346) pulse shaper. UHMWPE is a semi-crystalline, ductile polymer. It has high impedance mismatch with respect to Aluminum 7075-T651. So it took much time to reach equilibrium (at around 24μs) than the other materials and maintained decent equilibrium till the rest of the loading duration.

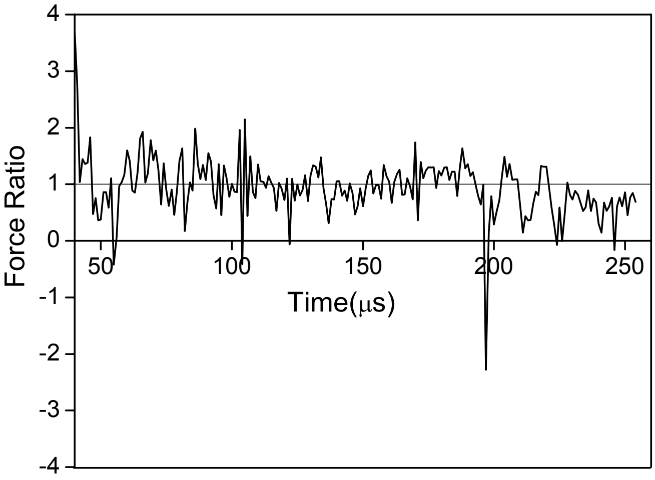

Figure 7. Force equilibrium condition of Polyurethane using Type 10 pulse shaper

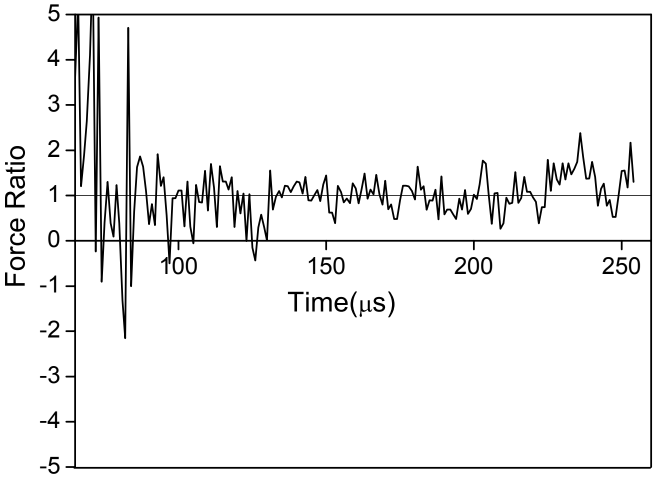

Figure 8. Force equilibrium condition of Polyurethane syntactic foam using Type 9 pulse shaper

Force ratio curve for polyurethane elastomer using Type-10 (thickness = 1.6mm, diameter = 4.76mm and t/d = 0.336) pulse shaper is shown in Figure 7. Since the impedance of polyurethane is very low when compared to Aluminum 7075-T651, it is expected that attaining force equilibrium condition is very difficult. Due to the low mechanical impedance, nearly all the compressive wave is reflected back in the form of tensile to the incident bar and very less is transmitted to the transmission bar. The oscillations in the figure are due to very low magnitude of transmission pulse. It can be seen from the figure that, equilibrium was achieved only after 50μs indicating that experimental result was valid only after this time [13]. This proves that attaining equilibrium at early stages of loading is very difficult for soft materials. So due to several oscillations of force ratio curve shown in Figure 7, exact initiation time of force equilibrium condition for polyurethane specimens is not reported.

Figure 8 shows the force ratio curve for polyurethane syntactic foam specimens using Type-9 (thickness = 1.6mm, diameter = 6.35mm and t/d = 0.251) pulse shaper. Even for this material as in the case of polyurethane elastomer, equilibrium was not achieved until 70μs [13]. As this material is much softer and has very high mechanical impedance, it took more time than polyurethane elastomer to reach equilibrium. Due to several oscillations of force ratio curve for Type-9 pulse shaper as shown in Figure 9, again the exact initiation of force equilibrium condition for polyurethane syntactic foam specimen is not reported. Better equilibrium can be achieved by reducing the thickness of the specimen but they were some limitations on thickness restrictions of the specimen.

Table 3. Number of reverberations of different material to reach equilibrium

Material	***Number of reverberations***
Al 6061-T6	8
Plexiglas	9
Macor	21
UHMWPE	5
Polyurethane Elastomer	3
Polyurethane Foam	3

Table 3. shows the number of reverberations for different materials to reach equilibrium. For AL 6061-T6, due to less impedance mismatch, it took 8 reverberations to reach equilibrium. From the table, it can be noticed that Macor takes 21 reverberations (higher than other materials) even though it took less time to reach equilibrium than other materials because the wave speed of Macor is much greater than the other materials. Since the value of n increases with the wave speed and L being constant for all materials, materials with higher wave speed will have higher value of n. So it can be concluded here that due to high wave speed, some materials may have larger value of n but still it takes less time to reach equilibrium. On the contrast, if the wave speed of the material is less, then it takes much time for less number of reverberations.

CONCLUSIONS

In this paper, a detailed experimental study was conducted to investigate the effect of thickness to diameter ratio of the copper-182 alloy and annealed C11000 pulse shaper on force equilibrium conditions for six different types of materials. Following are the major outcomes of this study:

- For Aluminum 6061-T6, Type-2 pulse shaper provided force equilibrium initiation time at around 5μs and maintained equilibrium conditions for entire loading duration.
- For acrylic (Plexiglass) specimens, Type-5 initiated the equilibrium conditions at around 17μs and conditions were maintained for entire loading duration.
- For Macor specimens, Type-5 pulse shaper attains the force equilibrium at around 14μs and also maintains the equilibrium for the rest of the loading duration.
- For UHMWPE, Type-11 pulse shaper provided force equilibrium conditions. The initiation time of the equilibrium is at around 24µs and maintained till 150µs.
- For Polyurethane and syntactic foam materials, Type-10 and Type-9 respectively provided decent equilibrium conditions with several oscillations around desired force ratio of 1.0. The equilibrium was only achieved after 60µs proving that it is very difficult to get equilibrium for soft materials at early stages of loading.

REFERENCES

[1] Kolsky, H. An Investigation of the Mechanical Properties of Materials at very High Strain Rates of Loading. *Proceeding of Physics Society,* **62**, 676-700, 1949.

[2] Nicholas, T.: Material Behavior at High Strain Rates. *Impact Dynamics, Chap. 8, John Wiley & Sons, New York,* 1982.

[3] Davies, E. D. H. and Hunter, S. C.: The Dynamic Compression Testing of Solids by the method of the Split Hopkinson Pressure Bar. *Journal of the Mechanics and Physics of Solids,* **11**, 155-179, 1963.

[4] Duffy, J., Campbell, J. D., and Hawley, R. H.: On the Use of a Torsional Split Hopkinson Bar to Study Rate Effects in 1100-0 Aluminum. *ASME Journal of Applied Mechanics,* **37**, 83-91, 1971.

[5] Franz, C. E., Follansbee, P. S., and Wright, W. J.: New Experimental Techniques with the Split Hopkinson Pressure Bar. *8th international conference*, *ASME,* 1984.

[6] Follansbee, P. S.: The Hopkinson Bar Mechanical Testing, *metals handbook, 9th ed., ASM*, Metals Park, Ohio. **8**, 198-217, 1985.

[7] Nemat-Nasser, S., Issacs, J. B., and Starret, J. E.: Hopkinson Techniques for Dynamic Recovery Experiments. *Proceeding of Royal society of London, A*. **435**, 371-391, 1991.

[8] Chen, W., Zhang, B. and Forrestal, M. J.: A Split Hopkinson Bar Technique for Low-Impedance Materials. *Experimental Mechanics,* **39**, 81-85, 1999.

[9] Chen, W., Song, B., Frew, D. J., and Forrestal, M. J.: Dynamic Small Strain Measurements of a metal Specimen with a Split Hopkinson Pressure Bar. *Experimental Mechanics,* **43**, 20-23, 2003.

[10] Frew, D. J., Forrestal, M. J., and Chen, W.: Pulse Shaping Techniques for Testing Brittle Materials with a Split Hopkinson Pressure Bar. *Experimental Mechanics,* **42**, 93-106, 2002.

[11] Gray, G. T.: Classical Split-Hopkinson Pressure Bar Technique. ASM handbook, **8**, Mechanical Testing and Evaluation, *ASM International*, Materials Park, OH, 44073-0002, 2000.

[12] Yang, L.M., Shim, V. P. W.: An Analysis of Stress Uniformity in Split Hopkinson Pressure Bar Test Specimens. *International Journal of Impact Engineering*, **31**, 129-150, 2005.

[13] Song, B., Chen, W and Jiang, X., Split Hopkinson Pressure Bar Experiments on Polymeric Foams. *International of Journal Vehicle Design*, **37**, 185-198, 2005.

Proceedings of the SEM Annual Conference
June 7-10, 2010 Indianapolis, Indiana USA
©2010 Society for Experimental Mechanics Inc.

Interferometric Measurement Techniques for Small Diameter Kolsky Bars

Daniel T. Casem
US Army Research Laboratory
RDRL-WMP-B
Aberdeen Proving Ground, MD 21005-5069
dcasem@arl.army.mil

Stephen E. Grunschel
Post-Doctoral Fellow
US Army Research Laboratory
RDRL-WMP-B
Aberdeen Proving Ground, MD 21005-5069

Brian E. Schuster
US Army Research Laboratory
RDRL-WML-H
Aberdeen Proving Ground, MD 21005-5069

ABSTRACT

The use of optical measuring techniques for small diameter Kolsky bar experiments is discussed. The goal is to develop methods that can eliminate the need for more commonly used strain gages which become impractical as bar sizes decrease. The basic approach taken here is to adapt interferometer-based methods, used commonly in pressure-shear plate impact experiments, to high-rate Kolsky bar experiments. A Normal Displacement Interferometer (NDI) is used to measure the motion of the free end of the transmitter bar and provide a measurement of the transmitted pulse. Similarly, the incident and reflected pulses are measured with a Transverse Displacement Interferometer (TDI) utilizing a diffraction grating at the midpoint of the incident bar. Both techniques are applied to 1.59 mm diameter steel pressure bars. In the case of the transmitter bar, measurements are also made with the traditional strain gage instrumentation and comparisons between the two are made. The incident bar measurements made via TDI are validated with a simple bar impact against a single incident bar, i.e., without a specimen or transmitter bar. The possible application of these methods to smaller systems is also discussed.

INTRODUCTION

The Split Hopkinson Pressure Bar (SHPB), or Kolsky Bar [1, 2], is a device commonly used for determining the stress-strain response of materials in the strain-rate range of 10^3-10^4/s. The most common arrangement, used for compression testing, is shown in Fig. 1. A specimen is placed between two long, thin, linear elastic bars, known as the *incident bar* and the *transmitter bar*. A projectile impacts the incident bar, which generates a stress wave (the *incident pulse*) that travels down the bar where it is measured by a set of strain gages at the mid-point. It then continues to the end of the bar where it begins to compress the specimen. The impedance mismatch at the specimen results in the creation of a *reflected pulse* which travels back up the incident bar where it is measured by the same set of strain gages used to measure the incident pulse. As the specimen is compressed, a third pulse, called the *transmitted pulse,* propagates into the transmitter bar where it is measured by a set of strain gages at that bar's midpoint. It is assumed that the incident and reflected pulses are short enough that they do

T. Proulx (ed.), *Dynamic Behavior of Materials, Volume 1*, Conference Proceedings of the Society for Experimental Mechanics Series,
DOI 10.1007/978-1-4419-8228-5_70, © The Society for Experimental Mechanics, Inc. 2011

not overlap at the measurement location. Similarly, the transmitted pulse must be short enough that it does not interfere with its own reflection from the free end of the transmitter bar.

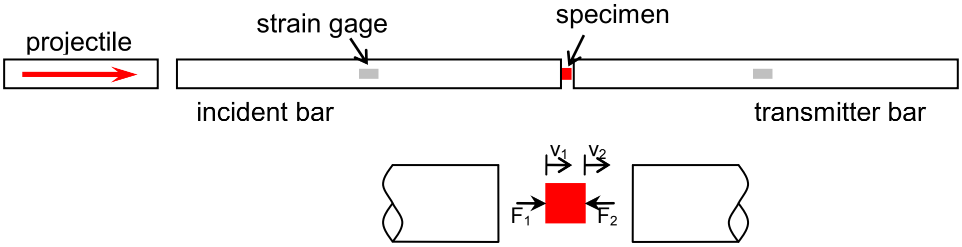

Figure 1 – A basic compressive Kolsky bar.

The force and motion at the interfaces between the bars and specimen can be found from the measured strain signals using the following equations.

$$F_1 = (\varepsilon_i + \varepsilon_r)EA_b \tag{1}$$

$$F_2 = \varepsilon_t EA_b \tag{2}$$

$$v_1 = (\varepsilon_i - \varepsilon_r)c_0 \tag{3}$$

$$v_2 = \varepsilon_t c_0 \tag{4}$$

Here A_b and c_0 are the cross-sectional area and wave speed of the bars. ε_i, ε_r, and ε_t, are the compressive strains due to the incident, reflected, and transmitted pulses at the time at which they act at the specimen. This requires translating the signals in time by the transit times between the specimen and gages, or possibly a frequency-based dispersion correction [3-5]. As long as the specimen remains in contact with the bars, these forces and velocities also act at the ends of specimen. If the specimen is in equilibrium (i.e., the effect of wave propagation in the specimen is negligible), we have the condition that $F_1 = F_2$ and from eqns. (1) and (2)

$$\varepsilon_i + \varepsilon_r = \varepsilon_t . \tag{5}$$

In the case of straightforward stress-strain testing, the engineering stress and strain-rate in the specimen can be determined:

$$\sigma_S = \frac{F_1}{A_0} \tag{6}$$

$$\dot{\varepsilon}_S = \frac{v_1 - v_2}{L_0} \tag{7}$$

Specimen strain is determined by integrating the strain-rate with time. Further simplifications are available but these are the basic equations needed for the analysis. Also note that under the assumption of equilibrium, only two of the three pulse are required to determine the response of the specimen. In practice, ε_r and ε_t are preferred. However, if all three pulses are measured independently, specimen equilibrium ($F_1 = F_2$) can be confirmed.

Two factors limit the maximum strain-rate that can be achieved during a given test. The first is related to the time required for a specimen to reach quasi-static equilibrium. As a general rule, smaller specimens equilibrate faster than larger specimens [6]. The second has to do with the dispersion characteristics of the bars. In the analysis of pressure bar signals, it is assumed that the wave propagation within the bars is one-dimensional. For pulses with wavelengths that are short in comparison to the diameter of the bar, this assumption is increasingly violated. This leads to an effective rise-time that limits the temporal resolution of measurements made by the bars [7]. Since high rate tests result in high frequency, short duration signals, this ultimately limits the maximum strain-rates that can be performed with a given bar diameter while maintaining a sufficiently one-dimensional state of stress in the bars.

It is clear that by reducing bar size, and correspondingly the specimen size, higher rate tests can be achieved. This has been recognized by numerous researchers who have built small systems based on this idea, both as Kolsky bar systems and also in Direct Impact (DI) configurations [8-14]. One difficulty encountered with this approach is the use of strain gages. As bar sizes decrease, their use becomes less practical for a variety of reasons, e.g., gage installation and alignment, decreased sensitivity associated with lower bridge excitations, and electrical connections becoming more cumbersome. For this reason we are adapting interferometer-based techniques used commonly in pressure-shear plate impact experiments [15] to the Kolsky bar method. These methods provide robust, non-contact measurements of the bar displacement that can be used to replace the strain-gage measurements under conditions encountered with miniaturized systems. Two applications of these techniques to 1.59 mm diameter steel pressure bars[1] are described in the following sections. In the first case, a Normal Displacement Interferometer (NDI) is used to measure the motion of the free end of the transmitter bar and provide a measurement of the transmitted pulse. In a second application, the incident and reflected pulses are measured with a Transverse Displacement Interferometer (TDI) utilizing a diffraction grating at the midpoint of the incident bar.

TRANSMITTER BAR – NDI MEASUREMENTS OF THE TRANSMITTED PULSE

In most cases with a Kolsky Bar, the end of the transmitter bar can be left free for the duration of the test. Therefore the motion at that free-surface can be measured with an NDI. The optical setup is shown in Fig. 2. The end of the transmitter bar is polished to a reflective finish and serves as the moving mirror in the interferometer. The interference of a laser beam reflected from the transmitter bar combined with a beam reflected from stationary mirrors produces an intensity variation that can be monitored with photodetectors. An example NDI signal from a Kolsky bar test is shown in Fig. 3. A displacement equal to half of the laser wavelength produces a 2π phase variation in the signal, or one fringe. The distance, d, that the free surface of the transmitter bar travels is therefore given by

$$d = \frac{\lambda}{2} n \,, \tag{8}$$

where λ is the wavelength of the laser and n is the number of fringes observed. The velocity of the free-end of the bar can be determined by differentiating with respect to time. The particle velocity due to the transmitted pulse is half the measured free-surface velocity,

$$v_t = \frac{1}{2} \dot{d} \,. \tag{9}$$

This velocity is related to the strain in the transmitted pulse by

$$\varepsilon_t = v_t / c_0 \,. \tag{10}$$

Thus the measurement made with the NDI can be used to replace the strain gage measurement of the transmitted pulse.

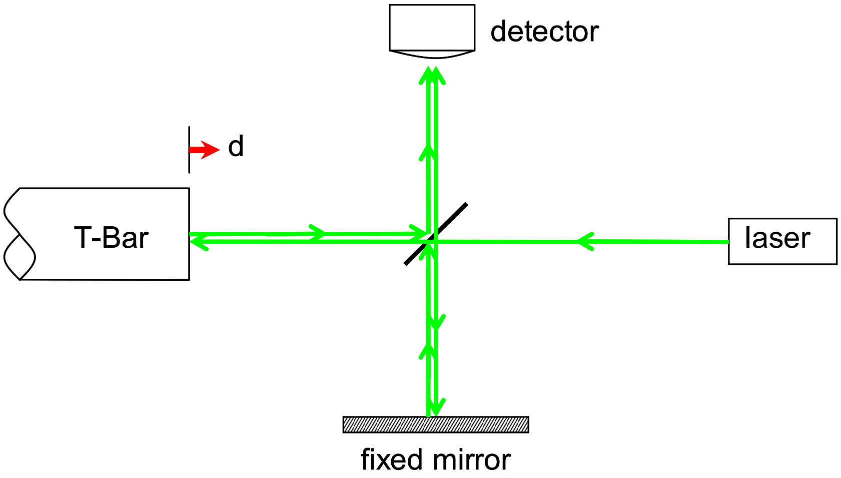

Figure 2 - An NDI used to measure the displacement of the end of the transmitter bar.

---

[1] Specific details of the Kolsky bar used during this research can be found in [8].

In a preliminary test on a copper alloy, the transmitted pulse was measured using the standard strain gage arrangement and an NDI simultaneously. A 5 mW HeNe laser with a 632 nm wavelength was used as a light source and the detector was an Electro-Optics Technology, Inc. model ET-2020 with a 200 MHz bandwidth. Figure 4a shows the strain signals measured using the strain gages during the test. The corresponding stress-strain curve is plotted with the strain-rate in Fig. 4b. The measurement of the transmitted pulse with both the NDI and the transmitter bar strain gage is shown in Fig. 5. Good agreement is obtained.

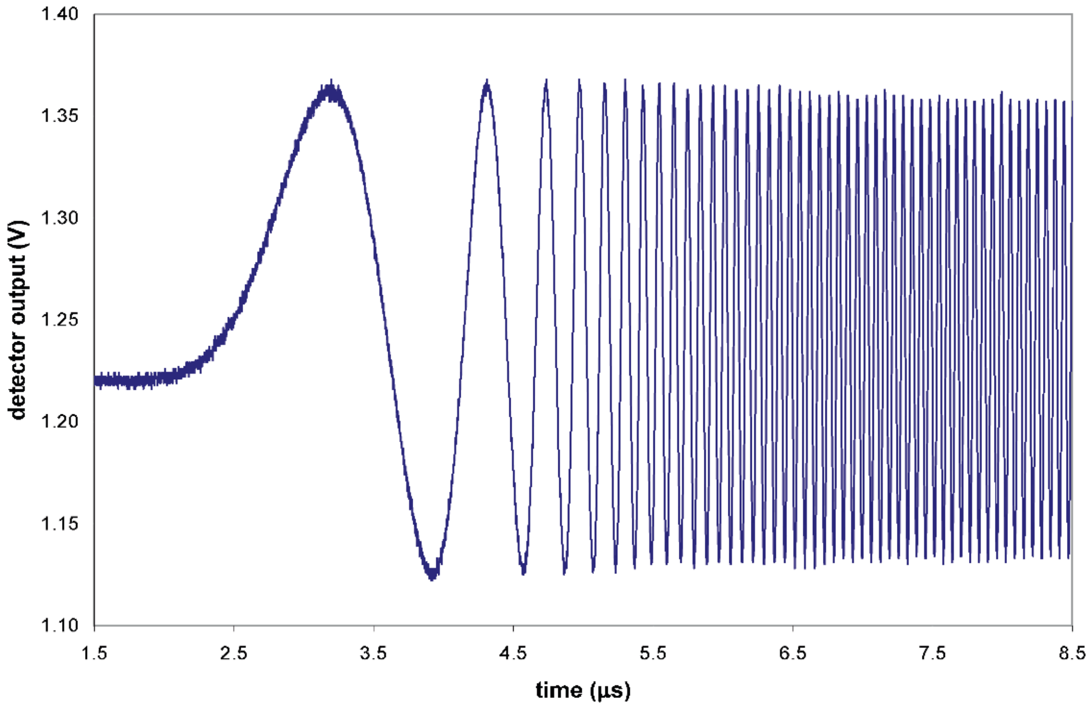

Figure 3 - Photodetector output from an NDI measuring the free-surface motion of the transmitter bar.

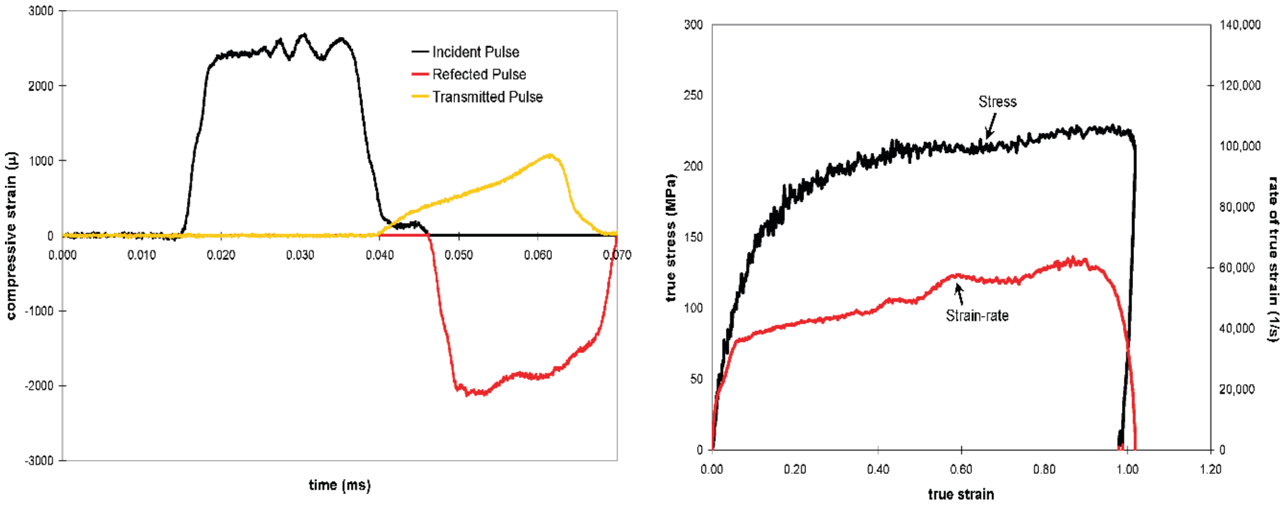

(a) (b)

Figure 4 - (a) Strain signals from an experiment with a 1.59 mm SHPB, and (b) the resulting stress-strain curve (black) and strain-rate (red).

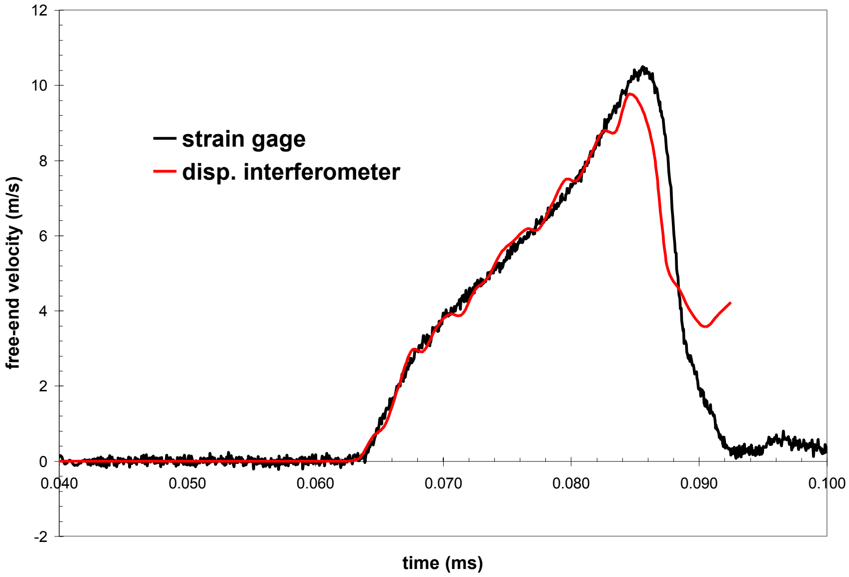

Figure 5 - The particle velocity due the transmitted pulse measured by the strain gage (black) and the NDI (red).

INCIDENT BAR – TDI MEASUREMENTS OF THE INCIDENT AND REFLECTED PULSES

Since no free-end of the incident bar is available during a Kolsky bar test, another NDI cannot be readily used. As an alternative, a TDI measurement near the midpoint of the bar (i.e., traditional strain gage location) allows the measurement of the bar displacement due to the incident and reflected pulses. Differentiation of the displacement over time leads to the particle velocity due to these pulses, v_i and v_r, respectively. These quantities are related to the traditional strain measurements by

$$v_i = \varepsilon_i c_0 \tag{11}$$

$$v_r = -\varepsilon_r c_0 \tag{12}$$

where v_i and v_r are positive for “down-range” motions of the bar. These equations can be then used in eqns. (1) and (3) to calculate the force and motion at the specimen/incident bar interface. The TDI is formed by combining two beams diffracted off a grating. Figure 6 shows the basic optical setup.

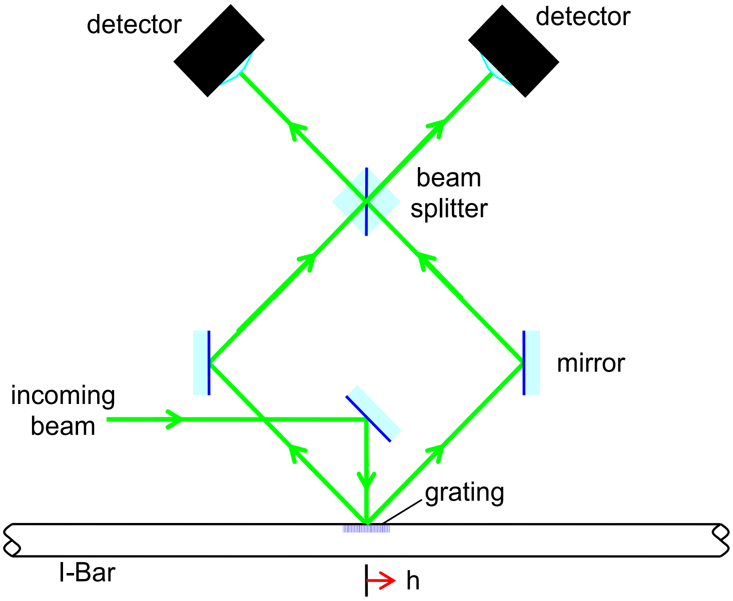

Figure 6 - An incident bar with a TDI.

Motion of the incident bar (in the direction along the axis of the bar) equal to half of the line spacing of the grating will produce a 2π phase variation in the signal, or one fringe. The distance, h, that the grating on the incident bar travels is given by

$$h = \frac{p}{2} n , \qquad (13)$$

where p is the line spacing of the grating and n is the number of fringes. More details about the TDI can be found in [16].

To demonstrate the use of the TDI, a simple bar impact experiment was performed. An aluminum striker bar (15.2 mm long, 1.59 mm diameter) impacts the steel incident bar described above (47.6 mm long). There is no specimen or transmitter bar in this experiment, i.e., the end of the bar is free. For this preliminary investigation, a ~300 micron wide flat was polished onto the side of the incident bar. The grating was then machined directly into the bar with a Focused Ion Beam (FIB) at an accelerating voltage of 30kV and a beam current of 1nA. Figure 7 shows SEM images of the grating. The line spacing is 1.6 μm, and each individual line is 0.5 μm wide and 0.5 μm deep. The removed material is minimal and the grating has essentially no effect on the wave propagation in the bar. Note that the flat extends the entire length of the bar, so that the entire bar has a uniform impedance. A 5W Nd:YVO_4 Coherent VERDI laser, with a 532nm wavelength, and Thorlabs PDA10A silicon amplified detectors, with 150 MHz bandwidths, were used in the optical setup of the TDI. The grating was located 20 mm from the free-end. Therefore two square pulses with durations of 6.0 μs were expected, separated by 2.1 μs.

Figure 8 shows the particle velocity measured by the TDI, along with the TDI trace signal used in its calculation. The square profiles due to the incident pulse and its reflection can be clearly seen, along with the familiar Pochhammer-Chree oscillations that arise due to dispersion. Note that this experiment required the use of rather large polycarbonate sabots on the projectile to fit a 3.85 mm bore gun. The effect of these sabots leads to further deviations from the expected incident pulse.

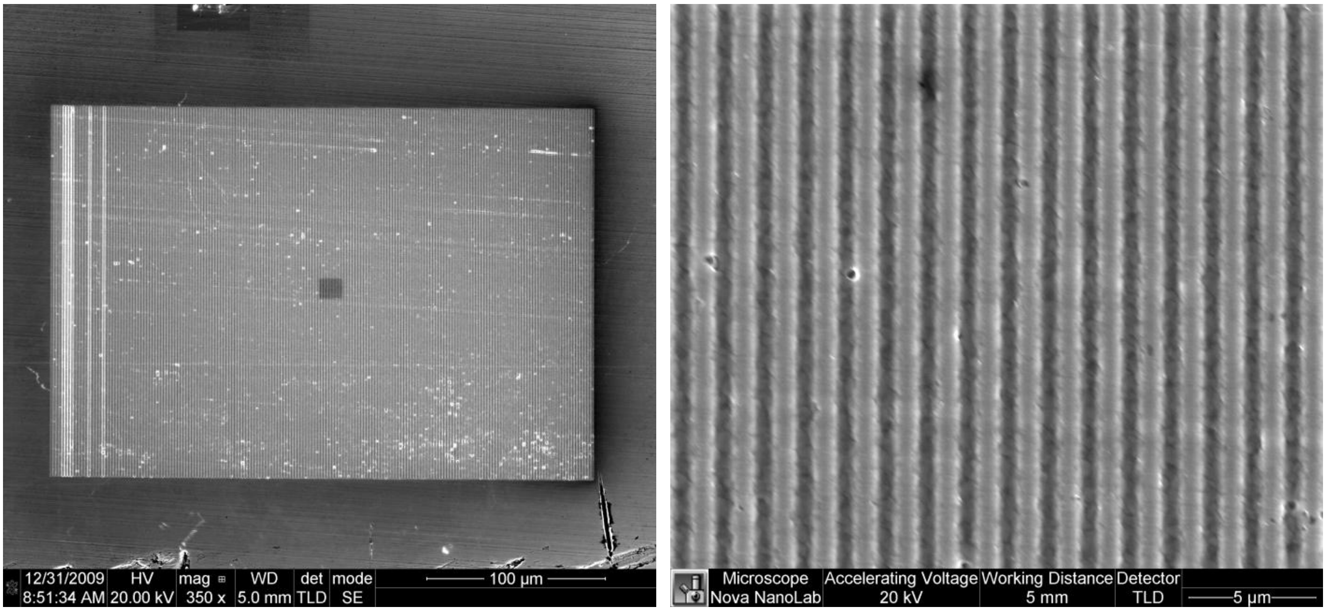

(a)

(b)

Figure 7 - SEM images of the grating used for the TDI. (a) A view of the entire grating area, and (b) a close up of the individual lines.

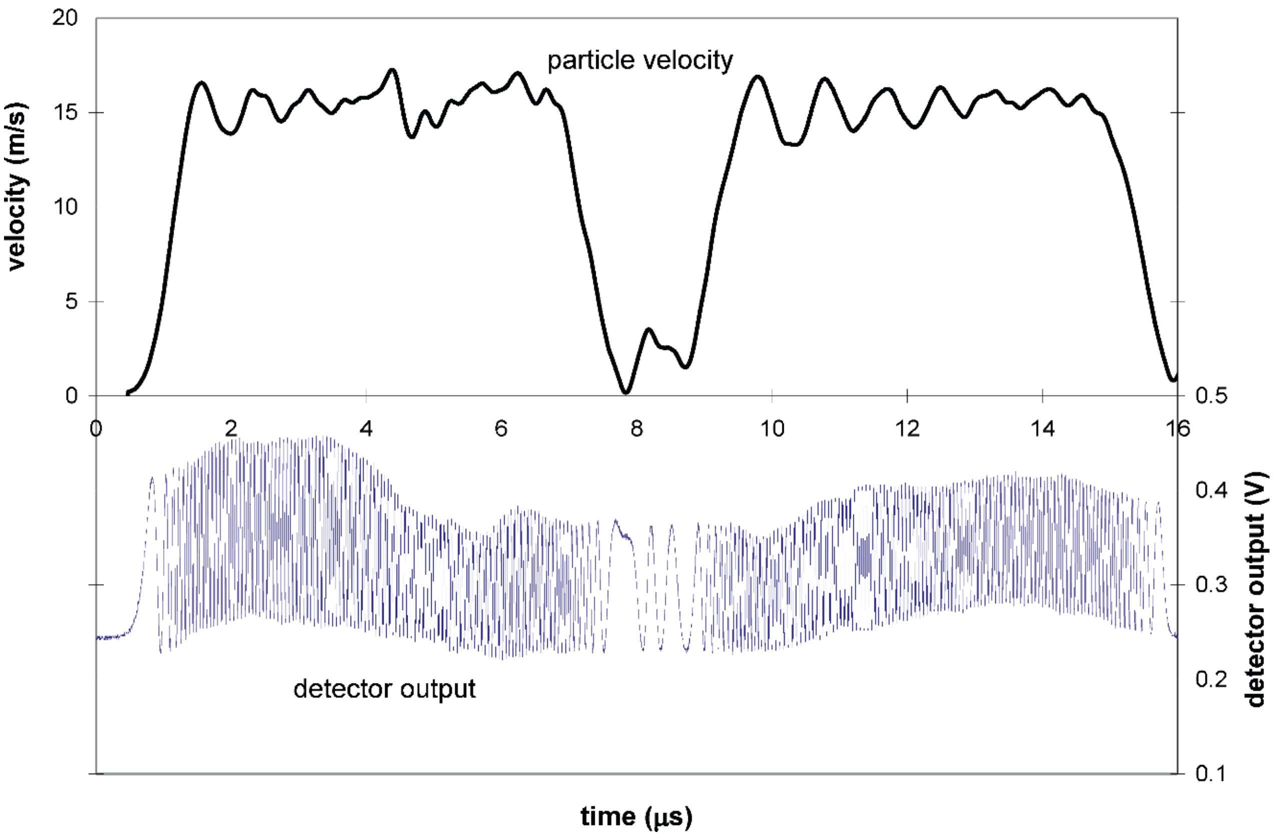

Figure 8 - Particle velocity at the grating as measured by the TDI. The detector output is also shown.

DISCUSSION AND CONCLUSION

This preliminary investigation has shown that optical techniques (NDI and TDI) can be used to replace strain gages as a means to measure the necessary pulses for a Kolsky bar analysis. These techniques have been applied to 1.59 mm diameter bars. Although this was shown in two separate examples, both methods can easily be applied simultaneously. A more rigorous investigation is underway to further validate the data acquired with these techniques.

As a practical matter, the use of standard strain gage techniques is limited to bar diameters of ~ 1.5 mm or greater. However, the use of these optical techniques can permit further miniaturization. Although additional complications due to bar manufacturing, alignment, and specimen preparation may arise, it is expected that the current instrumentation should be sufficient for application to bars as small as 0.4 mm diameter. This would permit testing of specimens as small as 100 μm at rates as high as 500k/s.

As a final note, consideration has been given to the application of these methods to various direct impact configurations, which also use pressure bars to measure specimen response. However, the Kolsky bar method is superior for in several respects given that it provides a more direct verification of specimen equilibrium, simplifies specimen recovery, and also permits the use of pulse shapers. For these reasons, future work will emphasize the Kolsky bar method.

REFERENCES

[1] Kolsky, H., Proc. Phys. Soc. B, 62, pp. 676-700, 1949.

[2] Follansbee, P.S., “The Hopkinson Bar,” Metals Handbook, 8 (9), American Society for Metals, Metals Park, OH, p. 198-217, 1985.

[3] Gorham, D.A., “A Numerical Method for the Correction of Dispersion in Pressure Bar Signals,” J. Phys. E:Sci. Instrum., 16, pp. 477-479, 1983

[4] Follansbee, P.S., Franz, C., “Wave Propagation in the Split-Hopkinson Pressure Bar”, J. Eng. Mat. Tech., 105, p. 61, 1983.

[5] Gong, J.C., Malvern, L.E., Jenkins, D.A., "Dispersion Investigation in the Split-Hopkinson Pressure Bar,” J. Eng. Mat. Tech., 112, pp. 309-314, 1990.

[6] Davies, E.D., Hunter, S.C., “The Dynamic Compression Testing of Solids by the Method of the Split-Hopkinson Pressure Bar,” J. Mech. Phys. Solids, 11, p. 155, 1963.

[7] Ames, R.G., “Limitations of the Hopkinson Pressure Bar for High-Frequency Measurements,” in Shock Compression of Condenser Matter, 2005 (M.D. Furnish, M. Elert, T.P. Russell, C.T. White, eds.) pp.1233-1237.

[8] Casem, D.T., “A Small Diameter Kolsky bar for High-rate Compression,” Proc. of the 2009 SEM Annual Conference and Exposition on Experimental and Applied Mechanics, Albuquerque, NM, June 1-4, 2009.

[9] Gorham, D.A., “Measurements of Stress-Strain Properties of Strong Metals at Very High Rates of Strain,” In: Proc. Conf. on Mech. Prop. at High Rates of Strain, conf. no. 47, Oxford, March 16, 1979.

[10] Gorham, D. A., Pope, P.H., Field, J.E., “An Improved Method for Compressive Stress-Strain Measurements at Very High Strain-Rates,” Proc. R. Soc. Lond. A, 438, pp. 153-170, 1992.

[11] Safford N.A., “Materials testing up to 10^5/s using a Miniaturized Hopkinson Bar with Dispersion Corrections,” In: Proc. 2nd Intl. Symp. on Intense Dynamic Loading and its Effects, Sichuan University Press, Chengdu, China, p. 378, 1992.

[12] Kamler, F., Niessen, P., Pick, R.J., “Measurement of the Behavior of High Purity Copper at Very High Rates of Strain,” Canadian Journal of Physics, 73, 295-303, 1995.

[13] Jia, D., Ramesh, K.T., “A Rigorous Assessment of the Benefits of Miniaturization in the Kolsky Bar System”, Experimental Mechanics, 44, pp. 445-454, 2004.

[14] Malinowski, J.Z., Klepaczko, J.R., Kowalewski, Z.L., “Miniaturized Compression Test at Very High Strain Rates by Direct Impact,” Experimental Mechanics, 2007, 47, p 451-463.

[15] Clifton, R.J., Klopp, R.W., “Pressure-Shear Plate Impact Testing,” Metals Handbook, 8 (9), American Society for Metals, Metals Park, OH, p. 230-239, 1985.

[16] Kim, K.S., Clifton, R.J., and Kumar, P., “Combined Normal-Displacement and Transverse-Displacement Interferometer with an Application to Impact of y-cut Quartz,” J. App. Phys., 48(10), pp. 4132-4139, 1977.

Proceedings of the SEM Annual Conference
June 7-10, 2010 Indianapolis, Indiana USA
©2010 Society for Experimental Mechanics Inc.

A Kolsky Bar with a Hollow Incident Tube

O. Guzman[1], D.J. Frew[2], W. Chen[3]

[1]Graduate Student, Purdue University, West Lafayette IN 47906 oguzman@purdue.edu

[2] Dynamic Systems and Research, Albuquerque, NM

[3]Professor, Purdue University, West Lafayette IN 47906

ABSTRACT This paper presents a novel dynamic experimental technique by modifying a Kolsky tension bar. Pulse shaping has been developed in Kolsky compression bars in order to subject the specimen to the desired dynamic testing conditions. Pulse shaping methods in Kolsky tension bars are not as mature as compression techniques. Developing an apparatus that can utilize the better-understood compression pulse shaping methods is then advantageous. A modified Kolsky tension bar where a hollow incident tube is used to carry the incident stress waves has been developed. The incident tube also acts as a gas gun barrel that houses the striker for impact. The striker impacts on the end of the incident tube through compression pulse shapers that are attached to the end cap. In order to accommodate free travel of the striker pressure-release slots are added to the tube. The effect of discontinuities on a stress pulse and impedance mismatches are discussed. Preliminary data will be shown for the elastic region of a 4140 steel sample.

Introduction

The Kolsky bar, also known as the Split Hopkinson Pressure Bar (SHPB), was originally developed by Kolsky [1] in 1949. The Kolsky bar is commonly used to investigate material behavior in the dynamic region for compression, tension, shear and torsion testing. Material behavior can be attained using the Kolsky bar for strain rates of 10^2-10^4 s^{-1}. The compression bar technique is well understood in terms of loading the specimen at a desired strain rate and in dynamic equilibrium using pulse shaping. Analytical methods for pulse shaping in compression were expanded and coded by Frew et al.; his work subsequently increased the ability to predict incident waveforms [2]. Pulse shaping in tension has generally been determined by experimental method in order to reach dynamic equilibrium. Chen et al. successfully used polymer disks to test polymer samples in tension [3]. Tension testing in Kolsky bars has matured slowly due to the constraints with interfaces between the incident and transmission bar, the uncertainty of gage dimensions on tensile specimens, and an open loop system for pulse shaping.

The Kolsky tension bar has gone through several different modifications and designs over the years. Harding et al. tested steel in tension by applying a compression pulse to a hollow weight bar. This compressive pulse then reflected off the free end of a yoke that was connected to the specimen and an inertia bar causing the specimen to undergo tension [4]. Hauser then modified Harding's design by simplifying the loading method [5]. In 1968, Lindholm et al. designed a different configuration by using a solid incident bar and a hollow transmission tube combined with a "hat" shaped specimen. The hat specimen was sandwiched between the bar and the tube, and a thin gage section would undergo a tensile wave [6]. Nicholas used a typical compression setup, but threaded the specimen on the incident and transmission bar with a collar over the specimen. A compressive wave would pass through the collar, not affecting the threaded specimen, and then reflect off the free-end of the transmission bar in tension [7]. Kwata et al. loaded the specimen by using an impact hammer on the input end of the bar [8].

T. Proulx (ed.), *Dynamic Behavior of Materials, Volume 1*, Conference Proceedings of the Society for Experimental Mechanics Series, DOI 10.1007/978-1-4419-8228-5_71, © The Society for Experimental Mechanics, Inc. 2011

Kwata's experimentation method was improved later on by other groups by using a striker to apply the impact and using a long incident bar after the impact end [13 14]. Ogawa's method loaded the incident bar by impacting a flange on the incident end, while using a hollow striker. Ogawa's design was used to investigate the dynamic hysteresis loop response of iron [9]. Staab et al. used a similar design as Ogawa, but used a clamp setup to load the specimen [10]. The principle behind the Kolsky tension bar has been generalized by Gray [11].

This experimental setup will use a traditional impact condition that occurs in a compression bar by loading the system with a solid striker. The impact condition allows a cylindrical pulse shaper to be used during testing where proven analytical models exist. The impact generates an incident tension wave, which travels through the gun barrel as it would in an incident bar, passes through a set of adaptors, and eventually into the specimen.

Experimental technique

Design characteristics

The experiments were conducted by using both an incident and transmission tube. Adaptors were used to attach the specimen to both the incident and transmission ends. The incident tube also had a hardened end cap attached to the impact end to transfer the load from the cap to the incident tube. An overview of the system is shown in Figure 1, a detailed view of the impact end is shown in Figure 2.

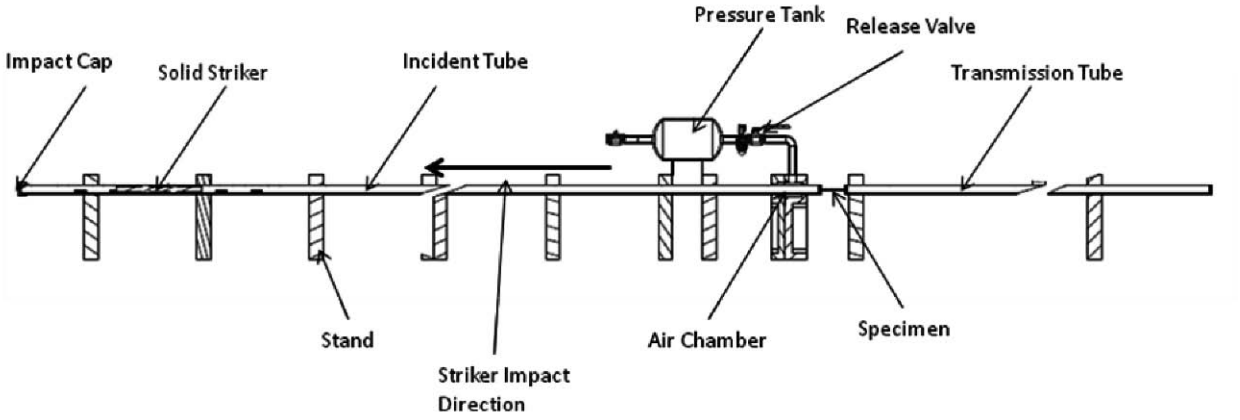
Pressure Tank
Release Valve
Impact Cap
Solid Striker
Incident Tube
Transmission Tube
Stand
Striker Impact Direction
Air Chamber
Specimen

Fig. 1. Schematic of the system

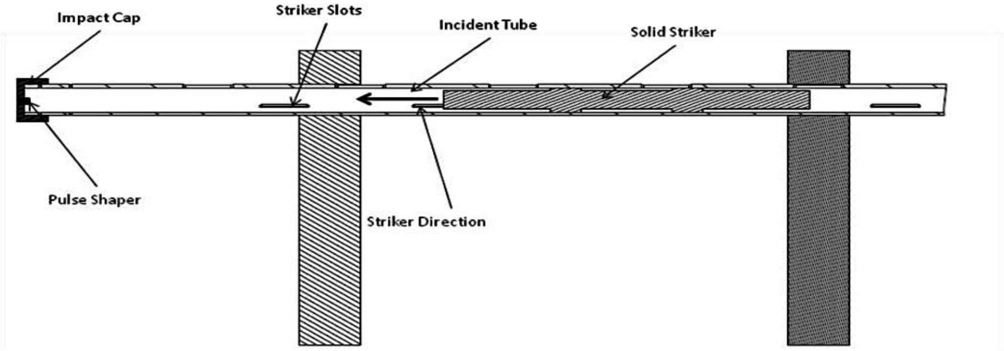
Impact Cap
Striker Slots
Incident Tube
Solid Striker
Pulse Shaper
Striker Direction

Fig. 2. Detailed view of impact end

The pressure system for this design differs from other setups because the pressure is transferred in the radial direction in the incident tube. Three slots of an appropriate dimension were machined on specimen end of the incident tube to allow the pressure to push the striker. Compressed air was used to propel the solid striker to the impact end. Slots of equivalent cross sectional area were chosen instead of holes so that the incident wave traveling through the incident tube would have minimal distortion on the wave propagation. Slot dimensions on the pressure input side were determined by equating a minimal area that would avoid choked flow. The specimen is held in place with a pair of adaptors that are attached to the inner diameter of the incident and transmission tube by using fine threads. Brass bushings that are clamped on by stands are used to support the incident and transmission tubes. The incident tube rides on a pair of O-rings in order to maintain air pressure in the compressed air chamber during operation. These O-rings were subsequently removed in order to determine the cause of issues that will be discussed in the later part of this paper. The impact end has a cap that is threaded onto the outer diameter of the incident tube. The striker impacts the cap and causes a tensile wave to travel through the incident tube.

The incident tube has an outer diameter of 3.175-cm, an inner diameter of 2.54-cm, and a length of 2.438-m. Cross-sectional areas were matched between the incident, transmission tubes, and the solid striker. The incident and transmission tubes were machined using a gun-drilling process and the outer diameter was turned to the appropriate dimension. All of the parts were machined out of A2 grade tool steel in order to accommodate a stable heat-treating process. Both the specimen adaptors and the impact cap were heat-treated to a hardness of 48Rc in an argon atmosphere so minimal oxidation would occur during the heat-treat process. The specimen dimensions are a 1.27-cm gage diameter and an open (not threaded) gage length of 1.016-cm. The specimen was a 4140 steel sample with a harness of 48Rc +/- 1Rc.

During experimentation the position of the incident tube pressure hole became a concern due to the effect the hole may have on the reflected wave. In order to circumvent this issue, a tube of equivalent cross-sectional area was attached to the current setup. An adaptor of sufficient stiffness was used to attach both tubes, and resistor strain gages were placed at the midpoint of the tube. The adaptor had a length of 1.21-m.

Data acquisition system and reduction

Resistor strain gages (1000-ohm) were used on the incident tube in pairs, and were then connected to a Wheatstone bridge in a way to remove bending waves during loading. The Wheatstone bridge is then connected to a pre-amplifier that transfers data to a Tektronix® digital oscilloscope. The transmission tube has a both a pair of resistor strain gages and semi conductor strain gages for low amplitude waves. The semi-conductor strain gages were calibrated by connecting the incident and transmission bar and viewing the difference between the resistor and semi conductor strain gage measurements on the transmission side. The resistor strain gages were placed in the middle of the incident tube so that both the incident and reflected wave could be accurately picked up in the oscilloscope without overlap. Both the resistor and semi-conductor strain gages were placed as close to the specimen on the transmission side because only the initial transmission pulse is used for data reduction.

Data reduction in the Kolsky tension bar is similar to data reduction in a compression bar. It assumes homogeneous elastic deformation in an impedance-matched incident and transmission tubes [11]. Assuming these conditions the strain rate can be determined by using just the reflected wave in Equation (1).

$$\dot{\varepsilon}(t) = -\frac{2c_o}{L}\varepsilon_R(t) \qquad (1)$$

where L is the original length of the specimen, $\varepsilon_R(t)$ is the time varying reflected strain, and c_o is the speed of sound within the incident tube. The speed of sound is defined as the squared root of the ratio of the Young’s Modulus and the density of the material in Equation (2). For A2 tool steel the Young’s modulus is 213-GPa, the density is 7870-kg/m^{3,} and the speed of sound is 5200-m/s. Using the same dynamic equilibrium assumptions the stress in the specimen can be computed by using just the transmitted wave as shown in Equation (3).

$$c_o = \sqrt{\frac{E_o}{\rho_o}} \tag{2}$$

$$\sigma(t) = \frac{A_o E_o}{A} \varepsilon_{\tau}(t) \tag{3}$$

Where E_o is the Young’s Modulus, A_o is the cross-sectional area, and $\varepsilon_T(t)$ is the time varied transmitted strain within the transmitted tube, and A is the cross-sectional area in the specimen. The strain within the specimen can be described by the integral of the time varying reflected strain Equation (4).

$$\varepsilon(t) = -\frac{2c_o}{L}\int_0^{\tau} \varepsilon_R(t)\,d\tau \tag{4}$$

Using these assumptions strain and stress history can be computed within the specimen.

Experimental results

Experiments were conducted with two different bar configurations, one with the adaptors attached directly to the incident tube, and the other with the 1.21-m incident tube appendage attached to the original setup. The appendage was used to bypass the effect of the pressure slots during loading and unloading.

The mismatch was determined to be caused by the specimen adaptors that were attached to the end of the incident and transmission tubes. Tests were run with both .610-m and .305-m long A2 strikers. Rise times in the loading period in both cases were 50-µs, which is higher than the typical ~20-µs [14]. This can be attributed to possible deformation in the threads on the impact cap end during initial loading. Figure 3 shows a typical experimental record from using the adaptor connected directly to the incident tube, and Figure 4 shows a record with the appendage attached. The data in Figure 3 shows a mismatch in terms of both amplitude and waveform of the incident and reflected pulses. Figure 4 also shows a slightly lower mismatch, but when the waveforms are plotted against each other the initial loading period matches quite closely as shown in Figure 5.

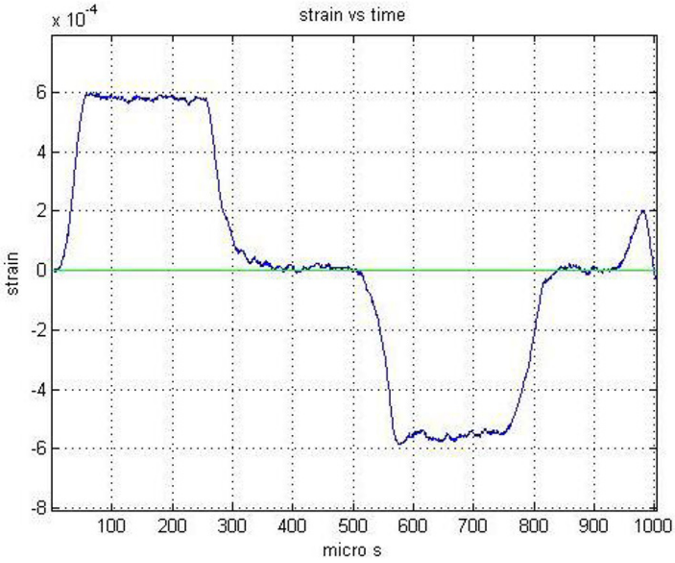

Fig. 3. Incident tube data for a .610-m striker without incident tube appendage

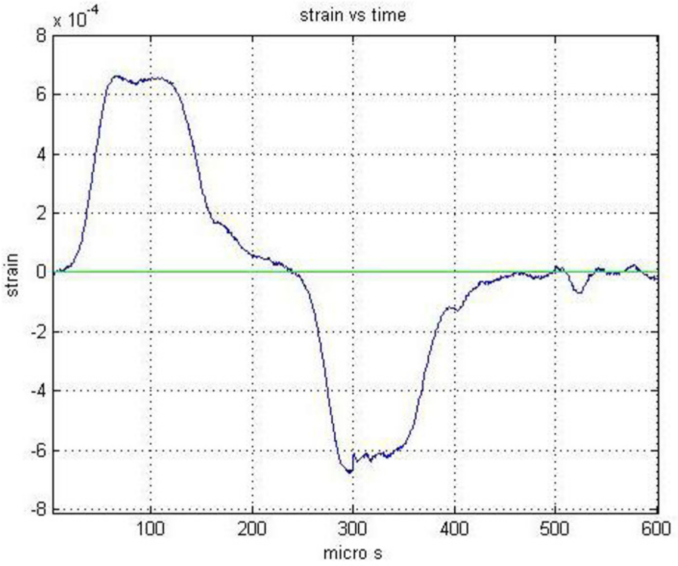

Fig. 4. Incident tube data for a .305-m striker with incident tube appendage

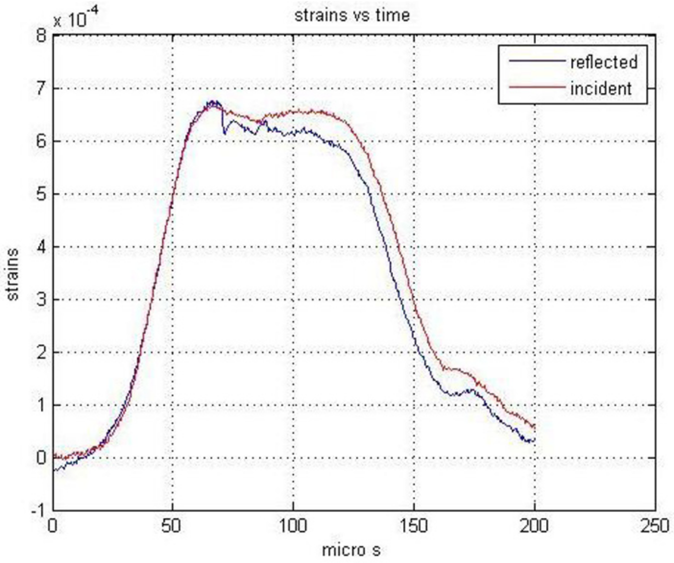

Fig. 5. Wave matching for a .305-m striker with incident tube appendage

Figure 5 still shows an amplitude mismatch after the initial loading period in the reflected wave. The free end in this experiment had no adaptor attached. The only reason the waves should have not matched exactly would be due to a lower cross-sectional area on the free end because of threading. The adaptor/clamp effect has been observed previously, which has been documented by Nie et al. during the testing of soft materials in a tension setup [12]. Nie tested various clamp sizes in order to determine which clamp would have a minimal affect on the 1-D wave propagation. Nie approached the problem in two ways, by decreasing the clamp mass, and using pulse shaping to lower the clamp effects [12]. In this set of experiments pulse shaping was used as a viable solution and a redesign to the incident and transmission tube are being considered before presentation at the conference. 4140 Steel specimens were tested in the elastic region to determine how both the reflected and transmitted waves would react to the large adaptor size. Matched waveforms of the steel specimens are shown in Figure 6.

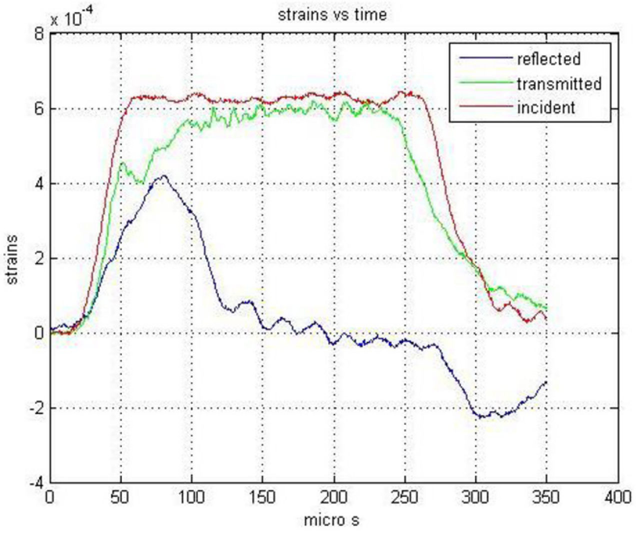

Fig. 6. Wave matching for a .610-m striker without incident tube appendage

Since the 4140 specimen has a high stiffness, the majority of the incident wave is transferred to the transmission tube. The initial loading period in the transmitted wave has a linear period for the initial 50-μs and then a nonlinear period for the next 50-μs. The initial linear period is due to the elastic loading of the specimen where the next 50-μs could be due to the load transferring over from the specimen to the transmission tube. The reflected pulse has an initial linear increase and then a drop. This period ends at about 120-μs, which is the initial elastic response of the specimen. At about 270-μs a reflection of the elastic response occurs. The wave amplitudes obviously shows that the system is not in dynamic equilibrium, but the elastic response is apparent, refinement of the system will be necessary before stress strain curves of smaller plastically deforming materials can be accurately calculated using Equations 3 and 4. Pulse shaping was also attempted using a thin disk of annealed copper. Pulse shaping had a minimal positive effect to the adaptor mismatch as shown in Figure 7. As expected, pulse shaping removes some of the higher frequency noise during the ramp period, but does little to drastically improve the lack of dynamic equilibrium within the specimen.

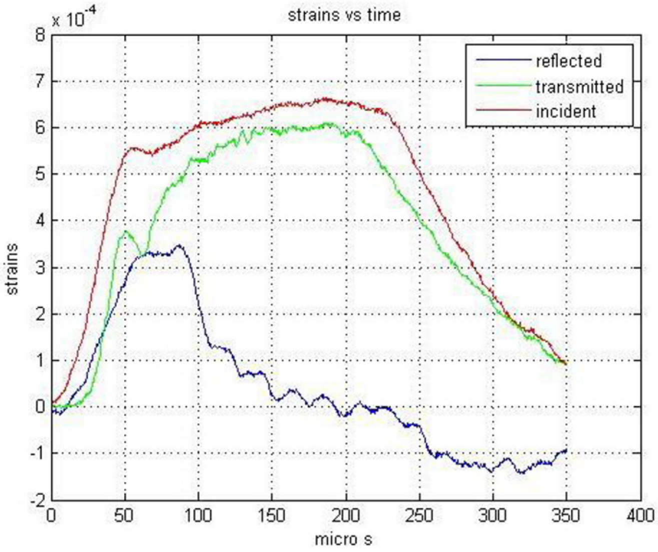

Figure 7. Wave matching for a .610-m striker with pulse shaping

Conclusions

A new Kolsky tension bar was designed and tested using hollow incident and transmission tubes and cylindrical 4140 steel samples. The apparatus applied heritage concepts in tension bars, and facilitated the use of pulse shaping from compression bars directly on the tension bar for testing conditions control. Elastic material behavior was viewed in the reflected wave and the ability to pulse shape by using a compressive technique was shown. Dynamic equilibrium was not able to be obtained with the current setup due to effects of the large specimen adaptors on the incident and transmission ends. Modifications to the design in order to accommodate dynamic equilibrium and material behavior via stress strain curves will be presented in the SEM conference.

References

[1]H. Kolsky, An investigation of the mechanical properties of materials at very high strain rates of loading, Proceedings of the Royal Society of London B62 (1949) 676-700

[2] D.J Frew, M. J. Forrestal and W. Chen, Pulse Shaping Techniques for Testing Elastic-plastic Materials with a Split Hopkinson Pressure Bar, Exp. Mech. V45 No2 (2005) 186-195

[3]W. Chen, F. Lu, and M. Chang, Tension and compression tests of two polymers under quasi-static and dynamic loading, Polymer Testing 21 (2002) 113-121

[4]J. Harding, E. O. Wood and J. D. Campbell, Tensile Testing of Materials at Impact Rates of Strain, Journal of Mechanical Engineering Science 2 (1960) 88-96

[5]F. E. Hauser, Technique for Measuring Stress-strain relation at High Strain Rate. Exp. Mech. 6 (1966) 88-96

[6]U.S. Lindholm and L.M. Yeakley, High Strain rate Testing: Tension and Compression, Exp. Mech. 8 (1968) 1-9

[7]T. Nicholas, Tensile Testing of Materials at High Rates of Strain, Exp. Mech. 21 (1981) 177-188

[8] K. Kwata, K. Hashimoto, S. Kurokawa and N. Kanayama, A New Testing Method for the Characterization of Materials in High-velocity Tension, Mechanical Properties at High Rate of Strain, ed. J. Harding, Inst of Phys. Conf Ser. No. 47, (1979) 71-80

[9]K. Ogawa, Impact-tension Compression Test by Using a Split-Hopkinson Bar, Exp. Mech. 24 (1984) 81-86

[10]G.H. Staab and A. Gilat, A Direct-tension Split Hopkinson Bar for High Strain-rate Testing, Exp. Mech. 31 (1991) 232-235

[11]G. T. Gray, Classic Split Hopkinson Pressure Bar Technique ASM V8 Mechanical Testing (1999) 17-20

[12]X. Nie, B. Song, Y. Ge, W.W. Chen and T. Weerasooriya, Dynamic Tensile Testing of Soft Materials, Exp. Mech. 49 (2009) 451-458

[13]Fu S., Wang Y. and Wang Y., Tension testing of polycarbonate at high strain rates, Polymer Testing 28 (2009) 724-729

[14] M Li, R. Wang and M.-B. Han, A Kolsky Bar: Tension, Tension-tension, Exp. Mech. 33 (1993) 7-14